Digitized Theses — Digitized Special Collections

1994

Analysis Of Initial Stresses, Long Term Deformation And Rock Lining Interaction In Tunnels

Ashraf Mohamed Hefny

Follow this and additional works at: https://ir.lib.uwo.ca/digitizedtheses

Analysis of Initial Stresses,
Long Term Deformation and
Rock Lining Interaction in Tunnels

VOLUME 1

BY

Ashraf Mohamed Hefny

Faculty of Engineering Science

Department of Civil Engineering

Submitted in partial fulfilment
of the requirements for the degree of
Doctor of Philosophy

Faculty of Graduate Studies
The University of Western Ontario
London, Ontario
April 1994

ABSTRACT

For the design of underground structures in rocks, the initial stresses in the rock mass are a pre-requisite for any analysis. The hydraulic fracturing technique is the only practical method for determining these initial stresses at great depth. For vertical fractures, existing solutions for calculation of stresses are satisfactory. For horizontal or mixed-mode fractures, appropriate solutions are required.

Closed-form solutions for horizontal and mixed-mode fractures including strength anisotropy are developed and applied to several case histories. The reinterpreted horizontal stresses agreed with results derived from convergence measurements and they are also consistent with field observations of excavation performance, indicating that the stresses are correct and readily applicable to practice. Stress values obtained using the conventional method in these cases are too low and may lead to unsafe design.

With the initial stresses correctly determined, the stability of tunnels immediately after excavation may be evaluated. For this purpose, Closed-form solutions for the stresses and displacements around unlined circular tunnels in cross-anisotropic rocks such as shales are derived. For convenience of application, design charts are prepared for the determination of stresses and displacements for given values of initial stresses and the elastic parameters.

After the stability conditions during construction are satisfied, the long-term deformation and consequent stress built-up in the lining are important design considerations, so as to ensure that the structural integrity of the lining is not affected. An experimental study is carried out to investigate the characteristics of the time-

dependent deformation of Queenston Shale. The study has shown that Queenston Shale exhibits long-term time-dependent deformation upon stress relief and that the deformation is non-linearly stress dependent. This deformation is represented by a model consisting of three Kelvin units connected in series. The predicted swelling deformations using this model are in good agreement with the measured values in laboratory tests.

Using the theory of viscoelasticity, closed-form solutions for the time-dependent stresses and displacements in the rock mass and the lining of tunnels driven in swelling rocks are derived. A semi-analytical approach is then developed to account for the increase of the values of the moduli of rock as the pressure built-up behind the lining increases with time. It is shown that this solution taking into account stress-dependency of swelling reduces significantly the final stresses and displacements in the lining and the final pressure built-up behind the lining. Therefore, use of the analytical method developed will lead to a more economical design.

ACKNOWLEDGEMENTS

TABLE OF CONTENTS

VOLUME 1

* * *

VOLUME 2

LIST OF TABLES

LIST OF FIGURES

CHAPTER 1

INTRODUCTION

For the design of underground structures in rocks for various purposes, the states of initial stresses in the rock mass are required. For structures located at great depths, the hydraulic fracturing test for stress measurements is the only practical method.

For vertical fractures, the conventional theory for calculation of stresses from test results is satisfactory and often used in practice. For mixed-mode fractures (combination of horizontal and vertical fractures), the conventional theory for vertical fractures has been used by adopting the arbitrary assumption that the vertical fractures were initiated before the horizontal ones by the first breakdown pressure. This assumption may lead to incorrect results if the horizontal fractures are initiated before the vertical fractures. For horizontal fractures, the only available solution is Ljunggren and Amadei's method. However, this method leads to very high ranges of stresses which are not accurate and cannot be adopted in design. Therefore, for horizontal or mixed-mode fractures, appropriate solutions are required.

It is the objective of the first part of this thesis to develop and check the reliability of a new theory for evaluation of the *in situ* stresses from hydraulic fracturing test results. The method developed deals with different modes of fractures (horizontal and vertical as well as mixed-mode fractures) and takes into account strength anisotropy, where appropriate. The method enables the determination of which fracture (horizontal or vertical) occurs first at the first breakdown pressure during the test, so that appropriate stress calculation may be carried out.

The first part of the thesis consists of four chapters (Chapter 2 to Chapter 5). In Chapter 2, a critical review of the conventional theory and other available theories for the calculation of *in situ* stresses from hydraulic fracturing test results is presented.

The new theory, the Modified Stress Path (MSP) method, is developed in the third chapter. Experimental requirements for the measurements of rock parameters relevant to the specific stress paths in hydraulic fracturing tests are, also, discussed in Chapter 3.

In Chapter 4, the method developed is used to reanalyze three case records and the reinterpreted stresses are compared to those obtained from other methods and from back analysis of field observations of underground structures.

Chapter 5 deals with the evaluation of the initial stresses in Queenston Shale at Sir Adam Beck Niagara Generating Station Number 3 (SABNGS NO. 3) site. Most of the fractures formed in 1984, 1990, and 1992 investigations are either horizontal or mixed-mode fractures. The conventional theory for vertical fractures was used previously to calculate the initial stresses in the site from the mixed-mode fractures by arbitrarily assuming that the vertical fractures were formed before the horizontal fractures at the first breakdown pressures. The method developed (MSP) is used to reinterpret the initial stresses and the results are compared with those previously obtained from the conventional theory and it is shown that the use of the conventional theory for mixed-mode fractures may lead to unsafe design. The method developed is then used to analyze the hydraulic fracturing test results for the 1990 and 1992 investigations. The effect of the strength anisotropy on the solution is discussed.

The estimation of the distribution of stresses and displacements around tunnels is

of crucial importance for the design and construction considerations. Closed-from solutions for the stresses and displacements around tunnels excavated in isotropic elastic rocks are well known. However, for tunnels driven in cross-anisotropic rocks, only the distribution of stresses resulting from loading in one direction is known. The solution for the displacement is not given in tne literature.

Part II of this thesis (Chapter 6) contains the complete derivation of closed-form solutions for both stresses and displacements around circular unlined tunnels driven in cross-anisotropic rocks. The solutions are given as functions of the *in situ* state of stress, the anisotropic strength parameters of the rock, and the dimensions of the tunnel. The effects of the different parameters affecting the solution are investigated. The solutions developed are, then, used to analyze a case history and to show the importance of adopting these correct solutions in case of tunnels driven in cross-anisotropic rocks (such as shales). Design charts for the stresses and displacements around tunnels are also provided in this chapter.

The problem of structural cracking of lining of tunnels under high *in situ* horizontal stress and driven in swelling rocks is well recognized. The release of the *in situ* stress due to excavation works acts as an initiating mechanism for time-dependent deformation to take place. With time, the pressure behind the lining is built-up and finally may lead to distress of the lining. The available closed-form solutions for the tangential stresses in lining are suitable for short-term swelling and for cases where the parameters of the rock are constant with ti.... .

For the proposed SABNGS No.3 project, twin diversion tunnels will be excavated deep in Queenston Shale. Experiments on Queenston Shale have shown that its time-

dependent swelling upon stress relief continues for a very long period of time and that the swelling is nonlinearly dependent on the stress applied. It is the objective of part III (Chapter 7 to Chapter 11) of the thesis to study and model the swelling behaviour of Queenston Shale.

In Chapter 7, the previous time-dependent deformation studies performed on Queenston Shale are reviewed. The results of the experimental study carried out during the course of this thesis are outlined. The mechanism of swelling of Queenston Shale is also discussed. Experiments devoted to study the effect of load-water sequence on the swelling behaviour of Queenston Shale and the mechanism of swelling are presented.

Modelling of the long-term time-dependent deformation of Queenston Shale is discussed in Chapter 8. The nonlinear relationship describing the change of deformation parameters of the rock with the level of stress applied is derived. Comparisons between the predicted and measured swelling strains of Queenston Shale samples under different applied pressures are presented.

In Chapter 9, the theory of linear viscoelasticity is used to derive closed-form solutions for the stresses and displacements around unlined tunnels driven in swelling rocks idealized by a generalized 7-element Kelvin model (a spring and 3 Kelvin units connected in series).

The closed-form solutions derived for unlined tunnels are extended to include the case of time-rock-lining interaction in Chapter 10. In the solutions, both the rock and the lining posses time-dependent deformation properties. The time elapsed between the excavation of tunnel and the installation of lining is also considered in the solutions.

In Chapter 11, a semi-analytical solution (nonlinear pressure step-wise approach)

is introduced to account for the change of the values of deformation parameters of rock as the reactive pressure behind the lining increases with time. The method developed is then used to evaluate the stresses and displacements in the rock and lining for the proposed twin tunnels for SABNGS No.3 project. The effects of the different parameters on the obtained solutions are also studied.

Finally, based on the results and conclusions obtained from each part of the thesis, a summary and general conclusions are provided in Chapter 12.

PART I

EVALUATION OF INITIAL STATE OF STRESS
IN THE GROUND USING
THE HYDRAULIC FRACTURING TECHNIQUE

(Chapter 2-5 inclusive)

CHAPTER 2

REVIEW OF METHODS OF ESTIMATION OF

INITIAL STATE OF STRESS IN THE GROUND USING

HYDRAULIC FRACTURING TECHNIQUE

2.1 INTRODUCTION

For the rational design of underground structures in rocks for various purposes, the magnitudes and directions of the initial stresses in the rock mass must be known. While there are several methods available for *in situ* measurements of stresses, the only practical technique for determination of stresses at great depths is the hydraulic fracturing method. In tests where the fractures are clearly vertical, the current method of interpretation (Hubbert and Willis 1957; Haimson and Fairhurst 1969) applies, and the results obtained are usually unambiguous and reliable. For cases where the fractures are horizontal or inclined or mixed mode (combination of horizontal and vertical), appropriate solutions of the problem are required.

In the following sections, the method of hydraulic fracturing test is described and followed by a critical review of the available methods of estimating the initial state of stress in the ground.

2.2 METHOD OF HYDRAULIC FRACTURING TEST

The test procedure is described in "Suggested Method for Rock Stress Determination," published by the International Society for Rock Mechanics (Kim and Franklin 1987), and in the published works of Haimson who has made important

7

progress in the development of the hydrofracturing technique (see e.g. Haimson 1978a). For convenience of relating the test procedure to the available methods of initial stress calculation presented subsequently and to the theoretical development of the solutions presented in the next chapter, the test method is described.

The first step is to select the depths in the borehole. The choice of the test zones is made based on the fracture characteristics of recovered cores or on inspection of the drillhole wall by an optical or acoustic logging tool. Zones that appear to be free of fractures are usually chosen for hydrofracturing stress measurements. This implies that the stress condition on the walls of the test hole should not exceed the stress condition at failure, by a selected failure criterion.

The next step is to insert a borehole device consisting of two inflatable packers, with a straddled interval as illustrated in Figure 2.1. The pressure in the straddled interval is increased by pumping water at a constant flow rate until a critical value P_{c1}, the breakdown pressure (Fracture Initiation Pressure, Figure 2.2), is reached and a fracture occurs. After maintaining the pumping for a short time to extend the fracture beyond the borehole zone influence (about three times the borehole diameter), the injection is stopped and the hydraulic system is sealed or "shut-in", yielding the shut-in pressure, P_s. The pressurization cycle is repeated several times to obtain the fracture reopening pressure, P_{c2}, and additional measurements of the shut-in pressure.

The last step is to obtain the inclination and the direction of the induced hydrofractures at the borehole wall. This is performed with the use of an impression packer and a magnetic orienting instrument, Figure 2.1.

2.3 CONVENTIONAL METHOD (MAXIMUM TENSILE STRESS METHOD) FOR INITIAL STRESS CALCULATIONS

In this method, the vertical *in situ* stress is considered to be one of the principal stresses in the ground, and the fracture is assumed to develop perpendicular to the least horizontal principal stress. The stress distribution around the borehole is given by the Kirsch solution for stress distribution around a circular hole (see e.g. Obert and Duvall 1967) in an infinite, linearly elastic, homogeneous, unfractured, isotropic medium loaded at infinity. The minimum tangential stress at the perimeter of the hole is

$$\sigma_{\theta min} = 3\sigma_h - \sigma_H \qquad (2.1)$$

where σ_h = the minimum horizontal *in situ* stress

σ_H = the maximum horizontal *in situ* stress

For a hole with an internal pressure P_i, the value of the minimum tangential stress is

$$\sigma_{\theta min} = 3\sigma_h - \sigma_H - P_i \qquad (2.2)$$

As the internal pressure is increased, the minimum tangential stress is reduced, finally to a value of the tensile strength of the rock (T). The injection pressure at this stage is P_{ci}, the breakdown pressure (fracture initiation pressure, Figure 2.2). Therefore, the condition for formation of the vertical fracture is

$$3\sigma_h - \sigma_H - P_{ci} = -T \qquad (2.3)$$

The fracture once formed will continue to propagate as long as the internal pressure is greater than the stress normal to the plane of the fracture. When pumping

is stopped, the internal pressure decreases (Figure 2.2). The recorded value of shut-in pressure, P_s, is the value for the closing of the fracture, and is assumed equal to σ_h, giving

$$\sigma_h = P_s \qquad (2.4)$$

Substitution for σ_h in Eq. 2.3 leads to

$$\sigma_H = 3P_s - P_{cl} + T \qquad (2.5)$$

Equations 2.4 and 2.5 are commonly used to determine the minimum and the maximum horizontal stresses respectively. In these equations, P_s and P_{cl} are measured directly at the test zone (i.e. they represent the total pressure at the test zone). If the values of P_s and P_{cl} are recorded at the ground surface, the value of P_H, the head pressure at the depth of the test, should be added to P_s and P_{cl} values. Therefore, Eqs. 2.4 and 2.5 become, respectively,

$$\sigma_h = P_s + P_H \qquad (2.6)$$

and

$$\sigma_H = 3P_s - P_{cl} + T + 2P_H \qquad (2.7)$$

The tensile strength, T, may be obtained by considering the fracture reopening pressure, P_{c2} (Figure 2.2), of the second cycle (Bredehoeft et al. 1976) in Eq. 2.3 using P_{c2} in place of P_{cl} and putting $T=0$

(c)   The results of stresses computed by the MSP method agree closely with those

determined by the USBM method as reported by Lo and Lukajic (1984) (see

Figure 4.2 for USBM result, Test OH2-3).

Sample calculations for the MSP method are shown in Appendix 4A, using results

of Test UN1-3 with mixed-mode fractures. The calculated stress paths are shown in

Figure 4.4. It is clear from Figure 4.4 that only stress path II reaches the failure

envelope Therefore, the vertical fracture occurs first in the mixed-mode fractures and

the stresses may be calculated accordingly by equations corresponding to stress path II

in Table 2.1.

From Tables 4.1 and 4.2, it may be observed that for shallow depths both the

effective stress principle and total stress principle yields almost the same results which

are in agreement with the USBM results. This occurs because for shallow depths the

pore water pressure represents only a small fraction of the calculated stresses. On the

other hand, for deep depths, the maximum horizontal stresses are higher than those

calculated using the effective stress principle. The USBM method was not conducted at

these deep locations. This emphasizes the importance of deciding which equations should

be used in estimating the *in situ* horizontal stresses.

4.3   CASE HISTORY 2 - *IN SITU* STRESS AT LAVIA IN FINLAND

In 1985, hydraulic fracturing stress measurements were conducted down to a

depth of 500 m in a vertical borehole in Precambrian Granodiorite at Lavia in Finland

(Ljunggren and Amadi 1989). Vertical fractures were found in only seven tests of 23

tests performed. The majority of the tests showed horizontal or subhorizontal fractures.

rocks such as granite. There is, however, a slight inconsistency in applying the principle of effective stress in Eq. 2.11. The theory of fracture so far has been derived consistently by consideration of total stresses in σ_H, σ_h, $\sigma_{\theta min}$ and P_i. If effective stress principle is invoked for the solution of the problem, then the effect of transient flow under pressure P_i on the stress distribution around the borehole should be considered and tensile strength determined in terms of effective stress. It should be noted that hydrofracturing tests are usually completed within a few minutes and the effect of transient flow in impermeable (intact) rock is negligible. For consistency, Eq. 2.5 should be used in the analysis of vertical fractures in hydraulic fracturing tests.

It should be noted that the use of Eq. 2.11 for many rocks at shallow depths resulted in σ_H magnitudes consistent with those determined by other techniques (see e.g. Lo 1981). However, because these depths are shallow, the pore pressure is a small fraction of the calculated stress and the use of either Eq. 2.11 or Eq. 2.5 would lead to the same conclusion.

Schmitt and Zoback (1989) suggested the following equation for the calculation of σ_H:

$$P_{cl} = 3\sigma_h - \sigma_H + T - \beta P_o \qquad (2.13)$$

where β ranges between 0 and unity. When $\beta = 0$, Eq 2.13 is the same as Eq. 2.3 and it is suitable for nonporous rocks. In the case of $\beta = 1$, Eq. 2.13 is the same as Eq. 2.11 and it is suitable for porous rocks which are impermeable to the injected fluid. Because of the difficulty of estimating the parameter β, Schmitt and Zoback (1989) did not

analyze any actual field data using Eq. 2.13, and this equation has not been used in practice.

2.4 EQUATION FOR POROUS ROCK

Haimson and Fairhurst (1967) suggested the use of the following equation, for maximum horizontal stress determination, for porous rocks into which fracturing fluid infiltrates prior to fracture initiation:

$$P_{ci} = \frac{3\sigma_h - \sigma_H + T - \alpha\frac{1-2v}{1-v}P_o}{2 - \alpha\frac{1-2v}{1-v}} \qquad (2.14)$$

where

v = Poisson's ratio

α = Biot poro-elastic parameter

The value of α ranges between 0 and unity. $\alpha = 0$ for low porosity rocks and $\alpha = 1$ for highly-porous compressible rocks. Due to the difficulty to measure the parameter α, Eq. 2.14 has not been used in practice.

It should be noted that there is inconsistency between Eq. 2.10 and Eq. 2.14. Equation 2.14 becomes the same as Eq. 2.10 when both the denominator and the coefficient of P_o in Eq. 2.14 are equal to unity. This requires that $\alpha = 1$ and $v = 0$ which refers to the case of highly-porous rocks. On the other hand, Eq. 2.10 requires that the rock is impermeable to the fracturing fluid.

Schmitt and Zoback (1989) proposed the following equation to be used when the

fluid infiltrates the rock before fracture initiation:

$$P_{cl} = \frac{3\sigma_h - \sigma_H + T - \alpha\frac{1-2\nu}{1-\nu}P_o}{1+\beta-\alpha\frac{1-2\nu}{1-\nu}}$$

(2.15)

The value of β ranges between 0 and unity. Equation 2.15 has the advantage of the ability to represent Eq. 2.3 when $\alpha = \beta = 0$. The higher the values of α and β are, the more porous is the rock. The authors used Eq. 2.15 to estimate the value of β for Valders limestone from a laboratory hydraulic fracturing experimental data but the value of β increased unexpectedly as the value of α decreased. Schmitt and Zoback did not analyze any actual field hydraulic fracturing data using this method. It seems that the difficulty of determining α and β limited the use of Eq. 2.15 in practice.

2.5 CORNET AND VALETTE'S METHOD

In 1984 Cornet and Valette suggested two methods for initial stress calculations. In these methods the orientation of the fracture is not necessarily perpendicular to that of the minimum principal stress. The first method is based on the measurements of the instantaneous shut-in pressure for fracture planes with various dips and strikes. The second method makes use of both shut-in pressures and reopening pressures for fractures parallel to the borehole axis.

In these methods, the stress field is assumed to vary linearly with depth and the lateral variation of the stress field is ignored. The horizontal stress values at a test location cannot be predicted from only that test data but rather from a large number of

tests conducted at different depths. At least six hydraulic tests are required if both the shut-in pressure and the reopening pressure are measured for each test, while a minimum of 12 hydraulic tests are required if only the shut-in pressure is measured.

Cornet and Valette analyzed hydraulic fracturing test data at two different sites to show the applicability of their technique. At the first test site, Le Mayet de Montagne in France, the stress field was not previously known. Therefore it is not possible to test the reliability of their method from the results of this site. At the second test site, Waterloo (Wisconsin), the results were satisfactory for the minimum horizontal stress, poor for the orientation of horizontal stresses and very poor for the maximum horizontal stress, according to the computed standard deviations.

The disadvantage of Cornet and Valette's method may be summarised as follows. The method makes use of the shut-in pressure and the reopening pressure and ignores the first breakdown pressure, usually, the best well defined quantity in hydraulic fracturing tests. The method requires the assumption of the linearity of the stress field with depth. The lateral variation of stress field is also ignored. In addition, a large number of tests is required to estimate the state of stress.

2.6 COMMENTS ON CONVENTIONAL METHOD OF INTERPRETATION OF HYDRAULIC FRACTURE TESTS

It is clear from the discussion in the previous sections that the conventional method is the only practical method to use from the previously mentioned methods. However, it applies to the case of vertical fracturing only. The conventional method has also been used for subvertical fractures (Haimson *et al.* 1989 and Haimson 1992). In

these cases, the inclination of the fracture is ignored and the fracture is dealt with as if it were a vertical fracture.

In the cases where both vertical and horizontal fractures are found in impression packer tests, some researchers assume that the vertical fracture is initiated before the horizontal fracture by the first breakdown pressure and they use the conventional theory to estimate the horizontal stresses (see e.g. Haimson and Lee 1980; Haimson 1985). These calculated values could be correct if the vertical fracture is formed with the first breakdown pressure before the horizontal fracture. However. the calculated values based on this assumption would be erroneous if the horizontal fracture is initiated by the first breakdown pressure before the vertical fracture.

From the previous discussion, it is clear that the conventional method should be used only for the cases of development of unambiguous vertical fractures. It is therefore necessary to develop a more appropriate technique suitable for the analysis of various fractures commonly encountered in hydrofracturing tests in different types of rocks under different stress regimes.

2.7 LJUNGGREN AND AMADEI'S METHOD

Recognizing the limitations of the conventional method, Ljunggren *et al.* (1988) and Ljunggren and Amadei (1989) introduced a new method of calculation suitable for initial stress determination when the hydrofractures are either vertical or horizontal. The method uses Hoek and Brown's failure criterion (Hoek and Brown 1980) instead of the maximum tensile stress failure criterion. As in the case of the conventional method, the test location is assumed to be intact and free of fractures before performing the test. The

essential steps of the method may be summarized as follows:

(a)   The initial state of stresses at the cylindrical surface of the test section before test

is obtained by a three-dimensional analytical solution for the stresses around a

circular hole in an infinite, linearly elastic and homogeneous continuum loaded

at infinity (Leeman and Hayes 1966). These initial stresses (before test) are

functions of the unknown maximum and minimum horizontal stresses. It should

be noted that for the case where the axis of the test hole is aligned with the

direction of the vertical principal stress, the results of the solutions by Kirsch and

Leeman and Hayes are identical (Eqs. 3.11 to 3.13 in next Chapter).

(b)   The changes of stresses are obtained by the elastic solution of a thick-walled

cylinder under internal pressure, with the external radius approaching infinity.

The final state of stress at failure is obtained by superposition of the stress

changes to the initial state of stress obtained in (a) above.

(c)   The final stresses obtained in (b) must satisfy the Hoek and Brown criterion of

failure.

The simultaneous imposition of conditions (b) and (c) leads to three useful stress

inequalities at failure, resulting in three corresponding sets of equations applicable to

vertical and horizontal fractures. Ljunggren and Amadei's solution may be considered

as a stress path method often employed in geotechnical engineering. For convenience

of reference, the stress path designation is shown in Figure 2.3 and the stress inequalities

and the corresponding equations from which the stresses are calculated are summarized

in Table 2.1.

At failure, the tensile fracture (which is not necessarily vertical) is assumed to

develop perpendicular to the minimum principal stress. This method requires a knowledge of the breakdown and shut-in pressures (obtained from the hydraulic fracturing tests), the uniaxial compressive strength, Poisson's ratio, and the tensile strength of the rock. To calculate the state of stress, after deciding on the type of fracture (horizontal or vertical), substitution in the equations in Table 2.1 for a corresponding stress path is required. In the case of vertical fractures, the solution yields unique values of horizontal stresses as in the case of the conventional method. In the case of horizontal fractures, however, the method does not predict a single value for the minimum or maximum horizontal stresses but rather a very wide range of stresses. The reasons for this are that the solution is in terms of the difference of the horizontal stresses ($\sigma_H - \sigma_h$) and the conditions are in terms of inequalities. Ljunggren and Amadei (1989) and Bjarnason et al. (1989) faced this problem in calculating the virgin state of stress at Lavia in Finland when the fractures were horizontal. The ranges of the predicted maximum and minimum horizontal stress were typically 15 MPa (see Tables 2 and 4 in Ljunggren and Amadei 1989, and Tables 4.3 and 4.4 in Chapter 4). The same problem in using this method was encountered by Martin (1990) in calculating the horizontal stresses in Granite in Southeastern Manitoba. A stress range of about 30 MPa was obtained.

In the following Chapter, the method of Ljunggren and Amadei is modified so that the inadmissible stresses are eliminated from the obtained range of stresses, with the result that the calculated stress range is reduced considerably. The procedure for this reduction technique is given. Since some rocks exhibit intrinsic anisotropy, especially shaly rocks, Hoek and Brown's failure criterion is modified to take into account the

strength anisotropy in hydrofracturing calculations. The proposed experimental program necessary for such modification and the deduction of the required parameters are formulated. In addition, the method is extended to include the case of calculating the state of stress when the hydrofractures are mixed-mode fractures (combined horizontal and vertical fractures). For convenience, the method developed will be referred to as the Modified Stress Path (MSP) method.

TABLE 2.1 Summary of the possible stress paths during hydraulic fracturing tests (modified from Ljunggren and Amadei 1989)

Stress Path	Type of Fracture	Condition at Failure	Corresponding Equation Using Hoek & Brown Failure Criterion
I	vertical	$\sigma_z > \sigma_r > \sigma_\theta,\ \sigma_\theta < 0$	$\sigma_z = \sigma_\theta + \sqrt{(m\sigma_c\sigma_\theta + \sigma_c^2)}$ or, $\sigma_{zo} - 2\nu(\sigma_H - \sigma_h) = 3\sigma_h - \sigma_H - P_{cl} + \sqrt{\{m\sigma_c(3\sigma_h - \sigma_H - P_{cl}) + \sigma_c^2\}}$
II	vertical	$\sigma_r > \sigma_z > \sigma_\theta,\ \sigma_\theta < 0$	$\sigma_r = \sigma_\theta + \sqrt{(m\sigma_c\sigma_\theta + \sigma_c^2)}$ or, $P_{cl} = 3\sigma_h - \sigma_H - P_{cl} + \sqrt{\{m\sigma_c(3\sigma_h - \sigma_H - P_{cl}) + \sigma_c^2\}}$
III	horizontal	$\sigma_r > \sigma_\theta > \sigma_z,\ \sigma_z < 0$	$\sigma_r = \sigma_z + \sqrt{(m\sigma_c\sigma_z + \sigma_c^2)}$ or, $P_{cl} = \sigma_{zo} - 2\nu(\sigma_H - \sigma_h) + \sqrt{\{m\sigma_c(\sigma_{zo} - 2\nu(\sigma_H - \sigma_h)) + \sigma_c^2\}}$

Note:

σ_z = $\sigma_{zo} - 2\nu(\sigma_H - \sigma_h)$
σ_{zo} = the overburden pressure
ν = Poisson's ratio
σ_r = radial pressure (at failure, $\sigma_r = P_{cl}$)
P_{cl} = the breakdown pressure
σ_θ = $3\sigma_h - \sigma_H - P_{cl}$
σ_c = the uniaxial compressive strength
m = constant for Hoek and Brown's failure criterion
σ_H, σ_h = the maximum and minimum horizontal in-situ stresses respectively
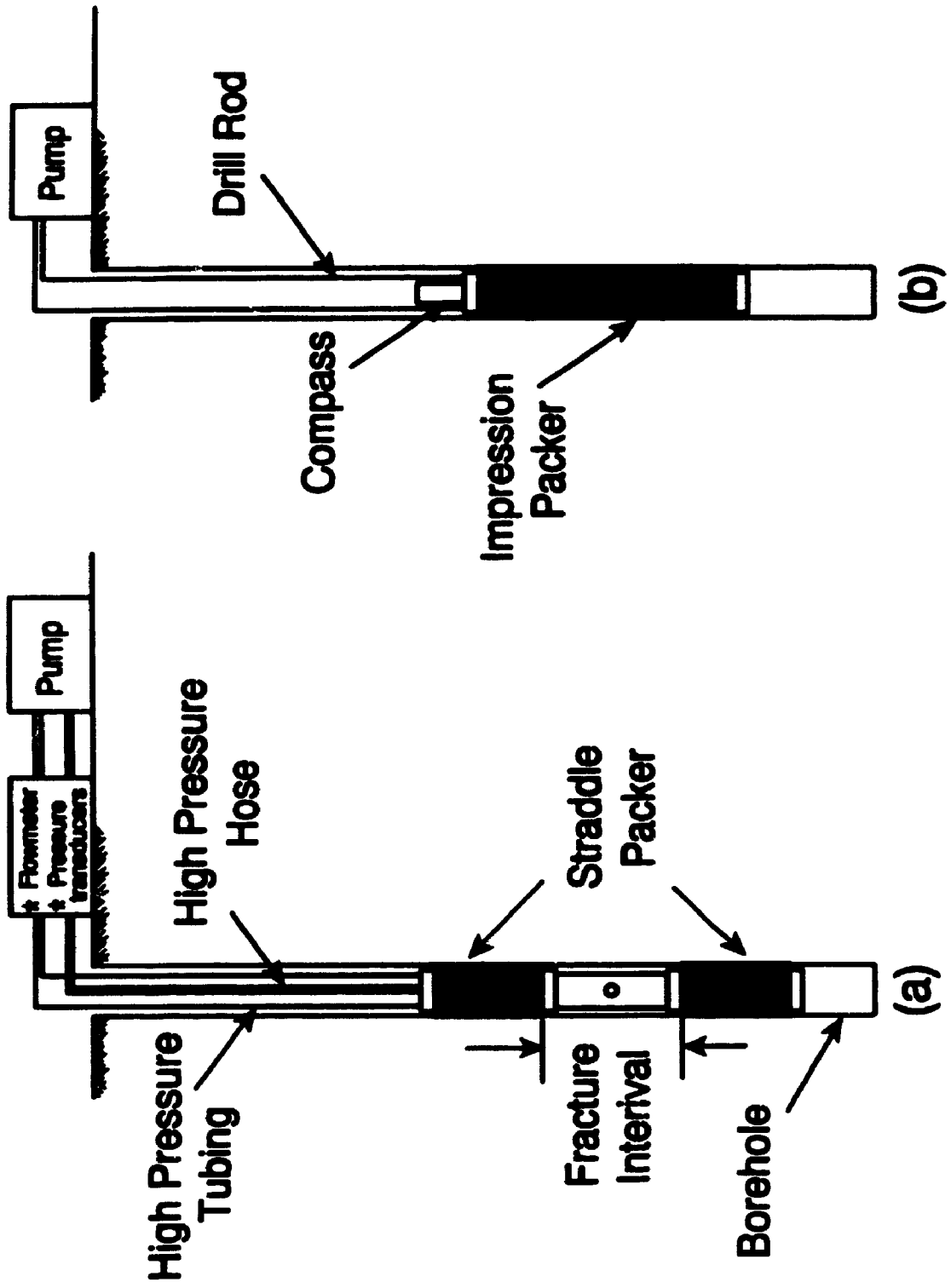
Figure 2.1 Schematic representation of (a) hydraulic fracturing testing (b) impression packer
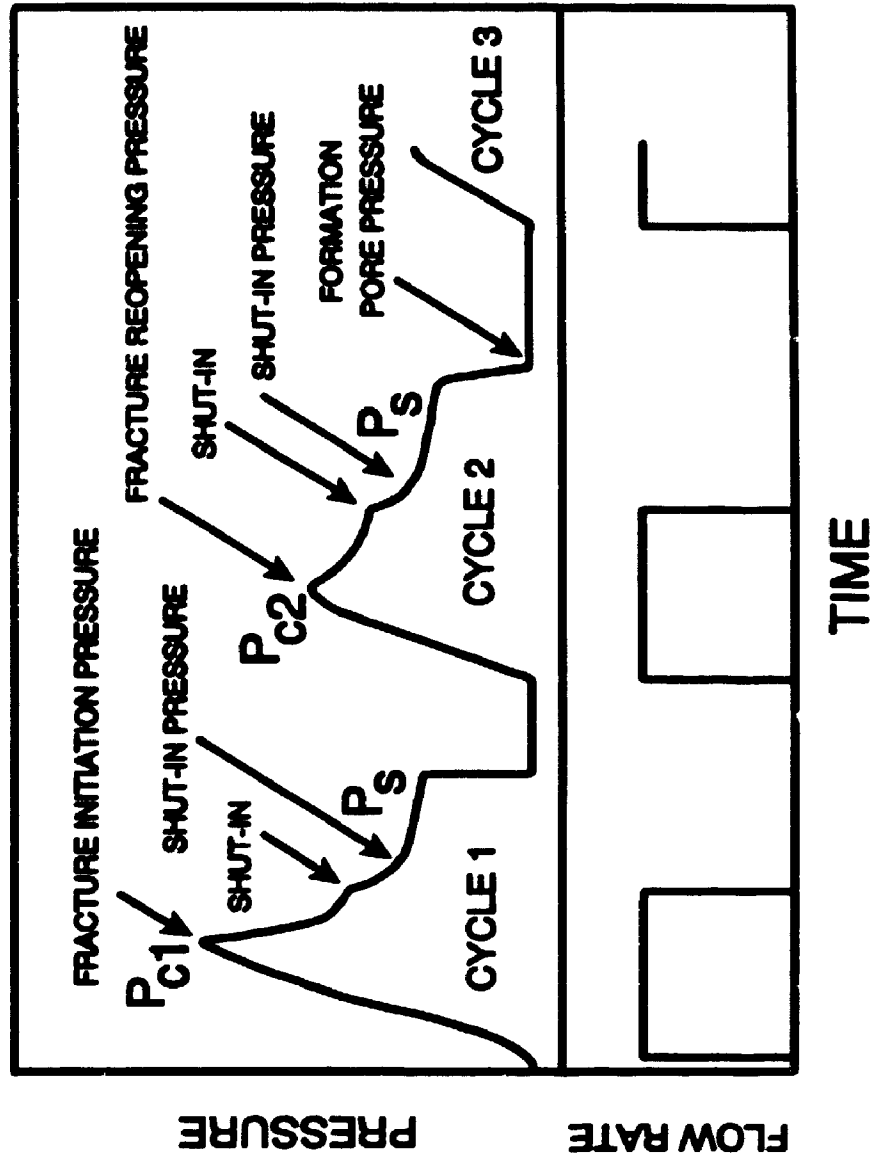
Figure 2.2 Idealised hydraulic fracturing pressure-time record
(ISRM - Kim and Franklin 1987)

(a) Stress Path I

Requirements at
Failure (F)

$\sigma_z > \sigma_r > \sigma_\theta$, $\sigma_\theta < 0$

$\sigma_z = \sigma_\theta + \sqrt{(m\sigma_c\sigma_\theta + \sigma_c^2)}$

(b) Stress Path II

Requirements at
Failure (F)

$\sigma_r > \sigma_z > \sigma_\theta$, $\sigma_\theta < 0$

$\sigma_r = \sigma_\theta + \sqrt{(m\sigma_c\sigma_\theta + \sigma_c^2)}$

(c) Stress Path III

Requirements at
Failure (F)

$\sigma_r > \sigma_\theta > \sigma_z$, $\sigma_z < 0$

$\sigma_r = \sigma_z + \sqrt{(m\sigma_c\sigma_z + \sigma_c^2)}$
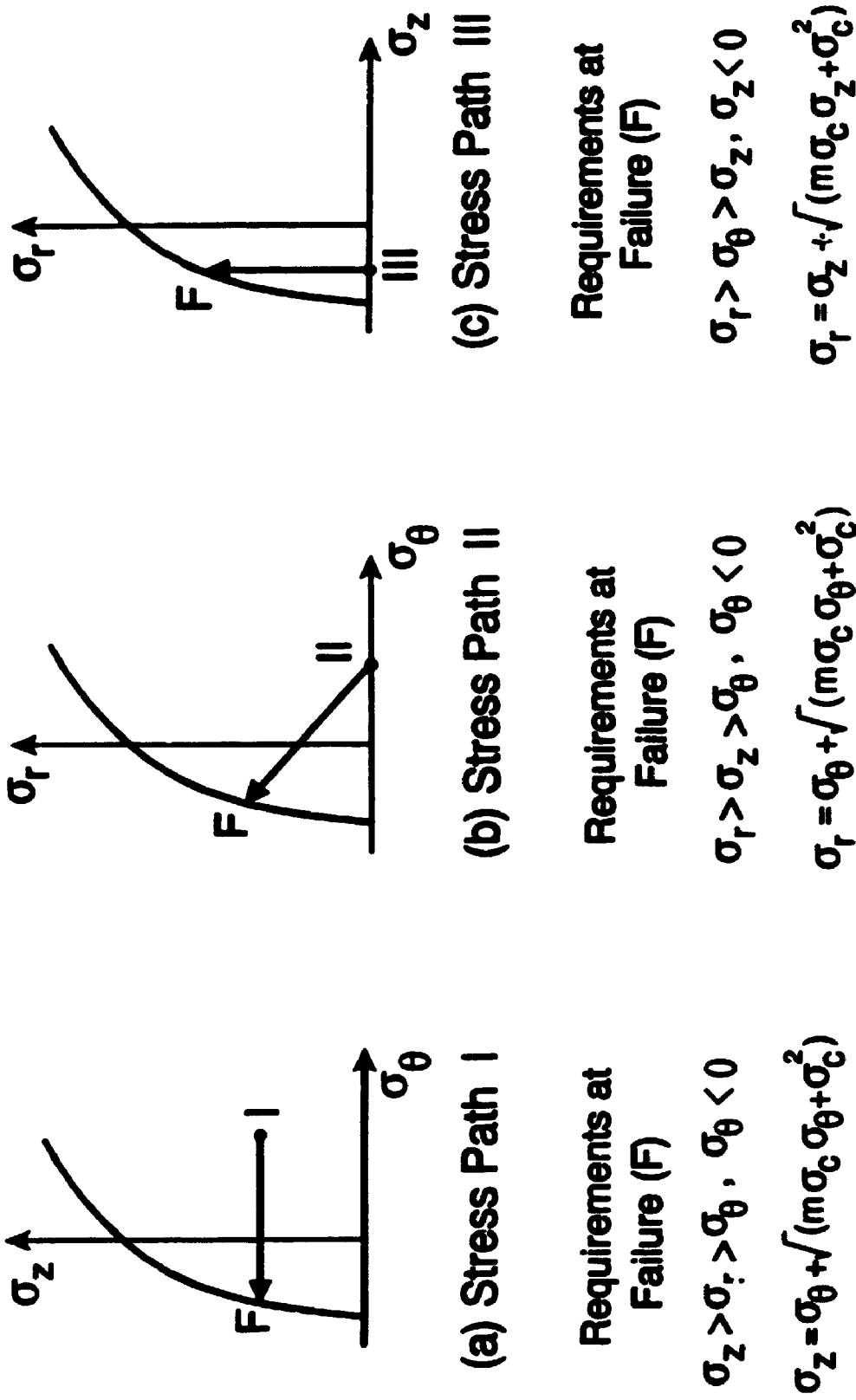
Figure 2.3 Possible stress paths during hydraulic fracturing tests
(a) & (b) vertical fracture   (c) horizontal fractures
(Modified from Ljunggren and Amadei 1989)

CHAPTER 3

THE MSP METHOD

FOR THE INTERPRETATION OF HORIZONTAL AND MIXED-MODE

FRACTURES IN HYDRAULIC FRACTURING TESTS IN ROCKS

3.1 INTRODUCTION

In Chapter 2, a critical review of the available methods for the prediction of *in situ* horizontal stresses from hydraulic fracturing tests was presented. The advantage and disadvantage of each method were clarified. It has been shown that the conventional method is the only practical method for stress determination when the hydrofractures are vertical. It has been shown also that although Ljunggren and Amadei's method is able to analyze horizontal fractures, it produces very wide ranges of the calculated stresses with the result that the calculated stresses are not suitable for design.

In this Chapter, the method of Ljunggren and Amadei is modified so that the inadmissible stresses are eliminated from the obtained range of stresses, with the result that the calculated stress range is reduced considerably. The developed method (Modified Stress Path (MSP) method, Hefny and Lo 1992a) enables the determination of the *in situ* stresses when mixed-mode fractures (combination of horizontal and vertical) are encountered, as recorded by the packer impression. This method takes into account the strength anisotropy of rock. Results of hydraulic fracturing tests in several case histories reanalyzed using the method developed will be presented in the next Chapter.

fluid infiltrates the rock before fracture initiation:

$$P_{cI} = \frac{3\sigma_h - \sigma_H + T - \alpha\frac{1-2v}{1-v}P_o}{1 + \beta - \alpha\frac{1-2v}{1-v}}$$ (2.15)

The value of β ranges between 0 and unity. Equation 2.15 has the advantage of the ability to represent Eq. 2.3 when $\alpha = \beta = 0$. The higher the values of α and β are, the more porous is the rock. The authors used Eq. 2.15 to estimate the value of β for Valders limestone from a laboratory hydraulic fracturing experimental data but the value of β increased unexpectedly as the value of α decreased. Schmitt and Zoback did not analyze any actual field hydraulic fracturing data using this method. It seems that the difficulty of determining α and β limited the use of Eq. 2.15 in practice.

2.5 CORNET AND VALETTE'S METHOD

In 1984 Cornet and Valette suggested two methods for initial stress calculations. In these methods the orientation of the fracture is not necessarily perpendicular to that of the minimum principal stress. The first method is based on the measurements of the instantaneous shut-in pressure for fracture planes with various dips and strikes. The second method makes use of both shut-in pressures and reopening pressures for fractures parallel to the borehole axis.

In these methods, the stress field is assumed to vary linearly with depth and the lateral variation of the stress field is ignored. The horizontal stress values at a test location cannot be predicted from only that test data but rather from a large number of

to Figure 2.3. In all stress paths, the fracture is assumed to develop with the occurrence of the first breakdown pressure and perpendicular to the least principal stress. These stress paths are the loci of points defined by the radial, tangential, and vertical stresses on the borehole wall at the test location.

(a)   Stress Path I

The first possible stress path that causes a vertical hydrofracture is shown in Figure 2.3-a. Point I in the figure represents the initial stresses after drilling the hole and before performing the test, while point F represents the final stress state at the formation of the fracture. At fracture formation, the following inequality of stresses must be satisfied:

$$\sigma_z > \sigma_r > \sigma_\theta, \quad \sigma_\theta < 0 \tag{3.3}$$

where: σ_z is the vertical stress at the test location.

$$\sigma_z = \sigma_{zo} - 2v(\sigma_H - \sigma_h)$$

(refer to Appendix 3A for the derivation of the value oi σ_z at the location of minimum tangential stress on the periphery of the borehole assuming plane strain conditions)

σ_{zo} is the overburden pressure.

v is the Poisson's ratio

σ_H, σ_h are the maximum and minimum *in situ* horizontal stresses, respectively.

σ_r is the radial stress and it is equal to the breakdown pressure (P_{cl})

at the time of initiation of the fracture.

σ_θ is the least tangential stress at the periphery of the borehole

$\sigma_\theta \;\; = 3\sigma_h - \sigma_H - P_{cl}$ at time of initiation of the fracture

Therefore, the failure criterion may be written as

$$\sigma_{zo} - 2\nu(\sigma_H - \sigma_h) = 3\sigma_h - \sigma_H - P_{cl} + \sqrt{m\sigma_c(3\sigma_h - \sigma_H - P_{cl}) + \sigma_c^2} \tag{3.4}$$

(b)   **Stress Path II**

The other possible stress path for formation of a vertical hydrofracture is shown in Figure 2.3-b. The corresponding inequality for this case is

$$\sigma_r > \sigma_z > \sigma_\theta \; , \;\;\;\; \sigma_\theta < 0 \tag{3.5}$$

or,

$$P_{cl} > \sigma_{zo} - 2\nu(\sigma_H - \sigma_h) > 3\sigma_h - \sigma_H - P_{cl} \tag{3.6}$$

The major principal stress at failure is the breakdown pressure while the minor principal stress is the minimum tangential stress at the periphery of the hole. Therefore, the relation between stresses at failure takes the following form:

$$P_{cl} = 3\sigma_h - \sigma_H - P_{cl} + \sqrt{m\sigma_c(3\sigma_h - \sigma_H - P_{cl}) + \sigma_c^2)} \tag{3.7}$$

(c)   Stress Path III

Figure 2.3-c shows the possible stress path for initiating a horizontal hydrofracture at the breakdown stage. The following inequality of stresses at fracture formation should be satisfied:

$$\sigma_r > \sigma_\theta > \sigma_z , \quad \sigma_z < 0 \tag{3.8}$$

or,

$$P_{cl} > 3\sigma_h - \sigma_H - P_{cl} > \sigma_{zo} - 2v(\sigma_H - \sigma_h) \tag{3.9}$$

In this case, the fracture is formed perpendicular to σ_z, the minimum principal stress at failure. The value of the breakdown pressure, P_{cl}, is the major principal stress. The failure criterion becomes

$$P_{cl} = \sigma_{zo} - 2v(\sigma_H - \sigma_h) + \sqrt{(m\sigma_c(r_{zo} - 2v(\sigma_H - \sigma_h)) + \sigma_c^2)} \tag{3.10}$$

Using Eqs. 3.9 and 3.10, the difference between the maximum and the minimum horizontal *in situ* stresses could be estimated when horizontal fractures are initiated. A range of values for both stresses will be obtained. It is important to note that the stress range is obtained by forcing the value of σ_θ to be the intermediate principal stress. In other words, σ_θ can take any value between P_{cl}, the major principal stress at failure, and σ_z, the minor principal stress.

3.2.3   Inadmissible Stresses

In the framework of solutions discussed in the previous sections, the following

additional requirement must be satisfied. The state of stress at the circumference of the test section before test must be below failure, otherwise premature pretest failure would occur rendering the test results meaningless. The application of this condition will eliminate ranges of stress calculated that are inadmissible.

3.2.4 Procedure for Elimination of Inadmissible Stresses

To eliminate the inadmissible stresses, the initial stresses before test will be examined. The range of the initial minimum horizontal tangential stress, $\sigma_{\theta i}$, (location of potential horizontal fracturing) is computed using the calculated values of the maximum and minimum horizontal stresses (see Sec. 3.2.2 and Table 2.1). After drilling the hole and before performing the test, the expressions for the stresses at the circumference at location of potential hydrofracturing (see Figure 3.1) are

$$\sigma_{\theta i} = 3\sigma_h - \sigma_H = \sigma_{1i} \tag{3.11}$$

$$\sigma_r = 0 \tag{3.12}$$

$$\sigma_z = \sigma_{zo} - 2v(\sigma_H - \sigma_h) = \sigma_{3i} \tag{3.13}$$

where

σ_H, σ_h = the maximum and minimum *in situ* horizontal stress values respectively.

$\sigma_{1i}, \sigma_{2i}, \sigma_{3i}$ = the major, intermediate, and minor initial principal stresses respectively at the start of the test.

σ_r = the radial stress

σ_z = the vertical stress at the test location

σ_{zo} = the overburden pressure (before test hole was drilled)

v = Poisson's ratio

From Eqs. 3.11 and 3.13, it may be seen that there is a range of σ_{θ_i} but only one value of σ_z because $(\sigma_H - \sigma_h)$ is single-valued. The next step is to calculate the maximum value of σ_1, (σ_{1max}), which lies on the failure envelope and corresponds to the single value of σ_z (Figure 3.2). The value of σ_{1max} represents the failure condition for a point with a minor principal stress equal to σ_z. Comparing this value of σ_{1max} with the calculated range of σ_{θ_i}, three cases would appear (Figure 3.2):

1. σ_{1max} >   the range of the values of σ_{θ_i}

2. σ_{1max} <   the range of the values of σ_{θ_i}

3. σ_{1max} lies on the range of the values of σ_{θ_i}

It is clear that if we have Case 1, all stresses calculated are admissible and no reduction could be done for the calculated range of the horizontal stress. On the other hand, Case 2 is an inadmissible condition because it indicates failure before performing the test. For Case 3, all the range of σ_{θ_i} above the failure envelope is inadmissible (premature failure) and has to be discarded. Only the range of σ_{θ_i} under the failure envelope is considered and a reduced range of σ_{θ_i} is obtained. The last step is to substitute the value of σ_{1max} for σ_{θ_i} in Eq. 3.11. Knowing the value of the difference between σ_H and σ_h, which

is already computed from the equation corresponding to stress path III in Table 2.1, new upper limit values for the maximum and minimum horizontal stresses can be obtained. Therefore, a narrower range of both the maximum and the minimum horizontal stresses can be estimated.

Experience gained from the analysis of results of hydraulic fracturing tests from several case histories (Chapters 4 and 5) has shown that Case 1 and Case 2 never appear and only Case 3 arises. These results are consistent with theoretical considerations of stress conditions at fracture according to the inequality of stress path III in Table 2.1. In the following the theory behind this fact will be discussed.

At first, the value of σ_{1max} discussed in Cases 1, 2 and 3 above is examined. The stress ranges of σ_h and σ_H are obtained by allowing the value of σ_θ at failure to be the intermediate principal stress (refer to stress path III in Section 3.2.2 and Table 2.1). In other words, σ_θ at fracturing can take any value between the radial stress ($=P_{ci}$) which is the major principal stress at failure (the upper limit of σ_θ) and σ_z which is the minor principal stress (the lower limit of σ_θ). It can be concluded also that the value of σ_{1max} should be equal to the value of P_{ci} (the major principal stress at failure).

Secondly, the upper limit of the initial tangential stress, $\sigma_{\theta i}$, before the test is examined. According to the elastic solution for thick-walled cylinder under an internal pressure, P_i, (when the outer radius approaches infinity), the tangential stress at the inner radius after applying the internal pressure (P_i) is equal to $-P_i$. Therefore, in

hydrofracturing tests the value of final tangential stress is less than the initial tangential stress. The final tangential stress will be equal to the difference between the initial tangential stress and the radial pressure at fracturing, P_{cl}, $(\sigma_\theta = \sigma_{\theta_l} - P_{cl})$. Realizing that the upper limit of the final tangential stress equals to P_{cl} as discussed above, the value of the upper limit of initial tangential stress should always be equal to twice the value of P_{cl}. Comparing this value of the upper limit of initial tangential stress $(=2P_{cl})$ with the value of σ_{1max} $(=P_{cl})$, it can be concluded that the upper limit of σ_{θ_l} should lie above the failure criterion. Therefore, Case 1 never appears in the solution and only Case 2 and 3, so far, could be obtained.

Finally, the lower limit of the initial tangential stress is examined. As discussed above, the value of the tangential stress at fracturing lies between σ_z (which is tensile for case of horizontal fracturing) and P_{cl}. This means that the lower limit of the final tangential stress is tensile and is equal to σ_z. Therefore, the value of the lower limit of initial tangential stress equals to $(P_{cl} + \sigma_z)$. Comparing this value with the value of σ_{1max} $(=P_{cl})$, it can be concluded that the lower limit of σ_{θ_l} should lie below the failure envelope, because σ_z is tensile. Therefore, it could be concluded that only Case 3 of the three cases discussed above will always be obtained. This guarantees that reduction can always be done for the calculated range of stresses.

For convenience, the complete steps of calculating the initial horizontal stresses from horizontal fractures are summarized in Figure 3.3.

3.2.5 Which Hydrofracture Has Been Initiated First?

Until recently, the maximum tensile stress method has been the only available technique for calculations of the state of stress from the hydraulic fracturing test results. The validity of this method is limited to the case of unambiguous vertical fracture formation. However, this method has been used to calculate the state of stress where both horizontal and vertical fractures have been developed. In the calculations, it was necessary to assume arbitrarily that the vertical fracture was initiated with the first breakdown pressure and before the horizontal hydrofracture. Intuitively, the stresses calculated could be correct if the vertical fractures were formed with the first breakdown pressure before the horizontal fractures. However, the calculated values based on this assumption would be erroneous if the horizontal fractures were initiated by the first breakdown pressure and before the vertical fractures.

The MSP method offers a direct way of calculating the state of stress for the mixed-mode fractures, without using any arbitrary assumptions. In the case when both horizontal and vertical fractures are recorded by the impression packer, the first breakdown pressure will satisfy only one of the three stress paths discussed previously in Sec. 3.2.2. By following the three stress paths successively until the breakdown stage, it will be found that only one stress path hits the failure envelope at the first breakdown pressure. The stress path thus found will define the type of fracture (horizontal or vertical). This fracture is considered to be initiated first and the state of stress should be calculated using the corresponding equations. It should be noted that stress path III implies forcing the tangential stress at failure to take all the possible values that make it the intermediate principal stress. Therefore, checking stress path III should only be

carried out after checking stress path I and II and making sure that they are not satisfied.

Examples of application of this procedure will be given for the hydrofracturing test at sites where combined fractures were encountered. In Chapter 4, this method will be used to re-analyze the hydrofracturing test results for the Darlington Generating Station site where mixed-mode fractures were encountered. State of stress was calculated, previously, at these test locations using the conventional theory of vertical fractures, Haimson 1978b. Calculations of the state of stress in the SABNGS No.3 site where mixed-mode hydrofractures were formed will be given in Chapter 5. The obtained results will be compared with those obtained using the conventional theory of vertical fractures by Haimson (1985).

3.3   EXTENSION OF THE MSP METHOD

3.3.1   Modified Hoek and Brown's Failure Criterion for Anisotropic Rocks

For Rocks which exhibit strength anisotropy, such as shales, the method of calculating the virgin state of stresses should take strength anisotropy into account. For shales, Hoek and Brown (1980) recognized that the strength behaviour would be anisotropic. If a failure criterion is adopted, such as Hoek and Brown's failure criterion, and considering that there are three different stress paths with different relationships between stresses at failure, strength anisotropy indicates the existence of three failure envelopes. To define these failure envelopes, a strictly specified series of tests matching the condition of failure for each of the three stress paths should be performed. In the following, the relevant tests for obtaining each of the three failure envelopes will be discussed. Four types of tests are required to define each envelope: tensile strength test,

tests for the part of the envelope where σ_3 is negative (tensile), uniaxial compression test, and tests for the part of the envelope where σ_3 is positive (compressive).

(a)   Envelope For Stress Path I

In the case of stress path I, a vertical fracture is encountered. The proposed types of tests required are illustrated in Figure 3.4. The condition at failure indicates that the vertical stress is the major principal stress and the horizontal stresses are the minor and intermediate principal stresses. Therefore, the tensile strength that should be adopted in this case is that representing vertical fracturing, T_h, i.e. the tensile stress is applied in the horizontal direction. A series of biaxial compression-tension tests or triaxial compression-compression-tension tests would determine that part of the failure envelope where σ_3 is less than zero. In this group of tests, the vertical direction is the direction of the major principal stress. The uniaxial compressive strength obtained by applying the stress in the vertical direction ,i.e. for vertically oriented samples, σ_{cv}, is relevant for this stress path. For the part of the envelope where σ_3 is positive, a series of triaxial compression tests for vertically oriented samples is required.

(b)   Envelope For Stress Path II

Stress path II also represents vertical fracturing. However, the condition at failure indicates that both the major and the minor principal stresses are horizontal. Therefore, T_h should also be determined to represent such a vertical fracture. A series

of biaxial compression-tension tests or triaxial compression-compression-tension tests, where one of the horizontal directions is the direction of major principal stress and the other is the direction of the tensile stress, could be adopted for the determination of part of the envelope where σ_3 is tensile. In this case, $\text{th}^{\sim}$ ₋₋ue of the uniaxial compressive strength in the horizontal direction, σ_{ch}, represents the suitable value for this envelope. A series of triaxial compression tests on h rizontally cored samples represents the part of the envelope where σ_3 is positive.

(c) Envelope For Stress Path III

Stress path III represents the condition of horizontal fracturing. At failure, the major principal stress is horizontal, while the minor principal stress is vertical. In this case, it is clear that the tensile strength from samples cored in the vertical direction and fractured in the horizontal direction represents well this mode of fracture. A series of biaxial compression-tension tests or triaxial compression-compression-tension tests, where the vertical direction is the direction of the tensile stress, would represent the part of the envelope for $\sigma_3 < 0$. The value of the uniaxial compression test for horizontally cored samples, σ_{ch}, is appropriate for this failure condition. A series of triaxial compression tests for horizontally cored samples is required to complete the envelope in the region where $\sigma_3 > 0$.

Figure 3.4 and Table 3.1 summarize the type of tests and applied stress states required for obtaining the three failure envelopes needed to represent the strength

anisotropy of the rock.

(d)   Effect of Poisson's Ratio

The importance of the effect of Poisson's ratio on calculated stresses has been pointed out by Ljunggren and Amadei (1989). From the analysis of test data in several case histories (to be discussed in Chapters 4 and 5), similar effects of Poisson's ratio have been found and the importance of this effect is confirmed. It should be noted that for stress paths I and III, the Poisson's effect relates to the effect of horizontal stress on vertical strain. The correct Poisson's ratio is therefore v_{hv}, the ratio for the effect of

horizontal stress on vertical strain, in the theory of deformation of cross-anisotropic media (see e.g. Lo and Hori 1979). For stress path II, Poisson's ratio is not involved (see Table 3.2). An example illustrating the effect of Poisson's ratio on the calculated stresses will be given in Chapter 5.

3.4   APPROXIMATE METHOD FOR DETERMINATION OF PARAMETERS FOR THE MSP METHOD

Although the experimental methods described in the preceding section to determine the appropriate envelope will yield representative parameters, in practice, time and other constraints may not allow such a complete investigation. As an alternative, th·· required parameters may be determined approximately by the following procedure. Realizing that the hydrofracturing tests should be performed at locations where the rock is intact, the parameter "s" in Hoek and Brown's failure criterion is taken equal to unity. Only appropriate values of the parameter "m" are required to represent the three failure

envelopes. This parameter "m" may be obtained from Hoek and Brown criterion by knowing σ_c and T as shown in Appendix 3B. Therefore, the values of "m" for the three stress paths are

$$m_I = \frac{\sigma_{cv}}{T_h} - \frac{T_h}{\sigma_{cv}} \qquad (3.14)$$

$$m_{II} = \frac{\sigma_{ch}}{T_h} - \frac{T_h}{\sigma_{ch}} \qquad (3.15)$$

$$m_{III} = \frac{\sigma_{ch}}{T_v} - \frac{T_v}{\sigma_{ch}} \qquad (3.16)$$

Where, m_I, m_{II} and m_{III} are the values of the parameter "m" for the envelopes required to represent stress path I, II and III, respectively. In the case of $\sigma_{cv} = \sigma_{ch}$, which occurs quite often, we have only two envelopes, one for the vertical fractures and the other for horizontal fractures. The values for "m" become

$$m_I = m_{II} = \frac{\sigma_c}{T_h} - \frac{T_h}{\sigma_c} \qquad (3.17)$$

and the value of m_{III} is the same as in Eq. 3.16.

Figure 3.5 shows failure envelopes for the three stress paths as functions of the strength parameters T_h, T_v, σ_{ch} and σ_{cv}. Two cases representing the commonly observed strength behaviour of rocks are shown. The first is for $T_v < T_h$ and $\sigma_{ch} >$ σ_{cv}, while the second is for the case $T_v < T_h$ and $\sigma_{ch} = \sigma_{cv}$. A summary of the equations describing the possible stress paths during hydrofracturing tests, in terms of

the representative anisotropic strength parameters, is given in Table 3.2 and Figure 3.6.

These equations may be used for stress determination for hydraulic fracturing tests in

rocks with tensile strength anisotropy. The effect of the degree of strength anisotropy

on the calculated horizontal stresses will be studied in Chapter 5.

3.5 ANALYSIS OF SUBVERTICAL FRACTURES

One of the reasons for the formation of subvertical fractures is tensile strength

anisotropy. If at any stage of the test the tangential stress in any direction is equal to the

tensile strength of the rock in that direction, a fracture develops. The initiation of

subvertical fracture is not only a function of the directional tensile strength but also

depends on the state of stress during testing.

To analyze subvertical fractures, it has been assumed that these fractures are

vertical and that their deviation from the vertical results in negligible change in the

computed stress values (Haimson et al. 1989). This implies that the horizontal tangential

stress at any stage of the test was assumed equal to the actual stress normal to the

fracture. If the inclination of the fracture to the vertical is large and/or tensile strength

anisotropy is significant, this assumption may lead to unreliable results.

A direct method to calculate the horizontal stresses from subvertical fractures is

to introduce into the analysis the component of stress normal to the fracture at the

breakdown stage and shut-in stage together with the anisotropic tensile strength of the

rock. The closed form solutions for the maximum and minimum horizontal stresses,

respectively, at the test location obtained using this analysis are

$$\sigma_H = A_1 \ P_{cI} + B_1 \ P_s + C_1 \ \sigma_{zo} + D_1 \ T_n \tag{3.18}$$

and

$$\sigma_h = B_2 \ P_s + C_2 \ \sigma_{zo} \tag{3.19}$$

Where:

$$A_1 = -\frac{M^4}{F}$$

$$B_1 = \frac{3M^2 + 2\nu N^2}{F}$$

$$C_1 = \frac{-2N^2(M^2 + \nu N^2)}{F}$$

$$D_1 = \frac{M^2}{F}$$

$$F = M^2(M^2 + 2\nu N^2)$$

$$B_2 = \frac{1}{m^2}$$

$$C_2 = -\frac{n^2}{m^2}$$

$$M = \cos\beta$$

$$N = \sin\beta$$
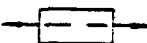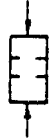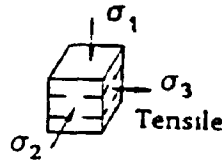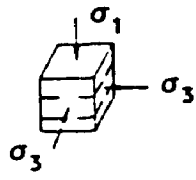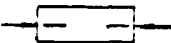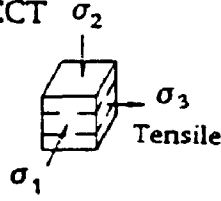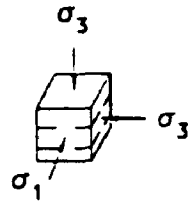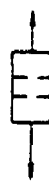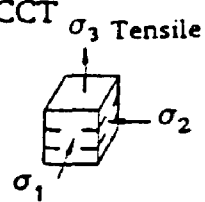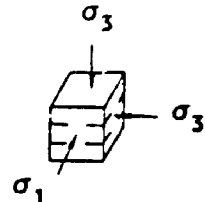
β = Angle between fracture plane and the vertical plane whose strike is parallel to the

direction of initial maximum horizontal stress

v = Poisson's ratio

Appendix 3C includes the complete derivation of the equations for calculating the *in situ* horizontal stresses using this analysis and an example of calculations.

TABLE 3.1   Tests required to determine the failure envelope representing the strength anisotropy in analysis of hydraulic fracturing tests

Stress Path	Required Tests			
	UT	UC	Envelope part for tensile min. stress	Envelope part for comp. min. stress
I	HCS	VCS	BCT or TCCT σ_1 σ_3 σ_2 Tensile	TC-VCS σ_1 σ_3 σ_3
II	HCS	HCS	BCT or TCCT σ_2 σ_3 σ_1 Tensile	TC-HCS σ_3 σ_3 σ_1
III	VCS	HCS	BCT or TCCT σ_3 Tensile σ_2 σ_1	TC-HCS σ_3 σ_3 σ_1

Note: HCS   Horizontally cored samples
VCS   Vertically cored samples
BCT   Biaxial compression-tension test
TCCT Triaxial compression-compression-tension test
TC   Triaxial compression test
UT   Uniaxial tension test
UC   Uniaxial compression test

TABLE 3.2 Summary of the equations of the possible stress paths in terms of the anisotropic strength parameters:

Stress Path	Type of Fracture	Condition at Failure	Corresponding Equation Using Modified Hoek & Brown Failure Criterion
I	vertical	$\sigma_z > \sigma_r > \sigma_\theta,\ \sigma_\theta < 0$	$\sigma_z = \sigma_\theta + \sqrt{(m_I \sigma_{cv}\sigma_\theta + \sigma_{cv}{}^2)}$ or, $\sigma_{zo} - 2\nu_{hv}(\sigma_H - \sigma_h) = 3\sigma_h - \sigma_H - P_{cl} + \sqrt{\{m_I\sigma_{cv}(3\sigma_h - \sigma_H - P_{cl}) + \sigma_{cv}{}^2\}}$
II	vertical	$\sigma_r > \sigma_z > \sigma_\theta,\ \sigma_\theta < 0$	$\sigma_r = \sigma_\theta + \sqrt{(m_{II}\sigma_{ca}\sigma_\theta + \sigma_{ca}{}^2)}$ or, $p_{cl} = 3\sigma_h - \sigma_H - P_{cl} + \sqrt{\{m_{II}\sigma_{ca}(3\sigma_h - \sigma_H - P_{cl}) + \sigma_{ca}{}^2\}}$
III	horizontal	$\sigma_r > \sigma_\theta > \sigma_z,\ \sigma_z < 0$	$\sigma_r = \sigma_z + \sqrt{(m_{III}\sigma_{ca}\sigma_z + \sigma_{ca}{}^2)}$ or, $P_{cl} = \sigma_{zo} - 2\nu_{hv}(\sigma_H - \sigma_h) + \sqrt{\{m_{III}\sigma_{ca}(\sigma_{zo} - 2\nu_{hv}(\sigma_H - \sigma_h)) + \sigma_{ca}{}^2\}}$

Notes:

(1) σ_z = $\sigma_{zo} - 2\nu_b(\sigma_H - \sigma_h)$

(2) σ_{zo} = the overburden pressure

(3) ν_{hv} = Poisson's ratio for the effect of horizontal stress on vertical strain

(4) σ_r = radial pressure (at failure, $\sigma_r = P_{cl}$)

(5) P_{cl} = the breakdown pressure

(6) σ_θ = $3\sigma_h - \sigma_H - P_{cl}$

(7) σ_H, σ_h = the maximum and the minimum horizontal in-situ stresses respectively

(8) σ_{cv}, σ_{ca} = uniaxial compressive strength for vertically and horizontally cored samples respectively

(9) m_I, m_{II}, m_{III} = constants for modified Hoek and Brown failure criterion

(a) Before Test

$\sigma_\theta = 3\sigma_h - \sigma_H$

$\sigma_r = 0$

$\sigma_z = \sigma_{zo} - 2V_{hv}(\sigma_H - \sigma_h)$

(b) During Test

$\sigma_\theta = 3\sigma_h - \sigma_H - P_i$

$\sigma_r = P_i$

$\sigma_z = \sigma_{zo} - 2V_{hv}(\sigma_H - \sigma_h)$

(c) At Fracturing

$\sigma_\theta = 3\sigma_h - \sigma_H - P_{c1}$

$\sigma_r = P_{c1}$

$\sigma_z = \sigma_{zo} - 2V_{hv}(\sigma_H - \sigma_h)$
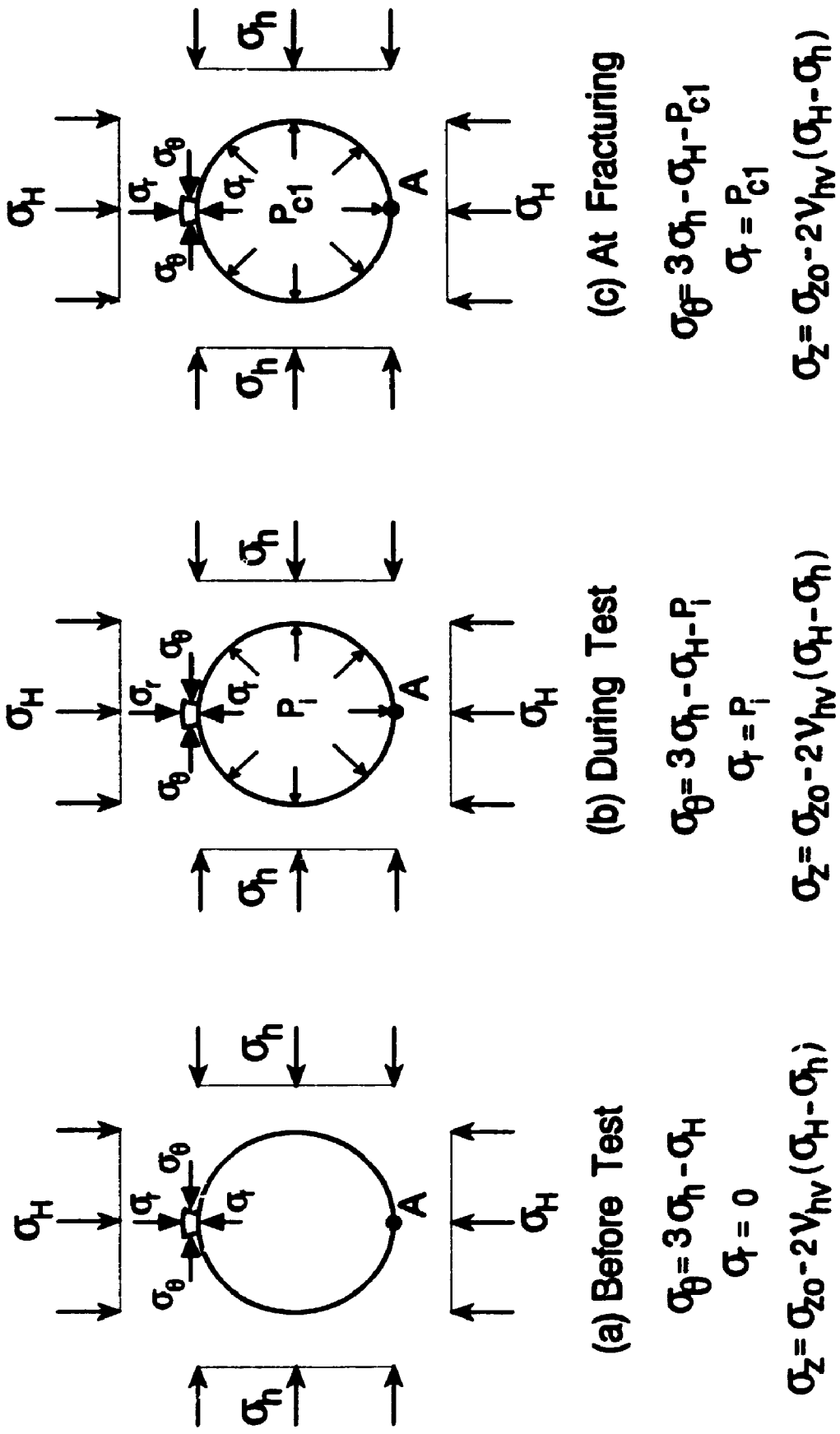
Figure 3.1 Stress condition at point A   (a) after drilling the test hole, before test

(b) during test   (c) at fracturing
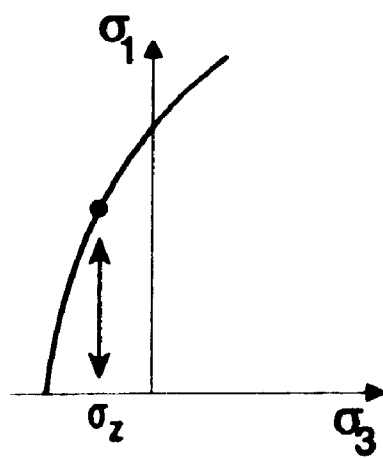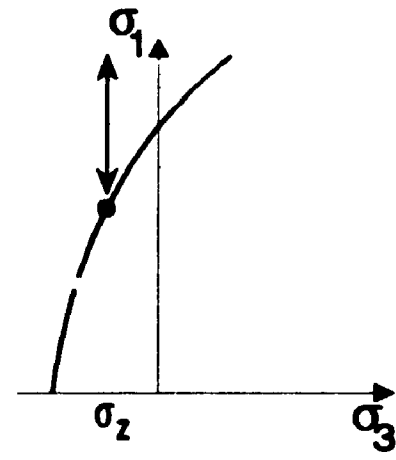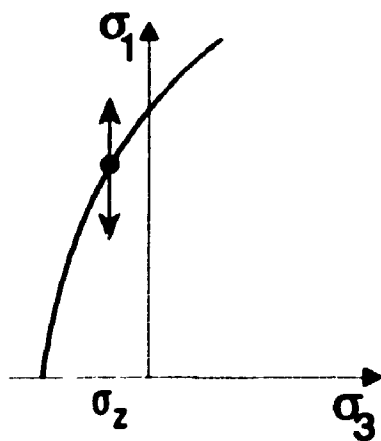
Figure 3.2 Different cases of the location of the range of the tangential stress with respect to the failure envelope (before performing the test)

Figure 3.3 Steps of calculations for horizontal fractures

1- Determine Hydraulic Fracture test data (at test location)

Pressure at test location = Pressure at G.S. + Head Pressure

Breakdown Pressure: P_{c1}

Shut-in Pressure: P_s

2- Establish Strength Parameters

particularly,

Tensile Strength: T_o

Uniaxial Comp. Strength: σ_{ch}

Poissons's ratio: ν_{bv}

Parameter 'm' for modified Hoek and Brown's failure criterion: m_{III}

3- Conditions and Relations at Failure

$$\sigma_r > \sigma_\theta > \sigma_z, \qquad \sigma_z < 0 \tag{3-1}$$

$$\sigma_r = P_{c1} = \sigma_z + \sqrt{(m_{III}\,\sigma_{ch}\,\sigma_z + \sigma_{ch}^2)} \tag{3-2-a}$$

$$\sigma_z = \sigma_{zo}\text{-}2\nu_{bv}(\sigma_H\text{-}\sigma_b)$$

$$P_{c1} = \{\sigma_{zo}\text{-}2\nu_{bv}(\sigma_H\text{-}\sigma_b)\} + \sqrt{\{m_{III}\,\sigma_{ch}\,|\sigma_{zo}\text{-}2\nu_{bv}(\sigma_H\text{-}\sigma_b)|+\sigma_{ch}^2\}} \tag{3-2-b}$$

4- Calculate the Difference Between the Major and Minor Initial Horizontal Stresses ($\sigma_D = \sigma_H\text{-}\sigma_h$)

Using Eq. (3-2-b) and after substitutions and arrangement, a quadratic equation in σ_D is obtained

$$a\,\sigma_D^2 + b\,\sigma_D + c = 0$$

Solution of this equation gives the value of σ_D

5- Calculate the Upper Bound of σ_H and σ_h

From stress condition at failure (Eq. 3-1),

$\sigma_r > \sigma_\theta$

$P_{c1} > 3\sigma_h\text{-}\sigma_H\text{-}P_{c1}$

$P_{c1} > 2\sigma_h\text{-}(\sigma_H\text{-}\sigma_h)\text{-}P_{c1}$

$$\sigma_h < (2P_{c1}+\sigma_D)/2$$

Similarly,

$$\sigma_H < (2P_{c1}+3\sigma_D)/2$$

6- Calculate the Lower Bound of σ_H and σ_h

The following condition at failure is used:

$\sigma_\theta > \sigma_z$, which leads to

$$\sigma_h > [\sigma_{zo}+\sigma_D(1\text{-}2\nu_{bv})+P_{c1}]/2$$

$$\sigma_H > [\sigma_{zo}+\sigma_D(3\text{-}2\nu_{bv})+P_{c1}]/2$$

7- Elimination of Inadmissible Stresses

In the $\sigma_\theta\text{-}\sigma_z$ plane, the stresses after drilling and before test must not exceed stress condition at failure.

From failure criterion, calculate the maximum permissible stress

$$\sigma_{\theta,\,per} = \sigma_z + \sqrt{[m_{III}\,\sigma_{ch}\,\sigma_z + \sigma_{ch}^2]}$$

$$= \sigma_{zo}\text{-}2\nu_{bv}(\sigma_H\text{-}\sigma_b) + \sqrt{[m_{III}\,\sigma_{ch}\{\sigma_{zo}\text{-}2\nu_{bv}(\sigma_H\text{-}\sigma_b)\}+\sigma_{ch}^2]}$$

$$\sigma_\theta = 3\sigma_h\text{-}\sigma_H < \sigma_{\theta,\,per}$$

$$\sigma_h < (\sigma_{\theta,\,per} + \sigma_D)/2$$

Similarly,

$$\sigma_H < (\sigma_{\theta,\,per} + 3\sigma_D)/2$$

Note :

BCT — Biaxial comp.-tension
TCCT — Triaxial comp.-comp.-tension
TC — Triaxial compression
VCS — Vertically cored sample
HCS — Horizontally cored sample
UC — Uniaxial compression
DT — Direct tension
- - — Horizontal direction
Th, Tv — Tensile strength in Hl. and Vl. direction, respectively
σ_{ch}, σ_{cv} — Uniaxial compressive strength in Hl. and Vl. direction, respectively
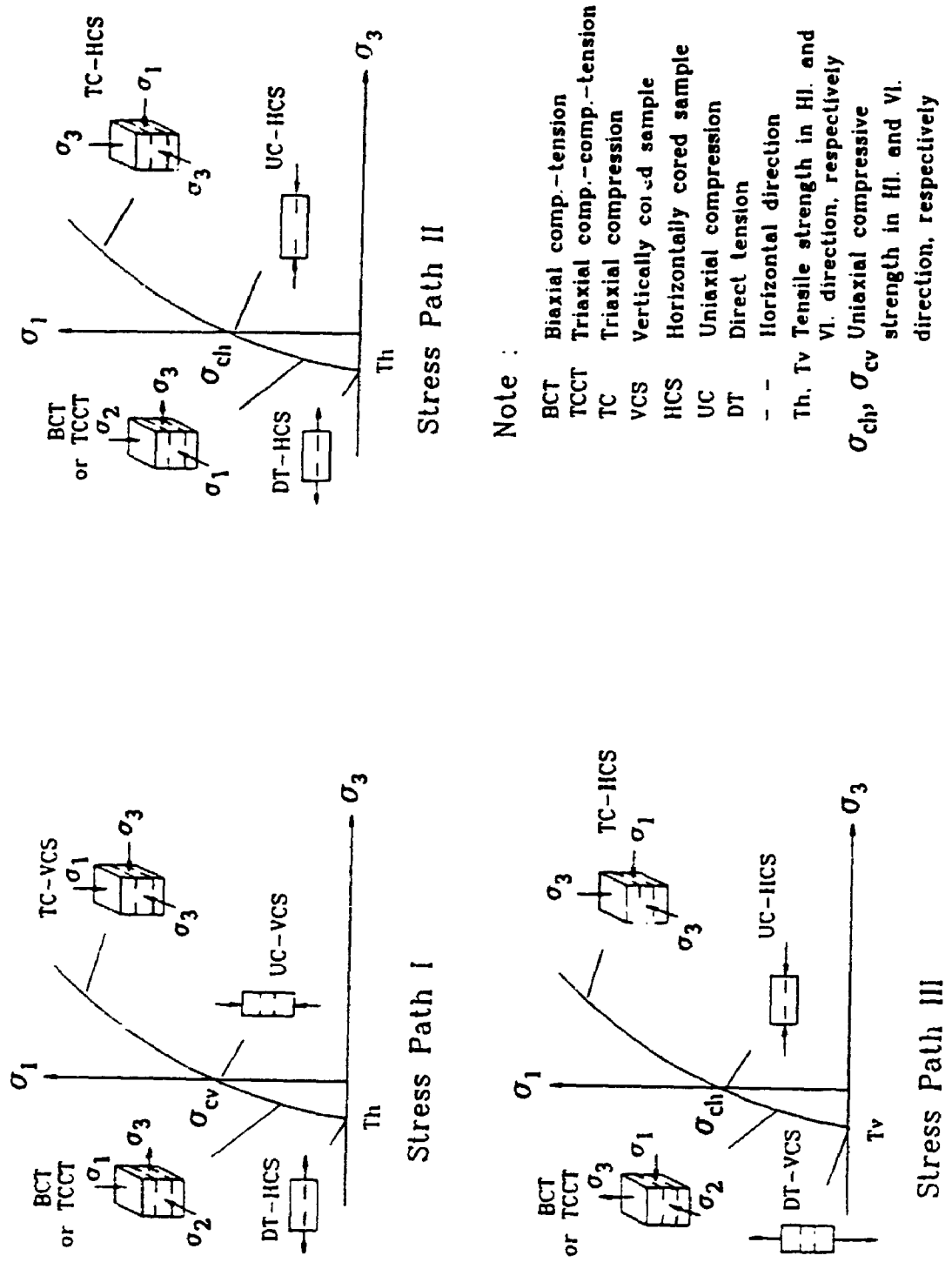
Figure 3.4 Tests required to determine the failure envelopes representing the strength anisotropy of the rock for the different stress paths
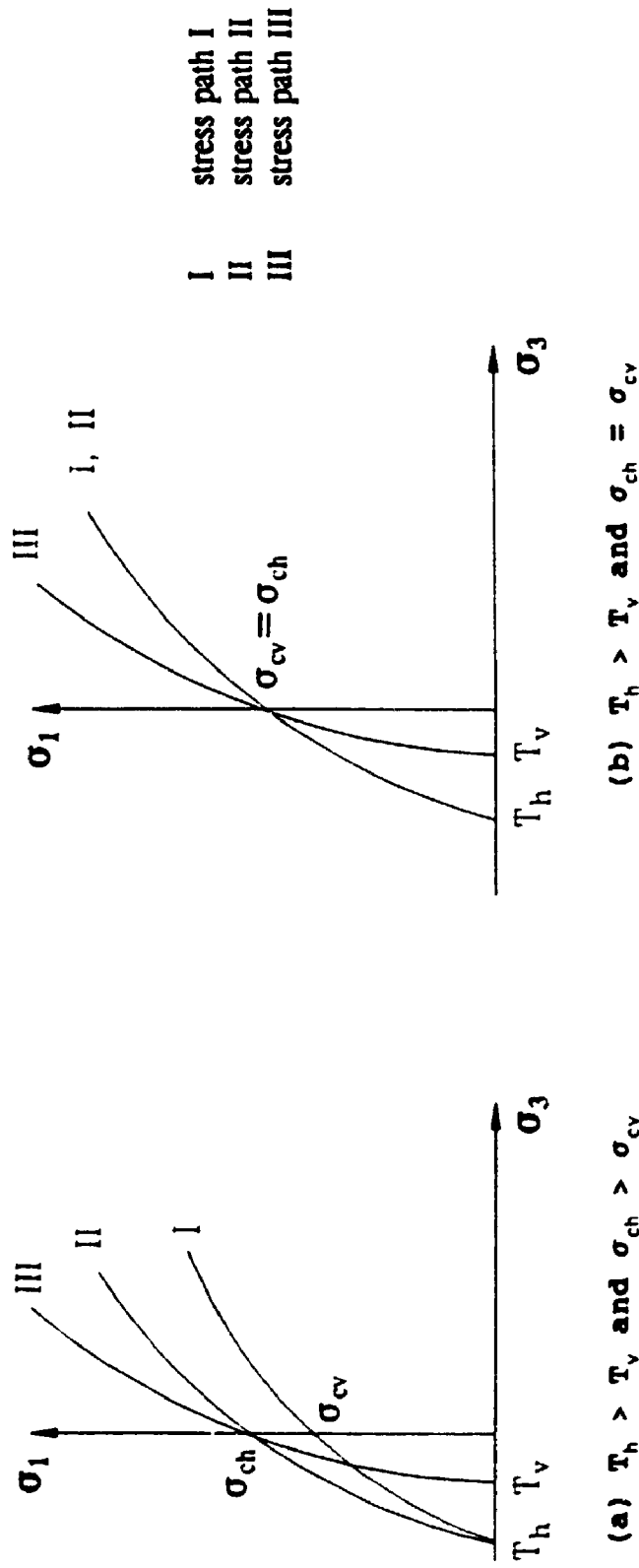
Figure 3.5 Modified Hoek and Brown failure envelopes in terms of strength parameters required to represent the different stress paths in hydraulic fracturing tests
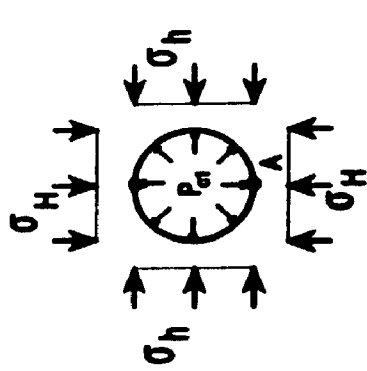
Figure 3.6 Parameters for modified Hoek and Brown failure criterion for anisotropic rocks

Stress Path I

$\sigma_z > \sigma_r > \sigma_\theta$, $\sigma_\theta < 0$

$\sigma_z = \sigma_\theta + \sqrt{(m_{I}\,\sigma_{cv}\,\sigma_\theta + \sigma_{cv}^2)}$
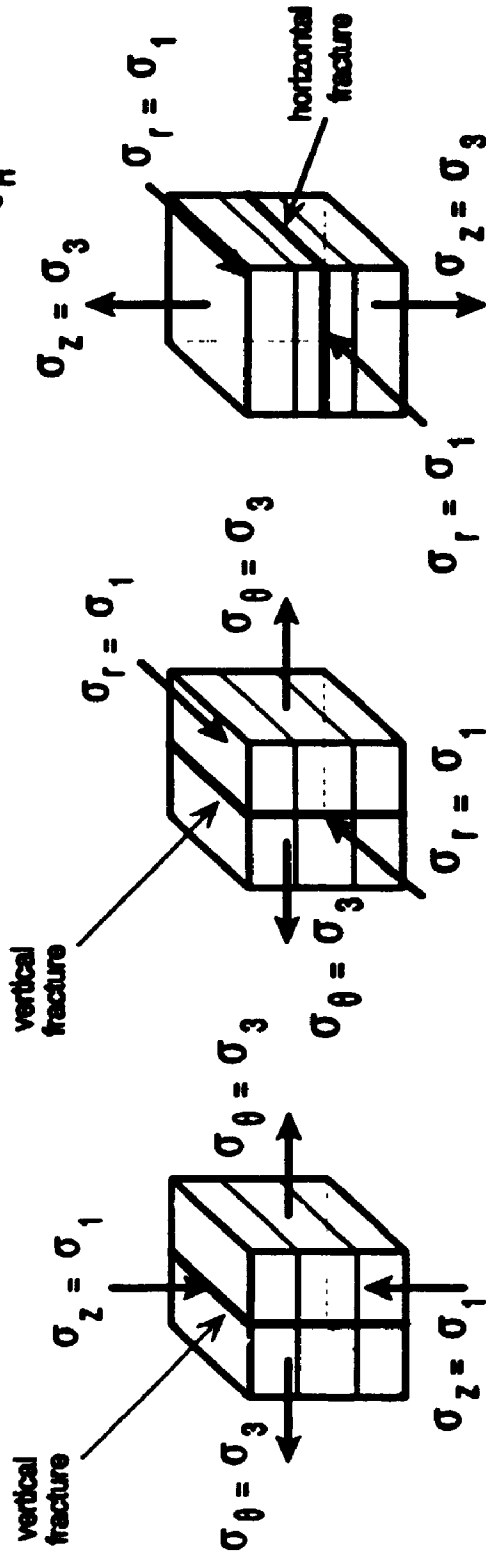
$m_{I} = \dfrac{\sigma_{cv}}{T_h} - \dfrac{T_h}{\sigma_{cv}}$

Stress Path II

$\sigma_r > \sigma_z > \sigma_\theta$, $\sigma_\theta < 0$

$\sigma_r = \sigma_\theta + \sqrt{(m_{II}\,\sigma_{ch}\,\sigma_\theta + \sigma_{ch}^2)}$

$m_{II} = \dfrac{\sigma_{ch}}{T_h} - \dfrac{T_h}{\sigma_{ch}}$

Stress Path III

$\sigma_r > \sigma_\theta > \sigma_z$, $\sigma_z < 0$

$\sigma_r = \sigma_z + \sqrt{(m_{III}\,\sigma_{ch}\,\sigma_z + \sigma_{ch}^2)}$

$m_{III} = \dfrac{\sigma_{ch}}{T_v} - \dfrac{T_v}{\sigma_{ch}}$

CHAPTER 4

APPLICATION OF THE MSP METHOD TO CASE HISTORIES

4.1 INTRODUCTION

In Chapter 3, the proposed MSP method, to calculate the state of stress when horizontal or mixed-mode fractures are encountered, has been developed. In this Chapter, three case histories of stress measurements by hydraulic fracturing tests will be reanalyzed using the MSP method. The first case history illustrates the ability of the MSP method to delineate the first fracture at first breakdown when mixed-mode fractures are recorded on the wall of the borehole by packer impression. The second and third case histories show the effectiveness of the MSP method in reducing the calculated range of maximum and minimum horizontal stresses by eliminating the inadmissible stress ranges. The third case history shows that the use of the MSP method in the analysis of horizontal fractures yields reliable stress values consistent with other stress measurements and field performance of underground structures.

The use of the MSP method in the case of anisotropic rocks will be presented in Chapter 5 where the *in situ* stresses in Queenston Shale at the Sir Adam Beck Niagara Generating Station No. 3 site are estimated.

4.2 CASE HISTORY 1 - DARLINGTON GENERATING STATION

The Darlington Generating Station is a nuclear generating facility located approximately 60 km east of the city of Toronto. For the design of the Cold Water Intake and Discharge Tunnels, both the USBM overcoring method and the

hydrofracturing method were used to determine the *in situ* state of stress. A total of ten hydrofracturing tests were conducted in a deep borehole (UN1) (Haimson 1978b). Figure 4.1 displays the borehole stratigraphy and hydrofracture test depths. Figure 4.2 shows the results of initial stress measurements obtained from the USBM overcoring method and the hydraulic fracturing method. The design envelopes suggested by Lo and Lukajic (1984) are also shown in Figure 4.2. It is clear from depths where both the USBM overcoring method and the hydrofracturing method were conducted that the hydrofracturing test results, calculated by Haimson (1978b) using the conventional method, are in good agreement with the USBM overcoring results.

Five of the ten hydrofracturing tests produced unambiguous vertical fractures, and four tests developed mixed-mode fractures. Only one test initiated an unambiguous horizontal fracture. Figure 4.3 shows the packer impressions for some of these tests (Haimson 1978b). The calculation of the initial stresses were done only for the tests that produced vertical fractures or mixed-mode fractures. Therefore, nine tests were used in the computations. The data for the test where an unambiguous horizontal fracture was formed, UN1-1, are not available and they were not included by Haimson in his report to Ontario Hydro. The conventional method was used in the analysis of the nine tests, although this method is suitable only for unambiguous vertical fractures. The use of the conventional method for the combined fractures implies that it was assumed that the vertical fractures were initiated by the first breakdown pressures and before the horizontal fractures. The calculated values would be erroneous if the horizontal fractures were initiated before the vertical fractures.

The measurements are reinterpreted using the proposed MSP method. The field

tensile strengths obtained from the hydrofracturing tests (as the difference between the first breakdown pressure and the reopening pressure, Eq. 2.9) are used in the analysis, as used by Haimson in 1978, so that stresses calculated may be compared. The uniaxial compression strength and Poisson's ratio for the Verulum Shaly Limestone, the Gull River Limestone, and the Granitic Gneiss were reported by Lo (1978), while the uniaxial compression strength and Poisson's ratio for the Lindsay Limestone were obtained by Lo (1981). The strength parameters for the Bobcaygeon Limestone are not available. Only one hydraulic fracture test was conducted in that rock layer, refer to Figure 4.1. In the calculations for that test, it is assumed that this rock has the same strength parameters as those for the Lindsay Limestone. Table 4.1 shows a comparison between initial stresses obtained by the MSP method and those obtained by Haimson (1978b) and reported in Haimson and Lee (1980) using the conventional method in terms of effective stress (Eq. 2.12). Table 4.2 shows a comparison between the stress values calculated by the MSP method and the conventional method in terms of total stress (Eq. 2.7).

From Table 4.2, the following observations may be made:

(a)   Using the MSP method, it is found that the four tests with mixed-mode fractures satisfy Stress Path II. Stress Path II is for vertical fractures. This indicates that the vertical fracture is formed with first breakdown pressure and before the horizontal fractures occurred.

(b)   The assumption that the vertical fracture was initiated with the first breakdown pressure before the horizontal fracture is correct for these tests. It should be noted that in other case histories to be presented in the next chapter, horizontal fracture occurs first in mixed-mode fracture, according to the MSP method analysis.

(c)   The results of stresses computed by the MSP method agree closely with those determined by the USBM method as reported by Lo and Lukajic (1984) (see Figure 4.2 for USBM result, Test OH2-3).

Sample calculations for the MSP method are shown in Appendix 4A, using results of Test UN1-3 with mixed-mode fractures. The calculated stress paths are shown in Figure 4.4. It is clear from Figure 4.4 that only stress path II reaches the failure envelope Therefore, the vertical fracture occurs first in the mixed-mode fractures and the stresses may be calculated accordingly by equations corresponding to stress path II in Table 2.1.

From Tables 4.1 and 4.2, it may be observed that for shallow depths both the effective stress principle and total stress principle yields almost the same results which are in agreement with the USBM results. This occurs because for shallow depths the pore water pressure represents only a small fraction of the calculated stresses. On the other hand, for deep depths, the maximum horizontal stresses are higher than those calculated using the effective stress principle. The USBM method was not conducted at these deep locations. This emphasizes the importance of deciding which equations should be used in estimating the *in situ* horizontal stresses.

4.3   CASE HISTORY 2 - *IN SITU* STRESS AT LAVIA IN FINLAND

In 1985, hydraulic fracturing stress measurements were conducted down to a depth of 500 m in a vertical borehole in Precambrian Granodiorite at Lavia in Finland (Ljunggren and Amadi 1989). Vertical fractures were found in only seven tests of 23 tests performed. The majority of the tests showed horizontal or subhorizontal fractures.

The stresses reported in the rock are shown in Tables 4.3 and 4.4. The use of Ljunggren and Amadei's method yielded a large stress range of both the maximum and minimum horizontal stresses. This calculated stress range was in the order of 20 MPa in most tests when the laboratory tensile strength, obtained from hydrofracturing tests on core specimens, was used in the analysis. The calculated stress range was about 15 MPa in most tests when the field tensile strength was used in the analysis. It is difficult to use results with such a wide range of values in design.

Using the data from Ljunggren and Amadei (1989), the results of hydrofracturing tests in which horizontal fractures were encountered are reanalyzed by the MSP method. Table 4.3 shows a comparison between the results obtained by Ljunggren and Amadi and those obtained by the MSP method, using the tensile strengths obtained from the laboratory. Table 4.4 gives a similar comparison for stresses calculated using the field hydrofracturing tensile strength. From Tables 4.3 and 4.4, it is clear that stress ranges determined have been considerably reduced by the MSP method. The reduction is from about 20 MPa to about 6 MPa, in the case of using the laboratory tensile strength, and from about 15 MPa to about 2 MPa for the case of using the field tensile strength. For example, the stress range obtained by Ljunggren and Amadei for the test at depth 116.5 m was 13 MPa (Table 4.4) whereas that obtained by using the MSP method is only 2.4 MPa.

4.4 CASE HISTORY 3 - *IN SITU* STRESS AT THE AECL UNDERGROUND RESEARCH LABORATORY, MANITOBA

To examine further the applicability of the proposed MSP method in estimating the initial state of stress from horizontal hydrofractures, the hydraulic fracturing test data at the AECL Underground Research Laboratory in Manitoba, (Martin 1990) are reanalyzed in this section.

The hydraulic fracturing technique was one of several methods used to determine the state of stress surrounding the AECL Underground Research Laboratory (URL) access shaft (Martin 1990). For relatively shallow depths, where the induced fractures were subvertical, the conventional method was used in the analysis. The results obtained are in good agreement with those obtained from the USBM overcoring method. However, at greater depth below Fracture Zone 2, the conventional method could not be used to analyze the hydrofracturing test data because the induced fractures in both test holes (URL6 and PH1) were subhorizontal. The method of Ljunggren and Amadei (1989) was employed to compute the stresses and the calculated values of the maximum horizontal stresses presented by Martin (1990) are shown in Figure 4.5. The ranges of the horizontal stresses determined were large, in the order of 30 MPa (the magnitude generally varying from 80 to 110 MPa). In addition, these values were considerably higher than those determined from convergence measurements which were carefully performed. If the values computed by this method were true, it would suggest that the horizontal excavation at the 420 level should experience extreme stability problems (Martin 1990).

Using the parameters obtained from a comprehensive laboratory testing program

and published by Martin (1990), the results of hydrofracturing tests in which horizontal fractures were encountered are reanalyzed by the MSP method. Table 4.5 shows the values of the horizontal stresses calculated before and after applying the proposed reduction technique. It is clear that after eliminating the inadmissible stresses, the stress range decreases from around 30 MPa to 2 MPa. The horizontal stresses determined using the MSP method and those calculated from convergence measurements are compared in Figure 4.6. It is clear that the results from both methods agree well from the 391 to 428 levels. More detailed examination of the results follows.

Referring to Figure 4.6, during the excavation of the shaft below Fracture Zone 2, failure of the wall was noticed and continued until the excavation reached Fracture Zone 1.9. This failure resulted in a V-shaped notch to a depth of 0.4 m beyond the excavation design perimeter. The development of the sidewall V-shaped notches was also observed at depths between 340 and 350 m. In addition, a horizontal excavation performed at the 420 level experienced crown spalling and the formation of V-shaped notches in the crown.

With this information, it is possible to compare the stability conditions as implied by the reinterpreted stresses with the field observations of the shaft and horizontal excavation.

Using the horizontal stresses determined (Table 4.5), the maximum stresses may be computed at appropriate depths to be compared with the uniaxial compressive strength. The uniaxial compressive strength of the grey granite ranges between 147 and 198 MPa with a mean value of 167 MPa.

The maximum compressive tangential stress on the wall of the shaft obtained from

test at depth 336.6 m ranges between 204 to 210 MPa. Comparing this value with the values of the uniaxial compressive strength of the rock, failure of the shaft wall around this depth is predicted. The depth of failure is also consistent with the theoretical value of 0.6 m from elastic solution.

At depths between 391 and 428 m, the maximum compressive tangential stress calculated from the corresponding tests ranges between 165 to 177 MPa suggesting that the rock at these locations is close to failure. This is in agreement with field observation that no local instability was reported.

At a horizontal excavation at the 420 level, the tangential stress at the crown was calculated using the lithostatic stress and the maximum horizontal stress obtained from the nearest hydraulic fracturing test at depth 425.1 m. The value obtained ranges between 192 to 200 MPa suggesting that the horizontal excavation at the 420 level would experience some crown spalling. This prediction is consistent with field observation that crown spalling and formation of V-shaped notches in the crown occurred.

It is evident, therefore, that the reinterpreted stresses are comparable not only to those deduced from the results of convergence measurements but are also consistent with field observations.

4.5   CONCLUSIONS

A method of analysis of hydraulic fracturing test dealing with different modes of fractures has been developed (Chapter 3). The method deals with horizontal and vertical fractures as well as mixed-mode fractures and takes into account strength anisotropy, where appropriate. The method includes the following features:

(a)   For vertical fractures, the determined stresses are essentially identical to the conventional maximum tensile stress theory.

(b)   For horizontal fractures, the range of horizontal stresses computed is much reduced so that the stresses determined are appropriate for engineering design.

(c)   For mixed-mode fractures, the method follows the stress paths during the test and determines whether the horizontal or the vertical fracture occurs first, so that appropriate stress calculations may be carried out.

Results of hydraulic fracturing tests in three case histories have been reanalyzed by the MSP method. From the results of the analyses, the following conclusions may be drawn:

(1)   For vertical, horizontal, or a combination of vertical and horizontal fractures, the method developed delineates the relevant stress path of the hydraulic fracturing tests from which the rock stresses may be determined. For mixed-mode fractures, it is possible to determine whether the vertical or the horizontal fracture occurs at the first breakdown pressure so that the stresses may be computed using the appropriate solution without uncertainty.

(2)   Application of the MSP method to the analysis of test data reduces considerably the stress range computed, to the extent that they are adequate for engineering purposes.

(3)   The reinterpreted horizontal stresses in the AECL Underground Research Laboratory are not only consistent with results deduced from convergence measurements but are also consistent with field observations of excavation performance.

The method of analysis presented is, therefore, of value for the determination of rock stresses in hydraulic fracturing tests for the design of underground structures in rocks.

TABLE 4.1   Comparison between values of initial horizontal stresses at the Darlington G.S. site, calculated by the conventional method and by the MSP method ("effective stress" analysis)

Test No.	El. (m)	Depth (m)	Min. H. Stress (MPa)	Max. H. Stress (MPa)		Fracture Mode	Stress Path
				MTS (Haimson and Lee 1980)	MSP		
UN1-2	37.3	74.7	9.27	13.96	13.38	HV	II
UN1-3	10.5	101.5	6.52	10.63	10.08	HV	II
UN1-10	-31.6	143.6	9.47	15.37	15.04	HV	II
UN1-9	-72.0	184.0	8.29	12.16	11.94	HV	II
UN1-4	-95.4	207.4	8.87	12.33	11.73	V	II
UN1-5	-116.0	228.0	10.52	17.22	17.20	V	II
UN1-6	-141.6	253.6	11.20	19.64	19.60	V	II
UN1-7	-164.0	276.0	10.62	18.34	18.32	V	II
UN1-8	-187.5	299.5	11.34	18.30	18.26	V	II

Note: MSP   Modified stress path method
        V   Vertical fracture
        HV   Mixed-mode fractures (horizontal and vertical)

TABLE 4.2 Comparison between values of initial horizontal stresses at the Darlington G.S. site, calculated by the conventional method and the MSP method ("total stress" analysis)

Test No.	El. (m)	Depth (m)	Min. H. Stress (MPa)	Max. H. Stress (MPa)		Fracture Mode	Stress Path
				MTS	MSP		
UN1-2	37.3	74.7	9.27	14.54	13.93	HV	II
UN1-3	10.5	101.5	6.52	11.49	10.89	HV	II
UN1-10	-31.6	143.6	9.47	16.65	16.27	HV	II
UN1-9	-72.0	184.0	8.29	13.82	13.54	HV	II
UN1-4	-95.4	207.4	8.87	14.23	13.54	V	II
UN1-5	-116.0	228.0	10.52	19.32	19.30	V	II
UN1-6	-141.6	253.6	11.20	21.98	21.96	V	II
UN1-7	-164.0	276.0	10.62	20.89	20.86	V	II
UN1-8	-187.5	299.5	11.34	21.09	21.04	V	II

Note:

MSP	Modified stress path method
V	Vertical fracture
HV	Mixed-mode fractures (horizontal and vertical fractures)
MTS	Conventional method (maximum tensile stress theory)

TABLE 4.3   Comparison between results of initial horizontal stresses, at Lavia in Finland, calculated by Ljunggren and Amadei (1989) and by the MSP method (using laboratory tensile strength)

Depth (m)	P_{cl} (MPa)	P_a (MPa)	T(lab) (MPa)	Ljunggren and Amadei 1989, Table 4		MSP	
				σ_a (MPa)	σ_H (MPa)	σ_a (MPa)	σ_H (MPa)
116.5	21.1	5.3	8.2	18.0-32.5	40.6-55.0	18.0-21.9	40.6-44.5
119.8	20.0	5.5	8.2	17.6-31.5	40.6-54.5	17.6-21.5	40.6-44.5
127.3	21.1	5.7	8.2	18.3-32.7	41.6-56.1	18.3-22.2	41.6-45.5
130.7	21.7	6.8	8.2	19.5-34.3	44.7-59.5	19.5-23.4	44.7-48.6
133.8	19.6	6.5	8.2	18.3-32.0	43.0-56.8	18.3-22.2	43.0-47.0
291.6	27.5	7.8	13.7	25.0-45.0	60.1-80.1	25.0-31.3	60.1-66.4
293.0	27.6	8.6	13.7	25.7-45.8	62.2-82.2	25.7-32.0	62.2-68.5
294.6	28.3	7.5	13.7	25.1-45.5	59.6-80.0	25.1-31.4	59.6-65.9
297.5	23.1	8.6	13.7	23.6-41.5	60.5-78.5	23.6-30.0	60.5-66.9
309.1	28.8	8.4	13.7	26.2-46.8	62.2-82.8	26.2-32.4	62.2-68.3
362.3	24.5	10.3	13.7	25.7-44.4	65.4-84.0	25.7-32.1	65.4-71.8
370.0	18.8	9.8	13.7	22.6-38.5	62.0-77.9	22.6-29.1	62.0-68.4
373.2	27.3	10.2	13.7	27.0-46.9	66.2-86.1	27.0-33.3	66.2-72.5
391.7	18.8	8.9	13.7	21.8-37.7	59.6-75.5	21.8-28.3	59.6-66.1
396.8	25.8	10.7	13.7	26.7-45.9	66.9-86.1	26.7-33.0	66.9-73.3

Note:
* The value of Poisson's ratio is 0.29
* σ_{∞} is taken equal to the value of P_a
* T   is the value of tensile strength extrapolated from laboratory measured tensile strength

TABLE 4.4   Comparison between results of initial horizontal stresses, at Lavia in Finland, calculated by Ljunggren and Amadei (1989) and by the MSP method. (using field tensile strength)

Depth (m)	P_{cl} (MPa)	P_s (MPa)	T(field) (MPa)	Ljunggren and Amadei 1989, Table 2		MSP	
				σ_a (MPa)	σ_H (MPa)	σ_a (MPa)	σ_H (MPa)
116.5	21.1	5.3	5.1	16.9-29.9	34.5-47.5	16.9-19.4	34.5-36.9
119.8	20.0	5.5	5.1	16.6-29.0	34.5-47.0	16.6-19.0	34.5-37.0
127.8	21.1	5.7	5.1	17.2-30.2	35.5-48.5	17.2-19.7	35.5-38.0
130.7	21.7	6.8	5.1	18.5-31.8	38.6-51.9	18.5-20.9	38.6-41.1
133.8	19.6	6.5	5.1	17.2-29.4	36.9-49.1	17.2-19.7	36.9-39.4
291.6	27.5	7.8	5.1	22.2-38.4	43.9-60.1	22.2-24.6	43.9-46.3
293.0	27.6	8.6	5.1	23.0-39.2	46.1-62.2	23.0-25.3	46.1-48.4
294.6	28.3	7.5	5.1	22.4-38.9	43.5-60.1	22.4-24.7	43.5-45.9
297.5	23.1	8.6	5.1	20.7-34.7	43.9-57.9	20.7-23.2	43.9-46.4
309.1	28.8	8.4	5.1	23.4-40.1	46.1-62.9	23.4-25.8	46.1-48.5
362.3	24.5	10.3	5.1	22.9-37.5	49.0-63.7	22.9-25.3	49.0-51.4
370.0	18.8	9.8	5.1	19.6-31.5	45.0-56.9	19.6-22.1	45.0-47.5
373.2	27.3	10.2	5.1	24.1-40.2	50.0-66.1	24.2-26.6	50.0-52.4
391.7	18.8	8.9	5.1	18.9-30.7	42.8-54.6	18.9-21.3	42.8-45.2
396.8	25.8	10.7	5.1	23.9-39.2	50.7-66.0	23.9-26.3	50.7-53.1

Note:

* The value of Poisson's ratio is 0.29
* σ_{ao} is taken equal to the value of P_s
* T   is the value of the field tensile strength

TABLE 4.5 Values of initial horizontal stresses before and after applying the reduction technique (AECL Underground Research Laboratory)

BH No.	Depth (m)	P_{cl} (MPa)	P_s (MPa)	Before Reduction		After Reduction	
				σ_b (MPa)	σ_H (MPa)	σ_b (MPa)	σ_H (MPa)
	336.6	37.75	20.71	37.8-59.3	80.8-102.3	37.8-40.4	80.8-83.4
	390.8	40.14	14.77	34.1-56.7	67.1-89.7	34.1-36.6	67.1-69.6
PH1	391.8	52.55	13.93	39.5-68.2	70.7-99.4	39.5-41.9	70.7-73.1
	425.1	49.76	13.27	37.6-64.9	67.8-95.1	37.6-40.0	67.8-70.2
	427.6	53.28	13.28	39.3-68.3	69.4-98.5	39.3-41.7	69.4-71.8

Note: $\nu = 0.3$
$\sigma_c = 167$ MPa
m = 30.54
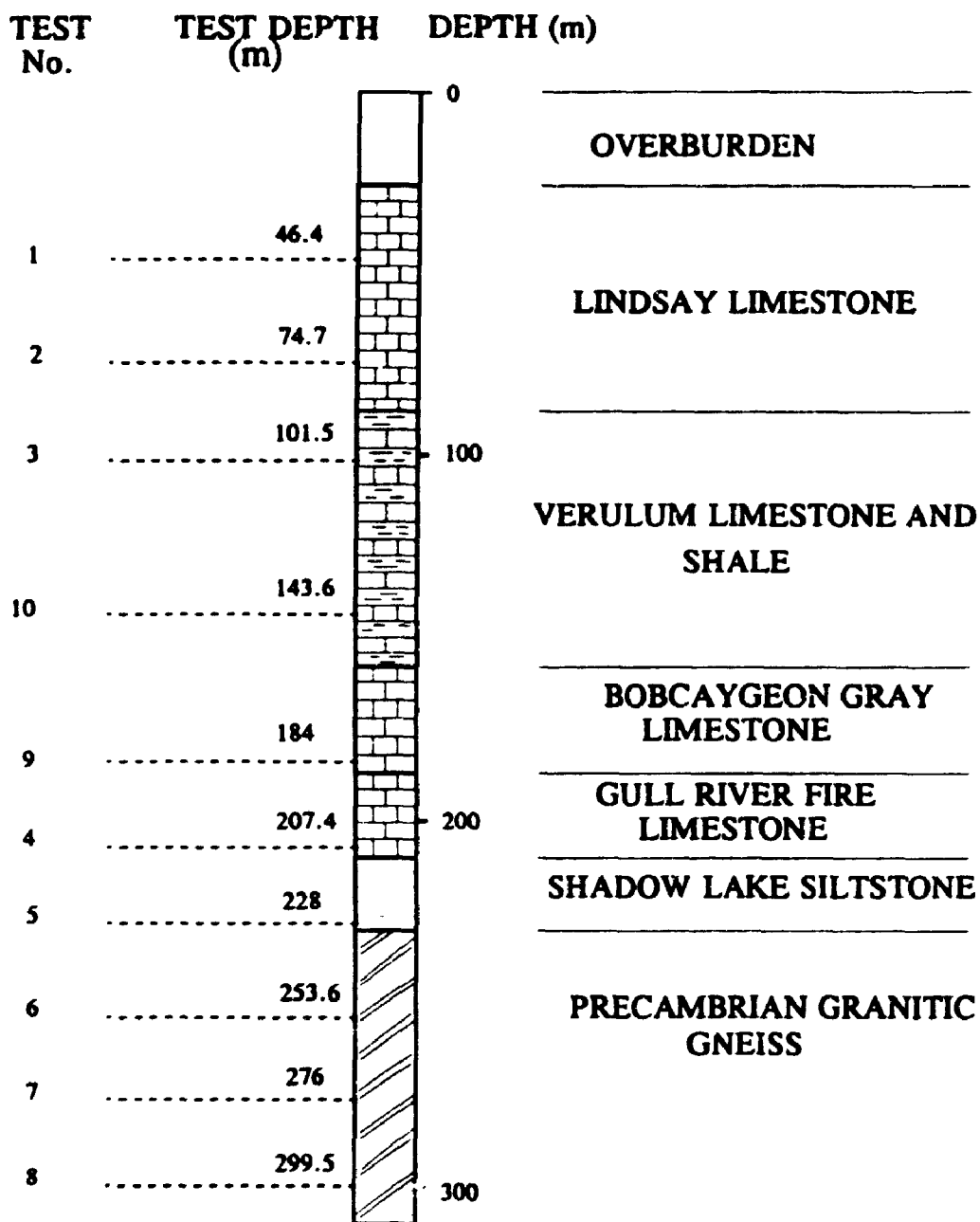
Figure 4.1 Borehole stratigraphy and hydraulic fracturing test depths
TEST HOLE UN-1 (DARLINGTON GENERATING STATION)
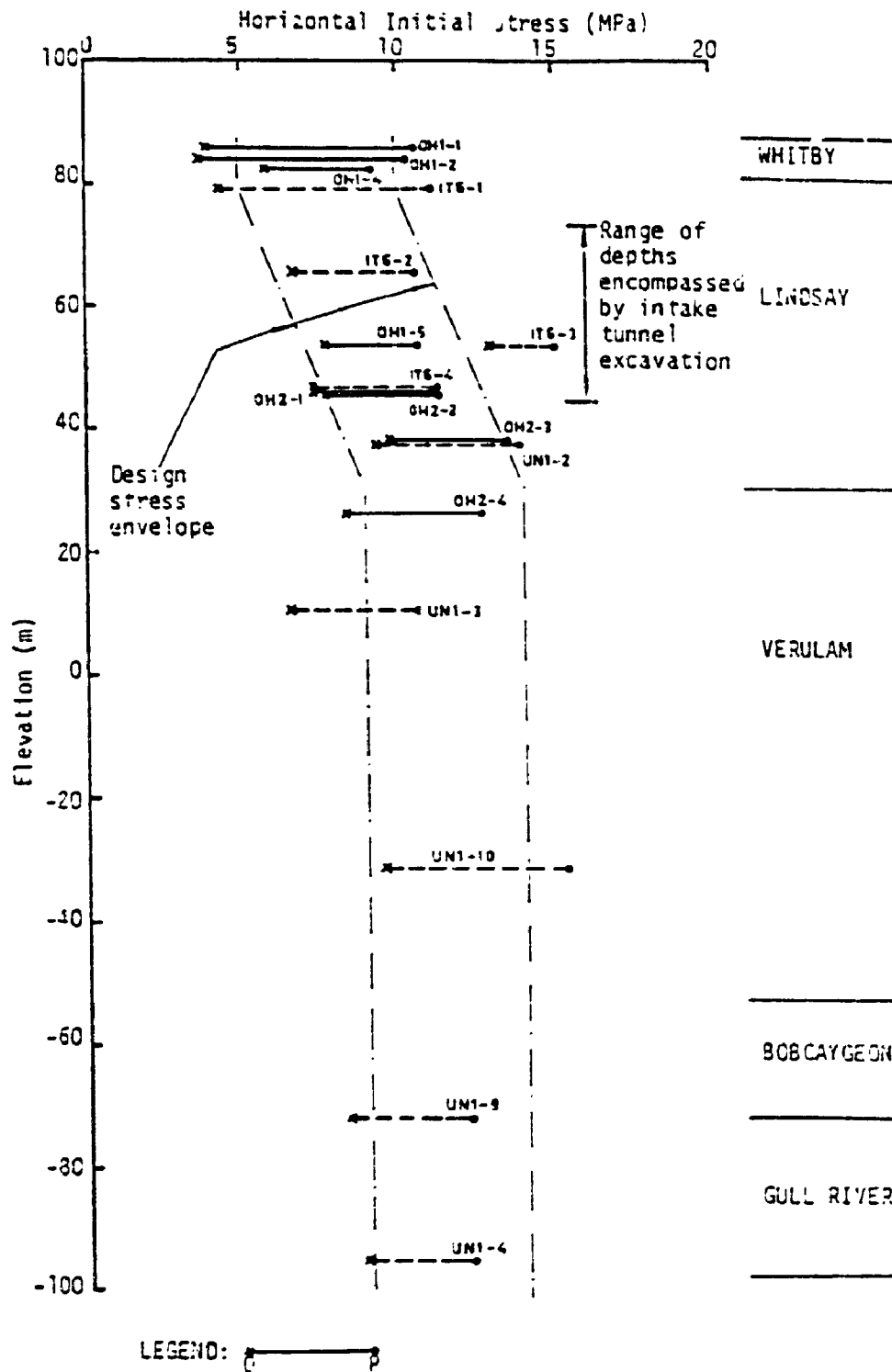
Figure 4.2   Initial stresses in the horizontal plane measured at the Darlington
Generating Station site
(borehole UN1-hydraulic fracturing stress measurements;
other boreholes-USBM deformation gauge)
(after Lo and Lukajic 1984)

| S | W | N | E | S |
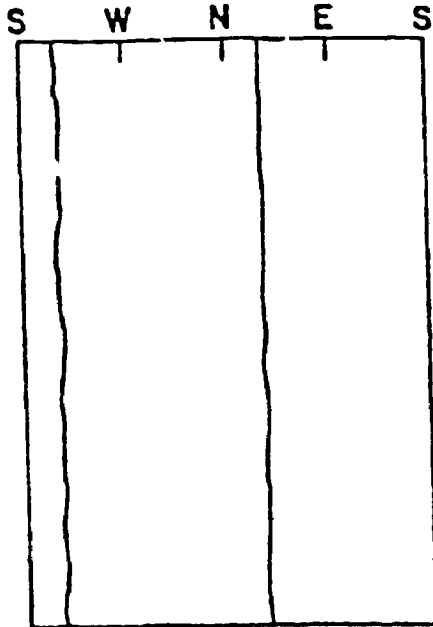
a- UN1/7
Vertical Fractures
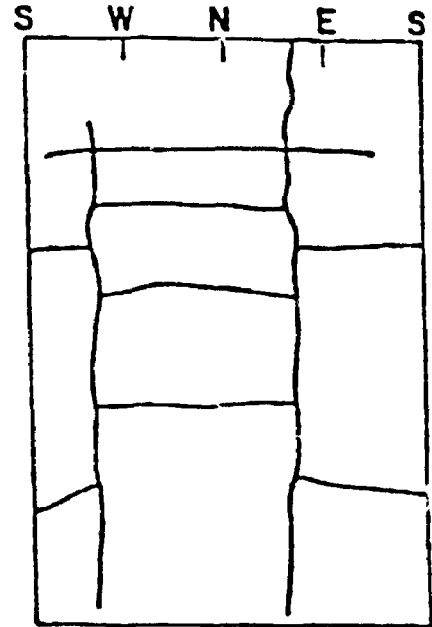
b- UN1/10
Mixed-Mode Fractures
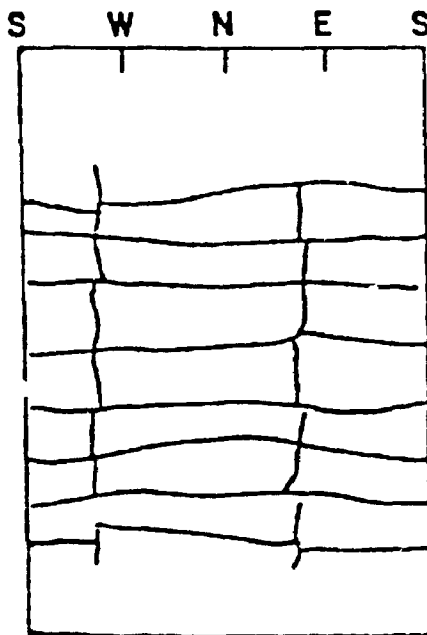
c- UN1/2
Mixed-Mode Fractures
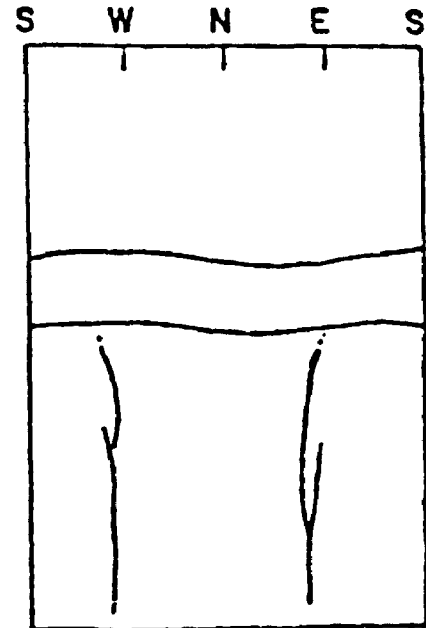
d- UN1/9
Mixed-Mode Fractures

Figure 4.3   Example of packer impressions (Darlinton G. S.): a- typical vertical fracture in Gneiss; b, c, and d- mixed mode fractures in Limestone (after Hamison 1978)
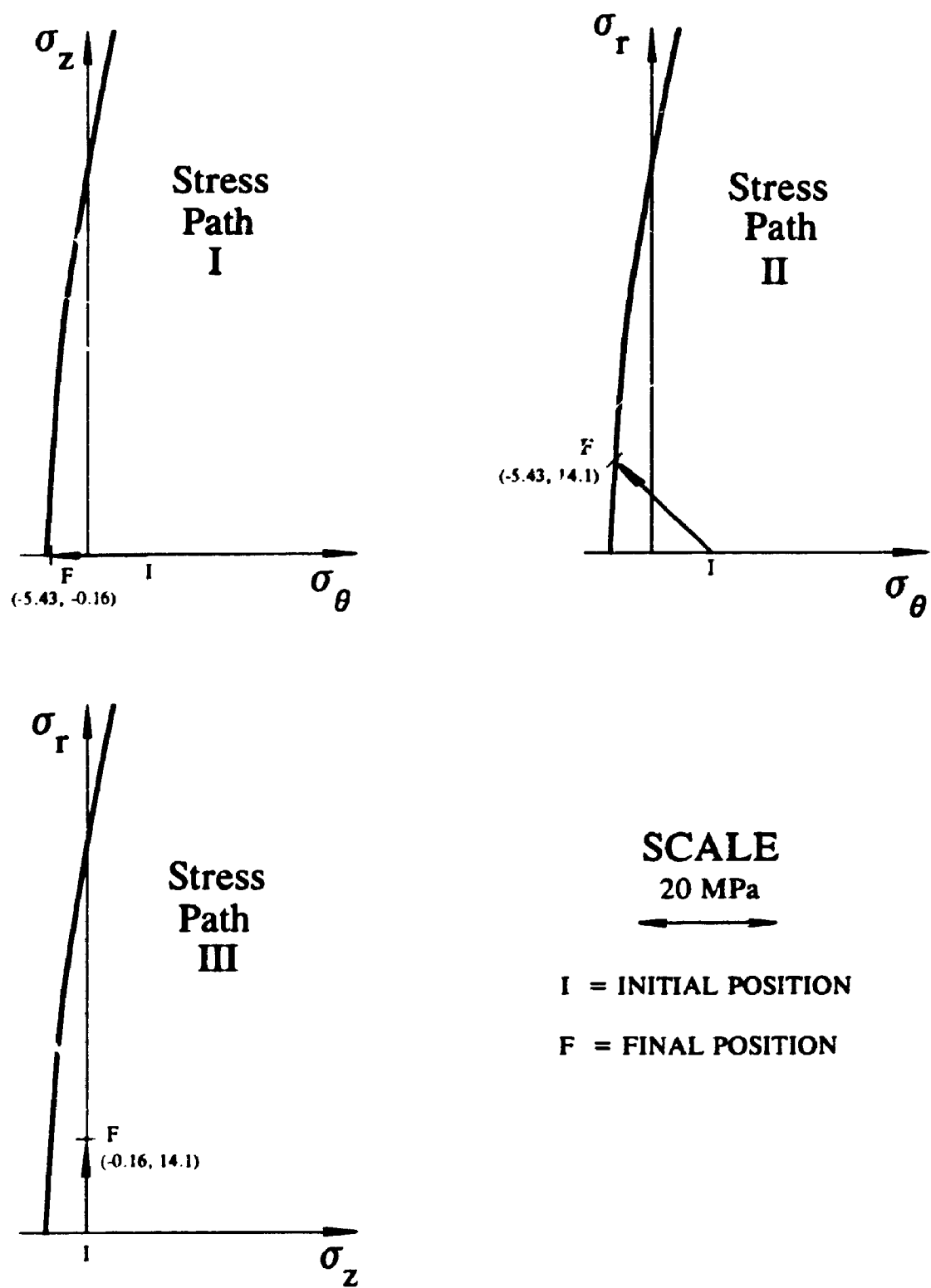
Figure 4.4 Different stress paths for Test UN1-3
(Darlington Generating Station)
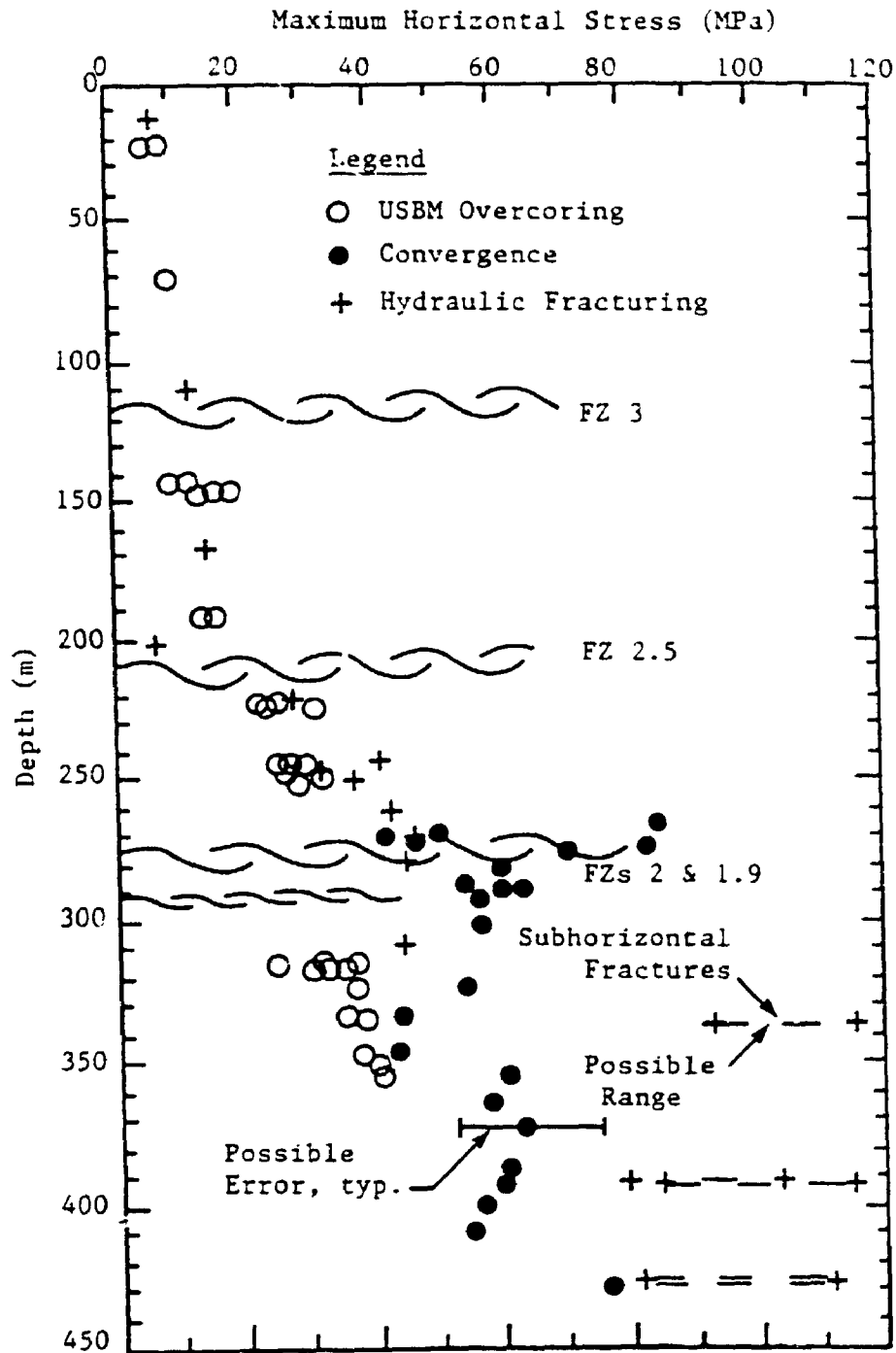
Figure 4.5   Maximum horizontal stress at the AECL Underground Research
Laboratory (after Martin 1990)
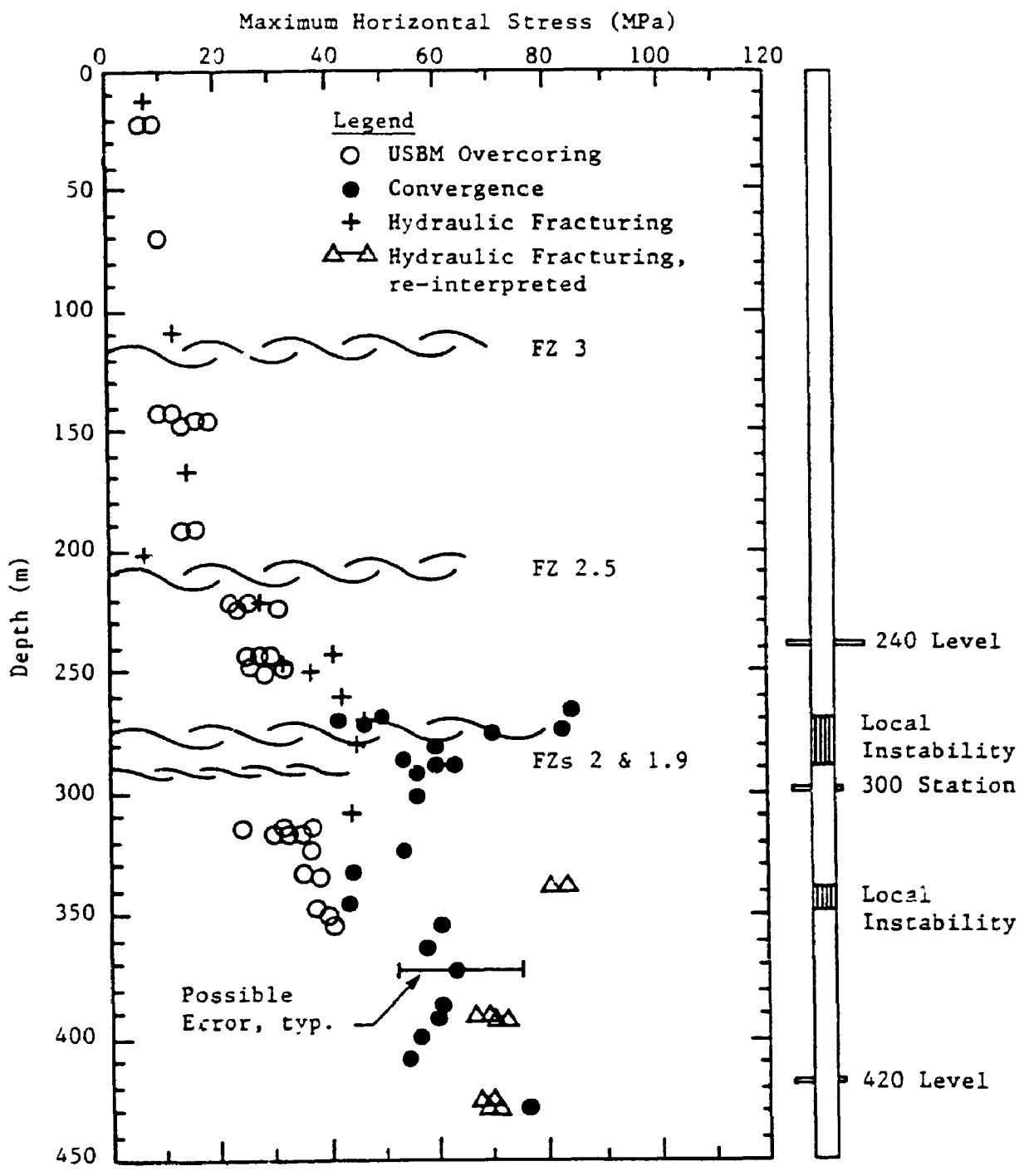
Figure 4.6　Maximum horizontal stress at the AECL Underground Research Laboratory (horizontal hydrofractures analyzed by the MSP method)

CHAPTER 5

EVALUATION OF THE INITIAL STATE OF STRESS

IN QUEENSTON SHALE AT SABNGS NO.3 SITE

5.1   INTRODUCTION

For the design of the Niagara Hydro Power Development project (NHPD), twin

tunnels, each of approximately 13 m diameter and 10 km long are required (Semec *et al.*

1986).   This project has also been referred to as Sir Adam Beck Niagara Generating

Station No.3 (SABNGS NO.3).   The tunnels will be mainly in Queenston Shale, a thinly-

bedded mudstone which exhibits important time-dependent deformation (Lo 1986; Lo and

Lee 1990).   In addition, the Powerhouse will be located underground, in the Queenston

Formation (Rigbey *et al.* 1992).

To determine the initial state of stress at the site, programs of hydraulic fracturing

tests were carried out in 1984, 1990, and 1992.

All the hydraulic fracturing tests conducted in 1984 and the majority of tests

conducted in 1990 and 1992 induced either horizontal or mixed-mode fractures (a

combination of horizontal and vertical frac.ures).   The ren... ing tests performed in 1990

and 1992 produced either vertical or subvertical fractures he ,acker impressions were

not taken.

The MSP method developed in Chapter 3 and presented by Hefny and Lo (1992a)

is adopted for stress determination in Queenston Shale since the method is capable of

analyzing horizontal and mixed-mode fractures.   This method takes into account tensile

strength anisotropy, a dominant characteristic of weakly bedded shales.

71

5.2   LOCATION AND GEOLOGY

The locations of the ten boreholes for hydraulic fracturing tests have been chosen so as to cover most of the area that will be occupied by the proposed diversion tunnels and powerhouse.   Figure 5.1 shows the location of the holes and the alignment of the proposed diversion tunnels.   Tests in boreholes NF3 and NF4 were conducted in 1984 by Haimson.   Tests in the other boreholes shown in the figure were carried out in 1990 and 1992 by Acres-Golder team.

The upstream segment of the diversion tunnels would start in an east-west direction from the edge of the Niagara River and extends inland in a curved path, Figure 5.1.   The tunnels at that part would be at a distance 0.6 Km or less from the Niagara River.   Two test boreholes, N..3 (1984) and NF32 (1990), are located along that proposed path.   The central segment of the tunnels would then run in a north-south direction and then change direction and cross under the buried St. Davids Gorge rising in a north-east direction to the outlet location.   Three boreholes, NF4 (1984), NF4A (1990), and NF28 (1990), are located along the north-south part of the proposed tunnels. In borehole SD6 stress measurements extended below the bottom of the gorge.   Stress measurements were also conducted in borehole NF30 located at the edge of the St. Davids Gorge.   One borehole, NF33, is located at the outlet of the proposed diversion tunnels.

In the area of generation facilities, the powerhouse complex would be located between the existing PGS reservoir and the Niagara River Gorge.   The penstock tunnels would extend from the headworks in the PGS reservoir in an East-West direction to an underground powerhouse oriented with its long axis approximately parallel to the river.

Stress measurements were performed in two boreholes, NF34 and NF35, in that area in 1990. In 1992, stress measurements were performed in borehole NF38 in the area of generation facilities near the Niagara River gorge, and in borehole NF31 which is more than half kilometre away from the gorge and lies between boreholes NF35 and NF33.

A detailed bedrock stratigraphy down to the Queenston shale, the deepest formation intersected by the holes, is given in Figure 5.2.

5.3   ANALYSIS OF TESTS PERFORMED IN 1984 INVESTIGATION

In 1984 investigation, a total of 7 tests were carried out within the Queenston Shale Formation (Semec et al. 1986; Haimson 1985). Four tests were conducted in borehole NF4 and three tests were conducted in borehole NF3. The test data are shown in columns (1) to (6) of Table 5.1. Figure 5.3 shows the packer impressions for the different tests in Queenston Shale except for test no. 18 which was not included by Haimson in his report to Ontario Hydro in 1985. It was stated, however, that the fracture was horizontal. It may be seen from Figure 5.3 that three tests (Test Nos. 5, 8 and 20) gave unambiguous horizontal fractures, while the remaining three tests yielded mixed-mode fractures. None of the seven tests yielded unambiguous vertical fractures. It is clear, therefore, that the "conventional" method, which deals with vertical fractures only, cannot be used in the analysis of any of these tests. However, Haimson calculated the values of the horizontal stresses in the rock from tests having mixed-mode fractures by assuming that the vertical fractures were initiated before the horizontal fractures by the first breakdown pressure. This assumption could lead to reasonable results if the vertical fractures were initiated before the horizontal fractures, as in the case of

Darlington Generating Station (Hefny and Lo 1992a). On the other hand, it could lead to unreliable results if the horizontal fractures occurred first (Lo and Hefny 1993). In the following sections, the MSP method which does not require this assumption is applied to calculate the initial state of stress in Queenston Shale.

5.3.1 Rock Parameters Used in Analysis

(a)   Tensile strength

If the tensile strength for the Queenston Shale is taken as the difference between the first breakdown pressure and the reopening pressure (columns 4 and 6, Table 5.1), the values would lie between 7.3 and 12.3 (Table 5.1), amounting to one third to one half the value of the uniaxial compressive strength. These values are considered to be very high and not representative. The values obtained in the laboratory from the splitting tensile strength test (Lee 1988) are used in the calculations. Two vertically oriented samples and one horizontally oriented sample were tested. The vertical samples failed across the bedding planes, while the horizontal specimen failed parallel to the bedding planes. The tensile strength for the horizontal direction (T_h) was found to be 4.6 MPa, while that in the vertical direction (T_v) was 3.4 MPa. The ratio of T_h/T_v is 1.35.

(b)   Uniaxial compressive strength

The value of the uniaxial compressive strength (σ_c) is obtained from 1987 investigation in borehole NF4A (Lee 1988) performed to study the behaviour of the Queenston Shale for the SABNGS NO.3 project. The values for the uniaxial

compressive strength in both the horizontal (σ_{ch}) and the vertical (σ_{cv}) directions were found to be 25 MPa.

(c)   The empirical constant (m)

Methods for the determination of strength parameters taking into account strength anisotropy in the modified Hoek and Brown failure criteria have been discussed in detail in Chapter 3 and by Hefny and Lo (1992a). From the uniaxial compressive strength and the tensile strength, the parameter "m", in the modified Hoek and Brown criteria may be determined (refer to Section 3.4 in Chapter 3). The values of "m" corresponding to the three stress paths (I, II, III) shown in Figure 5.4 are:

$$m_I = \frac{\sigma_{cv}}{T_h} - \frac{T_h}{\sigma_{cv}} \tag{5.1}$$

$$m_{II} = \frac{\sigma_{ch}}{T_h} - \frac{T_h}{\sigma_{ch}} \tag{5.2}$$

$$m_{III} = \frac{\sigma_{ch}}{T_v} - \frac{T_v}{\sigma_{cl.}} \tag{5.3}$$

For the case where $\sigma_{cv} = \sigma_{ch} = \sigma_c$, the value of m_I is equal to the value of m_{II} and is given by:

$$m_I = m_{II} = \frac{\sigma_c}{T_h} - \frac{T_h}{\sigma_c} \tag{5.4}$$

Substituting the values of σ_c, T_v and T_h in Eqs. 5.3 and 5.4, the values of "m" are found to be:

$$m_I = m_{II} = 5.25$$

and,

$$m_{III} = 7.22$$

(d) Poisson's ratio

Methods for the determination of deformation parameters in orthotropic elastic rock have been presented by Lo and Hori (1979). The relevant Poisson's ratio for the analysis of hydraulic fracturing tests is the Poisson's effect of horizontal stress on vertical strain, v_{hv}. The average value of v_{hv} from results of uniaxial compression tests was found to be 0.40.

5.3.2 Values of the Calculated Stresses

The results of stress computation for the seven tests using the MSP method are summarized in Table 5.1 (columns 9 and 12). For comparison, the stresses computed before the reduction of inadmissible stress state are also shown (columns 8 and 11). These latter values would correspond to the method of computation by Ljunggren and Amadei (1989). Values of stresses reported by Haimson (1985) are shown in columns (7) and (10) under the heading of maximum tensile stress theory (MTS).

In cases of having only horizontal fractures, the relations required to be satisfied for initiating such fractures are those for stress path III in Table 3.2. In the cases of mixed-mode fractures, it is not known which fracture occurred first. Therefore, substitutions in the equations of all the possible stress paths are required. Only one stress

path will satisfy the stress conditions defined by the failure envelope. This verified stress path indicates the type of fracture initiated by the first breakdown pressure before the other fractures occurred.

In all of the three tests where mixed-mode fractures occurred (NF4-6, NF4-7, and NF3-19, see Figure 5.3), computations show that only stress path III which is responsible for formation of horizontal hydrofracture is verified for each test. This observation indicates that the first breakdown pressures are responsible for initiating horizontal hydrofractures in all of the seven tests. As an example, the calculations required to check the different stress paths and to compute the state of stress from test NF4-6 are given in Appendix 5A. Figure 5.4 shows the different possible stress paths for test NF4-6. It is clear that stress path III is the only stress path that satisfies the failure criteria.

It may be seen from columns 8 and 9 (Table 5.1) that the ranges of the computed minimum horizontal stress σ_h for all the seven tests have been reduced from about 9 MPa to about 1 MPa. A similar observation may be made for the maximum horizontal stress (columns 11 and 12). It is evident, therefore, that the MSP method not only delineates the mechanism of failure in cases of mixed-mode fractures but also leads to narrow ranges for the maximum and minimum horizontal stresses computed. It is important to observe that the stresses calculated by the conventional method (column 7 in Table 5.1 and Figure 5.5) are much less than those calculated using the MSP method. Thus the arbitrary assumption that the first breakdown pressure initiates a vertical fracture first leads to stresses computed that are too low, which in turn may lead to unsafe design, if such stress values are adopted.

5.4   ANALYSIS OF TESTS PERFORMED IN 1990 INVESTIGATION

In addition to the seven tests that performed in 1984, a total of 39 tests in 8 boreholes were performed in Queenston Shale in 1990 investigation. The locations of the boreholes NF28, SD6, NF30, NF32, NF33, NF4A, NF34 and NF35 are shown in Figure 5.1. A variety of fractures were encountered in these tests, including unambiguous vertical fractures, unambiguous horizontal fractures, subvertical fractures, and mixed-mode fractures. The results of the hydraulic fracturing tests are analyzed using the MSP method.

5.4.1 Determination of Strength Parameters

To determine the strength parameters for the modified Hoek and Brown failure envelope, a test program was performed. The samples tested were recovered from depths below El. 40 m in borehole NF4A and below El. 110 m in borehole NF35(J1) and NF37(J2) corresponding generally to the depths where the majority of hydrofracturing tests were performed. The tests performed include triaxial compression tests, unconfined compression tests, direct tension and Brazilian tests. These tests were performed for both vertically and horizontally cored samples in order to determine the anisotropic parameters. A summary of the test requirements for the determination of strength parameters representing the different stress paths in the hydraulic fracturing tests was given in Figure 3.3. Figure 5.6 shows the results of the strength tests performed on the vertically cored samples. In this figure. the results of the Brazilian tests with tensile fracture across bedding planes are used to represent the tensile strength. Therefore, the results in this figure are relevant to stress path I. The variation of the results reveals the

effect of the shale content on the values of the strength parameters. Therefore, correlation between the shale content and the strength parameters governing the failure envelope is necessary. Figure 5.6 shows two failure envelopes. The upper curve could be represented by the following parameters:

σ_{cv} = 37 MPa

T_h = 4.2 MPa

m_I = 8.70

s = 1

These parameters were taken to represent the failure envelope for samples with shale content < 60 %. They represent the upper bound of parameters for the failure envelopes.

The lower envelope is taken to represent the failure for samples having shale content > 70%. This represents the lower bound of the strength parameters. The strength parameters values for this envelope are:

σ_{cv} = 12.5 MPa

T_h = 3.2 MPa

m_I = 3.65

s = 1

To obtain the parameters relevant to stress paths *II* and *III*, results of the tensile strength in the vertical direction (where failure is along the bedding planes) and the uniaxial compressive strength for horizontally cored samples should be considered.

Results of direct tension test showed that for samples of shale content less than 60%, the ratio of tensile strength normal and parallel to the bedding planes (T_h/T_v) equals to 4.2. This ratio is considered representative for the degree of tensile strength anisotropy for Queenston Shale.

The uniaxial compression tests for vertically and horizontally cored samples having the same shale content indicated that the uniaxial compressive strength in the vertical and horizontal directions are the same. However, because of the tensile strength anisotropy, the modified Hoek and Brown's criterion is anisotropic and Case (b) in Figure 3.4 appears.

Substituting the values of T_h, T_v, and σ_c into Eqs. 5.3 and 5.4, the values of "m" are found to be:

(a)   For shale content < 60%

$m_I = m_{II} = 8.7$

$m_{III} = 37$

(b)   For shale content > 70%

$m_I = m_{II} = 3.65$

$m_{III} = 16.4$

The value of Poisson's ratio for the effect of horizontal stress on vertical strain (ν_{hv}) is determined from the results of the uniaxial compression tests as 0.44.

The shale content in depths between El. 25 m and El. -20 m, where most of the hydraulic fracturing tests were performed in borehole NF4A, ranges between 30% to

70% and typically 60%. These values are also representative of the shale contents in range of depths where hydraulic fracturing tests were performed in borehole NF28. Therefore, the strength parameters obtained above for shale content ≤ 60% are used in the analysis of the hydraulic fracturing tests performed in these boreholes. The shale contents at depths between El. 85 m and El. 45 m, where all the hydraulic fracturing tests in the generating facilities area in boreholes NF34 and NF35 were performed, are generally higher than those along the tunnel alignment. Therefore, the strength parameters for shale content ≥ 70% are used in the analysis of hydraulic fracturing tests in the generation facilities area.

5.4.2 Discussion of Results

Typical results of the pressure-time and flow-time records of one of the hydraulic fracture tests are shown in Figure 5.7. The water was pumped at a constant flow rate of about 0.5 gal/min leading to increase in pressure in the test section. When a fracture was initiated, a sudden pressure drop occurred. Pumping was stopped and the pressure decay was monitored until a stable pressure was attained. The test cycle was then repeated.

Results of tests that are apparently unreliable, including: (a) those yielding unambiguous vertical fractures but giving negative maximum horizontal stress values, (b) those giving maximum horizontal stress less than the minimum horizontal stress (c) those giving reopening pressures higher than the first breakdown pressure, are discarded. These tests constitute about 30% of all the tests performed.

Table 5.2 summarizes the results of stress calculations using both the conventional

(MTS) method and the MSP method (columns 6 and 8; 7 and 9). It has been shown (Hefny and Lo 1992a) that the conventional method can be applied only for the analysis of vertical fractures, therefore only stress values obtained from vertical or mixed-mode hydrofractures that satisfy stress path I or II are shown in Table 5.2. It may be observed from Table 5.2, in cases of horizontal fractures or mixed-mode fractures which satisfied stress path III, that the ranges of the minimum and the maximum stresses calculated from each test are almost single values (the range is mostly 0.2 MPa). This is a direct result of MSP method which takes into account strength anisotropy and elimination of inadmissible stresses.

5.4.3   Regional Stress Regime at the Site (Central Part of the Proposed Tunnels)

Stress measurements conducted in boreholes along the straight North-South central portion of the tunnels, are in locations away from the existing topographic features. The initial stress values obtained from tests in these boreholes would be representative of the general initial stress regime at the site. These boreholes include NF4 (1984), NF4A (1990) and NF28 (1990), refer to Figure 5.1.

The distributions of maximum and minimum horizontal stresses (σ_H and σ_h, respectively) with elevation are shown in Figure 5.8. The vertical stress, σ_v, calculated as overburden pressure is also shown. From Figure 5.8 it may be observed that:

(i) The horizontal stresses in the rock are substantially higher than the vertical stress, as generally known in Southern Ontario.

(ii) The results of the 1984 tests, when correctly interpreted, agree well with the results of the 1990 investigations.

(iii) The computed ranges of stresses are very small, so that there is no difficulty of selection of values of σ_H and σ_h for design.

(iv) Both the maximum and minimum horizontal stresses increase approximately linearly with depth. The maximum horizontal stress increases from 14.5 MPa at El. 86 m to 24 MPa at El. -20 m. The minimum horizontal stress increases from 9 MPa at El. 86 m to 18 MPa at El. -20 m.

It should be noted that no impression packer test was performed in borehole NF4A. However, analyses of the results of hydraulic fracturing tests showed that the stress conditions at fracture for all the tests performed in NF4A satisfy only stress path III. This result indicates that the fractures induced by the first breakdown pressure are horizontal and is consistent with the mode of fracturing observed in borehole NF4 (see Table 5.1). It also illustrates the capability of the MSP method in the determination of stresses in the absence of any knowledge of the mode of fractures.

The value of the shut-in pressure in each test location where stress path III is satisfied (implying horizontal fractures) is taken as representative of the vertical stress at that location and the results are plotted in Figure 5.9. The solid line represents the overburden pressure distribution with depth. It may be observed that the vertical stress distributions with depth obtained from the hydraulic fracturing tests and the overburden pressures are comparable.

The direction of the regional maximum horizontal stress is calculated as the mean orientation of the vertical fractures obtained from impression packer tests that satisfied stress path II. The direction of the maximum horizontal stress in Queenston Shale is found to be in the northeast quadrant with a mean value of N65°E (Figure 5.10(a)). The

mean direction of the maximum horizontal stress in the Whirlpool layer overlying the Queenston shale is obtained from tests satisfied stress path II in the same boreholes and found to be N50°E. These directions are consistent with the orientations of the regional stresses previously measured in the Niagara Peninsula (Lo *et al.* 1979).

5.4.4 Horizontal Stresses at Other Locations of the Proposed Tunnels

(a) Downstream Part of the Tunnels

One borehole (NF33) is located at the outlet of the proposed diversion tunnels, and one successful test (test A2 at El. 18 m) was performed in this borehole. No packer impression was taken for this test. Application of the MSP method indicated that a horizontal fracture was initiated with the first breakdown pressure (only stress path III is satisfied). The maximum horizontal stress calculated from this test is 20.2-20.4 MPa and the minimum horizontal stress is 14.7-14.9 MPa. These values almost lie on the lines representing the regional horizontal stress distribution in Queenston Shale discussed in the previous section.

(b) Upstream Part of the Proposed Tunnels

Two test boreholes, NF3 and NF32, are located along the curved path of the upstream segment of the proposed diversion tunnels, Figure 5.1. The tunnels at that part would be at distance 0.6 Km or less from Niagara River. Results obtained from these two boreholes are shown in Figure 5.11. It may be seen that there is deviation from the general initial stress regime in Queenston Shale discussed in the previous section. In contrast to the trend of horizontal stress increasing with depth, both the maximum and

minimum horizontal stresses at the upstream portion of the proposed tunnels are constant with depth, down to El. 30 m. It is clear, also, that results of 1984 tests when properly interpreted and 1990 investigation are in good agreement. The representative value of the maximum horizontal stress is 15.8 MPa, while that of the minimum horizontal stress is 10.2 MPa. The ratio of the maximum to minimum horizontal stress is 1.6.

The maximum horizontal stress direction at this tunnel portion is determined as N65°E which is the same direction calculated for the maximum horizontal stress at the central portion of the tunnels.

(c)   Location of Borehole NF30 (Near the Edge of the Buried St. Davids Gorge)

Figure 5.12 shows the distribution of the maximum and minimum horizontal stresses, from tests performed in borehole NF30 near the edge of the buried St. Davids Gorge which is oriented northwest at this location. All the tests performed were below the bottom of the gorge. The distribution obtained is approximately constant with depth. This trend differs from that at the central portion of the tunnel and may be an indication of the effect of the proximity to the gorge on regional state of stress. From Figure 5.12, the representative value of the maximum horizontal stress is about 23 MPa and that of the minimum horizontal stress is about 13.5 MPa.

The direction of the maximum horizontal stress obtained at the test location is east-west, which is different from that obtained at the central portion of the tunnels (N65°E).

(d)   Location Below the Buried St. Davids Gorge (Borehole SD6)

Three hydraulic fracturing tests were performed in Queenston Shale in borehole SD6 which is drilled at the intersection of the proposed tunnels with the course of the buried St. Davids Gorge, Figure 5.1. The packer impressions for these tests showed that horizontal fractures were produced in the test locations, Figure 5.13. The first breakdown pressure, at each test location, and the successive reopening pressures are almost the same and sometimes the reopening pressure is higher than the first breakdown pressure. Figure 5.14 shows the pressure-time curve of three cycles of test C1 at depth 165.5 m. It may be seen that no true first breakdown pressures were obtained in these tests but rather, reopening pressures of approximately 2500 psi (17 MPa) were observed. Possible reasons for this phenomenon are that the horizontal fractures at these test locations are: (a) pre-existent incipient tensile fractures in Queenston formation due to the relief of the original lithostatic pressure and the formation of the valley, and/or (b) premature pretest fractures initiated after drilling the hole and before performing the tests due to horizontal stress concentration below the gorge. If the maximum pressure obtained from the first pressurization cycle is considered as a fracture initiation pressure, the results show that the horizontal stresses lie close to the regional trend as shown in Figure 5.15.

5.4.5 Horizontal Stresses at the Generation Facilities Area

Figure 5.16 shows the initial horizontal stress values in the area of generation facilities. These results were obtained from tests in boreholes NF34 and NF35 which were near Niagara Gorge, Figure 5.1. All the measurements in these boreholes were

above the riverbed. It may be observed from Table 5.2 and Figure 5.16 that the minimum and maximum horizontal stresses are approximately constant with depth in the Generation Facilities area. The representative value of the maximum horizontal stress at that location is interpreted as 9 MPa, while that of the minimum horizontal stress is only 4 MPa. The relatively low hor⋅ ⋅ntal stress values in that area reflect the effect of Niagara River Gorge on releasing the high horizontal stresses in nearby areas.

The directions of the maximum horizontal stress obtained from orientations of fractures from borehole NF35 are shown in Figures 5.1 and 5.10(b). It may be seen from these figures that the direction of the maximum horizontal stress is almost north-south (average N5°W), parallel to the Gorge direction. This observation is consistent with results of stress measurements reported for Ontario Power Generating Station (OPGS) (Lo *et al.* 1979).

5.5 ANALYSIS OF TESTS PERFORMED IN 1992 INVESTIGATION

IN 1992, 8 tests in two boreholes, NF31 and NF38, were performed in Queenston Shale. Vertical, subvertical, horizontal, and mixed-mode fractures were recorded by the packer impression for these tests. As for 1990 investigation, the analysis is performed using the strength parameters reported in section 5.4.1. As discussed in this section, the strength parameters for Queenston Shale in the area between borehole NF34 and NF35 are those for shale content > 70%. Therefore, these strength parameters are used in the analysis of tests performed in borehole NF38 since it is adjacent to borehole NF35. For borehole NF31, the strength parameters for shale content < 60% are used.

5.5.1 Discussion of Results

Table 5.3 shows a summary of the results of the analysis of hydraulic fracturing tests performed in 1992. Figure 5.17 shows a comparison between the stresses calculated from borehole NF38 and those computed from boreholes NF35 and NF34. It can be seen that there is a good agreement between results of tests performed in 1990 and those performed in 1992.

Borehole NF31 is in the zone between borehole NF35 and borehole NF33 at the outlet of the proposed tunnels. Therefore, stresses calculated from borehole NF31 are expected to be transitional stresses between the stresses near the gorge and those representing the general stress regime.

Figure 5.18 shows the stresses calculated from borehole NF31 and those representing the stresses near Niagara River gorge as well as the stresses representative for the general stress regime in the site. It can be seen from the figure that the stresses calculated from borehole NF31 are transitional stresses between the stresses in the two regions.

5.6 THE EFFECT OF TENSILE STRENGTH ANISOTROPY ON THE CALCULATED INITIAL HORIZONTAL STRESSES

To investigate the effect of tensile strength anisotropy on the horizontal stresses, test NF4-5 is examined. Figure 5.19 shows the relation between the ratio (T_h/T_v) and the calculated values of the maximum and minimum horizontal stress. It is clear from Figure 5.19 that the case of isotropic tensile strength $(T_h/T_v = 1)$ gives the highest values

of the horizontal stresses. As the ratio (T_h/T_v) increases, the horizontal stresses decrease. Moreover, the rate of decreasing is relatively high for low values of (T_h/T_v) and diminishes as the degree of anisotropy increases. Even a modest change in the degree of anisotropy from unity leads to a significant decrease in the horizontal stresses. For example, a change of (T_h/T_v) from unity to two decreases the maximum horizontal stress by 2.3 MPa, while changing this ratio from 5 to 20 decreases the maximum stress value only about 0.9 MPa. In addition, the calculated range of maximum and minimum horizontal stresses narrows as the tensile strength anisotropy increases. Therefore, even a small degree of tensile strength anisotropy impacts on the results significantly and anisotropic strength should be taken into consideration for stress determination.

5.7 EFFECT OF POISSON'S RATIO

Poisson's ratio has a significant effect on the calculated initial stresses (Hefny and Lo 1992a). The correct Poisson's ratio that should be adopted in the calculations is Poisson's ratio for the effect of horizontal stress on vertical strain v_{hv}. Figure 5.20 illustrates the effect of Poisson's ratio on the initial stress values. It can be seen from Figure 5.20 that a small change in Poisson's ratio leads to a significant change in initial stresses. For example, a change of v_{hv} of 0.40 to 0.3 (conventional value determined from uniaxial compression tests on vertical specimens) will increase the maximum horizontal stress value by 20%.

5.8 CONCLUSIONS

Investigations were performed in 1984, 1990, and 1992 to determine the *in situ* state of stress in Queenston Shale using the hydraulic fracturing tests. All the tests performed in 1984 and the majority of tests performed in 1990 and 1992 investigations initiated either horizontal or mixed-mode fractures. It was therefore necessary to develop a method of interpretation taking into account these modes of fractures and strength anisotropy of the shale.

Due to its capability of analyzing various modes of fracturing, the MSP method (developed in Chapter 3) is adopted to re-interpret the 1984 test data and to analyze the 1990 and 1992 test data. The 1984 test data were interpreted, previously, using the conventional theory of vertical fractures (Haimson 1985).

From the re-interpretation of 1984 test data, the following conclusions may be drawn:

(a)   Only stress path III representing horizontal fracturing is satisfied in all the tests performed in the 1984 investigation. Since all the observed modes of fracturing are horizontal, the results of analysis are in agreement with observations. It also indicates that the stresses can only be computed consistently with the MSP method taking into account horizontal fractures.

(b)   The assumption that vertical fracture is initiated before the horizontal fracture by the first breakdown pressure will lead to unsafe design, if these stresses computed were adopted.

From the interpretation of the hydraulic fracturing test data in the 1984, 1990, and 1992 investigations, the following conclusions may be drawn:

(1)   The results of hydraulic fracturing performed in 1984, when correctly interpreted, agree well with the results of 1990 investigation, both in the magnitudes of stresses computed and modes of fractures.

(2)   In tests in which packer impression tests are not available, it is possible, by the application of MSP method to determine which stress path the test results would follow, which mode of fracturing theoretically would occur, and thereby compute the magnitudes of stresses consistently without invoking assumptions other than that (i) the strength criterion (modified Hoek and Brown) should be satisfied and (ii) the inadmissible stress ranges should be eliminated.

(3)   The regional initial stress regime in the Queenston Shale are characterized as follows:

(i) the maximum horizontal stress increases linearly from 14.5 MPa at El. 86 m to 24 MPa at El. -20 m.

(ii) the minimum horizontal stress increases linearly from 9 MPa at El. 86 m to 18 MPa at El. -20 m.

(iii) The vertical stress is given closely by the overburden pressure.

(iv) The orientation of the maximum horizontal stress is approximately N65°E

(4)   Localized topographic features modify both the magnitude and direction of the regional stresses. In the powerhouse area, the maximum horizontal stress is approximately 9 MPa and is oriented parallel to the Gorge, consistent with previous observations made at the Ontario Power Generating Station.

(5)   The use of anisotropic strength envelopes is significant in (i) decreasing the

magnitude of stresses computed and (ii) narrowing the ranges of maximum and minimum horizontal stresses.

(6) Poisson's ratio has a significant effect on the calculated horizontal stresses and the relevant value is poisson's ratio for the effect of horizontal stress on vertical strain v_{hv}. The use of the conventional Poisson's ratio may lead to a significant increase in the calculated stress values.

TABLE 5.1   Values of initial horizontal stresses in Queenston Shale at the SABNGS No. 3 site (1984 hydraulic fracturing tests)

BH No.	Test No.	Depth (m)	P_{c1} (MPa)	P_s (MPa)	P_{c2} (MPa)	Min. Horizontal Stress (MPa)			Max. Horizontal Stress (MPa)			Fracture Mode	Stress Path
						MTS	Before Reduction	MSP	MTS	Before Reduction	MSP		
(1)	(2)	(3)	(4)	(5)	(6)	(7)	(8)	(9)	(10)	(11)	(12)	(13)	(14)
NF4	5	93.9	12.8	2.2			8.6-16.5	8.6-9.7		14.3-22.2	14.3-15.3	H	III
	8	98.5	12.6	2.4			8.7-16.6	8.7-9.8		14.5-22.4	14.5-15.6	H	III
	6	106.1	12.3	3.5	5.0	4.5	8.6-16.4	8.6-9.7	6.6	14.8-22.5	14.8-15.8	HV	III
	7	110.3	14.8	4.8	6.5	5.9	9.9-18.7	9.9-10.8	9.2	15.7-24.5	15.7-16.6	HV	III
NF3	18	105.0	16.3	2.4	4.0		10.5-20.0	10.5-11.3		15.8-25.2	15.8-16.6	H	III
	19	110.8	15.2	3.3	4.0	4.4	10.2-19.2	10.2-11.0	7.3	15.9-24.8	15.9-16.7	HV	III
	20	123.8	13.9	4.3	5.0	5.5*	9.8-18.3	9.8-10.7	8.4*	16.2-24.6	16.2-17.1	H	III

Note:
P_{c1} Breakdown pressure
P_s Shut-in pressure
P_{c2} Reopening pressure
MSP   Modified Stress Path Method
MTS   Conventional Method (Maximum Tensile Stress Theory) (values clculated by haimson in 1984)
*   Theses values are calculated by Haimson, in 1984, using the Conventional Method although the fracture in that test location is unambigeous horizontal fracture

TABLE 5.2 Values of initial horizontal stresses in Queenston Shale at the SABNGS No. 3 site (1990 hydraulic fracturing tests)

BH No.	Test No.	Depth (m)	P_s (MPa)	P_{el} (MPa)	Min. Horizontal Stress (MPa)		Max. Horizontal Stress (MPa)		Fracture Mode	Fracture Orientation	Stress Path
					MTS (6)	MSP (7)	MTS (8)	MSP (9)	(10)	(11)	(12)
(1)	(2)	(3)	(4)	(5)	(6)	(7)	(8)	(9)	(10)	(11)	(12)
NF28	G4	172.5	12.3	23.6	14.0	14.0	21.0	21.0	HV	N28°E	II
	G5	177.0	12.3	22.2	14.1	14.5	22.4	23.8	HV(12°)	S78°E	II
	G6	200.0	16.3	25.9		16.9-17.1		23.3-23.5	HV	N28°E	III
NF30	B2	170.0	12.1	21.1	13.8	14.0	22.8	23.6	SV(9°)	N86°E	II
	B3	187.0	12.1	20.7	14.0	14.1	23.5	23.9	SV(6°)	N85°E	II
	B5	212.0	10.1	16.6	12.2	12.2	22.1	22.1	V	N86°E	II
NF32	H5	167.0	6.9	13.2	8.6	8.6	15.1	15.1	HV	N65°E	II
	H6	136.0	9.9	13.2		9.3-10.3		17.2-26.2	H		III
NF33	A2	166.0	14.8	22.7	N/A	14.7-14.9	N/A	20.2-20.4	Not Measured	Not Measured	III
NF4A	03	117.0	12.8	19.9		12.3-12.7		16.5-16.9	Not Measured	Not Measured	III
	05	155.7	6.2	23.2		14.7-15.0		19.9-20.2			III
	06	169.7	7.9	27.1		16.9-17.1		22.4-22.6			III
	07	180.2	8.1	24.8	N/A	16.0-16.2	N/A	21.9-22.1			III
	08	188.7	11	26.5		17.0-17.2		23.0-23.2			III
	10	174.4	8.9	25.9		16.4-16.6		22.1-22.3			III
	12	200.1	8.5	26.2		17.1-17.3		23.5-23.7			III
NF34	K7	94.1	3.8	9.1	4.7	5.3	7.4	9.6	SV(27°)	N39°E	II
	K9	121.6	3.3	8.3	4.5	4.6	7.2	7.4	SV(9°)	N53°E	II

TABLE 5.2 (Continue)
Values of initial horizontal stresses in Queenston Shale at the SABNGS No. 3 site
(1990 hydraulic fracturing tests)

BH No.	Test No.	Depth (m)	P_o (MPa)	P_{ci} (MPa)	Min. H. stress (MPa)		Max. H. Stress (MPa)		Fracture Mode	Fracture Orientation	Stress Path
					MTS	MSP	MTS	MSP			
(1)	(2)	(3)	(4)	(5)	(6)	(7)	(8)	(9)	(10)	(11)	(12)
NF35	J1	128.0	2.8	4.6	4.1	4.1	9.6	9.6	V	N12°W	II
	J2	115.0	1.7	3.5	2.9	2.9	7.1	7.1	SV(4°)	N12°W	II
	J3	100.0	2.3	3.4	3.3	3.3	8.7	8.7	SV(6°)	N 8°W	II
	J4	95.0	3.7	6.2	4.7	4.7	10.0	10.0	V	N 7°E	II
	J5	88.0	2.8	3.6	3.7	3.7	9.8	9.8	V	N 8°W	II

Note:

P_o Shut-in pressure
P_{ci} Breakdown pressure
MTS   Conventional theory (Maximum tensile stress theory)
    (applied here only for unambiguous vertical and subvertical fractures and for mixed-mode fractures that satisfied stress path II)
MSP   Modified Stress Path Method
H   Horizontal fracture
V   Vertical fracture
SV   Subvertical fracture
HV   Mixed-mode fracture (horizontal and vertical or horizontal and subvertical)
N/A   Not applicable

TABLE 5.3   Values of initial horizontal stresses in Queenston Shale at the SABNGS No. 3 site (1992 hydraulic fracturing tests)

BH No.	Test No.	Depth (m)	P_s (MPa)	P_{cl} (MPa)	Min. H. stress (MPa)		Max. H. Stress (MPa)		Fracture Mode	Fracture Orientation	Stress Path
(1)	(2)	(3)	(4)	(5)	MTS (6)	MSP (7)	MTS (8)	MSP (9)	(10)	(11)	(12)
NF31	3	124.0	12.9	18.3		11.6-12.0		16.1-16.4	Not Measured	Not Measured	III
	4	86.0	6.9	14.8	7.8	8.1	11.9	12.9	SV(13°)	N6°W	II
	7	140.0	4.4	12.6		9.1-9.5		14.2-14.6	Not Measured	Not Measured	III
	8	150.0	10.3	23.8	11.8	11.8	14.3	12.0	Not Measured	Not Measured	II
NF38	1	130.0	3.1	7.4	4.4	4.5	7.7	8.1	SV(14°)	N34°W	II
	2	105.0	1.7	5.6	2.8	2.8	4.9	3.5	HV	N46°E	II
	3	90.0	2.8	8.7		6.1-6.4		9.2-9.4	H		III
	4	76.0	3.5	5.8		4.5-4.8		7.5-7.8	H		III

Note:

P_s	Shut-in pressure
P_{cl}	Breakdown pressure
MTS	Conventional method (Maximum tensile stress theory) (applied here only for unambiguous vertical and subvertical fractures and for mixed-mode fractures that satisfied stress path II)
MSP	Modified Stress Path Method
H	Horizontal fracture
V	Vertical fracture
SV	Subvertical fracture
HV	Mixed-mode fractures (horizontal and vertical)
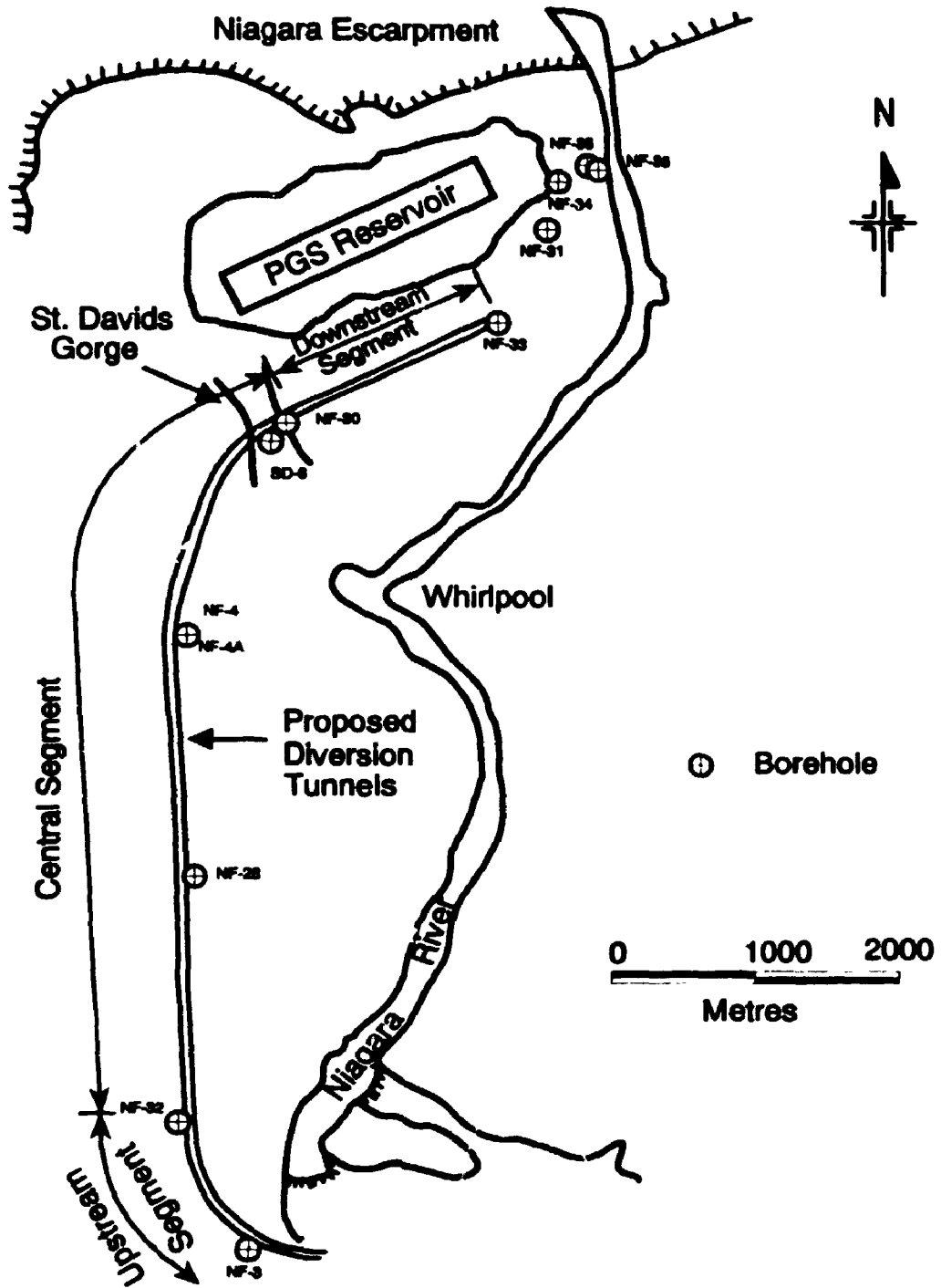
Figure 5.1 Locations of hydraulic fracture boreholes

AGE	GROUP	FORMATION	MEMBER	BRIEF DESCRIPTION	DEPTH (m)	EL (m) 181.82	SYMBOL
				OVERBURDEN	12.81	169.01	
MIDDLE SILURIAN	ALBEMARLE GROUP	LOCKPORT	GOAT ISLAND	MASSIVE DOLOMITE CHERT BEDS AT THE BASE	18.00	163.82	
			GASPORT	GREY CRINOIDAL DOLOMITE LIMESTONE	24.31	157.51	
			DECEW	GRAY DOLOMITE AND MUDSTONE	28.90	152.92	
	CLINTON GROUP (UPPER)	ROCHESTER		DARK GREY CALCAREOUS SHALE DOLOMITE INTERBEDDED	44.19	137.63	
		IRONDEQUOIT		GREY TO REDDISH DOLOMITE LIMESTONE	47.61	134.21	
	(LOWER)	REYNALES		LIGHT GREY DOLOMITE	50.07	131.75	
		NEAHGA		GREEN SHALE	52.40	129.42	
		THOROLD		WHITE SANDSTONE	54.76	127.06	
LOWER SILURIAN	CATARACT GROUP	GRIMSBY		GREEN BEDDED SANDSTONE WITH RED SHALE INTERBEDS	68.78	113.04	
		POWER GLEN		GREY SHALE TO WHITE CALCAREOUS SANDSTONE	79.38	102.44	
		WHIRLPOOL		LIGHT GREY CROSSBEDDED SANDSTONE	87.59	94.23	
UPPER ORDOVICIAN	QUEENSTON FORMATION	QUEENSTON		REDDISH MUDSTONE, SHALE, SILTSTONE AND FINE SANDSTONE			

Legend:

- LIMESTONE
- DOLOMITE
- SHALE
- SILTSTONE
- CHERT
- SANDSTONE

Figure 5.2 Detailed bedrock stratigraphy at SABNGS No. 3 site
(section at Boreholes NF4 & NF4A)
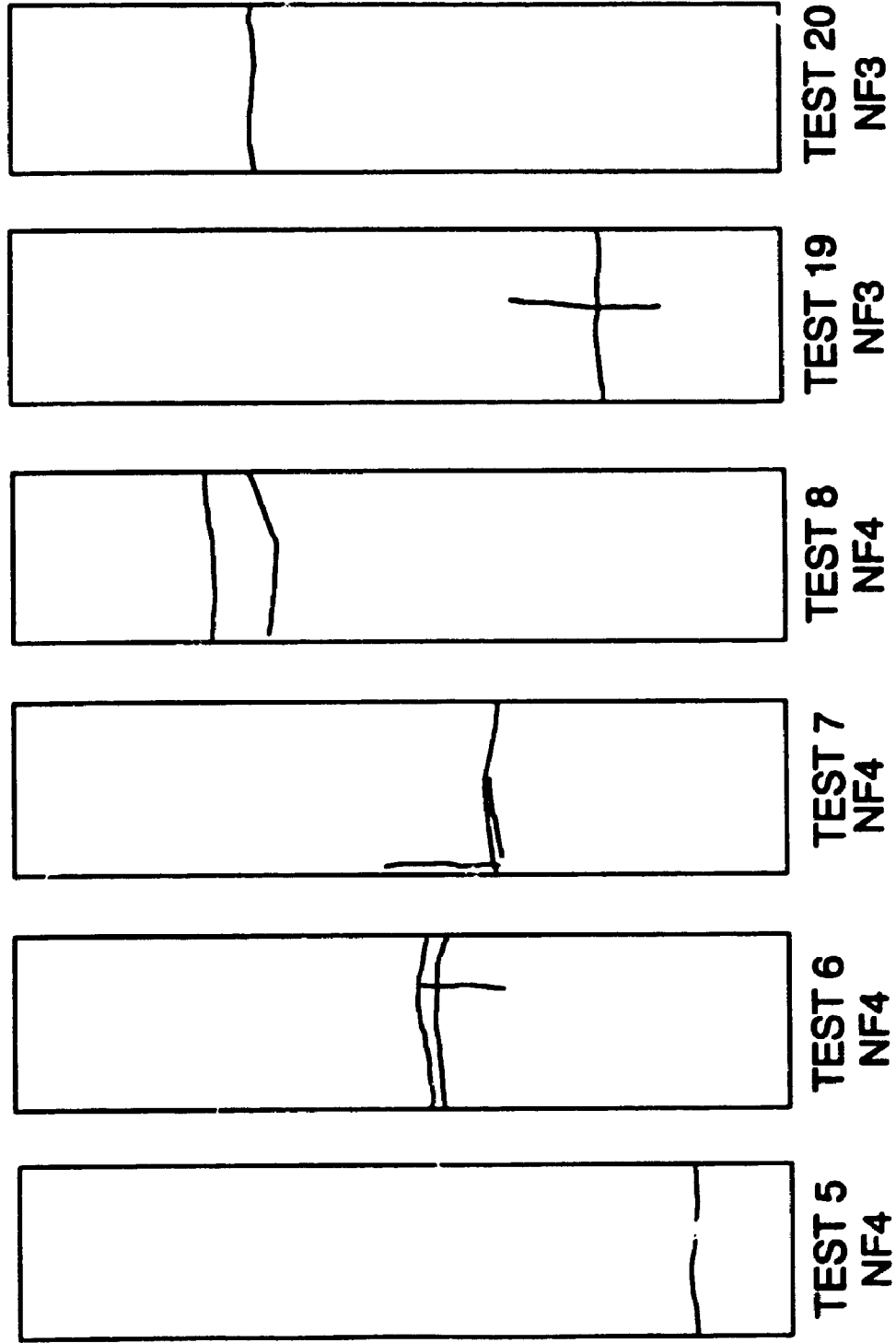
Figure 5.3 Packer impressions for tests in Queenston Shale (1984 investigation)
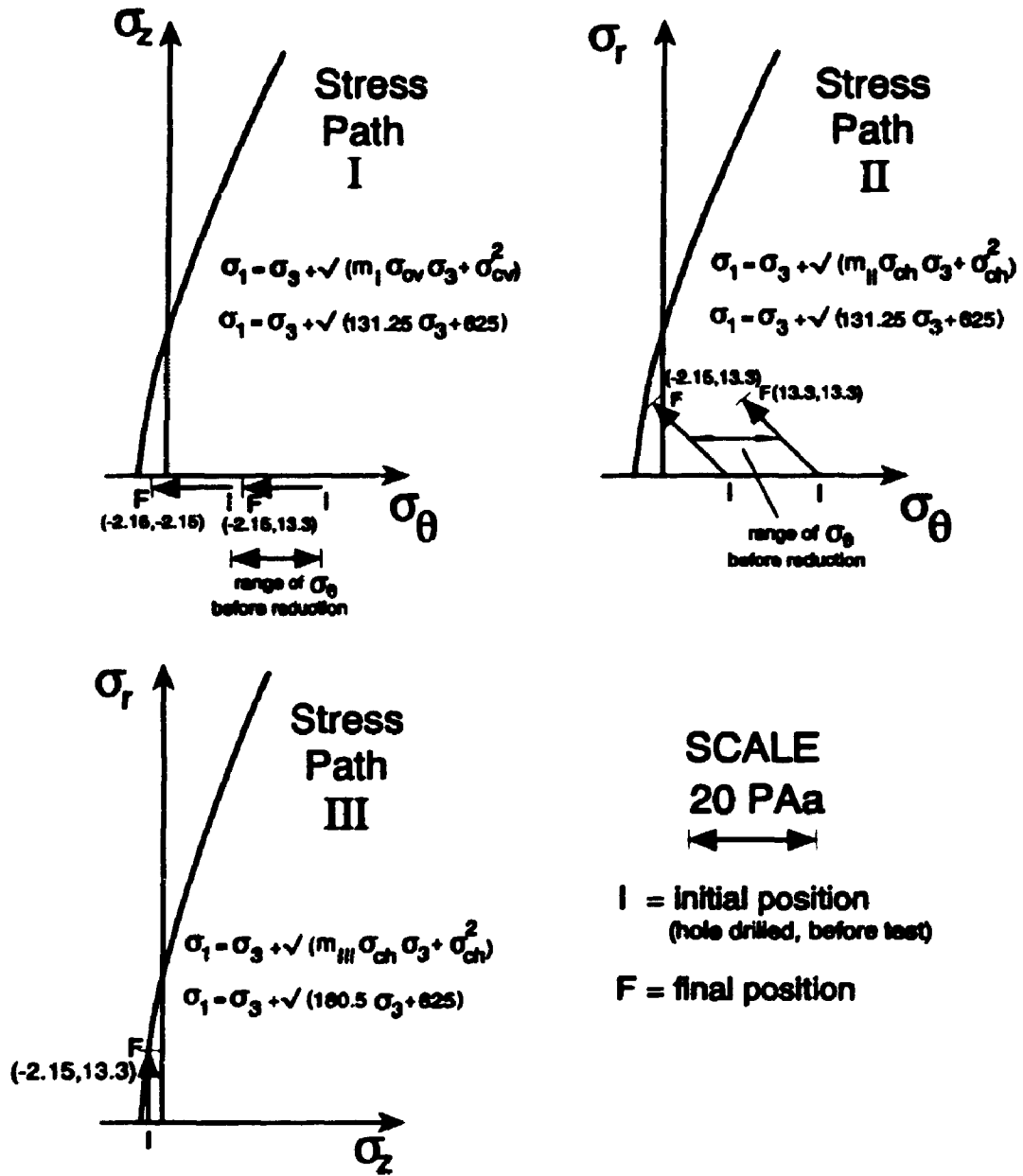
Figure 5.4 Different possible stress paths for test NF4-6
(Queenston Shale - SABNGS No. 3 site)
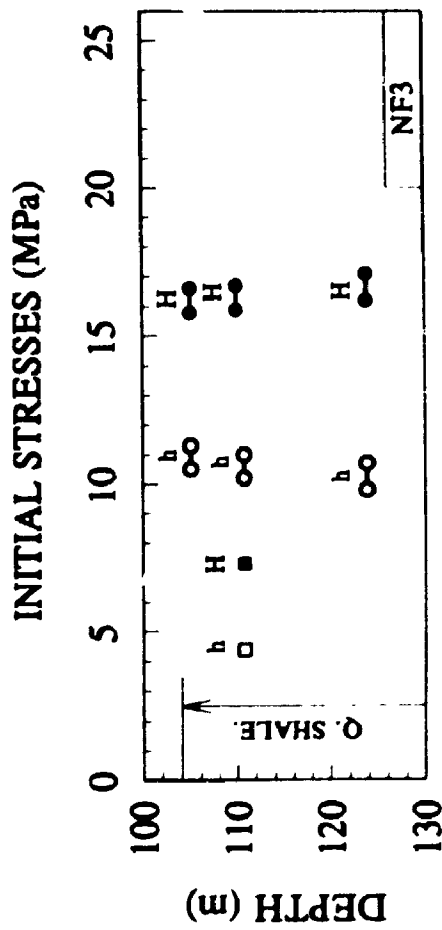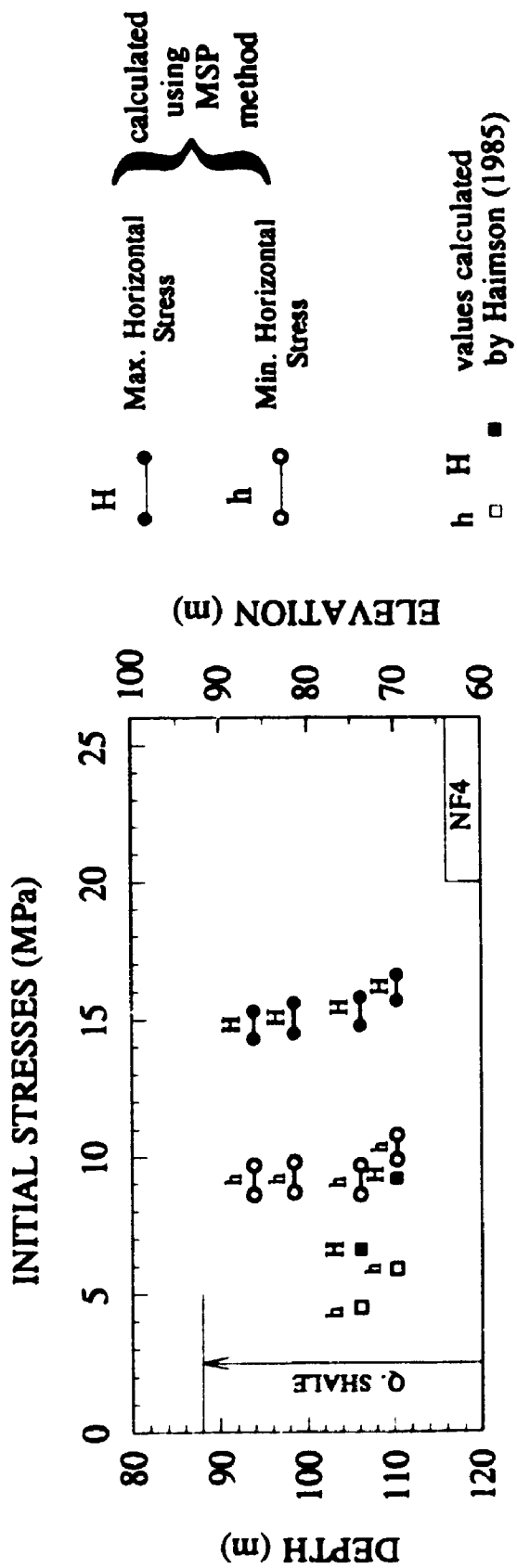
Figure 5.5 Initial horizontal stresses in Queenston Shale at SABNGS No. 3 site (calculated from 1984 hydrofracturing stress measurements)
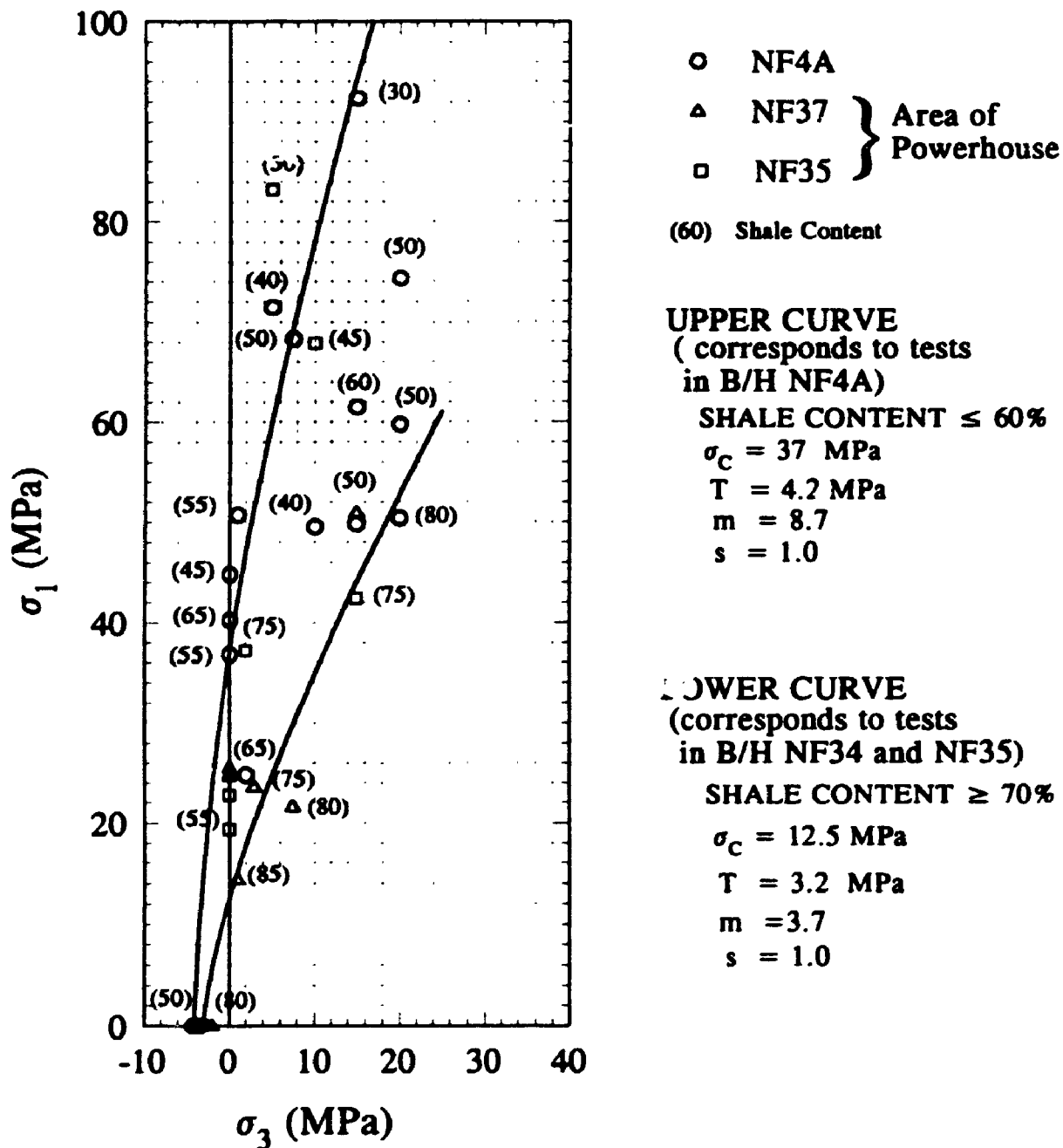
Figure 5.6 Correlation between shale content and failure envelopes

Borehole NF34 Test K7 depth 94.1 m, Queenston Shale
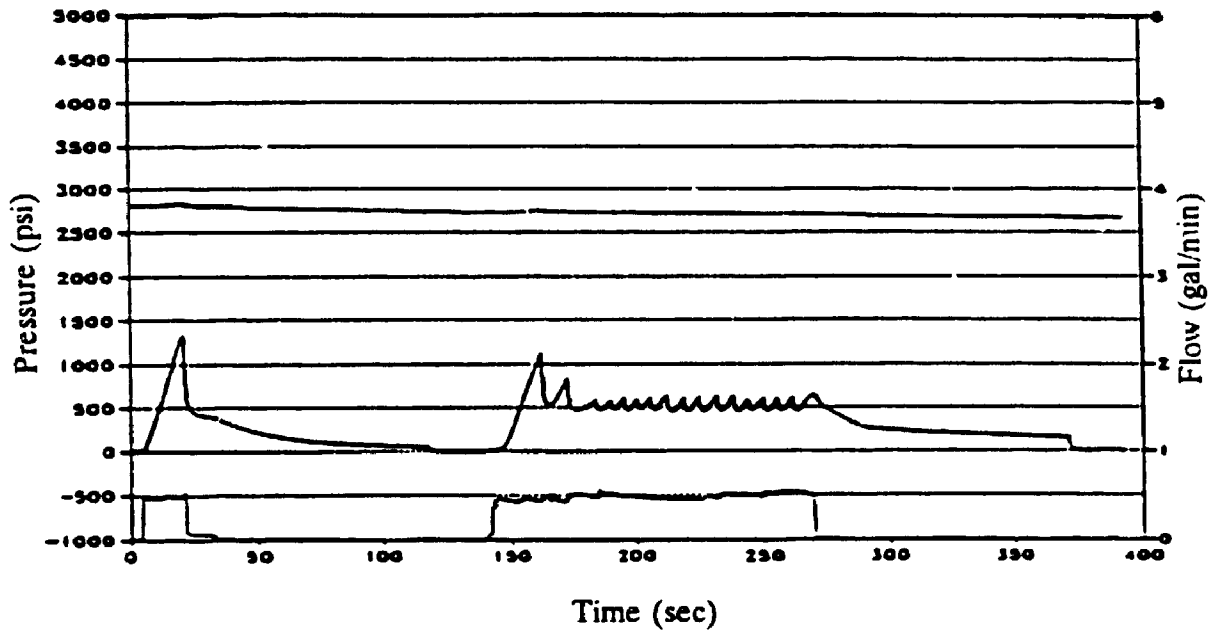
Figure 5.7 Pressure-time record for Test K7
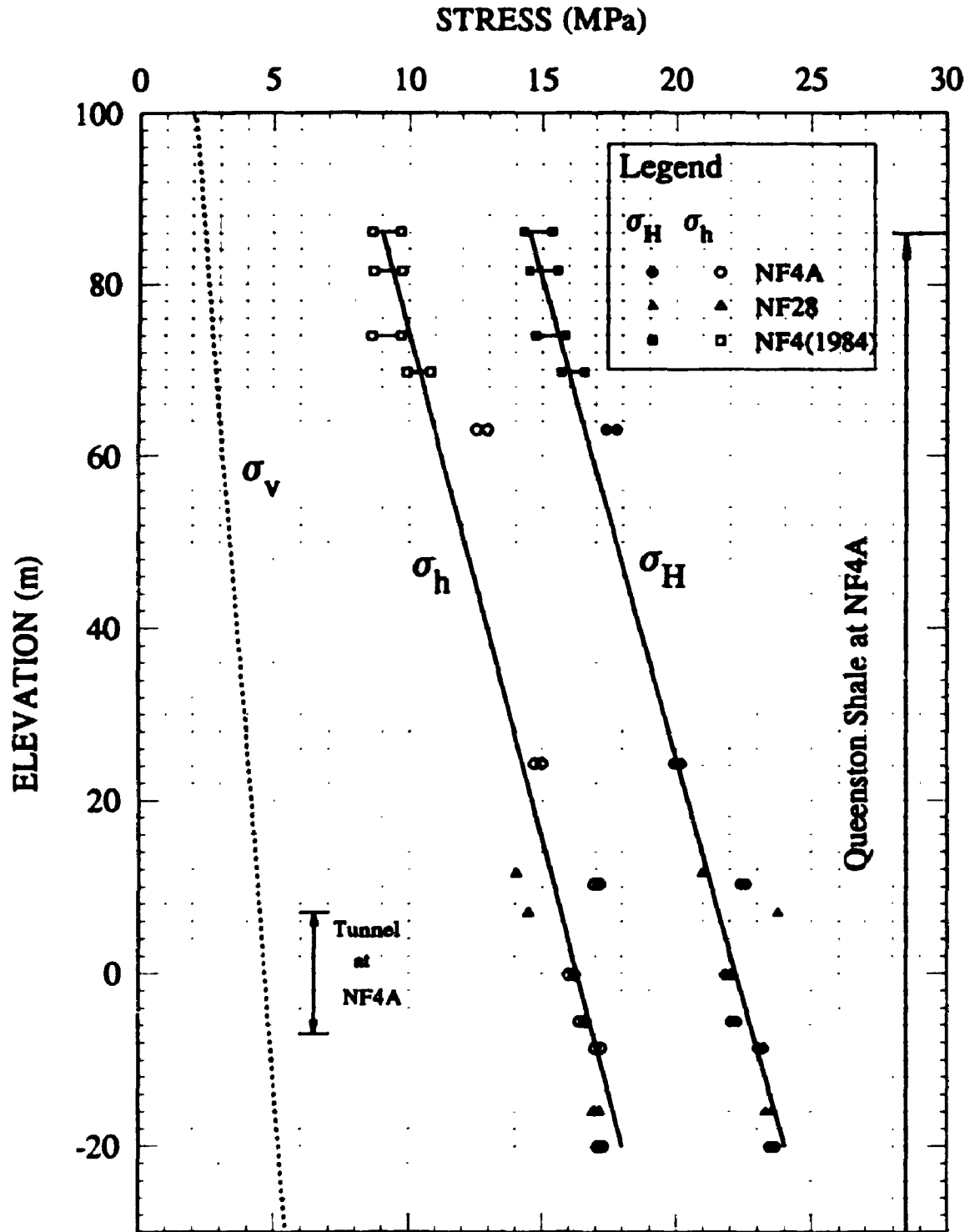
Figure 5.8 Initial horizontal stresses in Queenston Shale at SABNGS No. 3
site (central segment of the proposed diversion tunnels)
(REGIONAL STRESS REGIME)
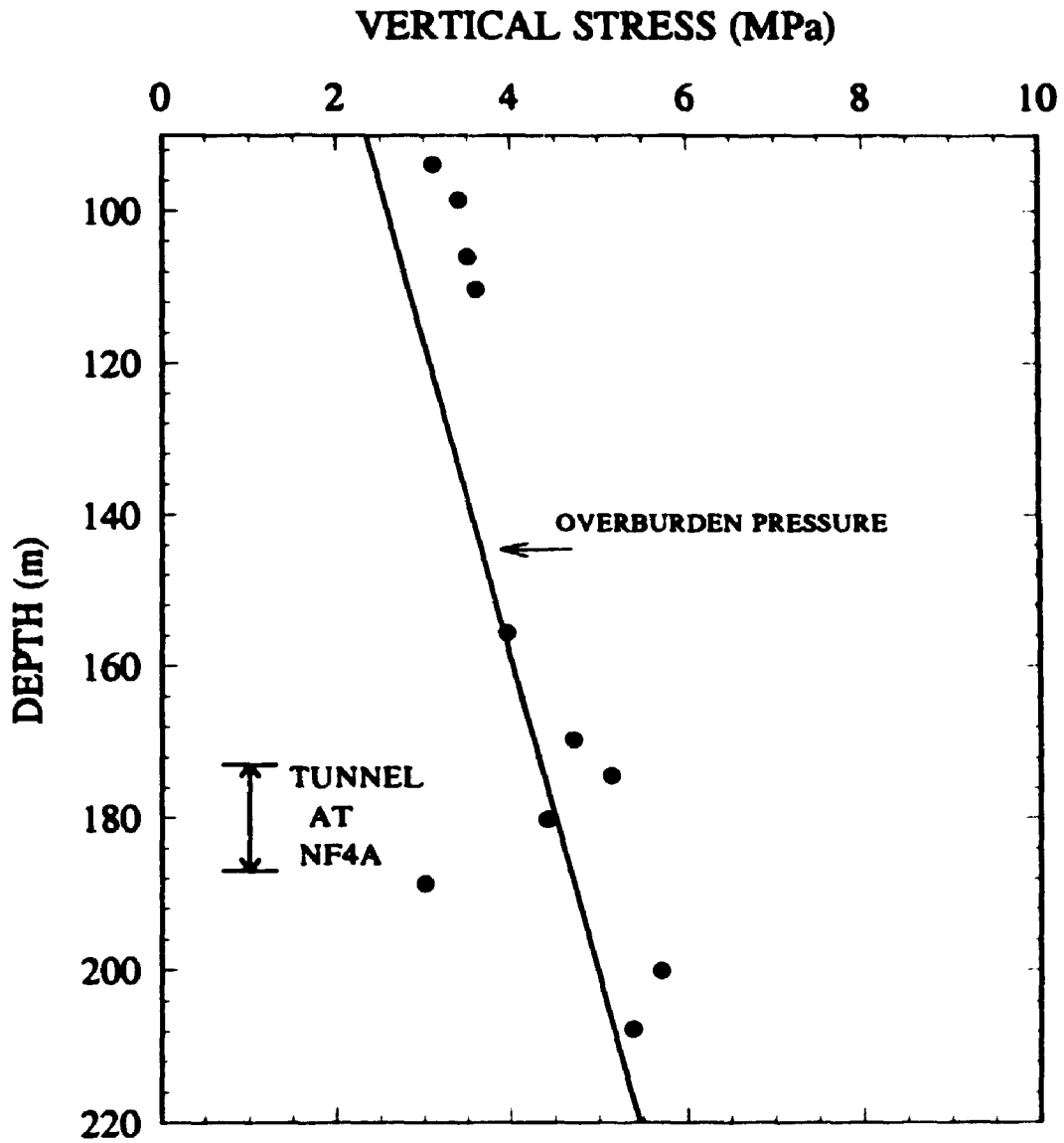
Figure 5.9 Comparison between vertical stresses calculated from hydraulic
fracturing stress measurements (in Boreholes NF4 and NF4A)
nd the overburden pressure

N5°W

BOREHOLE NF35 (J)
(NEAR NIAGARA RIVER GORGE)
(b)

N65°E

Queenston Formation
Whirlpool Formation

(CENTRAL PORTION OF THE TUNNELS)
(a)
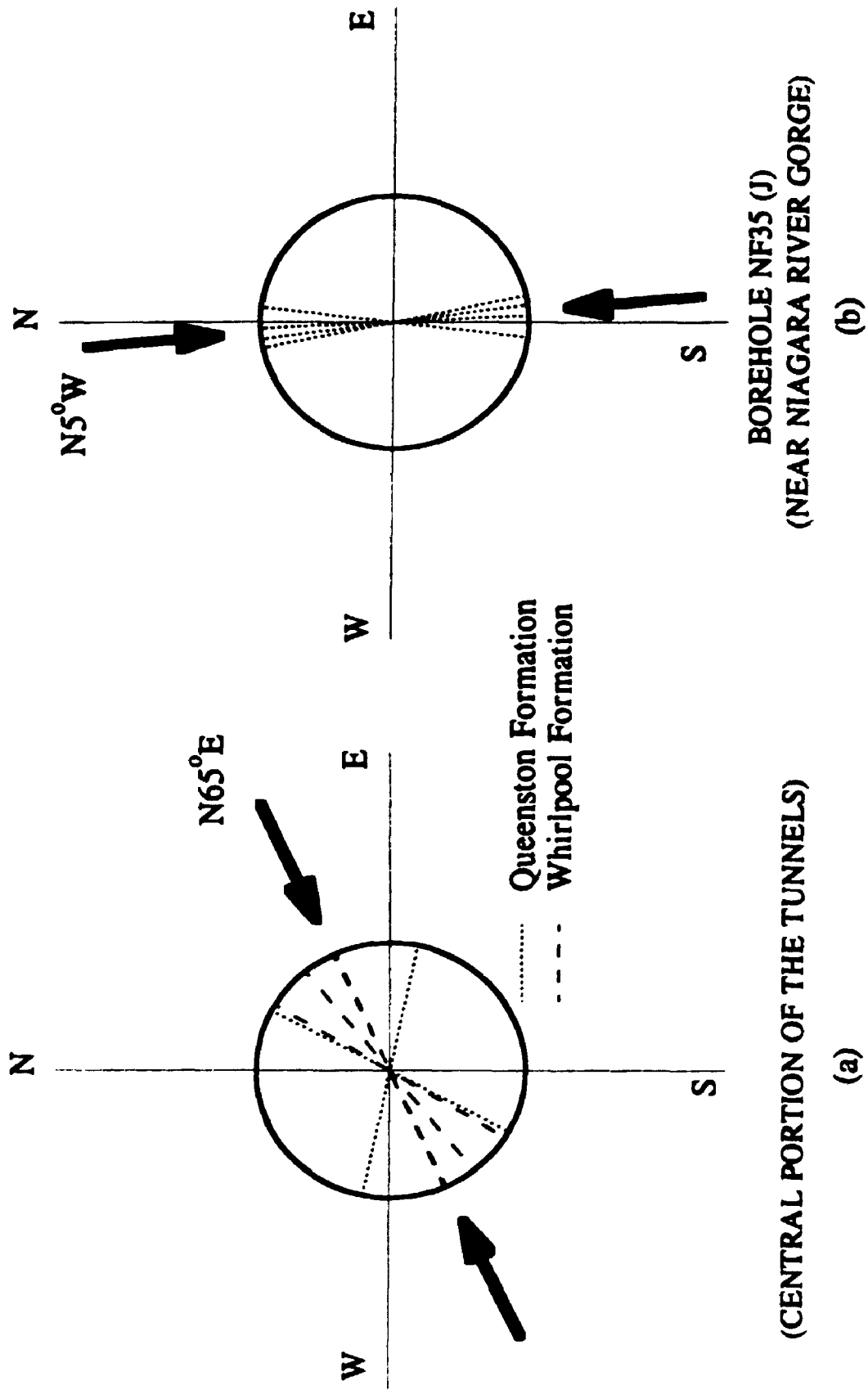
Figure 5.10 Direction of maximum horizontal stress in Queenston Shale
at SABNGS No. 3 site
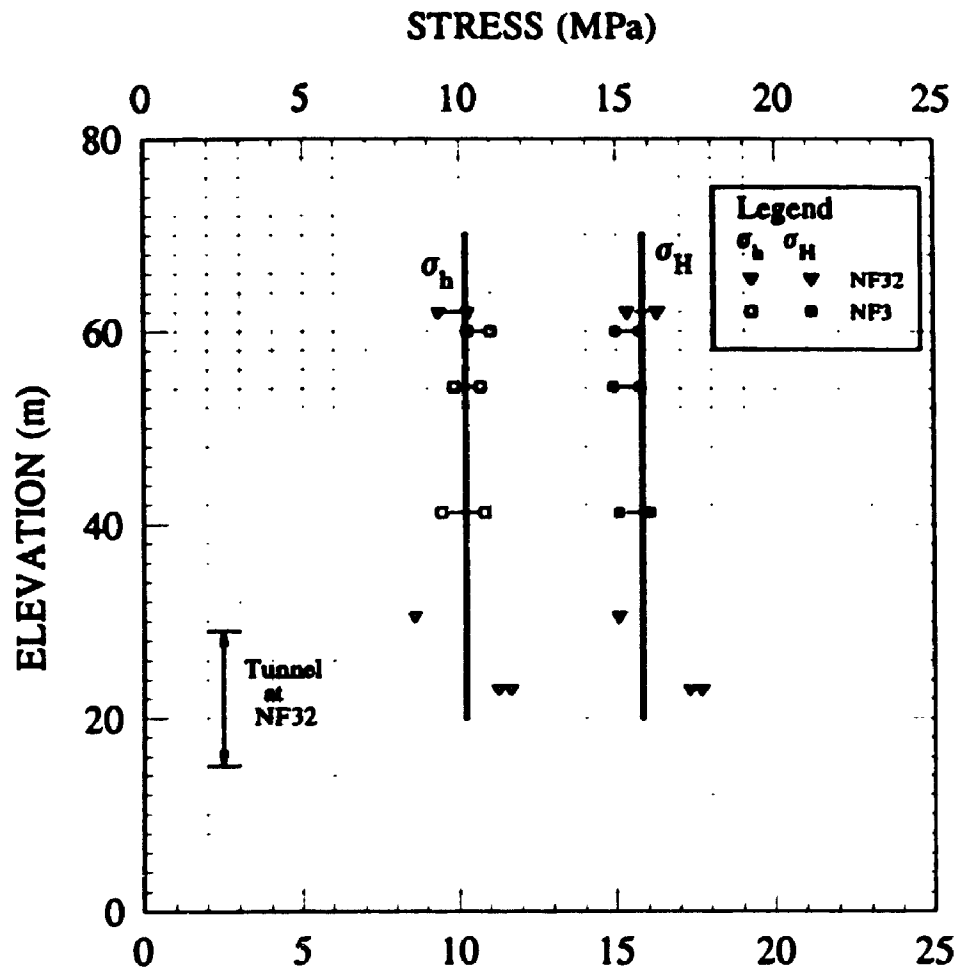
Figure 5.11   Initial horizontal stresses in Queenston Shale at SABNGS No. 3
site (upstream the proposed tunnel)

STRESS (MPa)
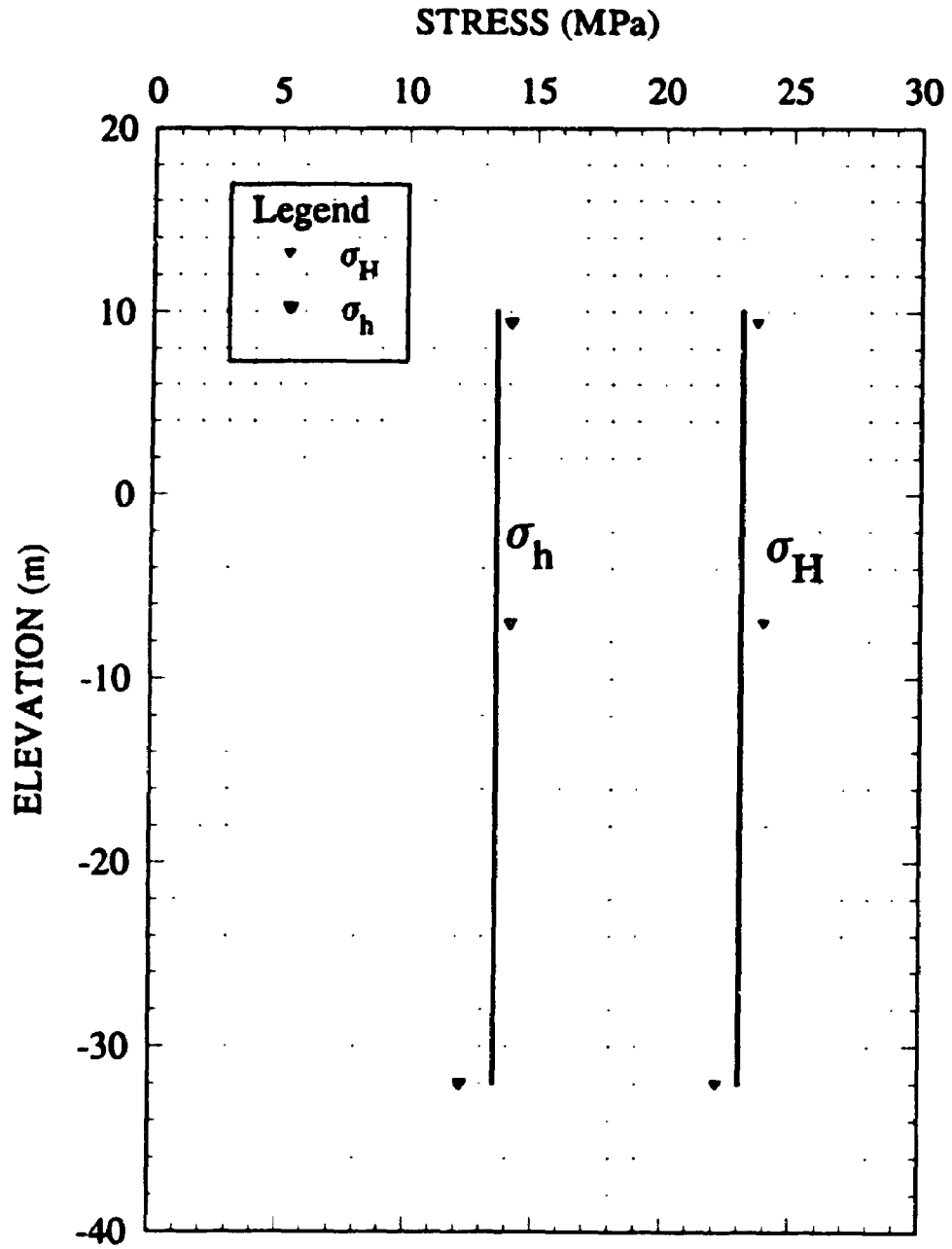
Figure 5.12 Initial horizontal stresses in Queenston Shale at the edge of the buried St. Davids Gorge (results from hydraulic fracturing tests in Borehole NF30)

150

82

216

TEST C1
DEPTH: 165.5 m
FORMATION: QUEENSTON
BOREHOLE: SD-6

TEST C2
DEPTH: 190.7
FORMATION: QUEENSTON
BOREHOLE: SD-6

TEST C3
DEPTH: 190 7 m
FORMATION: QUEENSTON
BOREHOLE: SD-6
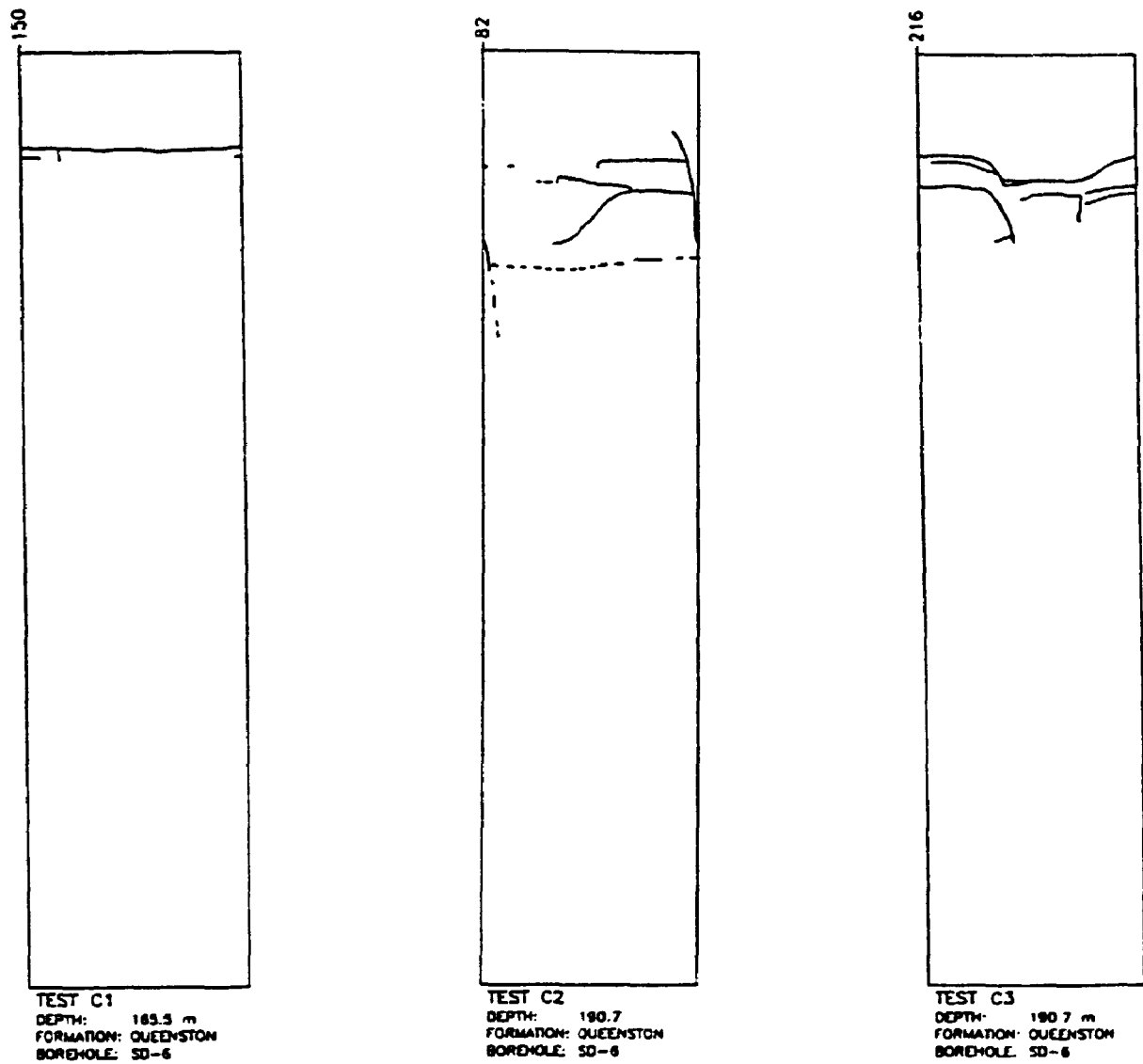
Figure 5.13   Packer impression for tests in Borehole SD6
(below the buried St. Davids Gorge)
(Queenston Shale - SABNGS No. 3 site)
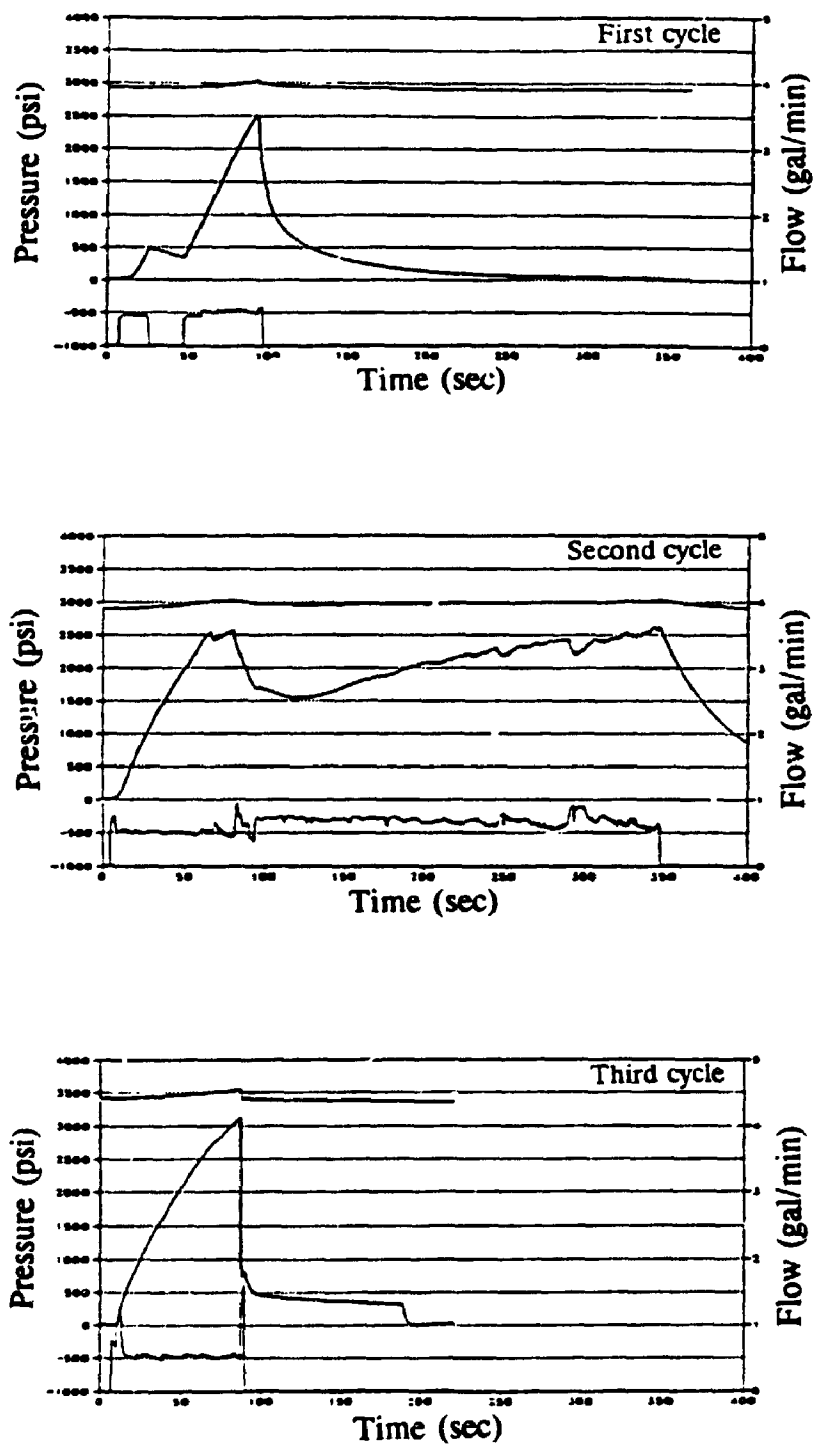
Figure 5.14   Pressure-time record for Test SD6-C1
              (below the buried St. Davids Gorge)
              (Queenston Shale - SABNGS No. 3 site)
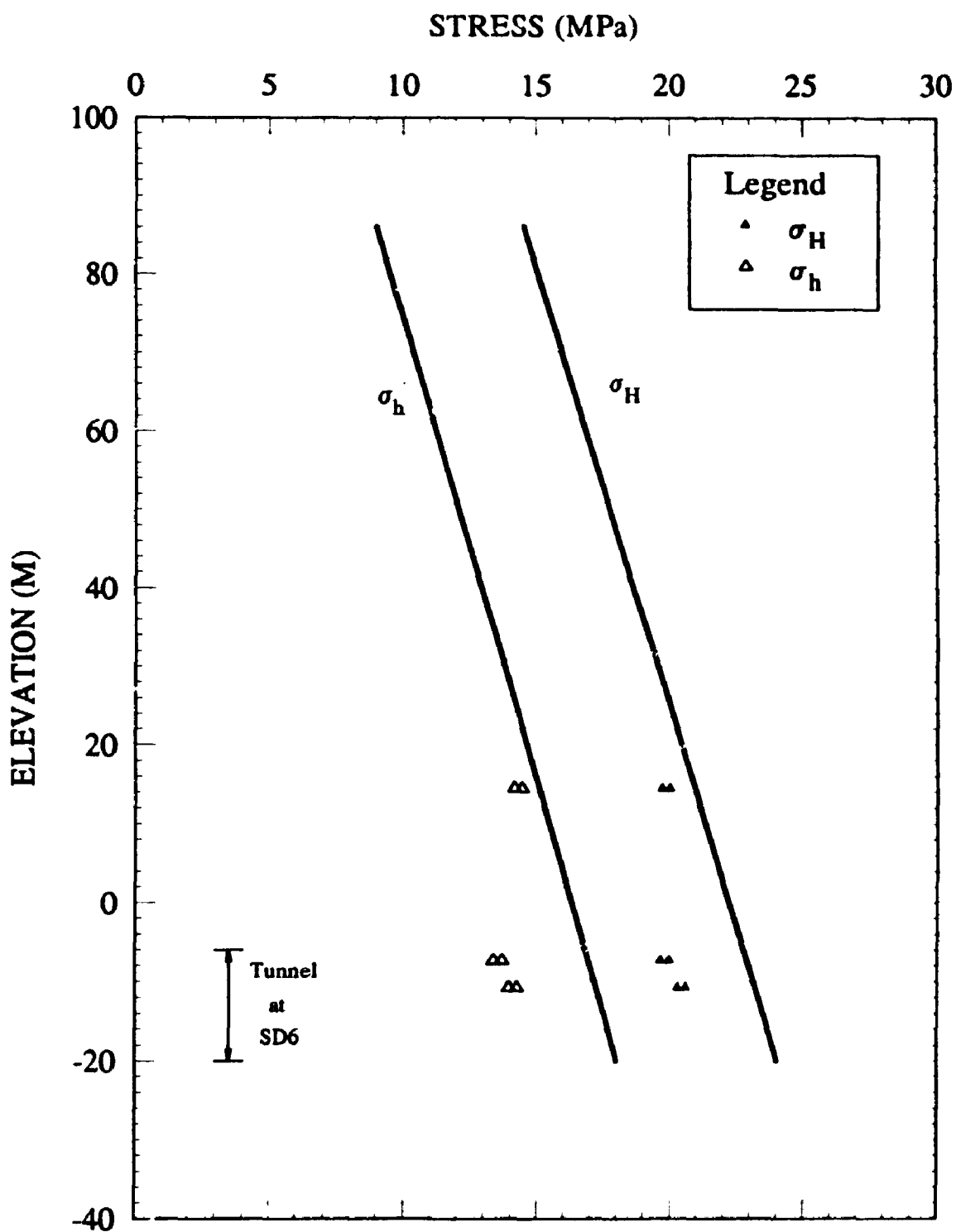
Figure 5.15 Initial horizontal stresses in Queenston Shale below the buried St. Davids
Gorge relative to the regional stress regime in the site
(calculated from tests in Borehole SD6)
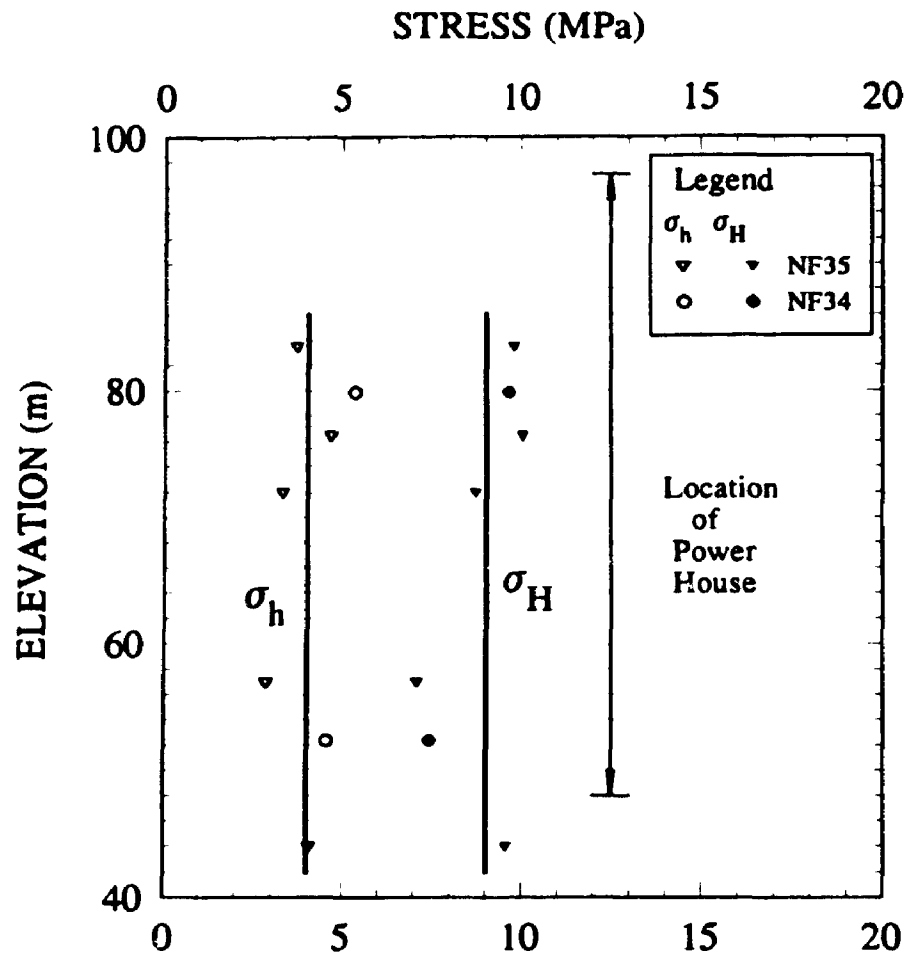
Figure 5.16 Initial horizontal stresses at the area of generation
facilities (Queenston Shale at SABNGS No. 3 site)
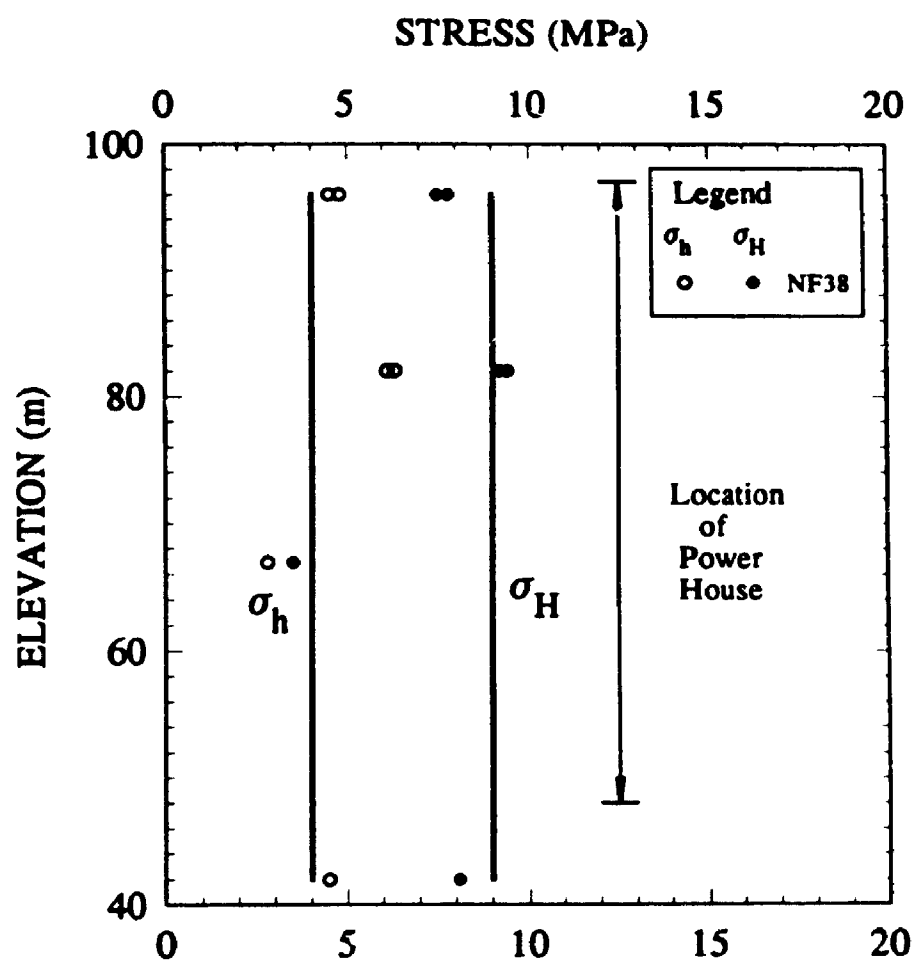
Figure 5.17 Comparison between initial horizontal stresses calculated
from hydraulic fracturing tests in Borehole NF38 (1992)
and those calculated from the 1990 investigation (the solid
vertical line) at the area of generation facilities
(Queenston Shale at SABNGS No. 3 site)
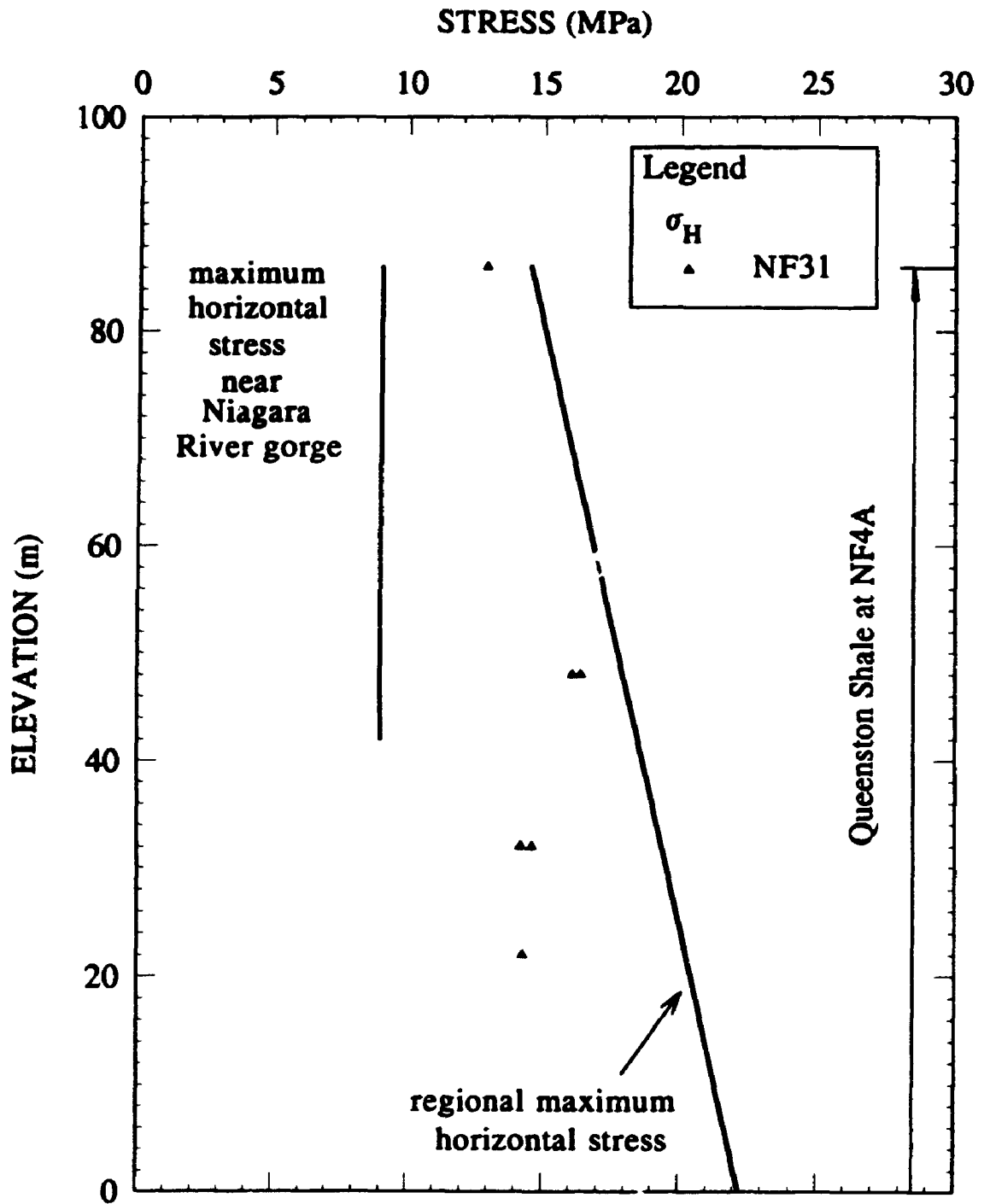
Figure 5.18 Comparison between the initial maximum horizontal stresses calculated from tests in Borehole NF31 and the regional maximum horizontal Stress and the maximum horizontal stress near Niagara River Gorge
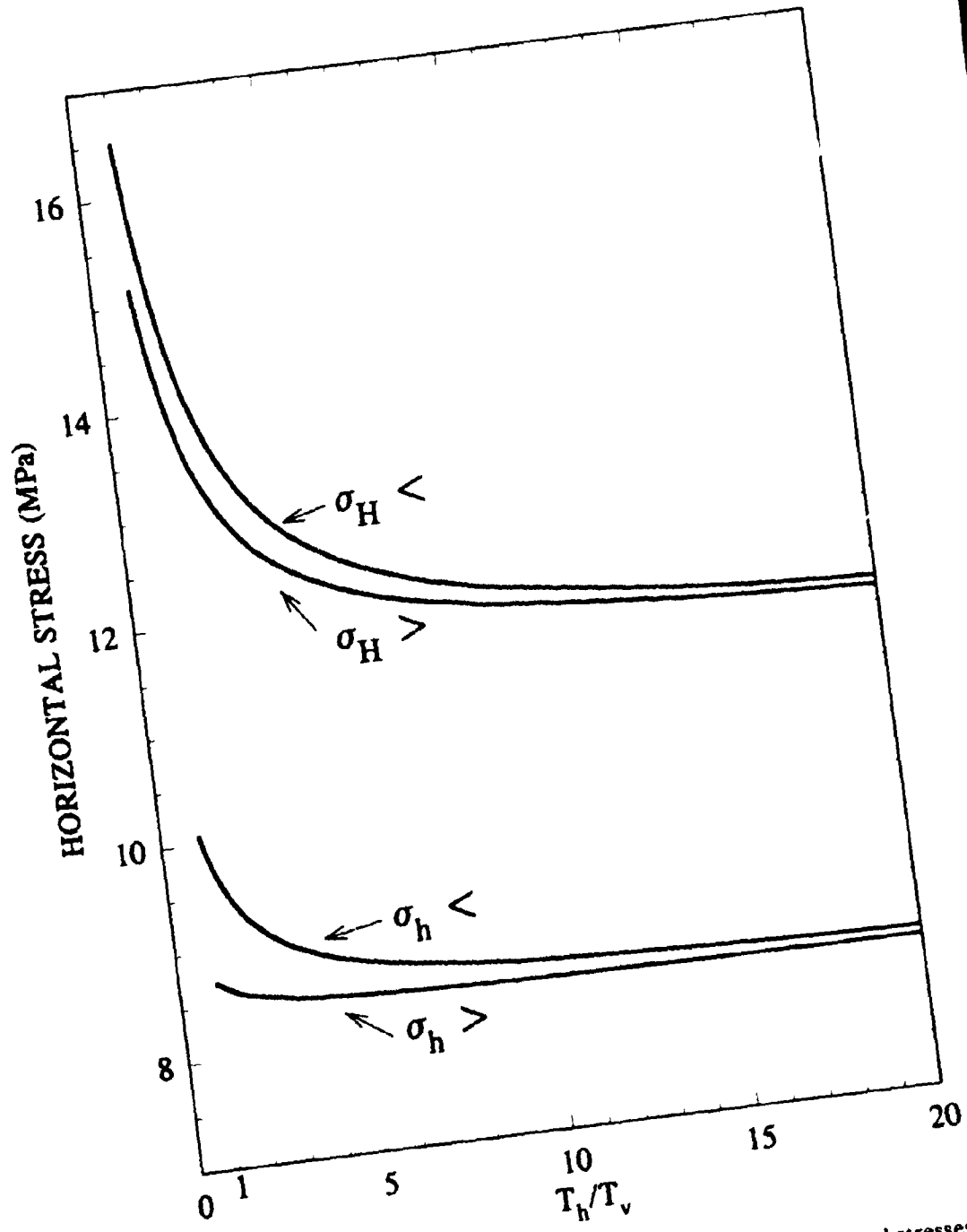
Figure 5.19 Effect of tensile strength anisotropy on initial horizontal stresses (Test NF4-6 is used in the analysis)
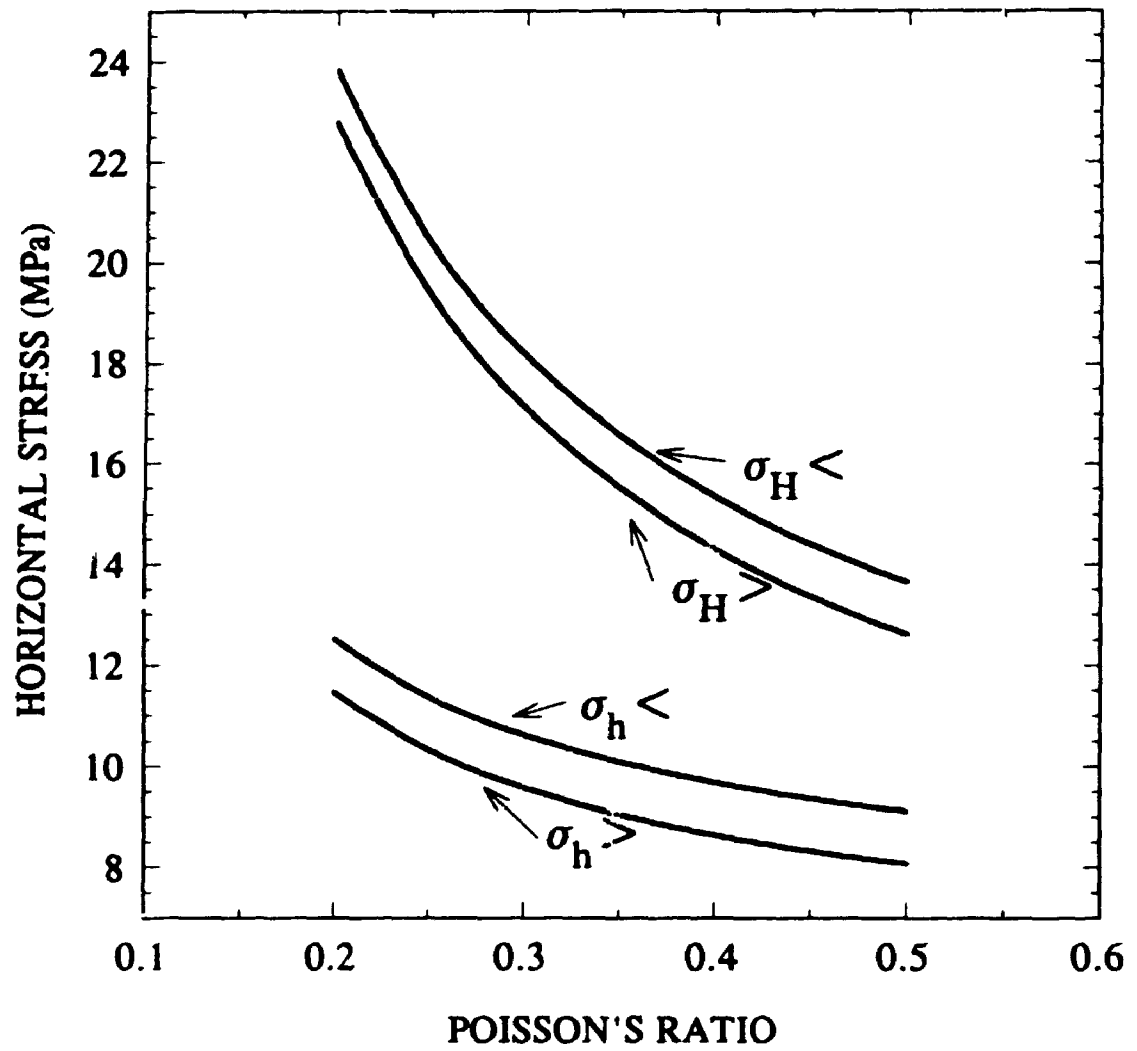
Figure 5.20 Effect of Poisson's ratio on initial horizontal stresses
(Test NF4-5 is used in the analysis)

PART II

STRESSES AND DEFORMATIONS AROUND
AN UNLINED TUNNEL DRIVEN IN
CROSS ANISOTROPIC MEDIUM

(Chapter 6 inclusive)

117

CHAPTER 6

STRESSES AND DISPLACEMENTS AROUND AN UNLINED TUNNEL

DRIVEN IN CROSS-ANISOTROPIC ROCKS

6.1 INTRODUCTION

When a tunnel is excavated in a rock mass, the initial state of stress is altered, resulting in changes of positions of the points in the medium relative to one another (i.e. strains and displacements are created). The determination of the state of stress and displacements due to excavation are of importance for applications in rock engineering. The elastic solution for stresses around a circular hole in an infinite plate subjected to a uniaxial stress (refer to Figure 6.1) was obtained by Kirsch (1898) and reported by many authors (see e.g. Timoshenko and Goodier 1951). The compressive stress concentration at points B and B' is $3P_z$. Mindlin (1939) investigated the more general case of a biaxial stress field. Three cases were studied: (a) case of hydrostatic pressure ($K_o=1$), where K_o is the initial stress ratio, (b) case of $K_o = v/1-v$, where v is Poisson's ratio, and (c) case of no lateral stress. The effect of proximity of boundary on the stress concentration under horizontal *in situ* stress was given by Mindlin (1948). In Figure 6.2, the stress concentration factor (σ_θ/P_x) at three points M, A, and A' is plotted against the embedment ratio c/a, where σ_θ is the compressive tangential stress induced by the horizontal stress P_x. It is obvious from Figure 6.2 that high stress concentration occurs at the crown for small values of c/a and as the value of c/a increases, the compressive

stress concentration factor approaches that of the classical case of uniaxial stress field ($\sigma_\theta/P_x = 3$). The elastic solution for the tangential stresses around a hole in an infinite medium under general biaxial stresses is known in the literature as Kirsch solution and has often been employed in design (see e.g. Obert and Duvall 1967). The elastic solution for the displacement around a pre-existing hole in an infinite plate is given by Obert and Duvall (1967) and Jaeger and Cook (1976). However, this solution is not relevant for tunnel design since it does not represent the actual case of deformation due to *in situ* stress relief at the tunnel boundary resulting from the excavation. The elastic solution for the displacement resulting from the relief of *in situ* stress was investigated by Yuen (1979).

It is evident, however, that for sedimentary rocks such as shales, the deformation behaviour is anisotropic. The effects of anisotropy on stresses and displacements resulting from underground excavations have not been studied in detail. The stress distribution around a circular hole in an infinite orthotropic (cross-anisotropic) plate loaded at infinity from one direction was studied by Green and Taylor (1939 and 1945). Using Green and Taylor solution, Lo and Morton (1976) computed the tangential stress on the surface of a tunnel in rock with various cases of anisotropy. However, the solutions for the displacements are not studied in the literature.

In this work, closed form solutions for the stresses and displacements along the circumference of tunnels driven in cross-anisotropic rocks are derived. An example of utilizing the theoretical solution for design analysis is given. Different factors affecting the resulting stresses and displacements, including the initial stress ratio and the degree of anisotropy, are studied. Design charts have been prepared for the determination of

stresses and displacements for given values of initial stress ratio (K_o) and the elastic

parameters (Hefny and Lo 1992b)

6.2 CONSTITUTIVE RELATIONSHIPS

For an elastic isotropic material, only two material parameters are required to

represent the stress-strain relationships. However, in the case of cross-anisotropic

material, properties are different in the horizontal and vertical directions and five

independent parameters are involved in the constitutive relationships. Consider the

problem as shown in Figure 6.3, where a tunnel is driven along the z-axis such that axes x

and z are horizontal and lie on the plane of isotropy. The cross section lies on the

vertical plane ($x - y$ plane) which is the plane of anisotropy. The problem is a plane

strain problem where the components ϵ_z, ϵ_{xz} and ϵ_{yz} vanish everywhere. Therefore, the

constitutive relationships are given as

$$\begin{Bmatrix} \epsilon_x \\ \epsilon_y \\ \epsilon_{xy} \end{Bmatrix} = \begin{bmatrix} S_{11} & S_{12} & 0 \\ S_{21} & S_{22} & 0 \\ 0 & 0 & S_{33} \end{bmatrix} \begin{Bmatrix} \sigma_x \\ \sigma_y \\ \tau_{xy} \end{Bmatrix} \tag{6.1}$$

Where, S_{11}, S_{22}, S_{33}, S_{12}, and S_{21} are deformation coefficients and related to the

material parameters as follows:

$$S_{11} = \frac{1 - v_h^2}{E_h} \qquad\qquad S_{22} = \frac{1 - v_{hv}v_{vh}}{E_v}$$

$$S_{12} = S_{21} = -\frac{v_{vh}(1 + v_h)}{E_v} \qquad\qquad S_{33} = \frac{1}{G_{vh}}$$

(6.2)

where:

$E_v =$ elastic modulus in vertical direction

$E_h =$ elastic modulus in horizontal direction

$v_{vh} =$ Poisson's ratio for effect of vertical stress on horizontal strain

$v_{hv} =$ Poisson's ratio for effect of horizontal stress on vertical strain

$v_h =$ Poisson's ratio for effect of horizontal stress on horizontal strain

$G_{vh} =$ independent shear modulus in vertical plane

From energy considerations (Hearmon 1961; Poulos and Davis 1974), the following relationships among the elastic parameters must be satisfied:

$$\frac{E_v}{v_{vh}} = \frac{E_h}{v_{hv}}$$

(6.3)

$$1 - v_h > 0 \qquad 1 + v_h > 0 \qquad 1 - v_h - 2v_{hv}v_{vh} > 0$$

(6.4)

For the case of isotropy the conditions that,

$$E_h = E_v = E , \qquad and \qquad v_{hv} = v_{vh} = v_h - v$$

(6.5)

are necessary conditions but not sufficient to insure isotropy. A final condition is:

$$G_{vh} = G = \frac{E}{2(1 + v)}$$

(6.6)

6.3   METHOD OF CALCULATIONS

The final stresses due to tunnel excavation in the cross-anisotropic rock may be obtained by the superposition of stresses resulting from two ca.es (Figure 6.3): case (a) where the infinite medium loaded by the initial state of stress (before excavating the tunnel), and case (b) of releasing the initial stresses at the boundary of the excavated tunnel. The displacements in the medium due to the excavation of the tunnel result directly from case (b).

The problem of finding the stresses and displacements in an infinite medium with an opening loaded at the circular boundary was reduced by Green and Zerna (1968) to the problem of finding two complex potentials $V(z)$ and $W(z)$ satisfying the boundary conditions. The symbol z now represents the complex variable:

$z = x + iy$ in cartesian coordinates, or

$z = re^{i\theta}$ in polar coordinates

The boundary conditions for stresses at $r=a$, where a is the radius of the tunnel, are represented by $p(ae^{i\theta})$ and $q(ae^{i\theta})$ for normal and shear stresses respectively. The complex potentials could be represented in a power series as

$$V(z) = \sum_{n=0}^{\infty} (R_n + iS_n)\frac{a^n}{z^n}$$

$$W(z) = \sum_{n=0}^{\infty} (-U_n + iT_n)\frac{a^n}{z^n}$$

(6.7)

where:

$$R_n = \frac{1}{\pi} \int_0^{2\pi} p(ae^{i\theta}) \cos n\theta \, d\theta \qquad\qquad S_n = \frac{1}{\pi} \int_0^{2\pi} p(ae^{i\theta}) \sin n\theta \, d\theta$$

$$T_n = \frac{1}{\pi} \int_0^{2\pi} q(ae^{i\theta}) \cos n\theta \, d\theta \qquad\qquad U_n = \frac{1}{\pi} \int_0^{2\pi} q(ae^{i\theta}) \sin n\theta \, d\theta \qquad (6.8)$$

$$R_o = U_o = \frac{1}{2\pi} \int_0^{2\pi} p(ae^{i\theta}) \, d\theta \qquad\qquad -S_o = T_o = \frac{1}{2\pi} \int_0^{2\pi} q(ae^{i\theta}) \, d\theta$$

so that S_n, R_n and U_n, T_n are respectively the Fourier coefficients in the expansions of $p(ae^{i\theta})$

and $q(ae^{i\theta})$ in Fourier Series. Therefore,

$$p(ae^{i\theta}) = R_o + \sum_{n=1}^{\infty} (R_n \cos n\theta + S_n \sin n\theta) \qquad (6.9\text{-a})$$

$$q(ae^{i\theta}) = T_o + \sum_{n=1}^{\infty} (T_n \cos n\theta + U_n \sin n\theta) \qquad (6.9\text{-b})$$

The complex potentials $V(z)$ and $W(z)$ in Eq. 6.7 are obtained through Eqs. 6.8 and 6.9.

The solution for the tangential stresses at the boundary of the hole in terms of these complex potentials is

$$\sigma_\theta = \frac{(1 + \gamma_1 e^{-2i\theta})(1 + \gamma_2 e^{-2i\theta}) V(z) + 2(1 - \gamma_1\gamma_2 e^{-4i\theta}) W(z)}{2(1 - \gamma_1 e^{-2i\theta})(1 - \gamma_2 e^{-2i\theta})}$$
$$+ \frac{(1 + \bar{\gamma}_1 e^{2i\theta})(1 + \bar{\gamma}_2 e^{2i\theta}) \bar{V}(\bar{z}) + 2(1 - \bar{\gamma}_1\bar{\gamma}_2 e^{4i\theta}) \bar{W}(\bar{z})}{2(1 - \bar{\gamma}_1 e^{2i\theta})(1 - \bar{\gamma}_2 e^{2i\theta})} \qquad (6.10)$$

where: $\bar{V}(\bar{z})$ and $\bar{W}(\bar{z})$ are the conjugates of the complex potentials $V(z)$ and $W(z)$ respectively.

$$\gamma_1 = \frac{\alpha_1 - 1}{\alpha_1 + 1}, \quad |\gamma_1| < 1 \qquad \gamma_2 = \frac{\alpha_2 - 1}{\alpha_2 + 1}, \quad |\gamma_2| < 1 \qquad \text{(6.11-a)}$$

$$\alpha_1^2 \alpha_2^2 = \frac{S_{11}}{S_{22}} \qquad \alpha_1^2 + \alpha_2^2 = \frac{2S_{12} + S_{33}}{S_{22}} \qquad \text{(6.11-b)}$$

The displacement, in terms of complex variables, is $D = u_x + iu_y$, where u_x is the displacement in x-direction and u_y is the displacement in y-direction. At the circumference of the tunnel $r = |z| = a$, it has been shown by Green and Zerna (1968) that the displacement D may be expressed in terms of two complex functions $f(z)$ and $g(z)$ and their conjugates $\overline{f}(\overline{z})$ and $\overline{g}(\overline{z})$ as

$$D = \delta_1 f(z) + \overline{\rho}_1 \overline{f}(\overline{z}) + \delta_2 g(z) + \overline{\rho}_2 \overline{g}(\overline{z}) \qquad \text{(6.12)}$$

The functions $f(z)$ and $g(z)$ are defined by their derivatives $f'(z)$ and $g'(z)$ which are functions of the complex potentials $W(z)$ and $V(z)$, which have been determined;

$$f'(z) = \frac{(1 + \gamma_2 \frac{a^2}{z^2})V(z) + (1 - \gamma_2 \frac{a^2}{z^2})W(z)}{4(\gamma_1 - \gamma_2)} \qquad \text{(6.13-a)}$$

$$g'(z) = -\frac{(1 + \gamma_1 \frac{a^2}{z^2})V(z) + (1 - \gamma_1 \frac{a^2}{z^2})W(z)}{4(\gamma_1 - \gamma_2)} \qquad \text{(6.13-b)}$$

where δ_1, δ_2, ρ_1, and ρ_2 are functions of the elastic constants and given by:

$$\begin{aligned}
\delta_1 &= (1 + \gamma_1)\beta_2 - (1 - \gamma_1)\beta_1 & \delta_2 &= (1 + \gamma_2)\beta_1 - (1 - \gamma_2)\beta_2 \\
\rho_1 &= (1 + \gamma_1)\beta_2 + (1 - \gamma_1)\beta_1 & \rho_2 &= (1 + \gamma_2)\beta_1 + (1 - \gamma_2)\beta_2
\end{aligned} \qquad \text{(6.14)}$$

where:
$$\beta_1 = S_{12} - \alpha_1^2 S_{22} \qquad \beta_2 = S_{12} - \alpha_2^2 S_{22} \qquad \text{(6.15)}$$

It should be noted that the symbols used in Eqs. 6.14 and 6.15 are different from those used by Green and Zerna.

In general, two cases arise:

(a) $\bar{\gamma}_1 = \gamma_1$, $\qquad \bar{\gamma}_2 = \gamma_2$

so that γ_1 and γ_2 are real. In this case, $\bar{\rho}_1 = \rho_1$ and $\bar{\rho}_2 = \rho_2$ (i.e. ρ_1 and ρ_2 are real)

(b) $\bar{\gamma}_2 = \gamma_1$, $\qquad \bar{\rho}_1 = \rho_2$

so that γ_1 and γ_2 are complex conjugates. In this case, $\rho_2 = \bar{\rho}_1$ and $\rho_1 = \bar{\rho}_2$ (i.e. ρ_1 and ρ_2

are complex conjugates).

For isotropic media, $\alpha_1 = \alpha_2 = 1$, therefore,

$$\gamma_1 = \gamma_2 = \delta_1 = \delta_2 \to 0 \qquad \rho_1 = \rho_2 \to \frac{-2(1+v)}{E} \qquad (6.16)$$

Equation (6.10), with the aid of Eqs. (6.7) and (6.11), is the formal solution for

the tangential stress, while equation (6.12), with the aid of Eqs. (6.7), (6.13), (6.14), and

(f 15), is the formal solution for the radial displacement. In the following sections, these

formal solutions will be reduced to engineering quantities.

6.4 CLOSED FORM SOLUTIONS OF THE STRESSES AND DISPLACEMENTS

Consider a tunnel driven in a cross-anisotropic rockmass acting upon by the initial

stresses P_v and P_h as shown in Figure 6.3. Utilizing the theory discussed in the

previous section, the closed form solution for the tangential stresses along the

circumference of the circular tunnel is derived as

$$\sigma_\theta = \frac{2 + 2(\gamma_1 + \gamma_2)^2 - 2\gamma_1^2\gamma_2^2 - 4(\gamma_1 + \gamma_2)\cos 2\theta}{(1 + \gamma_1^2 - 2\gamma_1\cos 2\theta)(1 + \gamma_2^2 - 2\gamma_2\cos 2\theta)} P_o$$
$$+ \frac{4(\gamma_1 + \gamma_2) - 4(1 + \gamma_1\gamma_2)\cos 2\theta}{(1 + \gamma_1^2 - 2\gamma_1\cos 2\theta)(1 + \gamma_2^2 - 2\gamma_2\cos 2\theta)} Q_o \qquad (6.17)$$

where: P_o is the hydrostatic initial stress component ($\frac{P_h + P_v}{2}$)

Q_o is the deviatoric initial stress component ($\frac{P_h - P_v}{2}$)

The solutions derived for the radial displacements (u_a) and the tangential displacements (u_θ), respectively, are

$$u_a = \frac{a}{2(\gamma_1 - \gamma_2)} \{P_o(\gamma_2\rho_1 - \gamma_1\rho_2) + Q_o(\rho_1 - \rho_2) \qquad (6.18)$$
$$+ [P_o(\gamma_2\delta_1 - \gamma_1\delta_2) + Q_o(\delta_1 - \delta_2)]\cos 2\theta\}$$

$$u_\theta = \frac{a}{2(\gamma_1 - \gamma_2)}[P_o(\gamma_1\delta_2 - \gamma_2\delta_1) + Q_o(\delta_2 - \delta_1)]\sin 2\theta \qquad (6.19)$$

The complete derivation of Eqs. 6.17 to 6.19 is given in Appendix 6A.

6.4.1 Case of Pressure Tunnel

The tangential stresses at the circumference of a pressure tunnel of an internal pressure (P_i) in a cross-anisotropic rock is given by Eq. 6.17 with the substitution of $(P_o - P_i)$ in place of (P_o). Therefore, the solution for the tangential stresses in case of pressure tunnel is

$$\sigma_\theta = \frac{2 + 2(\gamma_1 + \gamma_2)^2 - 2\gamma_1^2\gamma_2^2 - 4(\gamma_1 + \gamma_2)\cos2\theta}{(1 + \gamma_1^2 - 2\gamma_1\cos2\theta)(1 + \gamma_2^2 - 2\gamma_2\cos2\theta)}(P_o - P_i)$$
$$+ \frac{4(\gamma_1 + \gamma_2) - 4(1 + \gamma_1\gamma_2)\cos2\theta}{(1 + \gamma_1^2 - 2\gamma_1\cos2\theta)(1 + \gamma_2^2 - 2\gamma_2\cos2\theta)}Q_o \qquad (6.20)$$

The radial and tangential displacements resulting from the internal pressure are given by Eqs. 6.18 and 6.19 respectively with the substitution of $(-P_i)$ in place of (P_o) and $(Q_o = 0)$. Therefore, the radial and tangential displacements in the case of pressure tunnel, respectively, are

$$u_a = \frac{aP_i}{2(\gamma_1 - \gamma_2)} \{(\gamma_1\rho_2 - \gamma_2\rho_1) + (\gamma_1\delta_2 - \gamma_2\delta_1)\cos2\theta\} \qquad (6.21)$$

$$u_\theta = \frac{aP_i}{2(\gamma_1 - \gamma_2)}(\gamma_2\delta_1 - \gamma_1\delta_2)\sin2\theta \qquad (6.22)$$

6.5 COMPARISON TO SOME CASES OF KNOWN SOLUTIONS

(a) Green and Taylor Solution for Stresses

Closed form solutions for displacements on the circumference of an excavated tunnel in an elastic cross-anisotropic medium resulting from the relief of the *in situ* stress have not been obtained in the literature. However, the stress distribution around a pre-existing hole in an infinite plate loaded at infinity from one direction is known (Green and Taylor 1939 and 1945). For an elastic medium, the stress distribution from a pre-existing hole or from stress relief at the hole boundary in pre-loaded medium should be the same. Therefore, the closed form solutions for stresses, when $P_v = 0$, should reduce to that given by Green and Taylor.

Under the existence of a uniform pressure T parallel to the horizontal direction

(x-axis) the tangential stress σ_θ at the hole boundary is given by Green and Taylor as

$$\sigma_\theta = \frac{T(1 + \gamma_1)(1 + \gamma_2)(1 + \gamma_1 + \gamma_2 - \gamma_1\gamma_2 - 2\cos 2\theta)}{(1 + \gamma_1^2 - 2\gamma_1\cos 2\theta)(1 + \gamma_2^2 - 2\gamma_2\cos 2\theta)} \qquad (6.23)$$

This corresponds to the case of: $P_v=0$ and $P_h=T$. Therefore, $P_o = Q_o = T/2$. Substituting

for the values of P_o and Q_o in Eq. 6.17, an identical solution as given by Green and

Taylor is obtained (Eq. 6.23).

(b) Case of Isotropic Medium

The solutions for the stresses and displacements for the case of a tunnel excavated

in elastic isotropic rocks are well known (see e.g. Yuen 1979). The tangential stresses

and the radial and tangential displacements at the circumference of the tunnel wall, in

terms of the hydrostatic and deviatoric components of initial stresses, are, respectively:

$$\sigma_\theta = 2P_o - 4Q_o\cos 2\theta \qquad (6.24)$$

$$u_a = \frac{a(1+v)}{E}[P_o + (3-4v)Q_o\cos 2\theta] \qquad (6.25)$$

$$u_\theta = -\frac{a(1+v)}{E}Q_o(3-4v)\sin 2\theta \qquad (6.26)$$

Taking the limit of σ_θ, u_a, and u_θ in Eqs. 6.17, 6.18, and 6.19, respectively, as

$$\gamma_1 = \gamma_2 = \delta_1 = \delta_2 \to 0 \qquad \text{and} \qquad \rho_1 = \rho_2 \to \frac{-2(1+v)}{E},$$

Eqs. 6.17, 6.18, and 6.19 are reduced to Eqs. 6.24, 6.25, and 6.26 respectively. The

complete derivation is given in Appendix 6B.

6.6 EXAMPLE OF DESIGN ANALYSIS

For the design of Sir Adam Beck Niagara Generating Station (SABNGS) No. 3 project, twin tunnels, each of approximately 13 m diameter and 10 Km long are required. The tunnels will be excavated in Queenston Shale at depths of 150 to 200 m. The five independent parameters required to describe the deformation behaviour of Queenston Shale, using the theory of elastic orthotropic (cross-anisotropic) material, were determined using the method presented by Lo and Hori (1979). Typical values for the parameters obtained are: $E_h = 15.8$ GPa, $E_v = 10.5$ GPa, $G_{vh} = 3.95$ GPa, $v_{vh} = 0.3$, and $v_h = 0.3$, implying, $E_h/E_v = 1.5$, $E_h/G_{vh} = 4$, and $v_{hv} = 0.44$. The values of E_v and v_{vh} are usually taken to represent the elastic parameters of the material if the theory of elastic isotropic material is adopted.

The initial stresses at a typical cross section of the tunnels at depth 200 m from the ground surface are: $P_v = 5.2$ MPa and $P_h = 21$ MPa, giving: $K_o = 4$, $P_o = 13.1$ MPa, and $Q_o = 7.9$ MPa.

Using the values of the five elastic parameters discussed above and Eqs. 6.2 and 6.11, the following values of γ_1 and γ_2 are obtained:

$$\gamma_1 = 0.1432 \qquad \gamma_2 = -0.2296$$

The values of δ_1, δ_2, ρ_1, and ρ_2 are obtained, using Eq. 6.14, as

$$\delta_1 = 7.813 \times 10^{-5} \qquad \delta_2 = -5.625 \times 10^{-5}$$

$$\rho_1 = -2.368 \times 10^{-4} \qquad \rho_2 = -2.269 \times 10^{-4}$$

The tangential stresses and radial displacements are obtained by substituting the values of P_o, Q_o, γ_1, γ_2, δ_1, δ_2, ρ_1, and ρ_2 in Eqs. 6.17 and 6.18, respectively. For comparison, the corresponding values of stresses and displacements, assuming the rock is isotropic, are also calculated using Eqs. 6.21 and 6.22.

Figure 6.4 shows the distributions of the tangential stresses and radial displacements at the circumference of the tunnels for the two cases considered (isotropic and cross-anisotropic). A summary of the stresses and displacements obtained at the crown and the springline is given in Table 6.1. The differences between the two cases are represented as percentages of the results obtained for the cross-anisotropic case. From Figure 6.4 and Table 6.1, the following observations may be made:

(a) Compressive stress concentration at the crown-invert with a stress concentration factor of 3 is predicted by the anisotropic theory. The assumption of isotropy leads to a small difference of only 9%.

(b) Both isotropic and anisotropic theories predict tangential tensile stress at the springline. However, consideration of anisotropy leads to significantly lower values, the difference in magnitude being as much as 170%.

(c) Both theories predict inward displacements at the springline; consideration of anisotropy gives lower predicted values by 27%.

(d) At the crown-invert, the predicted direction of elastic displacements depends on the theory used, although the magnitudes of displacements are small.

These observations are significant in the interpretation of results of field monitoring of stresses and displacements in test adits and during construction of tunnels.

6.7 EFFECTS OF ANISOTROPIC ELASTIC PARAMETERS AND K_o ON STRESSES AND DISPLACEMENTS

The five elastic parameters characterizing the deformation behaviour of the rock (E_v, E_h, v_h, v_{vh}, and G_{vh}) can be determined using the method described by Lo and Hori (1979). Experience gained from testing of different shaly rocks from Southern Ontario showed that the elastic parameters generally vary within the following ranges:

v_{vh}: 0.2 to 0.4 v_h: 0.2 to 0.4 E_h/E_v: 1 to 2 E_h/G_{vh}: 3 to 10

In situ stress measurements in the same rock formations showed that the stress ratios (K_o) generally lie in the range of 3 to 30 (Lo 1986). These ranges of values are used to study the effect of v_h, v_{vh}, E_h/G_{vh}, and K_o on the tangential stresses and radial displacements. For the presentation of results, stresses and displacements are expressed in dimensionless forms. The tangential stress σ_θ is normalized by the initial stress hydrostatic component P_o, and the radial displacement u_a is expressed by the dimensionless displacement $\Omega = \dfrac{u_a E_h}{a P_o}$. The results are shown in Figures 6.5 and 6.6.

(a) Effect of v_h

Referring to Figures 6.5-a and 6.6-a, it may be observed that the effects of v_h on both the tangential stresses and radial displacements are negligible.

(b) Effect of v_{vh}

The effect of v_{vh} on the tangential stress and radial displacement is shown on Figures 6.5-b and 6.6-b respectively. It may be observed from Figure 6.5-b that the effect of v_{vh} on the tangential stresses is small. The effects of v_{vh} on the displacements (Figure 6.4-b) however, show some interesting and significant features. Starting from the crown-invert region, the effect of v_{vh} progressively increases towards the springline. At the springline, an increase of v_{vh} from 0.2 to 0.4 leads to a change of Ω from -0.1 to 0.5. Therefore, not only the magnitude of Ω is affected, but also the direction of displacement is altered, for the case considered.

(c) Effect of E_h/G_{vh}

Figures 6.5-c and 6.6-c show the effect of E_h/G_{vh} on the tangential stresses and radial displacements respectively. It may be observed from Figure 6.5-c that as the value of E_h/G_{vh} increases, the compressive tangential stresses at both the springline and the crown increase, with higher stress concentration at the crown. It may be seen from Figure 6.6-c that the radial displacements at both the crown and the springline are highly sensitive to the value of E_h/G_{vh}, increasing with E_h/G_{vh}. Therefore, E_h/G_{vh} is an important deformation parameter to consider in predicting displacements.

(d) Effect of K_o

The effects of K_o on the tangential stress and radial displacement are shown on Figures 6.5-d and 6.6-d, respectively. It may be observed from Figure 6.5-d that the compressive stress concentration increases at the crown as the value of K_o increases. On the other hand, the stress at the springline decreases and becomes tensile as the value of K_o increases.

It is obvious from Figure 6.6-d that the dimensionless displacement factor (Ω) at the springline increases (indicating greater inward displacement) as the value of K_o increases. At the crown-invert, the value of Ω decreases and then changes to outward displacement as K_o increases.

Under isotropic stress condition ($K_o = 1$), it is well known that the assumption of isotropy will lead to uniform stresses and displacements. It is interesting to note that Figures 6.5(d) and 6.6(d) show that both the stress and displacement are nonuniform for $K_o = 1$. This is a direct result of material anisotropy, which induces shear stresses and distortion even under external uniform pressure.

It may be concluded from the previous discussion that the elastic parameters controlling the degree of anisotropy of the rock have significant effects on stresses and displacements around the tunnel, and should be taken into consideration in design analysis.

6.8 CHARTS FOR DETERMINATION OF STRESSES AND DISPLACEMENTS

To facilitate calculation of stresses, Figures 6.7, 6.8, and 6.9 show the relationships of σ_θ/P_o with K_o, for different values of E_h/G_{vh} and E_h/E_v. These figures are for v_{vh} =0.2, 0.3, and 0.4, respectively.

From Figures 6.7, 6.8, and 6.9, it may be seen that the effect of E_h/E_v on stresses at the crown is negligible, for any value of K_o. At the springline, the magnitude of stress decreases slightly as E_h/E_v increases from 1 to 2.

The relationships for the dimensionless displacements Ω with K_o for v_{vh} =0.2, 0.3 and 0.4 are shown in Figures 6.10, 6.11, and 6.12 respectively. It is obvious from these figures that the radial displacement at the springline is insensitive to the value of E_h/E_v. On the other hand, the magnitude and direction of the radial displacement at the crown-invert is highly sensitive to E_h/E_v, specially for values of v_{vh} higher than 0.2. For Example, for the case of v_{vh} =0.4 (Figure 6.11), as E_h/E_v increases, the displacement changes direction from outward to inward displacement generally for values of K_o higher than 6. This is an important factor that should be taken into consideration in prediction of displacements.

6.9 CONCLUSIONS

The stresses and displacements around an unlined tunnels driven in cross-anisotropic rocks have been investigated. Closed form solutions for the stresses and

displacements are derived utilizing the stress potentials developed by Green and Zerna (1968).

The effects of anisotropy of the initial stress system and the elastic parameters on the stresses and displacements are studied. From the results of this investigation, the following conclusions may be drawn:

(a) The effects of v_h on both of the tangential stress and radial displacements are negligible.

(b) At the crown-invert, the magnitude and direction of the radial displacement are sensitive to the value of v_{vh}.

(c) The compressive stress at the crown increases with increasing E_h/G_{vh}. The radial displacements around the tunnel are highly sensitive to the value of E_h/G_{vh}, increasing substantially as E_h/G_{vh} increases.

(d) As the value of K_o increases, the compressive stress concentration at the crown-invert increases and the stress at the springline decreases and changes to tensile.

The dimensionless displacement factor (Ω) at the springline increases (indicating greater inward displacement) as the value of K_o increases. In contrast, the value of Ω at the crown decreases and then changes to outward displacement as K_o increases.

(e) The radial displacement at the springline is insensitive to E_h/E_v for any value of K_o. On the other hand, the magnitude and direction of the radial displacement at the crown-invert is highly sensitive to the value of E_h/E_v, specially for values of v_{vh} greater than

0.2.

For convenience of application, charts (Figures 6.7 to 6.12) have been prepared for the determination of stresses and displacements for given values of initial stresses and the elastic parameters.

It is believed that the results presented would be useful not only for ready determination of stresses and displacements for design considerations, but also for the interpretation of results of field monitoring in test adits and during construction.

0.2.

TABLE 6.1   ^tresses and Displacements at the Circumference of a Tunnel Driven in Queenston Shale

Stresses (MPa)						Displacements (mm)					
Springline			Crown			Springline			Crown		
iso-tropic	aniso-tropic	% diff	iso-tropic	aniso-tropic	% diff	iso-tropic	aniso-tropic	% diff	iso-tropic	aniso-tropic	% diff
-5.4	-2.0	170	57.8	63.4	8.8	21.9	17.2	27	-0.9	1.2	178

Remote Boundary

$$P_z$$

$$P_z = \gamma z$$

$$P_z$$

$$\sigma_\theta(B) = 3P_z$$

$$\sigma_\theta(A) = -P_z$$
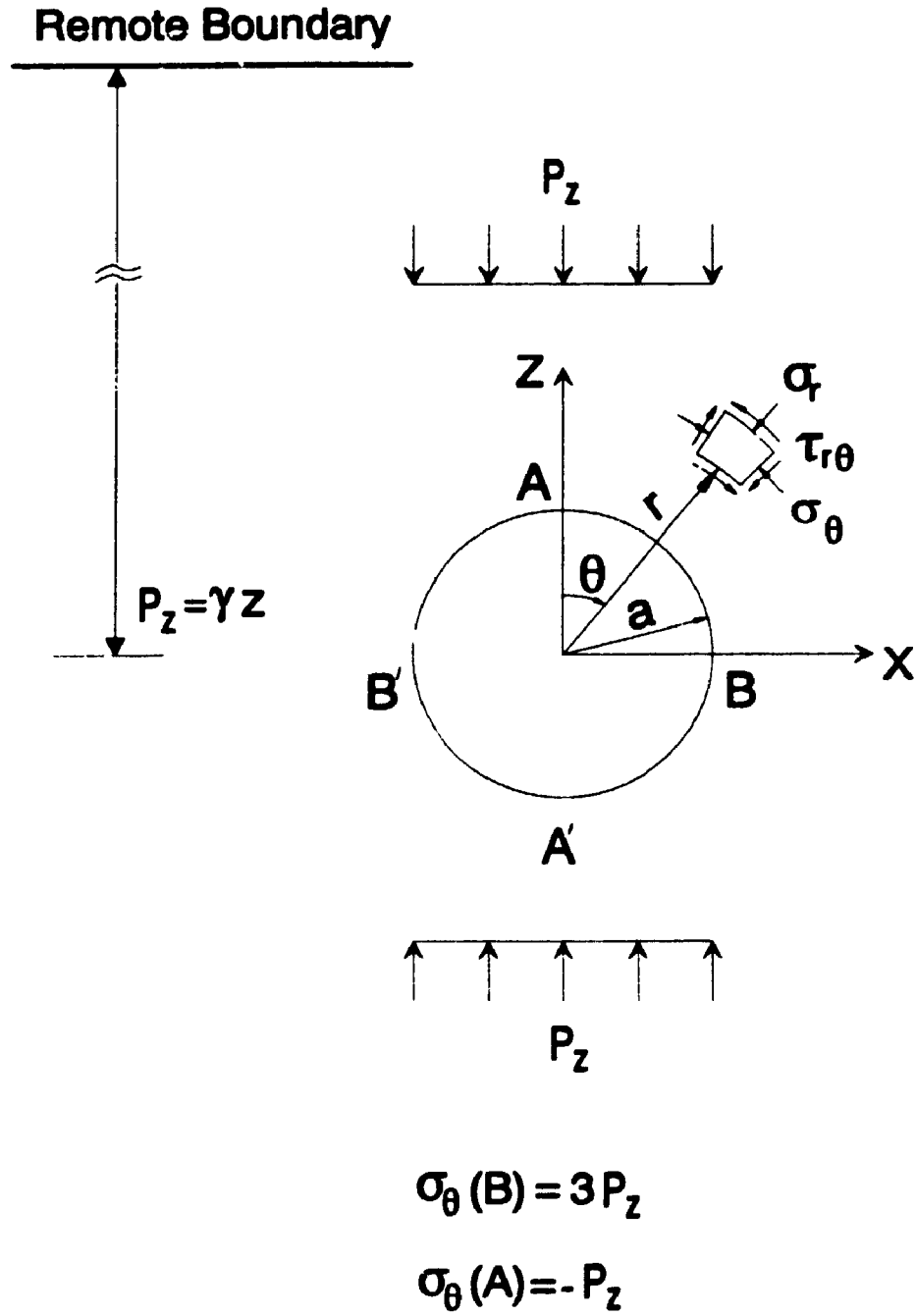
Figure 6.1 Stresses around a circular opening
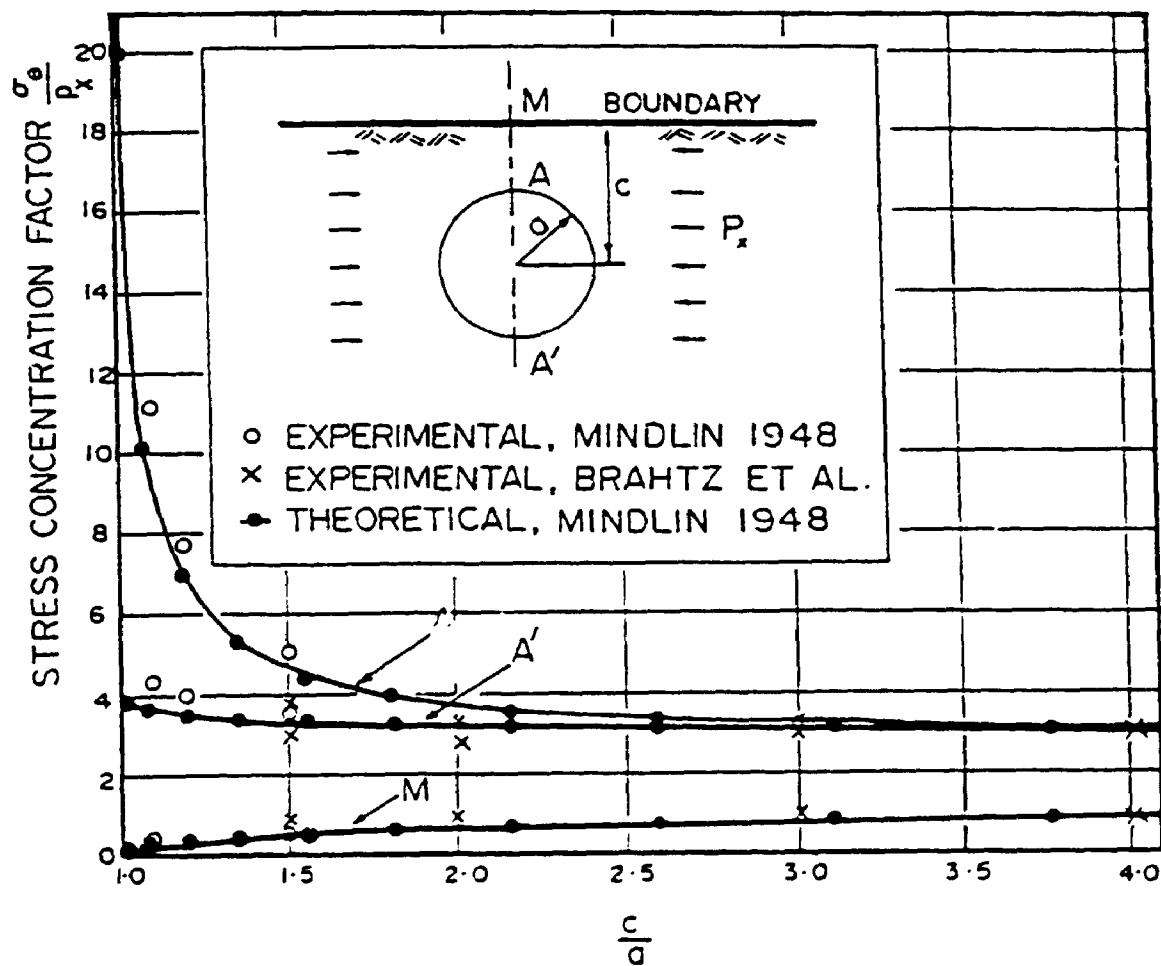
Figure 6.2   The effect of proximity of boundary on the stress concentration under horizontal *in situ* pressure (after Mindlin 1948)

(A)
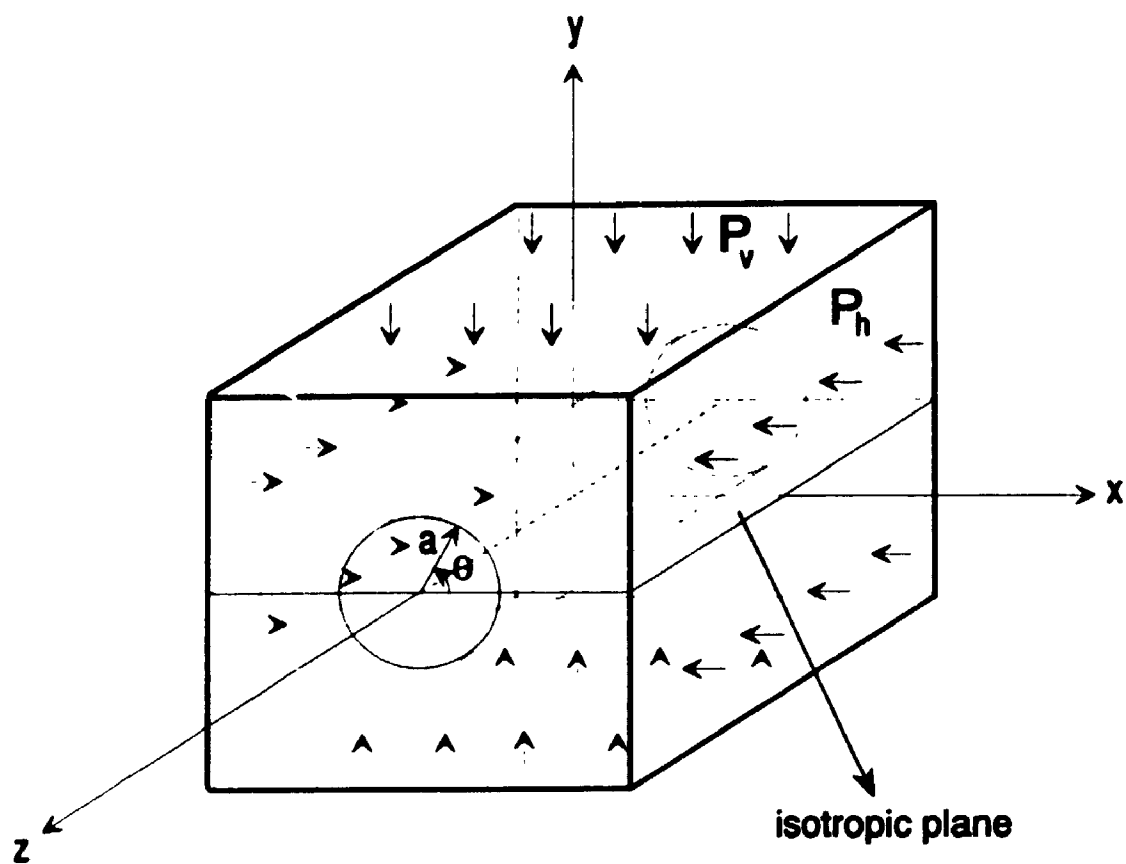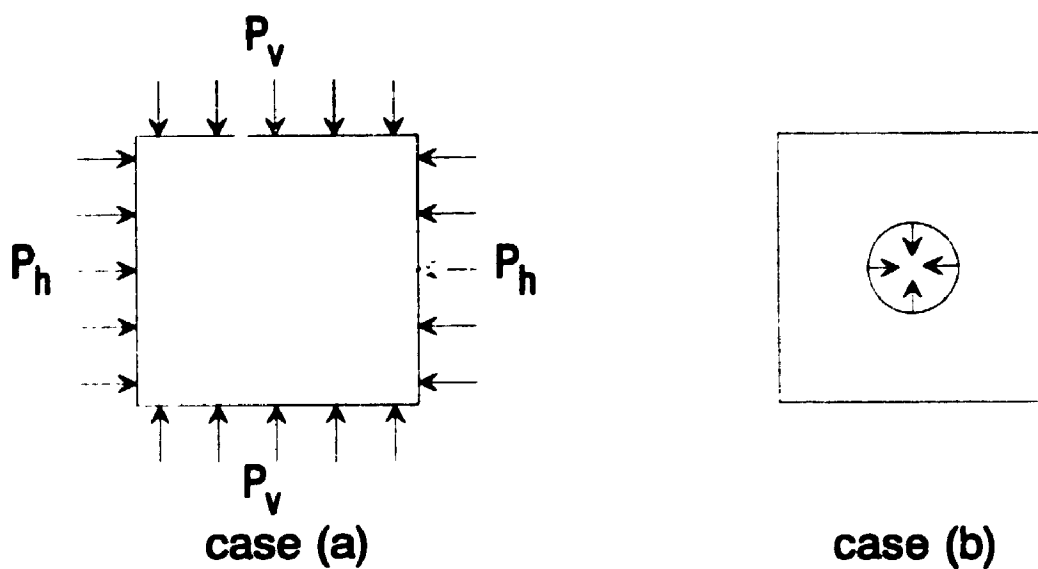
(B)

Figure 6.3 (A) Idealization of the problem

(B) Loading cases considered
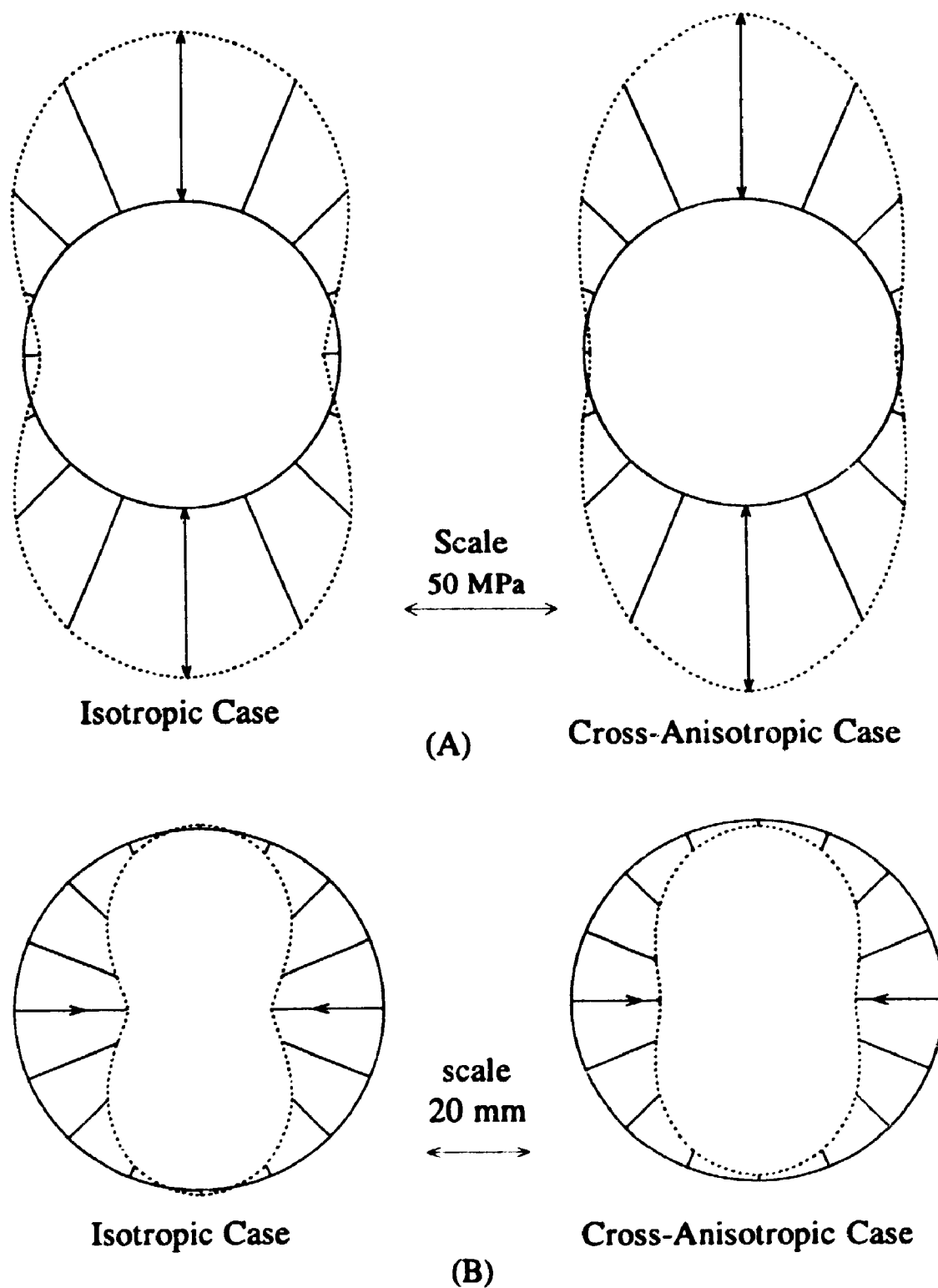
Figure 6.4 (A) Tangential stresses and (B) Radial displacements at the circumference
of the proposed tunnels in Queenston Shale for the SABNGS No. 3 project
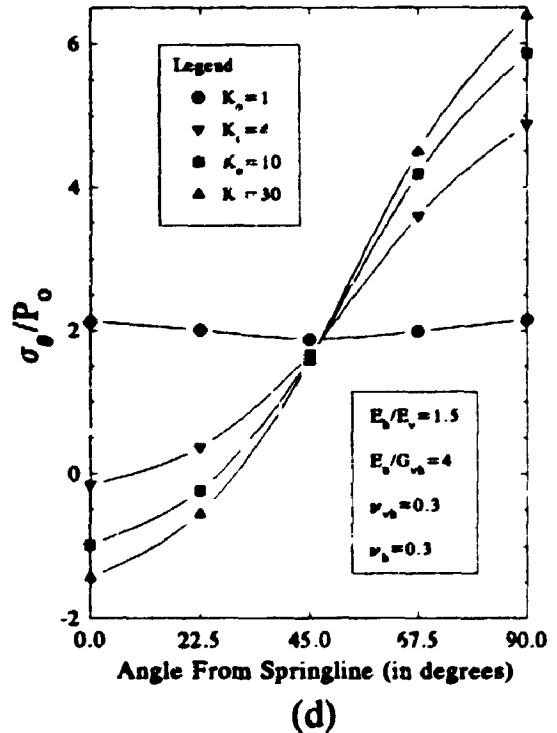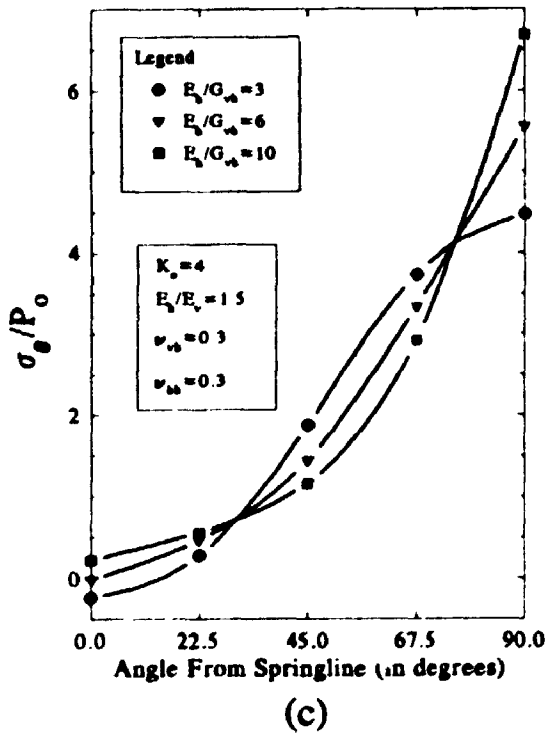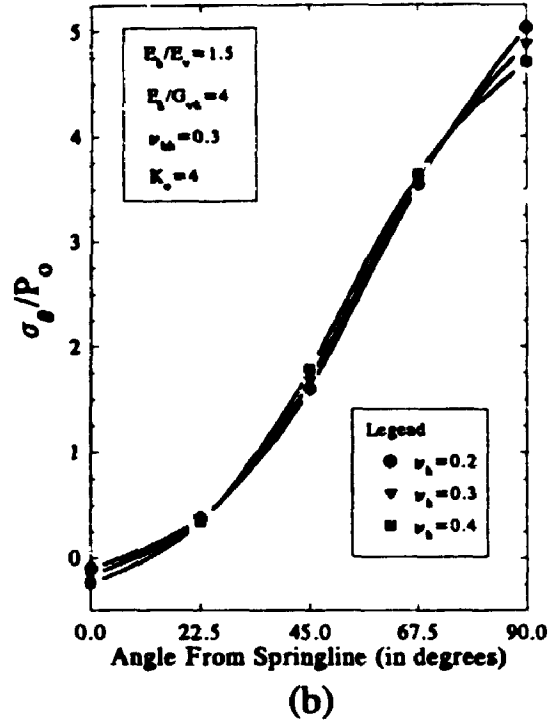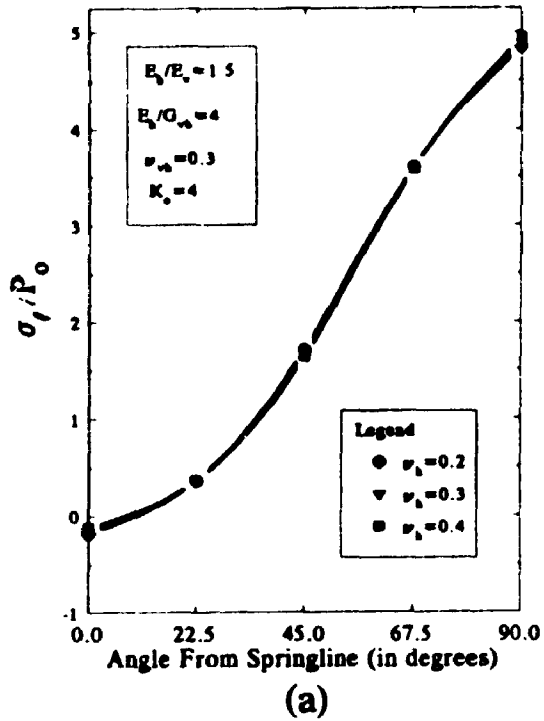
Figure 6.5 Effect of: (a)ν_h, (b)ν_{vh}, (c)E_h/G_{vh}, (d)Ko on the distribution of tangential stress
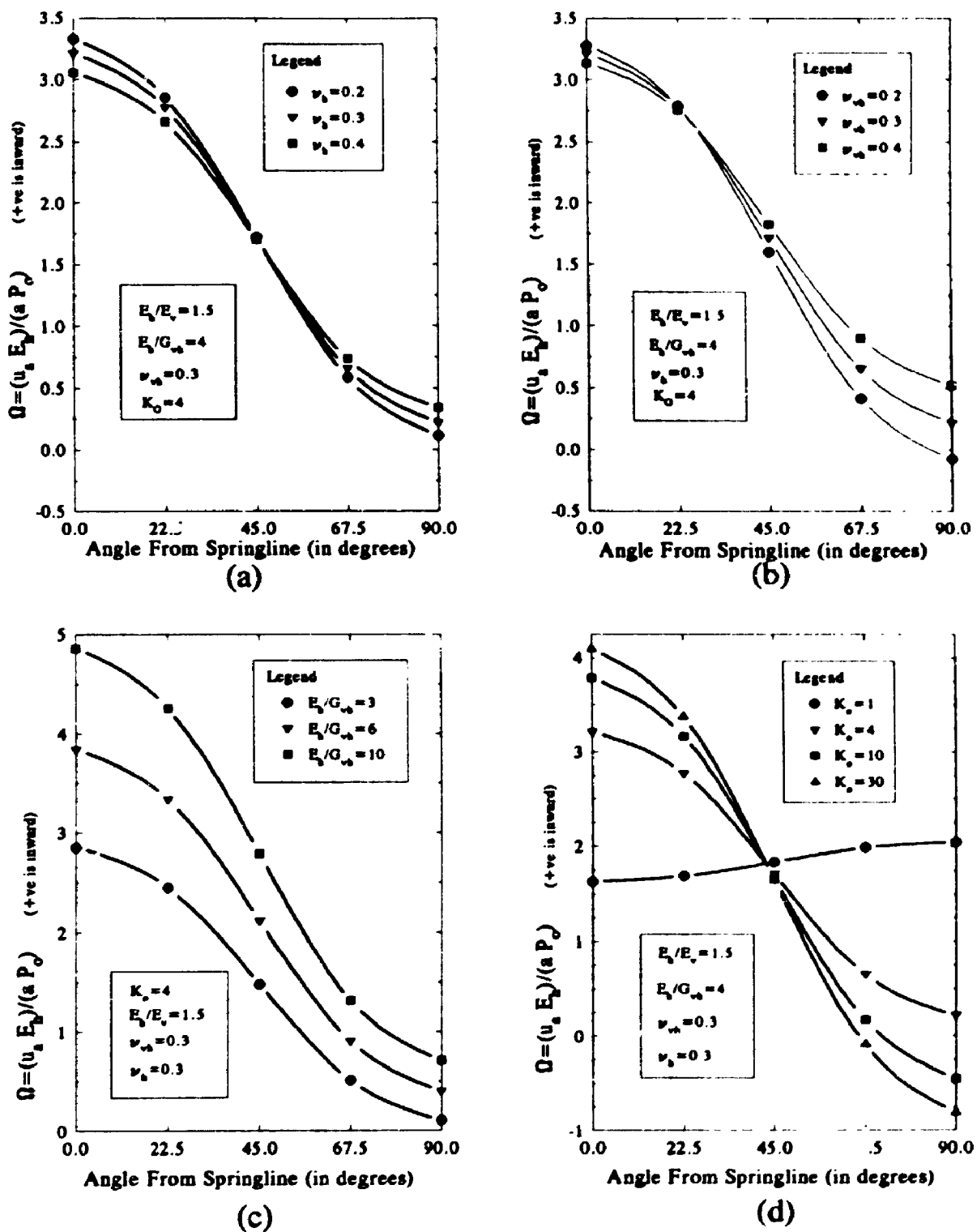
Figure 6.6 Effect of: (a)ν_h, (b)ν_{vh}, (c)E_h/G_{vh}, (d)K_o on the distribution of radial displacement at the circumference of a tunnel driven in a cross-anisotropic medium
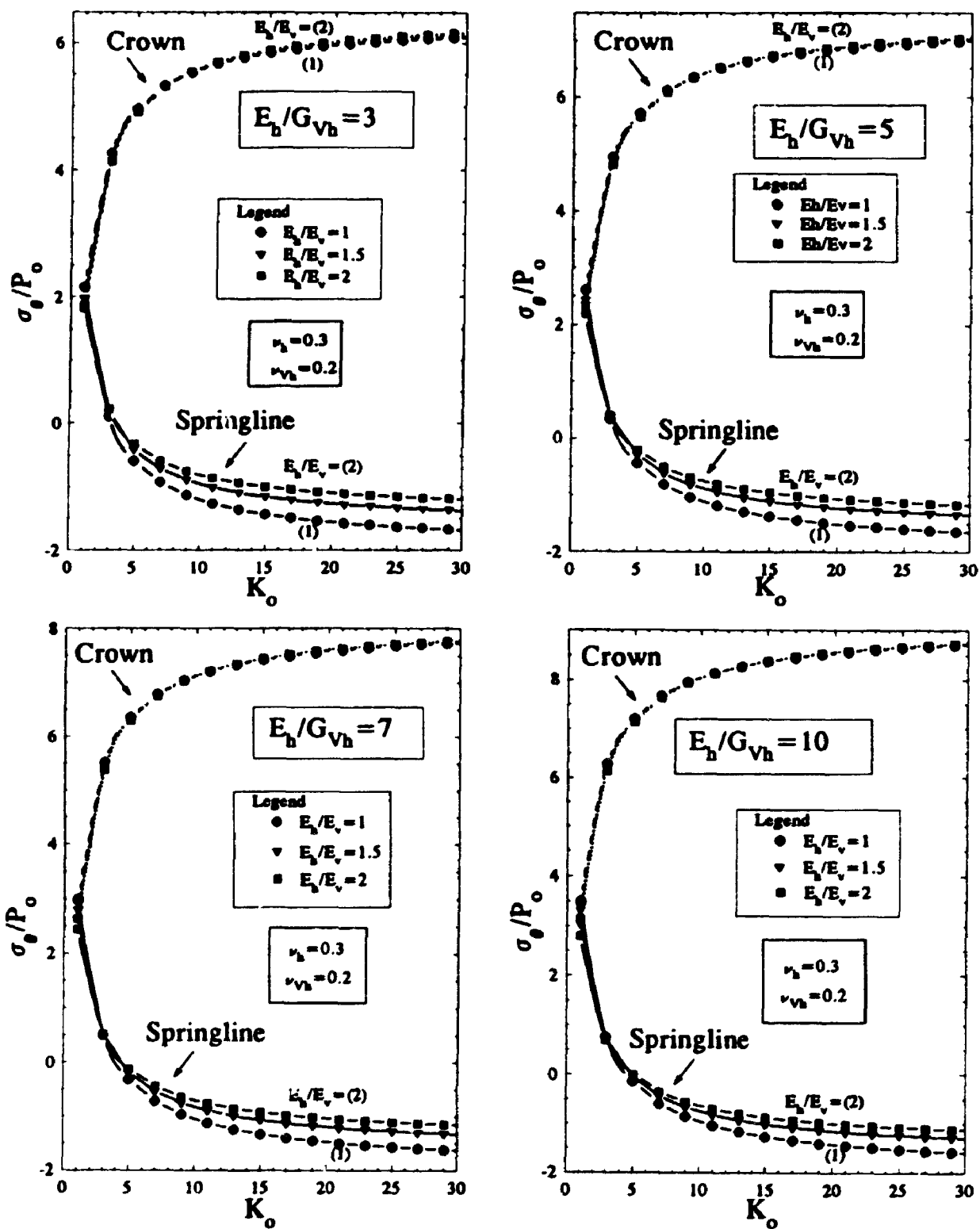
Figure 6.7 Tangential stresses at the circumference of a tunnel driven in a cross-anisotropic medium (ν_{vh}=0.2)
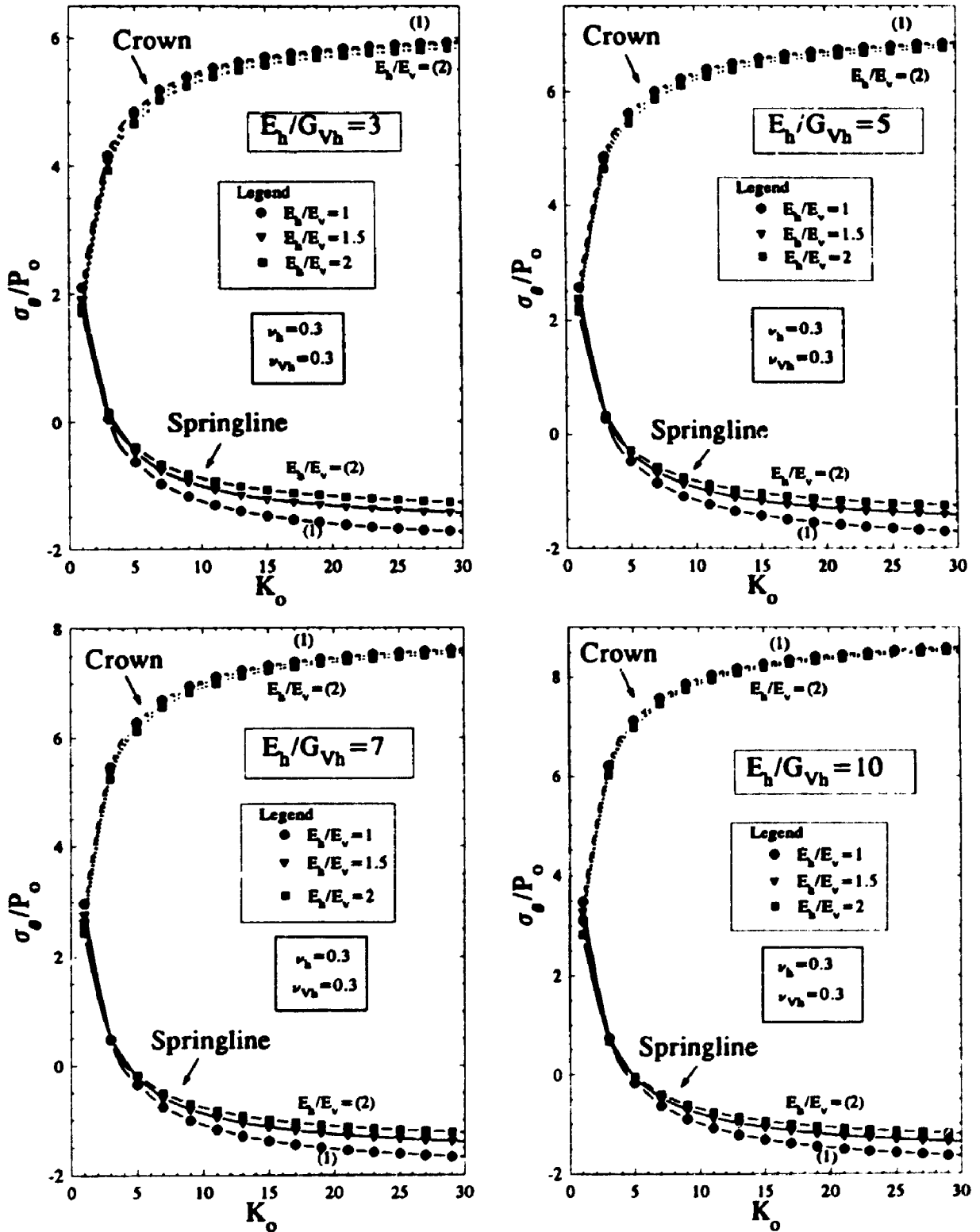
Figure 6.8 Tangential stresses at the circumference of a tunnel driven in a cross-anisotropic medium (ν_{vh}=0.3)
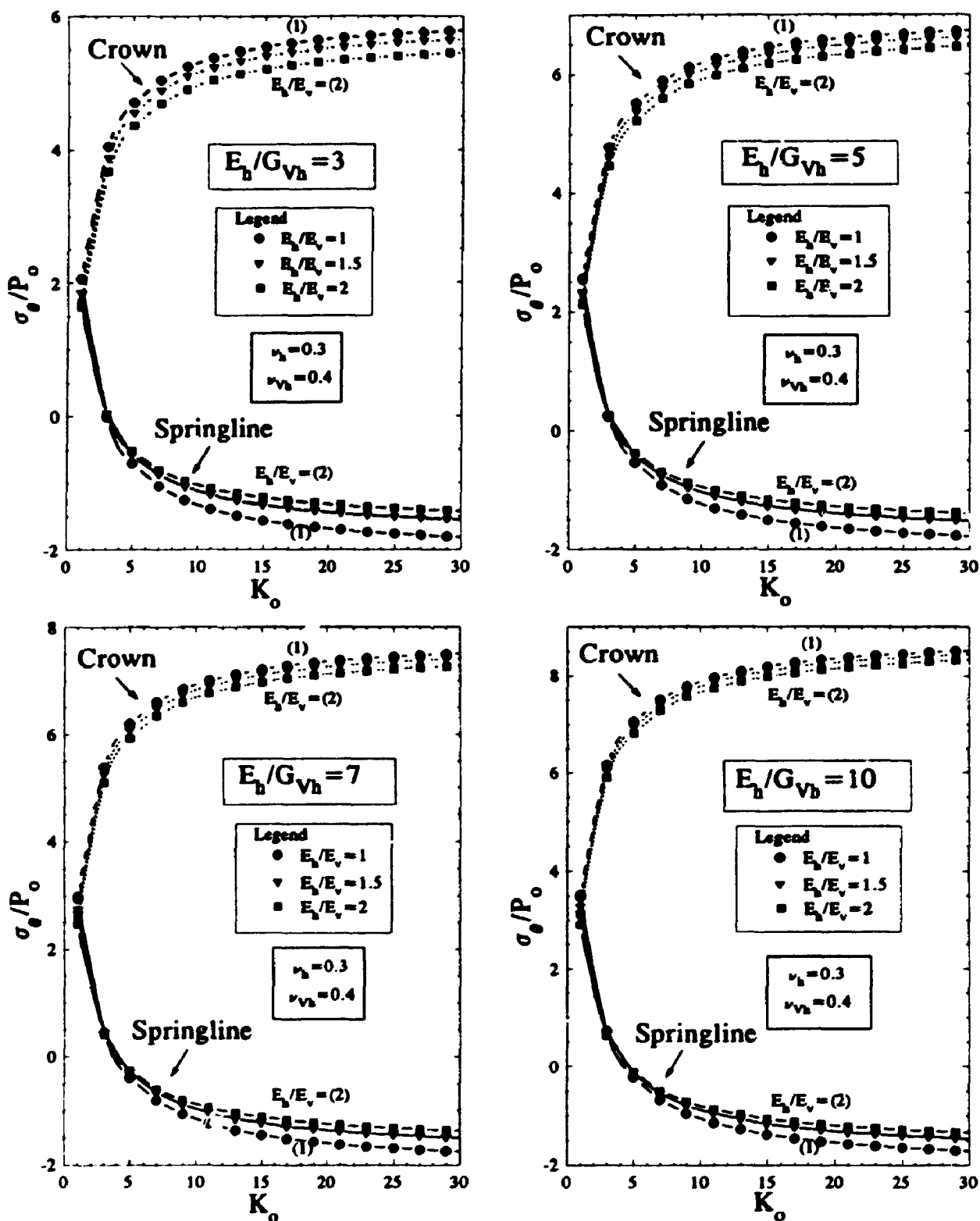
Figure 6.9 Tangential stresses at the circumference of a tunnel driven in a cross-anisotropic medium ($\nu_{vh}=0.4$)
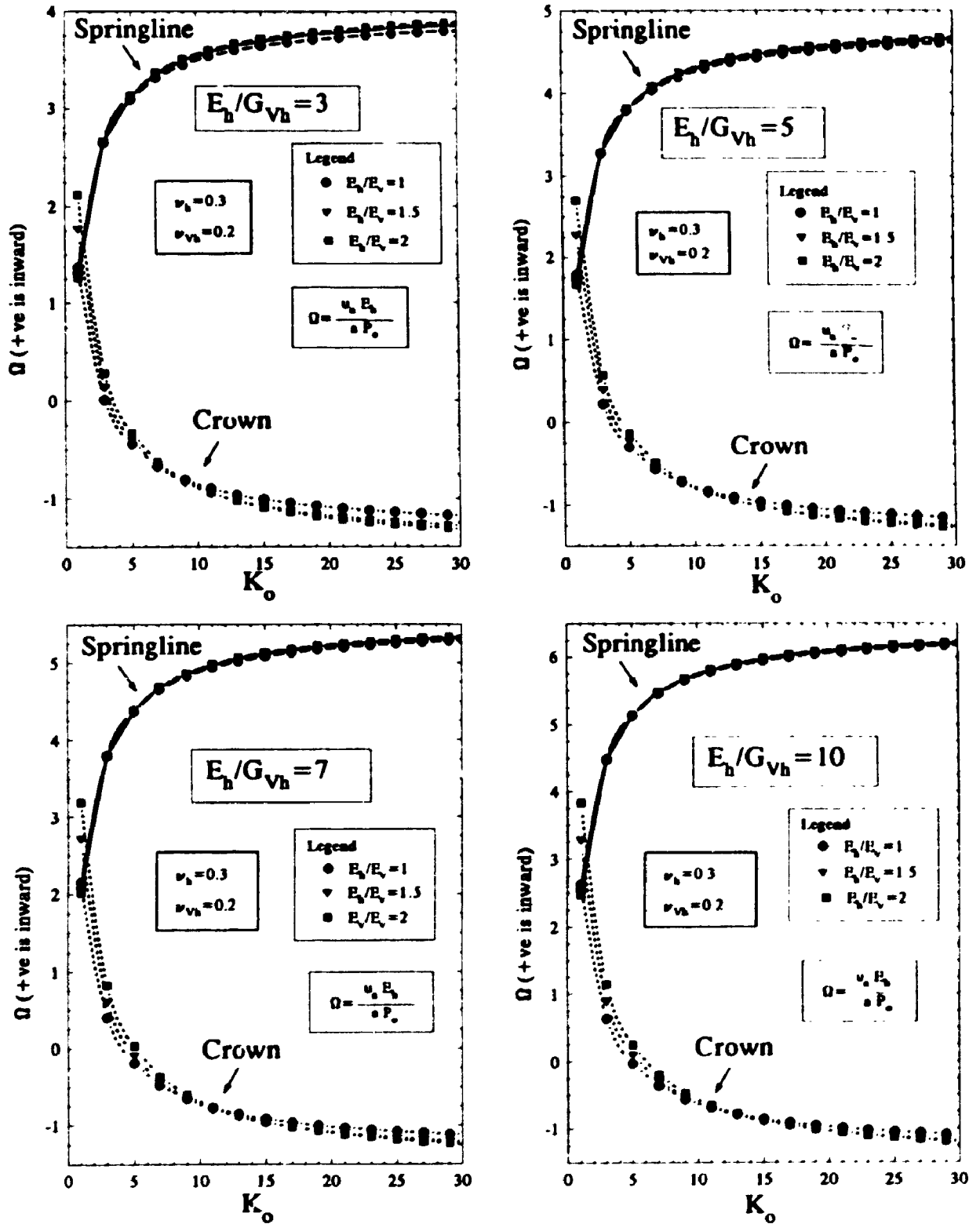
Figure 6.10 Radial displacements at the circumference of a tunnel driven in a cross-anisotropic medium $(\nu_{vh}=0.2)$
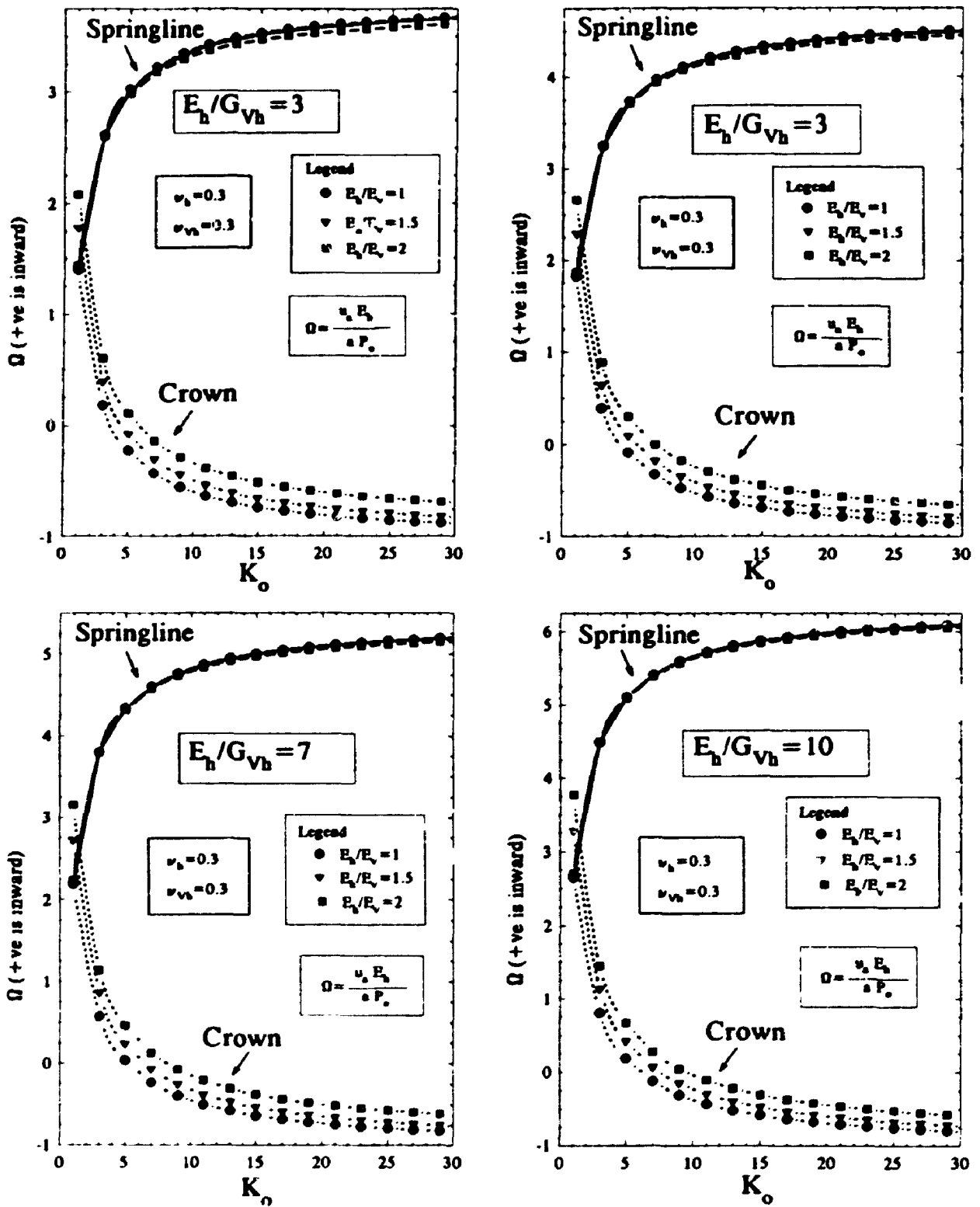
Figure 6.11 Radial displacements at the circumference of a tunnel driven in a cross-anisotropic medium (ν_{vh}=0.3)
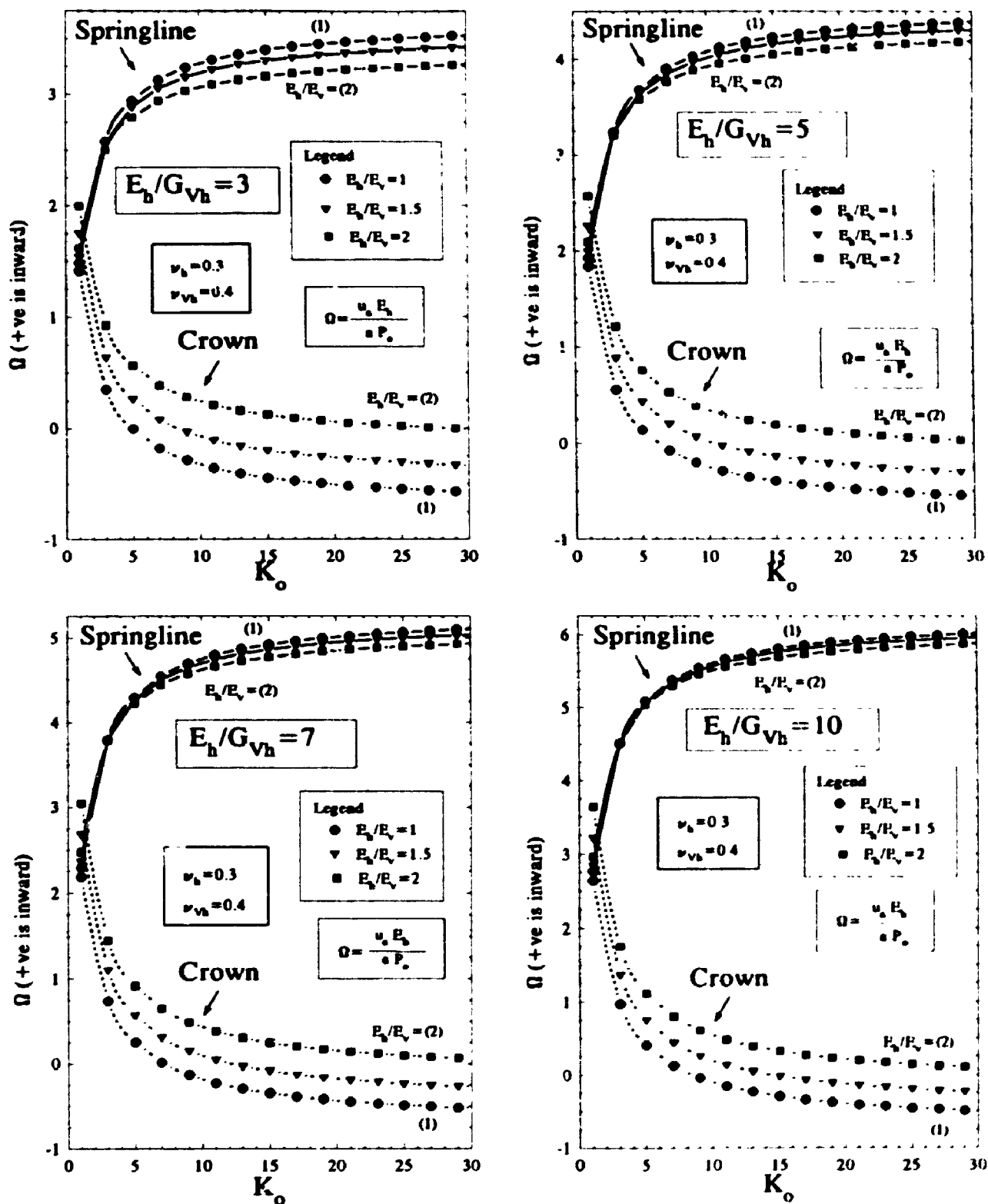
Figure 6.12 Radial displacements at the circumference of a tunnel driven in a cross-anisotropic medium (ν_{vh}=0.4)

PART III

TIME DEPENDENT DEFORMATION OF
QUEENSTON SHALE
AND
ROCK-LINING-TIME INTERACTION
IN TUNNELS

(Chapter 7-11 inclusive)

CHAPTER 7

RESULTS OF TIME-DEPENDENT DEFORMATION TESTS

PERFORMED ON QUEENSTON SHALE AND MECHANISM OF SWELLING

(SABNGS NO. 3 PROJECT)

7.1 INTRODUCTION

For the design of Sir Adam Beck Niagara Generating Station (SABNGS) No. 3 project, two diversion tunnels each of diameter 13 m and 10 km long will be excavated in Queenston Shale. The tunnels will be excavated as deep as 200 m below the ground surface. In addition, the powerhouse for the project will also be located in Queenston Shale.

One of the most important characteristics of Queenston Shale is the time-dependent deformation due to initial stress relief. Several distress problems of lining for unnels constructed in swelling shales in Southern Ontario have been reported (Lo and Yuen 1981). Queenston Shale is not only characterised by time-dependent swelling deformation due to stress relief but also the deformation continues for a long period of time.

Testing on Queenston S'ale to determine its time-dependent deformation behaviour began in 1984 at the University of Western Ontario under the supervision of Professor K.Y. Lo and has continued to the time of writing of this thesis (1994). Testing programs include free swell tests and semi-confined swell tests. Table 7.1 contains a summary of tests performed on Queenston Shale since 1984. Tests especially devoted to the study of the mechanism of swelling are not included in this table and will be

discussed at the end of this chapter. Tests for the study of long-term time-dependent deformation (5 tests) of Queenston Sha'e are also not listed in Table 7.1 and will be discussed in Chapter 8.

7.2 RESULTS OF FREE SWELL TESTS

The method of free swell test was developed at the University of Western Ontario to study the swelling behaviour of shales from Southwestern Ontario. Simplicity and inexpensivity of the free swell test have made it a practical way for the assessment of potential "rock squeeze" problems. Since the early 1970s, this method has been implemented extensively in many projects (Lo *et al.* 1978; Lo 1986).

In a free swell test, the swelling strains due to the relief of initial field stress are monitored with time in the vertical and two orthogonal horizontal directions. A plot of th.^ swelling strain versus logarithm of the elapsed time is used to determine a very useful index called the swelling potential, which can be determined for both the vertical and horizontal directions. The swelling potential has been defined by Lo *et al.* (1978) as the value of the average slope of swelling strain versus logarithm (to the base 10) of elapsed time curve between 10 and 100 days. The swelling potential is a good measure of the ability of the shale to deform with time when the initial stresses are released.

7.2.1 1984 to 1989 Investigations

In 1984 investigation, 6 free swell tests on samples recovered from borehole NF 7 between depths 79 and 122 m (elevations 94 m to 81 m) were carried out (Lee 1988). The horizontal swelling potential and the calcite content for all samples tested are

summarized in Table 7.2. It can be seen from Table 7.2 that. in general, as calcite content increases, swelling potential decreases.

For the 1985 to 1987 investigations (Lo and Lee 1990), 11 samples recovered from borehole NF4A were tested as follows: 3 samples between depths 95 and 98 m (elevations 85 to 82 m) in 1985 investigation, 3 samples between depths 101 and 106 m (elevations 79 to 74 m) in 1986 investigation, and 5 samples between depths 110 and 115 m (elevations 70 to 65 m) in 1987 investigation. Test results of the 11 free swell tests are summarized in Table 7.3. From Table 7.3 the following observations can be made:

1- The vertical swelling potential is higher than the horizontal swelling potential. The ratio of vertical to horizontal swelling potential is 1.3 to 1.9.

2- The swelling potentials in the horizontal directions are virtually identical. Th's observation indicates that the swelling behaviour for Queenston Shale in the horizontal direction is isotropic.

3- There is no general trend of swelling potential variation with depth, however, as observed for tests on samples from borehole NF7, there is a high tendency for the swelling potential to increase as calcite content decreases.

A total of 27 free swell tests were conducted in 1989 investigation on samples recovered from boreholes SD2 and SD3 (Lo 1989): 14 samples were from borehole SD2 between depths 212 and 248 m (elevations -32 to -68 m) and 13 samples were from borehole SD3 between depths 197 and 235 m (elevations -14 to -52 m). Tables 7.4 and 7.5 summarize test results for the 1989 investigation for samples recovered from SD2 and SD3 respectively. The vertical and horizontal swelling potentials in the two boreholes are plotted against depth in Figures 7.1 and 7.2.

From Tables 7.4 and 7.5 and Figures 7.1 and 7.2, the following observations can be made:

1- As observed for borehole NF4A, the horizontal swelling is generally isotropic. This observation indicates that in the horizontal plane, the time-dependent deformation is not sensitive to the difference in magnitude of initial horizontal stresses.

2- The vertical swelling potential is higher than the horizontal swelling potential. The ratio of vertical to horizontal swelling potential is 1.2 to 3.2, except for some samples with low shale contents that showed higher ratio (e.g. sample of test FSQ/SD3-5 having 15% shale and 85% siltstone showed 13% ratio). It should be noticed that some other tests of low shale content did not show the same behaviour.

3- For tests on samples taken from borehole SD-2, the values of the vertical swelling potential vary between 0.13% and 0.46%, with an average value of 0.29%. The values of the swelling potential in the horizontal direction vary between 0.03% and 0.23%, and the average value is 0.13%. Swelling potential from test FSQ/SD2-14 which was carried out on a fine-grained sandstone indicated zero swelling potential in both the vertical and horizontal directions. This test may be regarded as a control test. This observation implies that a certain amount of shale content must exist in order for time-dependent deformation to take place.

4- For tests on samples taken from borehole SD-3, the values of the vertical swelling potential vary between 0.10% and 0.30%, with an average value of 0.21%. In the horizontal direction, the values of the swelling potential vary from 0.01% to 0.24%, with an average value of 0.1%

5- As observed for tests in previous investigations, there is no general trend of variation

of swelling potential versus depth and there is a tendency for the swelling potential to increase as calcite content decreases and shale content increases.

In his study of time-dependent deformation of Queenston Shale, Lo (1989) provided a three-dimensional diagram conceptually illustrating the influence of calcite content and shale content on the swelling potential (Figure 7.3). It may be seen from the figure that for a given calcite content (*BB'*), swelling potential increases with shale content (*BB''*). For a given shale content (*AA'*), on the other hand, swelling potential decreases with the increase in calcite content (*A''A'*). Lo (1989) showed also that if both shale content and calcite content are determined on a free swell test specimen, it is then possible to interpret the results either on the swelling potential-calcite content plane with a family of lines corresponding to different values of shale content (Figure 7.4(a)), or on the swelling potential-shale content plane with a family of lines corresponding to different values of calcite content (Figure 7.4(b)). Therefore, the shale content and the calcite content are essential factors influencing the amount and rate of swelling (Lo et al. 1978).

To illustrate his theory, Lo (1989) plotted the horizontal swelling potential against the calcite content (Figure 7.5) for free swell test samples recovered from boreholes NF4A, SD-2, and SD-3 (1985 to 1989 investigations). The family of lines shown divides the plane into regions of certain shale content ranges. Although there is scatter, the trend as discussed earlier is generally followed.

7.2.2 1990 Investigation

In 1990 investigation, during the course of this thesis, free swell tests on 13 samples recovered from borehole NF4A and on 11 samples recovered from borehole NF37 have been carried out. Samples from borehole NF4A were recovered from depths between 151 and 224 m (elevation 29 to -44 m), representing relatively deep depths of Queenston Shale. Samples from borehole NF37 were recovered from depths between 72 and 108 m (elevation 100 to 64 m), representing relatively shallow depths of Queenston Shale.

Figures 7.6 and 7.7 show typical records for the swelling strain versus logarithm of elapsed time for free swell tests performed on samples recovered from boreholes NF4A and NF37 respectively. Details of results of all tests performed in 1990 investigation are compiled ι٢. Appendix 7A. Values of swelling potential in three orthogonal directions for samples tested in this investigation and taken from boreholes NF4A and NF37 are summarized and compared in Tables 7.6 and 7.7 respectively. Calcite content determined from each sample after testing is also listed in these tables. The vertical and average horizontal swelling potentials are plotted against depth in Figures 7.8 and 7.9. From Tables 7.6 and 7.7 and Figures 7.8 and ι.9, it can be seen that all the observations recorded earlier from previous investigations (1984 to 1989) generally apply for the 1990 investigation. The ratio of vertic΄ to horizontal swelling potential is between 1.2 and 2.0 for samples taken from both boreholes, except for some samples where separation of bedding planes was noticed during testing leading to a higher ratio (refer to the notes in Tables 7.6 and 7.7). ٢or the tests on samples taken from borehole NF4A, the values of the swelling potential in the vertical direction vary

from 0.18% to 0.69%, with an average of 0.29%. In the horizontal direction, the values of the swelling potential vary from 0.11% to 0.31%, and the average value is 0.22%.

For the tests on samples taken from borehole NF37, the values of swelling potential in the vertical direction vary from 0.13% to 0.53%, with an average value of 0.37%. In the horizontal direction, the values of swelling potential vary from 0.07% to 0.34%, and the average value is 0.23%.

The average horizontal swelling potential is plotted against the calcite content for samples taken from boreholes NF4A and NF37 (1990 investigation) in Figure 7.19. The values in brackets are the shale contents. The same family of lines obtained from previous investigations for Queenston Shale and given by Lo (1989) is drawn on the figure. It is obvious that, although there is some scatter, the theory as given by Lo (1989) is generally followed and the previously obtained family of lines apply to the 1990 investigation.

7.2.3 Summary of Observations on Results of Free Swell Tests on Queenston Shale

The observations on the results of all free swell tests conducted since 1984 investigation can be summarized as follows:

1-   The horizontal swelling is generally isotropic regardless of the area and the depth. It can be concluded, therefore, that the horizontal swelling is independent of the difference between the major and minor initial horizontal stress.

2-   The ratio of vertical to horizontal swelling potential (RSP) in general varies between 1.2 and 2. This observation is recorded for all tests except for samples where separation of bedding planes was noticed and for some samples from

boreholes SD-2 and SD-3 where RSP reached a value as much as 15. It was noticed and reported by Lo (1989) that samples from boreholes SD-2 and SD-3 contained more frequent occurrence of siltstone and sandstone than other samples tested. It can be concluded, therefore, that the structure of the samples taken from boreholes SD-2 and SD-3 is more complex than the structure of other samples tested. For such samples of complex structure, the monitored vertical swelling corresponds to the average vertical swelling of the sample, while the monitored horizontal swelling corresponds to a local swelling of layers dominant at the measurement level (due to sample heterogeneousity) rather than the average horizontal swelling. Therefore, a deviation from the normal value of RSP is expected from such samples. The value of RSP, therefore, may be regarded as an index for the structure complexity of the sample. A sample of RSP value between 1.2 and 2 may be regarded as a homogenous sample, otherwise the structure of the sample is complex and the sample is regarded as a heterogenous sample.

3-   The calcite content and the shale content control the amount and rate of swelling. The swelling potential decreases as the shale content decreases and the calcite content increases. The calcite content acts as a cementing agent lessening the swelling of the sample. In other words, it can be said that the increase in shale content and the decrease in calcite content decrease the time-dependent deformation modulus of the swelling rock, amounting to a higher swelling strain at any time.

4-   From each individual investigation, it is noticed that there is no definite trend of

variation of swelling potential with depth. Comparing the results of tests conducted on samples taken from borehole NF4A at different elevations, it is observed that there is a general trend of decrease of swelling potential with depth regardless the increase of initial stresses with depth (refer to Chapter 5). The variation of the vertical and horizontal swelling potentials for samples taken from borehole NF4A are plotted against depth in Figures 7.11 and 7.12. The variation of calcite content and shale content is also shown in these figures. From Figures 7.11 and 7.12 it can be seen that

(a) macroscopically, there is a trend of decrease of swelling potential with depth,

(b) there is no definite trend of variation of shale content with depth, however, the shale content varies from sample to sample, and

(c) macroscopically, there is a trend of increase of calcite content with depth.

Plotting the variation of swelling potential, shale content, and calcite content (obtained from all samples tested since 1984) against elevation, Figures 7.13 and 7.14, supports the observations a, b, and c above made from borehole NF4A. The important observation of the macroscopic decrease of swelling potential with depth may be mainly attributed to the noticeable macroscopic increase of calcite content with depth which acts as a cementing agent suppressing the swelling and increasing the value of time-dependent deformation modulus of shale. However, as discussed before, in microscopic scale, both the shale content and the calcite content affect the swelling potential of Queenston shale.

7.3   SEMI-CONFINED SWELL TESTS

The semi-confined swell test has been developed in the 1970s (Wai 1977; modified by Lee 1988) to study the stress dependency of the time-dependent deformation of swelling rocks. Since then, results of semi-confined tests have been employed in practice (see e.g. Trow and Lo 1989). In this test, a vertical load is applied on the sample in a temperature-controlled room $(10 \pm 2°c)$. This load is perpendicular to the bedding planes for vertically oriented samples and parallel to the bedding planes for horizontally oriented samples. The vertical swelling strain (loading direction) is monitored by a dial gauge, and the lateral strains in two orthogonal horizontal directions are monitored by strain gauges.

In general the tests are performed in groups (series). Samples in each group usually are chosen within one meter of the core to decrease the probability of variation of maerial. The samples in each group are loaded with different constant loads.

7.3.1   1985 to 1989 Investigations

In 1985 to 1987 investigations, 27 semi-confined swell tests, representing 9 groups of tests, on samples recovered from borehole NF4A at depths 95 to 112 m (elevations 85 to 68 m) were carried out (Lee 1988). Samples of three from the nine groups were loaded perpendicular to the bedding planes (vertically oriented samples), while the rest were loaded parallel to the bedding planes (horizontally oriented samples). The resul's of semi-confined swell tests from 1985 to 1987 investigations are summarized in Table 7.8. The effects of applied pressures on swelling potential in the vertical and horizontal directions are shown in a semi-log scale in Figures 7.15 and 7.16 respectively.

It may be seen that the swelling potential in both the vertical and the horizontal directions approximately decreases linearly with logarithm of applied pressure.

In 1989 investigation, 11 semi-confined swell tests were performed: 4 vertically oriented and 7 horizontally oriented (Lo 1989). All the samples were recovered from borehole SD-3 at depths from 209 to 219 m (elevations -26 to -36 m). Table 7.9 summarizes the results of the semi-confined tests for the 1989 investigation. The effect of the applied pressure on the vertical and horizontal swelling potentials is shown in Figures 7.17 and 7.18. The numbers in brackets in the figures are the values of calcite content determined on the samples subsequent to the tests. It may be seen that the higher the applied pressure on the specimen, the greater the suppression of the swelling potential is. In addition, it can be observed that the swelling potential is linearly decreasing with logarithm of applied pressure.

7.3.2 **1990 and 1992 Investigations**

In 1990 investigation and during the course of this thesis, 11 semi-confined swell tests were performed: 6 tests on samples recovered from borehole NF4A at depths from 180 to 181 m (elevations 0 to -1 m) and 5 tests on samples recovered from borehole NF37 at depths from 97 to 98 m (elevations 75 to 74 m). All samples in this investigation were loaded parallel to the bedding planes (horizontally oriented samples).

Table 7.10 summarizes the results of semi-confined swell tests for the 1990 investigation. The suppression effect of the applied pressures on the swelling potential is shown in Figures 7.19 and 7.20 for samples from boreholes NF4A and NF37 respectively. As observed from results of the previous investigations (1985 to 1987), it

can be seen from Table 7.10 and Figures 7.19 and 7.20 that the applied pressure has a suppression effect on the swelling potential and that the suppression increases as the value of applied pressure increases. It can be also seen that the swelling potential linearly decreases with logarithm of the applied pressure.

In 1992 investigation, 3 samples recovered from borehole NF43 were tested. The samples were loaded perpendicular to the bedding planes (vertically oriented samples). One of the samples was subjected to zero pressure as in free swell tests, but was tested in the temperature-controlled room and the horizontal swelling was monitored using strain gauges as in semi-confined tests.

Table 7.11 summarizes the results of semi-confined tests performed in 1992 investigation. The suppression effect of the applied pressure as discussed above is obvious from comparison of the swelling potentials of the three tests.

7.3.3 Discussion of Results

The most important observations on the results of semi-confined swell tests (Tables 7.8 to 7.11 and Figures 7.15 to 7.20) are that:

1- the time-dependent swelling deformation decreases as the applied pressure increases (stress dependency and suppression effect)

2   the applied pressure in one direction not only suppresses the swell deformation in that direction but also reduces the deformation in the other two orthogonal directions (Poisson's effect, see Lo and Lee 1990)

3- the time-dependent deformations in all three directions approximately decrease linearly with logarithm of the applied pressure. The scatter may be attributed to

the material variation in the specimens, such as the calcite content and shale content.

In their representations of the suppression effect of the applied pressure (σ_a) on time-dependent swelling deformation, Lo and Lee (1990) and Huang (1992) introduced two indices: the critical applied pressure (σ_c) and the slope (S) of the swelling potential-logarithm of applied pressure line (α-logσ_a).

The critical applied pressure (σ_c) is defined as the value of applied pressure where the straight line α-logσ_a intersects the axis of log σ (see e.g. Figure 7.19). When σ_a is larger than or equal to σ_c, the time-dependent deformation is completely suppressed and no swelling occurs. On the other hand, when σ_a is less than σ_c, time-dependent swelling deformation occurs but it is suppressed to a certain amount according to the value of σ_a. Therefore, the value of critical applied pressure σ_c may be taken as a characteristic index of stress-dependency of the time-dependent deformation of a rock. The smaller the value of σ_c, the easier to suppress the time-dependent swelling deformation of the rock.

Lo and Lee (1990), expressed the stress-dependent swelling potential, $\alpha(\sigma)$, by the following equation:

$$\alpha(\sigma) = S(\log \sigma_c - \log \sigma_a) \tag{1}$$

where σ_c was taken as a reference pressure. The value S is the slope of α-logσ_a line and it measures the sensitivity of the swelling deformation to stress change. The larger

the value of S, the more sensitive the swelling deformation is to the applied pressure (σ_a).

7.4   MECHANISM OF SWELLING

Lee and Lo (1993) provided a comprehensive review of swelling mechanisms for clay, clay shales, anhydrite, and black shale. A review of these mechanisms of swelling can also be found in Balasubramonian (1972), Mitchell (1973 and 1976), Yong and Warkenin (1975), Lindner (1976), and Huang *et al.* (1986).

Lee and Lo (1993) concluded that the proposed mechanisms of swelling in literature (relating the swelling to chemical or biochemical action of minerals like pyrite, anhydrite or swelling of clay minerals) are not applicable for the long-term swelling of shales in Southern Ontario. In this section, the experimental study carried out by Lee and Lo (1993) on shales will be reviewed. The mechanism of swelling controlling the time-dependent behaviour of Queenston Shale is then discussed. An independent experimental study carried out to investigate and verify the effect of some of the factors controlling the mechanism of swelling for Queenston Shale is then followed.

7.4.1   Review of the Experimental Study by Lee and Lo (1993)

In Lee and Lo study, all the samples tested were recovered from 1983 and 1987 investigations of the SABNGS No. 3 project. Their experimental program included the following components:

(a)   Study of mineralogy of four shales.

(b)   Residual negativ̱ pore pressure measurement on the fresh Queenston Shale

the value of S, the more sensitive the swelling deformation is to the applied pressure

(σ_a).

7.4 MECHANISM OF SWELLING

Lee and Lo (1993) provided a comprehensive review of swelling mechanisms for clay, clay shales, anhydrite, and black shale. A review of these mechanisms of swelling can also be found in Balasubramonian (1972), Mitchell (1973 and 1976), Yong and Warkenun (1975), Lindner (1976), and Huang *et al.* (1986).

Lee and Lo (1993) concluded that the proposed mechanisms of swelling in literature (relating the swelling to chemical or biochemical action of minerals like pyrite, anhydrite or swelling of clay minerals) are not applicable for the long-term swelling of shales in Southern Ontario. In this section, the experimental study carried out by Lee and Lo (1993) on shales will be reviewed. The mechanism of swelling controlling the time-dependent behaviour of Queenston Shale is then discussed. An independent experimental study carried out to investigate and verify the effect of some of the factors controlling the mechanism of swelling for Queenston Shale is then followed.

7.4.1 Review of the Experimental Study by Lee and Lo (1993)

In Lee and Lo study, all the samples tested were recovered from 1983 and 1987 investigations of the SABNGS No. 3 project. Their experimental program included the following components:

(a) Study of mineralogy of four shales.

(b) Residual negative pore pressure measurement on the fresh Queenston Shale

samples.

(c) Swell test on artificially sedimented and consolidated clay samples prepared from the Queenston Shale.

(d) Free swell test in different ambient fluids for the Queenston Shale samples from 1987 investigation.

(e) Free swell test on the Queenston Shale samples from the 1983 coring.

(f) Swell tests in ambient fluid having different salt concentrations.

From the results of their study, the following conclusions were drawn:

(a) The shales contained abundant clay minerals but only traces of swelling clay minerals, in the form of vermiculite. There was no evidence of pyrite or anhydrite in the Queenston Shale.

(b) Results of free swell tests in different ambient fluids showed that the time-dependent swelling is associated with increase in water content of the sample. An outward salt concentration gradient from the sample to the ambient fluid was required for swelling to occur. The magnitude and rate of swelling increased with increasing outward gradient.

(c) Results of free swell tests on samples which had been preserved for 1700 days after recovery showed substantial swelling under an outward salt concentration gradient. This observation supported conclusion (b).

(d) During the swelling process, the salt concentration of the specimen decreased, while that of the ambient fluid increased. The volume of macro pores (100 to 300 um) and ultra-micro pores (less than 0.02 um) increased.

(e) Results of tests on reconstituted clay samples prepared from Queenston Shale

showed long-term swelling dependent on the outward salt concentration gradient, conclusion (b).

(f)   residual negative pore pressure exists in specimens of Queenston Shale, resulting from stress changes in recovery of the rock cores.

Based on these conclusions, the following necessary and sufficient conditions for the swelling of Queenston Shale were postulated:

(i)   the relief of initial stresses which serves as an initiating mechanism;

(ii)   the accessibility to water; and

(iii)   an outward salt concentration gradient from the pore fluid of the rock to the ambient fluid.

They concluded also that if none of these conditions is existing, no swelling will take place. If only one or two conditions are met, the shale may or may not swell.

7.4.2 Swelling Mechanism

Based on the experimental results, Lee and Lo (1993) concluded that the time-dependent swelling of shales from Southern Ontario does not occur because of the chemical or biochemical action of minerals like pyrite, anhydrite or swelling clay minerals, but because of the interaction of clay minerals and pore water solution with ambient fluid. The following swelling mechanism was proposed.

Shales studied swell as a result of the dilution of pore water salt concentration which results in the expansion of spacing between clay particles. Both processes of osmosis (liquid flow from low to high concentration region) and diffusion (ion transfer from high to low concentration region) are responsible for the dilution of pore water salt

concentration.

The available water is driven into the shale sample by the action of negative pore pressure and the process of osmosis. While water migrates into the sample in response to the concentration difference between pore water and ambient water. The diffusion of cations lowers the concentration of cations in the pore water solution. The decrease in the concentration of cations results in an increase in the repulsive force and an increase in the interparticle spacing, thus causing the expansion of sample. Since the process of dissipation of cations is a time dependent phenomenon, the swelling of shales is also a time-dependent process.

7.4.3 Experimental Study

To verify the findings of Lee and Lo (1993), a follow-up study is performed on six samples of Queenston Shale recovered from borehole NU-13 in 1993 investigation for the SABNGS No. 3 project. All the six samples were recovered from a 30 cm core to reduce the probability of material variation. The main objective of this study is to examine the effect of the following factors on swelling behaviour of Queenston Shale:

(a)   Importance of accessibility to water in order for swelling to occur.

(b)   Effect of time elapsed before submergence of samples and loading.

(c)   Effect of the sequence of loading and accessibility to water.

Figure 7.21 summarizes the testing program performed on the six samples. The testing program can be described as follows.

(a)   Loading Before Accessibility to Ambient Water

!-   Three samples were prepared for testing in semi-confined test (LW-1, LW-2, and

       LW-3). The diameter of each sample was approximately 6 cm and the hight was

       about 5 cm.

2-   The samples were placed in position in three semi-confined cells with rubber

       membrane around them to prevent loss of water from samples before accessibility

       to water.

3-   The three samples were subjected to different vertical pressures as follows:

Sample #	Pressure (MPa)
LW-1	0.05
LW-2	0.2
LW-3	2

4-   The vertical deformations of the samples were monitored using dial gauges for

       7 days during which the samples had no access to water.

5-   The rubber membrane were carefully cut and removed from around the samples.

       The water is then added in the cells around the samples to provide continuous

       accessibility to ambient water.

6-   The deformation w·th th   was monitored for more than 200 days before the tests

       were stopped.

(b)   Accessibility to Ambient Water Before Loading

1-   Three samples were prepared for testing in semi-confined test (WL-1, WL-2, and

       WL-3). The dimensions of the samples were similar to those in (a).

2-   The samples were placed in position in three semi-confined cells and then

submerged in water to provide continuous access to water from the beginning of the test.

3-   The three samples were subjected to a 0.2 MPa vertical pressure after different elapsed times from submergence as follows.

Sample #	Elapsed Time Before Loading (days)
WL-1	0
WL-2	7
WL-3	14

4-   The vertical deformation with time was monitored for more than 200 days before stopping the test.

Sample WL-1 can be considered as a reference test since both the load and water were provided at the beginning of the test.

7.4.4 Results and Discussion

Figures 7.22 to 7.27 show the time-swelling strain curve for the six samples tested. The swelling potentials resulted from the samples are summarized in Table 7.12.

From Figures 7.22 to 7.27 and Table 7.12, the following observations and conclusions can be made:

(1)   The swelling potential for sample LW-1 (applied pressure = 0.05 MPa) is higher than that for sample LW-2 (applied pressure = 0.2 MPa). Swelling potentials of samples LW-1 and LW-2 are higher than that of sample LW-3 where the applied pressure is 2 MPa. It is obvious that as the applied pressure increases, the swelling potential decreases.

(2)   The ambient water is an important factor for swelling to occur. No swelling is

observed when the ambient water was absent for 7 days (samples LW-1, LW-2, and LW-3). After the samples had accessibility to water, they began to swell. Samples in access to water from the start of test commence to swell at the beginning of the test (samples WL-1, WL-2, and WL-3). This is consistent with the conclusion of Lee and Lo (1993) that ambient water is an essential factor for swelling to occur.

(3)   Samples LW-2 and WL-1 have the same swelling potential (0.31%). In sample WL-1 (reference test), the load and water were applied at the start of the test. In sample LW-2, the load was applied at the start of test and the water after 7 days. Both samples were subjected to the same stress value (0.2 MPa). It may be inferred, therefore, that the application of the load before the accessibility to water does not change the swelling potential of the sample. This may be attributed to the fact that the salt concentration inside sample LW-2 did not change during the first 7 days (no diffusion occurred due to the absence of the ambient water). Thus, the outward salt concentration gradient after adding the water is the same as that for sample WL-1 at start of test, leading to the same swelling potential. This is also in support of Lee and Lo conclusion that the salt concentration gradient is a crucial factor controling the time-dependent deformation of shales from Southern Ontario.

(4)   Comparing the swelling potentials of samples WL-i , WL-2 and WL-3 to each other, the following conclusion can be drawn. The longer the sample is subjected to ambient water before load application, the less the swelling potential it shows after loading. This can be attributed to the fact that the longer the sample is subjected to water, the more salt is diffused from sample before loading. Therefore, the sample subjected to water for longer period of time before loading will loose more salt by

diffusion and will have less salt concentration gradient and consequently less osmotic pressure after loading. Consequently, this leads to less swelling potential after load application. This observation, also, confirms Lee and Lo theory (1993) of mechanism of swelling for shales in Southern Ontario.

In the following Chapter, the long-term time-dependent deformation of Queenston Shale will be modelled using a generalized Kelvin model of three units connected in series. The measured time-dependent free swell strains will be compared to the predicted strains using this model. This model will also be used to predict the time-dependent strains under applied pressures using stress-dependent deformation parameters for the three units.

7.5 CONCLUSIONS

Several testing programs have been carried since 1984 to determine the time-dependent deofrmation characteristics of Queenston Shale for the design of the SABNGS No. 3 project. The testing porgrams include free swell tests and semi-confined swell tests. The most important conclusions drawn from the results of the `· :¬.cct¹gɑ`tions are

1- The horizontal swelling is generally isotropic regardless the area and the depth. It can be concluded, therefore, that the horizontal swelling is independent of the difference between the major and minor initial horizontal stress.

2- The ratio of vertical to horizontal swelling potential (RSP) may be regarded as an index for the structure complexity of the sample. A sample of RSP value between 1.2 and 2 may be regarded as a homogenous sample, otherwise the structure of the sample is complex and the sample is regarded as a heterogenous

sample.

3- The calcite content and the shale content control the amount and rate of swelling. The swelling potential decreases as the shale content decreases and the calcite content increases. The calcite content acts as a cementing agent lessening the swelling of the sample.

4- From each individual investigation, it is noticed ι at there is no definite trend of variation of swelling potential with depth. Plotting the variation of swelling potential, shale content, and calcite content (obtained from all samples tested since 1984) against elevation reveals the following conclusions:

(a) macroscopically, there is a trend of decrease of swelling potential with depth.

(b) there is no definite trend of variation of shale content with depth, however, the shale content varies from sample to sample.

(c) macroscopically, there is a trend of increase of calcite content with depth. The important observation of the macroscopic decrease of swelling potential with depth may be mainly attributed to the noticeable macroscopic increase of calcite content with depth which acts as a cementing agent suppressing the swelling and increasing the value of time-dependent deformation modulus of shale. However, as discussed before, in microscopic scale, both the shale content and the calcite content affect the swelling potential of Queenston Shale.

5- The time-dependent swelling deformation decreases as the applied pressure increases (stress dependency and suppression effect)

6- The applied pressure in one direction not only suppresses the swell deformation in that direction but also reduces the deformation in the other two orthogonal

directions.

7-   The time-dependent deformations in all three directions approximately decrease linearly with logarithm of the applied pressure. The scatter may be attributed to the material variation in the specimens, such as the calcite content and shale content.

The study carried out in 1993 investigation supported the postulation of Lee and Lo (1993) that the following conditions are necessary and sufficient for the swelling of Queenston Shale:

(i)   the relief of initial stresses which serves as an initiating mechanism;

(ii)   the accessibility to water; and

(iii) an outward salt concentration gradient from the pore fluid of the rock to the ambient fluid.

TABLE 7.1   Summary of time-dependent deformation tests on Queenston Shale

Year of Test	Borehole	Depth (m)	Elevation (m)	Number of Tests	
				Free Swell	Semi-Confined Swell Groups(Samples)
1984	NF7	77 to 127	96 to 46	6	1(3)
1985	NF4A	95 to 98	85 to 82	3	3(9)
1986	NF4A	101 to 106	79 to 74	3	3(9)
1987	NF4A	110 to 115	70 to 65	5	3(9)
1989	SD2	212 to 248	-32 to -68	14	-
	SD3	197 to 235	-14 to -52	13	2(11)
1990	NF4A	151 to 224	29 to -44	14	1(6)
	NF37	72 to 108	100 to 64	11	1(5)
1992	NF43	158 to 164	114 to 8	1	1(2)
Total				70	15(54)

Note: Tests devoted to the study the long-term time-dependent deformation of Queenston Shale and those specially devoted to study the mechanism of swelling are not included in this table.

TABLE 7.2   Results of free swell tests on Queenston Shale for SABNGS No. 3
(Borehole NF7 - 1984 investigation)

Test No.	Depth (m)	Horizontal Swelling Potential (% /Log Cycle)	Calcite Content (%)
FS/Q1	79.45	0.30	2.1
FS/Q2	89.10	0.27	7.8
FS/Q3	94.82	0.31	4.0
FS/Q4	102.82	0.32	3.1
FS/Q5	109.70	0.33	4.1
FS/Q6	121.50	0.28	6.4
Average		0.30	4.6

(after Lee 1988)

TABLE 7.3   Summary of results of free swell tests on Queenston Shale for SABNGS No. 3
(Borehole NF4A - 1985 to 1987 investigations)

Year of Investigation	Borehole	Sample No.	Depth (m)	Dimensions (mm)		Unit weight (g/cm3)	Wave Velocity (km/sec)	σ_v[1] (MPa)	Swelling Potential[2] (% /Log Cycle of Time)		Calcite Content (%)
				Diameter	Height				Horizontal	Vertical	
1985	NF4A	FS1	95.64	60.66	66.71	2.68	3.88	2.51	0.32	0.48	3.7
		FS2	97.08	60.86	67.19	2.67	3.93	2.54	0.24	0.39	4.9
		FS3	97.68	60.97	6?.16	2.68	3.90	2.57	0.24	0.45	4.1
1986	NF4A	FS1	101.39	60.45	67.94	2.68	3.91	2.67	0.31	0.41	3.5
		FS2	102.26	60.92	57.38	2.68	3.94	2.69	0.34	0.51	3.7
		FS3	105.80	61.07	64.90	2.66	3.56	2.66	0.27	0.42	3.5
1987	NF4A	FS1	110.64	60.90	58.50	2.66	3.48	2.89	0.30	0.49	4.5
		FS2	110.70	60.90	61.10	2.68	3.57	2.90	0.34	0.54	4.7
		FS3	112.78	60.84	62.32	2.67	3.80	2.95	0.24	0.38	8.5
		FS4	112.84	60.80	62.28	2.67	3.58	2.96	0.24	0.41	6.4
		FS5	114.33	60.88	62.38	2.66	3.92	2.98	0.22	0.37	5.4

Notes: (1) σ_v = the initial overburden pressure.

(after Lo and Lee 1990)

TABLE 7.4   Summary of results of free swell tests on Queenston Shale for SABNGS No. 3 (Borehole SD2 - 1989 investigation)

Sample No	Depth (m)	Dimensions (mm)		Weight (g)	Compressive Wave Velocity (km/sec)	Calcite Content (%)	Swelling Potential (%)			Lithology
		Height	Diameter				Vertical	Horizontal		
FSQ/SD2-1	212.21	27.8	26.6	41.03	3.63	14.9	0.38	0.17	0.18	red shale (80%) siltstone (20%)
FSQ/SD2-2	216.21	27.5	26.6	40.22	3.82	12.6	0.28	0.12	0.13	red shale (75%) siltstone (25%)
FSQ/SD2-3	219.87	27.0	26.6	40.07	3.53	17.4	0.25	0.11	0.12	red shale (70%) siltstone (30%)
FSQ/SD2-4	224.60	25.1	25.5	?.08	3.83	14.7	0.15	0.06	0.08	red shale (20%) siltstone (80%)
FSQ/SD2-5	226.28	27.8	26.5	40.89	3.78	17.4	0.32	0.08*	0.12*	red shale (60%) siltstone (40%)
FSQ/SD2-6	228.23	28.1	26.7	41.89	4.14	11.2	0.14	0.03	0.03	green&red shale (25%) siltstone (75%)
FSQ/SD2-7	230.08	29.3	26.6	44.02	3.21	4.9	0.43	0.17	0.17	red shale (80%) siltstone (20%)
FSQ/SD2-8	231.97	27.4	26.6	40.54	3.68	9.5	0.19	0.10	--	red shale (30%) siltstone (70%)
FSQ/SD2-9	234.05	28.4	26.7	41.62	3.53	12.2	0.37	0.13*	0.21*	red shale (60%) siltstone (40%)
FSQ/SD2-10	235.89	27.5	26.6	40.56	4.10	13.7	0.13	0.06	0.08	red shale (15%) siltstone (85%)
FSQ/SD2-11	239.88	28.3	26.6	41.70	3.58	4.9	0.31	0.15	0.17	red shale (60%) siltstone (40%)
FSQ/SD2-12	244.42	26.7	26.6	39.85	3.43	4.6	0.46	0.22	0.22**	red shale (90%) siltstone (10%)
FSQ/SD2-13	247.69	26.6	26.6	39.34	3.42	5.8	0.42	0.23	0.23***	red shale (90%) siltstone (10%)
FSQ/SD2-14	244.08	28.2	26.6	41.49	4.73	15.7	0	0	0	reddish fine sandstone

Notes: .   specimen heterogeneous
    -   specimen was cracked at 26th day
    ¦   specimen was influenced by crack after 30 days

(after Lo 1989)

TABLE 7.5 Summary of results of free swell tests on Queenston Shale for SABNGS No. 3
(Borehole SD3 - 1989 investigation)

Sample No.	Depth (m)	Dimension (mm)		Weight (g)	Compressive Wave Velocity (km/sec)	Calcite Content (%)	Swelling Potential (%)			Lithology
		Height	Diameter				Vertical	Horizontal		
FSQ/SD3-1	197.67	44.8	44.8	187.02	3.60	12.1	0.23	0.13	0.15	red shale (80%) siltstone (20%)
FSQ/SD3-2	201.82	44.4	44.8	193.54	4.05	14.8	0.26	0.08	0.10	red shale (70%) siltstone (30%)
FSQ/SD3-3	206.12	42.2	44.8	189.62	3.88	11.7	0.12	0.08	0.08	red shale (20%) siltstone (80%)
FSQ/SD3-4	209.11	44.8	46.4	195.70	4.02	12.9	0.30	0.11	0.12	red shale (80%) siltstone (20%)
FSQ/SD3-5	212.00	44.9	44.8	187.19	4.54	22.9	0.13	0.01	0.01	green shale (15%) red siltstone (85%)
FSQ/SD3-6	214.49	46.1	44.9	194.67	4.25	21.6	0.22	0.07	0.09	red shale (35%) siltstone (65%)
FSQ/SD3-7	215.54	46.8	44.8	196.49	4.00	10.3	0.26	0.11	0.13	red shale (50%) siltstone (50%)
FSQ/SD3-8	217.96	46.9	44.8	197.55	4.24	16.6	0.23	0.15	0.17	red shale (70%) siltstone (30%)
FSQ/SD3-9	220.04	46.9	44.9	197.55	4.70	18.0	0.10	0.04	0.05	red shale (15%) siltstone (85%)
FSQ/SD3-10	221.86	45.1	44.7	187.99	4.36	19.1	0.26	0.03	0.03	red shale (40%) siltstone (60%)
FSQ/SD3-11	226.07	45.3	44.5	188.92	3.90	6.3	0.27	0.08	0.09	red shale (40%) siltstone (60%)
FSQ/SD3-12	228.69	46.0	44.6	191.53	4.26	11.2	0.13	0.07	0.07	red shale (20%) siltstone (80%)
FSQ/SD3/13	234.05	46.5	44.9	196.00	4.17	5.6	0.26	0.19*	0.24*	red shale (85%) siltstone (15%)

Note. * specimen heterogeneous

(after Lo 1989)

TABLE 7.6   Summary of results of free swell tests on Queenston Shale for SABNGS No. 3
(Borehole NF4A - 1990 investigation)

Sample No.	Depth (m)	Dimensions (mm)		Unit Weight (g/cm³)	Compressive Wave Velocity (km/sec)	Calcite Content (%)	Swelling Potential (%)		Lithology
		Height	Diameter				Vertical	Horizontal	
FSQ/NF4A-1	151.85	58.9	61.0	2.69	4.48	6.3	0.28	0.20	0.25	red shale (65%) siltstone (35%)
FSQ/NF4A-2	157.30	58.1	61.1	2.66	3.58	4.4	0.46	0.31	0.31	red shale (70%) siltstone (30%)
FSQ/NF4A-3	161.86	60.5	61.0	2.67	3.88	8.4	0.31	0.21	0.24	red shale (75%) siltstone (25%)
FSQ/NF4A-4	167.50	60.9	61.0	2.68	4.09	7.0	0.33	0.24	0.24	red shale (70%) siltstone (30%)
FSQ/NF4A-5	174.49	57.2	61.0	2.67	4.27	3.6	0.34	0.25	0.25	red shale (65%) siltstone (35%)
FSQ/NF4A-6	180.84	61.0	61.0	2.67	4.24	6.6	0.69	0.34	0.33	red shale (80%) siltstone (20%)
FSQ/NF4A-7	186.41	59.3	61.0	2.67	3.95	5.0	0.28	0.22	0.24	red shale (65%) siltstone (35%)
FSQ/NF4A-8	192.16	59.6	60.9	2.66	3.70	8.8	0.29	0.23	0.25	red shale (65%) siltstone (35%)
FSQ/NF4A-9	197.82	60.1	16.0	2.68	4.03	20.7	0.19	0.15	0.15	red shale (65%) siltstone (35%)
FSQ/NF4A-10	204.37	58.6	61.0	2.67	3.55	9.7	0.38*	0.14	0.14	red shale (75%) siltstone (25%)
FSQ/NF4A-11	204.29	57.4	61.0	2.65	4.19	13.8	0.20	0.13	0.12	red shale (55%) siltstone (45%)
FSQ/NF4A-12	210.44	61.0	61.0	2.67	4.33	14.7	0.18	0.11	0.11	red shale (70%) siltstone (30%)
FSQ/NF4A-13	219.10	59.5	61.1	2.70	3.77	6.8	0.27	0.23	0.17	red shale (70%) siltstone (30%)
FSQ/NF4A-14	223.87	61.4	61 1	2.67	4.09	7.5	0.30	0.24	0.22	red shale (75%) siltstone (25%)

Notes: Bedding plane separation noticed

TABLE 7.7   Summary of results of free swell tests on Queenston Shale for SABNGS No. 3
(Borehole NF37 - 1990 investigation)

Sample No.	Depth (m)	Dimensions (mm)		Unit Weight (g/cm³)	Compressive Wave Velocity (km/sec)	Calcite Content (%)	Swelling Potential (%)		Lithology
		Height	Diameter				Vertical	Horizontal	
FSQ/NF37-1	72.12	62.5	60.8	2.68	4.16	2.6	0.28	0.22	red shale (75%) siltstone (25%)
FSQ/NF37-2	76.16	59.4	60.5	2.63	3.96	5.0	0.49	0.25	red shale (80%) siltstone (20%)
FSQ/NF37-3	80.12	60.^	60.6	2.62	3.31	4.5	0.65*	0.29	red shale (85%) siltstone (15%)
FSQ/NF37-4	85.57	53.4	60.9	2.64	3.87	4.8	0.42	0.31	red shale (65%) siltstone (35%)
FSQ/NF37-5	91.16	52.7	60.7	2.65	3.74	3.8	0.37	0.27	red shale (70%) siltstone (30%)
FSQ/NF37-6	93.50	58.6	60.9	2.66	3.73	4.4	0.41*	0.17	red shale (60%) siltstone (40%)
FSQ/NF37-7	96.02	62.8	60.6	2.67	3.95	5.8	0.53	0.33	red shale (65%) siltstone (35%)
FSQ/NF37-8	99.81	59.0	60.7	2.65	3.73	5.6	0.46*	0.34	red shale (65%) siltstone (35%)
FSQ/NF37-9	100.60	55.9	60.8	2.64	4.74	15.9	0.13	0.07	red shale (40%) siltstone (60%)
FSQ/NF37-10	104.10	64.0	60.8	2.68	3.98	5.1	0.37	0.29	red shale (70%) siltstone (30%)
FSQ/NF37-11	107.23	58.6	60.6	2.68	3.99	4.5	0.37	0.23	red shale (60%) siltstone (40%)

NOTES: *   Bedding plane seperation noticed

TABLE 7.8   Summary of results of modified semi-confined swell test on Queenston Shale for SABNGS No. 3 (Borehole NF4A - 1985, 1986, and 1987 investigations)

Year of Investigation	Sample No	Depth (m)	Dimension (mm) Diameter	Dimension (mm) Height	Unit Weight (g/cm³)	Compressive Wave Velocity (km/sec)	σ_vo (MPa)	σ_c (MPa)	Swelling Potential (%) HM	Swelling Potential (%) HN	Swelling Potential (%) V	Calcite Content (%)
1985	MSC/V1	95.56	41.83	100.15	2.67	3.75	2.50	0.027	0.20	0.21	0.265	3.9
	MSC/V2	95.46	41.80	86.49	2.67	3.76	2.50	0.132	0.19	0.17	0.22	4.1
	MSC/V3	97.47	41.80	67.56	2.68	3.67	2.56	0.691	0.17	0.155	0.14	3.6
	MSC/HM1	96.47	32.15	49.70	2.66	3.98	2.51	0.096	0.19	0.22	0.245	3.0
	MSC/HM2	97.29	32.22	49.51	2.68	4.05	2.56	0.342	0.15	0.135	0.18	3.0
	MSC/HM3	97.20	32.23	48.05	2.68	3.91	2.55	1.855	0.04	0.115	0.15	2.4
	MSC/HN1	96.53	32.25	49.13	2.66	3.98	2.52	0.036	0.24	0.15	0.26	3.2
	MSC/HN2	96.43	32.22	48.3	2.67	4.05	2.52	0.342	0.18	0.125	0.22	3.5
	MSC/HN3	97.17	32.19	49.94	2.67	3.92	2.54	1.960	0.11	0.04	0.145	3.7
	MSC/V1	101.99	41.98	73.70	2.68	3.60	2.67	0.019	0.21	0.21	0.24	3.8
	MSC/V2	102.14	41.98	95.20	2.68	3.53	2.68	0.131	0.23	0.17	0.22	4.0
	MSC/V3	101.85	41.94	60.54	2.67	3.59	2.66	0.687	0.14	0.14	0.195	4.1
1986	MSC/HM1	101.00	32.18	48.40	2.67	4.10	2.64	0.036	0.18	0.165	0.24	4.0
	MSC/HM2	101.04	32.20	50.08	2.67	4.04	2.65	0.358	0.125	0.12	0.22	4.0
	MSC/HM3	100.96	32.17	48.44	2.67	4.04	2.64	1.866	0.04	0.125	0.165	2.8
	MSC/HN1	101.69	32.15	50.80	2.67	3.91	2.66	0.036	0.16	0.15	0.27	4.1
	MSC/HN2	101.57	32.24	50.32	2.68	3.90	2.66	0.355	0.16	0.16	0.205	3.6
	MSC/HN3	101.63	32.15	51.08	2.68	3.87	2.66	1.868	0.06	0.025	0.16	3.5
	MSC/V1	111.57	42.01	76.00	2.66	3.91	2.91	0.025	0.175	0.14	0.22	3.7
	MSC/V2	111.48	42.12	61.68	2.64	3.97	2.88	0.25	0.125	0.105	0.185	5.1
	MSC/V3	111.78	42.09	62.72	2.66	3.84	2.92	2.38	0.15	0.10	0.08	3.8
1987	MSC/HM1	110.89	32.32	48.16	2.66	4.17	2.89	0.025	0.155	0.21	0.25	5.6
	MSC/HM2	110.95	32.26	48.10	2.61	4.28	2.84	0.25	0.125	0.18	0.24	5.3
	MSC/HM3	110.83	32.18	47.96	2.68	4.12	2.91	2.42	0.05	0.105	0.19	4.5
	MSC/HN1	111.21	32.20	48.18	2.62	4.17	2.85	0.025	0.22	0.195	0.30	3.8
	MSC/HN2	111.26	32.23	47.80	2.66	4.07	2.90	0.26	0.22	0.145	0.29	3.8
	MSC/HN3	111.41	32.21	48.04	2.66	4.20	2.91	2.42	0.11	0.04	0.13	3.7

Notes: σ_c = the applied pressure on the specimen
σ_vo = the initial overburden pressure
H = horizontally cored samples (pressure is applied parallel to the bedding plane)

(after Lo and Lee 1989)

TABLE 7.9 Summary of results of modified semi-confined swell tests on Queenston Shale for SABNGS No. 3 (Borehole SD3 - 1989 investigation)

Sample No.	Depth (m)	Dimensions (mm) Height	Dimensions (mm) Diameter	Unit Weight (g/cc)	Comp. Wave Velocity (km/sec)	Calcite Content (%)	Swelling Potential (%) HM	Swelling Potential (%) HN	Swelling Potential (%) V	Applied Pressure (MPa)	Lithology
SSQ/SD3-V1	216.50	77.1	44.7	2.69	3.59	14.4	0.20	0.19	0.30	0.02	red shale (70%) siltstone (30%)
SSQ/SD3-V2	217.48	78.9	44.8	2.65	4.18	22.4	0.16	0.14	0.15	0.10	red shale (35%) siltstone (65%)
SSQ/SD3-V3	217.40	75.9	44.8	2.67	4.05	19.2	0.13	0.10	0.11	0.26	red shale (56.5) siltstone (50%)
SSQ/SD3-V4	218.04	77.5	44.7	2.69	4.10	19.5	0.11	0.09	0.06	1.02	red shale (60%) siltstone (40%)
SSQ/SD3-H1*	215.28	36.5	32.2	2.66	4.90	30.3	0.17	0.19	0.26	0.02	red shale (30%) siltstone (70%)
SSQ/SD3-H2*	215.20	32.8	32.4	2.67	3.86	13.9	0.13	0.14	0.17	0.10	red shale (80%) siltstone (20%)
SSQ/SD3-H3*	215.13	34.3	32.4	2.65	4.04	26.5	0.01	0.03	0.06	1.00	red shale (55%) siltstone (45%)
SSQ/SD3-H11*	211.45	34.7	32.6	2.64	3.67	8.5	0.18	0.21	0.29	0.05	red shale (90%) siltstone (10%)
SSQ/SD3-H12	211.40	34.5	32.4	2.64	3.75	7.6	0.06	0.08	0.14	0.50	red shale (90%) siltstone (10%)
SSQ/SD3-H13*	211.35	34.7	32.4	2.64	3.81	6.3	0.00	0.02	0.03	1.50	red shale (90%) siltstone (10%)
SSQ/SL3-H14*	209.56	33.1	32.4	2.64	4.41	22.5	0.00	0.00	0.00	3.00	red shale (50%) siltstone (50%)

Notes: * Specimen is loaded parallel to the bedding planes (HM direction)

(after Lo 1990)

TABLE 7.10 Summary of results of modified semi-confined tests on Queenston Shale from SABNGS No. 3 site (Boreholes NF4A and NF37 - 1990 investigation)

Borehole No.	Sample No.	Depth (m)	Dimensions (mm)		Unit Weight (g/cm³)	Compressive Wave Velocity (km/sec)	Applied Pressure (X-Dir.) (MPa)	Swelling Potential (%)			Calcite Content (%)
			Height	Diameter				Horizontal		Vertical	
								X	Y	Z	
NF4A	MSC/NF4A-1	180.37	50.6	32.7	2.61	4.49	0.02	0.25	0.27	-	3.7
	MSC/NF4A-2	180.56	50.4	32.5	2.67	4.46	0.05	-	0.25	0.41	4.4
	MSC/NF4A-3	180.75	47.3	32.5	2.73	3.97	0.10	0.20	0.24	-	4.3
	MSC/NF4A-4	180.86	50.2	32.4	2.68	4.42	0.30	0.16	-	0.28	-
	MSC/NF4A-5	180.92	47.7	32.4	2.68	4.41	1.00	0.08	-	0.42	4.3
	MSC/NF4A-6	181.18	49.0	32.4	2.67	4.49	3.00	0.00	0.20	0.18	6.4
NF37	MSC/NF37-1	97.48	49.0	32.4	2.67	4.23	0.01	0.18	0.32	0.37	4.1
	MSC/NF37-2	97.85	51.3	32.4	2.69	4.20	0.03	0.21	-		2.6
	MSC/NF37-3	98.16	49.6	32.4	2.64	4.31	0.10	0.17	-	-	5.1
	MSC/NF37-4	98.60	50.5	32.4	2.65	4.28	0.30	0.14	0.18	0.24	-
	MSC/NF37-5	98.10	49.4	32.4	2.69	4.28	1.00	0.13	0.18	-	3.9

TABLE 7.11   Summary of modified semi-confined swell test results on Queenston Shale from SABNG: No. 3 site
(Borehole NF43 - 1992 investigation)

Sample No.	Depth (m)	Dimensions (mm)		Unit Weight (g/cc)	Comp. Wave Velocity (km/sec)	Calcite Content (%)	Swelling Potential (%)			Applied Pressure (MPa)	Lithology
							Horizontal		Vertical		
		Height	Diameter				X	Y	Z		
FSQ/NF43-1	158.97	55.6	42.1	2.69	4.06	2.0	0.26	0.25	0.33	0.0	red shale (65%) siltstone (35%)
MSC/NF43-V1	163.66	51.0	42.1	2.66	3.99	8.0	0.2	0.20	0.06	1.0	red shale (55%) siltstone (45%)
MSC/NF43-V2	163.72	51.5	42.1	2.65	3.96	7.8	0.14	0.15	0.04	3.0	red shale (65%) siltstone (45%)

TABLE 7.12 Summary of semi-confined swell test results on Queenston Shale from SABNGS No. 3 site
(Borehole NU-13 - 1993 investigation)

Sample No.	Depth (m)	Dimensions (mm)		Unit Weight (g/cc)	Comp. Wave Velocity (km/sec)	Time before Load application (days)	Time before submergence (days)	Vertical Swelling Potential (%)	Applied Pressure (MPa)
		Height	Diameter						
NU-13/LW-1	2.34	45.70	63.26	2.69	4.44	0	7	0.45	0.05
NU-13/LW-2	2.29	47.28	63.24	2.68	4.46	0	7	0.31	0.20
NU-13/LW-3	2.24	45.20	63.20	2.67	4.47	0	7	0.10	2.00
NU-13/WL-1	2.19	49.18	63.24	2.67	4.28	0	0	0.31	0.20
NU-13/WL-2	2.14	47.66	63.36	2.63	4.33	7	7	0.25	0.20
NU-13/WL-3	2.09	49.80	63.22	2.63	4.33	14	14	0.23	0.20
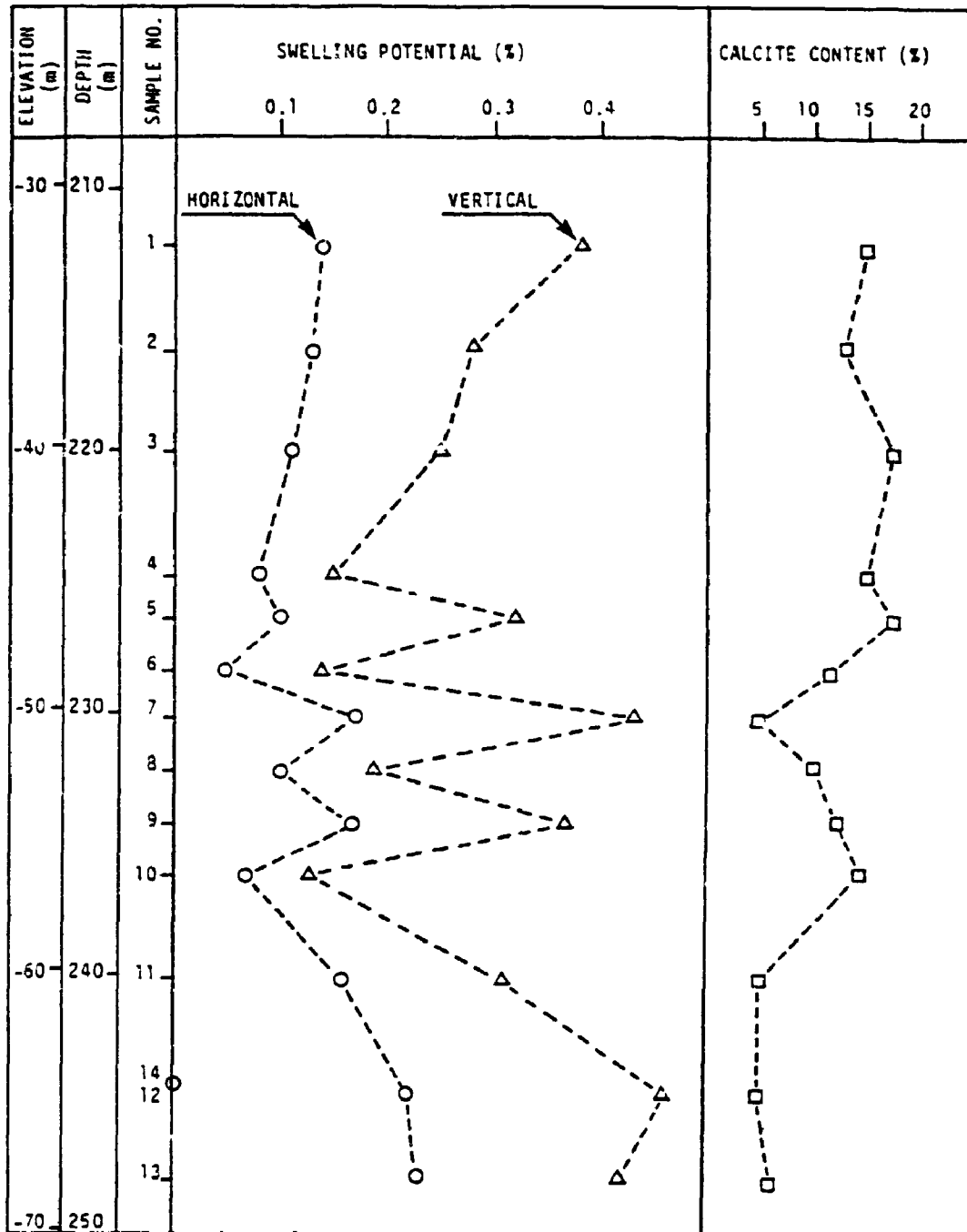
Figure 7.1   Variation of swelling potential with depth in Borehole SD-2
(after Lo 1989)
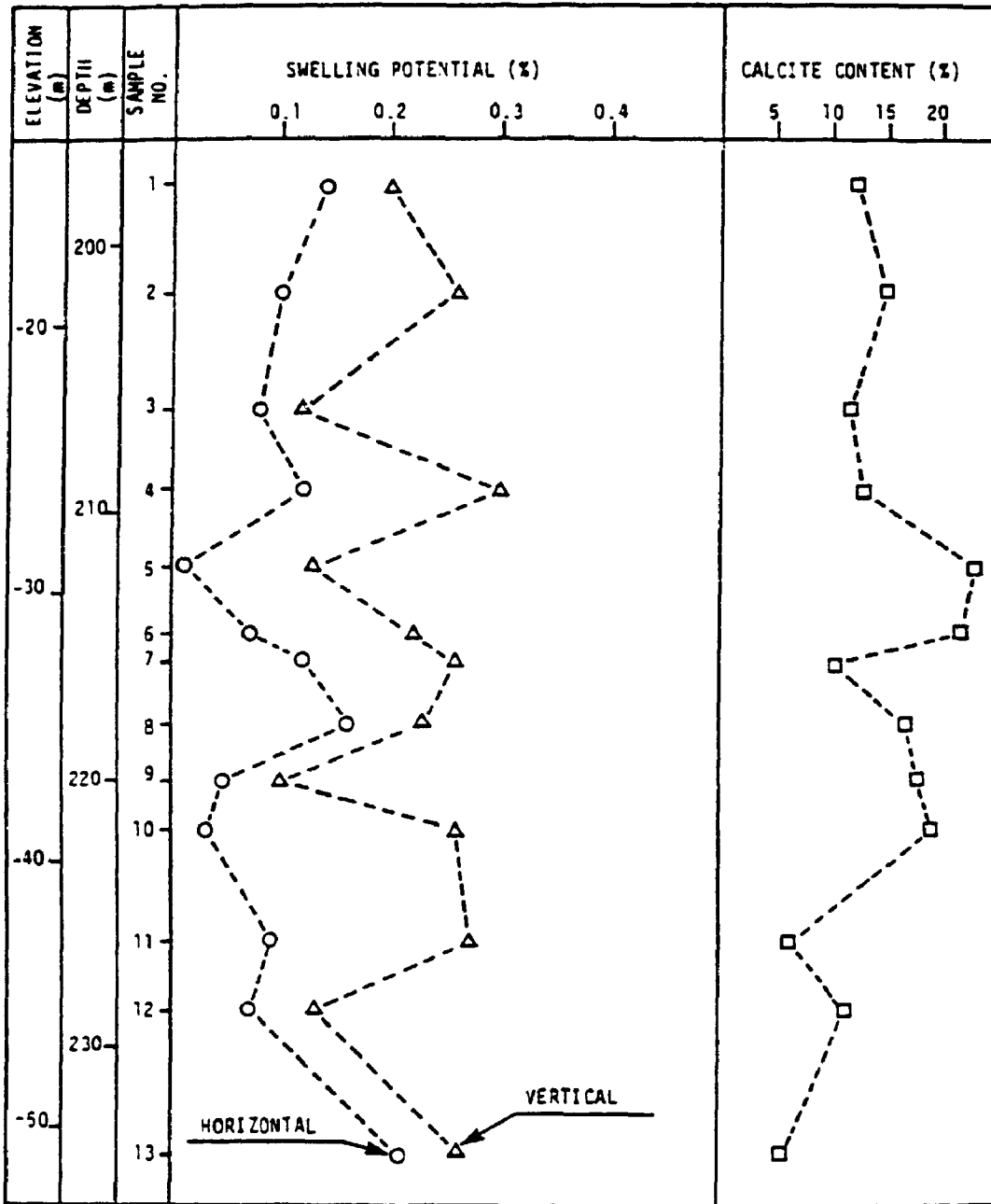
Figure 7.2   Variation of swelling potential with depth in Borehole SD-3
(after Lo 1989)
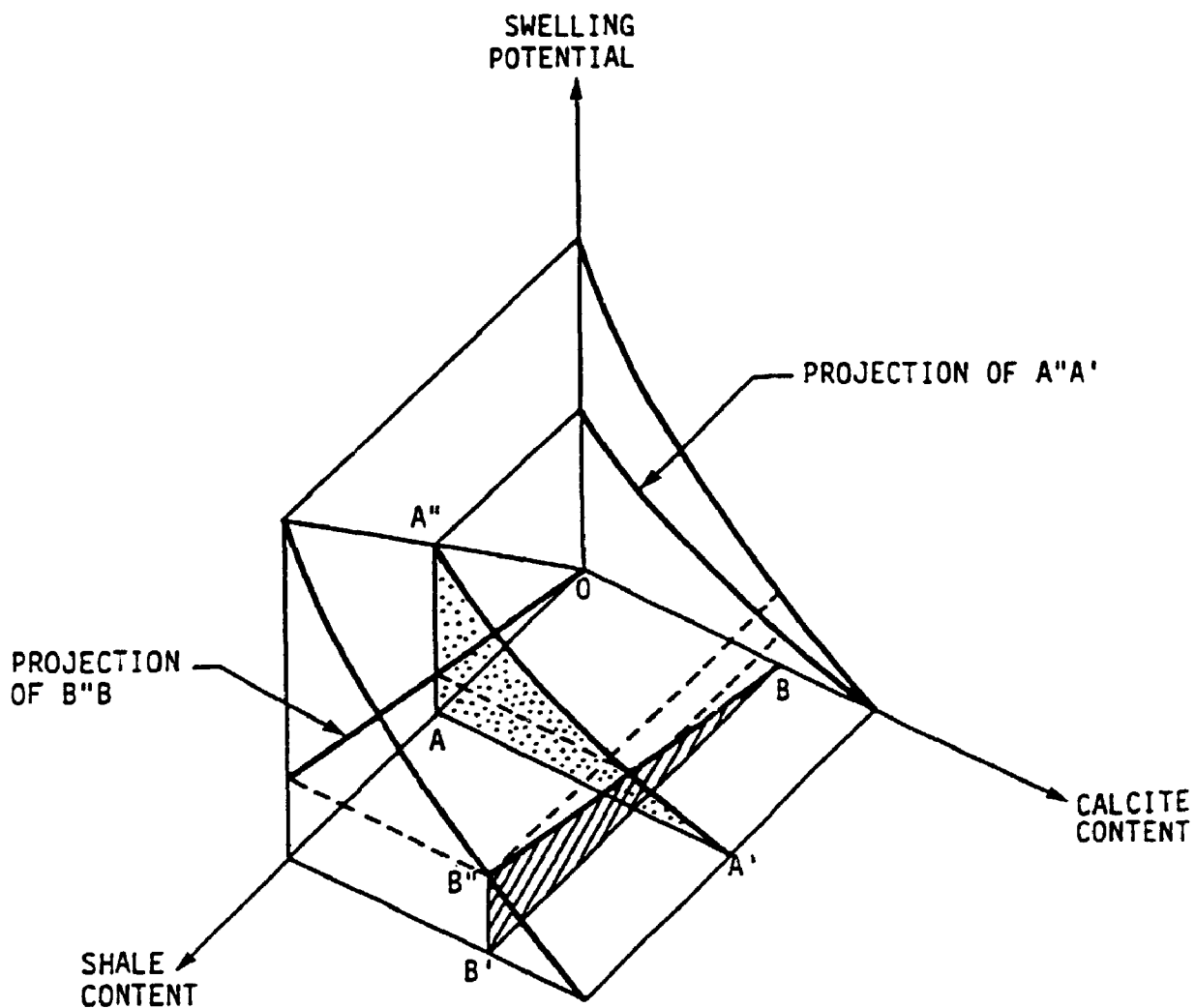
Figure 7.3   Conceptual illustration of influence of calcite content and shale content on
swelling potential (after Lo 1989)
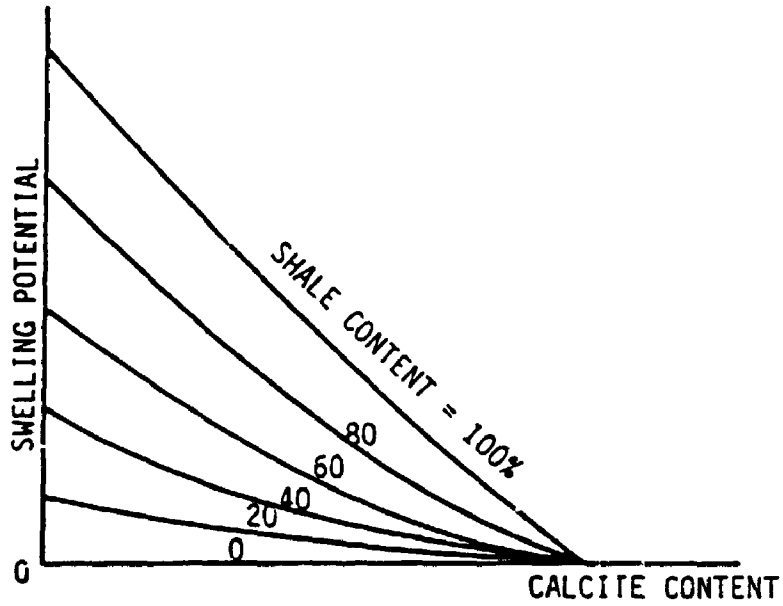
Figure 7.4a   Conceptual relationship between swelling potential and calcite content
(after Lo 1989)
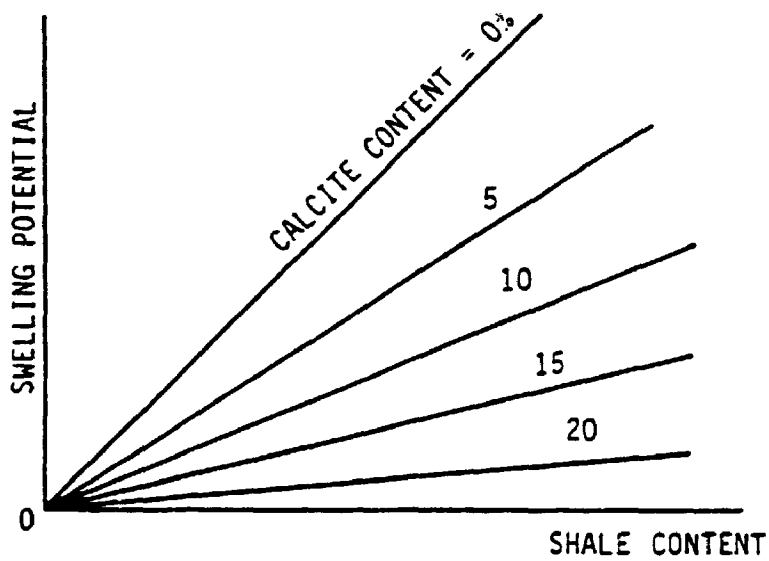
Figure 7.4b   Conceptual relationship between sweling potential and shale content
(after Lo 1989)
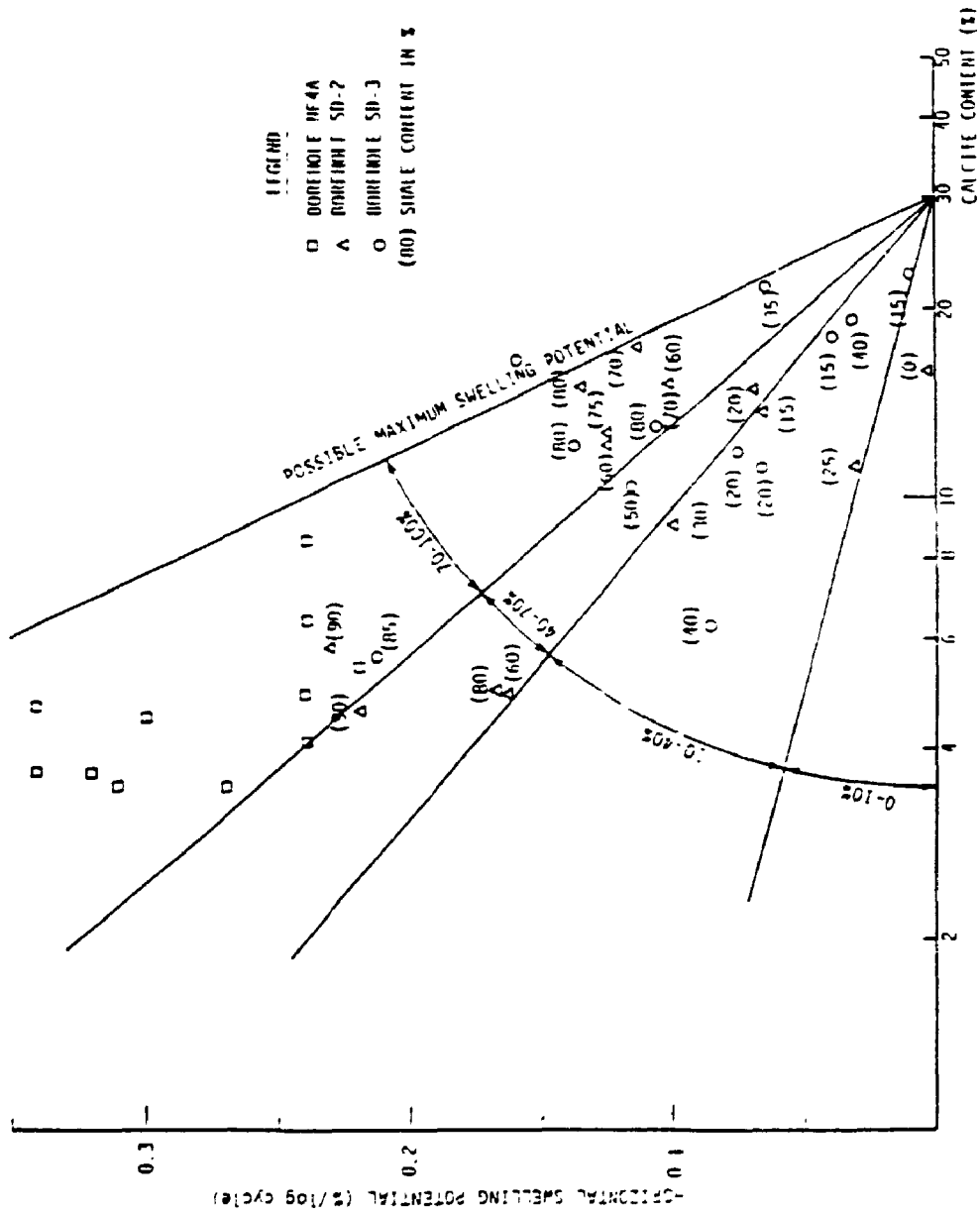
Figure 7.5   Effect of calcite content on swelling potential 1985 to 1989 investigations (after Lo 1989)
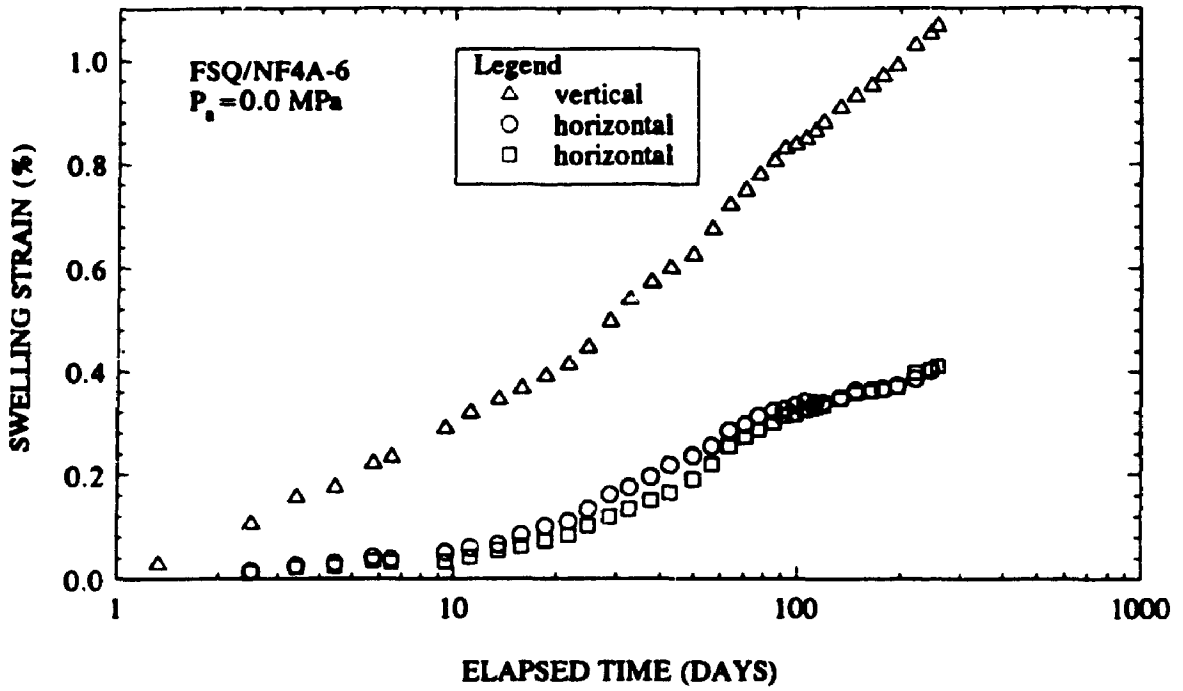
Figure 7.6 Results of free swell tests on Queenston Shale at SABNGS No. 3 site
Test NF4A-6 (1990 investigation)
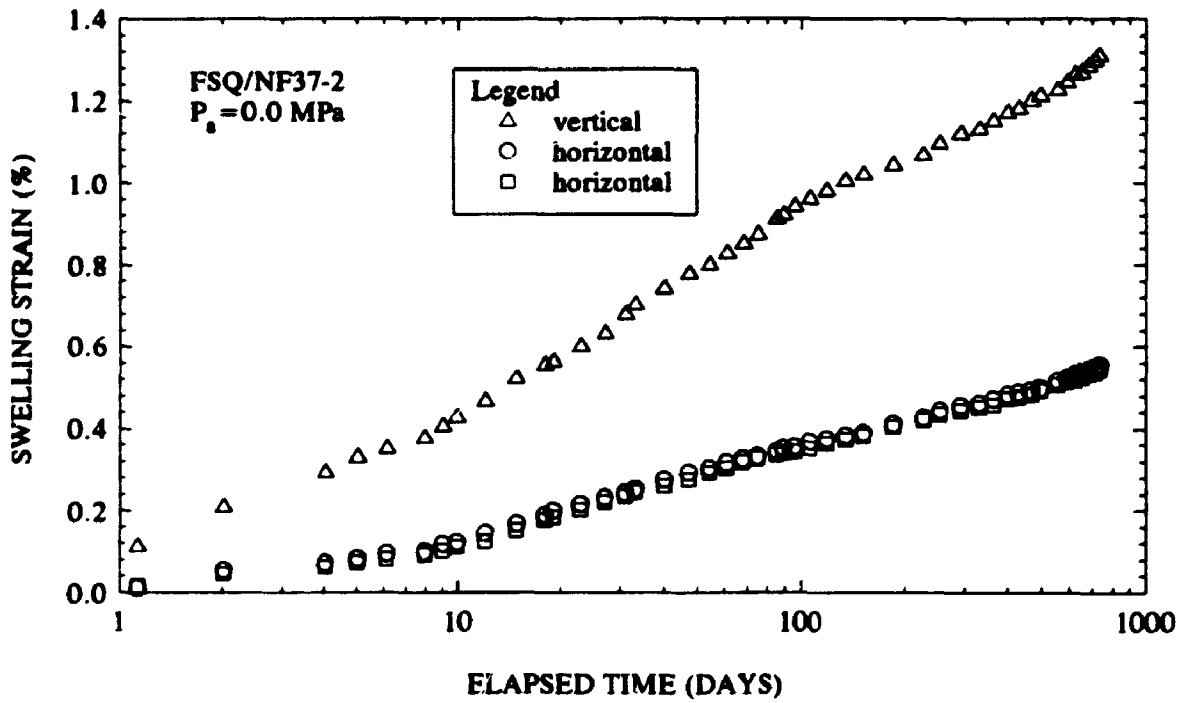
Figure 7.7 Results of free swell tests on Queenston Shale at SABNGS No. 3 site
Test NF37-2 (1990 investigation)
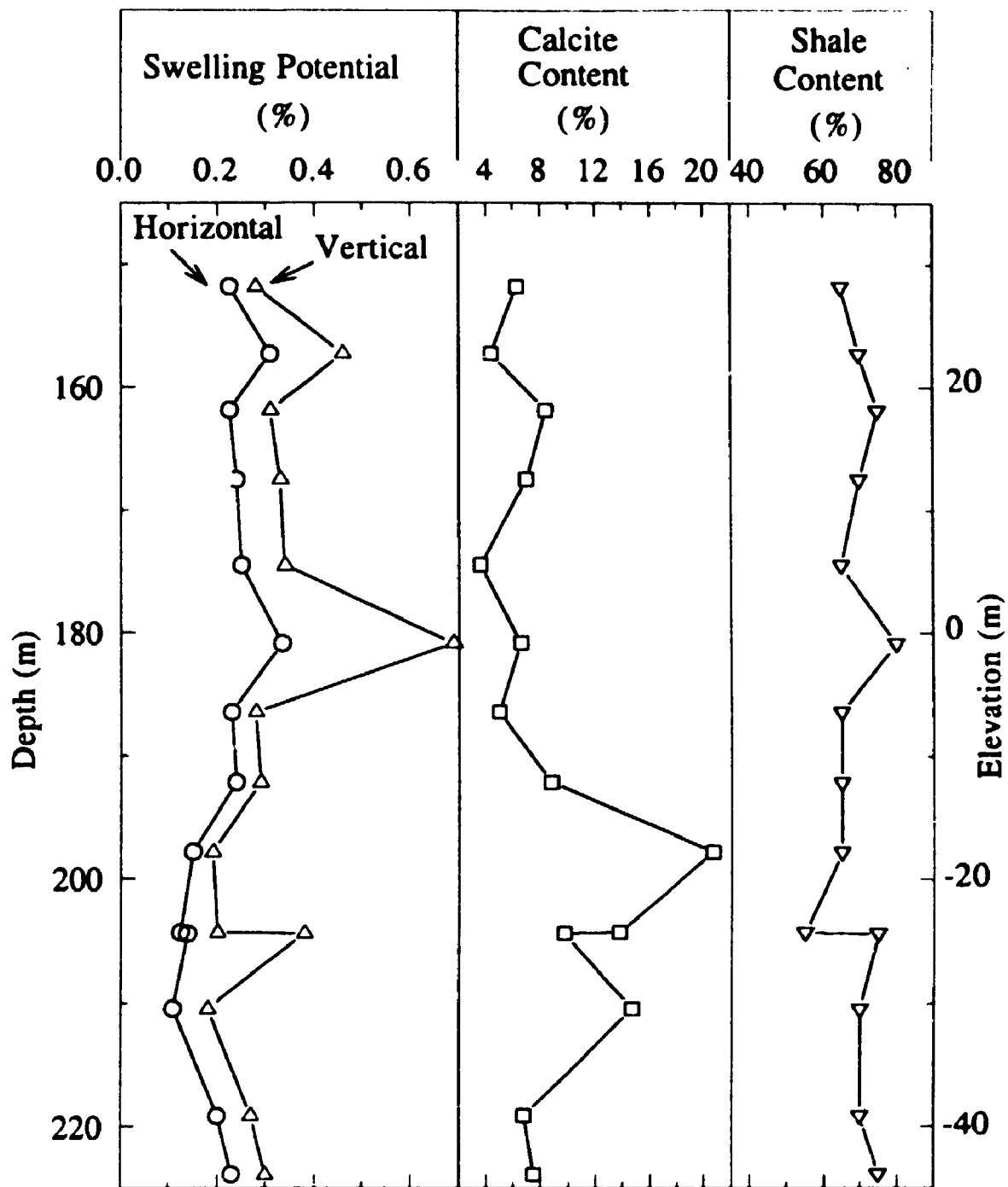
Figure 7.8 Variation of swelling potential, calcite content and shale content
with depth in Borehole NF4A (1990 investigation)
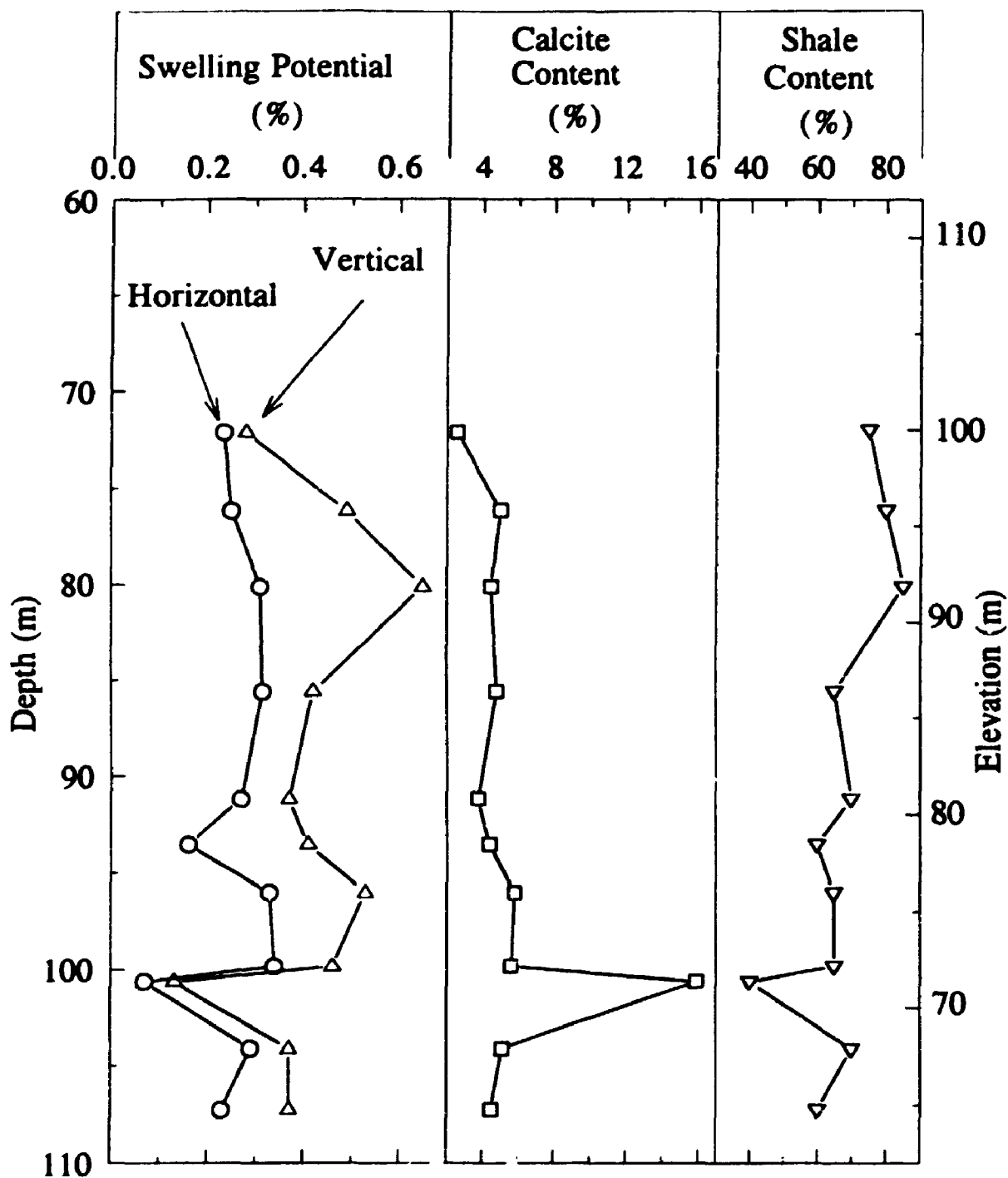
Figure 7.9 Variation of swelling potential, calcite content and shale content with depth in borehole NF37 (1990 investigation)
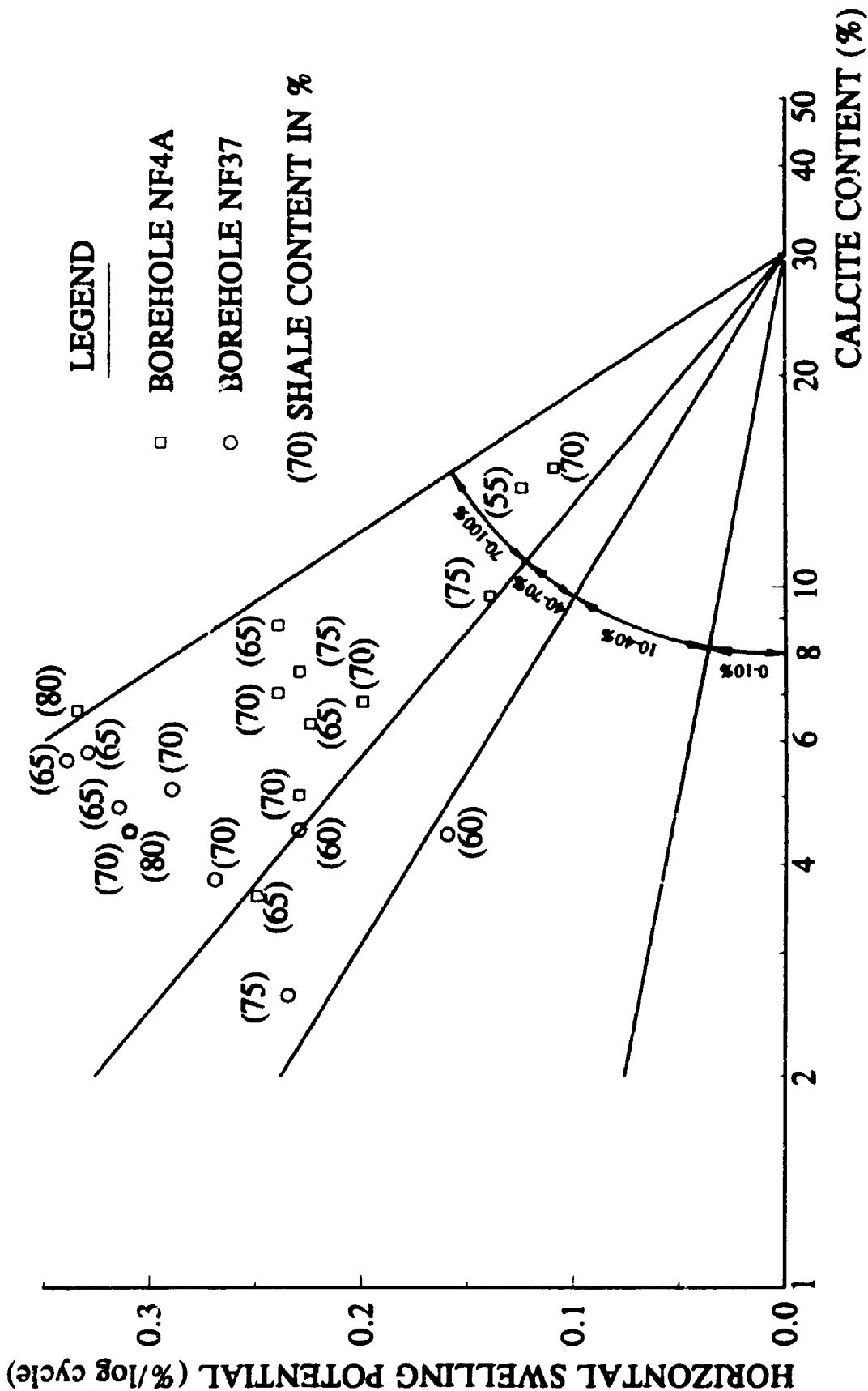
Figure 7.10 Effect of calcite content on swelling potential (1990 investigation)
(The shown boundaries are those obtained by Lo (1989) for Queenston Shale)
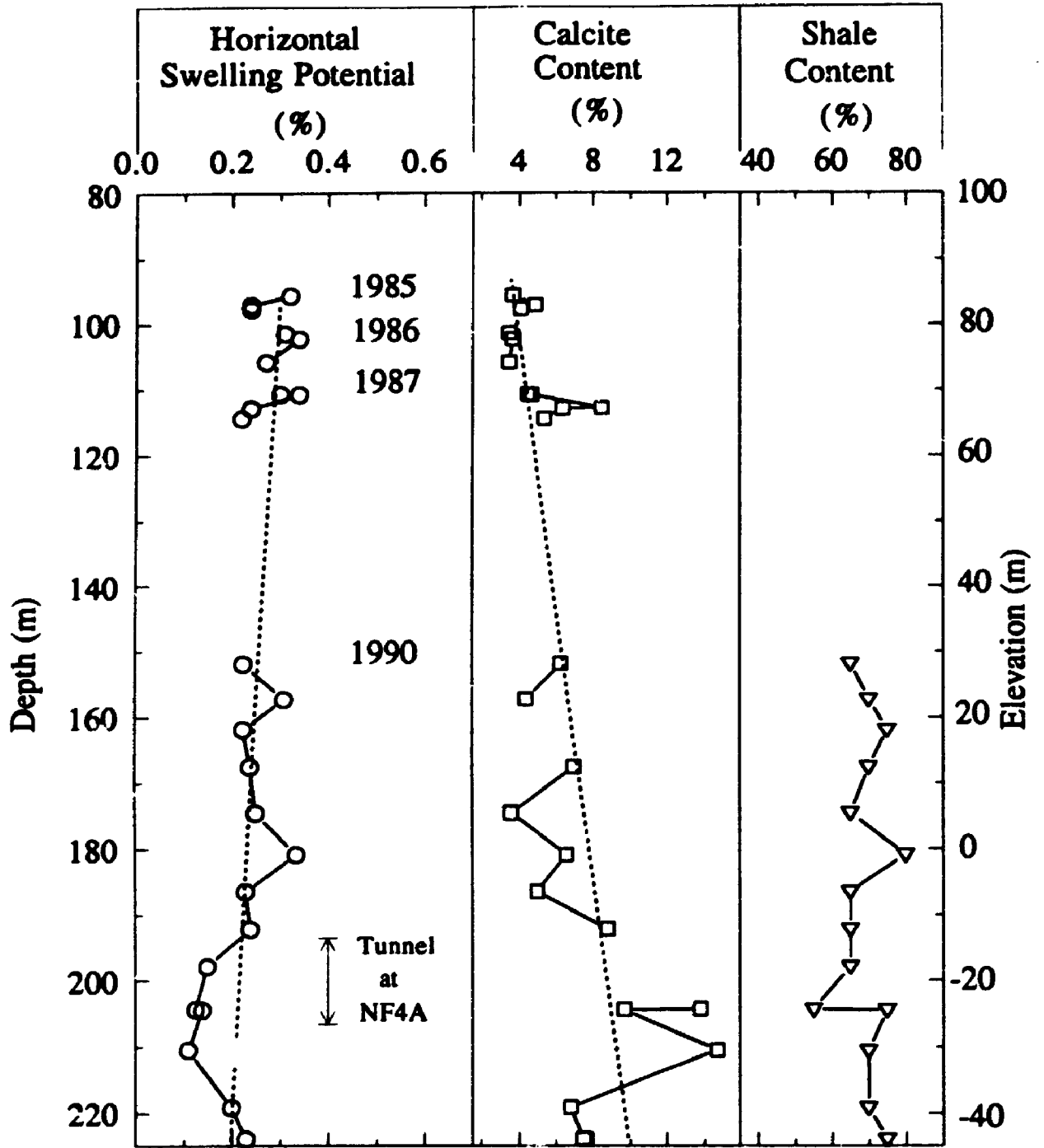
Figure 7.11 Variation of horizontal swelling potential, calcite content and shale content with depth in Borehole NF4A (1985 to 1990 investigations)
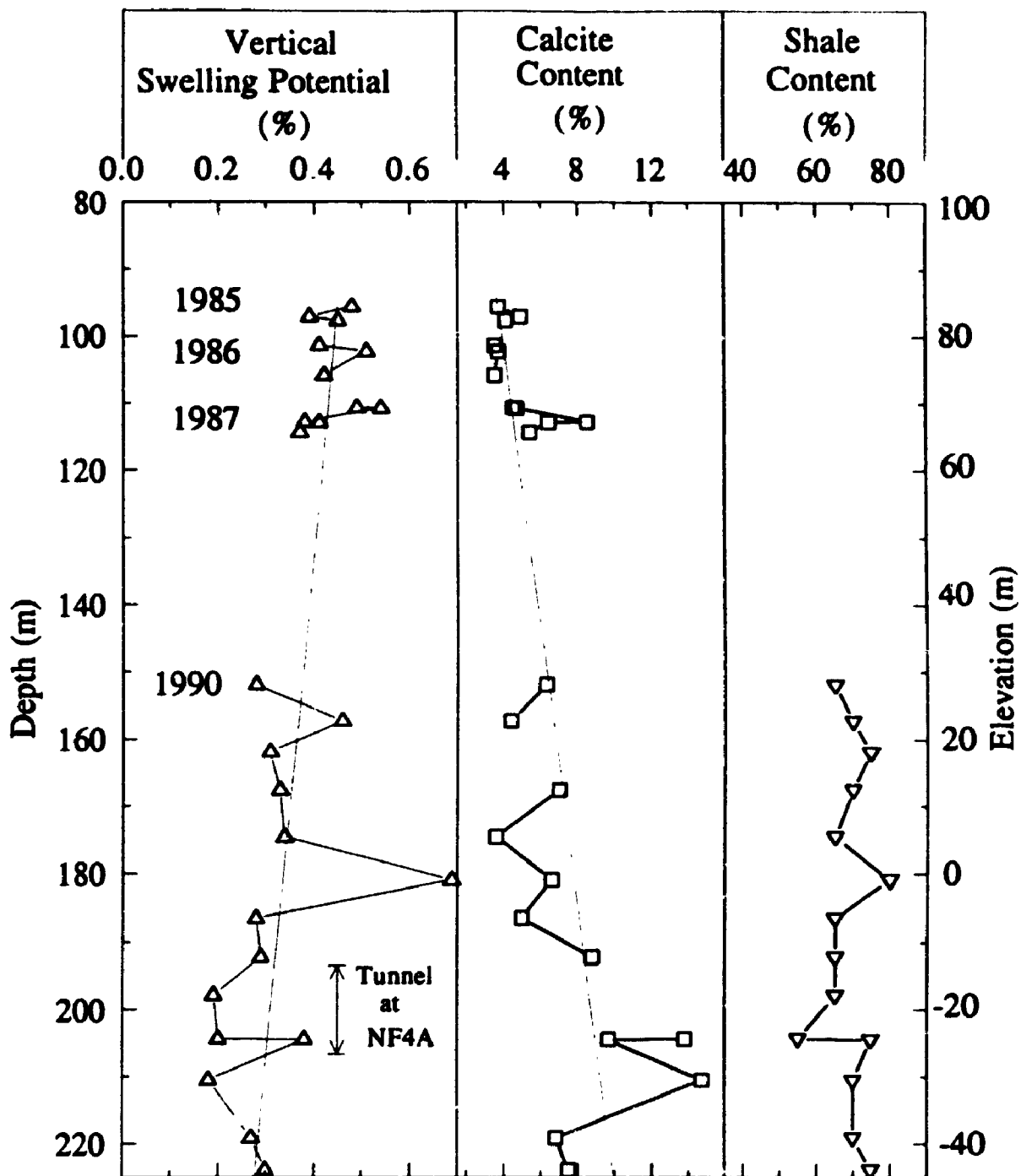
Figure 7.12 Variation of vertical swelling potential, calcite content and shale content with depth in Borehole NF4A (1985 to 1990 investigations)
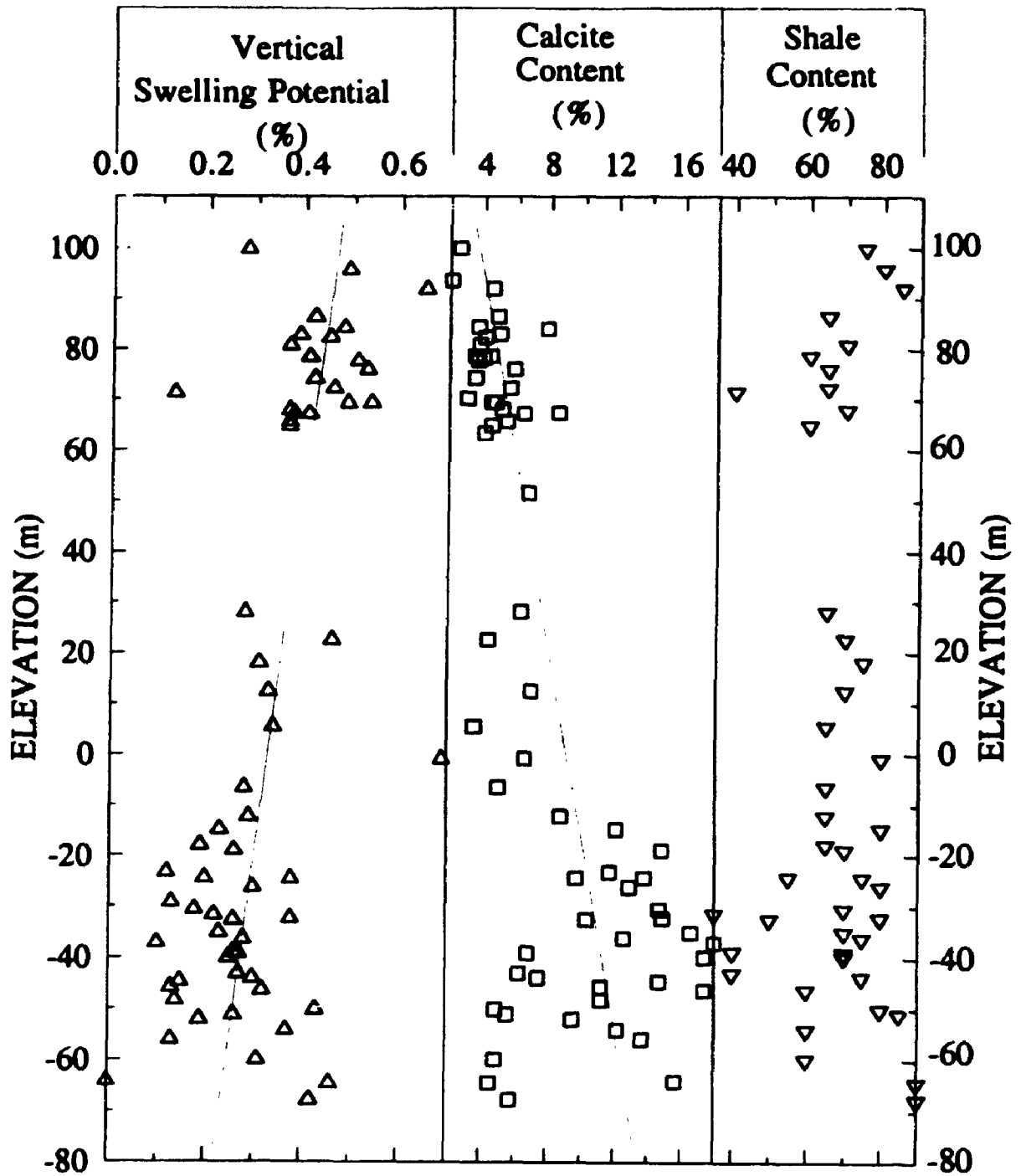
Figure 7.13 Variation of vertical swelling potential, calcite content and shale content with depth for Queenston Shale (1985 to 1990 investigations)
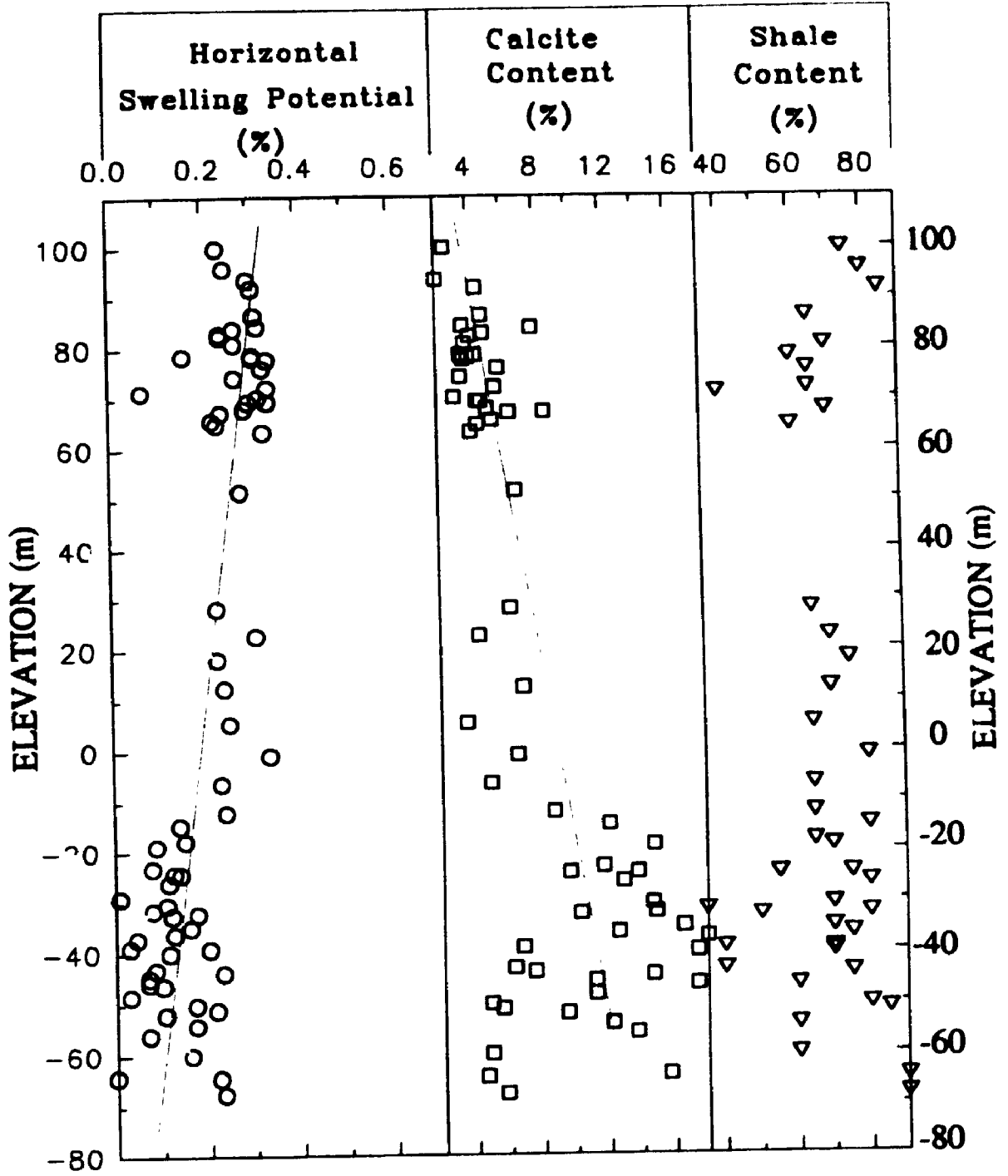
Figure 7.14 Variation of horizontal swelling potential, calcite content and shale content with depth for Queenston Shale (1985 to 1990 investigation)
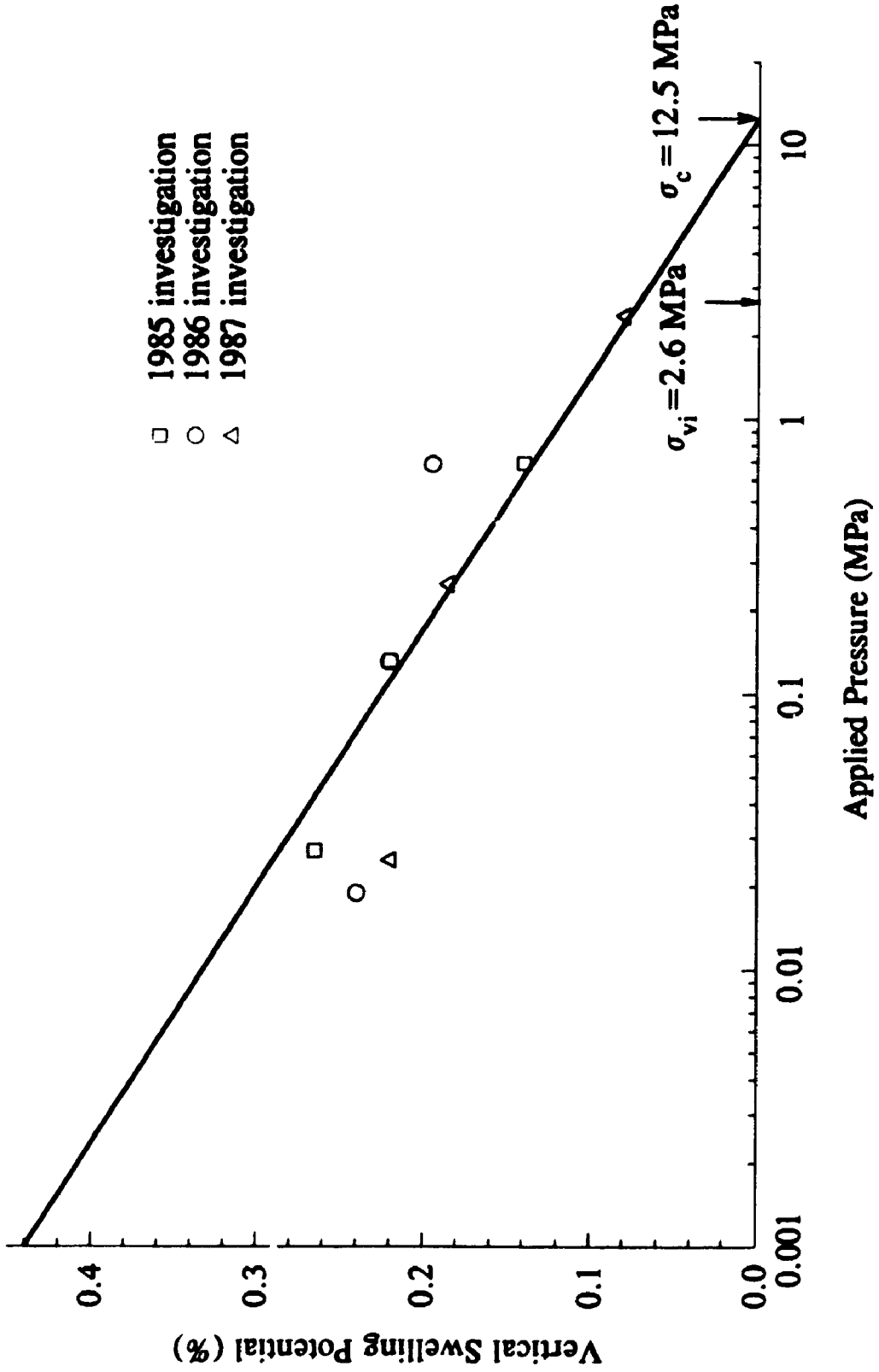
Figure 7.15 Effect of applied pressure on vertical swelling potential for Queenston Shale for the 1985 to 1987 investigations (Borehole NF4A)
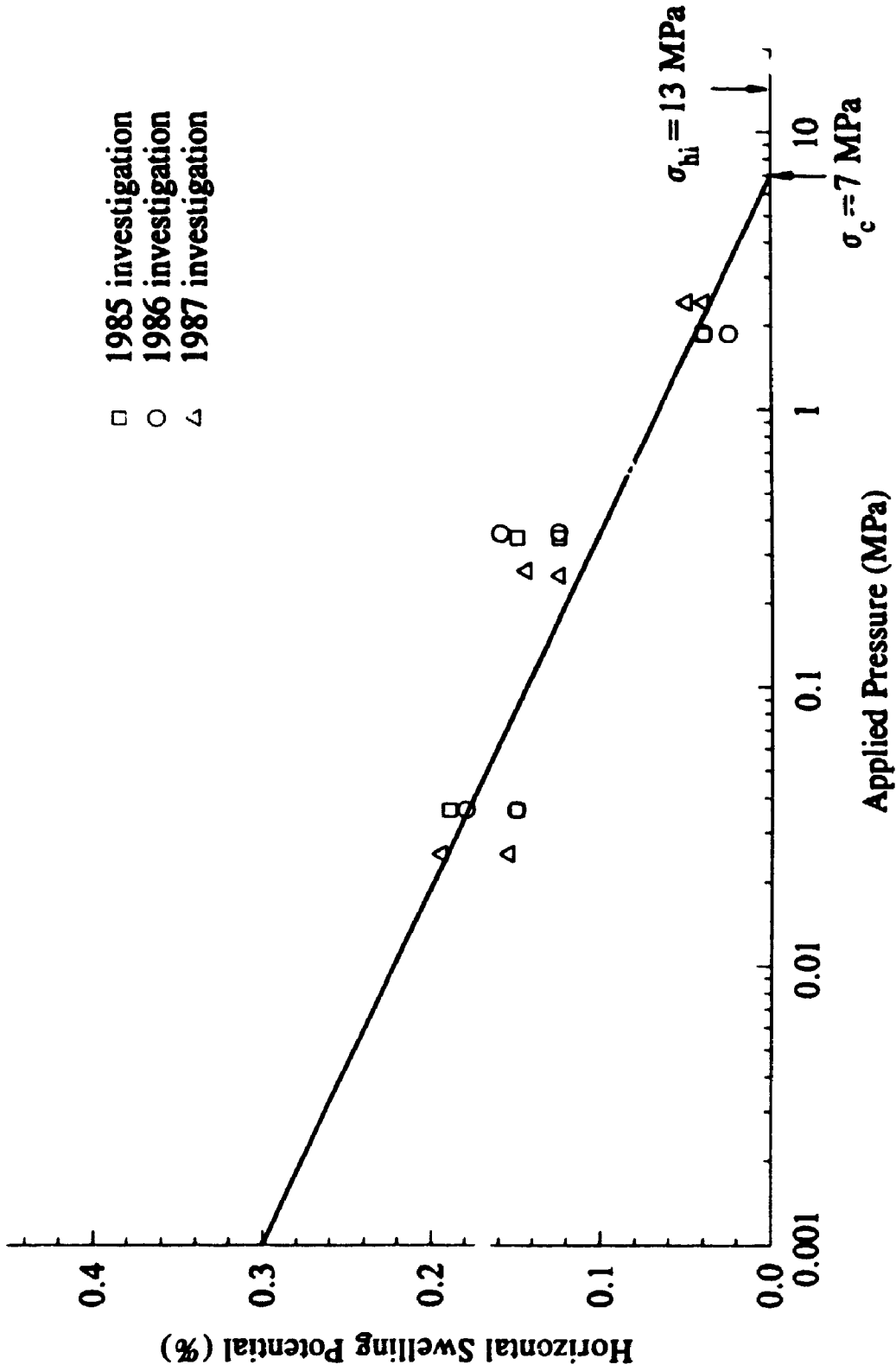
Figure 7.16 Effect of Applied Pressure on Horizontal Swelling Potential for Queenston Shale for the 1985 to 1987 investigations (Borehole NF4A)
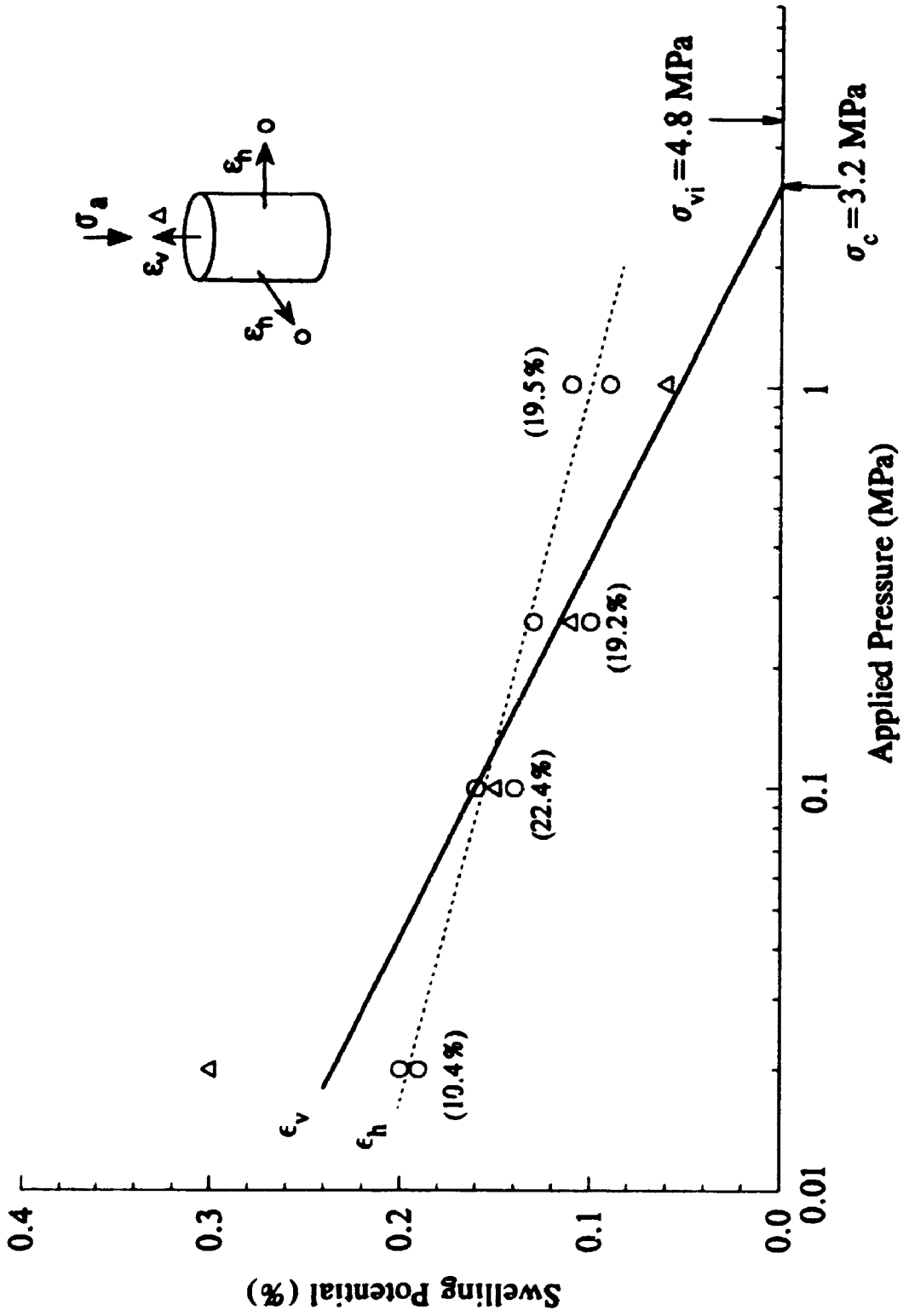
Figure 7.17 Effect of applied pressure on swelling potential of vertical samples of Queenston Shale for the 1989 Investigation (Borehole SD3)
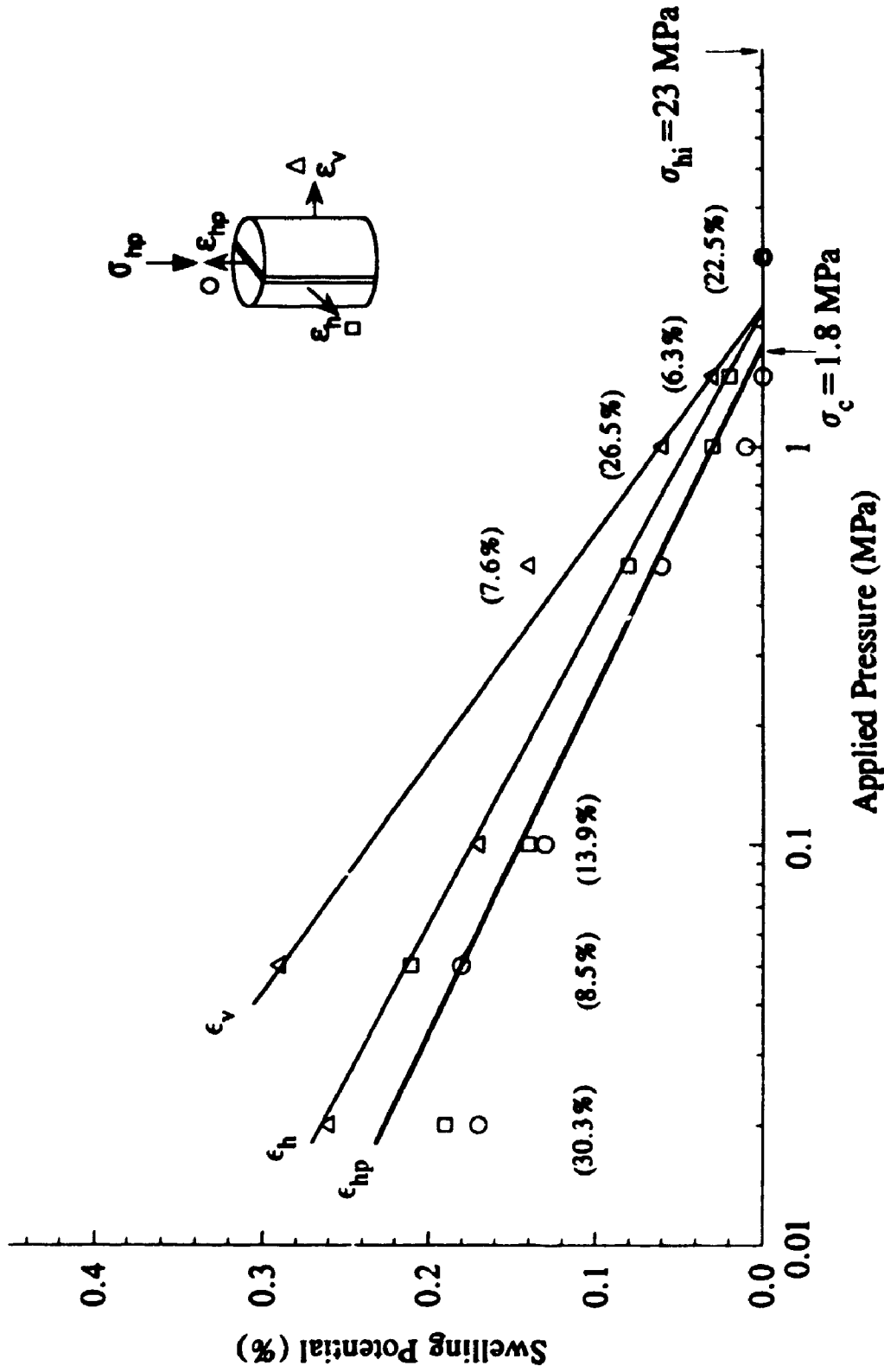
Figure 7.18 Effect of applied pressure on swelling potential on horizontal samples of Queenston Shale for the 1989 Investigation (Borehole SD3)
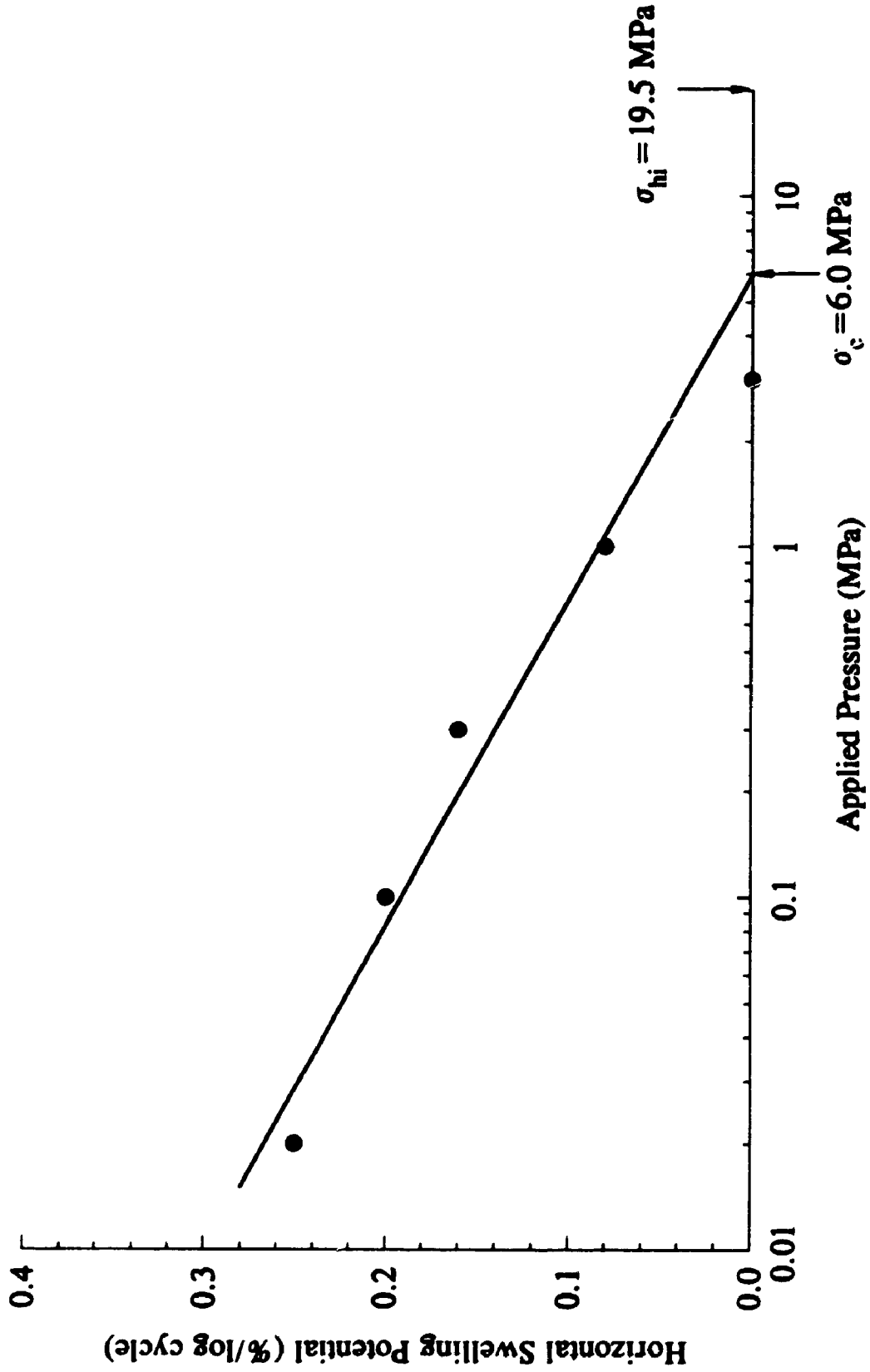
Figure 7.19 Effect of applied pressure on horizontal swelling potential of Queenston Shale for the 1990 investigation (Borehole NF4A)
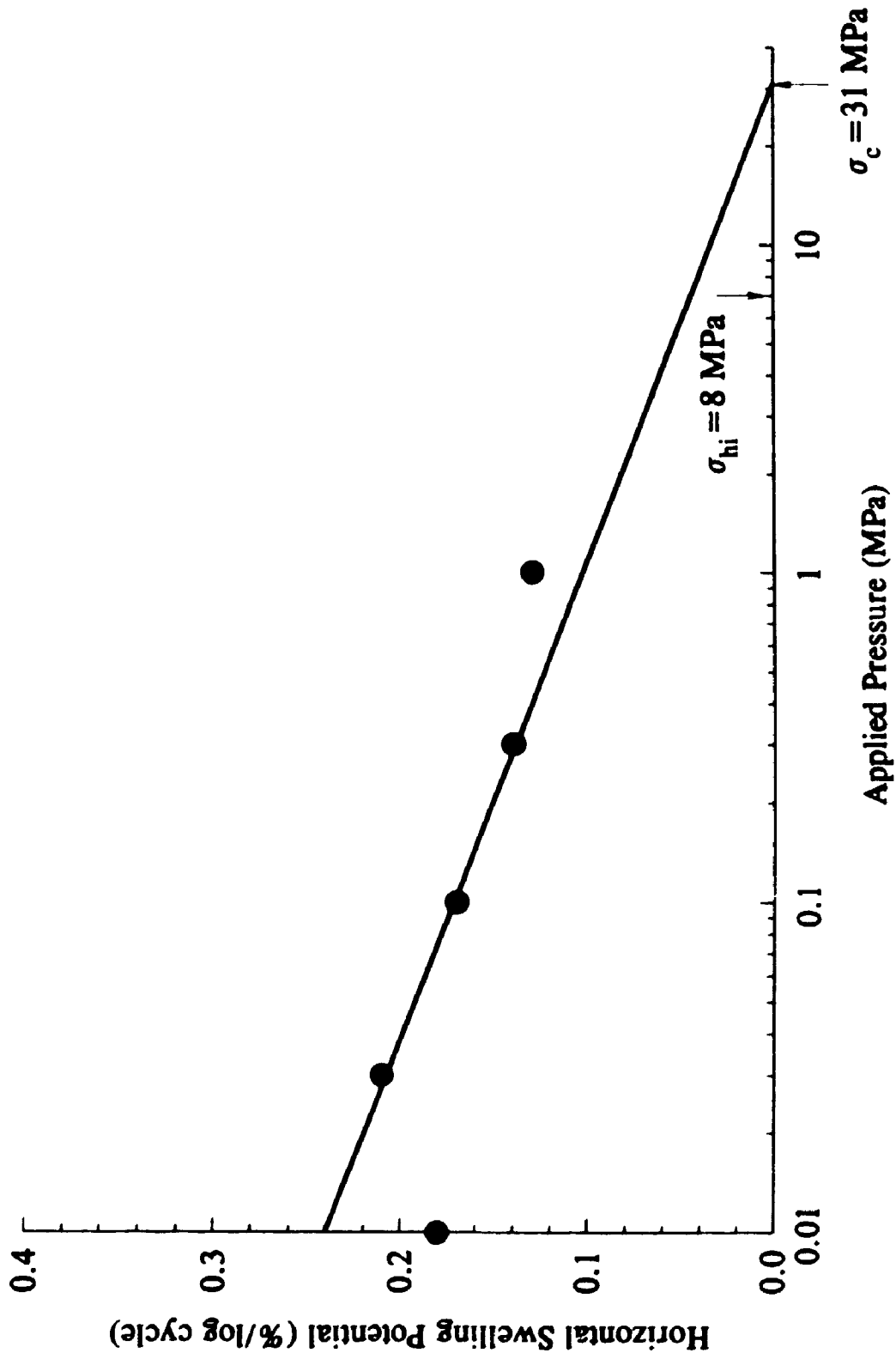
Figure 7.20 Effect of applied pressure on horizontal swelling potential of Queenston Shale
for the 1990 Investigation (Borehole NF37)

SAMPLE #	LW1	LW2	LW3	WL1 (reference)	WL2	WL3
STEP 1	σ_a	σ_a	σ_a	σ_a		
STEP 2	σ_a	σ_a	σ_a	σ_a	σ_a	σ_a
t_L(days)	0	0	0	0	7	14
t_w(days)	7	7	7	0	0	0
σ_a (MPa)	0.05	0.2	2	0.2	0.2	0.2
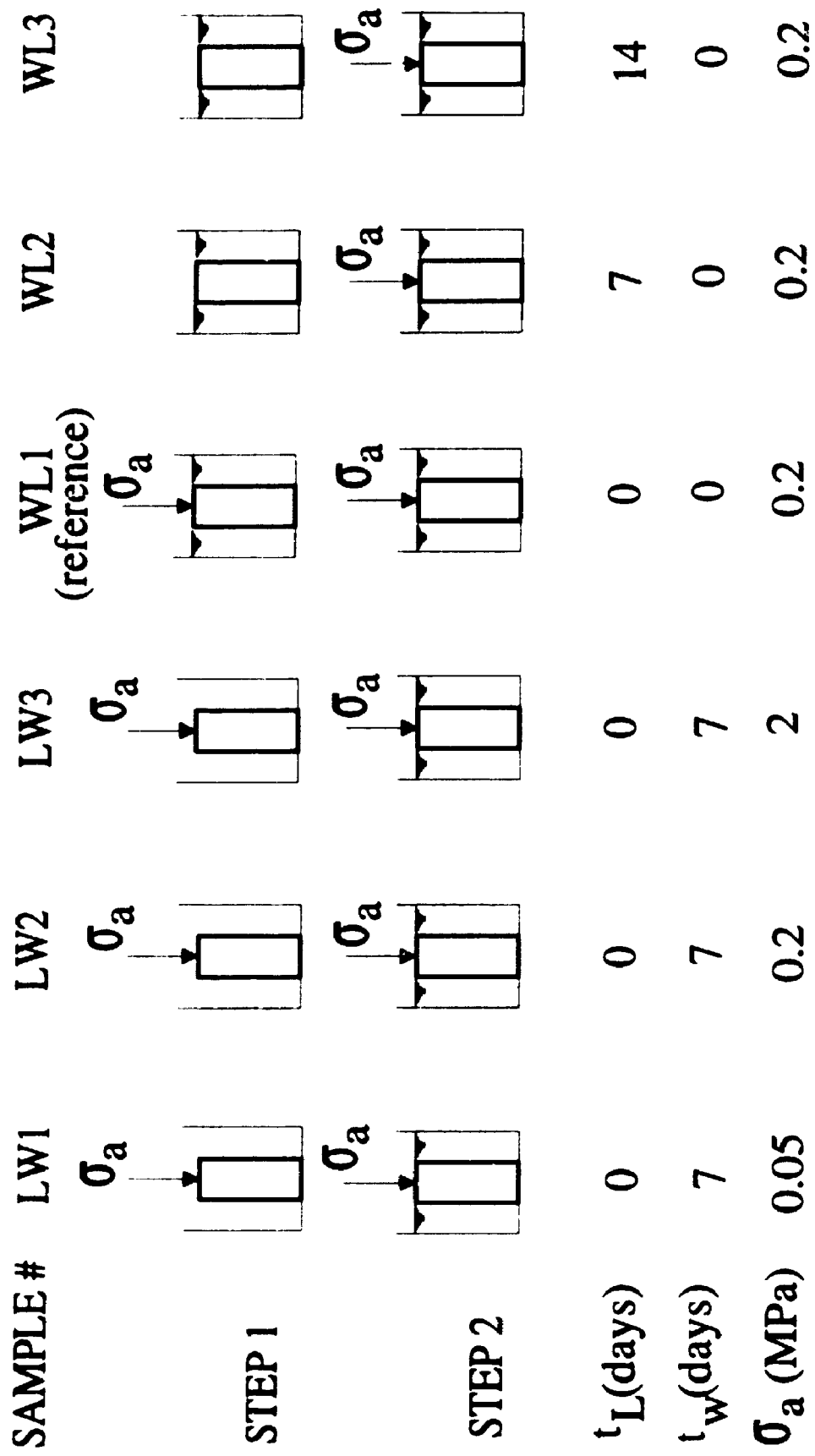
Figure 7.21 Schematic diagram showing the testing program performed on Queenston Shale (1993 investigation) to study the load-water sequence on swelling behaviour
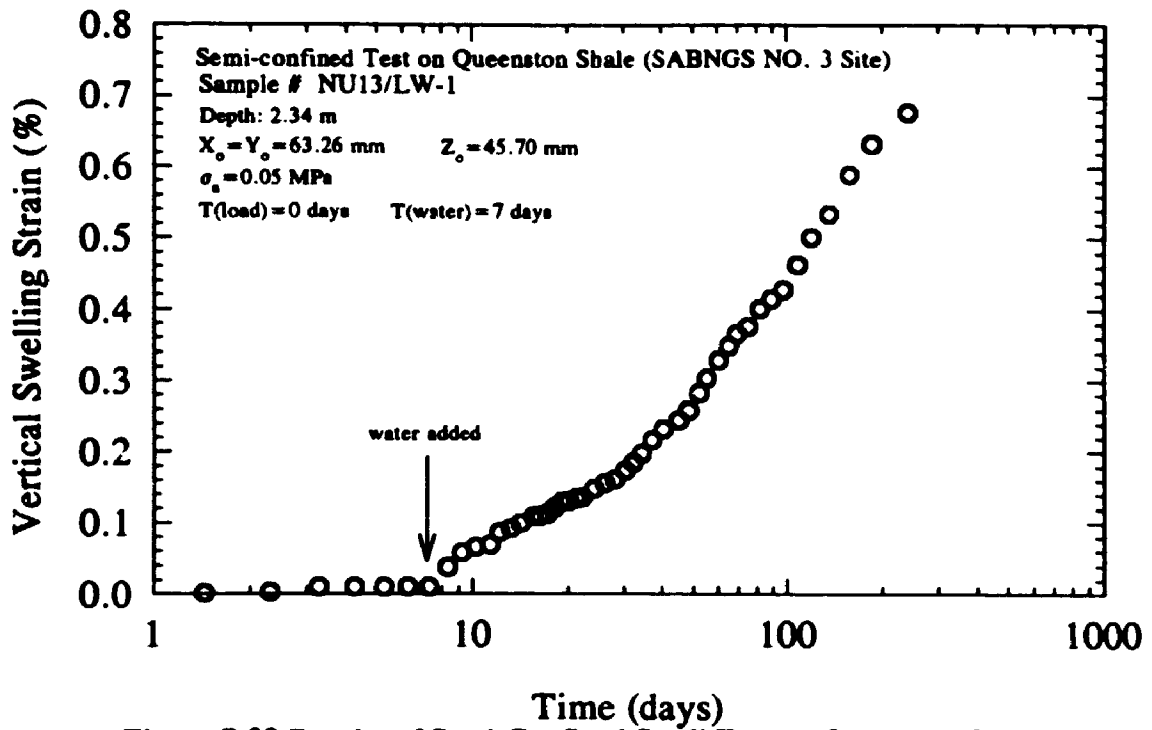
Figure 7.22 Results of Semi-Confined Swell Test on Queenston Shale
Test NU-13/LW-1 (1993 Investigation)
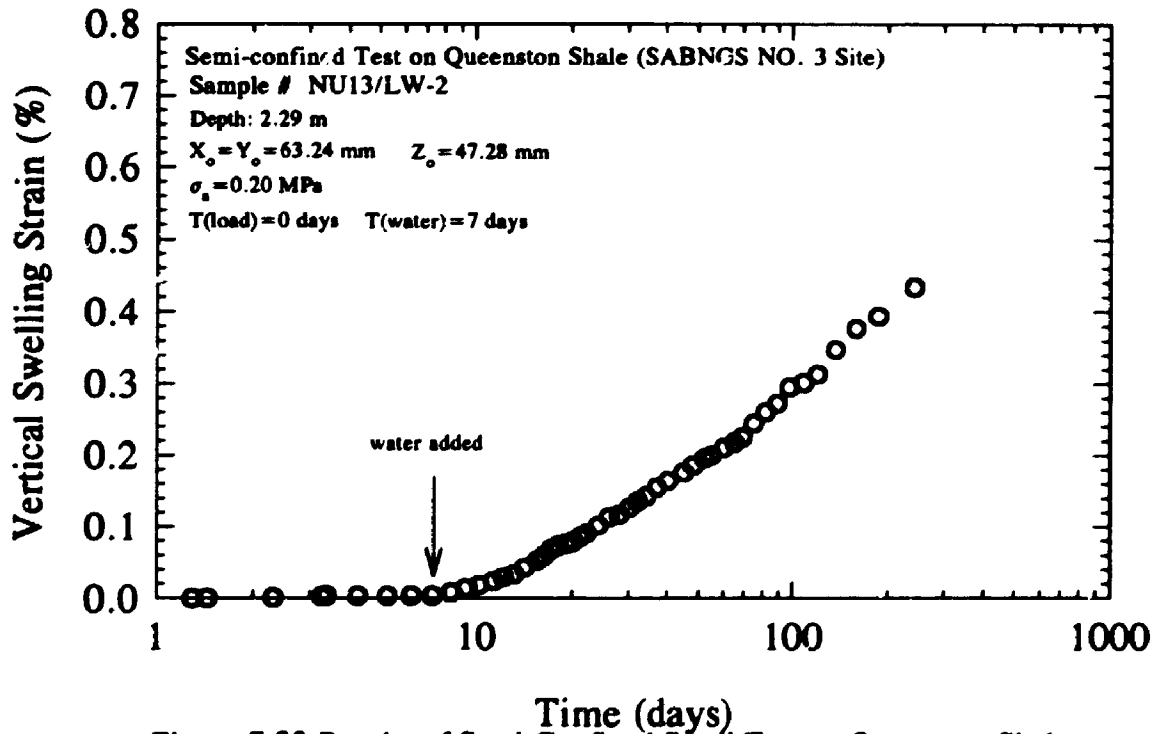
Figure 7.23 Results of Semi-Confined Swell Test on Queenston Shale
Test NU-13/LW-2 (1993 Investigation)
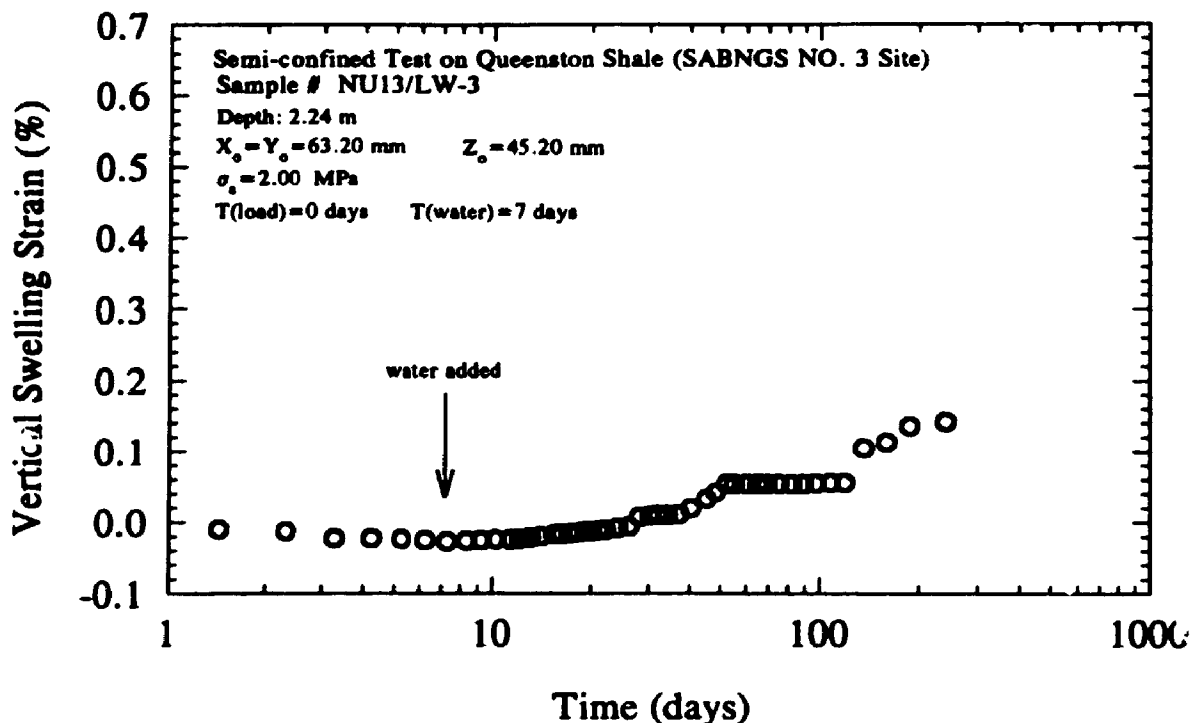
Figure 7.24 Results of Semi-Confined Swell Test on Queenston Shale
Test NU-13/LW-3 (1993 Investigation)
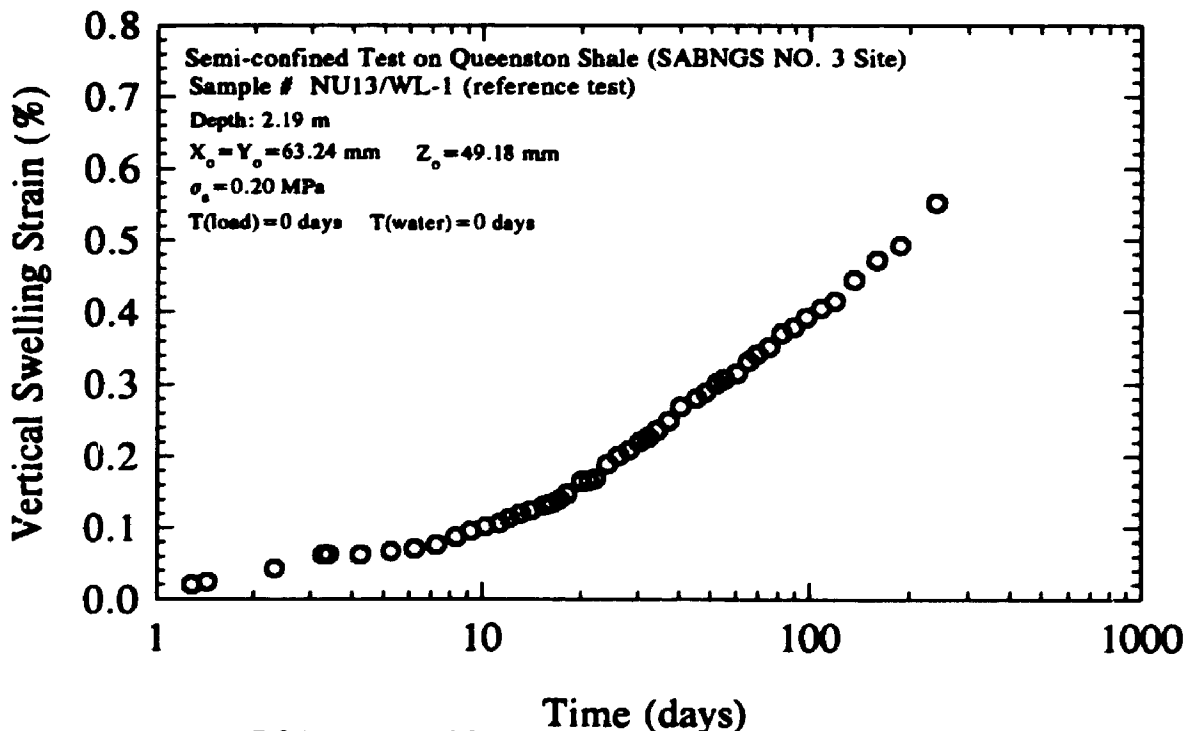
Figure 7.25 Results of Semi-Confined Swell Test on Queenston Shale
Test NU-13/WL-1 (1993 Investigation)
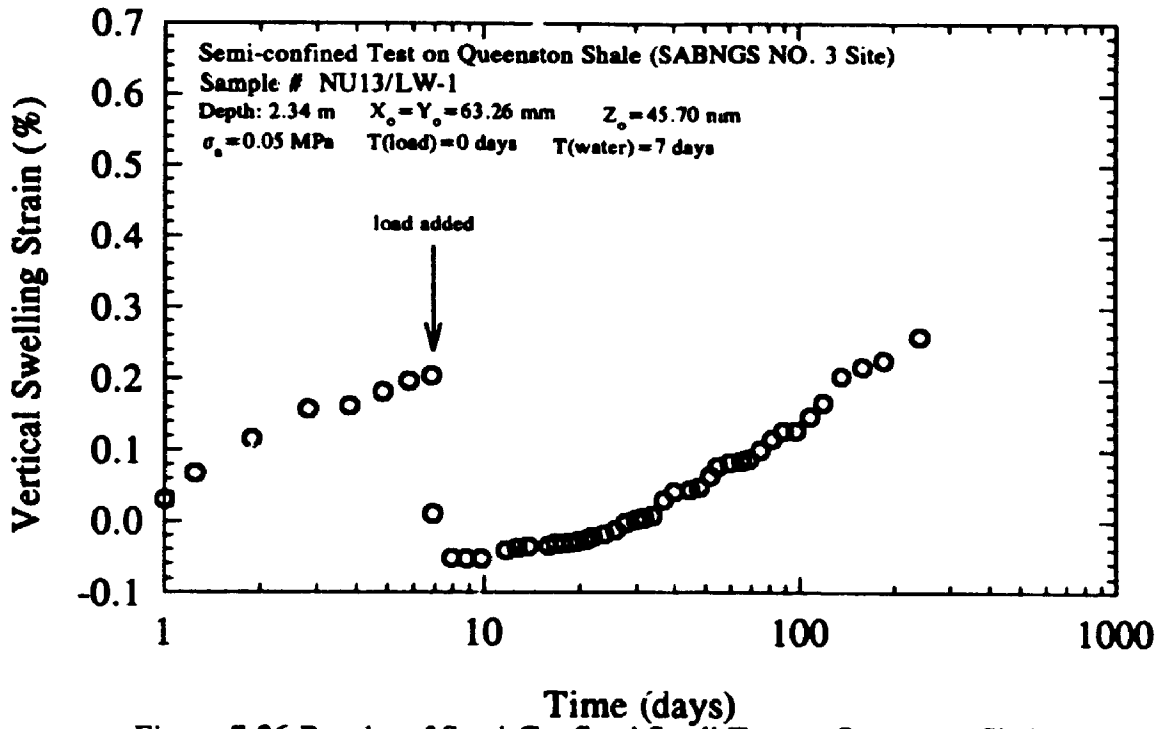
Figure 7.26 Results of Semi-Confined Swell Test on Queenston Shale
Test NU-13/WL-2 (1993 Investigation)
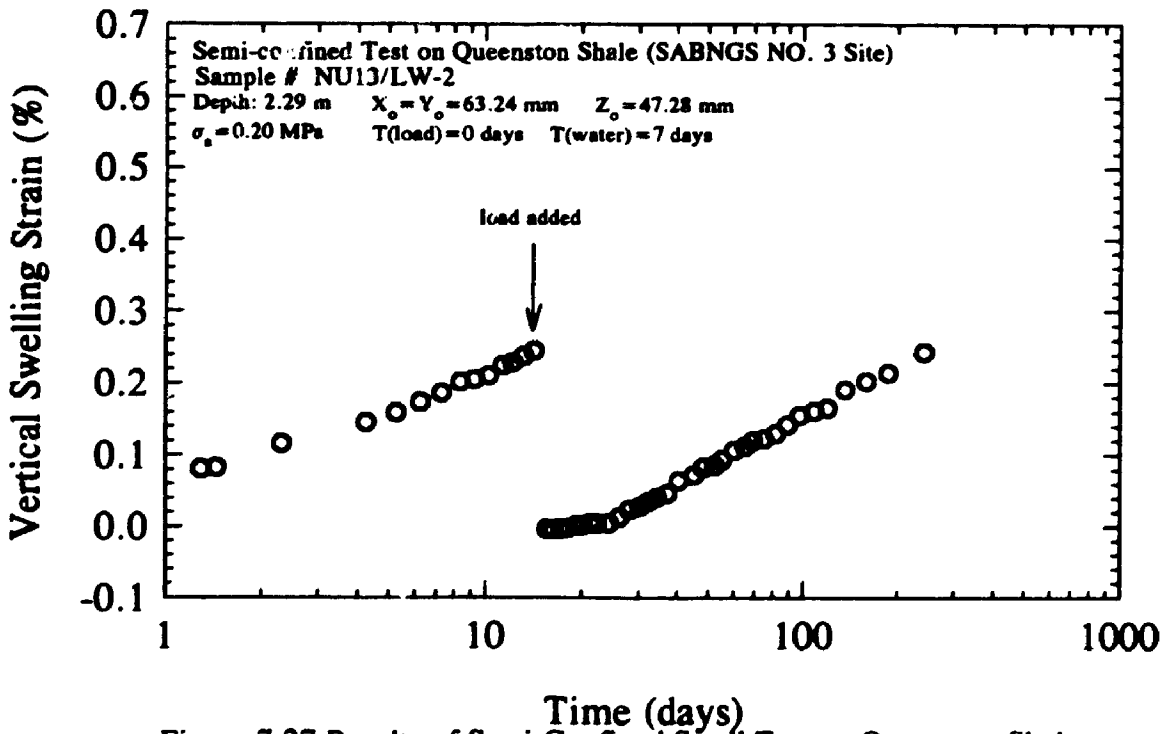
Figure 7.27 Results of Semi-Confined Swell Test on Queenston Shale
Test NU-13/WL-3 (1993 Investigation)

CHAPTER 8

MODELLING OF LONG-TERM TIME-DEPENDENT DEFORMATION

AND STRESS DEPENDENCY FOR QUEENSTON SHALE

8.1   INTRODUCTION

Investigations since 1984 on time-dependent deformation of Queenston Shale have shown that Queenston Shale exhibits important swelling characteristics upon stress relief. Two of the most important characteristics are that the swelling continues for very long period of time and that it is nonlinearly dependent on the applied stress.

In this chapter, the rheological model consisting of three Kelvin units connected in series is adopted to describe the nonlinear long-term swelling behaviour of Queenston Shale. This model was originally used by Huang (1992) to describe the swelling behaviour of Queenston Shale. In his formulation, however, the effect of the initial stress relief on the swelling was ignored and different rate parameters were used to represent deformation of samples from different boreholes. In this study, the initial stress value is introduced into the formulation and it is shown that only one set of rate parameters calculated from long-term swell tests can be used to represent adequately the swelling behaviour of Queenston Shale at different locations.

The same model is also used to predict the stress-dependent swelling strain for Queenston Shale. Equations relating the deformation moduli of the three Kelvin units under free swell strain to those under any applied stress are derived. The predicted swelling strains using this model are compared to the measured values.

8.2 MODELLING OF LONG-TERM TIME-DEPENDENT DEFORMATION

8.2.1 Long-Term Tests

In addition to the swelling tests discussed in Chapter 7, another 5 free swell tests have been started in 1986 and devoted to examine the long-term time-dependent deformation of Queenston Shale. The five samples were recovered from borehole NF4A at a depth of 103 m from the ground surface (elevation 77 m). Three of the five tests (NF4A/L1, NF4A/L2, and NF4A/L3) lasted for about 1260 days before converting them into semi-confined swell tests under different applied pressures. The other two free swell tests (NF4A/L4, and NF4A/L5) are still running till present (early 1994), more than 2700 days (≈ 8 years) since start of testing.

The swelling strains for the five tests are plotted in normal scale against time in Figures 8.1 to 8.5 and in semi-logarithmic scale in Figures 8.6 to 8.10. Table 8.1 summarizes the results of the five free swell tests. In this table, the value of the average slope of the curve of swelling strain versus logarithm of time between 10 and 100 days is denoted α_{10-100} and that between 100 and 1000 days is denoted $\alpha_{100-1000}$. The values of α_{10-100} and $\alpha_{100-1000}$ are indices of swelling potentials (strain per log cycle of time as defined by Lo et al. 1978). From Figures 8.1 to 8.10 and Table 8.1, the following observations can be made:

1- The values of swelling strain increment from 100 to 1000 days are larger than those from 10 to 100 days, indicating that the swelling potential (strain per log cycle of time) is increasing with time, that the swelling deformation may last for long time, and that the long-term swelling deformation is highly nonlinear with

time.

2- In the vertical direction, the average value of α_{10-100} for the five tests is 0.37% and that of $\alpha_{100-1000}$ is 0.44%. In the horizontal direction, the average value for the five tests of α_{10-100} is 0.2% and that of $\alpha_{100-1000}$ is 0.28%.

3- After 2700 days and up to the present (early 1994), time-dependent swell deformation is still developing although the swelling rate decreases gradually with time.

4- The rate of swelling of samples (NF4A/L1, NF4A/L2, and NF4A/L3) after converting them into semi-confined tests is decreased due to the applied pressure.

8.2.2 Modelling of Long-Term Deformation

To represent the time-dependent deformation of geotechnical materials several empirical laws and rheological models have often been employed (see e.g. Goodman (1980), Lo and Yuen (1981), and Lo and Lee (1990)). The method introduced by Lo and Lee (1981) for modelling the swelling behaviour of Queenston Shale is dependent on the assumption that the relationship between the swelling strain and logarithm of time is linear. Therefore this method will be suitable only for representation of short-term deformation. Huang (1992) showed that the logarithm law, the multipower law, a Kelvin body, and a Burger body can only represent the short term time-dependent deformation of Queenston Shale. The ineptitude of different models to represent the swelling deformation of Queenston Shale is due to the high nonlinearity of the long-term time-dependent swelling deformation as discussed above.

Huang (1992) showed that the rheological model consisting of a series of Kelvin units can represent the nonlinear long-term time-dependent deformation of Queenston Shale to a high degree of accuracy. The parameters of this model can be obtained by a nonlinear regression analysis. For this model (Figure 8.11), the time-dependent swelling strain can be expressed as

$$\varepsilon(t) = \sigma \sum_{i=1}^{n} \frac{1}{E_i} (1 - e^{-\lambda_i t}) \qquad (8.1)$$

where $\varepsilon(t)$ = time-dependent swelling strain under stress relief σ,

σ = stress relief under which swelling occurs,

n = the number of Kelvin units adopted,

E_i = deformation modulus of the ith unit,

λ_i = parameter controlling the swelling rate of the ith unit

$$\lambda_i = \frac{E_i}{\eta_i},$$

η_i = viscosity of the dash pot in the ith unit, and

t = elapsed time

It was shown by Huang (1992) that a model consisting of three Kelvin units connected in series well represents the long-term swelling behaviour of Queenston Shale. For a model of two units, not only it gives poor representation but also the choice of the parameters λ_i is critical. Any small change in the value of λ_i may affect the accuracy of the predicted results. For a model of more than three units, a negligible to no better

representation may be obtained, the number of parameters increases, and some of the values of E_i may be negative which has no physical meaning.

Using a model of three Kelvin units connected in series, the parameters obtained from regression analysis for the five long-term free swell tests of Queenston Shale are listed in Table 8.2 for the vertical direction and Table 8.3 for the horizontal direction (obtained based on the first 1260 days of test results, Huang (1992)). The average values of the rate parameters λ_i of the five tests are also shown in the tables. It can be seen from Tables 8.2 and 8.3 that the average value of λ_1 is the same for the vertical and horizontal directions. There is, also, negligible difference between the average values of the parameter λ_2 and λ_3 in the two directions. For engineering purposes, therefore, the average set of values of the parameters λ_i in the vertical and horizontal directions may be used to represent the long-term time-dependent deformation of Queenston Shale for both directions.

The representative average values of λ_i in the vertical and horizontal directions are

$$\lambda_1 = 0.11, \qquad \lambda_2 = 0.028, \text{ and } \qquad \lambda_3 = 0.0018 \qquad (8.2)$$

Since these values are adequately calculated from long-term swell tests, they will be considered as the governing swelling rate parameters for Queenston Shale at this site regardless the depth and location. The variation of swelling strain from a free swell test to another will be dependent only on the deformation moduli of the three Kelvin units, keeping the rate parameters λ_i constant. Using the rate parameters obtained in Eq. 8.2,

the values of moduli E_1, E_2, and E_3 for each free swell test in both directions are calculated using the least-squares method and listed in Table 8.4. The predicted swelling strains using the values of λ_i and E_i listed in Table 8.4 are plotted against time and compared to the measured values in Figures 8.12 to 8.16. From these figures, the following two important observations can be made:

1-   the predicted values of swelling strain agree well with the measured values.

2-   the predicted curves of swelling strain versus elapsed time for tests NF4A-L4 and NF4A-L5, whose parameters were obtained on the basis of the test results during the first 1260 days, can represent the results of the free swell test up to the present (more than 2700 days) reasonably well. This important observation shows that the model not only represents the swelling strain within the period of time the parameters are calculated but also predicts adequately the strain for even much higher values of time.

Parameters Representing the Overall Behaviour of the Long-Term Tests

The representative values of E_i for the overall behaviour are the values of E_i that give the average swelling strain of the five tests at any time. Using Eq. 8.1 and the deformation moduli of the five tests, the average swelling strain of the five tests at any time is

$$\varepsilon(t) = \frac{\sigma}{5} \sum_{j=1}^{5} \sum_{i=1}^{3} \frac{1}{E_{ij}}(1-e^{-\lambda_i t}) \qquad (8.3)$$

where i is the unit number and j is the test number. Since λ_1, λ_2, and λ_3 are the same for the five tests, Eq. 8.3 can be written as

$$\varepsilon(t) = \frac{\sigma}{5}\left[(1-e^{-\lambda_1 t})\sum_{j=1}^{5}\frac{1}{E_{1j}} + (1-e^{-\lambda_2 t})\sum_{j=1}^{5}\frac{1}{E_{2j}} + (1-e^{-\lambda_3 t})\sum_{j=1}^{5}\frac{1}{E_{3j}}\right] \qquad (8.4)$$

From Eq. 8.1, the average swelling strain can be directly expressed as

$$\varepsilon(t) = \sigma\left[\frac{1}{E_1}(1-e^{-\lambda_1 t}) + \frac{1}{E_2}(1-e^{-\lambda_2 t}) + \frac{1}{E_3}(1-e^{-\lambda_3 t})\right] \qquad (8.5)$$

where E_1, E_2, and E_3 are the representative deformation moduli of the overall behaviour. Comparing Eq. 8.4 to 8.5, the following expression for the representative moduli is obtained:

$$\frac{1}{E_i} = \frac{1}{5}\sum_{j=1}^{5}\frac{1}{E_{ij}} \qquad (8.6)$$

The representative values of E_i in both the vertical and horizontal directions calculated using Eq. 8.6 are as follows:

in the vertical direction

$E_1 = 3080$ MPa $E_2 = 730$ MPa $E_3 = 420$ MPa

in the horizontal direction

$E_1 = 19610$ MPa $E_2 = 9950$ MPa $E_3 = 3240$ MPa

The swelling strains calculated using the above set of parameters in both the vertical and horizontal directions are plotted and compared to the calculated swelling strains for

individual tests in Figure 8.17. From this figure, it can be observed that the representative values of E_i estimate quite well the average strains of the five tests at any time for both the vertical and horizontal directions.

8.3 STRESS-DEPENDENCY OF TIME-DEPENDENT DEFORMATION

In addition to the long-term time-dependent deformation, the nonlinear stress-dependency of the deformation is an important characteristic of Queenston Shale (refer to Chapter 7). It has been shown from the results of the semi-confined tests analyzed in Sec. 7.3 that:

1- Under an applied stress less than the critical stress (σ_c), there is a suppression effect on the time-dependent swelling deformation of Queenston Shale.

2- Under an applied stress equal to or higher than σ_c, no time-dependent deformation occurs

3- The swelling potential is not linear to the applied stress (σ_a), however, it is linear to the logarithm of the applied stress.

Extensive study on the swelling behaviour of Queenston Shale (Lee 1988) has shown that the swelling potential and the time-dependent deformations at any time (less than 100 days) are linear to the logarithm of the applied stress. In 1990 investigation, semi-confined swell tests lasted for more than 500 days and results have shown that the time-dependent deformations at any time over 100 days are also linear to the logarithm of applied stress (Figure 8.18).

To relate the swelling strain resulting from a semi-confined swell test to that from

the free swell test, the equivalent free swell stress (σ_e) was introduced by Huang (1992),

refer to Figure 8.19. The equivalent free swell stress can be defined as the minimum

applied stress under which the suppression effect of the stress begins to be effective. In

other words, for any applied stress less than σ_e, the resulting swelling strain (ε_a) equals

to the free swell test strain (ε_o), while for an applied stress higher than σ_e, a strain less

than ε_a is obtained with its magnitude dependent on the value of the applied stress.

From this discussion, it is obvious that σ_e is referred to as the equivalent free swell

stress because under σ_e the resulting strain ε_e is equal to the free swell strain. As will

be shown later, the value of σ_e is very small, usually less than 0.02 MPa.

The swelling strain at time t under an applied stress σ_a between σ_e and σ_c is

denoted $\varepsilon_a(t)$ (Figure 8.19) and can be related to the free swell strain, $\varepsilon_e(t)$, by the

following relationship:

$$\varepsilon_a(t) = \frac{\log \sigma_c - \log \sigma_a}{\log \sigma_c - \log \sigma_e} \varepsilon_e(t) \tag{8.7}$$

where $\dfrac{\varepsilon_e(t)}{\log \sigma_e - \log c_e}$ is the slope of the straight line between σ_e and σ_c at time t.

8.3.1 Modelling of Stress-Time-Dependent Deformation by Three Kelvin Units Connected in Series

It has been shown in Sec. 8.2 that the rheological model consisting of three

Kelvin units connected in series well represents the results of long-term time-dependent deformation of free swell tests. In this section, the model will be extended to include modelling of the results of semi-confined swell tests.

In his formulation of the problem, Huang (1992) ignored the effect of initial stress value σ_o on the swelling strain of semi-confined tests. He considered that the swelling strain is resulting from the relief of the difference between the critical stress σ_c and the applied stress σ_a, although in modelling the free swell test results he considered that the deformation is resulting from the relief of the initial stress. This discrepancy led to a sudden huge decrease in the deformation moduli, of the three Kelvin units, within a very small change in stress (between stress relieves σ_o and $\sigma_o - \sigma_c$).

In this section, the initial stress value is introduced into the formulatic. which overcomes the discrepancy given by Huang's formulation and leads to smooth rational values of deformation moduli.

Assuming that the swelling strain $\varepsilon(t)$ is dependent on the stress relief σ, it has been able (Sec. 8.2) to express the free swell strain by the following expression:

$$\varepsilon(t) = \sum_{i=1}^{3} \frac{\sigma}{E_i} (1 - e^{-\lambda_i t}) \qquad (8.8)$$

Under applied stress, the resulting swelling strain is less than the free swell strain and the relation between the applied stress and the resulting strain is nonlinear (linear in logarithmic scale). For applied stress higher than the critical stress σ_c, the strain is completely suppressed and no time-dependent deformation occurs. Results of semi-confined tests since 1985 have shown that in general the critical stress value is

considerably below the initial stress value σ_o. Mechanically, the suppression of the swelling strain for the general case ($\sigma_c < \sigma_o$) can be regarded as the combination of the effects of two factors (refer to Figure 8.20):

1- Suppression due to reduction of stress relief: under applied stress σ_a, the stress relief σ_r is less than the initial stress value σ_o considered with the free swell strain ($\sigma_r = \sigma_o - \sigma_a$), leading to lower strain values.

2- Suppression due to apparent stiffening effect: as the applied load on the sample increases, the sample apparently becomes more stiffer towards the time dependent deformation and the values of deformation moduli increase, leading to a lower strain value than that would be obtained if only factor (1) above is considered (Figure 8.20).

The effects of both factors can be considered in the generalized Kelvin model expressed by Eq. 8.8 by letting $\sigma = \sigma_o - \sigma_a$ (factor 1) and by constructing a nonlinear relationship between the deformation moduli E_i and the applied stress (factor 2).

According to the above discussion, the rate parameters λ_i are considered stress independent and only the deformation parameters E_i are stress dependent. Consequently, the equivalent swelling strain ε_e under applied stress σ_e can be given by the following equation:

$$\varepsilon_e(t) = (\sigma_o - \sigma_e) \sum_{i=1}^{3} \frac{1}{E_{ie}}(1 - e^{-\lambda_i t}) \tag{8.9}$$

where E_{ie} is a stress-dependent modulus for the ith Kelvin unit under applied stress σ_e.

From Eqs. 8.7 and 8.9, the swelling strain $\varepsilon_a(t)$ under applied stress σ_a can be written as

$$\varepsilon_a(t) = \frac{(\log \sigma_c - \log \sigma_a)(\sigma_o - \sigma_e)}{(\log \sigma_c - \log \sigma_e)(\sigma_o - \sigma_a)}(\sigma_o - \sigma_a) \sum_{i=1}^{3} \frac{1}{E_{ie}}(1 - e^{-\lambda_i t}) \tag{8.10}$$

Similar to Eq. 8.9, the swelling strain $\varepsilon_a(t)$ under applied stress σ_a can be written as

$$\varepsilon_a(t) = (\sigma_o - \sigma_a) \sum_{i=1}^{3} \frac{1}{E_{ia}}(1 - e^{-\lambda_i t}) \tag{8.11}$$

where E_{ia} is a stress-dependent modulus for the ith Kelvin unit under applied stress σ_a.

From Eqs. 8.10 and 8.11, the following relationship between E_{ia} and E_{ie} can be obtained:

$$E_{ia} = \frac{(\log \sigma_c - \log \sigma_e)(\sigma_o - \sigma_a)}{(\log \sigma_c - \log \sigma_a)(\sigma_o - \sigma_e)} E_{ie} \tag{8.12}$$

Equation 8.12 shows that the deformation parameter E_{ie} is an important quantity that should be determined in order to calculate the deformation parameters of the sample under any applied stress σ_a.

Since the free swell strain ε_o (under stress relief σ_o) is equal to the equivalent strain ε_e, then $\varepsilon_o = \varepsilon_e$. Therefore,

$$\sigma_o \sum_{i=1}^{3} \frac{1}{E_{io}}(1 - e^{-\lambda_i t}) = (\sigma_o - \sigma_e) \sum_{i=1}^{3} \frac{1}{E_{ie}}(1 - e^{-\lambda_i t}) \qquad (8.13)$$

After arrangement, a relationship between the deformation parameters of free swell test and those under equivalent stress is obtained

$$E_{ie} = \frac{\sigma_o - \sigma_e}{\sigma_o} E_{io} \qquad (8.14)$$

From results of semi-confined tests, the values of σ_e obtained are very small (usually less than 0.02 MPa), therefore, E_{ie} can be taken the same value as E_{io}.

8.3.2 Summary of Steps of Predicting the Time-Dependent Deformation

The method of predicting the time-dependent deformation for any sample of Queenston Shale under applied stress σ_a is summarized as follows:

1-   Using nonlinear regression analyses, determine the rate parameter λ_i and the deformation parameter E_{io} for each of the three Kelvin units from results of long-term free swell tests.

2-   From results of semi-confined tests, determine the critical stress σ_c and the equivalent free swell stress σ_e. The critical stress is the value of stress at the intersection of the swelling potential line with $\log \sigma$ axis. The equivalent free swell stress is the value of stress under which the resulting swelling potential is equal to the free swelling potential (Figure 8.19).

3-   Consider the deformation parameters E_{ie} for the three Kelvin units are equal to

the values of E_{io} or calculate E_u using Eq. 8.14.

4-   Under applied stress σ_a between σ_e and σ_c, calculate the corresponding values

of E_{ia} using Eq. 8.12.

5-   Calculate the swelling strain ε_u under the applied stress σ_a using Eq. 8.11.

6-   As σ_a approaches σ_c, the value of E_{ia} approaches infinity and for $\sigma_a \geq \sigma_c$ no

swelling strain occurs.

7-   For locations where no long-term free swell tests are performed, use a reliable

semi-confined test to calculate the values of E_{ia} for that test and the deformation

parameters for the other tests can be related to those from that test (this test will

be referred to as a reference test).

8.4   PREDICTION OF STRESS-TIME-DEPENDENT DEFORMATION OF QUEENSTON SHALE

In the following analysis, the method described in the previous section will be

implemented to predict the stress-time-dependent deformation of Queenston Shale at

different locations and different depths. The predicted strains will be compared to the

measured values both in the vertical and horizontal directions.

8.4.1   1985 to 1987 Investigations

As mentioned in Chapter 7, the semi-confined tests carried out in 1985 to 1987

investigations were on samples recovered from borehole NF4A at shallow depths of

Queenston Shale. The five long-term free swell tests were also for samples from the same borehole and within the same depths. Therefore, the deformation parameters obtained from these five tests can be used with Eqs. 8.11, 8.12 and 8.14 to predict the time dependent deformation for different samples under different applied pressures.

(A) Vertical Direction

From results of semi-confined tests on samples under applied stresses in the vertical direction. the critical stress σ_c and the equivalent free swell stress σ_e are determined as 12.5 MPa and 0.0035 MPa, respectively (refer to Figure 7.15). The initial vertical stress σ_{vi} at the test locations is 2.6 MPa.

The values of the deformation moduli E_i of the three Kelvin units under different stresses are calculated using Eq. 8.13 and listed in Table 8.5.

Typical predicted curves of swelling strains versus time under different applied stresses are compared to the measured strains from semi-confined tests in Figure 8.21. It can be seen that there is good agreement between the predicted and measured strain values.

(B) Horizontal Direction

The average initial horizontal stress at the depth at which the samples of the semi-confined tests were recovered is found to be about 12.0 MPa from results of hydrofracturing tests (refer to Chapter 5). The critical and equivalent free swell stresses under applied pressures in the horizontal direction are calculated as 7.0 and 0.01 MPa,

respectively (refer to Figure 7.16).

Using Eq. 8.12, the values of the deformation moduli of the three Kelvin units under different applied stresses are calculated and listed in Table 8.6. The variation of the deformation moduli in the horizontal direction with the applied stress is plotted in Figure 8.22. It can be seen that as the applied stress increases, the values of the deformation moduli of the three Kelvin units increase. The apparent stiffening effect discussed in the previous section is obvious from the increasing trend of E_i values as σ_a increases.

Typical predicted curves of swelling strain vs. time under different applied stresses are compared to the measured values from semi-confined tests in Figure 8.23. It can be seen that the results of the semi-confined tests can be predicted reasonably well using a model of three Kelvin units with stress-dependent deformation moduli.

8.4.2 1989 Investigation

In 1989 investigation, samples for semi-confined tests were recovered from borehole SD3 at depths from 209 to 219 m, representing the deep section of Queenston Shale. No long-term free swell tests were performed on that depth. Therefore, as discussed previously in Sec. 8.3, in calculating the stress-dependent moduli of the three Kelvin units, it is necessary to choose a semi-confined test as a reference test. As discussed in the previous sections, the rate parameters λ_i calculated from the five long term free swell tests will be used as the governing rate parameters for Queenston Shale regardless the location and depth.

(A)   Vertical Direction

The initial vertical stress at the test location is 4.8 MPa. The critical and the equivalent free swell stresses are calculated as 3.2 and 0.014 MPa, respectively (refer to Figure 7.17). The applied pressures on the samples ranged between 0.02 MPa and 1.02 MPa.

The semi-confined test   SD3-V3 is chosen as a reference test for the determination of the stress dependent moduli. The values of the stress-dependent deformation moduli calculated are listed in Table 8.7.

A comparison between the predicted swelling strains under different applied stresses and the measured strains from semi-confined tests is shown in Figure 8.24. It can be seen that the calculated strains are generally consistent with the measured values.

(B)   Horizontal Direction

The average horizontal initial stress at the depth from which the samples were recovered is 23 MPa, from results of hydraulic fracturing tests (refer to Chapter 5). The critical and equivalent free swell stresses are determined to be 1.8 and 0.05 MPa, respectively (refer to Figure 7.18). The applied pressures on the samples ranged from 0.02 to 3.0 MPa.

Using test SD3-H11 as a reference test, the deformation moduli under different applied stresses are calculated and summarized in Table 8.8.

The swelling strains predicted using the proposed model are calculated for different applied stresses and compared to the measured strains in Figure 8.25. It can be seen that the predicted and measured strains are in good agreement.

8.4.3 1990 Investigation

In 1990 investigation, 6 semi-confined tests on samples recovered from borehole NF4A and 5 tests from borehole NF37 were carried out. The samples from borehole NF4A were from depths between 180.37 m and 181.18 m, therefore they represent the deep section of Queenston Shale where the twin tunnels will be constructed. The samples from borehole NF37 were from depths between 97.48 m and 98.10 m in the area of the proposed power house. The loading direction for all the 11 tests performed in this investigation was parallel to the bedding planes, i.e. the horizontal direction.

(A) Borehole NF4A

The applied stresses, in the horizontal direction, on samples from borehole NF4A ranged from 0.02 MPa to 3.0 MPa. The average horizontal initial stress at the test depths is 19.5 MPa as determined from hydraulic fracturing measurements (Chapter 5). The critical stress and the equivalent free swell stress are determined as 6.0 MPa and 0.005 MPa, respectively, refer to Figure 7.19.

According to the method described in Sec. 8.3.2, test NF4A-11 is chosen as a reference test. From regression analysis and using the rate parameters determined previously from the long term free swell tests discussed in section 8.2, the deformation parameters for the three Kelvin units for this test are determined. Using Eq. 8.12, the deformation parameters under different applied stresses are calculated and they are listed in Table 8.9.

Using the deformation parameters listed in Table 8.9, the swelling strains under different applied stresses are calculated and compared to the measured strains in Figure

8.26. It can be seen that there is a good agreement between the predicted and the measured values.

(B)   Borehole NF37

The semi-confined test samples from borehole NF37 were loaded in the horizontal direction. The applied stresses on the samples ranged from 0.03 MPa to 1.0 MPa. The average initial horizontal stress at the test depths is 6.5 MPa as determined from hydraulic fracturing measurements (Chapter 5). The critical stress and the equivalent free swell stress are determined as 31 MPa and 0.007 MPa, respectively, refer to Figure 7.20.

To calculate the deformation parameters, test NF37-4 is chosen as a reference test. From regression analysis and using the rate parameters determined previously from the long term free swell tests discussed in section 8.2, the deformation parameters for the three Kelvin units for this test are determined. Using Eq. 8.12, the deformation parameters under different applied stresses are calculated and they are listed in Table 8.10.

Using the deformation parameters listed in Table 8.10, the swelling strains under different applied stresses are calculated and compared to the measured strains in Figure 8.27. It can be seen that there is good agreement between the predicted and the measured values.

8.4.4   1992 Investigation

In 1992 investigation, two semi-confined tests were performed on samples

recovered from borehole NF43. The applied stresses were in the vertical direction: 1.0 MPa on one sample and 3.0 MPa on the other. The initial vertical stress at samples location is 4.2 MPa. The critical stress determined from these two samples is 13.0 MPa, and the equivalent free swell test is 0.00012 MPa.

The stress dependent deformation moduli for the samples are determined twice: once by using sample NF43-V1 as the reference test and another by using test NF43-V2 as the reference test. The average of the two set of values for each test is considered as the representative set of deformation moduli for this test. A summary of the values of the deformation moduli obtained is shown in Table 8.11.

Figure 8.28 shows a comparison between the measured and the predicted swelling strains. It can be seen that the calculated swelling strains represent the measured strains reasonably well.

8.5   SUMMARY AND CONCLUSIONS

Results of five free swell tests started in 1986 and still in progress till present (early 1994) are presented in this chapter. These tests are devoted to examine the long-term time-dependent deformation of Queenston Shale. A rheological model consisting of three Kelvin units connected in series is adopted to describe the nonlinear long-term swelling behaviour of Queenston Shale. The same model is also used to predict the stress-dependent swelling strain for Queenston Shale. Equations relating the deformation moduli of the three Kelvin units under free swell to those under any applied stress are derived. The predicted swelling strains using this model are compared to the measured values. From this study, the following observations and conclusions are drawn:

a- The swelling deformations of Queenston Shale last for long time and the long-term swelling deformation is highly nonlinear with time: up to the present (more than 2700 days, - 8 years), time-dependent swell deformation is still developing although the swelling rate decreases gradually with time.

b- The rheological model consisting of three Kelvin units connected in series well represents the long-term swelling behaviour of Queenston Shale.

c- The predicted curves of swelling strain versus elapsed time, whose parameters were obtained on the basis of the test results during the first 1260 days, can represent the results of the free swell test up to the present (more than 2700 days) reasonably well. Therefore, the model not only represents the swelling strain within the period of time the parameters are calculated but also predicts adequately the strain for even much higher values of time.

d- One set of rate parameters, λ_i, calculated from long-term swell tests can be used to represent adequately the swelling behaviour of Queenston Shale at this site regardless the depth or location. The representative values of rate parameters, λ_i, are

$$\lambda_1 = 0.11, \qquad \lambda_2 = 0.028, \text{ and} \qquad \lambda_3 = 0.0018$$

The variation of swelling strain from a free swell test to another are dependent only on the values of deformation moduli of the three Kelvin units, keeping the rate parameters λ_i constant.

e- The suppression of the swelling strain under applied stress can be regarded as the combination of the effects of two factors:

1- Suppression due to reduction of stress relief: under applied stress σ_a, the stress

relief σ_r is less than the initial stress value σ_o considered with the free swell strain ($\sigma_r = \sigma_o - \sigma_e$), leading to lower strain values.

2-   Suppression due to a~~ ~~nt stiffening effect: as the applied load on the sample increases, the sample apparently becomes more stiffer towards the time-dependent deformation and the values of deformation moduli increase, leading to a lower strain value than that would be obtained if only factor (1) above is considered.

The effects of both factors can be considered in the generalized Kelvin model expressed by Eq. 8.8 by letting $\sigma = \sigma_o - \sigma_e$ (factor 1) and by constructing a nonlinear relationship between the deformation moduli E_i and the applied stress (factor 2). Accordingly, the rate parameters λ_i are considered stress independent and only the deformation parameters E_i are stress dependent.

f- The predicted stress-time-dependent strains, using the method developed, agree well with the measured values from different series of semi-confined swell tests in 1985 to 1992 investigations.

TABLE 8.1   Summary of swelling potentials in the vertical and horizontal directions
for the five long-term free swell tests on Queenston Shale

Sample No.	Depth (m)	Swelling Potential (% per log cycle of time)			
		Vertical Direction		Horizontal Direction	
		α_{10-100}	$\alpha_{100-1000}$	α_{10-100}	$\alpha_{100-1000}$
FSQ/NF4A-L1	103.28	0.43	0.45	0.27	0.27
FSQ/NF4A-L2	103.37	0.44	0.45	0.25	0.29
FSQ/NF4A-L3	103.69	0.41	0.42	0.19	0.28
FSQ/NF4A-L4	103.02	0.27	0.43	0.14	0.29
FSQ/NF4A-L5	103.10	0.28	0.46	0.15	0.27

TABLE 8.2 Parameters of Kelvin units that best fit the results of the five long-term free swell tests. (Vertical direction)

Sample No.	FSQ/NF4A-L1	FSQ/NF4A-L2	FSQ/NF4A-L3	FSQ/NF4A-L4	FSQ/NF4A-L5	Average Value of λ_i
λ_i	0.10	0.12	0.11	0.11	0.12	0.11
λ_2 (1/day)	0.039	0.030	0.020	0.020	0.020	0.026
λ_3	0.0030	0.0020	0.0016	0.0018	0.0014	0.002
E_1	6420	2870	1660	1590	2080	-
E_2 (MPa)	710	590	600	2110	1250	-
E_3	370	440	540	400	360	-

Note: initial vertical stress = 2.6 MPa

TABLE 8.3   Parameters of Kelvin units that best fit the results of the five long-term free swell tests. (Horizontal direction)

Sample No.	FSQ/NF4A-L1	FSQ/NF4A-L2	FSQ/NF4A-L3	FSQ/NF4A-L4	FSQ/NF4A-L5	Average Value of λ_i
λ_1	0.12	0.08	0.12	0.12	0.12	0.11
λ_2 (1/day)	0.030	0.044	0.035	0.020	0.024	0.031
λ_3	0.0020	0.0030	0.0010	0.0012	0.0010	0.0016
E_1	53180	17260	118630	39770	22530	-
E_2 (MPa)	4930	9930	6890	11430	9950	-
E_3	3770	3050	2640	2910	2840	-

Note: initial horizontal stress = 13.0 MPa

TABLE 8.4 Values of deformation moduli E_i for Kelvin units for the five long-term free swell tests.
(using λ_i = 0.11, 0.028, 0.0018)

Direction	Sample No.	FSQ/NF4A-L1	FSQ/NF4A-L2	FSQ/NF4A-L3	FSQ/NF4A-L4	FSQ/NF4A-L5	Representative E_i Value for Average Strain
Vertical	E_1	46480	2660	4540	2010	1970	3080
	E_2 (MPa)	490	580	520	1700	1730	730
	E_3	390	440	520	400	360	420
Horizontal	E_1	47630	49740	11380	23280	12000	19610
	E_2 (MPa)	4770	5060	30890	26290	39650	9950
	E_3	3770	3230	3030	3070	3210	3240

Notes: initial horizontal stress = 13.0 MPa
initial vertical stress = 2.6 MPa

TABLE 8.5   Values of deformation moduli E_i under applied stress σ_a in the vertical direction for "shallow section" of Queenston Shale at Borehole NF4A

σ_a (MPa)	Free Swell	0.027	0.131	0.25	0.691	2.38
E_1 (MPa)	3080	4063	5249	5822	5390	1285
E_2 (MPa)	730	963	1244	1380	1514	305
E_3 (MPa)	420	554	716	794	871	175

Notes: $\lambda_1 = 0.11$, $\lambda_2 = 0.028$, and $\lambda_3 = 0.0018$ 1/day

$\sigma_o = 2.6$ MPa

$\sigma_e = 0.0035$ MPa

$\sigma_c = 12.5$ MPa

TABLE 8.6   Values of deformation moduli E_i under applied stress σ_a in the horizontal direction for "shallow section" of Queenston Shale at Borehole NF4A

σ_a (MPa)	Free Swell	0.036	0.342	1.86	2.42
E_i (MPa)	19610	24309	41435	83063	98435
E_2 (MPa)	9950	12334	21024	42146	49945
E_3 (MPa)	3240	4016	6846	13723	16264

Notes: $\lambda_1 = 0.11$, $\lambda_2 = 0.028$, and $\lambda_3 = 0.0018$ 1/day

$\sigma_o = 13.0$ MPa

$\sigma_a = 0.01$ MPa

$\sigma_c = 7.0$ MPa

TABLE 8.7   Values of deformation moduli E_i under applied stress σ_a in the vertical direction for "deep section" of Queenston Shale at Borehole SD3

σ_a (MPa)	Free Swell	0.02	0.10	0.26	1.00
E_1 (MPa)	1710	1823	2624	3500	6322
E_2 (MPa)	12250	13056	18800	25072	45289
E_3 (MPa)	570	608	875	1167	2107

Notes: $\lambda_1 = 0.11$, $\lambda_2 = 0.028$, and $\lambda_3 = 0.0018$ 1/day

$\sigma_o = 4.8$ MPa

$\sigma_e = 0.014$ MPa

$\sigma_c = 3.2$ MPa

TABLE 8.8   Values of deformation moduli E_i under applied stress σ_a in the horizontal direction for "deep section" of Queenston Shale at Borehole SD3

σ_a (MPa)	Free Swell	0.05	0.10	0.50	1.00
E_i (MPa)	101	101	125	276	589
E_2 (MPa)	1345	1345	1664	3689	7861
E_3 (MPa)	37	37	46	101	216

Notes: $\lambda_1 = 0.11$, $\lambda_2 = 0.028$, and $\lambda_3 = 0.0018$ 1/day

$\sigma_o = 23$ MPa

$\sigma_e = 0.05$ MPa

$\sigma_c = 1.8$ MPa

TABLE 8.9 Values of deformation moduli E_i under applied stress σ_a in the horizontal Direction for "deep section" of Queenston Shale at location of Borehole NF4A (SABNGS No. 3 project, 1990 investigation)

σ_a (MPa)	Free Swell	0.01	0.02	0.1	0.3	1.0	3.0
E_1 (MPa)	9940	121200	12350	17130	23170	37330	86050
E_2 (MPa)	8080	9850	10040	13930	18840	30340	69960
E_3 (MPa)	4940	6030	6140	8520	11520	18560	42800

Notes: λ_i = 0.11, 0.028, and 0.0018

σ_o = 19.5 MPa

σ_e = 0.005 MPa

σ_c = 6.0 MPa

TABLE 8.10   Values of deformation moduli E_i under applied stress σ_a in the horizontal direction for Queenston Shale at location of Borehole NF37 (SABNGS No. 3 project, 1990 investigation)

σ_a (MPa)	Free Swell	0.03	0.10	0.30	1.00
E_1 (MPa)	20000	24080	28820	34530	41370
E_2 (MPa)	2640	3180	3800	4560	5460
E_3 (MPa)	1570	1890	2265	2710	3250

Notes: $\lambda_1 = 0.11$, $\lambda_2 = 0.028$, and $\lambda_3 = 0.0018$ 1/day

$\sigma_o = 6.5$ MPa

$\sigma_a = 0.007$ MPa

$\sigma_c = 31.0$ MPa

TABLE 8.11   Values of deformation moduli E_i under applied stress σ_a in the vertical direction for Queenston Shale at location of Borehole NF43 (SABNGS No. 3 project, 1992 investigation)

σ_a (MPa)	Free Swell	1.0	3.0
E_1 (MPa)	20000	24080	28820
E_2 (MPa)	2640	3180	3800
E_3 (MPa)	1570	1890	2265

Notes: $\lambda_1 = 0.11$, $\lambda_2 = 0.028$, and $\lambda_3 = 0.0018$ 1/day

$\sigma_o = 4.2$ MPa

$\sigma_a = 0.00012$ MPa

$\sigma_c = 13.0$ MPa
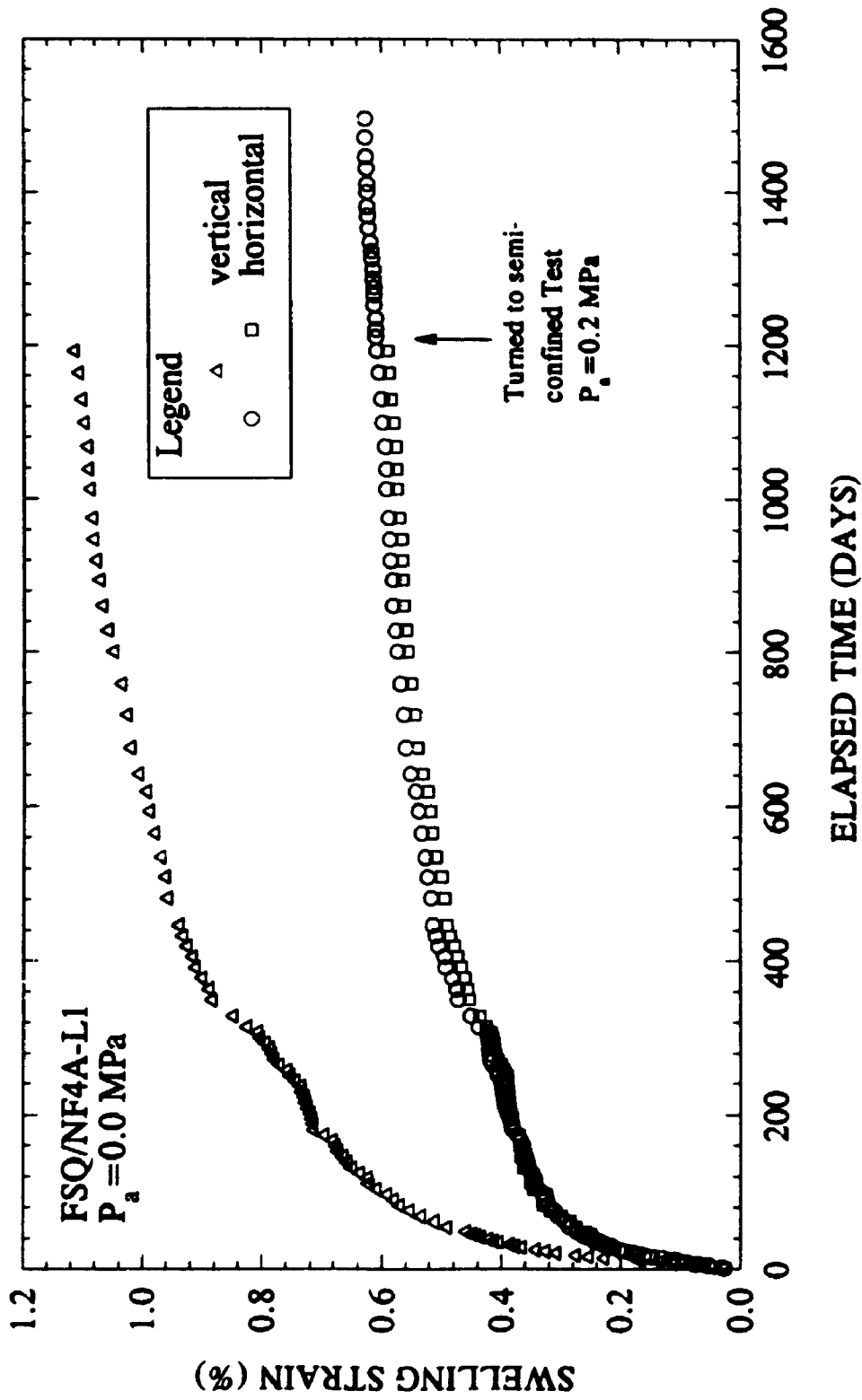
Figure 8.1 Measured swelling strain vs. elapsed time for a long-term free swell test on Queenston Shale (FSQ/NF4A-L1)
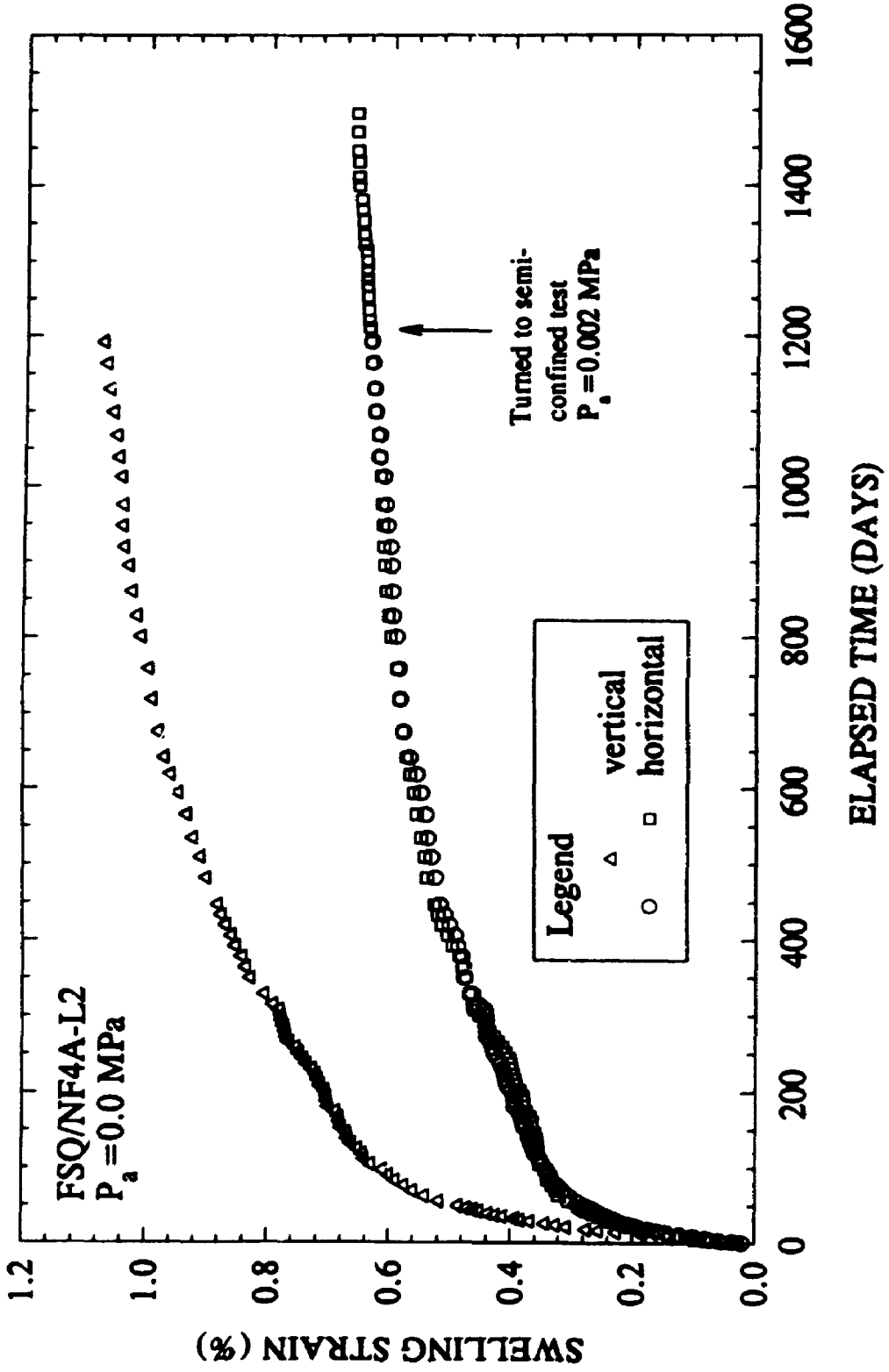
Figure 8.2 Measured swelling strain vs. elapsed time for a long-term free swell test on Queenston Shale (FSQ/NF4A-L2)
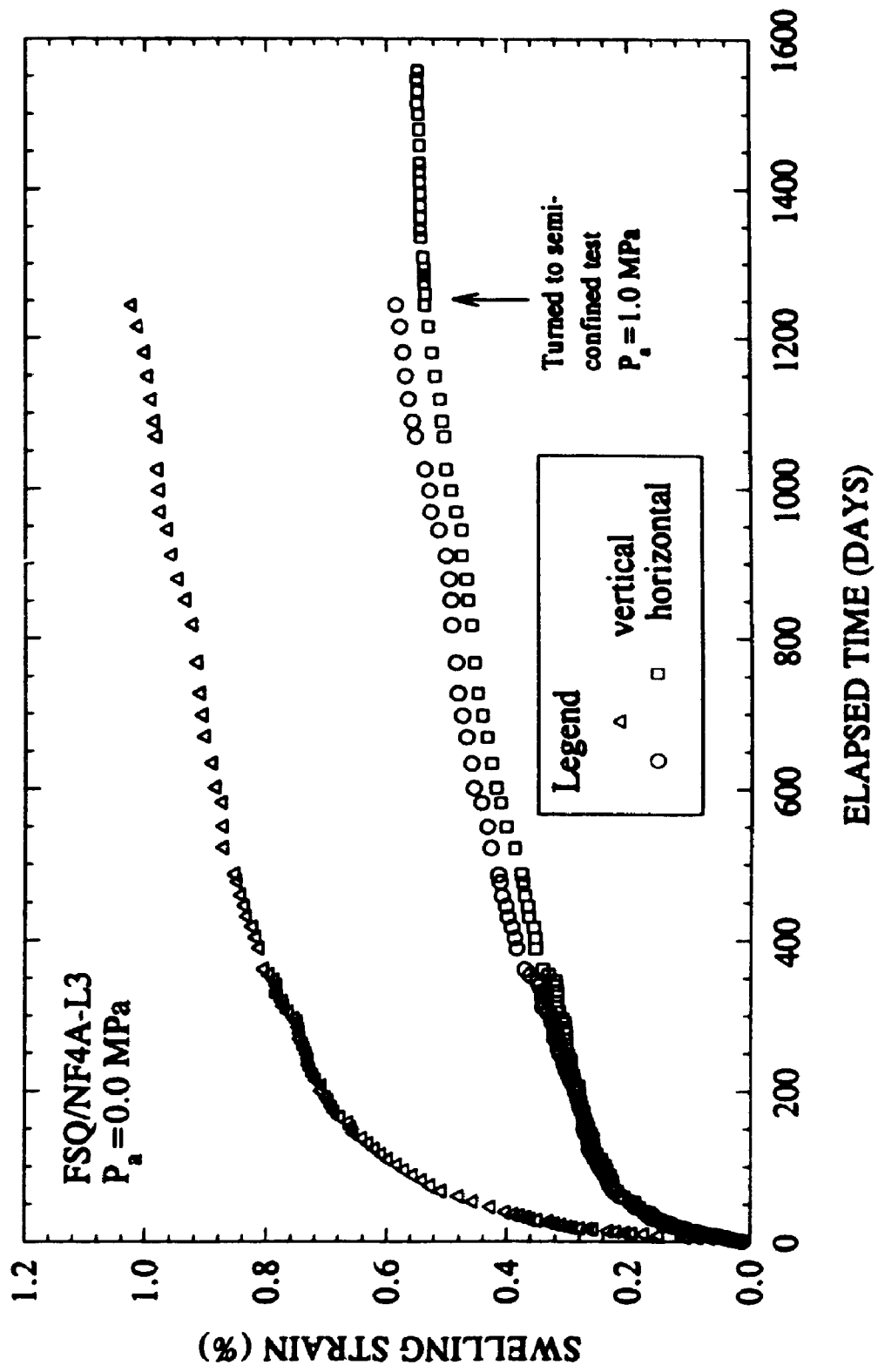
Figure 8.3 Measured swelling strain vs. elapsed time for a long-term free swell test on Queenston Shale (FSQ/NF4A-L3)
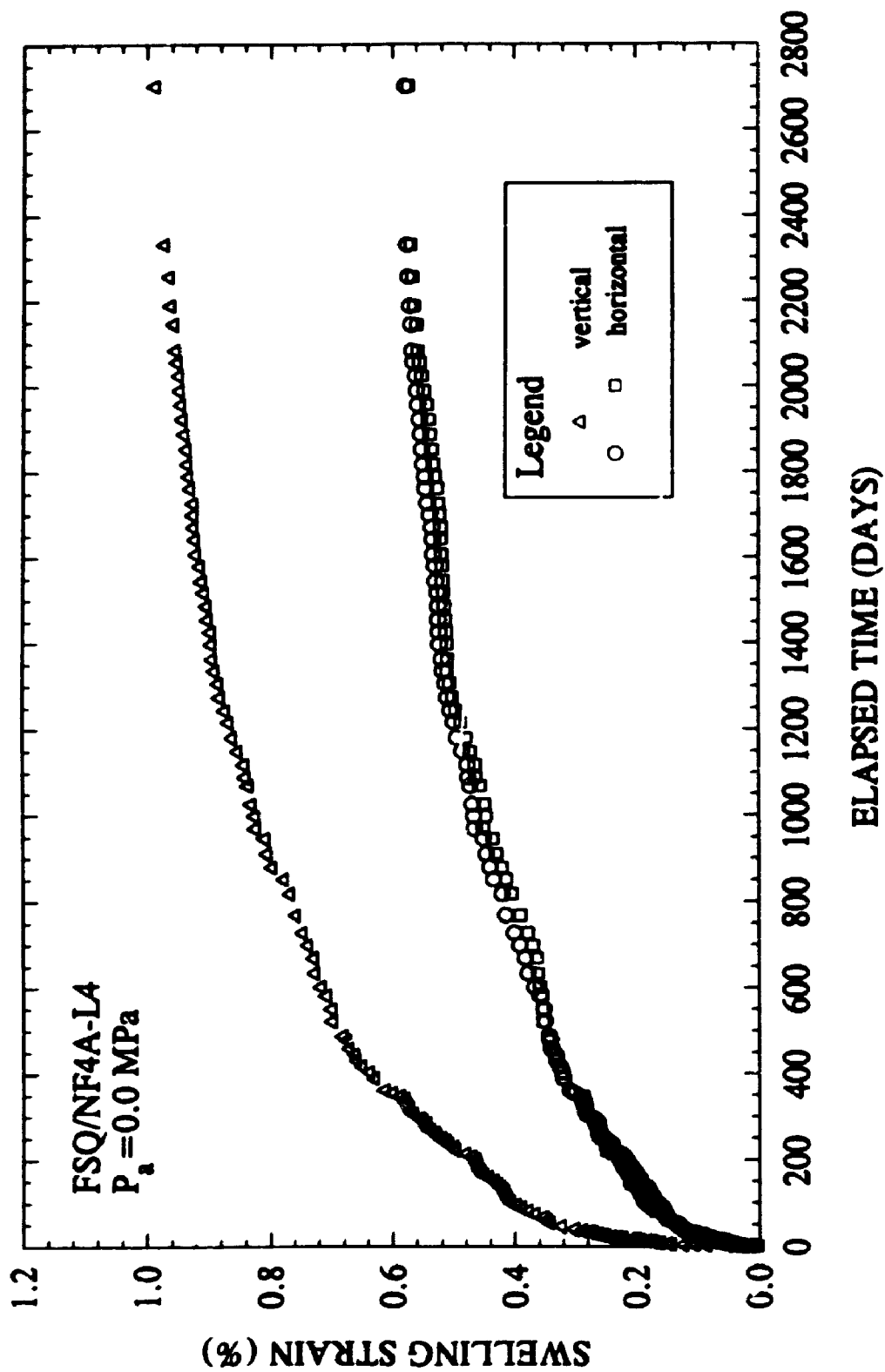
Figure 8.4 Measured swelling strain vs. elapsed time for a long-term free swell test on Queenston Shale (FSQ/NF4A-L4)
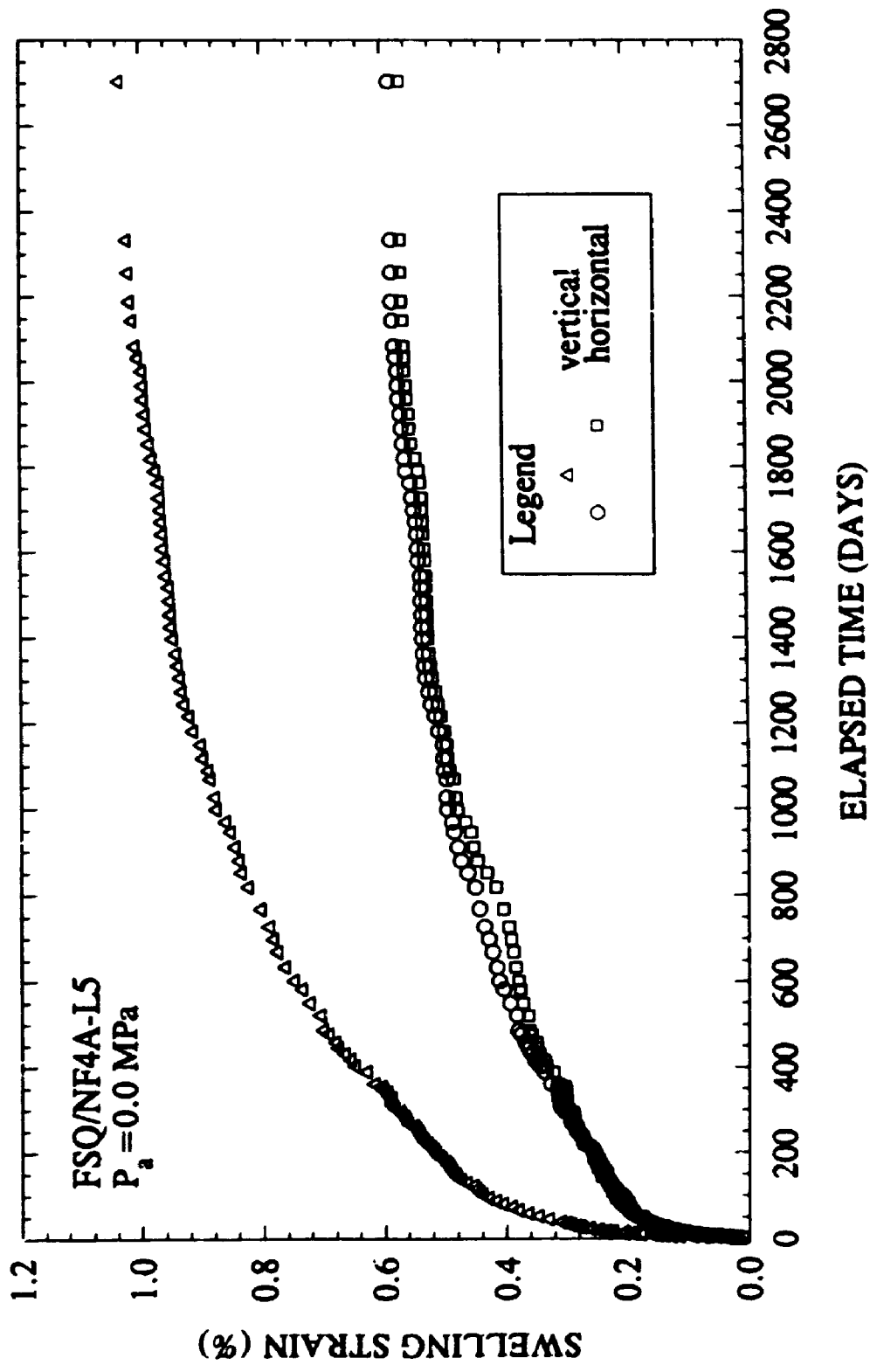
Figure 8.5 Measured swelling strain vs. elapsed time for a long-term free swell test on Queenston Shale (FSQ/NF4A-L5)
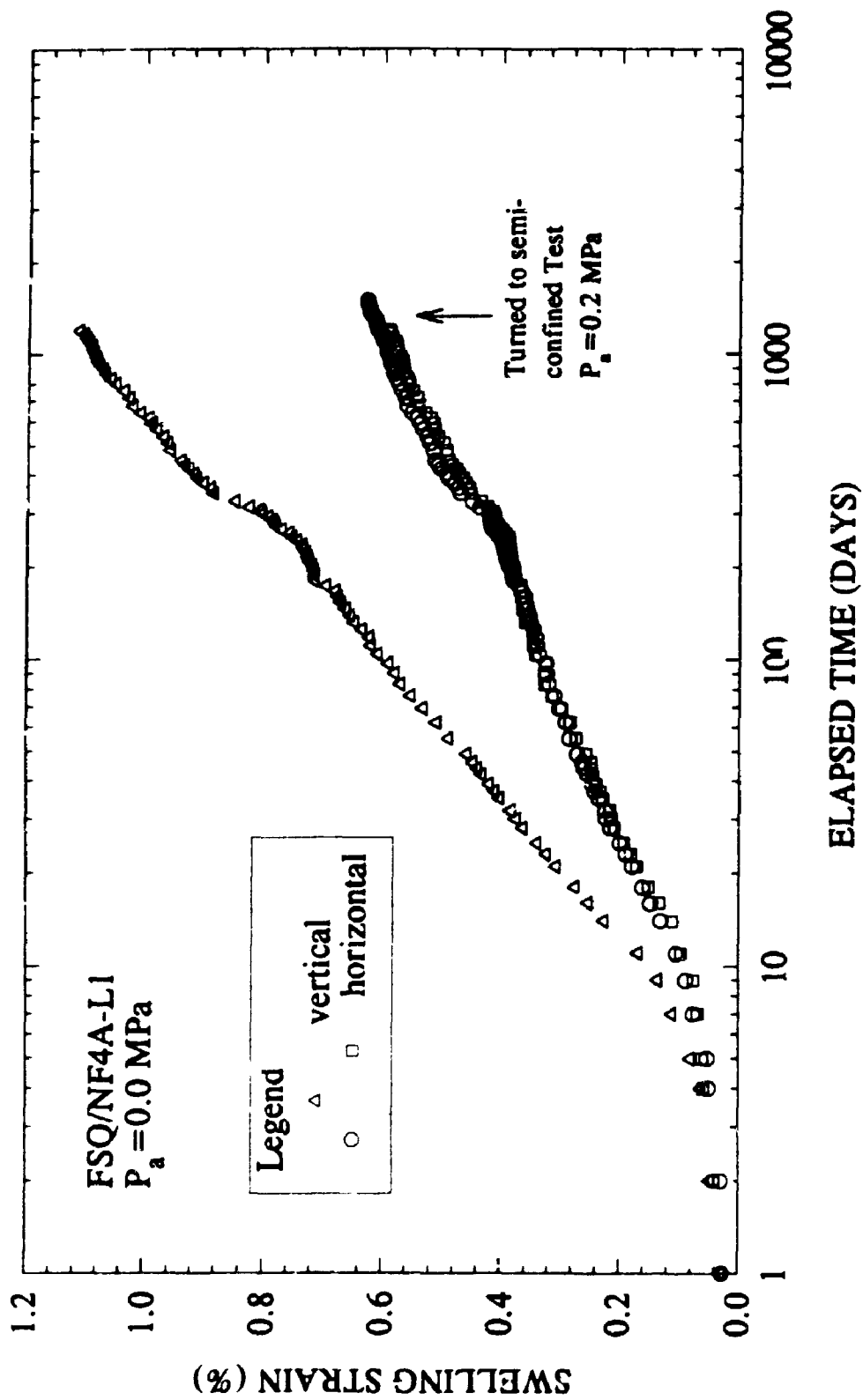
Figure 8.6 Measured swelling strain vs. elapsed time for a long-term free swell test on Queenston Shale (FSQ/NF4A-L1)
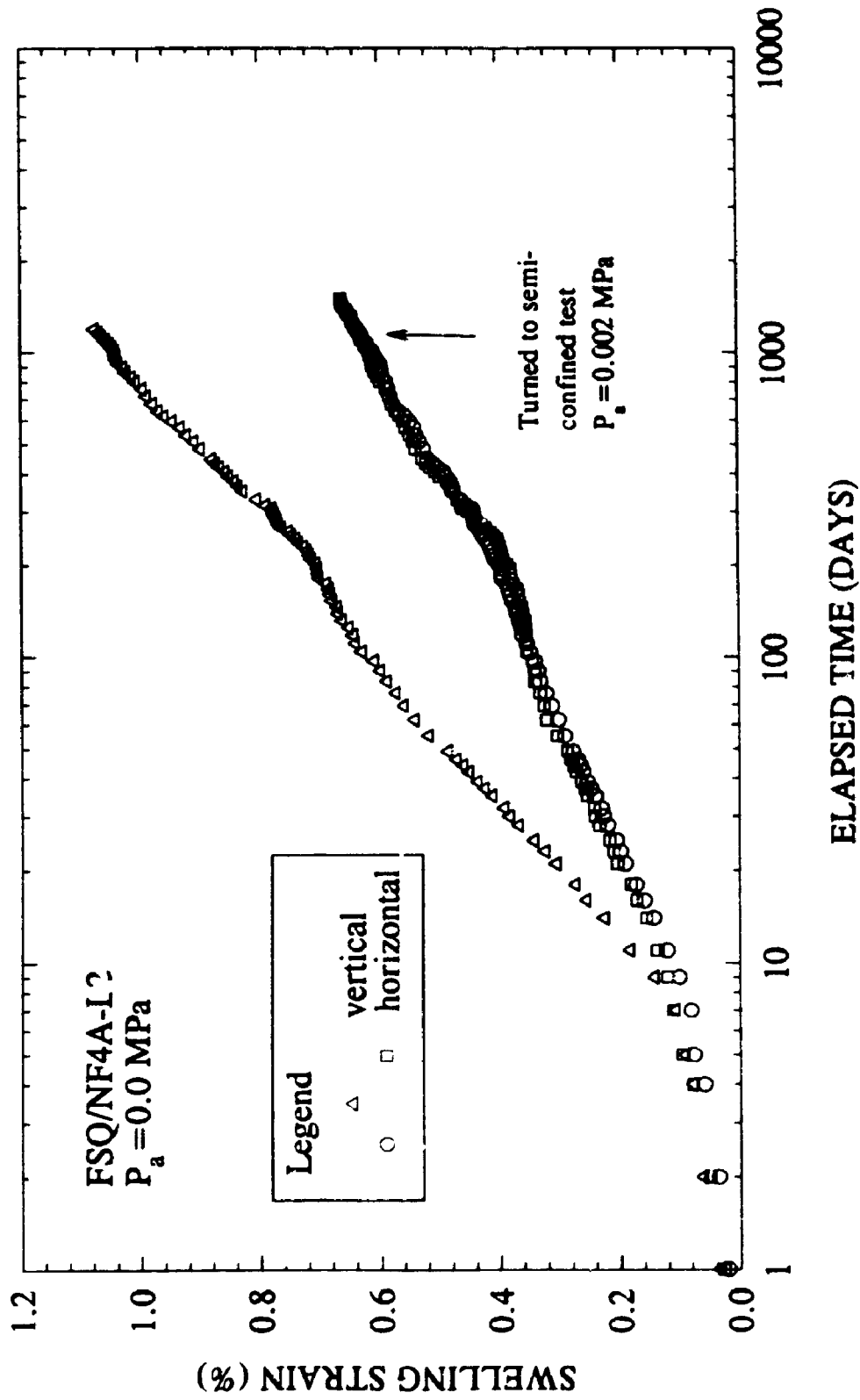
Figure 8.7 Measured swelling strain vs. elapsed time for a long-term free swell test on Queenston Shale (FSQ/NF4A-L2)
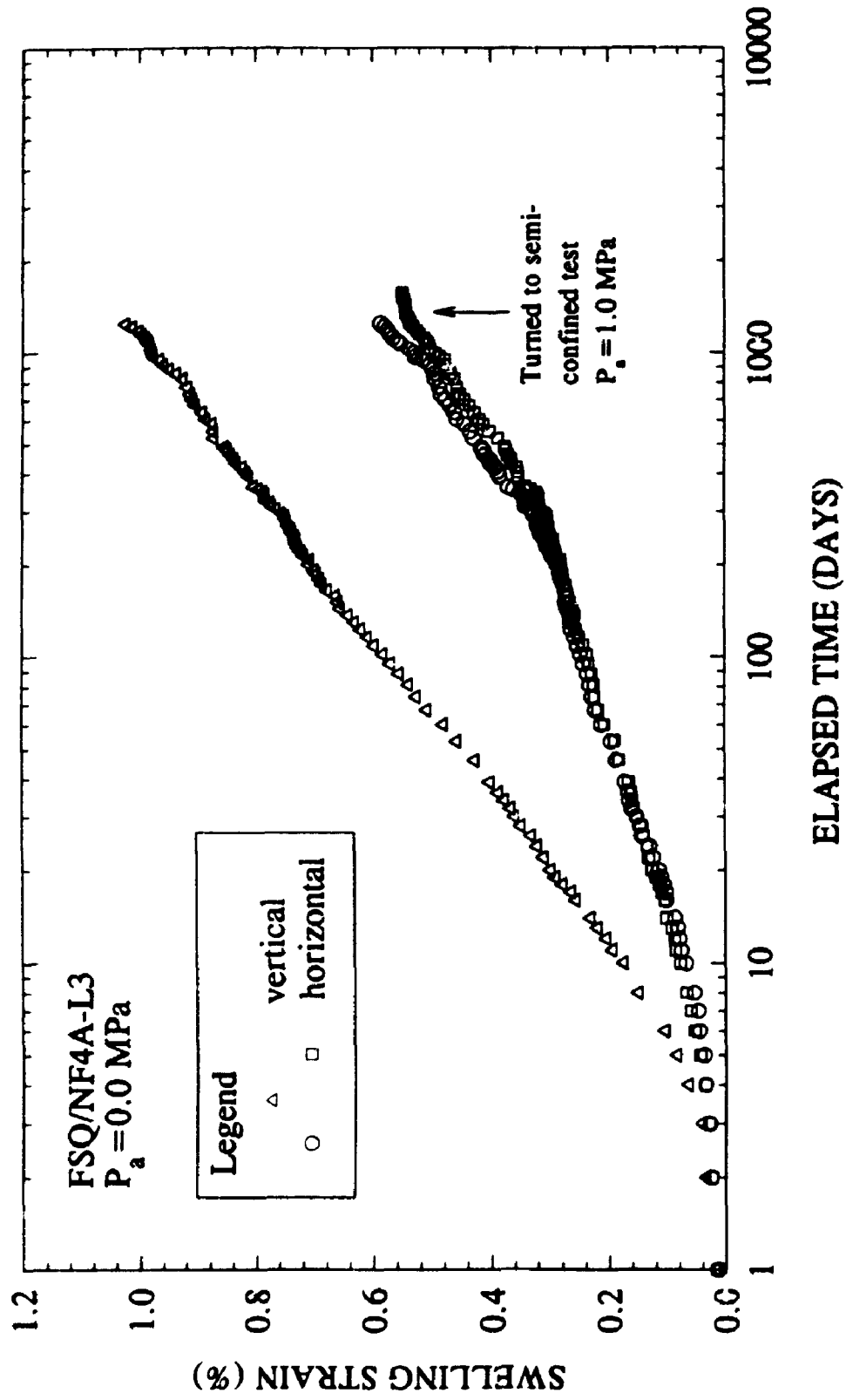
Figure 8.8 Measured swelling strain vs. elapsed time for a long-term free swell test on Queenston Shale (FSQ/NF4A-L3)
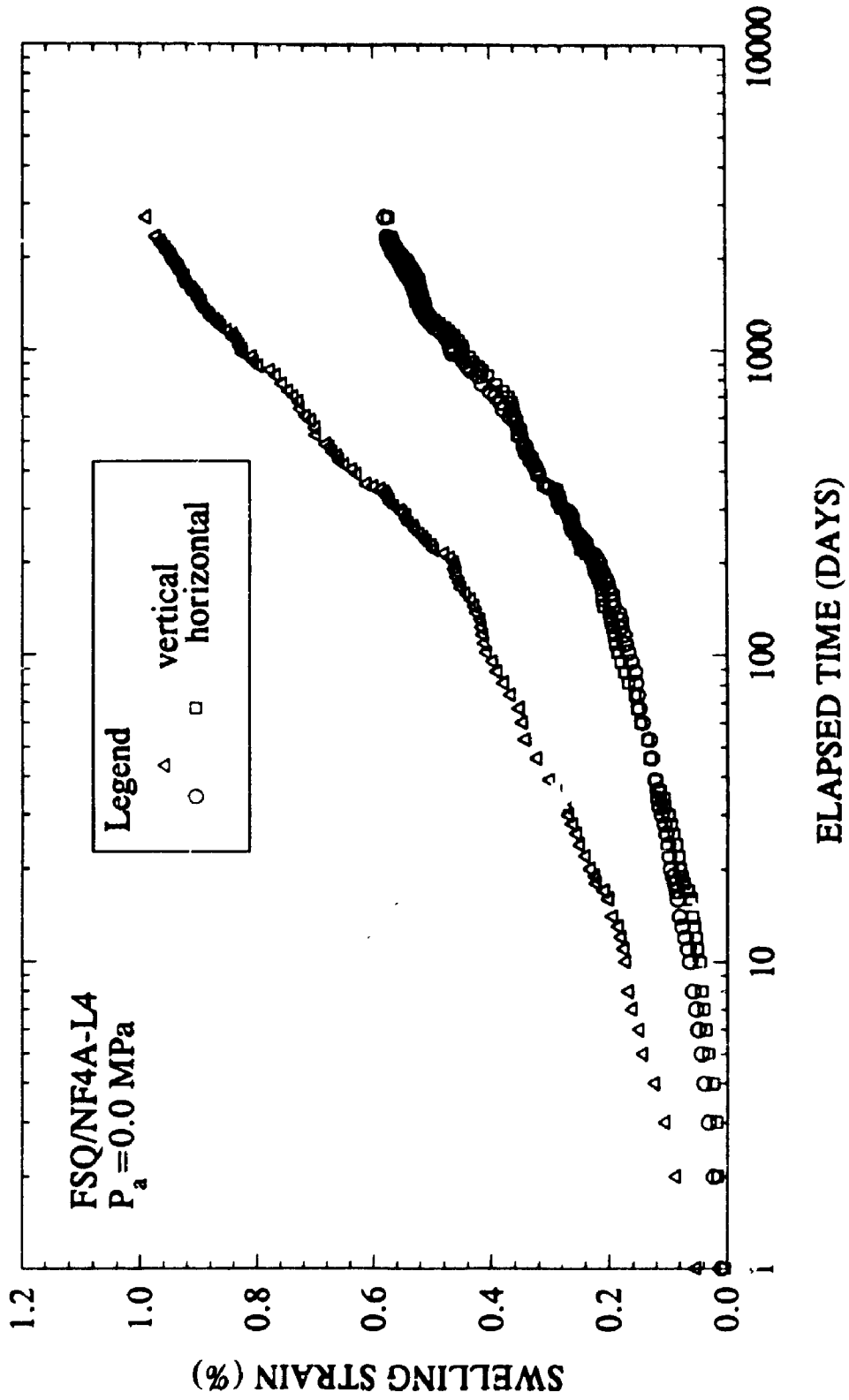
Figure 8.9 Measured swelling strain vs. elapsed time for a long-term free swell test on Queenston Shale (FSQ/NF4A-L4)
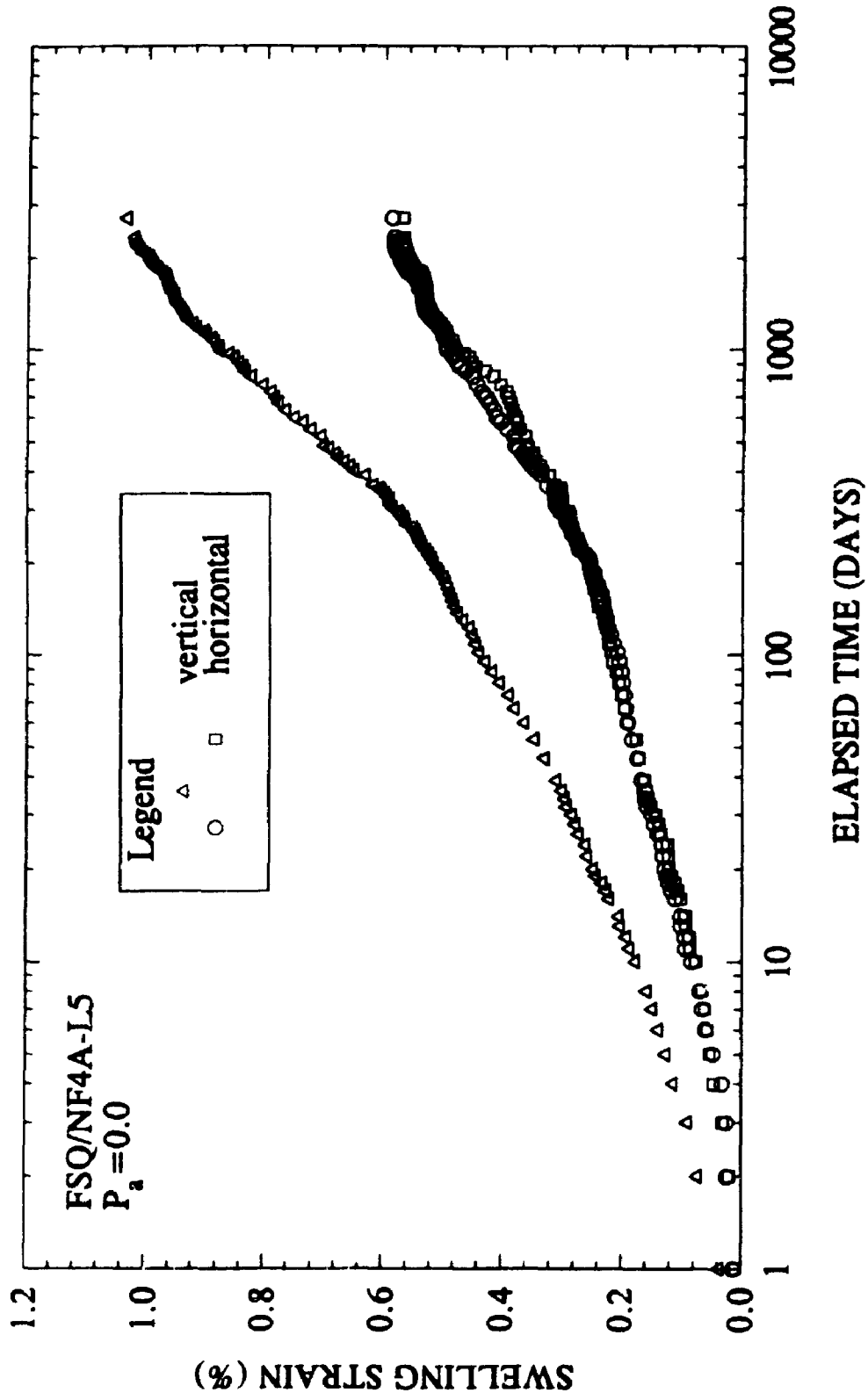
Figure 8.10 Measured swelling strain vs. elapsed time for a long-term free swell test on Queenston Shale (FSQ/NF4A)
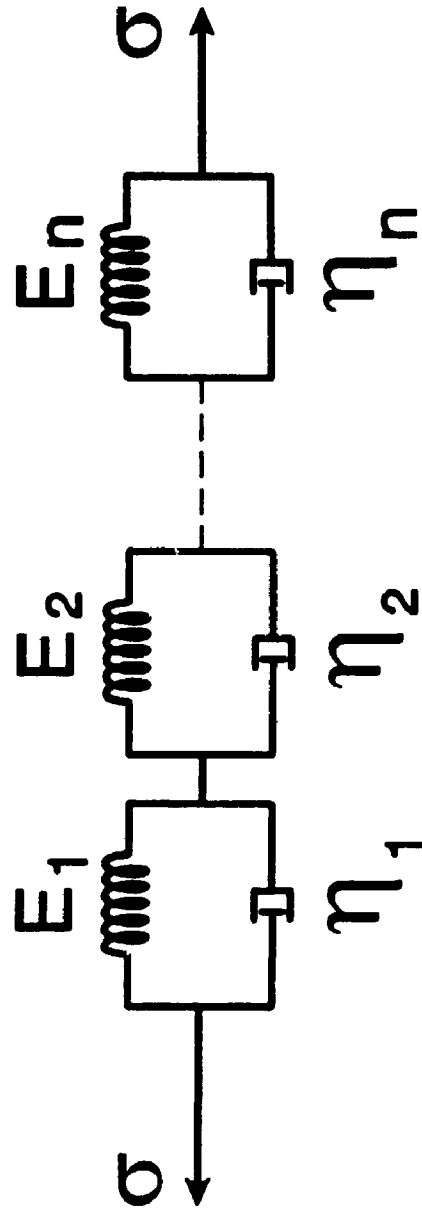
Figure 8.11 Generalized Kelvin model (representation of the long-term time-dependent deformation deformation of Queenston Shale)
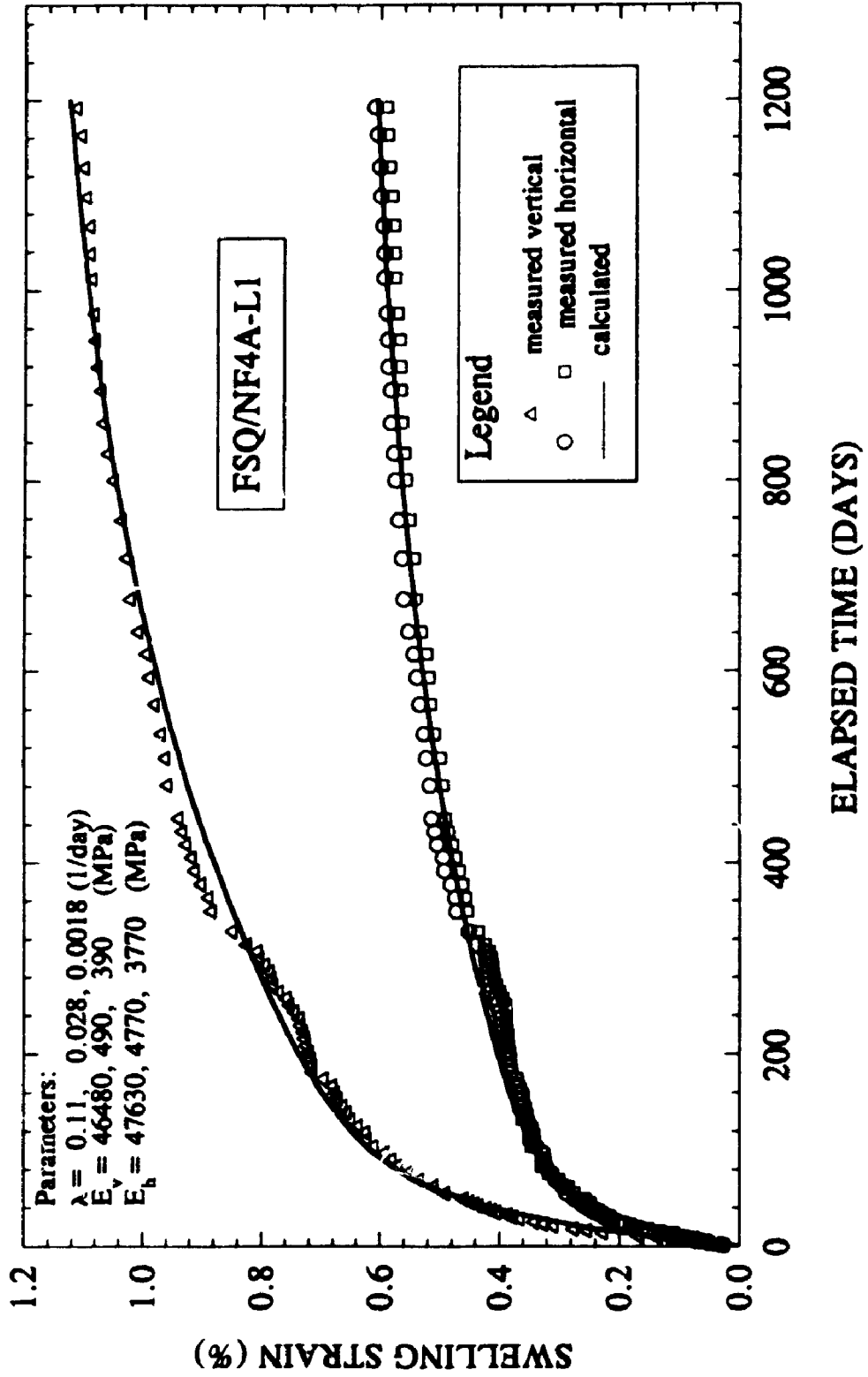
Figure 8.12 Measured and calculated swelling strain vs. elapsed time for a long-term free swell test on Queenston Shale (FSQ/NF4A-L1)
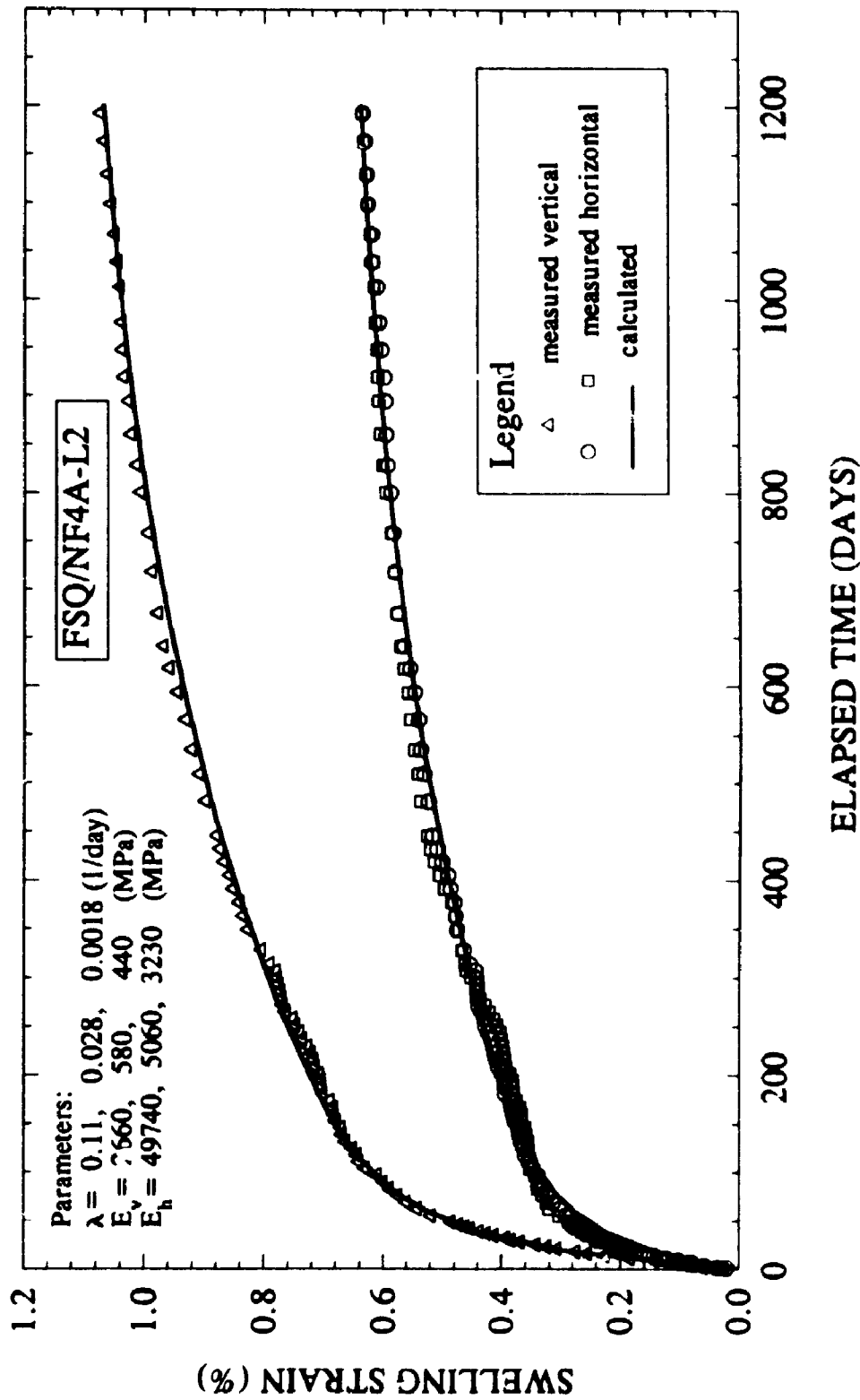
Figure 8.13 Measured and calculated swelling strain vs. elapsed time for a long-term free swell test on Queenston Shale (FSQ/NF4A-L2)
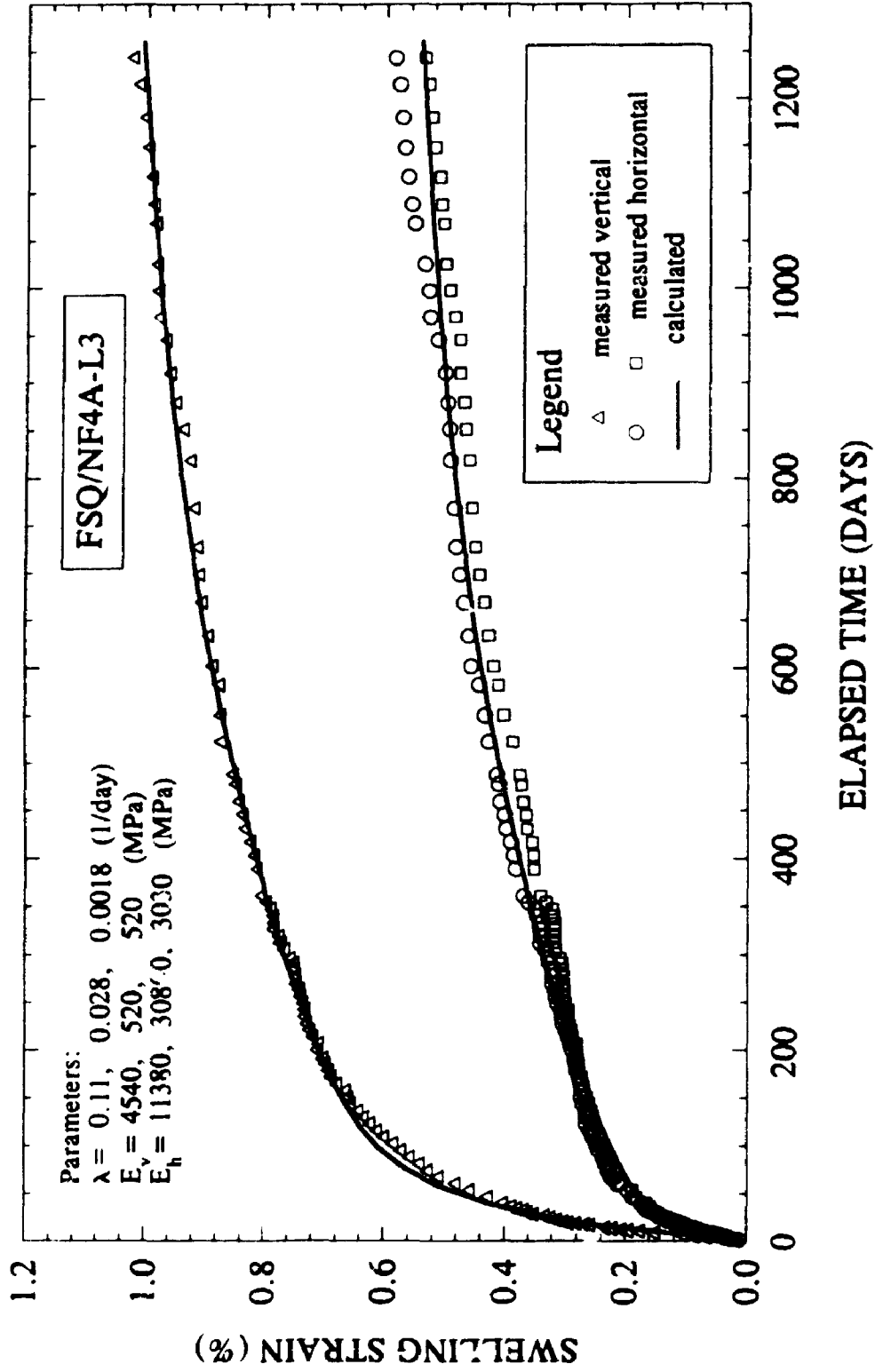
Figure 8.14 Measured and calculated swelling strain vs. elapsed time for a long-term free swell test on Queenston Shale (FSQ/NF4A-L3)
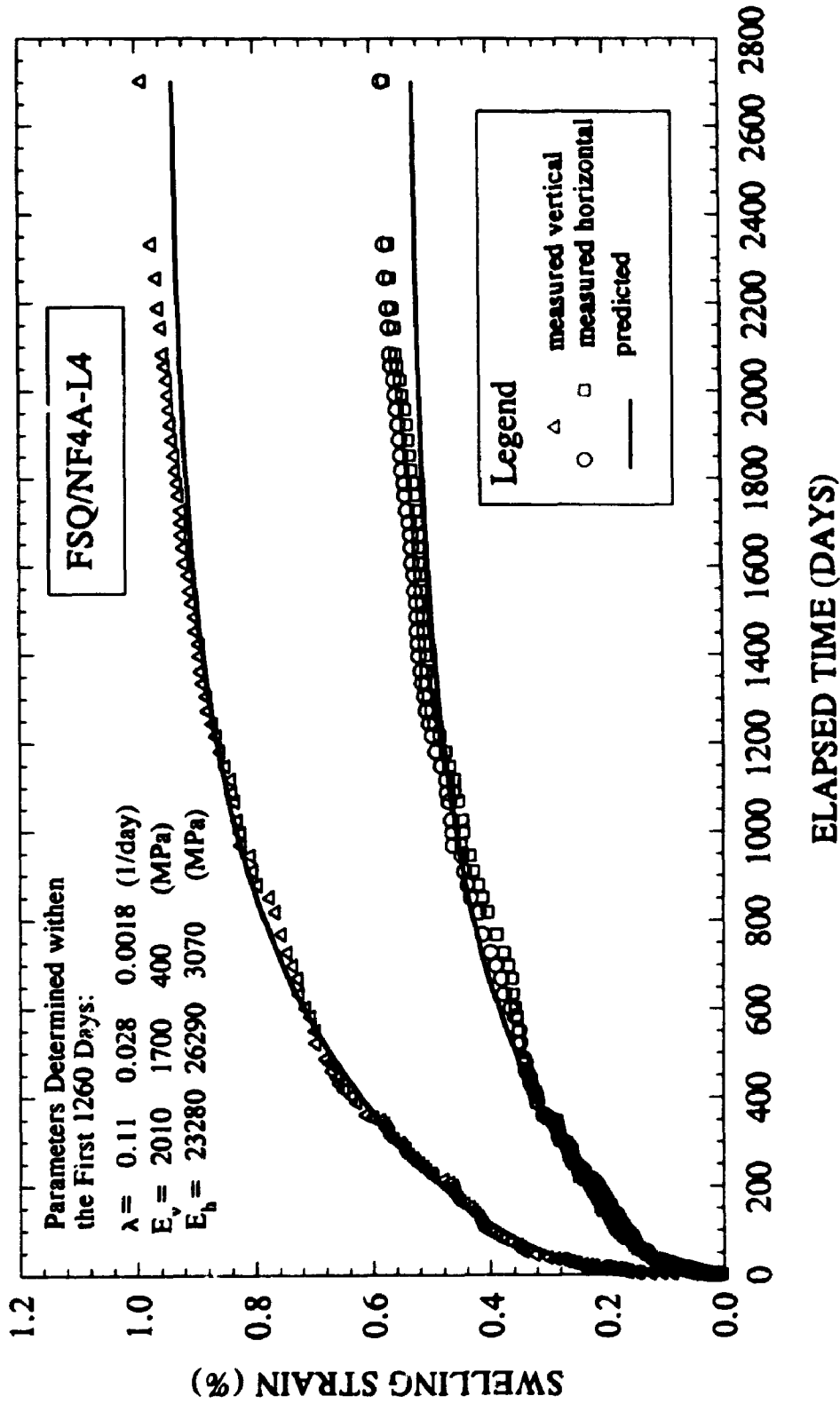
Figure 8.15 Measured and calculated swelling strain vs. elapsed time for a long-term free swell test on Queerston Shale (FSQ/NF4A-L4)
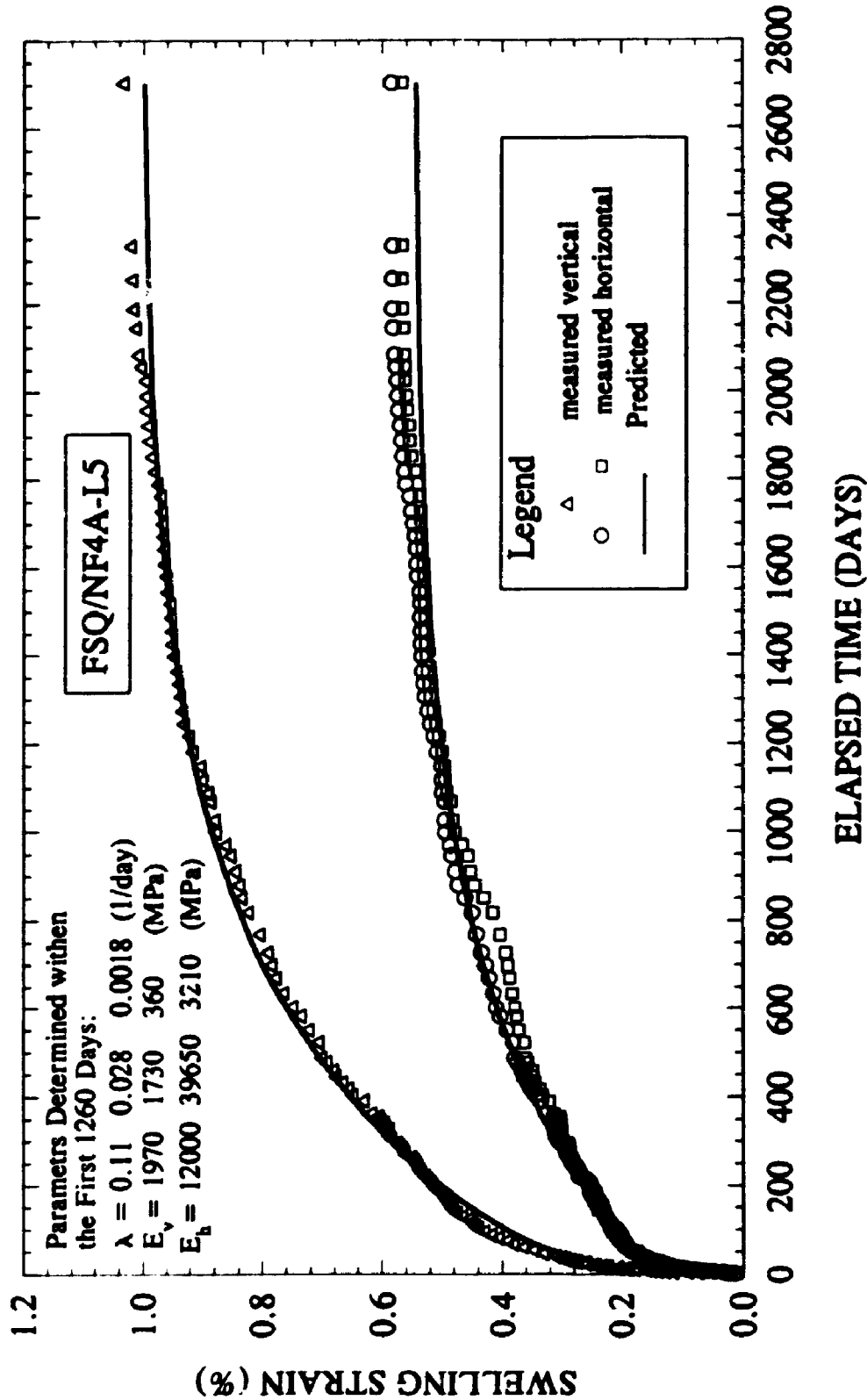
Figure 8.16 Measured and calculated swelling strain vs. elapsed time for a long-term free swell test on Queenston Shale (FSQ/NF4A-L5)
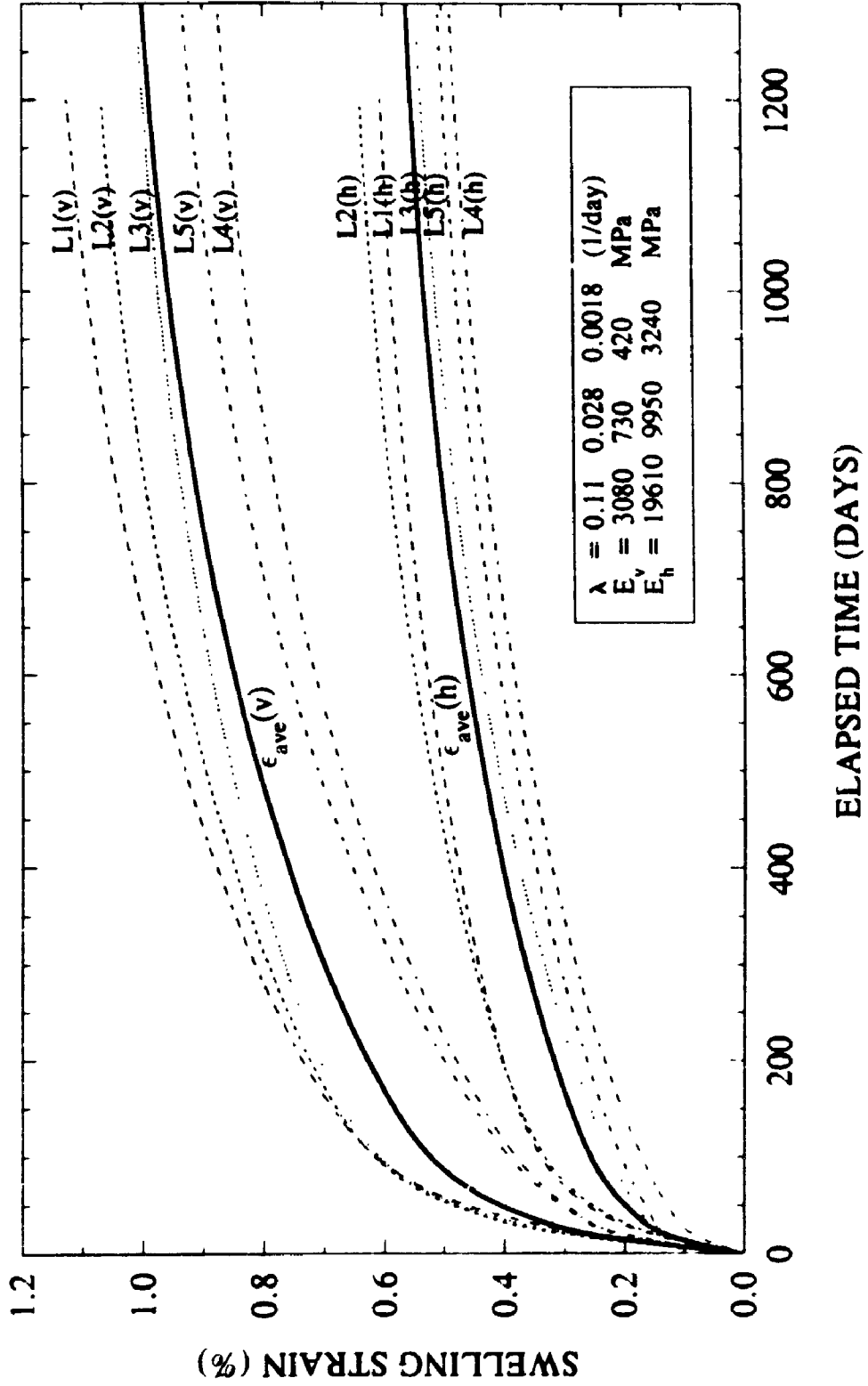
Figure 8.17 Comparison between the average swelling strain and swelling strains calculated for individual tests (L1 to L5)
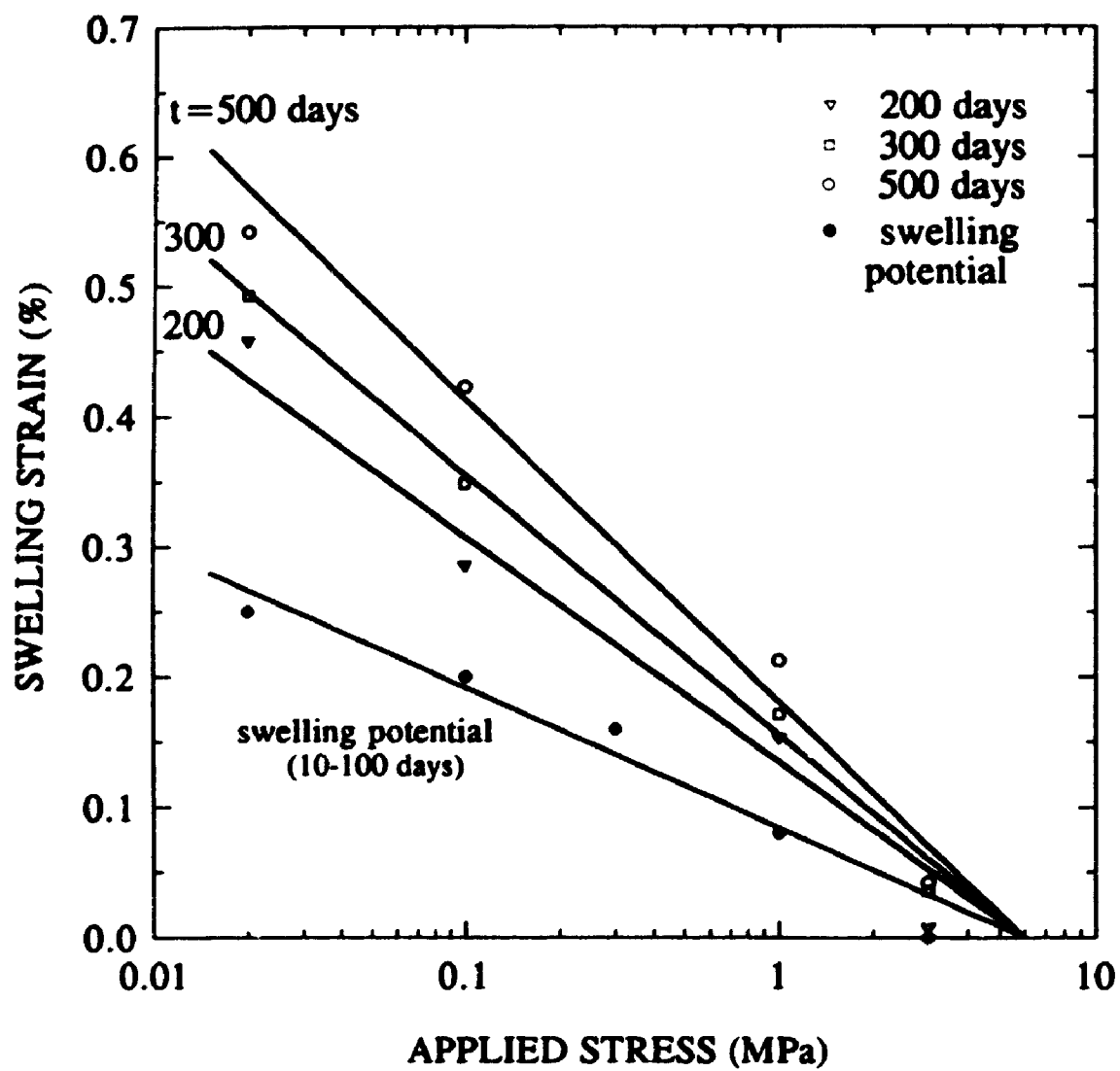
Figure 8.18 Typical isochronous swelling strain versus logarithm of applied stress, Queenston Shale
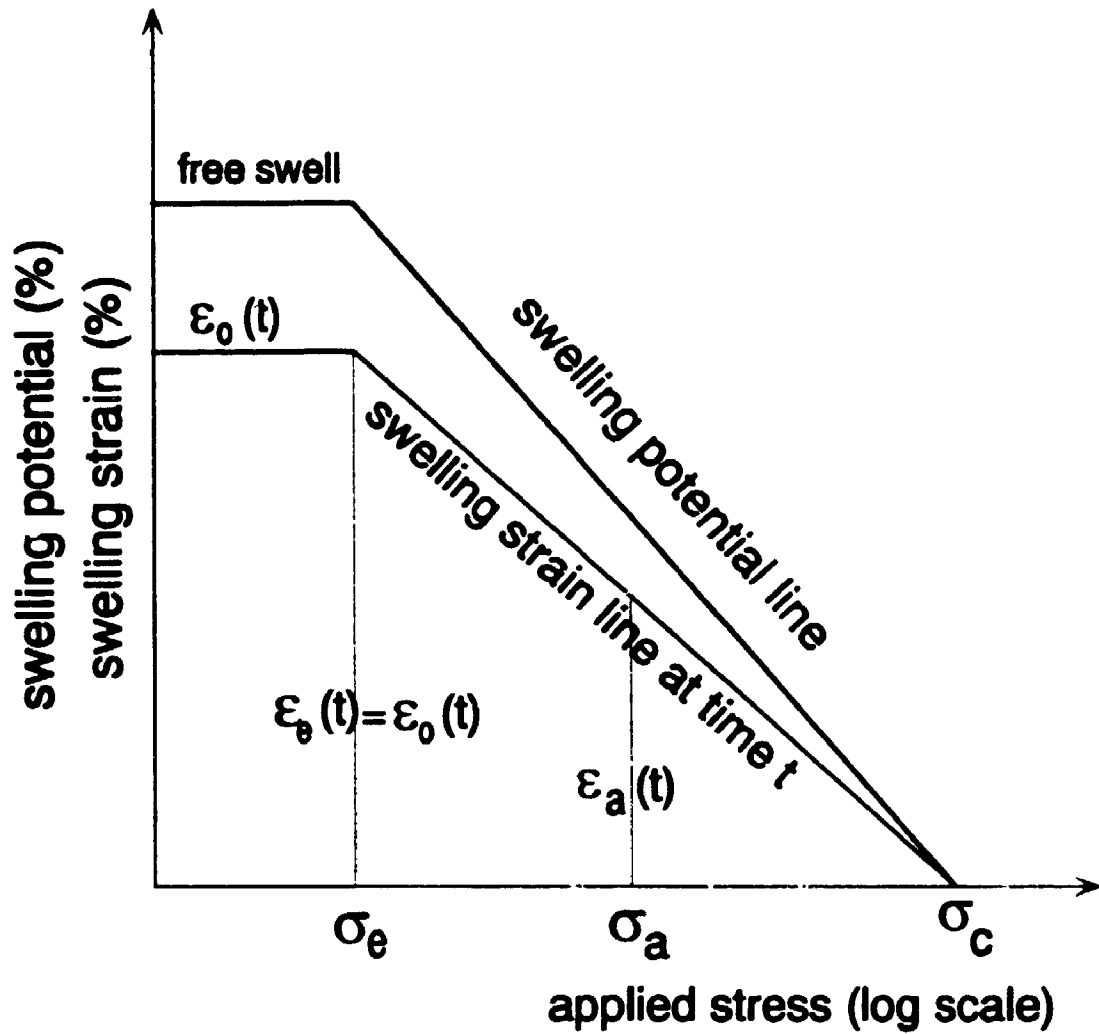
Figure 8.19 Idealization of relationship between swelling strain and applied stress
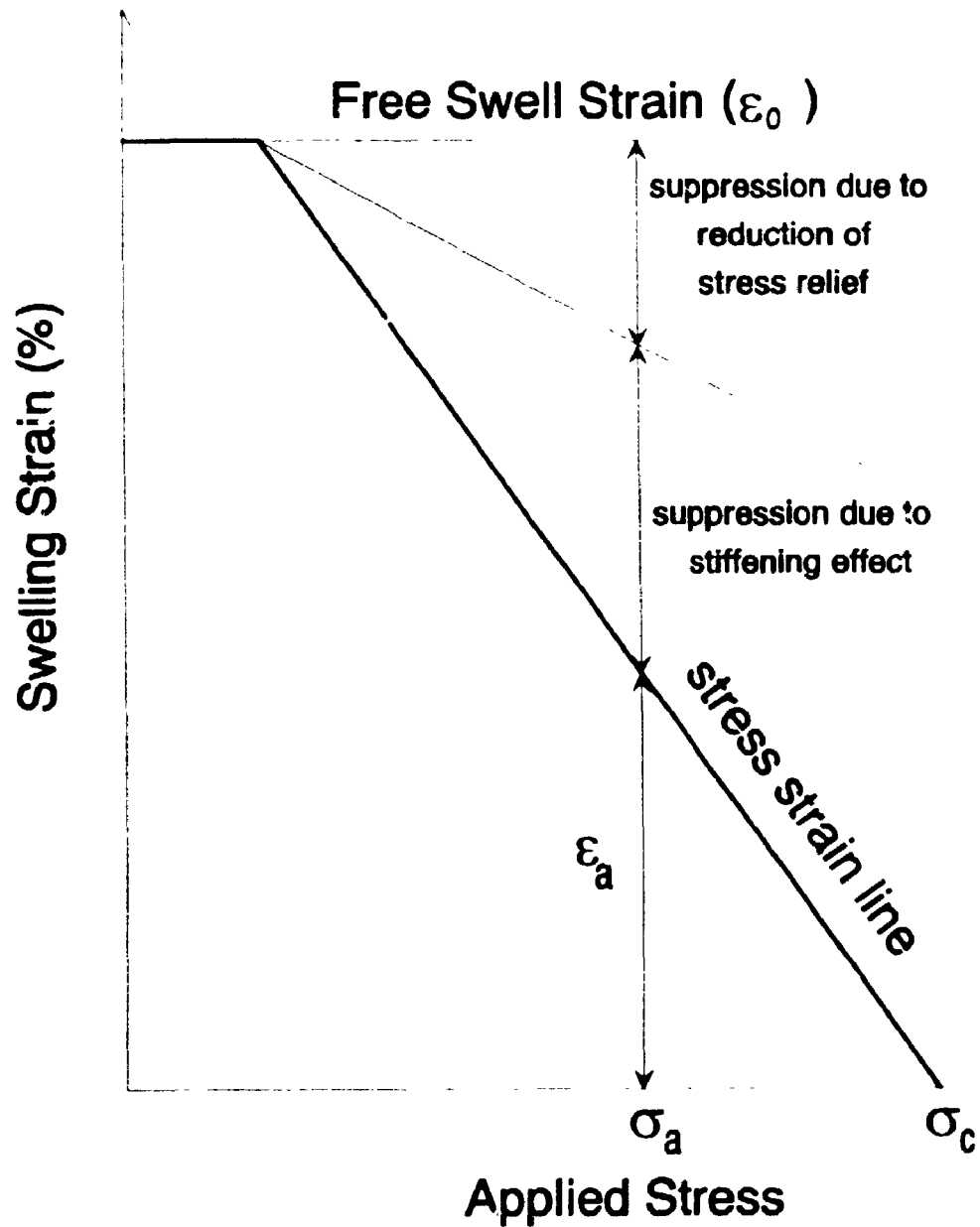
Figure 8.20 Schematic diagram showing factors affecting the suppression of swelling strain
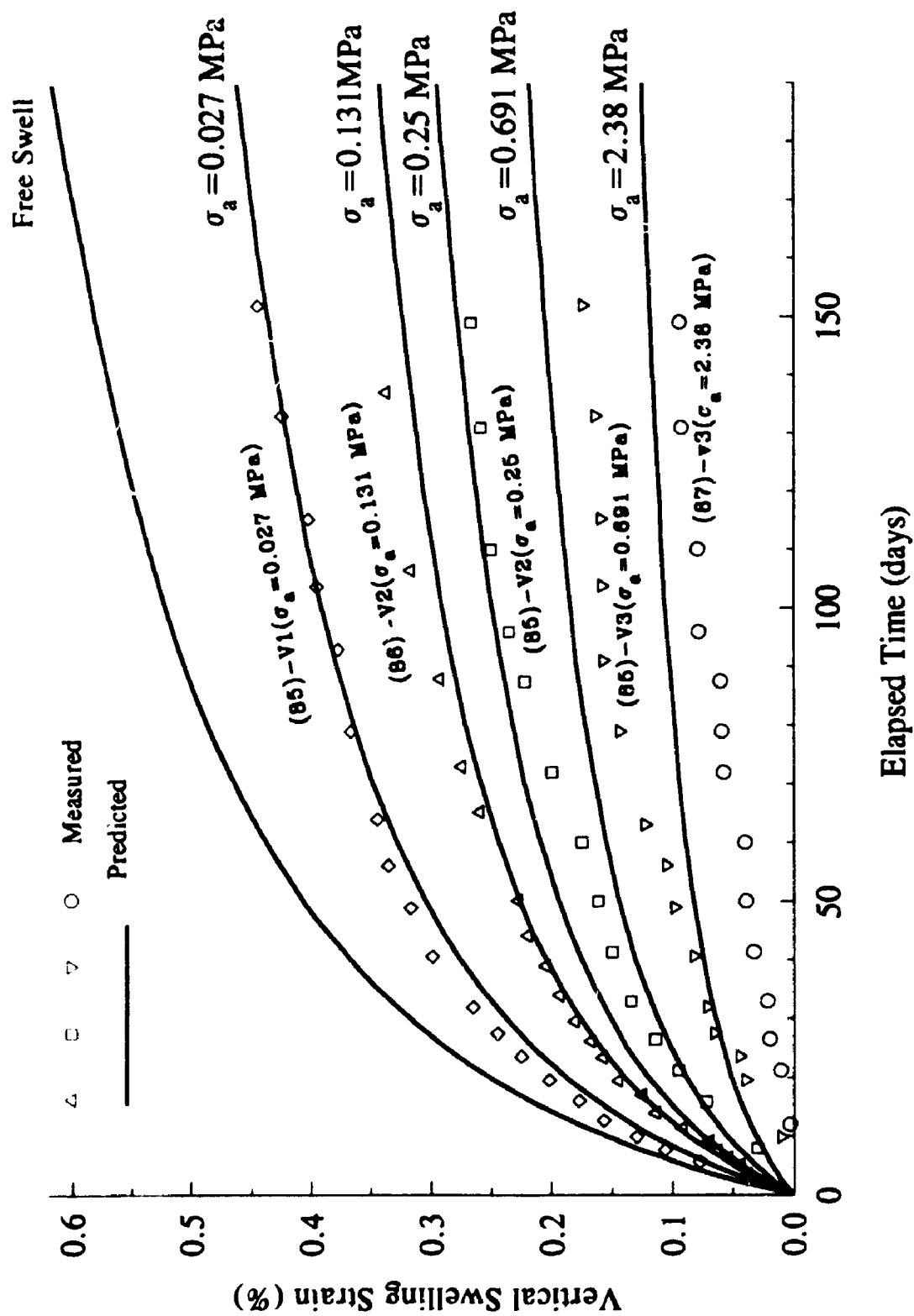
Figure 8.21 Typical measured and predicted vertical swelling strain vs. elapsed time under different applied pressures for Shallow Section of the Queenston Shale at location of Borehole NF4A (1985 to 1987 investigations)
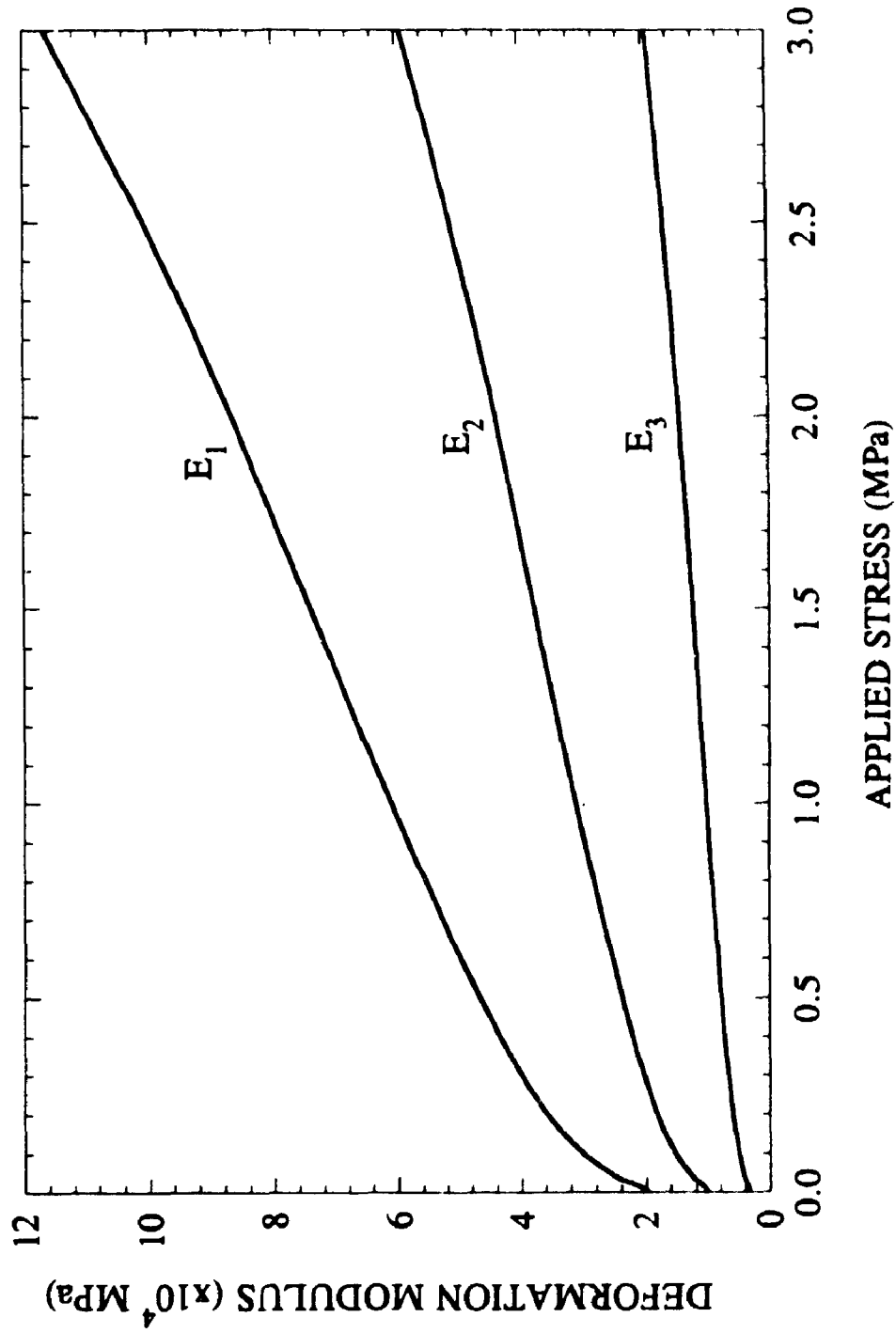
Figure 8.22 Variation of deformation modulus with applied stress in the horizontal direction for shallow section of Queenston Shale at Borehole NF4A
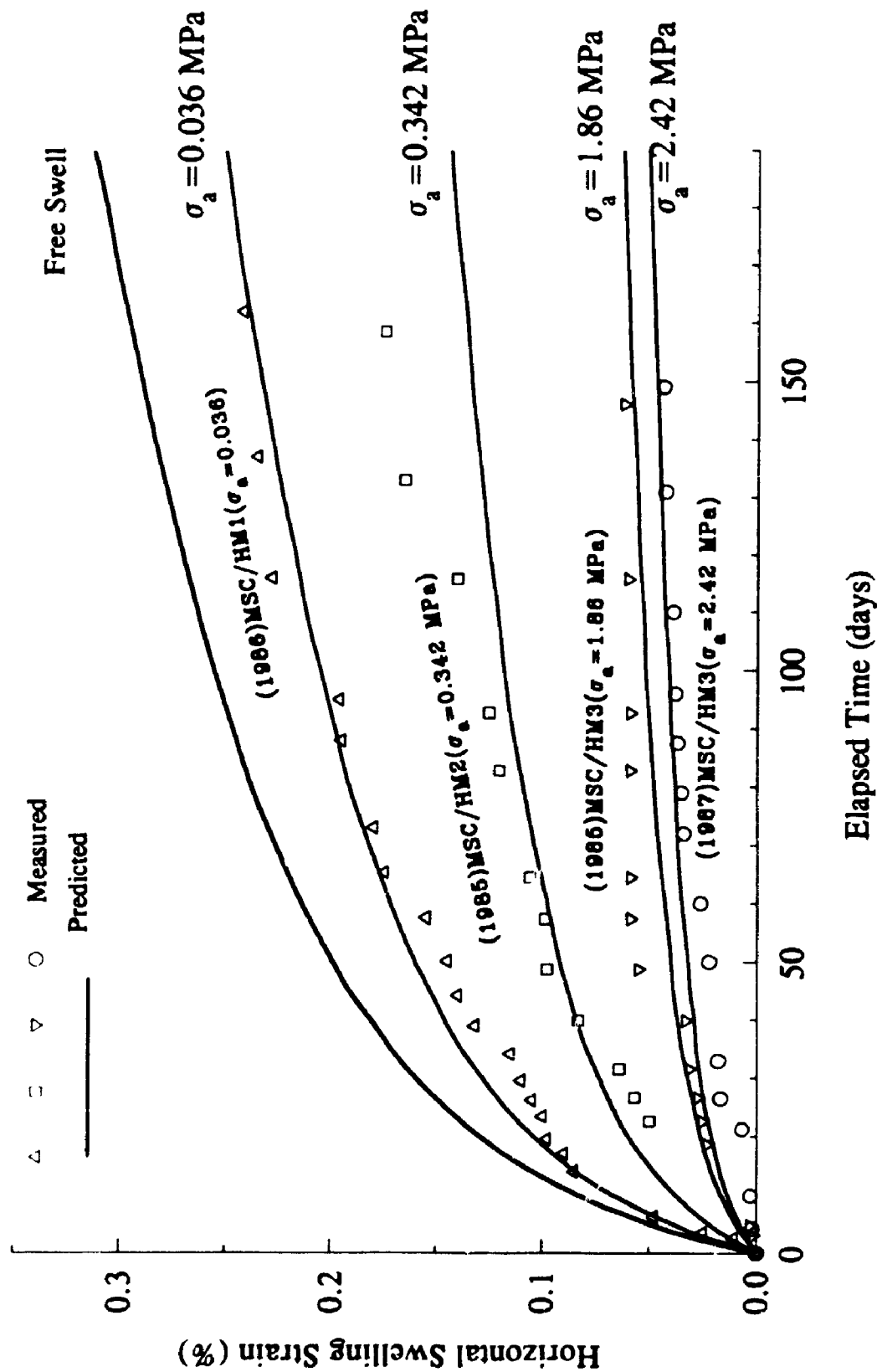
Figure 8.23 Typical measured and predicted horizontal swelling strain vs. elapsed time under different applied pressures for shallow section of the Queenston Shale at location of Borehole NF4A (1985 to 1987 investigations)
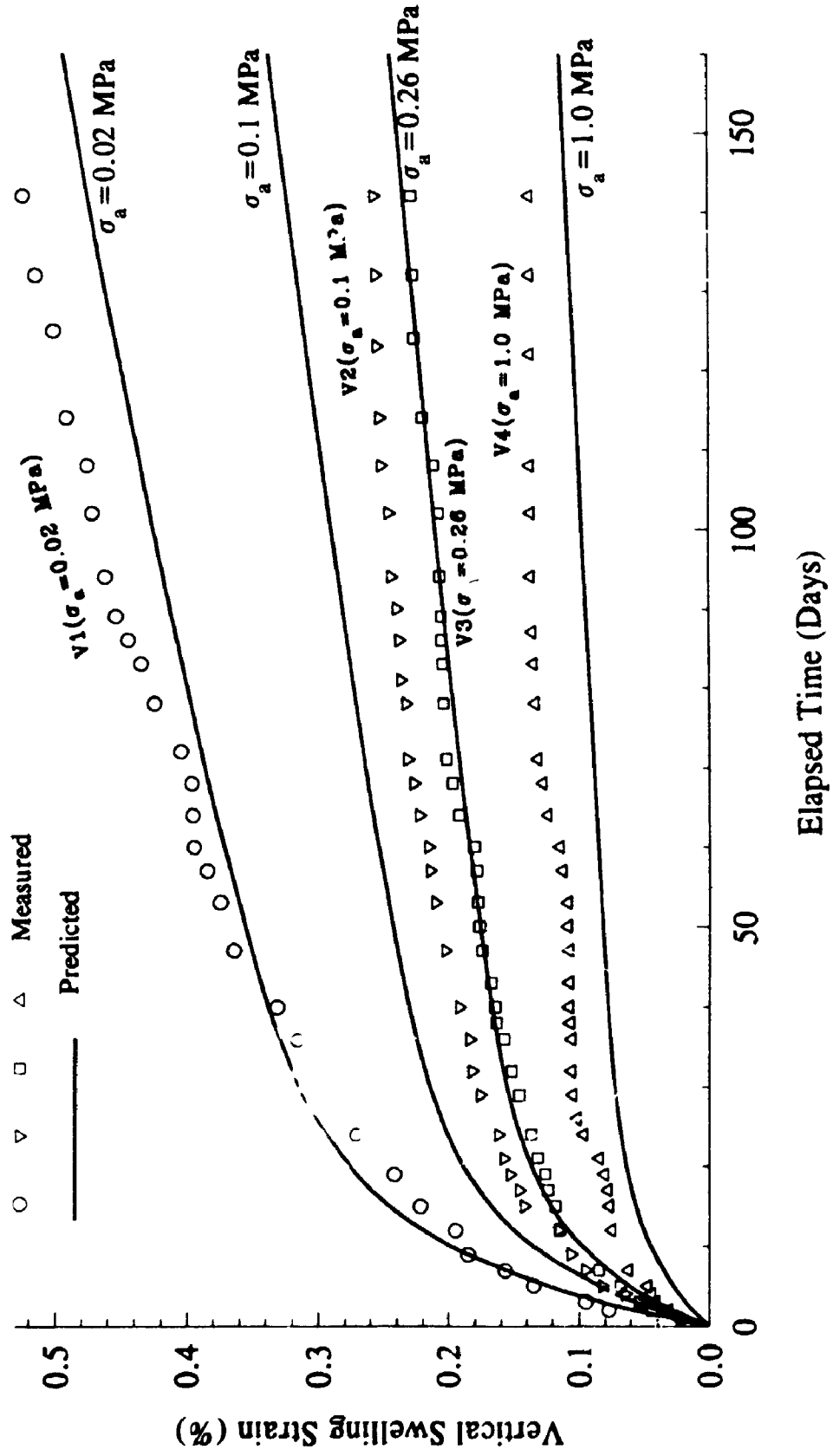
Figure 8.24 Typical measured and predicted vertical strain vs. elapsed time under different applied pressures for deep section of Queenston Shale at location of Borehole SD3 (1989 investigation)
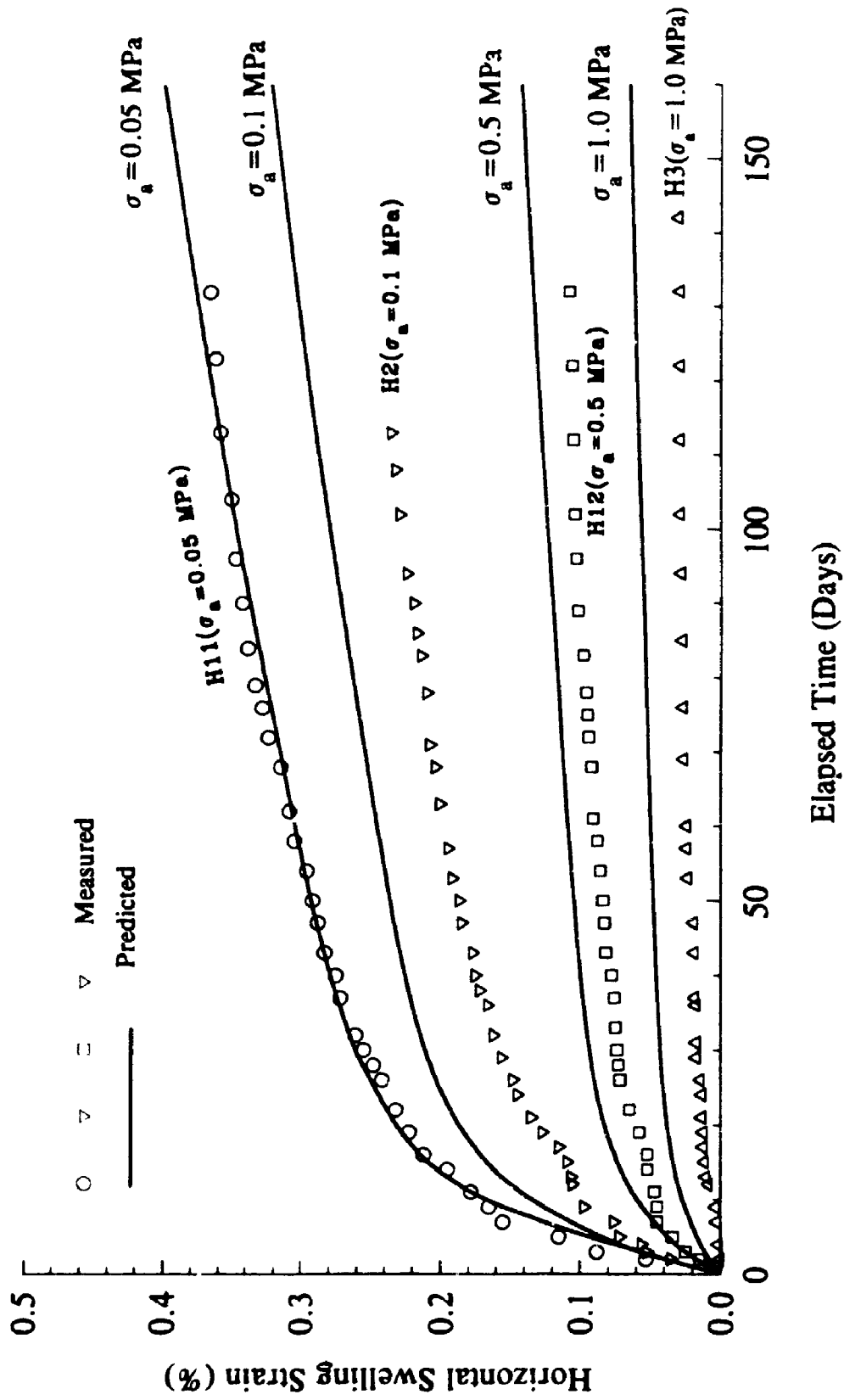
Figure 8.25 Typical measured and predicted horizontal swelling strain vs. elapsed time under different applied pressures for Deep Section of Queenston Shale at location of Borehole SD3 (1989 investigation)
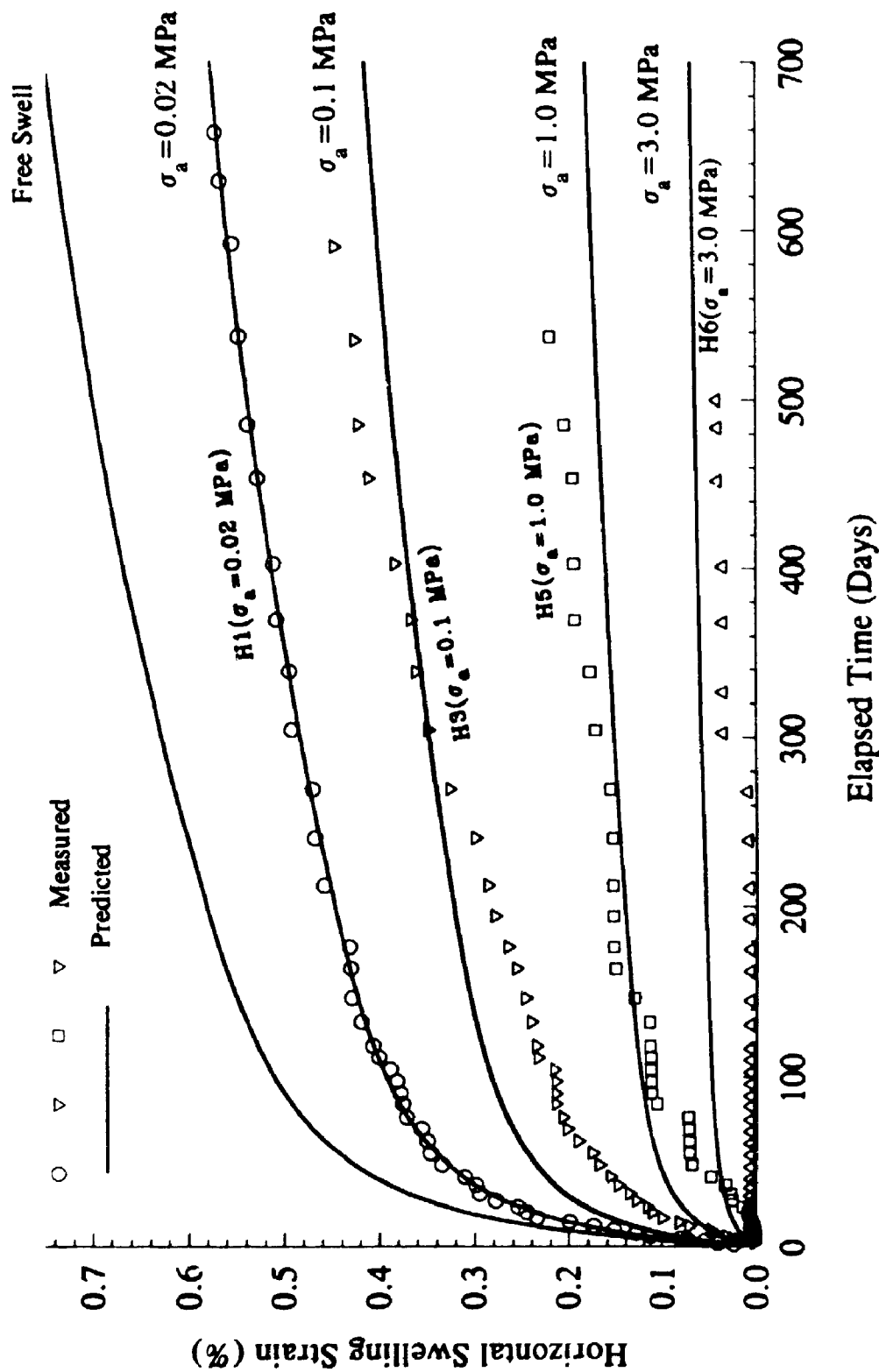
Figure 8.26 Typical measured and predicted horizontal swelling strain vs. elapsed time under different applied pressures for deep section of Queenston Shale (Borehole NF4A-1990 investigation)
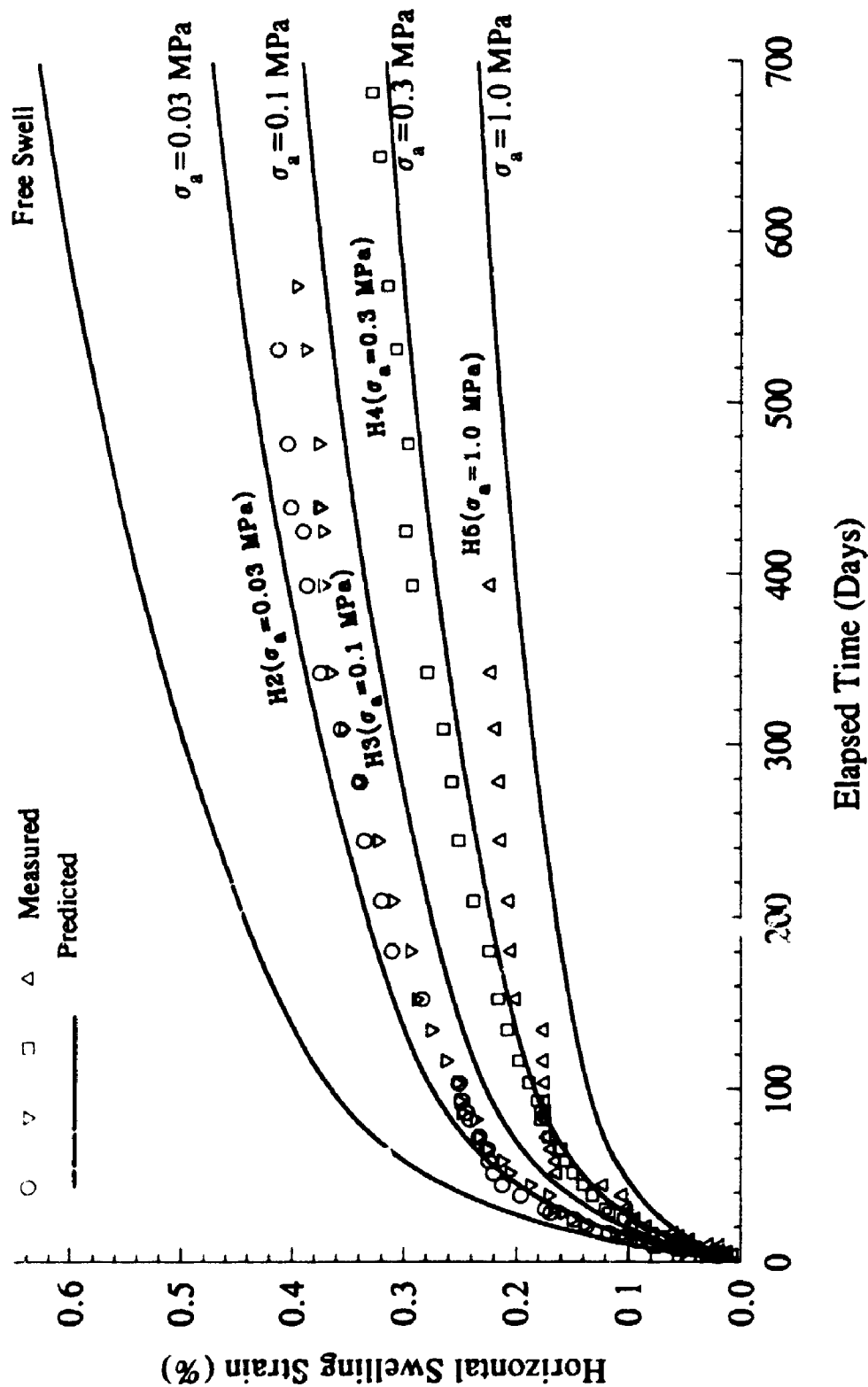
Figure 8.27 Typical measured and predicted horizontal swelling strain vs. elapsed time under different applied pressures for Samples of Queenston Shale (Borehole NF37-1990 investigation)
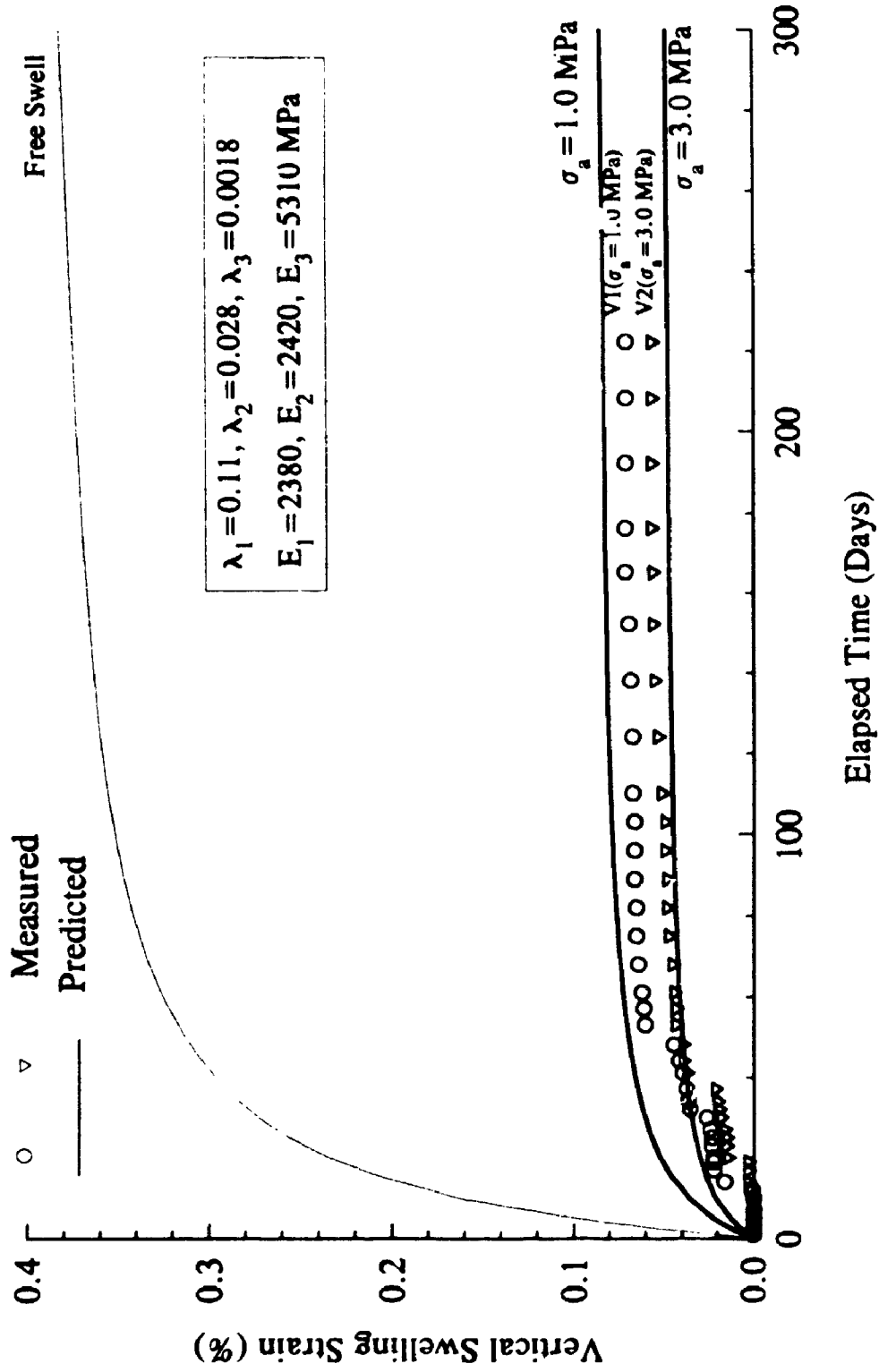
Figure 8.28 Typical measured and predicted horizontal swelling strain vs. elapsed time under different applied pressures for Qsamples of eenston Shale (Borehole NF43-Depth 163 m-1992 investigation)

CHAPTER 9

UNLINED TUNNELS DRIVEN IN VISCOELASTIC

ROCKS

9.1 INTRODUCTION

Distress in underground structures built in rocks exhibiting time-dependent deformation and subject to high horizontal stress is well known. Table 9.1 summarizes the effect of high horizontal stress and time-dependent deformation on underground structures (Lo and Yuen 1981).

Lo and Yuen (1981), showed in many case records that for lined circular tunnels the distress is manifested in the form of subhorizontal cracking at the springline. Invert heave up to 30 cm was measured in tunnels in Switzerland in 30 years (Berk and Grob 1972; Einstein and Bischoff 1975). Floor heave of about 45 cm in 3 years measured in tunnels in Germany was reported by Wittke and Pierau (1979).

Gill *et al.* (1970) and Gill and Dube (1974) studied the problem of rock-structure interaction for elastic lining. The case of viscoelastic lining was investigated by Curtis (1974, 1976) and Sakurai (1974). Lo and Yuen (1981) developed a theoretical solution for stresses and displacements in the lining and rock mass. Their solution takes into account the following important factors: (a) the initial stresses in the rock mass, (b) the time-dependent behaviour of the lining as well as that of the rock mass, and (c) the time elapsed between excavation and installation of the lining. Results of their solution were compared with several case histories in which severe cracking occurred and the comparison was satisfactory in Georgian Bay Shale and Shaly limestone. However,

because of the adoption of one Kelvin unit in their model, their solution is suitable only for rocks deforming for relatively short period of time, in the order of up to a few years.

In the light of results from Chapters 7 and 8, it can be seen that the time-dependent deformation of Queenston Shale occurs over a very long period of time. It has been shown in Chapter 8 that this long-term time-dependent deformation of Queenston Shale is well represented by a model consisting of three Kelvin units connected in series.

In this chapter, closed form solutions for the displacements around unlined tunnels driven in viscoelastic rocks are derived. The theory of linear viscoelasticity is adopted. The rock is idealized by a 7-element Kel/in model (a spring and 3 Kelvin units connected in series, refer to Figure 9.1). The law of correspondence between the elastic solution and viscoelastic solution is adopted to obtain the solutions.

In the next Chapter, the closed form solution developed will be extended to include the case of lined tunnel in viscoelatic rocks. The solutions obtained will be used to estimate the stresses in lining of the proposed tunnel for SABNGS No. 3 proje_t and all the parameters affecting the solution will be investigated.

9.2 CORRESPONDENCE PRINCIPAL

If the elastic solution of a particular problem is known, the associated problem in linear viscoelasticity may be solved by using the principle of correspondence (Flügge 1975) derived in Appendix 9A. The steps of solution may be summarized as follows:

(a) replace the displacements and stresses by their Laplace transforms.

(b) replace the actual loads by their Laplace transforms.

(c) replace the elastic parameters (K, G, E and v) in the elastic solution by the transformed operators given in Appendix 9A, Eqs. 9A.57 through 9A.59

$$2G \rightarrow \frac{\bar{Q}}{\bar{P}} \qquad 3K \rightarrow \frac{\bar{Q}'}{\bar{P}'} \qquad \text{(9.1a)}$$

$$E \rightarrow \frac{3\bar{Q}'\bar{Q}}{2\bar{P}'\bar{Q}' + \bar{P}'\bar{Q}} \qquad v \rightarrow \frac{\bar{P}\bar{Q}' - \bar{P}'\bar{Q}}{2\bar{P}\bar{Q}' + \bar{P}'\bar{Q}} \qquad \text{(9.1b)}$$

where K = bulk modulus of the rock

G = shear modulus of the rock

E = Young's modulus of the rock

v = Poisson's ratio of the rock

$\bar{P}$, $\bar{Q}$, $\bar{P}'$, and $\bar{Q}'$ are the Laplace transforms of the differential operators P, Q, P', and Q' respectively in the constitutive laws of a viscoelastic material, and they are polynomials in s, the transformation variable.

(d) inversion of the Laplace transforms will give the final viscoelastic solution.

9.3 ASSUMPTIONS

The following basic assumptions for the rock mass are considered during the derivation of the solution:

1) The rock mass is an infinite, elastic, linear viscoelastic material and acted upon by the initial stresses at infinity.

2) Both the dilatational and distortional behaviour of the rock mass are represented by a 7-element Kelvin model (a spring and 3 Kelvin units connected in series,

Figure 9.1).

3) Poisson's ratio of the rock mass is independent of time. Extensive study on Queenston Shale has shown that Poisson's ratio is independent of time (Lee 1988).

4) The tunnel is long enough to consider the problem a plane strain problem with one of the principal stresses parallel to the tunnel axis and the other two perpendicular to it in the vertical and horizontal directions.

9.4 ELASTIC STRESSES AND DISPLACEMENTS AROUND UNLINED TUNNELS

Since the method of analysis described above (the correspondence principle) requires the existence of the elastic solution of the problem, the elastic solutions of stresses and displacements around unlined tunnels are summarized in this section.

The elastic solution of stresses and displacements around unlined tunnels are well known (Jaeger and Cook 1976; Obert and Duvall 1967; and Yuen 1979). In terms of the initial hydrostatic (P_o) and deviatoric (Q_o) stress components, the radial, tangential and shear stresses respectively are

$$\sigma_{rR} = P_o(1 - \frac{R_2^2}{r^2}) + Q_o(1 + 3\frac{R_2^4}{r^4} - 4\frac{R_2^2}{r^2})\cos 2\theta \qquad (9.2)$$

$$\sigma_{\theta R} = P_o(1 + \frac{R_2^2}{r^2}) + Q_o(1 + 3\frac{R_2^4}{r^4})\cos 2\theta \qquad (9.3)$$

$$\tau_{r\theta R} = -Q_o(1 - 3\frac{R_2^4}{r^4} + 2\frac{R_2^2}{r^2})\sin 2\theta \qquad (9.4)$$

The radial and tangential displacements respectively are (Yuen 1979)

$$u_{rR} = \frac{R_2^2}{2G_R r}\left[P_o + Q_o(4 - 4v_R - \frac{R_2^2}{r^2})\cos 2\theta\right] \qquad (9.5)$$

$$v_R = -\frac{Q_o}{2G_R}\left[\frac{R_2^4}{r^3} + \frac{2R_2^2}{r}(1 - 2v_R)\right]\sin 2\theta \qquad (9.6)$$

where $P_o \quad = \dfrac{P_h + P_v}{2}$

$Q_o \quad = \dfrac{P_h - P_v}{2}$

$P_h, P_v \qquad =$ initial horizontal and vertical stresses in the rock mass respectively

$R_2 \qquad =$ radius of the unlined tunnel

$r \qquad =$ radial distance from the centre of the tunnel

$G_R, v_R \qquad =$ shear modulus and Poisson's ratio of the rock respectively

$\theta \qquad =$ angle measured from the springline of the tunnel

The subscript R stands for Rock.

9.5 VISCOELASTIC SOLUTION FOR THE STRESSES AND DEFORMATIONS AROUND A TUNNEL

Yuen (1979) showed that the final time-dependent deformation of the rock is independent of the Poisson's ratio. In addition, extensive study on Queenston Shale has shown that Poisson's ratio is independent of time (Lee 1988). Therefore, in the following investigation Poisson's ratio will be assumed to remain constant with time.

9.5.1 Solution For Stresses

As shown by Eqs. 9.2, 9.3, and 9.4, the stresses in the elastic rock mass are independent of the material parameters. Therefore, the viscoelastic stresses will be the same as given by these equations for elastic rock mass, according to the elastic-viscoelastic correspondence principle.

9.5.2 Solution For Radial Displacement

The elastic solution for the radial displacement is given by Eq. 9.5 and can be written in the following form:

$$u_R = \frac{1}{G_R} M_1 \tag{9.7}$$

where

$$M_1 = \frac{R_2^2}{2r} \left[P_o + Q_o(4 - 4v_R - \frac{R_2^4}{r^2})\cos 2\theta \right] \tag{9.8}$$

The initial stresses P_o and Q_o are applied at infinity and remain constant with time,

therefore,

$$P_o = P_o \Delta(t) \tag{9.9}$$

and

$$Q_o = Q_o \Delta(t) \tag{9.10}$$

where t = time variable

$\Delta(t)$ = the unit step function

= 0   for $t < 0$

= 1   for $t \geq 0$

The Laplace transforms of P_o (Eq. 9.9) and Q_o (Eq. 9.10) respectively are

$$\mathcal{L}(P_o) = \bar{P}_o = \frac{P_o}{s} \tag{9.11}$$

and

$$\mathcal{L}(Q_o) = \bar{Q}_o = \frac{Q_o}{s} \tag{9.12}$$

Since Poisson's ratio is assumed independent of time, the laplace transform of M_1 is

$\bar{M}_1 = \dfrac{M_1}{s}$. Application of the correspondence principle (Sec. 9.2) to Eq. 9.7 leads to the

following equation:

$$\bar{u}_R = \frac{2\bar{P}}{\bar{Q}} \frac{M_1}{s} \tag{9.13}$$

where u_R is replaced by its Laplace transform $\bar{u}_R$, M_1 by its Laplace transform $\frac{M_1}{s}$. and $2G_R$

by the transformed operators $\bar{P}$ and $\bar{Q}$ as given by Eq. 9.1

$$2G \rightarrow \frac{\bar{Q}}{\bar{P}} \tag{9.14}$$

where $\bar{Q}$ and $\bar{P}$ are polynomials in the transform variable s.

It has been shown in Chapter 8 that the long-term time-dependent deformation for Queenston Shale is well represented by a 6-element Kelvin model (three Kelvin units connected in series,. To include the elastic deformation of Queenston Shale, a spring should be connected in series to the three Kelvin units, consisting a 7-element Kelvin model. For this model, the transforms of the differential operators $\bar{P}$ and $\bar{Q}$ are given by the following expressions (see Appendix 9A):

$$\bar{P} = 1 + p'_{R1} s + p'_{R2} s^2 + p'_{R3} s^3 \tag{9.15}$$

and

$$\bar{Q} = q'_{R0} + q'_{R1} s + q'_{R2} s^2 + q'_{R3} s^3 \tag{9.16}$$

The coefficients p'_{R1}, p'_{R2}, p'_{R3}, q'_{R0}, q'_{R1}, q'_{R2}, and q'_{R3} can be expressed in terms of the elastic and viscoelastic parameters of the rock as follows (refer to Appendix 9A):

$$p'_{RI} = (G_{RI}G_{R2}\eta_{R3} + G_{RI}G_{R3}\eta_{R2} + G_{R2}G_{R3}\eta_{RI} + G_R G_{R2}\eta_{R3} + G_R G_{R3}\eta_{R2}$$
$$+ G_R G_{RI}\eta_{R3} + G_R G_{R3}\eta_{RI} + G_R G_{RI}\eta_{R2} + G_R G_{R2}\eta_{RI})$$
$$/ \{2(G_{RI}G_{R2}G_{R3} + G_R G_{R2}G_{R3} + G_R G_{RI}G_{R3} + G_R G_{RI}G_{R2})\} \quad (9.17)$$

$$p'_{R2} = (G_{RI}\eta_{R2}\eta_{R3} + G_{R2}\eta_{RI}\eta_{R3} + G_{R3}\eta_{RI}\eta_{R2} + G_R\eta_{R2}\eta_{R3}$$
$$+ G_R\eta_{RI}\eta_{R3} + G_R\eta_{RI}\eta_{R2})$$
$$/ \{4(G_{RI}G_{R2}G_{R3} + G_R G_{R2}G_{R3} + G_R G_{RI}G_{R3} + G_R G_{RI}G_{R2})\} \quad (9.18)$$

$$p'_{R3} = \frac{\eta_{RI}\eta_{R2}\eta_{R3}}{8(G_{RI}G_{R2}G_{R3} + G_R G_{R2}G_{R3} + G_R G_{RI}G_{R3} + G_R G_{RI}G_{R2})} \quad (9.19)$$

$$q'_{Ro} = \frac{2 G_R G_{RI}G_{R2}G_{R3}}{G_{RI}G_{R2}G_{R3} + G_R G_{R2}G_{R3} + G_R G_{RI}G_{R3} + G_R G_{RI}G_{R2}} \quad (9.20)$$

$$q'_{RI} = \frac{G_R G_{RI}G_{R2}\eta_{R3} + G_R G_{RI}G_{R3}\eta_{R2} + G_R G_{R2}G_{R3}\eta_R}{G_{RI}G_{R2}G_{R3} + G_R G_{R2}G_{R3} + G_R G_{RI}G_{R3} + G_R G_{RI}G_{R2}} \quad (9.21)$$

$$q'_{R2} = \frac{G_R G_{RI}\eta_{R2}\eta_{R3} + G_R G_{R2}\eta_{RI}\eta_{R3} + G_R G_{R3}\eta_{RI}\eta_{R2}}{2(G_{RI}G_{R2}G_{R3} + G_R G_{R2}G_{R3} + G_R G_{RI}G_{R3} + G_R G_{RI}G_{R2})} \quad (9.22)$$

$$q'_{R3} = \frac{G_r\eta_{RI}\eta_{R2}\eta_{R3}}{4(G_{RI}G_{R2}G_{R3} + G_R G_{R2}G_{R3} + G_R G_{RI}G_{R3} + G_R G_{RI}G_{R2})} \quad (9.23)$$

Substitution of Eqs. 9.15 and 9.16 into Eq. 9.13 leads to the following equation:

$$\bar{u}_R = \frac{2(1 + p'_{RI} s + p'_{R2} s^2 + p'_{R3} s^3)}{s(q_{Ro} + q'_{RI} s + q'_{R2} s^2 + q'_{R3} s^3)} M_1 \quad (9.24)$$

After arrangement, Eq. 9.24 can be written in the following form:

$$\bar{u}_R = \frac{(1 + p'_{RI} s + p'_{R2} s^2 + p'_{R3} s^3)}{s(s^3 + \dfrac{q'_{R2}}{q'_{R3}} s^2 + \dfrac{q'_{RI}}{q'_{R3}} s + \dfrac{q_{Ro}}{q'_{R3}})} \left(\frac{2M_1}{q'_{R3}}\right) \quad (9.25)$$

If $-\lambda_{RI}$, $-\lambda_{R2}$, and $-\lambda_{R3}$ are the roots of the following equation:

$$s^3 + \frac{q'_{R2}}{q'_{R3}} s^2 + \frac{q'_{R1}}{q'_{R3}} s + \frac{q'_{Ro}}{q'_{R3}} = 0$$

then, Eq. 9.25 can be expressed as

$$\bar{u}_R = \frac{(1 + p'_{R1} s + p'_{R2} s^2 + p'_{R3} s^3)}{s(s + \lambda_{R1})(s + \lambda_{R2})(s + \lambda_{R3})} \left(\frac{2M_1}{q'_{R3}}\right) \qquad (9.26)$$

where

$$\lambda_{R1} = 2\sqrt{-Q_1} \cos\left(\frac{\theta_1}{3}\right) - \frac{q'_{R2}}{q'_{R3}} = \frac{2G_{R1}}{\eta_{R1}} \qquad (9.27\text{a})$$

$$\lambda_{R2} = 2\sqrt{-Q_1} \cos\left(\frac{\theta_1}{3} + 120°\right) - \frac{q'_{R2}}{q'_{R3}} = \frac{2G_{R2}}{\eta_{R2}} \qquad (9.27\text{b})$$

$$\lambda_{R3} = 2\sqrt{-Q_1} \cos\left(\frac{\theta_1}{3} + 240°\right) - \frac{q'_{R2}}{q'_{R3}} = \frac{2G_{R3}}{\eta_{R3}} \qquad (9.27\text{c})$$

$$\theta_1 = \cos^{-1}\left(\frac{R}{\sqrt{-Q_1^3}}\right) \qquad (9.27\text{d})$$

$$R = \frac{9\frac{q'_{R2}}{q'_{R3}}\frac{q'_{R1}}{q'_{R3}} - 27\frac{q_{Ro}}{q'_{R3}} - 2\frac{q'_{R2}}{q'_{R3}}}{54} \qquad (9.27\text{e})$$

$$Q_1 = \frac{3\frac{q'_{R1}}{q'_{R3}} - \left(\frac{q'_{R2}}{q'_{R3}}\right)^2}{9} \qquad (9.27\text{f})$$

λ_{Ri} (where i can take any value of 1, 2, or 3) can be expressed as

$$\lambda_{Ri} = \frac{2G_{Ri}}{\eta_{Ri}} \tag{9.28}$$

where G_{Ri} and η_{Ri} respectively are the shear modulus of the spring and the viscosity coefficient of the dashpot in the i *th* Kelvin unit.

Using partial fractions, Eq. 9.26 can be written in the following form:

$$\bar{u}_R = \left[\frac{A_o}{s} + \frac{A_1}{s(s+\lambda_{R1})} + \frac{A_2}{s(s+\lambda_{R2})} + \frac{A_3}{s(s+\lambda_{R3})}\right]\left(\frac{2M_1}{q'_{R3}}\right) \tag{9.29}$$

where

$$A_o = p'_{R3} \tag{9.30a}$$

$$A_1 = \frac{(\lambda_{R2} - \lambda_{R3})(\lambda_{R1} p'_{R1} - \lambda_{R1}^2 p'_{R2} + \lambda_{R1}^3 p'_{R3} - 1)}{\lambda_{R2}\lambda_{R3}(\lambda_{R3} - \lambda_{R2}) + \lambda_{R1}\lambda_{R3}(\lambda_{R1} - \lambda_{R3}) + \lambda_{R1}\lambda_{R2}(\lambda_{R2}\lambda_{R1})} \tag{9.30b}$$

$$A_2 = \frac{(\lambda_{R3} - \lambda_{R1})(\lambda_{R2} p'_{R1} - \lambda_{R2}^2 p'_{R2} + \lambda_{R2}^3 p'_{R3} - 1)}{\lambda_{R1}\lambda_{R3}(\lambda_{R3} - \lambda_{R2}) + \lambda_{R1}\lambda_{R3}(\lambda_{R1} - \lambda_{R3}) + \lambda_{R1}\lambda_{R2}(\lambda_{R2}\lambda_{R1})} \tag{9.30c}$$

$$A_3 = \frac{(\lambda_{R1} - \lambda_{R2})(\lambda_{R3} p'_{R1} - \lambda_{R3}^2 p'_{R2} + \lambda_{R3}^3 p'_{R3} - 1)}{\lambda_{R2}\lambda_{R3}(\lambda_{R3} - \lambda_{R2}) + \lambda_{R1}\lambda_{R3}(\lambda_{R1} - \lambda_{R3}) + \lambda_{R1}\lambda_{R2}(\lambda_{R2}\lambda_{R1})} \tag{9.30d}$$

Inverse Laplace transform of Eq. 9.29 leads to the following solution of the time-dependent radial deformation of the unlined tunnel:

$$u_R(t) = \left[p'_{R3} + \frac{A_1}{\lambda_{R1}}(1 - e^{-\lambda_{R1}t}) + \frac{A_2}{\lambda_{R2}}(1 - e^{-\lambda_{R2}t}) + \frac{A_3}{\lambda_{R3}}(1 - e^{-\lambda_{R3}t})\right]\left(\frac{2M_1}{q'_{R3}}\right) \tag{9.31}$$

Eq. 9.31 can be written in the following form:

$$u_R(t) = J_R(t) u_R(elastic) \tag{9.32}$$

where

$$J_R(t) = \frac{2G_R}{q'_{R3}}\left[p'_{R3} + \frac{A_1}{\lambda_{RI}}(1-e^{-\lambda_{RI}t}) + \frac{A_2}{\lambda_{R2}}(1-e^{-\lambda_{R2}t}) + \frac{A_3}{\lambda_{R3}}(1-e^{-\lambda_{R3}t})\right] \tag{9.33}$$

or

$$J_R(t) = \left[1 + \phi_{RI}(1-e^{-\lambda_{RI}t}) + \phi_{R2}(1-e^{-\lambda_{R2}t}) + \phi_{R3}(1-e^{-\lambda_{R3}t})\right] \tag{9.34}$$

$$\frac{p'_{R3}}{q'_{R3}} = \frac{1}{2G_R} \tag{9.35a}$$

$$\phi_{RI} = \frac{2G_R A_1}{q'_{R3}\lambda_{RI}} = \frac{G_R}{G_{RI}} \tag{9.35b}$$

$$\phi_{R2} = \frac{2G_R A_2}{q'_{R3}\lambda_{R2}} = \frac{G_R}{G_{R2}} \tag{9.35c}$$

$$\phi_{R3} = \frac{2G_R A_3}{q'_{R3}\lambda_{R3}} = \frac{G_R}{G_{R3}} \tag{9.35d}$$

ϕ_{Ri}, where i can take any value of 1, 2, or 3, can be expresses as

$$\phi_{Ri} = \frac{G_R}{G_{Ri}} \tag{9.36}$$

$J(t)$ is a time-dependent function which relates the time-dependent deformation to the elastic deformation.

When $t = 0$

$$J_R(0) = 1 \tag{9.37}$$

and

$$u_R(0) = u_R(elastic) \tag{9.38}$$

When $t = \infty$

$$J_R(\infty) = 1 + \phi_{RI} + \phi_{R2} + \phi_{R3} \tag{9.39}$$

and

$$u_R(\infty) = (1 + \phi_{RI} + \phi_{R2} + \phi_{R3}) u_R(elastic) \tag{9.40}$$

In general, for a model of a spring and k Kelvin units, the time-dependent radial deformation takes the following form:

$$u_R(t) = J_R(t) u_R(elastic) \tag{9.41}$$

where

$$J_R(t) = 1 + \sum_{i=1}^{k} \phi_{Ri} (1 - e^{-\lambda_{Ri} t}) \tag{9.42}$$

ϕ_{Ri} represents the ratio of the final deformation resulting from the i th Kelvin unit to the elastic deformation and it is defined by Eq. 9.36. λ_{Ri} is an indicator to the rate at which the time-dependent deformation of the i th Kelvin unit is built up and it is defined by Eq. 9.28; a high value represents fast occurrence of the time-dependent deformation and vice versa.

9.5.3 Solution for Tangential Deformation

The method of analysis described in the preceding sections may be applied in a similar manner to solve for the time-dependent tangential deformation of the unlined tunnel. Thus, for a model consisting of a spring and k Kelvin units, similar to Eq. 9.41

$$v_R(t) = J_R(t) \, v_R(elastic) \qquad (9.43)$$

where

$$J_R(t) = 1 + \sum_{i=1}^{k} \phi_R(1-e^{-\lambda_i t}) \qquad (9.44)$$

9.5.4 Example of Design Analysis

As an example of utilizing Eq. 9.41 in practice, the final unrestricted time-dependent radial deformation of a typical section at depth 200 m of the circular twin tunnels proposed for the SABNGS No.3 project are calculated. As shown in Chapter 8, the elastic and time-dependent properties for Queenston Shale (the rock component in which the tunnels will be excavated) are

$E_R = 15800$ MPa $\qquad v_R = 0.3$

$\lambda_1 = 0.1100$ day^{-1} $\qquad \lambda_2 = 0.02800$ day^{-1} $\qquad \lambda_3 = 0.0018$ day^{-1}

$E_{R1} = 15000$ MPa $\qquad E_{R2} = 8080$ MPa $\qquad E_{R3} = 4940$ MPa

The elastic shear modulus is $G_R = \dfrac{E_R}{2(1+v_R)} = 6077$ MPa

The time dependent shear moduli are also calculated as

$$G_{R1} = 5769 \text{ MPa} \quad G_{R2} = 3108 \text{ MPa} \quad G_{R3} = 1900 \text{ MPa}$$

ϕ_R are calculated using Eq. 9.36

$$\phi_{R1} = \frac{G_R}{G_{R1}} = 1.1 \quad \phi_{R2} = \frac{G_R}{G_{R2}} = 2.0 \quad \phi_{R3} = \frac{G_R}{G_{R3}} = 3.2$$

The final time-dependent radial deformation are calculated using Eq. 9.41

$$u_R(\infty) = (1+1.1+2.0+3.2) \, u_R(elastic) = 7.3 \, u_R(elastic)$$

which indicates that the unrestricted final radial deformation is more than 7 times the elastic deformation.

9.6   SUMMARY

Closed form solutions for the displacements around unlined tunnels driven in viscoelastic rocks are derived using the theory of linear viscoelasticity. The rock is idealized by a 7-element Kelvin model (a spring and 3 Kelvin units connected in series). The law of correspondence between the elastic solution and viscoelastic solution is adopted to obtain the solutions. In the next chapter, the solution is extended to include the case of rock-lining-time interaction.

TABLE 9.1   Effect of high horizontal stresses and time-dependent deformation on
underground structures

Type of Structure	Short Term (during construction)	Long Term
Open excavation	(a) Heave and buckling of floor (b) Movement along bedding planes	(i) As (a) (ii) Long term deformation in unsupported excavation (iii) Stress increases in support system leading to distress
Tunnels	(a) Movement along bedding planes at or near springline (b) Local "failure" at crown and invert in soft rock (c) invert heave	(i) Displacements (inward) increases with time in unlined tunnels (ii) Stress increases in lining leading to distress

(after Lo and Yuen 1981)
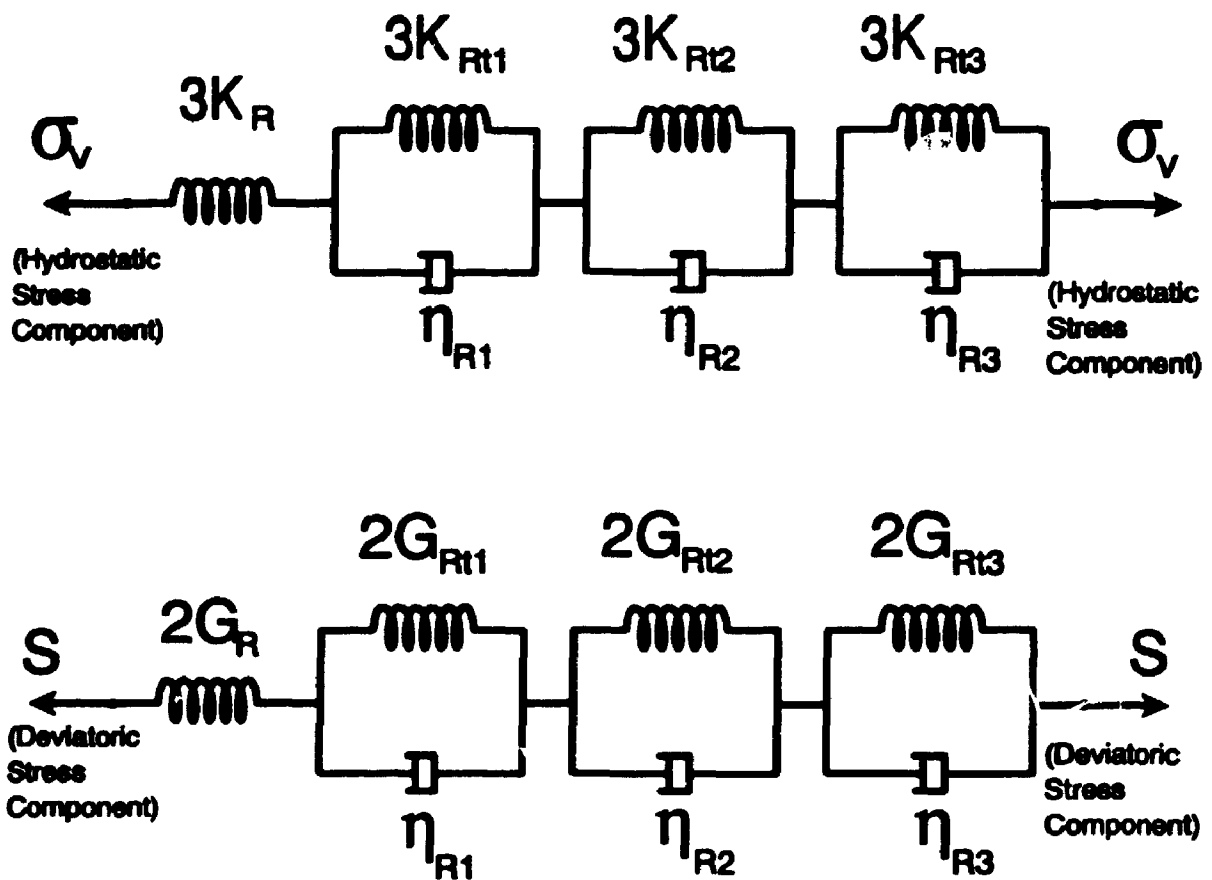
K_R = Elastic bulk modulus

G_R = Elastic shear modulus

K_{Rti} = Bulk modulus for the spring in the i th Kelvin unit

G_{Rti} = shear modulus for the spring in the i th Kelvin unit

η_{Ri} = Viscosity of dashpot for the i th Kelvin unit

λ_{Ri} = rate parameter for the i th Kelvin unit

$$\lambda_{Ri} = \frac{2G_{Rti}}{\lambda_{Ri}}$$

Figure 9.1 7-Element Kelvin model for hydrostatic and deviatoric stress components
for rock

CHAPTER 10

ROCK-LINING-TIME INTERACTION

OF CIRCULAR TUNNELS

10.1 INTRODUCTION

In Chapter 9, the closed form solutions for the unrestrained time-dependent displacements around a circular tunnel driven in a linear viscoelastic rock mass are derived. In the solutions obtained, the rock mass has been represented by a 7-element Kelvin model (a spring and 3 Kelvin units connected in series), a model which is capable of describing the long-term time-dependent deformation of swelling shales.

In this chapter, the rock-lining-time interaction of circular tunnels is considered. Closed form solutions for the stresses and displacements in the lininig and in the rock mass are derived. The geometry of the problem and the sign convention for the stresses and displacements are illustrated in Figure 10.1. The elastic and time-dependent deformations of the rock mass are idealized by a 7-element Kelvin model (Figure 9.1) and those for the lining are idealized by a 3-element Kelvin model. The correspondence principle derived in Chapter 9 is adopted to convert the elastic solution of the problem to its correspondent of time-dependent solution.

10.2 ASSUMPTIONS

Besides the basic assumptions for the rock mass mentioned in Chapter 9, the following basic assumptions are considered for the lining:

(1)   The lining is an isotropic linear viscoelastic material.

(2)   Both the dilatational and distortional behaviour of the lining are represented by

a 3-element Kelvin model. Poisson's ratio is independent of time.

10.3   ANALYSIS OF ROCK-LINING-TIME INTERACTION OF A CIRCULAR

TUNNEL UNDER INITIAL HYDROSTATIC STRESS COMPONENT, P_o

10.3.1   Summary of the Elastic Solutions of Rock-Lining Interaction

Since the correspondence principle will be adopted to convert the elastic solution

of the problem to its correspondent of time-dependent solution, the elastic solution of the

problem, which can be found in Yuen (1979), is summarized in this section.

(1)   Expression for the lining pressure, P_l

The lining pressure is defined as the radial stress at the rock-lining interface. For

the hydrostatic stress component, P_l is independent of θ

$$P_l = \frac{P_o}{1 + C_1 C_2} \tag{10.1}$$

where P_o = the initial hydrostatic stress component

$$P_o = \frac{P_h + P_v}{2}$$

P_h, P_v = the initial stresses in the horizontal and vertical directions

respectively

$$C_1 = \frac{E_R}{E_l}\frac{(1+v_l)}{(1+v_R)} = \frac{G_R}{G_l}$$ (10.2a)

$$C_2 = \frac{(1-2v_l)R_2^2 + R_1^2}{R_2^2 - R_1^2}$$ (10.2b)

v_R, v_l = Poisson's ratios for the rock mass and lining respectively

E_R, E_l = Young's moduli for the rock mass and lining respectively

G_R, G_l = the shear moduli for the rock mass and lining respectively

R_1, R_2 = the inner and outer radii of the lining respectively

The subscripts R and l refer to rock and lining respectively.

(2) Stress distribution in rock mass

The final radial stress in the rock mass after elastic rock-lining interaction is

$$\sigma_{rRh} = P_o\left(1 - \frac{R_2^2}{r^2}\right) + P_l\left(\frac{R_2^2}{r^2}\right)$$ (10.3a)

or

$$\sigma_{rRh} = P_o\left(1 - \frac{C_1 C_2}{1 + C_1 C_2}\frac{R_2^2}{r^2}\right)$$ (10.3b)

Where r is the distance from the point of interest to the center of the tunnel and the subscript h refers to the hydrostatic component. The expression for the tangential stress is

$$\sigma_{\theta Rh} = P_o \left(1 + \frac{R_2^2}{r^2} \right) - P_i \left(\frac{R_2^2}{r^2} \right) \tag{10.4a}$$

or

$$\sigma_{\theta Rh} = P_o \left(1 + \frac{C_1 C_2}{1 + C_1 C_2} \frac{R_2^2}{r^2} \right) \tag{10.4b}$$

while the shear stress is zero

$$\tau_{r\theta Rh} = 0 \tag{10.5}$$

(3) **Deformation in rock mass**

(i) **radial displacement,** u_{Rh}

$$u_{Rh} = \frac{(P_o - P_i)(1 + \nu_R)}{E_R} \frac{R_2^2}{r} \tag{10.6}$$

(ii) **tangential displacement,** v_{Rh}

$$v_{Rh} = 0 \tag{10.7}$$

(4) **equivalent moment and thrust in the lining**

The expression for the equivalent moment per unit length in the lining is

$$M_h = -\frac{P_l}{12}(R_2 - R_1)^2 \qquad (10.8a)$$

or

$$M_h = -\frac{P_o}{12(1 + C_1 C_2)}(R_2 - R_1)^2 \qquad (10.8b)$$

The expression for the equivalent thrust per unit length in the lining is

$$N_h = \frac{P_l(3R_2^2 + R_1^2)}{2(R_2 + R_1)} \qquad (10.9a)$$

or

$$N_h = \frac{P_o}{(1 + C_1 C_2)} \frac{(3R_2^2 + R_1^2)}{2(R_2 + R_1)} \qquad (10.9b)$$

(5)   Stresses in the lining

The radial and tangential stresses in the lining respectively are

$$\sigma_{rlh} = \frac{P_l(1 - \dfrac{R_1^2}{r^2})}{(1 - \dfrac{R_1^2}{R_2^2})} \qquad (10.10)$$

and

$$\sigma_{\theta lh} = \frac{P_l(1 + \frac{R_1^2}{r^2})}{(1 - \frac{R_1^2}{R_2^2})}$$

(10.11)

(i)   at the outer fibre $r = R_2$

$$\sigma_{rlh}(r=R_2) = P_l$$

(10.12a)

$$\sigma_{\theta lh}(r=R_2) = P_l \cdot \frac{R_1^2 + R_2^2}{R_2^2 - R_1^2}$$

(10.12b)

(ii)   at the inner fibre $r = R_1$

$$\sigma_{rlh}(r=R_1) = 0$$

(10.13a)

$$\sigma_{\theta lh}(r=R_1) = \frac{2P_l R_2^2}{R_2^2 - R_1^2}$$

(10.13b)

(6)   Deformation in lining

(i)   radial displacement

$$u_{lh} = \frac{C_2 (1 + v_l) r}{E_l} P_l$$

(10.14)

where

$$C_2 = \frac{1 - 2\nu_l + \left(\dfrac{R_1}{r}\right)^2}{1 - \left(\dfrac{R_1}{R_2}\right)^2} \tag{10.15}$$

(ii)   tangential displacement

$$v_{lh} = 0 \tag{10.16}$$

10.3.2   Viscoelastic Solution for Rock-Lining-Time Interaction Problem

The elastic solution for the rock-lining interaction problem, summarized in the previous section, is obtained for the imaginary case that the lining is installed in its place in the rock before excavation and then the initial stresses are released at the interface. Therefore, if the correspondence principle is utilized to obtain the time dependent solution, this solution will represent the imaginary case of placing the lining into the rock and instantaneously releasing the initial stresses at the interface at $t = 0$. In practice, however, the lining is installed at time $t = t_o$ after the tunnel excavation.

In this section, the correspondence principle will be used to obtain the expression for the time-dependent lining pressure assuming the lining is installed at $t_o - 0$. Then, the expression will be extended to include the case of $t_o > 0$.

From the elastic solution for rock-lining interaction under the action of hydrostatic stress component (P_o), the lining pressure is (refer to Sec. 10.3.1)

$$P_I = \frac{P_o}{1 + C_2 \dfrac{G_R}{G_I}} \qquad (10.17)$$

The associated problem in viscoelasticity can be formed using the principle of correspondence. Application of the correspondence principle to Eq. 10.17 yields the following equation:

$$\bar{P}_I = \frac{P_o}{s(1 + \dfrac{\bar{Q}_R}{\bar{P}_R} \dfrac{\bar{P}_I}{\bar{Q}_I} C_2)} \qquad (10.18)$$

where P_I is replaced by its Laplace transform $\bar{P}_I$, P_o by its Laplace transform $\dfrac{P_o}{s}$, and the elastic parameters (G_R and G_I) by the transformed operators ($\bar{P}_R$ and $\bar{Q}_R$) and ($\bar{P}_I$ and $\bar{Q}_I$) respectively as given by the following relationships:

$$G_R \rightarrow \frac{\bar{Q}_R}{2\bar{P}_R} \qquad G_I \rightarrow \frac{\bar{Q}_I}{2\bar{P}_I} \qquad (10.19)$$

(i)   for rock

The long-term time-dependent deformation of Queenston Shale is idealized by the 7-element Kelvin model shown in Figure ⸫ .. For this model,

$$\bar{P}_R = 1 + p'_{RI} s + p'_{R2} s^2 + p'_{R3} s^3 \qquad (10.20)$$

and

$$\bar{Q}_R = q'_{Ro} + q'_{RI} s + q'_{R2} s^2 + q'_{R3} s^3 \qquad (10.21)$$

Where the coefficients p'_{RI}, p'_{R2}, p'_{R3}, q'_{Ro}, q'_{RI}, q'_{R2}, and q'_{R3} can be expressed in terms of the elastic and viscoelastic parameters of the rock as follows (refer to Appendix 9A):

$$
\begin{aligned}
p'_{RI} = & (G_{RI}G_{R2}\eta_{R3} + G_{RI}G_{R3}\eta_{R2} + G_{R2}G_{R3}\eta_{RI} + G_R G_{R2}\eta_{R3} + G_R G_{R3}\eta_{R2} \\
& + G_R G_{RI}\eta_{R3} + G_R G_{R3}\eta_{RI} + G_R G_{RI}\eta_{R2} + G_R G_{R2}\eta_{RI}) \\
& / \{2(G_{RI}G_{R2}G_{R3} + G_R G_{R2}G_{R3} + G_R G_{RI}G_{R3} + G_R G_{RI}G_{R2})\}
\end{aligned}
\qquad (10.22a)
$$

$$
\begin{aligned}
p'_{R2} = & (G_{RI}\eta_{R2}\eta_{R3} + G_{R2}\eta_{RI}\eta_{R3} + G_{R3}\eta_{RI}\eta_{R2} + G_R\eta_{R2}\eta_{R3} \\
& + G_R\eta_{RI}\eta_{R3} + G_R\eta_{RI}\eta_{R2}) \\
& / \{4(G_{RI}G_{R2}G_{R3} + G_R G_{R2}G_{R3} + G_R G_{RI}G_{R3} + G_R G_{RI}G_{R2})\}
\end{aligned}
\qquad (10.22b)
$$

$$
p'_{R3} = \frac{\eta_{RI}\eta_{R2}\eta_{R3}}{8(G_{RI}G_{R2}G_{R3} + G_R G_{R2}G_{R3} + G_R G_{RI}G_{R3} + G_R G_{RI}G_{R2})}
\qquad (10.22c)
$$

$$
q'_{Ro} = \frac{2 G_R G_{RI}G_{R2}G_{R3}}{G_{RI}G_{R2}G_{R3} + G_R G_{R2}G_{R3} + G_R G_{RI}G_{R3} + G_R G_{RI}G_{R2}}
\qquad (10.23a)
$$

$$
q'_{RI} = \frac{G_R G_{RI}G_{R2}\eta_{R3} + G_R G_{RI}G_{R3}\eta_{R2} + G_R G_{R2}G_{R3}\eta_{RI}}{G_{RI}G_{R2}G_{R3} + G_R G_{R2}G_{R3} + G_R G_{RI}G_{R3} + G_R G_{RI}G_{R2}}
\qquad (10.23b)
$$

$$
q'_{R2} = \frac{G_R G_{RI}\eta_{R2}\eta_{R3} + G_R G_{R2}\eta_{RI}\eta_{R3} + G_R G_{R3}\eta_{RI}\eta_{R2}}{2(G_{RI}G_{R2}G_{R3} + G_R G_{R2}G_{R3} + G_R G_{RI}G_{R3} + G_R G_{RI}G_{R2})}
\qquad (10.23c)
$$

$$
q'_{R3} = \frac{G_r\eta_{RI}\eta_{R2}\eta_{R3}}{4(G_{RI}G_{R2}G_{R3} + G_R G_{R2}G_{R3} + G_R G_{RI}G_{R3} + G_R G_{RI}G_{R2})}
\qquad (10.23d)
$$

(b)   for lining

As mentioned at the beginning of this chapter, the concrete lining of the tunnel

is idealized in the analysis by the 3-element Kelvin model (a spring and one Kelvin unit connected in series). For this model,

$$\bar{P}_l = 1 + p'_{ll}s \qquad (10.24)$$

and

$$\bar{Q}_l = q'_{lo} + q'_{ll}s \qquad (10.25)$$

where

$$p'_{ll} = \frac{\eta_l}{2(G_l + G_k)} \qquad (10.26)$$

$$q'_{lo} = \frac{2G_lG_k}{G_l + G_k} \qquad (10.27a)$$

$$q'_{ll} = \frac{G_l\eta_l}{G_l + G_k} \qquad (10.27b)$$

Substitution of Eqs. 10.20, 10.21, 10.24 and 10.25 into Eq. 10.18 leads to the following expression:

$$\bar{P}_l = \frac{P_c}{s\left(1 + \frac{(q'_{Ro} + q'_{R1}s + q'_{R2}s^2 + q'_{R3}s^3)(1 + p'_{ll}s)C_2}{(1 + p'_{R1}s + p'_{R2}s^2 + p'_{R3}s^3)(q'_{lo} + q'_{ll}s)}\right)} \qquad (10.28)$$

After arrangement, Eq. 10.28 can be written in the following form:

$$\bar{F}_l = \frac{p_o}{b_4} \frac{(a_4s^4 + a_3s^3 + a_2s^2 + a_1s + a_o)}{s(s^4 + b_3s^3 + b_2s^2 + b_1s + b_o)} \qquad (10.29)$$

where

$$a_o = q'_{lo} \tag{10.30a}$$

$$a_1 = p'_{RI}q'_{lo} + q'_{II} \tag{10.30b}$$

$$a_2 = p'_{R2}q'_{lo} + p'_{RI}q'_{II} \tag{10.30c}$$

$$a_3 = p'_{R3}q'_{lo} + p'_{R2}q'_{II} \tag{10.30d}$$

$$a_4 = p'_{R3}q'_{II} \tag{10.30e}$$

$$b_o = \frac{(q'_{lo} + q'_{Ro}C_2)}{b_4} \tag{10.31a}$$

$$b_1 = \frac{(p'_{RI}q'_{lo} + q'_{II} + q'_{RI}C_2 + q'_{Ro}p'_{II}C_2)}{b_4} \tag{10.31b}$$

$$b_2 = \frac{(p'_{R2}q'_{lo} + p'_{RI}q'_{II} + q'_{R2}C_2 + q'_{RI}p'_{II}C_2)}{b_4} \tag{10.31c}$$

$$b_3 = \frac{(p'_{R3}q'_{lo} + p'_{R2}q'_{II} + q'_{R3}C_2 + q'_{R2}p'_{II}C_2)}{b_4} \tag{10.31d}$$

$$b_4 = p'_{R3}q'_{II} + q'_{R3}p'_{II}C_2 \tag{10.31e}$$

If $-\alpha_1$, $-\alpha_2$, $-\alpha_3$, and $-\alpha_4$ are the roots of the following polynomial of the transform variable s :

$$s^4 + b_3s^3 + b_2s^2 + b_1s + b_o = 0$$

Eq. 10.29 can take the following form:

$$\bar{P}_l = \frac{P_o}{b_4} \frac{a_4 s^4 + a_3 s^3 + a_2 s^2 + a_1 s + a_o}{s(s+\alpha_1)(s+\alpha_2)(s+\alpha_3)(s+\alpha_4)} \tag{10.32a}$$

where

$$\alpha_1 = \frac{Z_5}{\sqrt[4]{Z_4}} \tag{10.32b}$$

$$\alpha_2 = \frac{Z_6}{\sqrt[4]{Z_4}} \tag{10.32c}$$

$$\alpha_3 = \frac{Z_7}{\sqrt[4]{Z_4}} \tag{10.32d}$$

$$\alpha_4 = \frac{Z_8}{\sqrt[4]{Z_4}} \tag{10.32e}$$

$$
\begin{aligned}
Z_1 = \sqrt{3} \big(& 6 b_1^2 b_3^2 b_o + 4 b_1^3 b_3^3 + 128 b_o^2 b_2^2 - 16 b_o b_2^4 + 4 b_1^2 b_2^3 + 27 b_o^2 b_3^4 \\
& - b_1^2 b_3^2 b_2^2 + 192 b_1 b_3 b_o^2 - 18 b_2 b_1^3 b_3 - 144 b_o b_2 b_1^2 - 144 b_o^2 b_2 b_3^2 \\
& + 4 b_o b_3^2 b_2^3 - 256 b_o^3 + 27 b_1^4 + 80 b_1 b_3 b_o b_2^2 - 18 b_2 b_1 b_3^3 b_o \big)^{\frac{1}{2}}
\end{aligned}
\tag{10.32f}
$$

$$Z_2 = -\frac{b_2 b_1 b_3}{6} - \frac{4 b_o b_2}{3} + \frac{b_1^2}{2} + \frac{b_o b_3^2}{2} + \frac{b_2^3}{27} - \frac{Z_1}{18} \tag{10.32g}$$

$$Z_3 = -\frac{b_2 b_1 b_3}{6} - \frac{4 b_o b_2}{3} + \frac{b_1^2}{2} + \frac{b_o b_3^2}{2} + \frac{b_2^3}{27} + \frac{Z_1}{18} \tag{10.32h}$$

$$Z_4 = 3 b_3^2 - 8 b_2 + 12 \sqrt[3]{Z_3} + 12 \sqrt[3]{Z_2} \tag{10.32i}$$

$$Z_5 = \frac{b_3}{4} - \frac{\sqrt{3}\sqrt{Z_4}}{12} - \frac{\sqrt{6}}{12}\Big(3b_3^2\sqrt{Z_4} - 8b_2\sqrt{Z_4} - 6\sqrt[3]{Z_3}\sqrt{Z_4}$$

$$-6\sqrt[3]{Z_2}\sqrt{Z_4} - 3\sqrt{3}b_3^3 + 12\sqrt{3}b_3 b_2 - 24\sqrt{3}b_1\Big)^{\frac{1}{2}}$$

(10.32j)

$$Z_6 = \frac{b_3}{4} - \frac{\sqrt{3}\sqrt{Z_4}}{12} + \frac{\sqrt{6}}{12}\Big(3b_3^2\sqrt{Z_4} - 8b_2\sqrt{Z_4} - 6\sqrt[3]{Z_3}\sqrt{Z_4}$$

$$-6\sqrt[3]{Z_2}\sqrt{Z_4} - 3\sqrt{3}b_3^3 + 12\sqrt{3}b_3 b_2 - 24\sqrt{3}b_1\Big)^{\frac{1}{2}}$$

(10.32k)

$$Z_7 = \frac{b_3}{4} + \frac{\sqrt{3}\sqrt{Z_4}}{12} - \frac{\sqrt{6}}{12}\Big(3b_3^2\sqrt{Z_4} - 8b_2\sqrt{Z_4} - 6\sqrt[3]{Z_3}\sqrt{Z_4}$$

$$-6\sqrt[3]{Z_2}\sqrt{Z_4} + 3\sqrt{3}b_3^3 - 12\sqrt{3}b_3 b_2 + 24\sqrt{3}b_1\Big)^{\frac{1}{2}}$$

(10.32l)

$$Z_8 = \frac{b_3}{4} + \frac{\sqrt{3}\sqrt{Z_4}}{12} + \frac{\sqrt{6}}{12}\Big(3b_3^2\sqrt{Z_4} - 8b_2\sqrt{Z_4} - 6\sqrt[3]{Z_3}\sqrt{Z_4}$$

$$-6\sqrt[3]{Z_2}\sqrt{Z_4} + 3\sqrt{3}b_3^3 - 12\sqrt{3}b_3 b_2 + 24\sqrt{3}b_1\Big)^{\frac{1}{2}}$$

(10.32m)

After partial fractions, Eq. 10.32a becomes

$$\bar{P}_I = \frac{P_o}{b_4}\left(\frac{A_o}{s} + \frac{A_1}{(s+\alpha_1)} + \frac{A_2}{(s+\alpha_2)} + \frac{A_3}{(s+\alpha_3)} + \frac{A_4}{(s+\alpha_4)}\right)$$

(10.33)

A_o, A_1, A_2, A_3, and A_4 are determined by equating the coefficients of s in the

numerators of Eqs. 10.32a and 10.33:

$$A_o = \frac{a_o}{\alpha_1\alpha_2\alpha_3\alpha_4}$$

(10.34a)

$$A_1 = -\frac{a_4\alpha_1^4 - c_3\alpha_1^3 + a_2\alpha_1^2 - a_1\alpha_1 + a_0}{\alpha_1(\alpha_2 - \alpha_1)(\alpha_3 - \alpha_1)(\alpha_4 - \alpha_1)} \qquad (10.34b)$$

$$A_2 = -\frac{a_4\alpha_2^4 - a_3\alpha_2^3 + a_2\alpha_2^2 - a_1\alpha_2 + a_0}{\alpha_2(\alpha_1 - \alpha_2)(\alpha_3 - \alpha_2)(\alpha_4 - \alpha_2)} \qquad (10.34c)$$

$$A_3 = -\frac{a_4\alpha_3^4 - a_3\alpha_3^3 + a_2\alpha_3^2 - a_1\alpha_3 + a_0}{\alpha_3(\alpha_1 - \alpha_3)(\alpha_2 - \alpha_3)(\alpha_4 - \alpha_3)} \qquad (10.34d)$$

$$A_4 = -\frac{a_4\alpha_4^4 - a_3\alpha_4^3 + a_2\alpha_4^2 - a_1\alpha_4 + a_0}{\alpha_4(\alpha_1 - \alpha_4)(\alpha_2 - \alpha_4)(\alpha_3 - \alpha_4)} \qquad (10.34e)$$

Inverse transform of Eq. 10.33 yields

$$p_l(t) = \frac{p_o}{b_4}\left(A_o + A_1 e^{-\alpha_1 t} + A_2 e^{-\alpha_2 t} + A_3 e^{-\alpha_3 t} + A_4 e^{-\alpha_4 t}\right) \qquad (10.35)$$

Eq. 10.35 can also be expressed in the following form:

$$p_l(t) = \frac{p_o}{b_4}\left(A_o + A_1 + A_2 + A_3 + A_4 - A_1(1 - e^{-\alpha_1 t}) - A_2(1 - e^{-\alpha_2 t})\right.$$
$$\left. - A_3(1 - e^{-\alpha_3 t}) - A_4(1 - e^{-\alpha_4 t})\right) \qquad (10.36)$$

From Eq. 10.36, it can be seen that $A_o + A_1 + A_2 + A_3 + A_4$ is a term related to the time-independent lining pressure and $A_1(1 - e^{-\alpha_1 t})$ to $A_4(1 - e^{-\alpha_4 t})$ are terms related to the time-dependent lining pressure. The sum of the coefficients A_1 to A_4 controls the final time-dependent lining pressure. α_1 to α_4 are parameters governing the rate at which the pressure builds up.

Equation 10.36 represents the lining pressure-time relationship for the imaginary case of installing the lining into the viscoelastic rock and instantaneously releasing the initial hydrostatic component of stress (P_o) at the interface. If the lining is installed after time $t = t_o$ after the excavation of the tunnel, the only relevant parts in Eq. 10.36 are the time-dependent terms $A_1(1-e^{-\alpha_1 t'})$ to $A_4(1-e^{-\alpha_4 t'})$. These terms being derived from the imaginary case do not give the actual magnitude of the lining pressure but they do give the form of the expression of the rate of stress built-up.

Now, let the final lining pressure equal to P_{om}. The time-dependent lining pressure can be expressed by the following form:

$$P_L(t') = \frac{P_{om}}{A_s}\left[A_1(1-e^{-\alpha_1 t'}) + A_2(1-e^{-\alpha_2 t'}) + A_3(1-e^{-\alpha_3 t'}) + A_4(1-e^{-\alpha_4 t'})\right] \qquad (10.37)$$

where $A_s \quad = A_1 + A_2 + A_3 + A_4$

$t' \quad$ = new time variable

$\quad = t - t_o$

When $t' = 0$, all the terms in Eq. 10.37 vanish resulting in $P_L(0) - 0$. When $t' - \infty$,

$P_L(\infty) = P_{om}$.

By examining the time function in Eq. 10.37 using numerical study and reasonable ranges of parameters for the lining and the rock, the following observations are made: (a) α_2, α_3, and α_4 are much higher than α_1, and (b) the summation of the terms of α_2, α_3, and α_4 vanish after few days and only the term of α_1 controls the rate

of pressure built up behind the lining. Similar observations were made by Yuen (1979)

when he analyzed the problem using 3-element Kelvin model for the rock mass.

Therefore, for practical considerations, it is convenient to consider only the term of α_1

in the time function controlling the rate of pressure built up. Therefore, the expression

for the time-dependent lining pressure becomes

$$P_l(t) = P_{om} (1 - e^{\alpha t}) \tag{10.38}$$

where α is α_1 which is defined by Eq. 10.32b. It should be noted that α is a function

of all the model parameters of lining and rock and lining geometry and therefore the

approximation does not lead to loss of any important features of the solution.

The final lining pressure (P_{om}) can be determined from the condition of continuity

of deformation at the interface. The condition of continuity of deformation is that the

radial deformation of the lining at the interface must be equal to the free deformation of

the rock at the time interval from t_o to $t(t)$ plus the radial deformation of the rock due

to the reaction lining pressure (refer to Fig. 10.2), i.e.

$$u_{lh}(R_2, t) = u_{Rh}(R_2, t) - u_{Rh}(R_2, t_o) + u_{Rlh}(R_2, t) \tag{10.39}$$

The term in the left side of Eq. 10.39, $u_{lh}(R_2, t)$, represents the radial deformation of the

lining at the interface at time t after the installation of the lining. The first two terms

in the right side of Eq. 10.39, $u_{Rh}(R_2, t) - u_{Rh}(R_2, t_o)$, represent the free deformation of the

rock at the interface from the time of installation of the lining, t_o, till the time t. The

term $u_{Rlh}(R_2, t)$ represents the radial deformation of the rock at the interface due to the

reactive lining pressure.

(a) **Free deformation of rock at time (t)**

The free deformation of the rock is equal to the free elastic deformation multiplied by the time function $J_R(t)$ (refer to the derivation in Chapter 9). Therefore, at the interface, the free deformation of the rock after time t from the excavation of the tunnel is

$$u_{Rh}(R_2,\ t) = \frac{P_o(1+v_R)R_2}{E_R} J_R(t) \tag{10.40}$$

where

$$J_R(t) = 1 + \phi_{R1}(1-e^{-\lambda_{R1}t}) + \phi_{R2}(1-e^{-\lambda_{R2}t}) + \phi_{R3}(1-e^{-\lambda_{R3}t})$$

(b) **Free deformation of rock at time (t_o)**

The free deformation of the rock at the interface at the time of installation of the lining (t_o) can be obtained by substituting t_o for t in Eq. 10.40:

$$u_{Rh}(R_2,\ t_o) = \frac{P_o(1+v_R)R_2}{E_R} J_R(t_o) \tag{10.41}$$

(c) **Free deformation of rock for time interval from t_o to t**

The free deformation of the rock, at the interface for the time interval between the time of installation of the lining (t_o) and the time (t), equals to the difference

between Eq. 10.40 and Eq. 10.41.

(d)   **Radial deformation of rock due to reactive lining pressure $(P_r(t))$**

The reactive lining pressure $P_r(t)$ is zero at the time of installation of lining ($t' = 0$

or $t = t_o$) and it is monotonically increasing function with time (Eq. 10.38). At infinity,

the value of the lining pressure is $p_r(\infty) = P_{om}$. Since the reactive lining pressure is a

function of time and the time function $J_R(t)$ (in Eq. 10.40) relating the elastic

deformation to the viscoelastic deformation has been derived for a constant applie

pressure, the radial deformation of rock under the action of reactive pressure can not be

obtained directly by using this time function. Therefore, the deformation of the rock for

this case should be evaluated by the use of the hereditary integral which takes into

consideration the history of the applied load (Flügge 1975). Appendix 10A contains the

complete steps of derivation of the deformation of the rock using this technique. The

resulting radial deformation of the rock at the interface due to the reactive lining pressure

is

$$u_{RLh}(R_2, t') = \frac{-(1+\nu_R)R_2}{E_R} P_{om} R_h(t') \qquad (10.42)$$

where

$$R_h(r) = (1 - e^{-\alpha r}) - \frac{\phi_{RI} \lambda_{RI} e^{-\lambda_{RI} r}}{\alpha - \lambda_{RI}} (1 - e^{-(\alpha - \lambda_{RI}) r}) - \frac{\phi_{R2} \lambda_{R2} e^{-\lambda_{R2} r}}{\alpha - \lambda_{R2}} (1 - e^{-(\alpha - \lambda_{R2}) r})$$

$$- \frac{\phi_{R3} \lambda_{R3} e^{-\lambda_{R3} r}}{\alpha - \lambda_{R3}} (1 - e^{-(\alpha - \lambda_{R3}) r}) + \phi_{RI}(1 - e^{-\lambda_{RI} r}) + \phi_{R2}(1 - e^{-\lambda_{R2} r}) + \phi_{R3}(1 - e^{-\lambda_{R3} r})$$

(10.43)

At infinity, $R_h(\infty) = 1 + \phi_{RI} + \phi_{R2} + \phi_{R3}$

(e) Radial deformation of lining

Since the lining is subjected to the monotonically increasing lining pressure $p_i(r)$

(Eq. 10.38), the evaluation of the radial deformation requires the adoption of the hereditary integral as shown in Appendix 10A. The resulting radial deformation of the lining at the interface is

$$u_{lh}(R_2, r) = \frac{C_2 (1 + v_l) R_2}{E_l} P_{om} L_h(r)$$

(10.44)

where

$$L_h(r) = (1 - e^{-\alpha r}) - \frac{\phi_l e^{-\lambda_l r}}{\alpha - \lambda_l} (1 - e^{-(\alpha - \lambda_l) r}) + \phi_l(1 - e^{-\lambda_l r})$$

(10.45)

At infinity, $L_h(\infty) = 1 + \phi_l$

Continuity at the interface:

The continuity condition of radial displacement at the interface is given by Eq. 10.39. Substituting Eqs. 10.40, 10.41, 10.42 and 10.44 into Eq. 10.39 leads to the following relationship:

$$\frac{C_2(1+\nu_l)R_2}{E_l} P_{om} L_h(t') = \frac{(1+\nu_R)R_2 P_o}{E_R}\left[\phi_{RI}(e^{\lambda_{RI}t'_o} - e^{-\lambda_{RI}t'}) + \right.$$

$$\left. \phi_{R2}(e^{\lambda_{R2}t'_o} - e^{-\lambda_{R2}t'}) + \phi_{R3}(e^{-\lambda_{R3}t'_o} - e^{-\lambda_3 t'})\right] - \frac{(1+\nu_R)R_2}{E_R} P_{om} R_h(t') \tag{10.46}$$

After arrangement, Eq. 10.46 becomes

$$P_{om}\left[\left(\frac{E_R}{1+\nu_R}\frac{1+\nu_l}{E_l}C_2\right)L_h(t') + R_h(t')\right] = P_o\left[\phi_{RI}(e^{\lambda_{RI}t'_o} - e^{-\lambda_{RI}t'}) + \right.$$

$$\left. \phi_{R2}(e^{\lambda_{R2}t'_o} - e^{-\lambda_{R2}t'}) + \phi_{R3}(e^{-\lambda_{R3}t'_o} - e^{-\lambda_3 t'})\right] \tag{10.47}$$

Therefore,

$$P_{om} = \frac{\phi_{RI}(e^{\lambda_{RI}t'_o} - e^{-\lambda_{RI}t'}) + \phi_{R2}(e^{\lambda_{R2}t'_o} - e^{-\lambda_{R2}t'}) + \phi_{R3}(e^{-\lambda_{R3}t'_o} - e^{-\lambda_3 t'})}{C_1 C_2 L_h(t') + R_h(t')} P_o \tag{10.48}$$

Equation 10.48 should be satisfied for the time interval from ($t = t_o$ or $t' = 0$) to ($t = \infty$ or

$t' = \infty$). A direct relationship, which is independent of the time variables t and t', between the final reactive pressure P_{om} and the initial hydrostatic stress component P_o can be obtained by evaluating Eq. 10.48 at infinity

$$P_{om} = \frac{\phi_{RI}e^{-\lambda_{RI}t'_o} + \phi_{R2}e^{-\lambda_{R2}t'_o} + \phi_{R3}e^{-\lambda_{R3}t'_o}}{C_1 C_2(1+\phi_l) + (1+\phi_{RI}+\phi_{R2}+\phi_{R3})} P_o \tag{10.49a}$$

For perfectly rigid lining, $E_l \rightarrow \infty$. Therefore, $C_1 \rightarrow 0$ and the expression for P_{om} becomes

$$P_{rm} = \frac{\phi_{R1}e^{-\lambda_{R1}t_o} + \phi_{R2}e^{-\lambda_{R2}t_o} + \phi_{R3}e^{-\lambda_{R3}t_o}}{(1+\phi_{R1}+\phi_{R2}+\phi_{R3})} P_o \qquad (10.49b)$$

The expression for the lining pressure $P_l(t')$ is

$$P_l(t') = P_{om}(1-e^{-\kappa t'}) \qquad (10.50)$$

10.4 ANALYSIS OF ROCK-LINING-TIME INTERACTION OF A CIRCULAR TUNNEL UNDER INITIAL DISTORTIONAL STRESS COMPONENT, Q_o

10.4.1 Summary of the Elastic Solution of Rock-Lining Interaction

(1) Expression for the lining pressures

(A) no slip at the Interface

For no slip case, there are normal and tangential reactive pressures at the interface. The expression for the reactive normal pressure at the interface $(r=R_2)$ is

$$S_{nl}(\theta) = S_{nl}\cos 2\theta \qquad (10.51)$$

The expression for the reactive tangential pressure at the interface $(r=R_2)$ is

$$S_{tl}(\theta) = -S_{tl}\sin 2\theta \qquad (10.52)$$

where S_{nl} and S_{tl} are the maximum normal and tangential stresses occurring at the rock-lining interface at $\theta = 0°$ and $\theta = 45°$ respectively. θ is the angle measured from the springline (refer to Fig. 10.2). The expression for the maximum radial lining pressure S_{nl} is

$$S_{nl} = \frac{3(3-4v_R)Q_o}{C_3\left(K_e\bar{d}+\bar{C}\right) + (5-6v_R) + K_e(4-6v_R)}$$

(10.53)

where

Q_o = the initial deviatoric stress component = $\dfrac{P_h - P_v}{2}$

P_h, P_v = the initial stresses in the horizontal and vertical directions respectively

$$C_3 = \frac{E_R}{E_l}\frac{1+v_l}{1+v_R}\frac{1}{(1-h)^3} = \frac{G_R}{G_l}\frac{1}{(1-h)^3}$$

(10.54a)

$$K_e = \frac{S_u}{S_{nl}} = \frac{1-C_3(\bar{d}-\bar{C})}{1+C_3(\bar{C}_1-\bar{d})}$$

(10.54e)

$$\bar{C} = h^3(5-6v_l) + h^2(9-6v_l) + h(15-18v_l) + (3-2v_l)$$

(10.54c)

$$\bar{d} = h^3(4-6v_l) + h^2(12-6v_l) - 6v_l h + 2v_l$$

(10.54d)

$$\bar{C}_1 = h^3(5-6v_l) + h^2(9-6v_l) - h(9-6v_l) + (3-2v_l)$$

(10.54e)

$$h = (\frac{R_1}{R_2})^2$$

(10.54f)

The maximum tangential lining pressure S_u at 45° is

$$S_{tl} = K_e \cdot S_{nl} \tag{10.55}$$

(B) Full Slip at the Interface

Expression for the lining pressures

For full slip case, only the normal reactive pressure at the interface exists while the tangential reactive pressure is zero

$$S_{nl}(\theta) = S_{nl} \cos 2\theta \tag{10.56}$$

$$S_{tl}(\theta) = 0 \tag{10.57}$$

where S_{nl} is the maximum radial lining pressure at $\theta = 0°$ and is given by

$$S_{nl} = \frac{3Q_o(3 - 4v_R)}{C_3\bar{C} + (5 - 6v_R)} \tag{10.58}$$

(2) Deformation in lining

The expression for the elastic radial displacement of the lining is

At $r = R_2$

$$u_{ld,r-R_2} = \frac{(1 + v_l)R_2}{3E_l(1 - h)^3} [\bar{c}S_{nl} + \bar{d}S_{tl}] \cos 2\theta \tag{10.59a}$$

At $r = R_1$

$$u_{ld_{r-R_1}} = \frac{(1+v_l)}{E_l(1-h)^3} (\bar{A}'S_{nl} + \bar{B}'S_{ll}) \cos 2\theta \qquad (10.59b)$$

where

$$\bar{A}' = (2h^2+h+1)R_1 - h^2(h+3)\frac{R_2^4}{3R_1^3} + 2h(h^2+h+2)\frac{R_2^2}{R_1}$$

$$-v_l[2h(h^2+h+2)\frac{R_2^2}{R_1} + \frac{2}{3}(3h+1)\frac{R_1^3}{R_2^2}] \qquad (10.60a)$$

$$\bar{B}' = 2h^3R_1 - \frac{2}{3}h^3\frac{R_2^4}{R_1^3} + 2h^2(h+1)\frac{R_2^2}{R_1}$$

$$-v_l[2h^2(h+1)\frac{R_2^2}{R_1} + \frac{2}{3}(3h-1)\frac{R_1^3}{R_2^2}] \qquad (10.60b)$$

The expression for the elastic circumferential displacement of the lining is

At $r = R_2$

$$v_{ld_{r-R_2}} = \frac{-(1+v_l)R_2}{3E_l(1-h)^3} [\bar{d}S_{nl} + \bar{c}_1 S_{ll}] \sin 2\theta \qquad (10.61a)$$

At $r = R_1$

$$v_{ld_{r-R_1}} = \frac{-2(1+v_l)}{E_l(1-h)^3} [\bar{A}''S_{nl} + \bar{B}''S_{ll}] \sin 2\theta \qquad (10.61b)$$

where

$$\bar{A}'' = (2h^2+h+1)\frac{R_1}{2} - (3-2v_l)(3h+1)\frac{R_1^3}{6R_2^2} + h^2(h+3)\frac{R_2^4}{6R_1^3}$$

$$+ (1-2v_l)h(h^2+h+2)\frac{R_2^2}{2R_1}$$

$$(10.62a)$$

$$\bar{B}'' = h^2R_1 - (3-2v_l)(3h-1)\frac{R_1^3}{6R_2^2} + h^3\frac{R_2^4}{3R_1^3}$$

$$+ (1-2v_l)h^2(h+1)\frac{R_2^2}{2R_1}$$

$$(10.62b)$$

(3) Stresses in lining

The radial, tangential and shear stresses in the lining are

$$\sigma_{rld} = -(2A + \frac{6C}{r^4} + \frac{4D}{r^2})\cos2\theta \qquad (10.63)$$

$$\sigma_{\theta ld} = (2A + 12Br^2 + \frac{6C}{r^4})\cos2\theta \qquad (10.64)$$

$$\sigma_{r\theta ld} = (2A + 6Br^2 - \frac{6C}{r^4} - \frac{2D}{r^2})\sin2\theta \qquad (10.65)$$

where

$$A = \frac{1}{(1-h)^3}[-\frac{S_{nl}}{2}(2h^2+h+1) - S_{tl}h^2] \qquad (10.66a)$$

$$B = \frac{1}{(1-h)^3}[\frac{S_{nl}}{6R_2^2}(3h+1) + \frac{S_{tl}}{6R_2^2}(3h-1)] \qquad (10.66b)$$

$$C = \frac{1}{(1-h)^3} \left[-\frac{S_{n'} h^2}{6} (h+3) R_2^4 - \frac{S_{d} h^3 R_2^4}{3} \right] \qquad (10.66c)$$

$$D = \frac{1}{(1-h)^3} \left[\frac{S_{n'}}{2} h (h^2 + h + 2) R_2^2 + \frac{S_{d}}{2} h^2 (h+1) R_2^2 \right] \qquad (10.66d)$$

The tangential stress at $r = R_1$ is

$$\sigma_{\theta_{ld\,r-R_1}} = (2A + 12BR_1^2 + \frac{6C}{R_1^4}) \cos 2\theta \qquad (10.67a)$$

and at $r = R_2$ is

$$\sigma_{\theta_{ld\,r-R_2}} = (2A + 12BR_2^2 + \frac{6C}{R_2^4}) \cos 2\theta \qquad (10.67b)$$

(4)   Equivalent moments and thrusts

The equivalent moment and thrusts per unit length in the lining are

$$M_d = (\sigma_{\theta_{ld\,r-R_2}} - \sigma_{\theta_{ld\,r-R_1}}) \left(\frac{R_2 - R_1}{12} \right)^2 \qquad (10.68)$$

$$N_d = (\sigma_{\theta_{ld\,r-R_2}} + \sigma_{\theta_{ld\,r-R_1}}) \frac{(R_2 - R_1)}{2} \qquad (10.69)$$

(5)   Deformation in rock mass

The free radial and tangential displacements due to the removal of the initial deviatoric stress component respectively are

$$u_{Rd} = \frac{(1+v_R)}{E_R}[-\frac{Q_oR_2^4}{r^3} + \frac{4Q_oR_2^2}{r}(1-v_R)]\cos2\theta \qquad (10.70a)$$

$$v_{Rd} = -\frac{(1+v_R)}{E_R}[\frac{Q_oR_2^4}{r^3} + \frac{2Q_oR_2^2}{r}(1-2v_R)]\sin2\theta \qquad (10.70b)$$

The radial and tangential displacements of the rock mass due to the reactive lining pressure respectively are

$$u_{Rld} = \frac{(1+v_R)}{E_R}[(2S_{tl}+S_{nl})\frac{R_2^4}{3r^3} - 2(1-2v)(S_{nl}+S_{tl})\cdot\frac{R_2^2}{r}]\cos2\theta \qquad (10.71a)$$

$$v_{Rld} = \frac{(1+v_R)r}{E_R}[(S_{tl}+2S_{nl})\frac{R_2^4}{3r^4} + (1-2v)(S_{nl}+S_{tl})\frac{R_2^2}{r^2}]\sin2\theta \qquad (10.71b)$$

At $r = R_2$

$$u_{Rd_{r-R_2}} = \frac{1+v_R}{E_R}[Q_oR_2(3-4v_R)]\cos2\theta \qquad (10.72a)$$

$$v_{Rd_{r-R_2}} = -\frac{(1+v_R)}{E_R}[Q_oR_2(3-4v_R)]\sin2\theta \qquad (10.72b)$$

$$u_{Rld_{r-R_2}} = -\frac{(1+v_R)R_2}{3E_R}[(S_{nl}(5-6v_R)+S_{tl}(4-6v_R)]\cos2\theta \qquad (10.72a)$$

$$v_{Rld_{r-R_2}} = \frac{(1+v_R)R_2}{3E_R}[(S_{nl}(4-6v_R)+S_{tl}(5-6v_e)]\sin2\theta \qquad (10.72d)$$

The final displacements are obtained by combining the free displacement and the displacement from the reactive pressure.

(6)   Stresses in rock mass

The elastic radial, tangential and shear stresses in the rock mass due to the release of the initial deviatoric stress component respectively are

$$\sigma_{rRd} = [Q_o + \frac{R_2^4}{r^4}(3Q_o - 2S_{tl} - S_{nl}) - \frac{R_2^2}{r^2}(4Q_o - 2S_{tl} - 2S_{nl})]\cos 2\theta \qquad (10.73)$$

$$\sigma_{\theta Rd} = -[Q_o + \frac{R_2^4}{r^4}(3Q_o - 2S_{tl} - S_{nl})]\cos 2\theta \qquad (10.74)$$

$$\tau_{r\theta Rd} = -[Q_o - \frac{R_2^4}{r^4}(3Q_o - 2S_{tl} - S_{nl}) + \frac{R_2^2}{r^2}(2Q_o - S_{nl} - S_{tl})]\sin 2\theta \qquad (10.75)$$

10.4.2   Viscoelastic Solution for Rock-Lining-Time Interaction Problem

In this section, two cases at the rock-lining interface will be considered:

(a) case of no-slip at the interface, and (b) case of full slip at the interface.

(A)   Case of No Slip at the Interface

From the elastic solution for rock-lining interaction under the action of deviatoric stress component (P_o), the maximum radial lining pressure at $\theta = 0°$ is (refer to Sec. 10.4.1)

$$S_{nl} = \frac{3(3 - 4v_R) Q_o}{C_3(K_c \bar{d} + \bar{C}) + (5 - 6v_R) + K_c(4 - 6v_R)} \qquad (10.76)$$

where

$$K_e = \frac{S_{tl}}{S_{nl}} = \frac{1 - C_3(\bar{d} - \bar{C})}{1 + C_3(\bar{C}_1 - \bar{d})}$$

Putting

$$J_1 = 3(3 - 4v_R) \qquad\qquad (10.77a)$$

$$J_2 = 5 - 6v_R + K_e(4 - 6v_R) \qquad\qquad (10.77b)$$

$$J_3 = \frac{K_e\bar{d} + \bar{C}}{(1 - h)^3} \qquad\qquad (10.77c)$$

Eq. 10.76 becomes

$$S_{nl} = \frac{Q_o J_1}{J_2 + \dfrac{G_R}{G_l} J_3} \qquad\qquad (10.78)$$

Since v_R and v_l are constants with time, J_1, J_2 and J_3 are, therefore, independent of time. The associated problem in viscoelasticity can be formed using the principle of correspondence. Application of the correspondence principle to Eq. 10.78 yields the following expression:

$$\bar{S}_{nl} = \frac{Q_o J_1}{s(J_2 + \dfrac{\bar{Q}_R}{\bar{P}_R} \dfrac{\bar{P}_l}{\bar{Q}_l} J_3)} \qquad\qquad (10.79)$$

where S_{nl} is replaced by its laplace transform $\bar{S}_{nl}$, Q_o by its laplace transform $\dfrac{Q_o}{s}$, and

the elastic parameters (G_R and G_I) by the transformed operators ($\bar{P}_R$ and $\bar{Q}_R$) and ($\bar{P}_I$

and $\bar{Q}_I$) respectively as given by the following relationships:

$$G_R \rightarrow \frac{\bar{Q}_R}{2\bar{P}_R} \qquad G_I \rightarrow \frac{\bar{Q}_I}{2\bar{P}_I}$$

Putting $J_4 = \dfrac{J_3}{J_2}$, Eq. 10.79 becomes

$$\bar{S}_{nl} = \frac{Q_o J_1}{J_2 s} \left[\frac{1}{1 + \dfrac{\bar{Q}_R}{\bar{P}_R} \dfrac{\bar{P}_I}{\bar{Q}_I} J_4} \right] \tag{10.80}$$

Substitution of Eqs. 10.20, 10.21, 10.24 and 10.25 into Eq. 10.80 leads to

$$\bar{S}_{nl} = \frac{Q_o J_1}{J_2} \frac{1}{s\left(1 + \dfrac{(q'_{Ro} + q'_{RI}s + q'_{R2}s^2 + q'_{R3}s^3)(1 + p'_{II}s)}{(1 + p'_{II}s + p'_{R2}s^2 + p'_{R3}s^3)(q'_{Io} + q'_{II}s)} J_4\right)} \tag{10.81}$$

After arrangement, Eq. 10.81 can be written in the following form:

$$\bar{S}_{nl} = \frac{Q_o J_1}{J_2 e_4} \frac{(a_4 s^4 + a_3 s^3 + a_2 s^2 + a_1 s + a_o)}{s(s^4 + e_3 s^3 + e_2 s^2 + e_1 s + e_o)} \tag{10.82}$$

where

$$a_o = q'_{Io} \tag{10.83a}$$

$$a_1 = p'_{RI} q'_{Io} + q_{II} \tag{10.83b}$$

$$a_2 = p'_{R2}q'_{lo} + p'_{R1}q'_{ll} \tag{10.83c}$$

$$a_3 = p'_{R3}q'_{lo} + p'_{R2}q'_{ll} \tag{10.83d}$$

$$a_4 = p'_{R3}q'_{ll} \tag{10.83e}$$

$$e_o = \frac{(q'_{lo} + q'_{Ro}J_4)}{e_4} \tag{10.84a}$$

$$e_1 = \frac{(p'_{R1}q'_{lo} + q'_{ll} + q'_{R1}J_4 + q'_{Ro}p'_{ll}J_4)}{e_4} \tag{10.84b}$$

$$e_2 = \frac{(p'_{R2}q'_{lo} + p'_{R1}q'_{ll} + q'_{R2}J_4 + q'_{R1}p'_{ll}J_4)}{e_4} \tag{10.84c}$$

$$e_3 = \frac{(p'_{R3}q'_{lo} + p'_{R2}q'_{ll} + q'_{R3}J_4 + q'_{R2}p'_{ll}J_4)}{e_4} \tag{10.84d}$$

$$e_4 = p'_{R3}q'_{ll} + q'_{R3}p'_{ll}J_4 \tag{10.84e}$$

If $-\beta_1$, $-\beta_2$, $-\beta_3$, and $-\beta_4$ are the roots of the following polynomial in the transform variable s:

$$s^4 + e_3s^3 + e_2s^2 + e_1s + e_o = 0, \tag{10.85}$$

Eq. 10.85 can take the following form:

$$\bar{S}_{nl} = \frac{Q_oJ_1}{J_2 e_4} \frac{a_4s^4 + a_3s^3 + a_2s^2 + a_1s + a_o}{s(s+\beta_1)(s+\beta_2)(s+\beta_3)(s+\beta_4)} \tag{10.86a}$$

where

$$\beta_1 = \frac{Y_5}{\sqrt[4]{Y_4}} \tag{10.86b}$$

$$\beta_2 = \frac{Y_6}{\sqrt[4]{Y_4}} \tag{10.86c}$$

$$\beta_3 = \frac{Y_7}{\sqrt[4]{Y_4}} \tag{10.86d}$$

$$\beta_4 = \frac{Y_8}{\sqrt[4]{Y_4}} \tag{10.86e}$$

$$Y_1 = \sqrt{3}\left(6e_1^2 e_3^2 e_o + 4e_1^3 e_3^3 + 128 e_o^2 e_2^2 - 16 e_o e_2^4 + 4e_1^2 e_2^3 + 27 e_o^2 e_3^4\right.$$
$$\left. - e_1^2 e_3^2 e_2^2 + 192 e_1 e_3 e_o^2 - 18 e_2 e_1^3 e_3 - 144 e_o e_2 e_1^2 - 144 e_o^2 e_2 e_3^2 \right. \tag{10.86f}$$
$$\left. + 4e_o e_3^2 e_2^3 - 256 e_o^3 + 27 e_1^4 + 80 e_1 e_3 e_o e_2^2 - 18 e_2 e_1 e_3^3 e_o \right)^{\frac{1}{2}}$$

$$Y_2 = -\frac{e_2 e_1 e_3}{6} - \frac{4 e_o e_2}{3} + \frac{e_1^2}{2} + \frac{e_o e_3^2}{2} + \frac{e_2^3}{27} - \frac{Y_1}{18} \tag{10.86g}$$

$$Y_3 = -\frac{e_2 e_1 e_3}{6} - \frac{4 e_o e_2}{3} + \frac{e_1^2}{2} + \frac{e_o e_3^2}{2} + \frac{e_2^3}{27} + \frac{Y_1}{18} \tag{10.86h}$$

$$Y_4 = 3 e_3^2 - 8 e_2 + 12 \sqrt[3]{Y_3} + 12 \sqrt[3]{Y_2} \tag{10.86i}$$

$$Y_5 = \frac{e_3}{4} - \frac{\sqrt{3}\sqrt{Y_4}}{12} - \frac{\sqrt{6}}{12}\left(3e_3^2\sqrt{Y_4} - 8e_2\sqrt{Y_4} - 6\sqrt[3]{Y_3}\sqrt{Y_4}\right.$$

$$\left. - 6\sqrt[3]{Y_2}\sqrt{Y_4} - 3\sqrt{3}e_3^3 + 12\sqrt{3}e_3 e_2 - 24\sqrt{3}e_1\right)^{\frac{1}{2}}$$

(10.86j)

$$Y_6 = \frac{e_3}{4} - \frac{\sqrt{3}\sqrt{Y_4}}{12} + \frac{\sqrt{6}}{12}\left(3e_3^2\sqrt{Y_4} - 8e_2\sqrt{Y_4} - 6\sqrt[3]{Y_3}\sqrt{Y_4}\right.$$

$$\left. - 6\sqrt[3]{Y_2}\sqrt{Y_4} - 3\sqrt{3}e_3^3 + 12\sqrt{3}e_3 e_2 - 24\sqrt{3}e_1\right)^{\frac{1}{2}}$$

(10.86k)

$$Y_7 = \frac{e_3}{4} + \frac{\sqrt{3}\sqrt{Y_4}}{12} - \frac{\sqrt{6}}{12}\left(3e_3^2\sqrt{Y_4} - 8e_2\sqrt{Y_4} - 6\sqrt[3]{Y_3}\sqrt{Y_4}\right.$$

$$\left. - 6\sqrt[3]{Y_2}\sqrt{Y_4} + 3\sqrt{3}e_3^3 - 12\sqrt{3}e_3 e_2 + 24\sqrt{3}e_1\right)^{\frac{1}{2}}$$

(10.86l)

$$Y_8 = \frac{e_3}{4} + \frac{\sqrt{3}\sqrt{Y_4}}{12} + \frac{\sqrt{6}}{12}\left(3e_3^2\sqrt{Y_4} - 8e_2\sqrt{Y_4} - 6\sqrt[3]{Y_3}\sqrt{Y_4}\right.$$

$$\left. - 6\sqrt[3]{Y_2}\sqrt{Y_4} + 3\sqrt{3}e_3^3 - 12\sqrt{3}e_3 e_2 + 24\sqrt{3}e_1\right)^{\frac{1}{2}}$$

(10.86m)

After partial fractions, Eq. 10.86a becomes

$$\bar{S}_{nj} = \frac{Q_0 J_1}{J_2 e_4}\left(\frac{B_o}{s} + \frac{B_1}{(s+\beta_1)} + \frac{B_2}{(s+\beta_2)} + \frac{B_3}{(s+\beta_3)} + \frac{B_4}{(s+\beta_4)}\right)$$

(10.87)

B_o, B_1, B_2, B_3, and B_4 are determined by equating the coefficients of s in the

numerators of Eqs. 10.86a and 10.87:

$$B_o = \frac{a_o}{\beta_1\beta_2\beta_3\beta_4}$$

(10.88a)

$$B_1 = -\frac{a_4\beta_1^4-a_3\beta_1^3+a_2\beta_1^2-a_1\beta_1+a_o}{\beta_1(\beta_2-\beta_1)(\beta_3-\beta_1)(\beta_4-\beta_1)} \qquad (10.88b)$$

$$B_2 = -\frac{a_4\beta_2^4-a_3\beta_2^3+a_2\beta_2^2-a_1\beta_2+a_o}{\beta_2(\beta_1-\beta_2)(\beta_3-\beta_2)(\beta_4-\beta_2)} \qquad (10.88c)$$

$$B_3 = -\frac{a_4\beta_3^4-a_3\beta_3^3+a_2\beta_3^2-a_1\beta_3+a_o}{\beta_3(\beta_1-\beta_3)(\beta_2-\beta_3)(\beta_4-\beta_3)} \qquad (10.88d)$$

$$B_4 = -\frac{a_4\beta_4^4-a_3\beta_4^3+a_2\beta_4^2-a_1\beta_4+a_o}{\beta_4(\beta_1-\beta_4)(\beta_2-\beta_4)(\beta_3-\beta_4)} \qquad (10.88e)$$

Inverse transform of Eq. 10.87 yields

$$S_{nl}(t) = \frac{Q_o J_1}{J_2 e_4}\left(B_o+B_1e^{-\gamma_1 t}+B_2e^{-\gamma_2 t}+B_3e^{-\gamma_3 t}+B_4e^{-\gamma_4 t}\right) \qquad (10.89)$$

Eq. 10.89 can also be expressed in the following form:

$$S_{nl}(t) = \frac{Q_o J_1}{J_2 e_4}\left(B_o+B_1+B_2+B_3+B_4-B_1(1-e^{-\beta_1 t})-B_2(1-e^{-\beta_2 t})- \right.$$
$$\left. B_3(1-e^{-\beta_3 t})-B_4(1-e^{-\beta_4 t})\right) \qquad (10.90)$$

From Eq. 10.90, it can be seen that $B_o+B_1+B_2+B_3+B_4$ is a term related to the time-independent lining pressure and $B_1(1-e^{-\beta_1 t})$ to $B_4(1-e^{-\beta_4 t})$ are terms related to the time-dependent lining pressure. The sum of the coefficients B_1 to B_4 controls the final time-dependent lining pressure. β_1 to β_4 are parameters governing the rate at which the pressure builds up.

Equation 10.90 represents the lining pressure-time relationship if the lining is installed in the viscoelastic rock and then the initial deviatoric component of stress $(Q_o \cos 2\theta)$ is released at the interface. If the lining is installed after time $t = t_o$ after the excavation of the tunnel, the only relevant parts in Eq. 10.90 are the time-dependent terms $B_1(1-e^{-\beta_1 t})$ to $B_4(1-e^{-\beta_4 t})$. These terms do not give the real lining pressure but they give the form of the expression of the rate of stress built up.

Now, let the final lining pressure equal to Q_{om} at $\theta = 0$. Following the same line of discussion for the case of hydrostatic stress component, the time-dependent radial and tangential lining pressures, respectively, can be expressed as

$$S_{n}(t', \theta) = Q_{om}(1-e^{-\beta t'}) \qquad (10.91)$$

$$S_{t}(t', \theta) = KQ_{om}(1-e^{-\beta t'}) \qquad (10.92)$$

where $\beta \quad = \beta_1$

$t' \quad$ = new time variable

$\quad = t - t_o$

When $t'=0$, $S_{n}(0, \theta) = S_{t}(0, \theta) = 0$. When $t'=\infty$, $S_{n}(\infty, \theta) = Q_{om}\cos 2\theta$ and $S_{t}(\infty, \theta) = KQ_{om}\sin 2\theta$.

The final lining pressure Q_{om} and the value of the parameter K can be determined from the conditions of continuity of radial and tangential deformations at the interface.

(i)   Continuity of Radial Displacement

The condition of continuity of radial displacement at the interface is that the radial displacement of the lining must be equal to the free displacement of the rock at the time interval from the time of installation of lining t_o to $t(t')$ plus the radial displacement of the rock due to the reaction lining pressure, i.e.

$$u_{Ld}(R_2, t', \theta) = u_{Rd}(R_2, t, \theta) - u_{Rd}(R_2, t_o, \theta) + u_{Rld}(R_2, t', \theta) \qquad (10.93)$$

The term in the left side of Eq. 10.93, $u_{Ld}(R_2, t', \theta)$, represents the radial deformation of the lining at the interface at time t' after the installation of the lining. The first two terms in the right side of Eq. 10.93, $u_{Rd}(R_2, t, \theta) - u_{Rd}(R_2, t_o, \theta)$, represent the free deformation of the rock at the interface from the time of installation of the lining, t_o, till the time t'. The term $u_{Rld}(R_2, t', \theta)$ represents the radial deformation of the rock at the interface due to the reactive lining pressure.

(a)   Free radial deformation of rock at time (t)

The free radial deformation of the rock is equal to the free radial elastic deformation multiplied by the time function $J_R(t)$ (refer to the derivation in Chapter 9). Therefore, at the interface the free radial deformation of the rock after time t from the excavation of the tunnel is

$$u_{Rd}(R_2, t_o, \theta) = \frac{Q_o(1+v_R)R_2}{E_R} (3-4v_R)\cos 2\theta \, J_R(t) \qquad (10.94)$$

where

$$J_R(t) = 1 + \phi_{R1}(1-e^{-\lambda_{R1}t}) + \phi_{R2}(1-e^{-\lambda_{R2}t}) + \phi_{R3}(1-e^{-\lambda_{R3}t}) \qquad (10.95)$$

(b)   Free radial deformation of rock at time (t_o)

The free deformation of the rock at the interface at the time of installation of the

lining (t_o) can be obtained by substituting t_o for t in Eq. 10.94

$$u_{Rd}(R_2, t_o, \theta) = \frac{Q_o(1+v_R)R_2}{E_R} (3-4v_R)\cos 2\theta \, J_R(t_o) \qquad (10.96)$$

(c)   Free radial deformation for time interval from t_o to t

The free radial deformation of the rock at the interface for the time interval

between the time of installation of the lining (t_o) and the time t equals to the difference

between Eq. 10.94 and Eq. 10.96.

(d)   Radial deformation of rock due to reactive lining pressure

The reactive lining pressures ($S_{nl}(t')$ and $S_{tl}(t')$) are zero at the time of installation

of lining ($t'=0$ or $t=t_o$) and they are monotonically increasing with time (Eqs. 10.91 and

10.92). At infinity, the values of the radial and tangential lining pressures respectively

are $S_{nl}(\infty) = Q_{om}$ and $S_{tl}(\infty) = K.Q_{om}$. As in the case of hydrostatic stress component, the

deformation of the rock can be evaluated by the use of the hereditary integral which takes into consideration the history of the applied load. The resulting radial deformation of the rock at the interface due to the reactive lining pressure is

$$u_{Rld}(R_2, t', \theta) = \frac{-(1+v_R)R_2}{3E_R}(\bar{a} + K\bar{b})Q_{om}R_{nd}(t')\cos 2\theta \qquad (10.97)$$

where

$$\bar{a} = 5 - 6v_R \qquad (10.98a)$$

$$\bar{b} = 4 - 6v_R \qquad (10.98b)$$

$$R_{nd}(t') = (1-e^{-\beta t'}) - \frac{\phi_{RI}\lambda_{RI}e^{-\lambda_{RI}t'}}{\beta - \lambda_{RI}}\left(1-e^{-(\beta-\lambda_{RI})t'}\right) - \frac{\phi_{R2}\lambda_{R2}e^{-\lambda_{R2}t'}}{\beta - \lambda_{R2}}\left(1-e^{-(\beta-\lambda_{R2})t'}\right)$$

$$- \frac{\phi_{R3}\lambda_{R3}e^{-\lambda_{R3}t'}}{\beta - \lambda_{R3}}\left(1-e^{-(\beta-\lambda_{R3})t'}\right) + \phi_{RI}\left(1-e^{-\lambda_{RI}t'}\right) + \phi_{R2}\left(1-e^{-\lambda_{R2}t'}\right) + \phi_{R3}\left(1-e^{-\lambda_{R3}t'}\right) \qquad (10.99)$$

At infinity, $R_{nd}(\infty) = 1 + \phi_{RI} + \phi_{R2} + \phi_{R3}$

(e) Radial deformation of lining

Since the lining is subjected to the monotonically increasing lining pressure $S_n(t', \theta)$ (Eq. 10.91), the evaluation of the radial deformation of the lining requires the adoption of the hereditary integral. The resulting radial deformation of the lining at the interface is

$$u_{Ld}(R_2, t', \theta) = \frac{(1+v_l)R_2}{3E_l(1-h)^3}(\bar{C} + K\bar{d})Q_{om}L_{nd}(t')\cos 2\theta \qquad (10.100)$$

where

$$L_{nd}(t') = (1-e^{-\beta t'}) - \frac{\phi_l e^{-\lambda_l t'}}{\beta - \lambda_l}(1-e^{-(\beta - \lambda_l)t'}) + \phi_l(1-e^{-\lambda_l t'})$$ (10.101)

At infinity, $L_{nd}(\infty) = 1 + \phi_l$.

Condition of continuity at the interface:

The continuity condition of radial displacement at the interface is

$$u_{ld}(R_2, t', \theta) = u_{Rd}(R_2, t, \theta) - u_{Rd}(R_2, t_o, \theta) + u_{Rld}(R_2, t', \theta)$$ (10.102)

Substituting Eqs. 10.94, 10.96, 10.97 and 10.100 into Eq. 10.102 leads to the following expression:

$$\frac{(1 + v_l)R_2}{3E_l(1 - h)^3}(\bar{C} + K\bar{d})Q_{om}L_{nd}(t')\cos 2\theta$$
$$= \frac{Q_o(1 + v_R)R_2}{E_R}(3 - 4v_R)[J_R(t) - J_R(t_o)]\cos 2\theta$$ (10.103)
$$- \frac{(1 + v_R)R_2}{3E_R}(\bar{a} + K\bar{b})Q_{om}R_{nd}(t')\cos 2\theta$$

Putting $C_3 = \dfrac{1 + v_l}{1 + v_R}\dfrac{E_R}{E_l}\dfrac{1}{(1-h)^3}$, Eq. 10.103 becomes

$$3Q_o(3 - 4v_R)[J_R(t) - J_R(t_o)] = [C_3(\bar{C} + K\bar{d})L_{nd}(t') + (\bar{a} + K\bar{b})R_{nd}(t')]Q_{om}$$ (10.104)

(ii)   Continuity of Tangential Deformation

(a)   Free deformation of rock at time t

At the interface the free tangential deformation of the rock after time t from the excavation of the tunnel is

$$v_{R\theta}(R_2, t, \theta) = \frac{-Q_o(1+v_R)R_2}{E_R} (3-4v_R) J_R(t) \sin 2\theta \qquad (10.105)$$

(b)   Free tangential deformation of rock at time (t_o)

The free deformation of the rock at the interface at the time of installation of the lining (t_o) can be obtained by substituting t_o for t in Eq. 10.105

$$v_{R\theta}(R_2, t_o, \theta) = \frac{-Q_o(1+v_R)R_2}{E_R} (3-4v_R) J_R(t_o) \sin 2\theta \qquad (10.106)$$

(c)   Free tangential deformation of rock for time interval from t_o to t

The free radial deformation of the rock at the interface for the time interval between the time of installation of the lining (t_o) and the time (t) equals to the difference of Eqs. 10.105 and 10.106.

(d)   Tangential deformation of rock due to reactive lining pressure

As in Eq. 10.97, the time dependent tangential deformation of the rock at the interface due to the reactive lining pressure is

$$v_{Rld}(R_2, t', \theta) = \frac{(1+v_R)R_2}{3E_R} (\bar{b} + K\bar{a})Q_{om} R_{nd}(t') \sin 2\theta \qquad (10.107)$$

(e)   Tangential deformation of lining

As in Eq. 10.100, the time dependent tangential deformation of the lining at the interface due to the reactive lining pressure is

$$v_{ld}(R_2, t', \theta) = \frac{-(1+v_l)R_2}{3E_l(1-h)^3} (\bar{d} + K\bar{C}_1)Q_{om} L_{nd}(t') \sin 2\theta \qquad (10.108)$$

Condition of continuity at the interface

The continuity condition of tangential displacement at the interface is

$$v_{ld}(R_2, t', \theta) = v_{Rd}(R_2, t, \theta) - v_{Rd}(R_2, t_o, \theta) + v_{Rld}(R_2, t', \theta) \qquad (10.109)$$

Substituting Eqs. 10.105, 10.106, 10.107 and 10.108 into Eq. 10.109 leads to

$$\begin{aligned}
&\frac{-(1+v_l)}{3E_l(1-h)^3} (\bar{d} + \bar{C}_1 K)Q_{om} L_{nd}(t') \sin 2\theta \\
=\ &\frac{-Q_o(1+v_R)R_2}{E_R} (3-4v_R) [J_R(t) - J_R(t_o)]\sin 2\theta \\
&+ \frac{(1+v_R)R_2}{3E_R} (\bar{b} + \bar{a}K) Q_{om} R_{nd}(t') \sin 2\theta
\end{aligned} \qquad (10.110)$$

Putting $C_3 = \dfrac{1+v_l}{1+v_R} \dfrac{E_R}{E_l} \dfrac{1}{(1-h)^3}$, Eq. 10.110 becomes

$$3Q_o(3-4v_R)[J_R(t) - J_R(t_o)]$$
$$= \left[C_3(\bar{d}+\bar{C_1}K)L_{nd}(t') +(\bar{b}+\bar{a}K)R_{nd}(t')\right]Q_{om} \tag{10.111}$$

Solving Eqs. 10.104 and 10.110 simultaneously, the values of Q_{om} and K can be obtained. Comparing Eq. 10.104 to Eq. 10.111, it can be seen that the left hand sides of both equations are the same. Therefore, the right hand side of these two equations should be equal. Thus,

$$C_3(\bar{C}+K\bar{d})L_{nd}(t') + (\bar{a}+K\bar{b})R_{nd}(t')$$
$$= C_3(\bar{d}+K\bar{C_1})L_{nd}(t') + (\bar{b}+K\bar{a})R_{nd}(t') \tag{10.112}$$

After arrangement, the value of K can be expressed as

$$K = \frac{C_3(\bar{d}-\bar{C})L_{nd}(t') + (\bar{b}-\bar{a})R_{nd}(t')}{C_3(\bar{d}-\bar{C_1})L_{nd}(t') + (\bar{b}-\bar{a})R_{nd}(t')} \tag{10.113}$$

Since $\bar{b} - \bar{a} = (4-6v_R) - (5-6v_R) = -1$,

$$K = \frac{C_3(\bar{d}-\bar{C})L_{nd}(t') - R_{nd}(t')}{C_3(\bar{d}-\bar{C_1})L_{nd}(t') - R_{nd}(t')} \tag{10.114a}$$

After arrangement,

$$K = \frac{R_{nd}(t') + C_3(\bar{C}-\bar{d})L_{nd}(t')}{R_{nd}(t') - C_3(\bar{d}-\bar{C_1})L_{nd}(t')} \tag{10.114b}$$

Substituting the values of $R_{nd}(t')$ and L_{nd} at $t' = \infty$, Eqs. 10.99g and 10.101e, into Eq. 10.114b yields

$$K = \frac{(1 + \phi_{RI} + \phi_{R2} + \phi_{R3}) + C_3(\bar{C}-\bar{d})(1 + \phi_I)}{(1 + \phi_{RI} + \phi_{R2} + \phi_{R3}) - C_3(\bar{d}-\bar{C_1})(1 + \phi_I)} \tag{10.115}$$

The value of Q_{om} can be obtained by evaluating Eq. 10.104 at $t' - \infty$

$$\frac{Q_{om}}{Q_o} = \frac{3(3-4\nu_R)(\phi_{RI} e^{-\lambda_{RI} t'_o} + \phi_{R2} e^{-\lambda_{R2} t'_o} + \phi_{R3} e^{\lambda_{R3} t'_o})}{C_3(\bar{C}+K\bar{d})(1 + \phi_I) + (\bar{a}+K\bar{b})(1 + \phi_{RI} + \phi_{2} + \phi_{R3})} \tag{10.116}$$

For perfectly rigid lining, $E_I \rightarrow \infty$. Therefore, $C_3 \rightarrow 0$ and the final reactive lining pressure given by Eq. 10.116 becomes

$$\frac{Q_{om}}{Q_o} = \frac{3(3-4\nu_R)(\phi_{RI} e^{-\lambda_{RI} t'_o} + \phi_{R2} e^{-\lambda_{R2} t'_o} + \phi_{R3} e^{\lambda_{R3} t'_o})}{(\bar{a}+K\bar{b})(1 + \phi_{RI} + \phi_{R2} + \phi_{R3})} \tag{10.116}$$

The time-dependent distribution of radial pressure on the lining is

$$S_{n}(t', \theta) = Q_{om}(1 - e^{-\beta r'}) \cos 2\theta \tag{10.118}$$

The time-dependent distribution of tangential pressure on the lining is

$$S_{t}(t', \theta) = K Q_{om}(1 - e^{-\beta r'}) \sin 2\theta \tag{10.119}$$

(B) Case of Full Slip at the Interface

From the elastic solution for rock-lining interaction for full slip at the interface under the removal of deviatoric stress component (P_o), the maximum radial lining pressure at $\theta = 0°$ is (refer to Sec. 10.4.1)

$$S_{nl} = \frac{3(3-4v_R)Q_o}{C_3\bar{C} + (5-6v_R)} \qquad (10.120)$$

After arrangement,

$$S_{nl} = \frac{3(3-4v_R)Q_o}{(5-6v_R)\left[C_3\dfrac{\bar{C}}{(5-6v_R)} + 1\right]} \qquad (10.121)$$

Putting $J_7 = \dfrac{\bar{C}}{(5-6v_R)(1-h)^3}$, $J_1 = 3(3-4v_R)$ and $\bar{a} = 5-6v_R$ yields

$$S_{nl} = \frac{J_1 Q_o}{\bar{a}}\left[\frac{1}{1 + \dfrac{G_R}{G_l}J_7}\right] \qquad (10.122)$$

The associated problem in viscoelasticity can be formed using the principle of correspondence. Application of the correspondence principle to Eq. 10.122 yields the following equation:

$$\bar{S}_{nl} = \frac{Q_o J_1}{\bar{a}}\frac{1}{s(1 + \dfrac{\bar{Q}_R}{\bar{P}_R}\dfrac{\bar{P}_l}{\bar{Q}_l}J_7)} \qquad (10.123)$$

where S_{nl} is replaced by its laplace transform $\bar{S}_{nl}$, Q_o by its laplace transform $\dfrac{Q_o}{s}$, and the elastic parameters (G_R and G_l) by the transformed operators ($\bar{P}'_R$ and $\bar{Q}'_R$) and ($\bar{P}'_l$ and $\bar{Q}'_l$) respectively as given by the following relationships:

$$G_R \rightarrow \frac{\bar{Q}_R}{2\bar{P}_R} \qquad G_I \rightarrow \frac{\bar{Q}_I}{2\bar{P}_I}$$

Substitution of Eqs. 10.20, 10.21, 10.24 and 10.25 into Eq. 10.23 leads to

$$\bar{S}_{nI} = \frac{Q_o J_1}{\bar{a}} \; \frac{1}{s\left(1 + \dfrac{(q'_{Ro} + q'_{RI}s + q'_{R2}s^2 + q'_{R3}s^3)(1 + p'_{II}s)}{(1 + p'_{RI}s + p'_{R2}s^2 + p'_{R3}s^3)(q'_{Io} + q'_{II}s)} J_7\right)} \tag{10.124}$$

After arrangement, Eq. 10.124 can be written in the following form:

$$\bar{S}_{nI} = \frac{Q_o J_1}{\bar{a}\, g_4} \; \frac{(a_4 s^4 + a_3 s^3 + a_2 s^2 + a_1 s + a_o)}{s\,(s^4 + g_3 s^3 + g_2 s^2 + g_1 s + b_o)} \tag{10.125}$$

where

$$a_o = q'_{Io} \tag{10.126a}$$

$$a_1 = p'_{RI} q'_{Io} + q'_{II} \tag{10.126b}$$

$$a_2 = p'_{R2} q'_{Io} + p'_{RI} q'_{II} \tag{10.126c}$$

$$a_3 = p'_{R3} q'_{Io} + p'_{R2} q'_{II} \tag{10.126d}$$

$$a_4 = p'_{R3} q'_{II} \tag{10.126e}$$

$$g_o = \frac{(q'_{Io} + q'_{Ro} J_7)}{g_4} \tag{10.127a}$$

$$g_1 = \frac{(p'_{RI} q'_{Io} + q'_{II} + q'_{RI} J_7 + q'_{Ro} p'_{II} J_7)}{g_4} \tag{10.127b}$$

$$g_2 = \frac{(p'_{R2}q'_{l0} + p'_{R1}q'_{l1} + q'_{R2}J_7 + q'_{R1}p'_{l1}J_7)}{g_4} \tag{10.127c}$$

$$g_3 = \frac{(p'_{R3}q'_{l0} + p'_{R2}q'_{l1} + q'_{R3}J_7 + q'_{R2}p'_{l1}J_7)}{g_4} \tag{10.127d}$$

$$g_4 = p'_{R3}q'_{l1} + q'_{R3}p'_{l1}J_7 \tag{10.127e}$$

If $-\gamma_1$, $-\gamma_2$, $-\gamma_3$, and $-\gamma_4$ are the roots of the following polynomial in the transform variable s:

$$s^4 + g_3 s^3 + g_2 s^2 + g_1 s + g_o = 0 \tag{10.128}$$

Eq. 10.125 can be expressed as

$$\bar{S}_{nl} = \frac{Q_o J_1}{\bar{a} g_4} \frac{(a_4 s^4 + a_3 s^3 + a_2 s^2 + a_1 s + a_o)}{s(s+\gamma_1)(s+\gamma_2)(s+\gamma_3)(s+\gamma_4)} \tag{10.129a}$$

where

$$\gamma_1 = \frac{X_5}{\sqrt[4]{X_4}} \tag{10.129b}$$

$$\gamma_2 = \frac{X_6}{\sqrt[4]{X_4}} \tag{10.129c}$$

$$\gamma_3 = \frac{X_7}{\sqrt[4]{X_4}} \tag{10.129d}$$

$$Y_4 = \frac{X_8}{\sqrt[4]{X_4}}$$

(10.129e)

$$
\begin{aligned}
X_1 = \sqrt{3}\Big(&6g_1^2 g_3^2 g_0 + 4g_1^3 g_3^3 + 128 g_0^2 g_2^2 - 16 g_0 g_2^4 + 4g_1^2 g_2^3 + 27 g_0^2 g_3^4 \\
&- g_1^2 g_3^3 g_2^2 + 192 g_1 g_3 g_0^2 - 18 g_2 g_1^3 g_3 - 144 g_0 g_2 g_1^2 - 144 g_0^2 g_2 g_3^2 \\
&+ 4g_0 g_3^2 g_2^3 - 256 g_0^3 + 27 g_1^4 + 80 g_1 g_3 g_0 g_2^2 - 18 g_2 g_1 g_3^3 g_0\Big)^{\frac{1}{2}}
\end{aligned}
$$

(10.129f)

$$X_2 = -\frac{g_2 g_1 g_3}{6} - \frac{4g_0 g_2}{3} + \frac{g_1^2}{2} + \frac{g_0 g_3^2}{2} + \frac{g_2^3}{27} - \frac{X_1}{18}$$

(10.129g)

$$X_3 = -\frac{g_2 g_1 g_3}{6} - \frac{4g_0 g_2}{3} + \frac{g_1^2}{2} + \frac{g_0 g_3^2}{2} + \frac{g_2^3}{27} + \frac{X_1}{18}$$

(10.129h)

$$X_4 = 3g_3^2 - 8g_2 + 12\sqrt[3]{X_3} + 12\sqrt[3]{X_2}$$

(10.32i)

$$
\begin{aligned}
X_5 = \frac{g_3}{4} - \frac{\sqrt{3}\sqrt{Z_4}}{12} - \frac{\sqrt{6}}{12}\Big(&3g_3^2\sqrt{X_4} - 8g_2\sqrt{X_4} - 6\sqrt[3]{X_3}\sqrt{X_4} \\
&- 6\sqrt[3]{X_2}\sqrt{X_4} - 3\sqrt{3}g_3^3 + 12\sqrt{3}g_3 g_2 - 24\sqrt{3}g_1\Big)^{\frac{1}{2}}
\end{aligned}
$$

(10.129j)

$$
\begin{aligned}
X_6 = \frac{g_3}{4} - \frac{\sqrt{3}\sqrt{X_4}}{12} + \frac{\sqrt{6}}{12}\Big(&3g_3^2\sqrt{X_4} - 8g_2\sqrt{X_4} - 6\sqrt[3]{X_3}\sqrt{X_4} \\
&- 6\sqrt[3]{X_2}\sqrt{X_4} - 3\sqrt{3}g_3^3 + 12\sqrt{3}g_3 g_2 - 24\sqrt{3}g_1\Big)^{\frac{1}{2}}
\end{aligned}
$$

(10.129k)

$$
\begin{aligned}
X_7 = \frac{g_3}{4} + \frac{\sqrt{3}\sqrt{X_4}}{12} - \frac{\sqrt{6}}{12}\Big(&3g_3^2\sqrt{X_4} - 8g_2\sqrt{X_4} - 6\sqrt[3]{X_3}\sqrt{X_4} \\
&- 6\sqrt[3]{X_2}\sqrt{X_4} + 3\sqrt{3}g_3^3 - 12\sqrt{3}g_3 g_2 + 24\sqrt{3}g_1\Big)^{\frac{1}{2}}
\end{aligned}
$$

(10.129l)

$$X_s = \frac{g_3}{4} + \frac{\sqrt{3}\sqrt{X_4}}{12} + \frac{\sqrt{6}}{12}\left(3g_3^2\sqrt{X_4} - 8g_2\sqrt{X_4} - 6\sqrt[3]{X_3}\sqrt{X_4}\right.$$

$$\left. - 6\sqrt[3]{X_2}\sqrt{X_4} + 3\sqrt{3}g_3^3 - 12\sqrt{3}g_3g_2 + 24\sqrt{3}g_1\right)^{\frac{1}{2}} \tag{10.129m}$$

After partial fractions Eq. 10.129a becomes

$$\bar{S}_{nl} = \frac{Q_o J_1}{\bar{a}\,g_4}\left(\frac{G_o}{s} + \frac{G_1}{(s+\gamma_1)} + \frac{G_2}{(s+\gamma_2)} + \frac{G_3}{(s+\gamma_3)} + \frac{G_4}{(s+\gamma_4)}\right) \tag{10.130}$$

G_o, G_1, G_2, G_3, and G_4 are determined by equating the coefficients of s in the numerators of Eqs 10.129a and 10.130

$$G_o = \frac{a_o}{\gamma_1\gamma_2\gamma_3\gamma_4} \tag{10.131a}$$

$$G_1 = -\frac{a_4\gamma_1^4 - a_3\gamma_1^3 + a_2\gamma_1^2 - a_1\gamma_1 + a_o}{\gamma_1(\gamma_2 - \gamma_1)(\gamma_3 - \gamma_1)(\gamma_4 - \gamma_1)} \tag{10.131b}$$

$$G_2 = -\frac{a_4\gamma_2^4 - a_3\gamma_2^3 + a_2\gamma_2^2 - a_1\gamma_2 + a_o}{\gamma_2(\gamma_1 - \gamma_2)(\gamma_3 - \gamma_2)(\gamma_4 - \gamma_2)} \tag{10.131c}$$

$$G_3 = -\frac{a_4\gamma_3^4 - a_3\gamma_3^3 + a_2\gamma_3^2 - a_1\gamma_3 + a_o}{\gamma_3(\gamma_1 - \gamma_3)(\gamma_2 - \gamma_3)(\gamma_4 - \gamma_3)} \tag{10.131d}$$

$$G_4 = -\frac{a_4\gamma_4^4 - a_3\gamma_4^3 + a_2\gamma_4^2 - a_1\gamma_4 + a_o}{\gamma_4(\gamma_1 - \gamma_4)(\gamma_2 - \gamma_4)(\gamma_3 - \gamma_4)} \tag{10.131e}$$

Inverse transform of Eq. 10.130 gives

$$S_{nl}(t) = \frac{Q_o J_1}{\bar{a} g_4} \left(G_o + G_1 e^{-\gamma_1 t} + G_2 e^{-\gamma_2 t} + G_3 e^{-\gamma_3 t} + G_4 e^{-\gamma_4 t} \right) \tag{10.132}$$

Eq. 10.132 can also be expressed in the following form:

$$S_{nl}(t) = \frac{Q_o J_1}{\bar{a} g_4} \left(G_o + G_1 + G_2 + G_3 + G_4 - G_1(1 - e^{-\gamma_1 t}) - G_2(1 - e^{-\gamma_2 t}) \right.$$
$$\left. - G_3(1 - e^{-\gamma_3 t}) - G_4(1 - e^{-\gamma_4 t}) \right) \tag{10.133}$$

As for the no slip case, the function for the lining pressure distribution will be in the following form:

$$S_{nl}(t', \theta) = Q_{oms}(1 - e^{-\gamma t'}) \cos 2\theta \tag{10.134}$$

where γ is equal to γ_1

Q_{oms} is the final maximum radial pressure at $\theta = 0°$.

To solve for Q_{oms}, the continuity of radial displacement at the interface is considered.

(a)   **Free radial deformation of rock at time (t)**

Referring to Eq. 10.94, the free radial deformation of the rock at the interface after time t from the excavation of the tunnel is

$$u_{Rd}(R_2, t_o, \theta) = \frac{Q_o(1 + v_R)R_2}{E_R} (3 - 4v_R) \cos 2\theta \, J_R(t) \tag{10.135}$$

where

$$J_R(t) = 1 + \phi_{R1}(1-e^{-\lambda_{R1}t}) + \phi_{R2}(1-e^{-\lambda_{R2}t}) + \phi_{R3}(1-e^{-\lambda_{R3}t}) \qquad (10.136)$$

(b) Free radial deformation of rock at time t_o

The free deformation of the rock at the interface at the time of installation of the lining (t_o) can be obtained by substituting t_o for t in Eq. 10.135:

$$u_{Rd}(R_2, t_o, \theta) = \frac{Q_o(1+\nu_R)R_2}{E_R}(3-4\nu_R)\cos 2\theta\, J_R(t_o) \qquad (10.137)$$

(c) Free radial deformation for time interval from t_o to t

The free radial deformation of the rock at the interface for the time interval between the time of installation of the lining (t_o) and the time (t) equals to the difference of Eqs. 10.135 and 10.137.

(d) Radial deformation of rock due to reactive lining pressure

As in the no slip case, the hereditary integral may be adopted to calculate the deformation of the rock due to the time dependent reactive lining pressure. The resulting radial deformation of the rock at the interface due to the reactive lining pressure is

$$u_{Rld}(R_2, t', \theta) = \frac{(1+\nu_R)R_2}{3E_R}(\bar{a} + K\bar{b})Q_{oms}R_{nds}(t')\cos 2\theta \qquad (10.138)$$

where

$$R_{nds}(t') = (1-e^{-\gamma t'}) - \frac{\phi_{RI}\lambda_{RI}e^{-\lambda_{RI}t'}}{\gamma-\lambda_{RI}}\left(1-e^{-(\gamma-\lambda_{RI})t'}\right) - \frac{\phi_{R2}\lambda_{R2}e^{-\lambda_{R2}t'}}{\gamma-\lambda_{R2}}\left(1-e^{-(\gamma-\lambda_{R2})t'}\right)$$

$$- \frac{\phi_{R3}\lambda_{R3}e^{-\lambda_{R3}t'}}{\gamma-\lambda_{R3}}\left(1-e^{-(\gamma-\lambda_{R3})t'}\right) + \phi_{RI}\left(1-e^{-\lambda_{RI}t'}\right) + \phi_{R2}\left(1-e^{-\lambda_{R2}t'}\right) + \phi_{R3}\left(1-e^{-\lambda_{R3}t'}\right)$$

$$(10.139)$$

(e)   Radial deformation of lining

The resulting radial deformation of the lining at the interface is

$$u_{Ld}(R_2, t', \theta) = \frac{(1+v_l)R_2}{3E_l(1-h)^3}(\bar{C}+\bar{K}\bar{d})Q_{oms}L_{nds}(t')\cos2\theta \qquad (10.140)$$

where

$$L_h(t') = (1-e^{-\gamma t'}) - \frac{\phi_l\lambda_l e^{-\lambda_l t'}}{\gamma-\lambda_l}\left(1-e^{-(\gamma-\lambda_l)t'}\right) + \phi_l\left(1-e^{-\lambda_l t'}\right) \qquad (10.141)$$

At infinity, $L_{nds}(\infty) = 1 + \phi_l$.

The condition of continuity of radial deformation at the interface is

$$u_{Ld}(R_2, t', \theta) = u_{Rd}(R_2, t, \theta) - u_{Rd}(R_2, t_o, \theta) + u_{Rld}(R_2, t', \theta) \qquad (10.142)$$

Substituting Eqs. 10.135, 10.137, 10.138 and 10.140 into Eq. 10.142 yields

$$\frac{(1+v_I)R_2}{3E_I(1-h)^3}\,\bar{C}\,Q_{oms}\,L_{nds}(t')\cos2\theta$$

$$= \frac{Q_o(1+v_R)R_2}{E_R}\,(3-4v_R)\,[J_R(t) - J_R(t_o)]\cos2\theta \qquad (10.143)$$

$$-\frac{(1+v_R)R_2}{3E_R}\,\bar{a}\,Q_{oms}\,R_{nds}(t')\cos2\theta$$

Putting $C_3 = \dfrac{1+v_I}{1+v_R}\,\dfrac{E_R}{E_I}\,\dfrac{1}{(1-h)^3}$, Eq. 10.143 becomes

$$C_3\,\bar{C}\,Q_{oms}\,L_{nds}(t') = 3(3-4v_R)Q_o\left[\phi_{RI}(e^{-\lambda_{RI}t_o} - e^{-\lambda_{RI}t}) + \phi_{R2}(e^{-\lambda_{R2}t_o} - e^{-\lambda_{R2}t})\right.$$
$$\left. + \phi_{R3}(e^{-\lambda_{R3}t_o} - e^{-\lambda_{R3}t})\right] - \bar{a}\,Q_{oms}\,R_{nds}(t') \qquad (10.144)$$

After arrangement,

$$\frac{Q_{oms}}{Q_o} = \frac{3(3-4v_R)\left[\phi_{RI}(e^{-\lambda_{RI}t_o} - e^{-\lambda_{RI}t}) + \phi_{R2}(e^{-\lambda_{R2}t_o} - e^{-\lambda_{R2}t}) + \phi_{R3}(e^{-\lambda_{R3}t_o} - e^{-\lambda_{R3}t})\right]}{C_3\,\bar{C}\,L_{nds}(t') + \bar{a}\,R_{nds}(t')} \qquad (10.145)$$

Evaluating Eq. 10.145 at $t = t' = \infty$ gives the following expression for the final reactive

lining pressure:

$$\frac{Q_{oms}}{Q_o} = \frac{3(3-4v_R)\left(\phi_{RI}e^{-\lambda_{RI}t_o} + \phi_{R2}e^{-\lambda_{R2}t_o} + \phi_{R3}e^{-\lambda_{R3}t_o}\right)}{C_3\,\bar{C}\,(1+\phi_I) + \bar{a}\,(1+\phi_{RI}+\phi_{R2}+\phi_{R3})} \qquad (10.146)$$

The time-dependent distribution of radial pressure on the lining is

$$S_n(t', \theta) = \frac{Q_{oms}}{G_s}\left[G_1(1-e^{-\gamma_1 t'}) + G_2(1-e^{-\gamma_2 t'}) + G_3(1-e^{-\gamma_3 t'})\right.$$
$$\left. + G_4(1-e^{-\gamma_4 t'})\right]\cos2\theta \qquad (10.147)$$

For perfectly rigid lining, $E_l \rightarrow \infty$. Therefore, $C_3 \rightarrow 0$ and the final reactive lining pressure given by Eq. 10.146 becomes

$$\frac{Q_{oms}}{Q_o} = \frac{3(3-4v_R)\left(\phi_{RI}e^{-\lambda_{RI}t_o} + \phi_{R2}e^{-\lambda_{R2}t_o} + \phi_{R3}e^{-\lambda_{R3}t_o}\right)}{\bar{a}(1+\phi_{RI}+\phi_{R2}+\phi_{R3})} \tag{10.148}$$

10.5 SUMMARY OF TIME-DEPENDENT STRESSES AND DISPLACEMENTS IN ROCK AND LINING

10.5.1 Stresses and Displacements Resulting from Initial Hydrostatic Stress Component P_o

(1) Reactive lining pressure $P_i(t')$

$$P_i(t') = P_{om}(1 - e^{-\alpha t'})$$
(10.149)

where

$$P_{om} = \frac{\phi_{RI}e^{-\lambda_{RI}t'_o} + \phi_{R2}e^{-\lambda_{R2}t'_o} + \phi_{R3}e^{-\lambda_{R3}t'_o}}{C_1 C_2(1 + \phi_l) + (1 + \phi_{RI} + \phi_{R2} + \phi_{R3})} \, P_o$$
(10.150)

and t' is the time elapsed after the installation of the lining

(2) Stresses in lining

(a) Radial stress

$$\sigma_{rlh}(r, t') = \frac{P_i(t')(1 - \frac{R_1^2}{r^2})}{(1 - \frac{R_1^2}{R_2^2})}$$
(10.151)

At $r = R_1$

$$\sigma_{rlh}(R_1, t') = 0$$
(10.152)

At $r = R_2$

$$\sigma_{rth}(R_2, t') = P_i(t') \qquad (10.153)$$

(b)   Tangential stress

$$\sigma_{\theta th}(r, t') = \frac{P_i(t')\left(1 + \dfrac{R_1^2}{r^2}\right)}{\left(1 - \dfrac{R_1^2}{R_2^2}\right)} \qquad (10.154)$$

At $r = R_1$

$$\sigma_{\theta th}(R_1, t') = \frac{2\,P_i(t')}{\left(1 - \dfrac{R_1^2}{R_2^2}\right)} \qquad (10.155)$$

At $r = R_2$

$$\sigma_{\theta th}(r, t') = \frac{P_i(t')\left(1 + \dfrac{R_1^2}{R_2^2}\right)}{\left(1 - \dfrac{R_1^2}{R_2^2}\right)} \qquad (10.156)$$

(c)   Shear stress

$$\tau_{r\theta th}(r, t') = 0 \qquad (10.157)$$

(3)   Equivalent moment and thrust in lining

$$M_h(t') = -\frac{P_l(t')}{12}(R_2 - R_1)^2 \qquad (10.158)$$

$$N_h(t') = \frac{P_l(t')(3R_2^2 + R_1^2)}{2(R_2 + R_1)} \qquad (10.159)$$

(4)   Deformation in lining

$$u_{lh}(t') = \frac{C_2(1 + \nu_l)r}{E_l} P_{om} L_h(t') \qquad (10.160)$$

where

$$C_2' = \frac{1 - 2\nu_l + \left(\dfrac{R_1}{r}\right)^2}{1 - \left(\dfrac{R_1}{R_2}\right)^2} \qquad (10.161)$$

$$L_h(t') = (1 - e^{-\alpha t'}) - \frac{\phi_l \lambda_l e^{-\lambda_l t'}}{\alpha - \lambda_l}\left(1 - e^{-(\alpha - \lambda_l)t'}\right) + \phi_l(1 - e^{-\lambda_l t'}) \qquad (10.162a)$$

At infinity, $L_h(\infty) = 1 + \phi_l$

At $r = R_1$

$$u_{lh}(R_1, t') = \frac{C_2(1 + \nu_l)R_1}{E_l} P_{om} L_h(t') \qquad (10.163)$$

At $r = R_2$

$$u_{th}(R_1, t') = \frac{C_2(1+v_l)R_2}{E_l} P_{om} L_h(t')$$

(10.164)

(5)   Stresses in rock

(a)   radial stress

$$\sigma_{rRh}(r, t') = P_o - \left(\frac{R_2}{r}\right)^2 [P_o - P_l(t')]$$

(10.165)

(b)   Tangential stress

$$\sigma_{\theta Rh}(r, t') = P_o + \left(\frac{R_2}{r}\right)^2 [P_o - P_l(t')]$$

(10.166)

(c)   shear stress

$$\tau_{r\theta h}(r, t') = 0$$

(10.167)

(6)   Deformation in rock mass

(a)   Radial deformation

$$u_{Rh}(r, t) = \frac{R_2^2}{2G_R r} [P_o J_R(t) - P_{om} R_h(t')]$$

(10.168)

where

$$J_R(t) = 1 + \phi_{R1}(1-e^{-\lambda_{R1}t}) + \phi_{R2}(1-e^{-\lambda_{R2}t}) + \phi_{R3}(1-e^{-\lambda_{R3}t})$$

(10.169)

$$R_h(t') = (1 - e^{-\alpha t'}) - \frac{\phi_{R1} \lambda_{R1} e^{-\lambda_{R1} t'}}{\alpha - \lambda_{R1}} \left(1 - e^{-(\alpha - \lambda_{R1})t'}\right) - \frac{\phi_{R2} \lambda_{R2} e^{-\lambda_{R2} t'}}{\alpha - \lambda_{R2}} \left(1 - e^{-(\alpha - \lambda_{R2})t'}\right)$$

$$- \frac{\phi_{R3} \lambda_{R3} e^{-\lambda_{R3} t'}}{\alpha - \lambda_{R3}} \left(1 - e^{-(\alpha - \lambda_{R3})t'}\right) + \phi_{R1}\left(1 - e^{-\lambda_{R1} t'}\right) + \phi_{R2}\left(1 - e^{-\lambda_{R2} t'}\right) + \phi_{R3}\left(1 - e^{-\lambda_{R3} t'}\right) \tag{10.170}$$

At infinity, $J_R(\infty) = R_h(\infty) = 1 + \phi_{R1} + \phi_{R2} + \phi_{R3}$. Therefore,

$$u_{Rh}(r, \infty) = \frac{R_2^2}{2 G_R r} \left(1 + \phi_{R1} + \phi_{R2} + \phi_{R3}\right) (P_o - P_{om}) \tag{10.171}$$

(b)   **Tangential deformation**

$$v_{Rh}(r, t) = 0 \tag{10.172}$$

10.5.2   Stresses and Displacements Resulting from Initial Deviatoric Stress

Component Q_o

(A)   No Slip at Rock-lining interface

(1)   Reactive lining pressure

(a)   radial reactive pressure S_{nl}

$$S_{nl}(t', \theta) = S_{nl}(t')\cos 2\theta \qquad (10.173)$$

where $S_{nl}(t')$ is the radial lining pressure at the springline and θ is the angle from

springline. $S_{nl}(t')$ is given by

$$S_{nl}(t') = Q_{om}(1-e^{-\beta t'}) \qquad (10.174)$$

where Q_{om} is the final deviatoric lining pressure at the springline and it is given by

$$Q_{om} = \frac{3(3-4v_R)(\phi_{R1}e^{-\lambda_{R1}t_o} + \phi_{R2}e^{-\lambda_{R2}t_o} + \phi_{R3}e^{-\lambda_{R3}t_o})}{C_3(\bar{C}+K\bar{d})(1+\phi_l) + (\bar{a}+K\bar{b})(1+\phi_{R1}+\phi_{R2}+\phi_{R3})} Q_o \qquad (10.175)$$

Q_o is the initia' deviatoric stress component of the rock $(Q_o = \dfrac{P_h - P_v}{2})$

(b)   tangential lining pressure $S_{tl}(t', \theta)$

$$S_{tl}(t', \theta) = S_{tl}(t')\sin 2\theta \qquad (10.176)$$

where $S_{tl}(t')$ is the tangential lining pressure at $\theta = 45°$ and is defined as

$$S_d(t') = K S_{nd}(t')$$ (10.177)

(2)   Stresses in lining

(a)   Radial stress

$$\sigma_{rld}(r, t', \theta) = -\left(2A + \frac{6C}{r^4} + \frac{4D}{r^2}\right)\cos 2\theta$$ (10.178)

(b)   Tangential stress

$$\tau_{\theta ld}(r, t', \theta) = \left(2A + 12Br^2 + \frac{6C}{r^4}\right)\cos 2\theta$$ (10.179)

(c)   Shear stress

$$\sigma_{r\theta ld}(r, t', \theta) = \left(2A + 6Br^2 - \frac{6C}{r^4} - \frac{2D}{r^2}\right)\sin 2\theta$$ (10.180)

where

$$A = \frac{1}{(1-h)^3}\left[-\frac{S_{nl}(t')}{2}(2h^2 + h + 1) - S_d(t')h^2\right]$$ (10.181a)

$$B = \frac{1}{(1-h)^3}\left[\frac{S_{nl}(t')}{6R_2^2}(3h + 1) + \frac{S_d(t')}{6R_2^2}(3h - 1)\right]$$ (10.181b)

$$C = \frac{1}{(1-h)^3}\left[-\frac{S_{nl}(t')h^2}{6}(h + 3)R_2^4 - \frac{S_d(t')h^3R_2^4}{3}\right]$$ (10.181c)

$$D = \frac{1}{(1-h)^3} \left[\frac{S_{nd}(t')}{2} h(h^2 + h + 2)R_2^2 + \frac{S_d(t')}{2} h^2(h+1)R_2^2 \right]$$

(10.181d)

(3) Equivalent moment and thrust in lining

Equivalent moment

$$M_d(t', \theta) = [\sigma_{\theta ld}(R_2, t', \theta) - \sigma_{\theta ld}(R_1, t', \theta)] \frac{(R_2 - R_1)^2}{12}$$

(10.182)

Equivalent thrust

$$N_d(t', \theta) = [\sigma_{\theta ld}(R_2, t', \theta) + \sigma_{\theta ld}(R_1, t', \theta)] \frac{(R_2 - R.)}{2}$$

(10.183)

(4) Displacement in lining

(a) Radial displacement

At $r = R_2$

$$u_{ld}(R_2, \infty, \theta) = \frac{(1+v_l)R_2}{3E_l(1-h)^3} (\bar{C} + K\bar{d}) Q_{om} L_{nd}(t') \cos 2\theta$$

(10.184)

where

$$L_{nd}(t') = (1 - e^{-\beta t}) - \frac{\phi_l \lambda_l e^{-\lambda t}}{\beta - \lambda_l} (1 - e^{-(\beta - \lambda_l)t}) + \phi_l(1 - e^{-\lambda t})$$

(10.185)

At infinity, $L_{nd}(\infty) = 1 + \phi_l$. Therefore,

$$u_{ld}(R_2, \infty, \theta) = \frac{(1+v_l)R_2}{3E_l(1-h)^3} (\bar{C} + K\bar{d}) Q_{om} (1+\phi_l) \cos 2\theta \qquad (10.186)$$

At $r = R_1$

$$u_{ld}(R_1, t', \theta) = \frac{(1+v_l)}{E_l(1-h)^3} (\bar{A}' + K\bar{B}) Q_{om} L_{nd}(t') \cos 2\theta \qquad (10.187)$$

where

$$\bar{A}' = (2h^2+h+1)R_1 - h^2(h+3)\frac{R_2^4}{3R_1^3} + 2h(h^2+h\ 2)\frac{R_2^2}{R_1}$$

$$-v_l[\ 2h(h^2+h+2)\frac{R_2^2}{R_1} + \frac{2}{3}(3h+1)\frac{R_1^3}{R_2^2}\ ] \qquad (10.188)$$

$$\bar{B} = 2h^2R_1 - \frac{2}{3}h^3\frac{R_2^4}{R_1^3} + 2h^2(h+1)\frac{R_2^2}{R_1}$$

$$-v_l[\ 2h^2(h+1)\frac{R_2^2}{R_1} + \frac{2}{3}(3h-1)\frac{R_1^3}{R_2^2}\ ] \qquad (10.189)$$

When $t' \to \infty$,

$$u_{ld}(R_1, t', \theta) = \frac{(1+v_l)}{E_l(1-h)^3} (\bar{A}' + K\bar{B}) Q_{om} (1+\phi_l) \cos 2\theta \qquad (10.190)$$

(b)   Tangential displacement

At $r = R_2$

$$v_{ld}(R_2, t', \theta) = \frac{-(1+v_l)R_2}{3E_l(1-h)^3} [\bar{d} + K\bar{c}_1] Q_{om} L_{nd}(t') \sin 2\theta \qquad (10.191)$$

When $t' \to \infty$,

$$v_{ld}(R_2, \infty, \theta) = \frac{-(1+v_l)R_2}{3E_l(1-h)^3} [\bar{d} + K\bar{c}_1] Q_{om} (1+\phi_l) \sin 2\theta \qquad (10.192)$$

At $r = R_1$

$$v_{ld}(R_1, t', \theta) = -\frac{2(1+v_l)}{E_l(1-h)^3} (\bar{A}'' + K\bar{B}'') Q_{om} L_{nd}(t') \sin 2\theta \qquad (10.193)$$

where

$$\bar{A}'' = (2h^2+h+1)\frac{R_1}{2} - (3-2v_l)(3h+1)\frac{R_1^3}{6R_2^2} + h^2(h+3)\frac{R_2^4}{6R_1^3}$$

$$+ (1-2v_l)h(h^2+h+2)\frac{R_2^2}{2R_1} \qquad (10.194)$$

$$\bar{B}'' = h^2 R_1 - (3-2v_l)(3h-1)\frac{R_1^3}{6R_2^2} + h^3\frac{R_2^4}{3R_1^3}$$

$$+ (1-2v_l)h^2(h+1)\frac{R_2^2}{2R_1} \qquad (10.195)$$

When $t' \to \infty$,

$$v_{ld}(R_1, \infty, \theta) = -\frac{2(1+v_l)}{E_l(1-h)^3}(\bar{A}'' + K\bar{B}'')Q_{om}(1+\phi_l)\sin2\theta \qquad (10.196)$$

(5) Stresses in Rock Mass

(a) Radial Stress

$$\sigma_{rRd}(r, t, \theta) = \{Q_o + \frac{R_2^4}{r^4}[3Q_o - S_{nl}(t') - 2S_{tl}(t')]$$

$$-\frac{R_2^2}{r^2}[4Q_o - 2S_{nl}(t') - 2S_{tl}(t')]\}\cos2\theta \qquad (10.197)$$

When $t' \to \infty$, $S_{nl}(\infty) = Q_{om}$

$$\sigma_{rRd}(r, \infty, \theta) = \{Q_o + \frac{R_2^4}{r^4}[3Q_o - (1+2K)Q_{om}] - \frac{R_2^2}{r^2}[4Q_o - 2(1+K)Q_{om}]\}\cos2\theta \qquad (10.198)$$

(b) Tangential stress

$$\sigma_{\theta Rd}(r, t, \theta) = -\{Q_o + \frac{R_2^4}{r^4}[3Q_o - 2S_{tl}(t') - S_{nl}(t')]\}\cos2\theta \qquad (10.199)$$

When $t' \to \infty$, $S_{nl}(\infty) = Q_{om}$

$$\sigma_{\theta Rd}(r, \infty, \theta) = -\{Q_o + \frac{R_2^4}{r^4}[3Q_o - (1+2K)Q_{om}]\}\cos2\theta \qquad (10.200)$$

(c) **Shear stress**

$$\tau_{r\theta Rd}(r, t, \theta) = -\{Q_o - \frac{R_2^4}{r^4}[3Q_o - 2S_{tl}(t') - S_{nl}(t')]$$

$$+ \frac{R_2^2}{r^2}[2Q_o - S_{nl}(t') - S_{tl}(t')]\} \sin 2\theta \qquad (10.201)$$

When $t' \to \infty$, $S_{nl}(\infty) = Q_{om}$

$$\tau_{r\theta Rd}(r, \infty, \theta) = -\{Q_o - \frac{R_2^4}{r^4}[3Q_o - (1+2K)Q_{om}] + \frac{R_2^2}{r^2}[2Q_o - (1+K)Q_{om}]\} \sin 2\theta \qquad (10.202)$$

(6) **Displacements in Rock mass**

(a) **Radial displacement**

$$u_{rd}(r, t, \theta) = \{\frac{Q_o(1+v_R)}{E_R}[-\frac{R_2^4}{r^3} + \frac{4R_2^2}{r}(1-v_R)]J_R(t)$$

$$+ \frac{(1+v_R)}{E_R}(E' + KF')Q_{om}R_{nd}(t')\} \cos 2\theta \qquad (10.203)$$

where

$$E' = \frac{R_2^4}{3r^3} - 2(1-v_R)\frac{R_2^2}{r} \qquad (10.204\text{a})$$

$$F' = \frac{2R_2^4}{3r^3} - 2(1-v_R)\frac{R_2^2}{r} \qquad (10.204\text{b})$$

$$J_R(t) = 1 + \phi_{R1}(1-e^{-\lambda_{R1}t}) + \phi_{R2}(1-e^{-\lambda_{R2}t}) + \phi_{R3}(1-e^{-\lambda_{R3}t}) \qquad (10.204\text{c})$$

$$R_{nd}(t') = (1-e^{-\beta t'}) - \frac{\phi_{R1}\lambda_{R1}e^{-\lambda_{R1}t'}}{\beta - \lambda_{R1}}\left(1-e^{-(\beta-\lambda_{R1})t'}\right) - \frac{\phi_{R2}\lambda_{R2}e^{-\lambda_{R2}t'}}{\beta - \lambda_{R2}}\left(1-e^{-(\beta-\lambda_{R2})t'}\right)$$

$$- \frac{\phi_{R3}\lambda_{R3}e^{-\lambda_{R3}t'}}{\beta - \lambda_{R3}}\left(1-e^{-(\beta-\lambda_{R3})t'}\right) + \phi_{R1}\left(1-e^{-\lambda_{R1}t'}\right) + \phi_{R2}\left(1-e^{-\lambda_{R2}t'}\right) + \phi_{R3}\left(1-e^{-\lambda_{R3}t'}\right) \tag{10.205}$$

When $t' \to \infty$, $J_R(\infty) = R_{nd}(\infty) = 1 + \phi_{R1} + \phi_{R2} + \phi_{R3}$, therefore,

$$u_{nd}(r, \infty, \theta) = (1+\phi_{R1}+\phi_{R2}+\phi_{R3})\{\frac{Q_o(1+\nu_R)}{E_R}\,[-\frac{R_2^4}{r^3} + \frac{4R_2^2}{r}\,(1-\nu_R)]$$

$$+ \frac{(1+\nu_R)}{E_R}\,(E' + KF')\,Q_{om}\}\cos 2\theta \tag{10.206}$$

(b)   Tangential displacement

$$v_{Rd}(r, t, \theta) = \{\frac{-Q_o(1+\nu_R)}{E_R}\,[\frac{R_2^4}{r^3} + 2(1-2\nu_R)\frac{R_2^2}{r}\,(1-\nu_R)]\,J_R(t)$$

$$+ \frac{(1+\nu_R)}{E_R}\,(E'' + KF'')\,Q_{om}\,R_{nd}(t')\}\sin 2\theta \tag{10.207}$$

Where

$$E'' = \frac{R_2^4}{3r^3} + (1-2\nu_R)\frac{R_2^2}{r} \tag{10.208a}$$

$$F'' = \frac{2R_2^4}{3r^3} + (1-2\nu_R)\frac{R_2^2}{r} \tag{10.208b}$$

When $t' \rightarrow \infty$,

$$v_{Rd}(r, \infty, \theta) = (1 + \phi_{RJ} + \phi_{R2} + \phi_{R3}) \{ \frac{-Q_o(1 + v_R)}{E_R} [\frac{R_2^4}{r^3} + 2(1 - 2v_R)\frac{R_2^2}{r}(1 - v_R)]$$

$$+ \frac{(1 + v_R)}{E_R} (E^* + KF^*) Q_{om} \} \sin 2\theta \qquad (10.209)$$

(B)   Full Slip at Rock-lining interface

(1)   Reactive lining pressure

(a)   Radial lining pressure

$$S_{nl}(t', \theta) = S_{nl}(t') \cos 2\theta \qquad (10.210)$$

where $S_{nl}(t')$ is the radial lining pressure at the springline ($\theta = 0$) and it is given by

$$S_{nl}(t') = Q_{oms}(1 - e^{-\gamma t'}) \qquad (10.211)$$

where Q_{oms} is the final deviatoric lining pressure at the springline and it is defined as

$$Q_{oms} = \frac{3(3 - 4v_R)(\phi_{RJ}e^{-\lambda_{RJ}t'_o} + \phi_{R2}e^{-\lambda_{R2}t'_o} + \phi_{R3}e^{-\lambda_{R3}t'_o})}{C_3\bar{C}(1 + \phi_l) + \bar{a}(1 + \phi_{RJ} + \phi_{R2} + \phi_{R3})} Q_o \qquad (10.212)$$

(b)   Tangential lining pressure $S_{tl}(t', \theta)$

$$S_{tl}(t', \theta) = 0 \qquad (10.213)$$

(2) Stresses in lining

The solutions for the radial, tangential and shear stresses in the lining are given by Eqs. 10.78, 10.79 and 10.88. $S_{rr}(t')$ is defined by Eq. 10.211 and $S_{r\theta}(t') = 0$.

(3) Equivalent moment and thrust

The solutions for the moments and thrust in the liner are given by Eqs. 10.184 and 10.185.

(4) Displacements in lining

(a) Radial Displacement

At $r = R_2$

$$u_{ld}(R_2, \infty, \theta) = \frac{(1+v_l)R_2}{3E_l(1-h)^3} \bar{C} Q_{oms} L_{nds}(t') \cos 2\theta \tag{10.214}$$

where

$$L_h(t') = (1-e^{-\gamma t'}) - \frac{\phi_l \lambda_l e^{-\lambda_l t'}}{\gamma - \lambda_l} \left(1 - e^{(\gamma - \lambda_l)t'}\right) + \phi_l(1 - e^{-\lambda_l t'}) \tag{10.215}$$

At infinity, $L_{nds}(\infty) = 1 + \phi_l$

Therefore,

$$u_{ld}(R_2, \infty, \theta) = \frac{(1+v_l)R_2}{3E_l(1-h)^3} \bar{C} Q_{oms} (1 + \phi_l) \cos 2\theta \tag{10.216}$$

At $r = R_1$

$$u_{ld}(R_1, t', \theta) = \frac{(1+v_l)}{E_l(1-h)^3} \bar{A}' Q_{oms} L_{nds}(t') \cos 2\theta \qquad (10.217)$$

where

$$\bar{A}' = (2h^2+h+1)R_1 - h^2(h+3) \frac{R_2^4}{3R_1^3} + 2h(h^2+h+2) \frac{R_2^2}{R_1}$$
$$-v_l [2h(h^2+h+2) \frac{R_2^2}{R_1} + \frac{2}{3}(3h+1) \frac{R_1^3}{R_2^2}] \qquad (10.218)$$

When $t' \to \infty$,

$$u_{ld}(R_1, t', \theta) = \frac{(1+v_l)}{E_l(1-h)^3} \bar{A}' Q_{oms} (1+\phi_l) \cos 2\theta \qquad (10.219)$$

(b)   Tangential Deformation

At $r = R_2$

$$v_{ld}(R_2, t', \theta) = \frac{-(1+v_l)R_2}{3E_l(1-h)^3} \bar{d} Q_{oms} L_{nds}(t') \sin 2\theta \qquad (10.220)$$

When $t' \to \infty$,

$$v_{ld}(R_2, \infty, \theta) = \frac{-(1+v_l)R_2}{3E_l(1-h)^3} \bar{d} Q_{ons} (1+\phi_l) \sin2\theta \qquad (10.221)$$

At $r = R_1$

$$v_{ld}(R_1, t', \theta) = -\frac{2(1+v_l)}{E_l(1-h)^3} \bar{A}'' Q_{ons} L_{nds}(t') \sin2\theta \qquad (10.222)$$

where

$$\bar{A}'' = (2h^2+h+1)\frac{R_1}{2} - (3-2v_l)(?h+1)\frac{R_1^3}{6R_2^2} + h^2(h+3)\frac{R_2^4}{6R_1^3}$$

$$+ (1-2v_l)h(h^2+h+2)\frac{R_2^2}{2R_1} \qquad (10.223)$$

When $t' \to \infty$,

$$v_{ld}(R_1, \infty, \theta) = -\frac{2(1+v_l)}{E_l(1-h)^3} \bar{A}'' Q_{ons} (1+\phi_l) \sin2\theta \qquad (10.224)$$

(5) Stresses in rock mass

The solutions for the radial, tangential and shear stresses in the rock mass are given by Eqs. 10.197, 10.199 and 10.201 respectively in which the value of $S_{nl}(t')$ is given by Eq. 10.174 and $S_{ll}(t') = 0$.

(6)   Displacements in rock mass

(a)   Radial displacement

$$u_{rd}(r, t, \theta) = \{ \frac{Q_o(1+v_R)}{E_R} [- \frac{R_2^4}{r^3} + \frac{4R_2^2}{r} (1-v_R)] J_R(t)$$

$$+ \frac{(1+v_R)}{E_R} E' Q_{oms} R_{nds}(t') \} \cos 2\theta$$

(10.225)

where

$$E' = \frac{R_2^4}{3r^3} - 2(1-v_R) \frac{R_2^2}{r}$$

(10.226a)

$$J_R(t) = 1 + \phi_{RI}(1-e^{-\lambda_{RI}t}) + \phi_{R2}(1-e^{-\lambda_{R2}t}) + \phi_{R3}(1-e^{-\lambda_{R3}t})$$

(10.226b)

$$R_{nds}(t') = (1-e^{-\gamma t'}) - \frac{\phi_{RI}\lambda_{RI}e^{-\lambda_{RI}t'}}{\gamma - \lambda_{RI}}(1-e^{-(\gamma - \lambda_{RI})t'}) - \frac{\phi_{R2}\lambda_{R2}e^{-\lambda_{R2}t'}}{\gamma - \lambda_{R2}}(1-e^{-(\gamma - \lambda_{R2})t'})$$

$$- \frac{\phi_{R3}\lambda_{R3}e^{-\lambda_{R3}t'}}{\gamma - \lambda_{R3}}(1-e^{-(\gamma - \lambda_{R3})t'}) + \phi_{RI}(1-e^{-\lambda_{RI}t'}) + \phi_{R2}(1-e^{-\lambda_{R2}t'}) + \phi_{R3}(1-e^{-\lambda_{R3}t'})$$

(10.227)

When $t' \to \infty$, $J_R(\infty) = R_{nd}(\infty) = 1 + \phi_{RI} + \phi_{R2} + \phi_{R3}$, therefore,

$$u_{rd}(r, \infty, \theta) = (1+\phi_{RI}+\phi_{R2}+\phi_{R3})\{ \frac{Q_o(1+v_R)}{E_R} [- \frac{R_2^4}{r^3} + \frac{4R_2^2}{r} (1-v_R)]$$

$$+ \frac{(1+v_R)}{E_R} E' Q_{om} \} \cos 2\theta$$

(10.228)

(b)   Tangential displacement

$$v_{Rd}(r, t, \theta) = \{ \frac{-Q_o(1+v_R)}{E_R} [\frac{R_2^4}{r^3} + 2(1-2v_R)\frac{R_2^2}{r} (1-v_R)] J_R(t)$$

$$+ \frac{(1+v_R)}{E_R} E^{''} Q_{oms} R_{nds}(t') \} \sin 2\theta \qquad \qquad (10.229)$$

Where

$$E^{''} = \frac{R_2^4}{3r^3} + (1-2v_R)\frac{R_2^2}{r} \qquad \qquad (10.230)$$

When $t' \rightarrow \infty$.

$$v_{Rd}(r, \infty, \theta) = (1+\phi_{R1}+\phi_{R2}+\phi_{R3}) \{ \frac{-Q_o(1+v_R)}{E_R} [\frac{R_2^4}{r^3} + 2(1-2v_R)\frac{R_2^2}{r} (1-v_R)]$$

$$+ \frac{(1+v_R)}{E_R} E^{''} Q_{oms} \} \sin 2\theta \qquad \qquad (10.231)$$

10.5.3 Final Solutions

The final expressions for the stresses and displacements in the rock mass and lining are obtained by superimposing the values obtained from the hydrostatic and deviatoric stress components:

(1)   Reactive lining pressure at rock-lining interface

(a)   Radial lining pressure

$$P_L(t', \theta) = P_l(t') + S_{nl}(t', \theta) \qquad (10.232)$$

(b)   Tangential lining pressure

$$S_L(t', \theta) = S_{nl}(t', \theta) \qquad (10.233)$$

(2)   Stresses in the Lining

(a)   Radial stress

$$\sigma_{rL}(r, t', \theta) = \sigma_{rlh}(r, t') + \sigma_{rld}(r, t', \theta) \qquad (10.234)$$

(b)   Tangential stress

$$\sigma_{\theta L}(r, t', \theta) = \sigma_{\theta lh}(r, t') + \sigma_{\theta ld}(r, t', \theta) \qquad (10.235)$$

(5)   Stresses in rock mass

(a)   radial stress

$$\sigma_{rR}(r, t', \theta) = \sigma_{rRh}(r, t') + \sigma_{rRd}(r, t', \theta) \qquad (10.241)$$

(b)   tangential stress

$$\sigma_{\theta R}(r, t', \theta) = \sigma_{\theta Rh}(r, t') + \sigma_{\theta Rd}(r, t', \theta) \qquad (10.242)$$

(c)   Shear stress

$$\tau_{r\theta R}(r, t', \theta) = \tau_{r\theta Rh}(r, t') + \tau_{r\theta Rd}(r, t', \theta) \qquad (10.243)$$

(6)   Displacements in rock mass

(a)   Radial displacement

$$u_R(r, t, \theta) = u_{Rh}(r, t) + u_{Rd}(r, t, \theta) \qquad (10.244)$$

(b)   Tangential displacement

$$v_R(r, t, \theta) = v_{Rh}(r, t) + v_{Rd}(r, t, \theta) \qquad (10.245)$$

It should be noted that the solutions given by Lo and Yuen (1981) is a special case of the solutions derived in this chapter. The solutions obtained becomes the same as those given by Lo and Yuen if the rock model is degenerated into a spring and one Kelvin unit connected in series.

10.6 SUMMARY

In this chapter, the rock-lining-time interaction of circular tunnels driven in swelling rocks is investigated. Closed form solutions for the stresses and displacements and other engineering quantities of interest in the lining and in the rock are derived. In the solutions, the rock mass is idealized by a 7-element Kelvin model (a model which is capable of describing the long-term time-dependent deformation of swelling shales). The lining is idealized by a 3-element Kelvin model. The correspondence principle derived in Chapter 9 is adopted to convert the elastic solution of the problem to viscoelastic solution. It should be noted that the solutions presented pertain to the linear case in which the effect of reactive pressure in the moduli governing time-dependent deformation (viz. values of E_{Rm}) has not yet been taken into account. This problem dealing with "suppression effect" is treated in the next chapter.
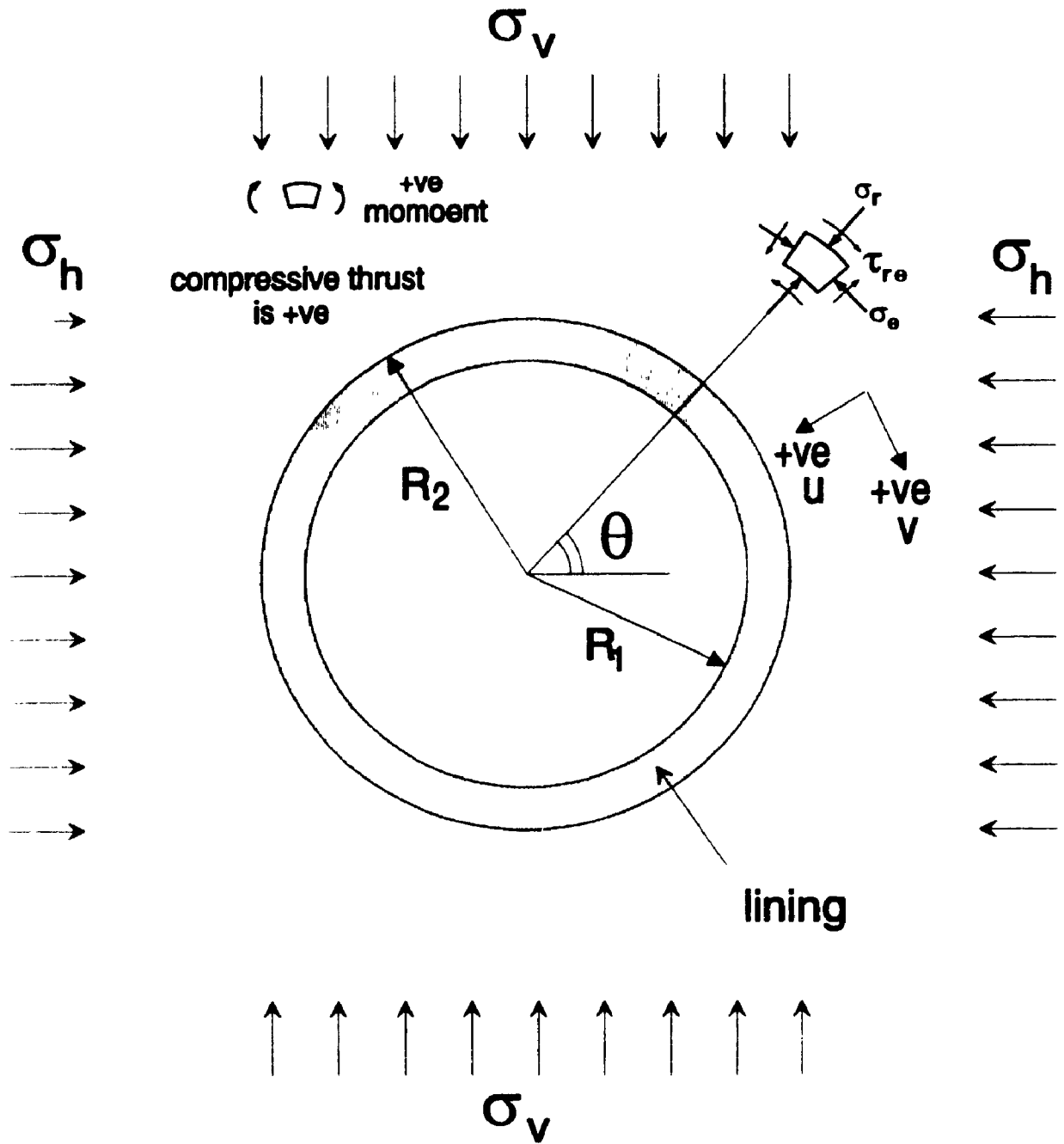
Figure 10.1 Sign convention, stress condition and geometry of the problem

radial deformation = free deformation + deformation of
of lining   of rock due to   rock due to
                  excavation   reactive force P_i
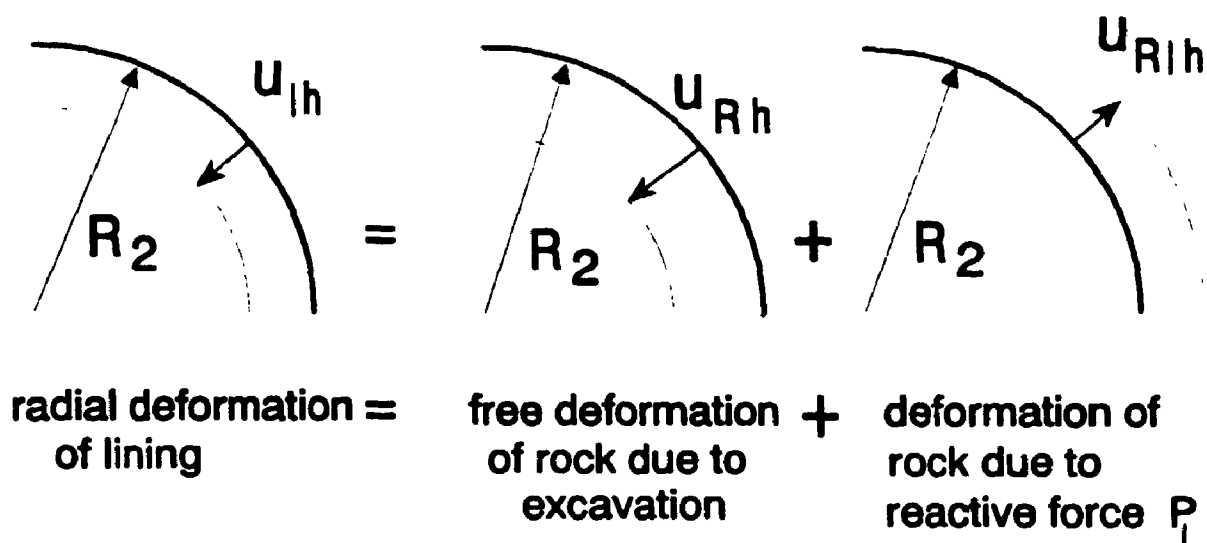
Figure 10.2(a) Continuity of radial displacement at interface $r=R_2$ for hyorostatic stress component P_0

deformation = free deformation + deformation of
of lining   of rock due to   rock due to
              excavation   reactive forces
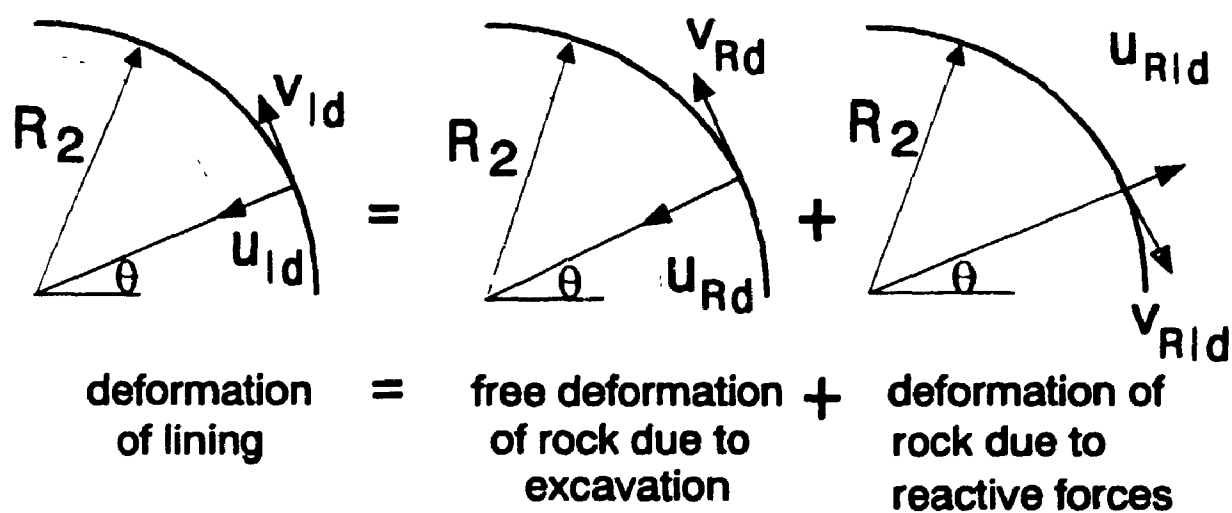
Figure 10.2(b) Continuity of displacements at interface $r=R_2$ for deviatoric stress component Q_0

CHAPTER 11

NONLINEAR ROCK-LINING-TIME INTERACTION METHOD

AND ITS APPLICATION ON SABNGS NO.3 PROJECT

11.1   INTRODUCTION

In Chapter 10, closed form solutions for the stresses and displacements in rock mass and lining have been obtained for the problem of swelling rocks around tunnels. The rock mass is characterized by the long-term time-dependent deformation and it is modelled by a generalized Kelvin model consisting of three Kelvin units and a spring connected in series. The solution obtained takes into account one set of deformation parameters which do not change with time.

For rocks such as Queenston Shale (Chapter 8), the deformation parameters are nonlinearly stress dependent, suggesting that the values of the deformation parameters E_{Rai} increase as the reactive pressure is accumulated behind the lining. The use of the deformation parameters obtained from the free swell test in the closed form solution will lead to a too conservative solution. An approach, therefore, allowing the update of the values of deformation parameters as the level of the accumulated reactive pressure increases should be adopted.

In this chapter, a pressure step-wise method is implemented for the use with the closed form solution obtained in Chapter 10 to account for the increase of values of deformation parameters of rock as the pressure level behind the lining increases. The method adopted is explained in the next section. In the subsequent sections, the developed method is used to calculate the stresses and displacements in the concrete

lining of the proposed tunnels for SABNGS NO. 3 project. The effects of the different parameters involved in the solution are studied by changing one parameter at a time in this study.

11.2   PRESSURE STEP-WISE METHOD

After the installation of lining, the reactive lining pressure increases from zero at $t` = 0$ to its final value at infinity. The final value of lining pressure is highly dependent on the time-dependent deformation parameters used in the analysis. The closed form solutions derived in Chapter 10 use only one set of parameters which does not change with the marching of time. For rocks such as Queenston Shale, however, these parameters are dependent on the stress level accumulated. Experiments (Chapters 7 and 8) showed that the values of the parameters controlling the amount of time-dependent deformation increase as the stress level increases, leading to a decrease in the forthcoming deformations and finally leading to a decrease in the final reactive lining pressure.

To take into account this "suppression effect", it is necessary to identify the 'equivalent applied pressure" at the rock-lining interface. In Chapter 8, it has been seen that the values of moduli controlling the time-dependent deformation are dependent on the level of applied pressure. In tunnel problems, it will be assumed that the values of rock moduli are dependent on the level of radial reactive pressure accumulated behind the lining along the tunnel perimeter. Since the reactive lining pressure at any time is in general not uniform along the tunnel perimeter, the average value along the perimeter will be taken as the "equivalent applied pressure" from which the updated values of rock

moduli at any time are calculated.

To account for the increase of the values of deformation parameters as the reactive lining pressure increases a pressure step-wise approach (semi-analytical method) is adopted (Figure 11.1). In this approach, the pressure accumulated behind the lining is assumed to increase in increments of equal magnitude (ΔP). The rock parameters are considered constant within each increment and they are updated at the beginning of each increment. For each increment of pressure, the time values at the beginning and end of the increment are calculated and then used with the corresponding parameters to calculate the increments of displacements and stresses in lining and rock within this time interval using the closed form solutions derived in Chapter 10. It should be emphasized at this point that the rate parameters, λ_{Ri}, are considered stress-independent quantities as discussed in Chapter 8 and their values should be kept constant in all the increments.

For example in the first pressure step, the pressure is increased from zero at $t^{`} = 0$ to $\Delta P$ at $t_1^{`}$ (Figure 11.1). The time $t_1^{`}$ at the end of the increment is calculated by solving Eq. 10.50 to find $t^{`}$ at pressure level equals ΔP. The deformation parameters for this pressure step are those from free swell test. Within the time interval between 0 and $t_1^{`}$, the increments of all the required quantities of stresses and displacements in rock and lining are calculated.

For the second pressure step, the pressure is increased from ΔP at $t_1^{`}$ to $2\Delta P$ at $t_2^{`}$. The deformation parameters for this step are calculated by substituting σ_a in Eq. 8.12 by the pressure level ΔP, the pressure at the beginning of the step. The time $t^{`}$

is known, calculated at the end of first pressure step. The time $t_2^{`}$ at the end of the second pressure step is calculated by solving Eq. 10.50 to find $t^{`}$ at pressure level equals $2\Delta P$. Within the time interval between ΔP and $2\Delta P$, the corresponding increments of stresses and displacements in the lining and in the rock are calculated. To update the stresses and displacements, the increments of stresses and displacements calculated from this step are added to the previously computed ones.

Similarly, for pressure step i, the pressure is increased from $(i-1)\Delta P$ at $t_{i-1}^{`}$ to $i\Delta P$ at $t_i^{`}$. The deformation parameters for this step are calculated by substituting σ_a in Eq. 8.12 by the pressure level $(i-1)\Delta P$, the pressure at the beginning of the step. The time $t_{i-1}^{`}$ is known, calculated at the end of pressure step $i-1$. The time $t_i^{`}$ at the end of pressure step i is calculated by solving Eq. 10.50 for $t^{`}$ at pressure level $i\Delta P$. Within the time interval between $t_{i-1}^{`}$ and $t_i^{`}$, the required increments of stresses and displacements are calculated and added to the previous computed ones to update the values.

The calculation procedures are repeated until the final pressure is reached. It should be noted that the size of the final pressure increment may be less than ΔP and it is calculated by subtracting the pressure at the beginning of the increment from the final pressure.

It is obvious that in the aforementioned method, the solution may be sensitive to the pressure-increment size ΔP. Therefore, a sensitivity study is performed to obtain the relevant step size. The results of the sensitivity analysis are discussed in the following section.

It should be noted that this "suppression problem" could be tackled by using a time step-wise approach instead of the pressure step-wise approach. However, the former approach requires very large number of time steps to obtain accurate solution, and the time infinity cannot be readily included for equal time steps.

11.3 ANALYSIS OF A TUNNEL IN QUEENSTON SHALE

In this study, a tunnel driven in Queenston Shale which has important time-dependent deformation characteristics will be analyzed. Experiments performed showed that Queenston Shale experiences long-term time-dependent deformations upon stress relief. The deformation with time is well represented by a model consisting of three Kelvin units connected in series, Chapter 7. It is also found that the time-dependent deformation is nonlinearly stress dependent. At a certain value of applied pressure called the critical pressure σ_c (Chapter 8), the deformation is suppressed completely.

Equations relating the deformation parameters of Kelvin units to the initial stress value and the critical pressure are derived in Chapter 8 (Eqs. 8.12).

The pressure step-wise approach mentioned in the previous section is adopted to calculate the time-dependent stresses and displacements in the lining and the rock at a typical section of the tunnel at depth 200 m. A "baseline" analysis for this tunnel section is performed first using the proposed parameters for design. The effect of the different parameters on design is studied by changing one parameter at a time and the results are compared with the "baseline" analysis.

11.3.1   Parameters Used in the "Baseline" Analysis

(1)   *In Situ* Stresses (refer to Chapter 5)

Vertical *in situ* stress: $P_v = 5.2$ MPa

Initial Stress Ratio: $K_o = 4$

(2)   Geometry of Lining (Proposed)

Inner radius of lining: $R_1 = 6.25$ m

Outer radius of lining: $R_2 = 6.80$ m

(3)   Elastic Parameters of Rock (Hefny and Lo 1992)

Young's modulus: $E_R = 15.8$ MPa

Poisson's ratio: $v_R = 0.3$ MPa

(4)   Initial Deformation Parameters for Time-Dependent Deformation of Rock (free swell, Chapter 7)

These parameters are calculated from the results of free swell test on samples recovered from borehole NF4A in 1990 investigation. Results of reliable tests (no separation of bedding planes during test period) are used to calculate the representative deformation parameters for the three Kelvin units (Tests: NF4A-1, NF4A-4, NF4A-6, and NF4A-13).

$E_{Rl} = 1.50 \times 10^4$ MPa

$E_{R2} = 8.08 \times 10^3$ MPa

$E_{R3} = 4.94 \times 10^3$ MPa

(5) Initial Viscosity Parameters of Rock (Chapter 7)

$\eta_{R1} = 136 \times 10^3$ MPa.day

$\eta_{R2} = 288 \times 10^3$ MPa.day

$\eta_{R3} = 274 \times 10^4$ MPa.day

(6) Other Parameters of Rock

(a) Critical Stress Ratio (CSR) (the ratio of the critical pressure σ_c to the initial stress σ_o, Figure 7.19):

$$CSR = 0.3$$

(b) Equivalent Stress Ratio ESR (the ratio of the equivalent stress σ_e, stress below which the deformation parameters are equal to those for free swell, to the initial stress σ_o) (see Chapter 8):

$$ESR = 0.03\%$$

(7) Parameters of Lining

The parameters of elastic and time-dependent deformation of lining are taken similar to those obtained for the concrete lining used in the Heart Lake Tunnel (Lo and

Yuen 1981).

Young's modulus: $E_l = 28.0 \times 10^3$ MPa

Poisson's ratio: $v_l = 0.2$

$E_{lt} = 14.0 \times 10^3$ MPa

$\eta_l = 1400 \times 10^3$ MPa.day

Tensile strength: $f_t = 3.5$ MPa

Compressive strength: $f_c = 28\text{-}40$ MPa (medium to high strength concrete, Beer and Johnston 1987)

The time elapsed before the installation of lining is taken 30 days in the "baseline" analysis.

11.3.2   Sensitivity Analysis

In this section, a sensitivity study is carried out to investigate the effect of the magnitude of pressure increment on the final solution.   Figure 11.2 shows the relationship between the final radial lining pressure ratio at springline and the magnitude of the pressure increment. The pressure at the springline is given as a ratio of computed pressure to the linear case (case of constant values of E_{R_m}, independent of stress). The pressure increment ΔP is given as a ratio to the initial hydrostatic stress $P_o \left(= \dfrac{\sigma_h + \sigma_v}{2} \right)$.

It can be seen from Figure 11.2 that for pressure increments less than 1% of P_o,

the final solution is insensitive to the increment magnitude. For pressure increments greater than 1% of P_o, as the increment magnitude increases, the sensitivity of the solution increases. For a step size approximately 20% of P_o and greater, the computed pressure approaches that of the linear case.

Based on the results of the above investigation, a pressure increment magnitude less than 1% of P_o should be used in the analysis to insure that the obtained solution is independent of the magnitude of the pressure increment. To obtain a smooth solution with time, a pressure increment of magnitude 0.3% of P_o is adopted. This leads to a total of 26 pressure increments in the "baseline" analysis.

11.3.3   Discussion of Results

The parameters listed in section 11.3.1 are used to calculate the stresses and displacements in the lining and rock. To show the effect of suppression of the accumulated pressure behind the lining on the calculated stresses and displacements, the solution from the linear case (case of no suppression where constant E_{Roi} values are used) is computed and compared to that obtained from the nonlinear case (pressure step-wise approach).

(1)   Displacement at interface

Figure 11.3 shows the change of radial displacement of rock at the springline at interface with time. The solid line represents the linear case whereas the dashed line represents the nonlinear case. The effect of lining installation is manifest from this

figure. Before the installation of the lining, the displacement increases rapidly while after installation, the rock deforms at much lower rates. It is also clear that the linear case leads to higher radial displacements.

(2) Final radial and tangential stresses in rock

The distributions of the final radial and tangential stresses in rock at both the springline and the crown are shown in Figures 11.4 and 11.5. The final radial stress in rock at the springline level (Figure 11.4) increases as the radial distance increases. More than ninety percent of the far field stress is reached at radial distance equal to 5 times R_2. The final tangential stress at the springline level rapidly increases as the radial distance increases until it slightly exceeds the value of the far field stress at distance about 1.7 R_2. Then it decreases to approach the value of the far field stress.

Above the crown, the radial stress in rock (Figure 11.5) rapidly increases from the interface pressure value to its peak value at distance about 1.5 R_2. The radial stress decreases afterwards as the radial distance increases to approach the far field stress. The tangential stress in rock above the crown (Figure 11.5) has its peak value at the interface and then it decreases rapidly to approach the far field stress.

(3) Distribution of final lining pressure

Figures 11.6 and 11.7 show the distribution of the final radial and tangential lining pressures for the cases of no slip (perfectly rough) and full slip (perfectly smooth) of interface, respectively.

For the case of no slip at interface (Figure 11.6a), the radial pressure gradually increases from its minimum value at springline to its maximum value at the crown-invert line. The maximum value of the tangential lining pressure occurs at 45° and decreases to zero at $\theta = 0^o$ and $\theta = 90^o$.

For the full slip case, the radial lining pressure has its maximum value at the springline and slightly decreases toward the crown-invert line (Figure 11.7). The tangential lining pressure is zero.

From Figures 11.6 and 11.7, it is obvious that the increase of the values of rock time-dependent deformation moduli as the lining pressure at the interface increases (nonlinear analysis) has a tremendous effect in reducing the final interface pressure built-up behind the lining.

(4) Distribution of final tangential stress in lining

The distributions of the final tangential stress in lining for the no slip and full slip cases are shown in Figures 11.8 and 11.9, respectively. For the no slip case, the tangential stress at both $r = R_1$ and $r = R_2$ decreases from its maximum at the crown to its minimum at the springline. The maximum compressive stress in the lining occurs at the inner face of the lining at the crown. At the inner face of lining at springline, a small value of tensile stress occurred for the "baseline" analysis, $K_o=4$. However, as will be seen later, for higher values of K_o, higher values of tensile stress are obtained at the inner face of the lining at the springline. From the results of analyses, it has been found that the inner face at the crown is the critical location for compressive stresses,

whereas the inner face at the springline is the critical location for tensile stresses.

From Figures 11.8 and 11.9 and Table 11.1 and by comparing the values of the final induced tangential stresses in the lining to the strength of the concrete in tension and compression, it can be seen that the final stresses calculated in the lining from the linear analysis are too high and exceeds the compressive strength of the lining at the crown at the inner and outer faces. It can, also, be seen that the stresses calculated from the nonlinear analysis are less than half those calculated from the linear case and that they are below the tensile and compressive strengths of the concrete lining. This shows the importance of adopting the nonlinear approach to obtain an economical and safe design for the lining.

(5) Distribution of final equivalent bending moment and axial thrust in the lining

The equivalent bending moment and axial thrust can be calculated from the fibre stresses in the lining at the inner and outer faces. The distribution is shown in figures 11.10 and 11.11 for the no slip and full slip cases, respectively. The equivalent bending moment has its maximum positive value at the springline and decreases gradually to zero and then becomes negative and increases to its maximum negative value at the crown. Positive bending moment causes tensile stress at the inner fibre.

The equivalent axial thrust is maximum and compressive at the crown and decreases gradually to its minimum compressive value at the springline. It should be noted that for higher values of K_a, the thrust may become tensile at the springline.

11.3.4   Effects of Different Parameters on Final Tangential Stress in Lining

(1)   Effect of R_1/R_2

Figure 11.12 shows the effect of the geometry ratio R_1/R_2 on the tangential stresses in lining at the inner and outer faces at the crown and the springline. It can be seen that at the springline there is a small effect on the tangential stresses at the outer face. At the inner face, although the magnitude of the tangential stresses slightly changes as R_1/R_2 changes, the sign of the stress is dependent on the value of R_1/R_2.

At the crown. the compressive tangential stresses increases at the inner and outer faces as the ratio R_1/R_2 increases. The sensitivity of the calculated stresses increases as R_1/R_2 increases.

(2)   Effect of Poisson's ratio of rock on the tangential stresses in lining

The effect of Poisson's ratio on the tangential stresses in lining at the springline and the crown is shown in Figure 11.13. It is clear that Poisson's ratio is an important parameter which strongly affects the results of the stresses especially at the springline. At the crown, as Poisson's ratio increases, the tangential stresses decreases at the inner and the outer faces. At the springline, for small values of Poisson's ratio, the tangential stress in the lining is tensile at both the inner and outer faces with a higher value at the inner face. As Poisson's ratio increases, the tensile stress decreases and then turns into compressive stresses.

(3) Effect of t_o and K_o on the tangential stresses in lining

The variation of final tangential stress in lining at the inner face at springline with time of installation of lining t_o and ratio of *in situ* horizontal to vertical stress K_o is illustrated in Figure 11.14. It can be seen from Figure 11.14 that both t_o and K_o play crucial roles in determining the tangential stresses in lining.

For $K_o = 1$, the tangential stress at the inner face is compressive and it decreases and then becomes tensile as K_o increases, for a given value of t_o. For $K_o > 5$, the tensile stress may exceed the tensile strength of the concrete which would cause distress in the lining.

For a given initial stress ratio K_o, an increase in t_o (the time lapse between excavation and lining installation) decreases the induced tensile stress in the lining.

(4) Effect of flexibility of lining

To study the effect of the deformation parameters of rock (Young's modulus and the three deformation moduli of Kelvin units) on the final tangential stress in lining, the following apparent flexibility parameters are defined.

$$F_e = \frac{G_R}{G_l}$$

$$F_l = \frac{G_{Re}}{G_{le}}$$

where:
$$\frac{1}{G_{Rt}} = \frac{1}{G_{Rt1}} + \frac{1}{G_{Rt2}} + \frac{1}{G_{Rt3}}$$

For perfectly rigid lining, $G_l \to \infty$, $F_e \to 0$. For elastic lining, $G_k \to \infty$, $F_t \to 0$.

Figures 11.15 and 11.16 show the effect of F_e and F_t on the tangential stress in lining for big range of values. The values of F_e and F_t are calculated by keeping the values of lining parameters constant and changing G_R and G_{Rt} of the rock.

From Figure 11.15, it is obvious that F_e has a small effect on the final tangential stress in lining especially for values of F_e greater than 1.

Figure 11.16 shows that the final tangential stress in lining is sensitive to the change in F_t. As F_t increases, the final tangential stresses everywhere in lining decrease. This implies that as the deformation moduli of the springs in Kelvin units for rock increases, the resulting final tangential stresses in lining decreases. This is expected since the increase of the values of deformation moduli of rock means that less final rock deformation will be developed and, therefore, less interactive lining pressure will be built-up behind the lining.

(5)   Effect of critical stress ratio (CSR)

The critical stress ratio (CSR) is defined as the ratio of the critical stress, the stress above which the swelling strain is completely suppressed, to the initial hydrostatic stress component P_o. Figure 11.17 shows the effect of CSR on the final tangential

stress in lining. It is obvious from the figure that the *CSR* is an important parameter affecting the values of compressive stresses calculated in the lining at the crown. As the *CSR* increases, the compressive stresses at the outer and inner face of the lining at the crown increases. For example, the increase of *CSR* from the value used in the "baseline" analysis (0.3) to 1, increases the maximum compressive stress at the inner face of the lining from about 26 MPa to about 32 MPa. At the spring line, the *CSR* has small effect on the tangential stresses in the lining.

11.4 SUMMARY AND CONCLUSIONS

Using the theory of linear viscoelasticity, closed form solutions for the stresses and displacements in the rock mass and tunnel lining have been derived in Chapter 10. The long-term time-dependent deformation of the rock is idealized by a model consisting of three Kelvin units connected in series. The time-dependent deformation of the lining is represented by a single Kelvin unit. The anisotropy of the initial stress system and the time elapsed between the excavation and the installation of the lining are accounted for. In this chapter, a semi-analytical solution (nonlinear pressure step-wise approach) is developed to allow for the increase of the values of deformation moduli of the model as the pressure level behind the lining increases. The developed method is then used to predict the stresses in the lining of a tunnel in Queenston Shale similar to these considered for the SABNGS No.3 project. The effects of the different parameters on the solution are investigated. From the results of this study, the following conclusion can be drawn:

(1)   The stresses and displacements calculated from the nonlinear approach (suppression of rock deformation as the lining pressure increases is accounted for) are considerably less than those calculated from the linear case (suppression is not accounted for).

(2)   The "baseline" analysis on the proposed dimensions of the tunnels shows that the stresses in lining do not exceed the tensile or the compressive strengths of the concrete.

(3)   The critical location in the lining for the compressive stress is the inner face at the crown and that for the tensile stress is the inner face at the springline.

(4)   Poisson's ratio of the rock is an important factor in the solution. As Poisson's ratio decreases, the compressive tangential stresses in the lining at the crown increase and the tensile stresses at the springline increase.

(5)   As the time elapsed between the excavation of the tunnel and the installation of the lining increases, the stresses induced in the lining decrease.

(6)   As the initial stress ratio increases, the tensile stress induced in the lining at the inner face at the springline increases. For the tunnel considered, ratios greater than 5 produce tensile stress which is higher than the tensile strength of the concrete.

(7)   The deformation moduli E_{Rei} for the three Kelvin units of the model play an important rule in the final solution. As the values of the moduli governing time-dependent deformation increase, the displacements and stresses induced in the lining decrease.

TABLE 11.1   Tangential stresses in lining calculated from the "baseline" analysis

Case	Tangential Stress (MPa)							
	No Slip Case				Full Slip Case			
	Crown		Springline		Crown		Springline	
	$r=R_1$	$r=R_2$	$r=R_1$	$r=R_2$	$r=R_1$	$r=R_2$	$r=R_1$	$r=R_2$
Linear	62.2	49.8	2.1	9.5	38.5	23.8	25.8	35.5
Nonlinear	26.1	21.8	-0.2	2.1	15.0	10.1	10.9	13.9

Note: Ultimate strength in compression for medium to high strength concrete is 28-40 MPa (Beer and Johnston 1987)
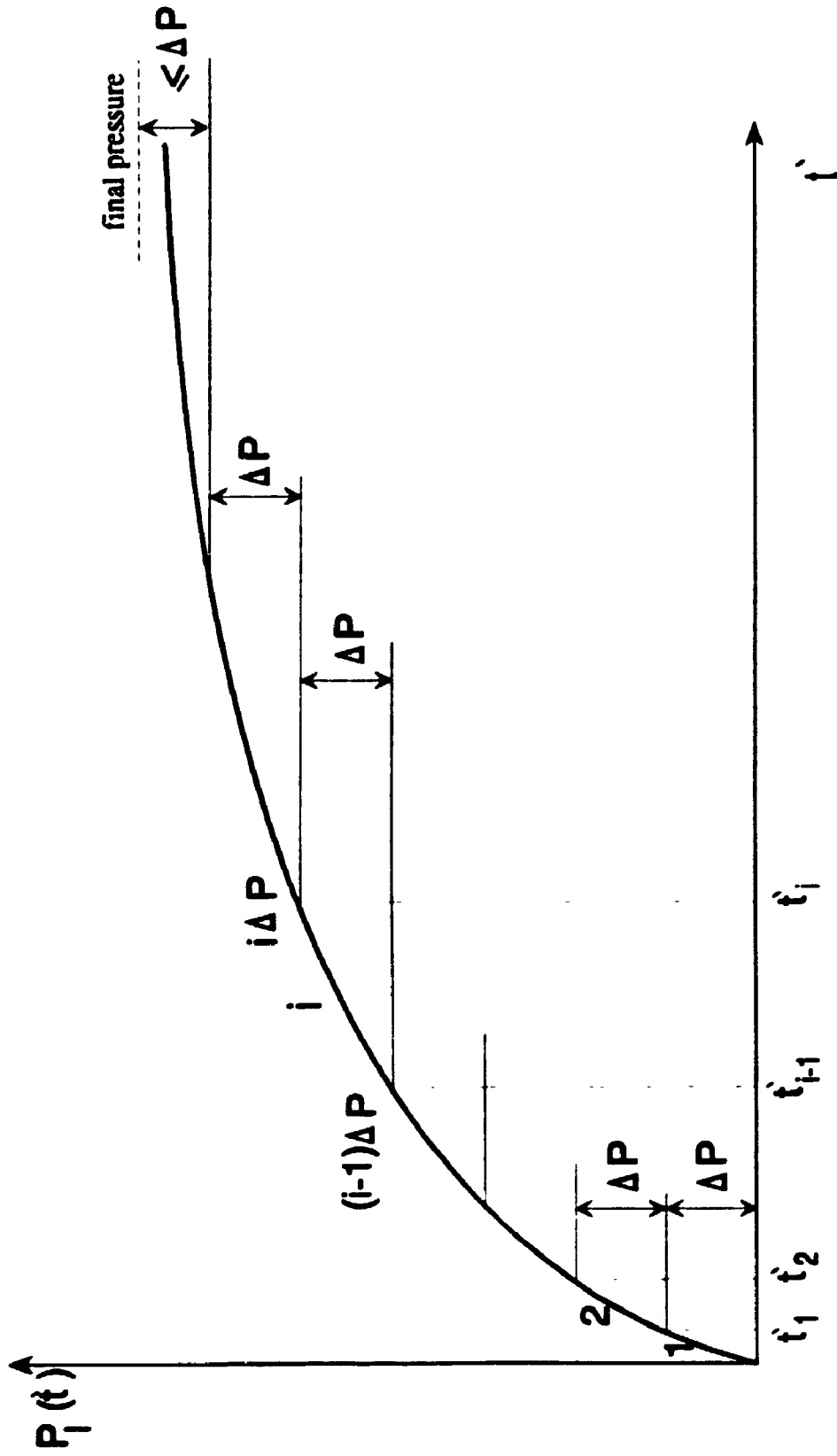
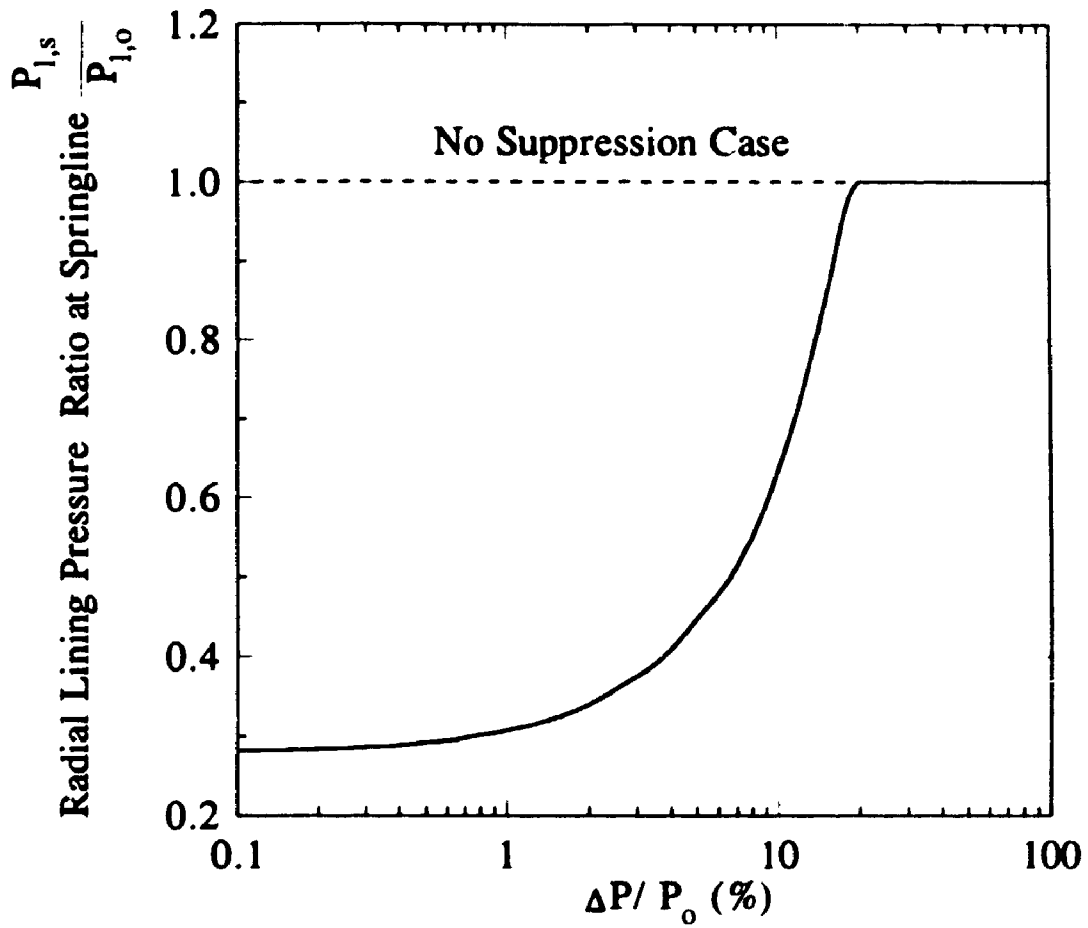Figure 11.1 Schematic diagram showing the pressure step-wise approach

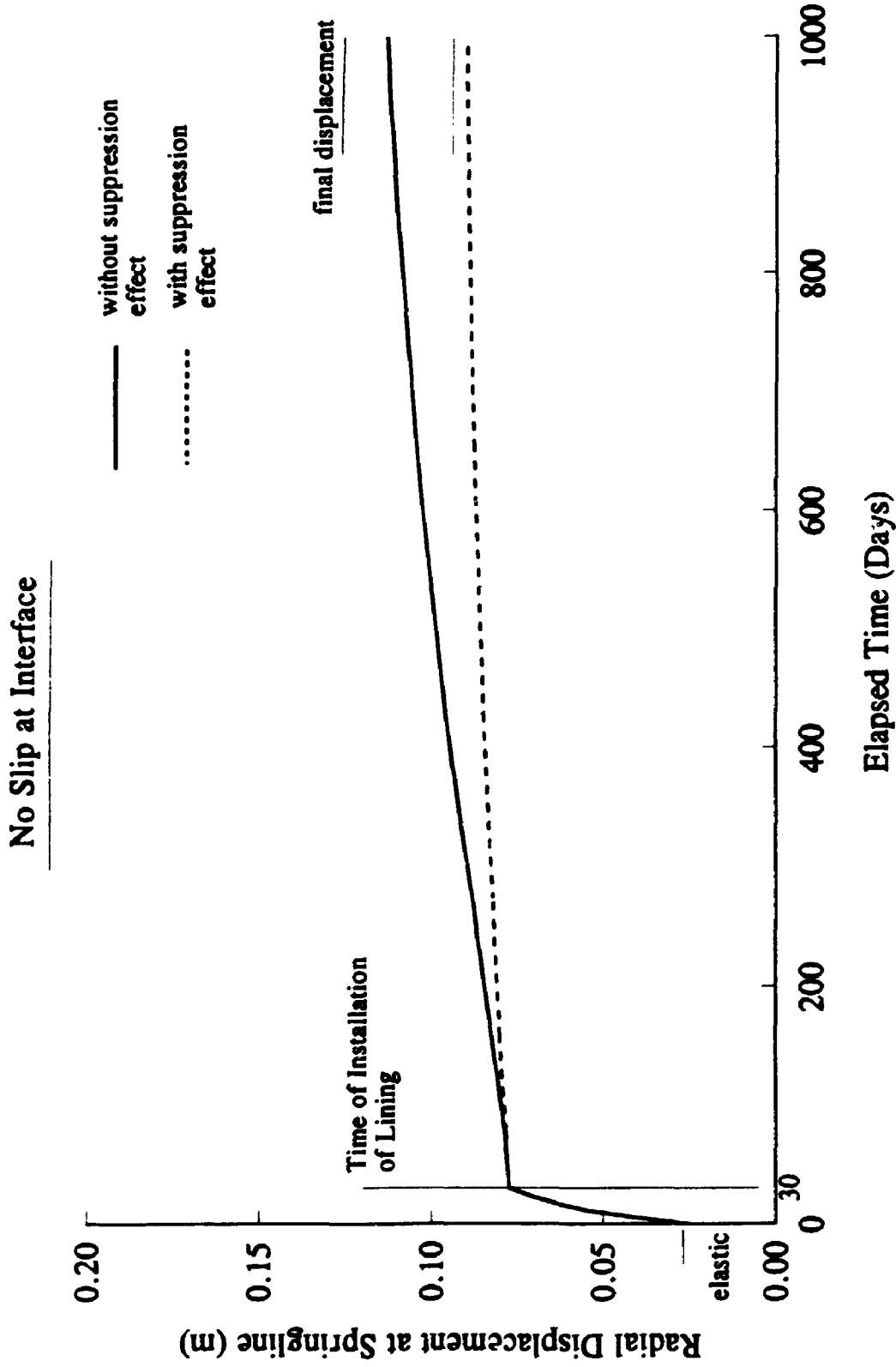Figure 11.2 Effect of pressure-increment size on the solution

Figure 11.3 Distribution of radial displacement at springline with time

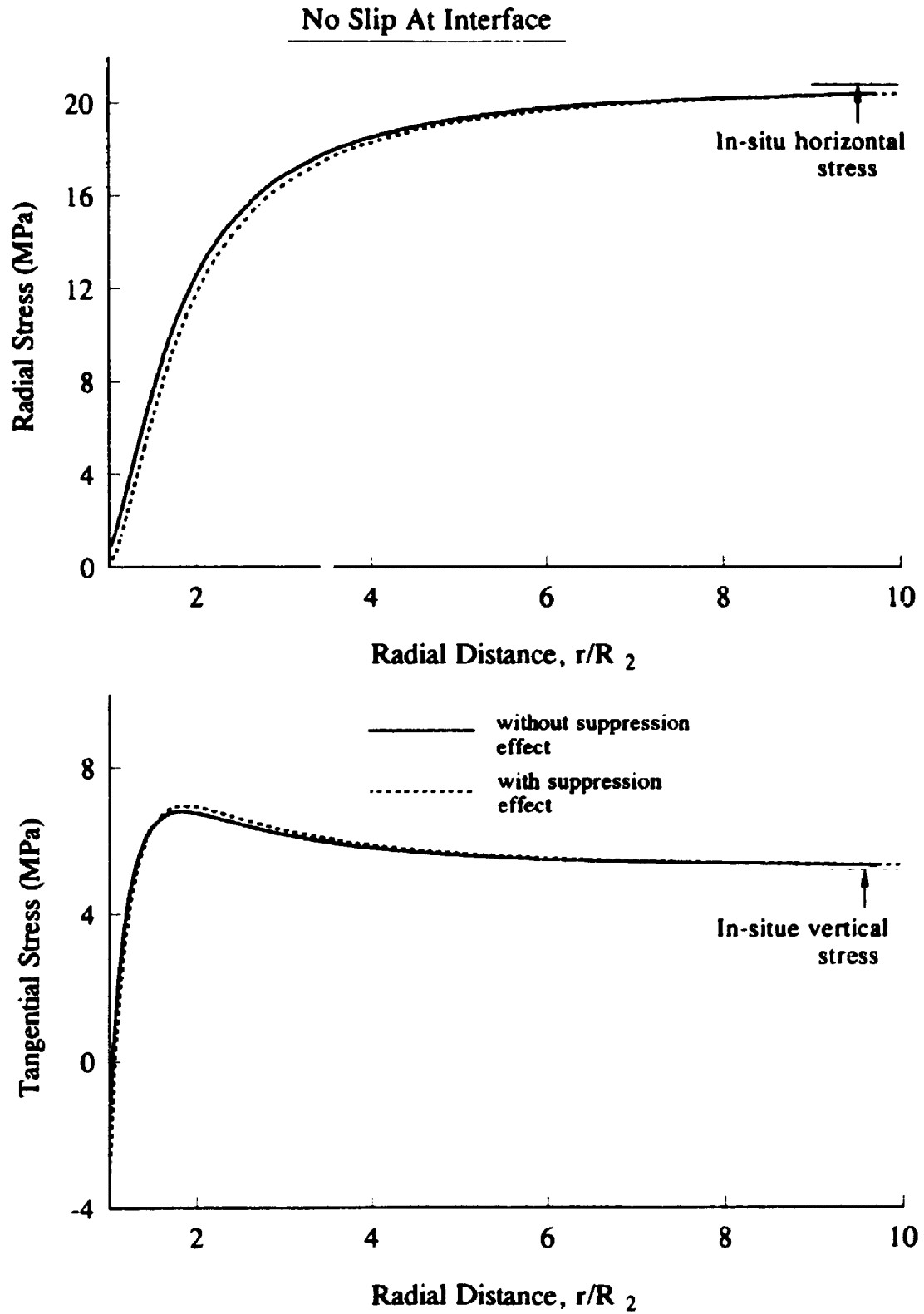Figure 11.4 Distribution of final radial and tangential stresses in rock at springline level with radial distance, r/R_2
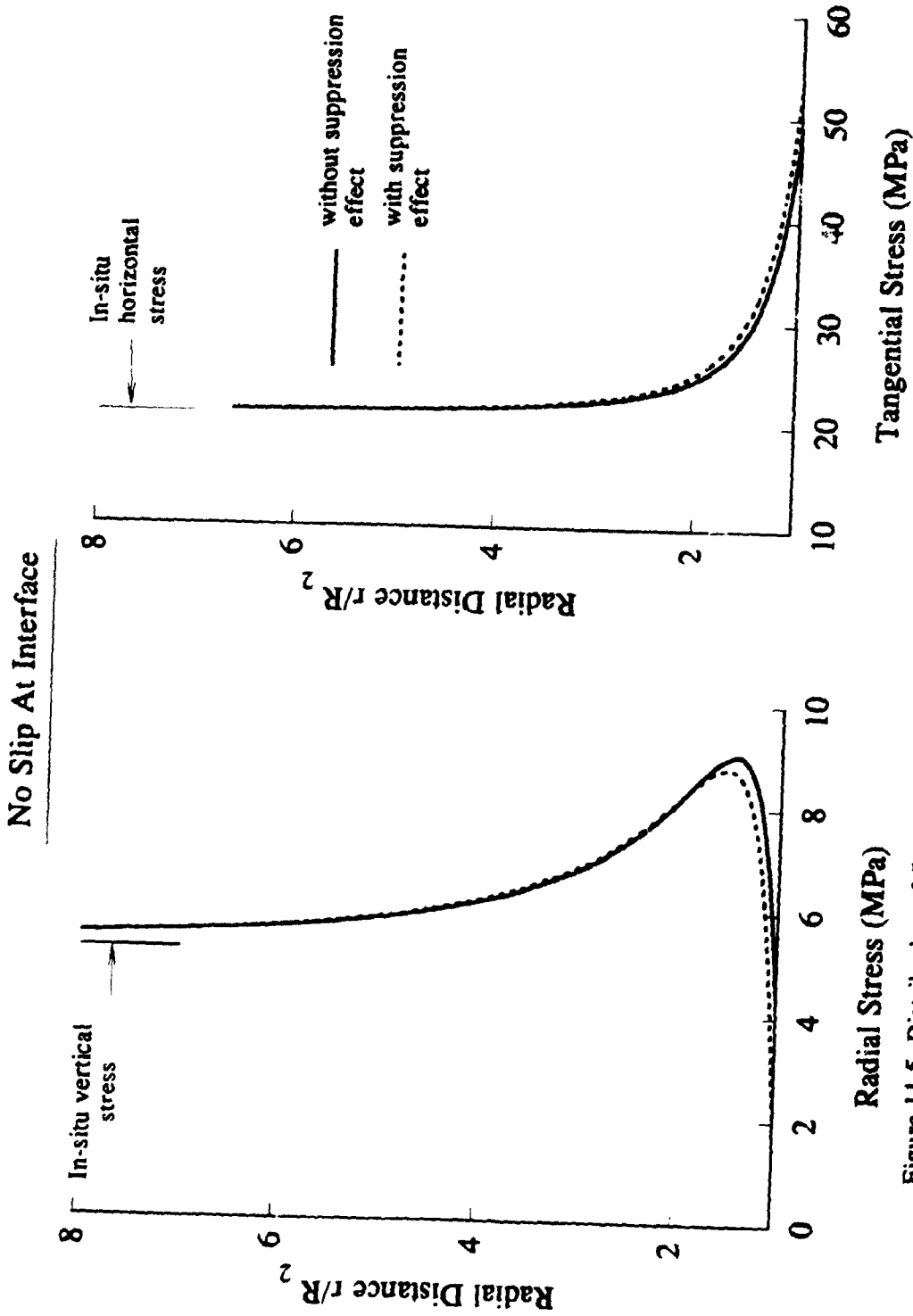
No Slip At Interface

Figure 11.5 Distribution of final radial and tangential stresses in rock above crown with radial distance, r/R₂

No Slip At Interface
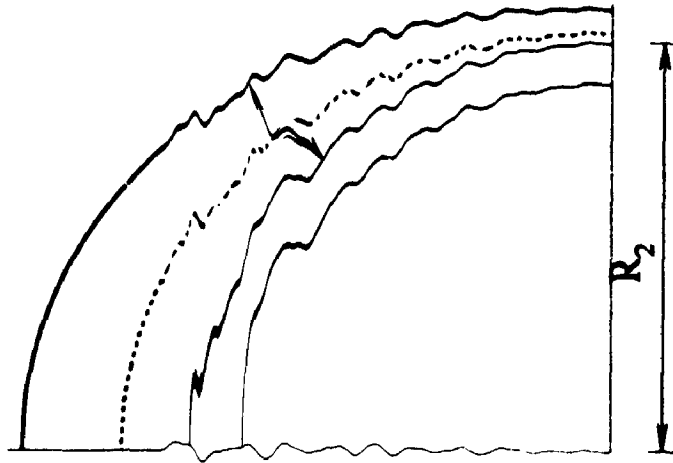
——— without suppression effect

·········· with suppression effect

Rock Data

$E_R = 15.8 \times 10^3$ MPa $\nu_R = 0.3$

$E_{R,t} = 15 \times 10^3$ MPa

$E_{R,2} = 8.06 \times 10^3$ MPa

$E_{R,3} = 4.943 \times 10^3$ MPa

$\eta_{R1} = 136 \times 10^3$ MPa.day

$\eta_{R2} = 288 \times 10^3$ MPa.day

$\eta_{R3} = 2740 \times 10^3$ MPa.day

Lining Data

$E_l = 28 \times 10^3$ MPa $\nu_l = 0.2$

$E_{lt} = 14 \times 10^3$ MPa

$\eta_l = 1400 \times 10^3$ MPa.day

$P_v = 5.2$ MPa
$K_o = 4$
$t_o = 30$ days
$R_2 = 6.8$ m
$R_1 = 6.25$ m

SCALE
5 MPa

R_2

(a) Final Radial Pressure

R_2
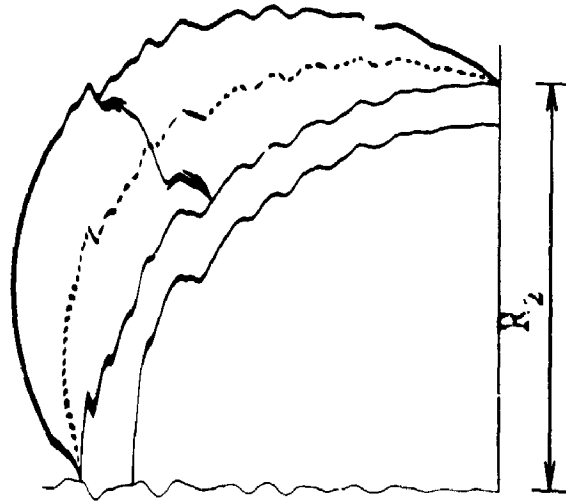
(b) Final Tangential Pressure

Figure 11.6 Distribution of final radial and tangential lining pressures at rock-lining interface

Full Slip At Interface

$P_v = 5.2$ MPa
$K_o = 4$
$t_o = 30$ days
$R_2 = 6.8$ m
$R_1 = 6.25$ m

Lining Data

$E_i = 28 \times 10^3$ MPa $\nu_i = 0.2$
$E_{it} = 14 \times 10^3$ MPa
$\eta_i = 1400 \times 10^3$ MPa.day

Rock Data

$E_R = 15.8 \times 10^3$ MPa $\nu_R = 0.3$
$E_{R1} = 15 \times 10^3$ MPa
$E_{R2} = 8.08 \times 10^3$ MPa
$E_{R3} = 4.94 \times 10^3$ MPa
$\eta_{R1} = 136 \times 10^3$ MPa.day
$\eta_{R2} = 288 \times 10^3$ MPa.day
$\eta_{R3} = 2740 \times 10^3$ MPa.day

SCALE
5 MPa

——— without suppression effect
·········· with suppression effect

R_2

(a) Final Radial Pressure

Figure 11.7 Distribution of final radial pressures at rock-lining interface

No Slip At Interface

——— without suppression
effect
.... with suppression
effect

Lining Data
$E_l = 28 \times 10^3$ MPa $\nu_l = 0.2$
$E_{lt} = 14 \times 10^3$ MPa
$\eta_l = 1400 \times 10^3$ MPa.day

Rock Data
$E_r = 15.8 \times 10^3$ MPa $\nu_r = 0.3$
$E_{r1} = 15 \times 10^3$ MPa
$E_{r2} = 8.08 \times 10^3$ MPa
$E_{r3} = 4.94 \times 10^3$ MPa
$\eta_{r1} = 136 \times 10^3$ MPa.day
$\eta_{r2} = 288 \times 10^3$ MPa.day
$\eta_{r3} = 2740 \times 10^3$ MPa.day

$P_v = 5.2$ MPa
$K_o = 4$
$t_o = 30$ days
$R_2 = 6.8$ m
$R_1 = 6.25$ m

SCALE
50 MPa

+ve compressive

(a) Final Tangential Stress
in Lining at $r = R_1$

(b) Final Tangential Stress
in Lining at $r = R_2$

Figure 11.8   Distribution of final tangential stress in lining

Full Slip At Interface

— without suppression effect

.... with suppression effect

Lining Data
$E_l = 28 \times 10^3$ MPa $\nu_l = 0.2$
$E_{lt} = 14 \times 10^3$ MPa
$\eta_l = 1400 \times 10^3$ MPa.day

Rock Data
$E_R = 15.8 \times 10^3$ MPa $\nu_R = 0.3$
$E_{R1} = 15 \times 10^3$ MPa
$E_{R2} = 8.08 \times 10^3$ MPa
$E_{R3} = 4.94 \times 10^3$ MPa
$\eta_{R1} = 136 \times 10^3$ MPa.day
$\eta_{R2} = 288 \times 10^3$ MPa.day
$\eta_{R3} = 2740 \times 10^3$ MPa.day

$P_v = 5.2$ MPa
$K_o = 4$
$t_o = 30$ days
$R_2 = 6.8$ m
$R_1 = 6.25$ m

SCALE
50 MPa

+ve compressive

(a) Final Tangential Stress in Lining at $r = R_1$

(b) Final Tangential Stress in Lining at $r = R_2$

Figure 11.9 Distribution of final tangential stress in lining

No Slip at Interface

—————— without suppression effect

.... with suppression effect

Lining Data

$E_1 = 28 \times 10^3$ MPa $\nu_1 = 0.2$

$E_{1t} = 14 \times 10^3$ MPa

$\eta_{1t} = 1400 \times 10^3$ MPa.day

SCALE
1 MN.m

+ve moment causes tensile stress at inner face

(a) Final Bending Moment

$P_v = 5.2$ MPa

$K_o = 20.8$ MPa

$t_o = 30$ days

$R_2 = 6.8$ m

$R_1 = 6.25$ m

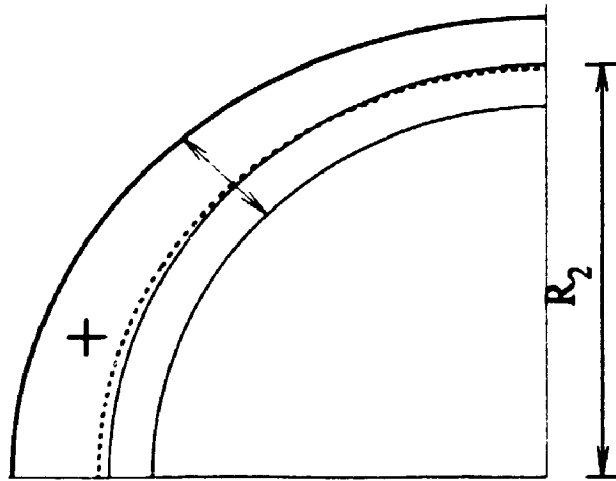**Rock Data**

$E_R = 15.8 \times 10^3$ MPa $\nu_R = 0.3$

$E_{Rt1} = 15 \times 10^3$ MPa

$E_{Rt2} = 8.08 \times 10^3$ MPa

$E_{Rt3} = 4.94 \times 10^3$ MPa

$\eta_{R1} = 136 \times 10^3$ MPa.day

$\eta_{R2} = 288 \times 10^3$ MPa.day

$\eta_{R3} = 2740 \times 10^3$ MPa.day

SCALE
50 MPa

+ve compressive thrust

(b) Final Axial Thrust

Figure 11.10 Distribution of final equivalent bending moment and equivalent axial thrust in lining

Full Slip at Interface

——— without suppression effect

·········· with suppression effect

Lining Data

$E_l = 28 \times 10^3$ MPa $\nu_l = 0.2$

$E_{lt} = 14 \times 10^3$ MPa

$\eta_{lt} = 1400 \times 10^3$ MPa.day

$P_v = 5.2$ MPa

$K_o = 20.8$ MPa

$t_o = 30$ days

$R_2 = 6.8$ m

$R_1 = 6.25$ m

Rock Data

$E_R = 15.8 \times 10^3$ MPa $\nu_R = 0.3$

$E_{R1} = 15 \times 10^3$ MPa

$E_{R2} = 8.08 \times 10^3$ MPa

$E_{R3} = 4.94 \times 10^3$ MPa

$\eta_{R1} = 136 \times 10^3$ MPa.day

$\eta_{R2} = 288 \times 10^3$ MPa.da;

$\eta_{R3} = 2740 \times 10^3$ MPa.day

SCALE
1 MN.m

+ve moment causes tensile stress at inner face

SCALE
50 MPa

+ve compressive thrust

R_2

(a) Final Bending Moment

R_2

(b) Final Axial Thrust

Figure 11.11 Distribution of final equivalent bending moment and equivalent axial thrust in lining

No Slip At Interface
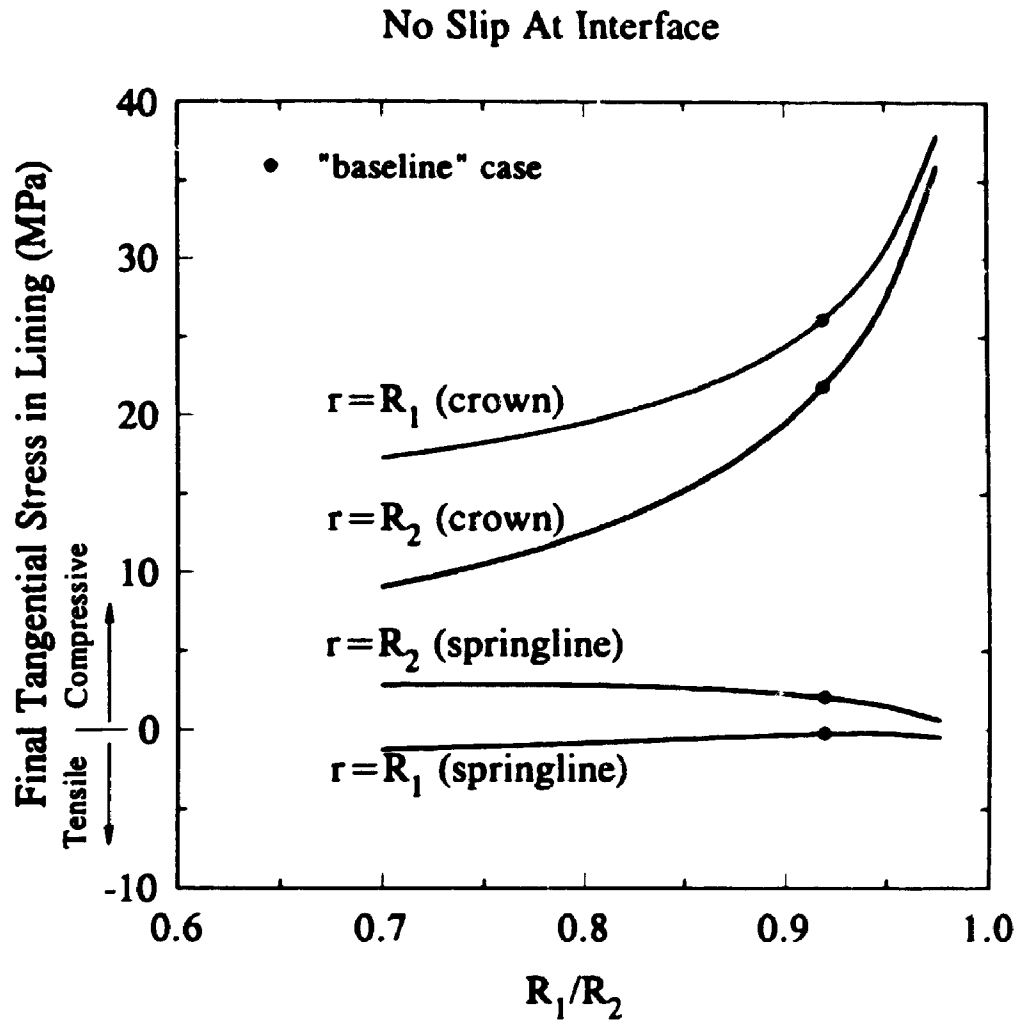
Figure 11.12 Effect of R_1/R_2 on tangential stresses in lining

No Slip At Interface
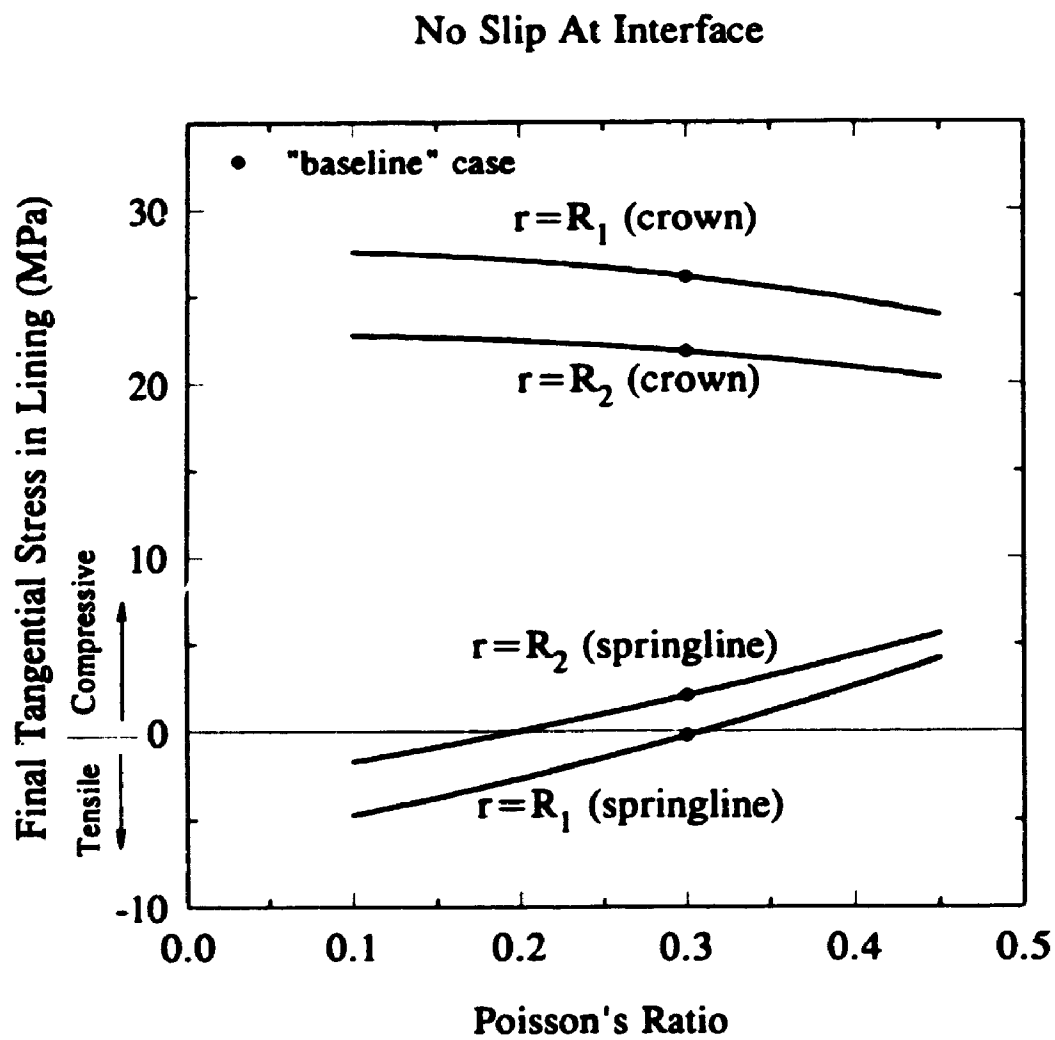
Figure 11.13 Effect of Poisson's ratio on tangential stresses in lining
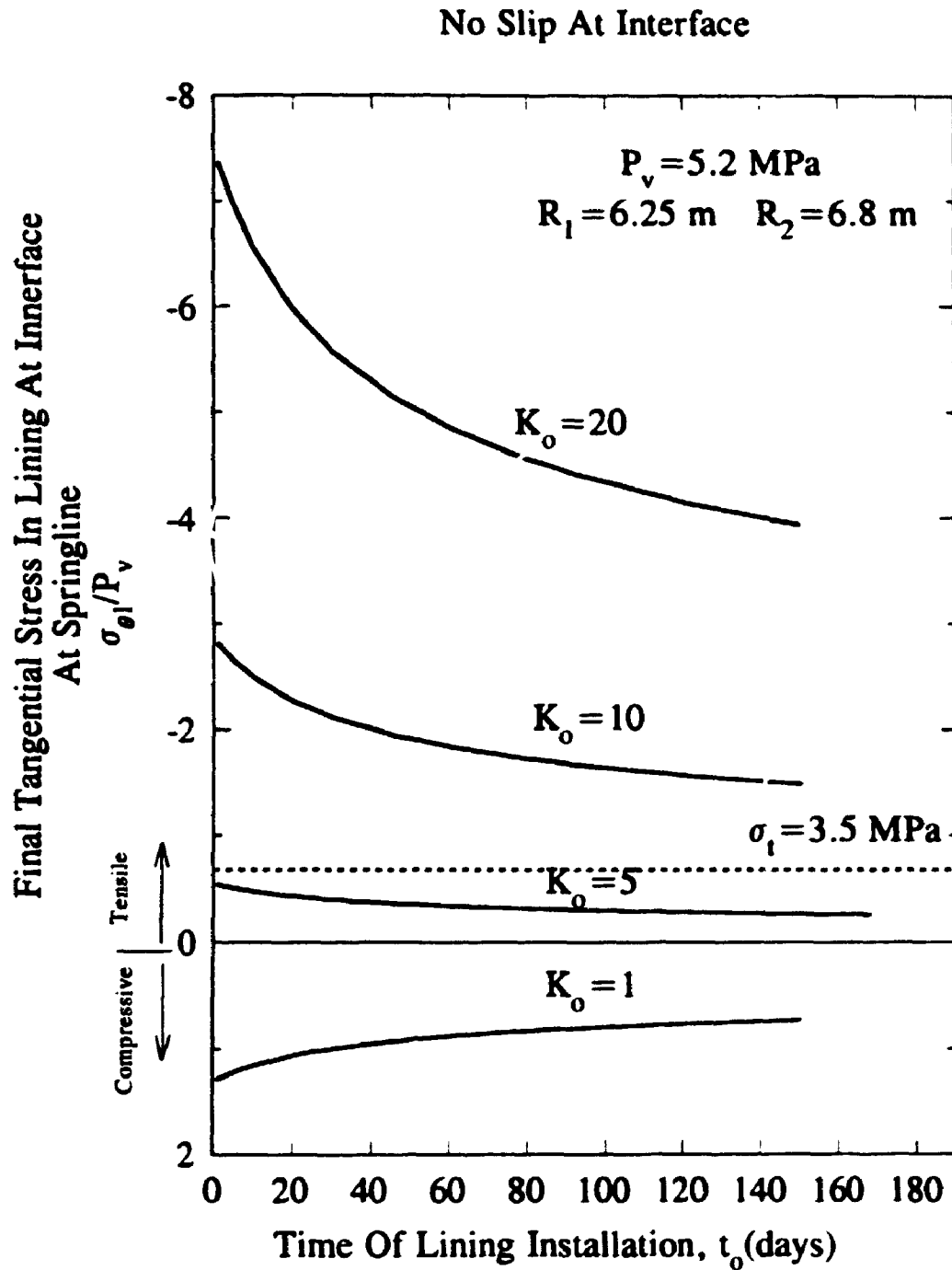
Figure 11.14 Variation of final tangential stress in lining at inner face at Springline with t_o and K_o

No Slip At Interface
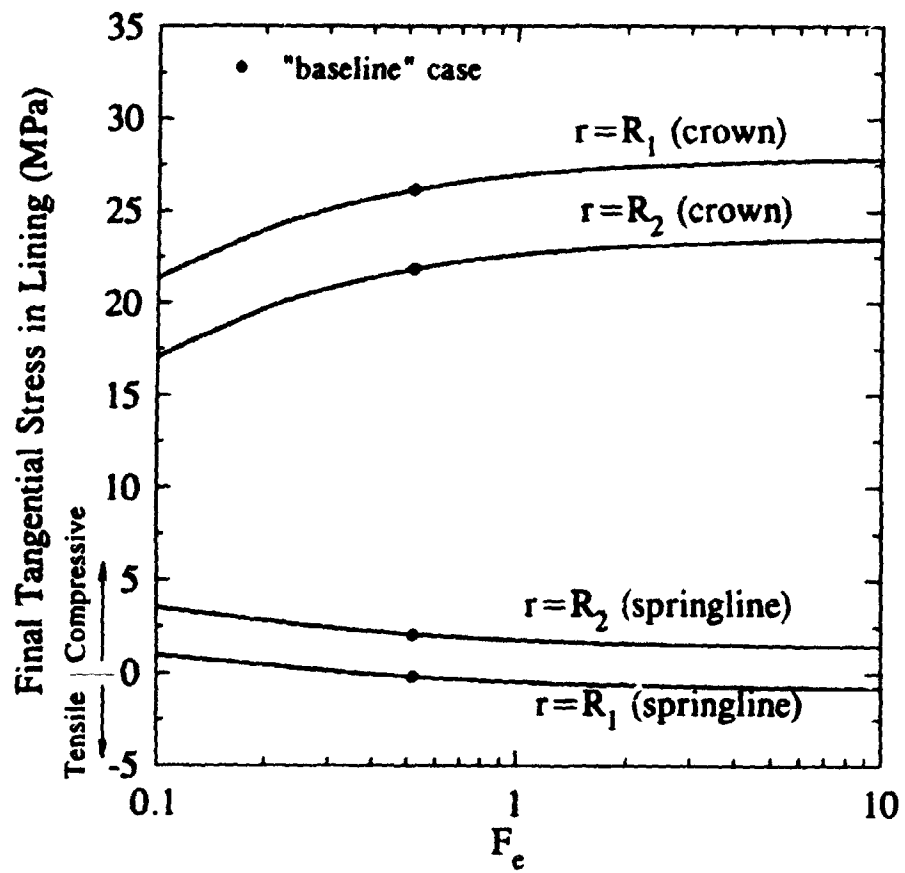
Figure 11.15 Variation of final tangential stress in lining with F_e

No Slip At Interface
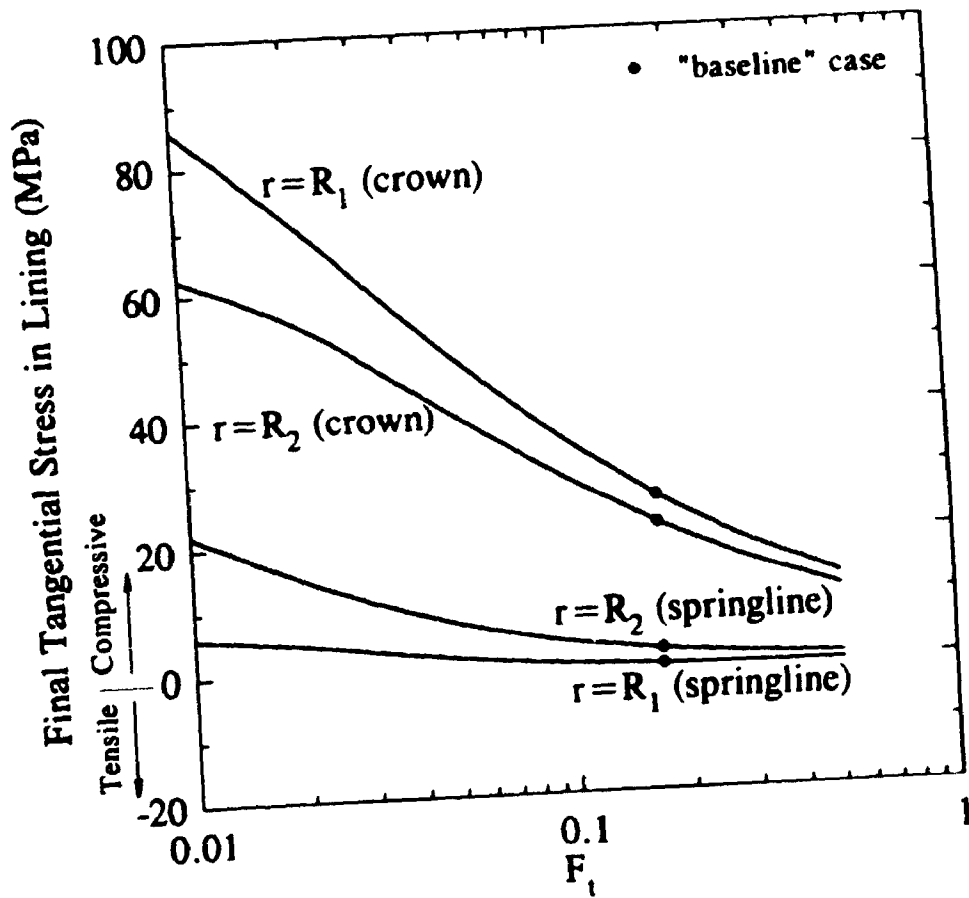
Figure 11.16 Variation of final tangential stress in lining with F_t
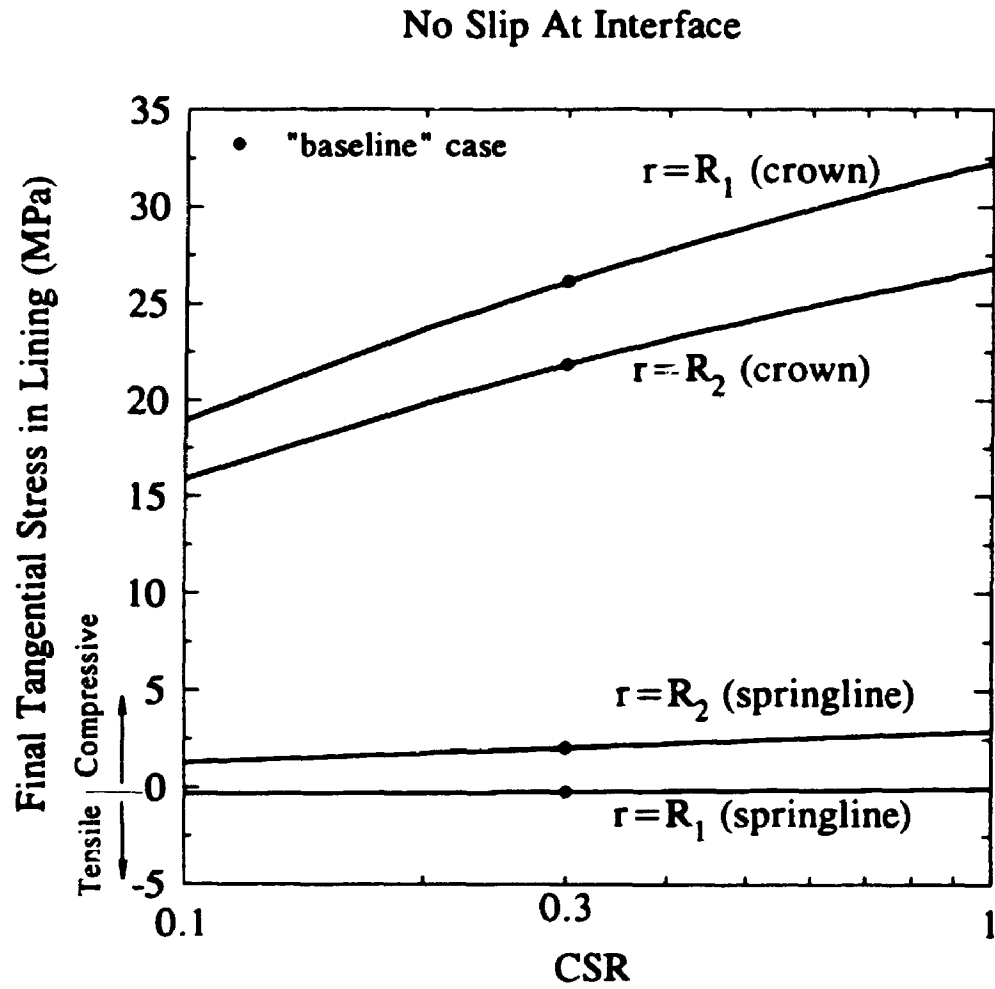
Figure 11.17 Variation of final tangential stress in lining with CSR

CHAPTER 12

SUMMARY AND CONCLUSIONS

The study carried out in this thesis essentially falls into three parts. The first part deals with the determination of initial stresses in rocks using the hydraulic fracturing test. The second part deals with stresses and displacements around unlined tunnels driven in cross-anisotropic rocks, which are representatives of shales in southern Ontario. The third part deals with the time-dependent deformation of Queenston Shale and the stresses and displacements around tunnels driven in swelling shales.

In part I, a new method, the Modified Stress Path (MSP) method, for the evaluation of initial stress in rocks from hydraulic fracturing test results is developed. This method is capable of analyzing horizontal and vertical fractures as well as mixed-mode fractures and takes into account strength anisotropy, where appropriate. For mixed-mode fractures, the method follows the stress paths during the test and determines whether the horizontal or the vertical fracture occurs first, so that appropriate stress calculations may be carried out without making any arbitrary assumptions regarding the fractures.

Results of hydraulic fracturing tests in several case histories were reanalyzed by the MSP method. From the results of the analyses, the following conclusions may be drawn:

(1)   For vertical, horizontal, or a combination of vertical and horizontal fractures, the method developed delineates the relevant stress path of the hydraulic fracturing tests from which the rock stresses may be determined. For mixed-mode fractures, it is possible to

determine whether the vertical or the horizontal fracture occurs at the first breakdown pressure, so the stresses may be computed using the appropriate solution without uncertainty.

(2)   Application of the MSP method to the analysis of test data reduces considerably the stress range computed, to the extent that they are adequate for engineering purposes.

(3)   The reinterpreted horizontal stresses in the AECL Underground Research Laboratory are not only consistent with results deduced from convergence measurements but are also consistent with field observations of excavation performance.

From the interpretation of the hydraulic fracturing test data in the 1984, 1990, and 1992 investigations in Queenston Shale, the following conclusions may be drawn:

(1)   The results of hydraulic fracturing performed in 1984, when correctly interpreted, agree well with the results of 1990 investigation, both in the magnitudes of stresses computed and modes of fractures.

(2)   In tests in which packer impression tests are not available, it is possible, by the application of MSP method to determine which stress path the test results would follow, which mode of fracturing theoretically would occur, and thereby compute the magnitudes of stresses consistently without invoking assumptions other than that (i) the strength criterion (modified Hoek and Brown) should be satisfied and (ii) the inadmissible stress ranges should be eliminated.

(3)   The regional initial stress regime in the Queenston Shale are characterized as follows:

(i) the maximum horizontal stress increases linearly from 14.5 MPa at El 86 m to 24 MPa at El -20 m.

(ii) the minimum horizontal stress increases linearly from 9 MPa at El 86 m to 18 MPa at El -20 m.

(iii) The vertical stress is given closely by the overburden pressure.

(iv) The orientation of the maximum horizontal stress is approximately N65°E.

(4) The use of anisotropic strength envelopes is significant in (i) decreasing the magnitude of stresses computed and (ii) narrowing the ranges of maximum and minimum horizontal stresses.

(5) Poisson's ratio has a significant effect on the calculated horizontal stresses and the relevant value is Poisson's ratio for the effect of horizontal stress on vertical strain v_{hv}.

The use of the conventional Poisson's ratio may lead to a significant increase in the calculated stress values.

With the initial stresses correctly determined, the stability of tunnels immediately after excavation may be evaluated. In part II of the thesis, closed form solutions for the distribution of stresses and displacements around unlined tunnels driven in cross-anisotropic rocks are derived. The effects of anisotropy of the initial stress system and the elastic parameters on the stresses and displacements are studied and a design example is analyzed. From the results of this investigation, the following conclusions may be drawn:

(a) The effects of v_h on both the tangential stress and radial displacements are negligible.

(b) At the crown-invert, the magnitude and direction of the radial displacement are sensitive to the value of v_{vh}.

(c) The compressive stress at the crown increases with increasing E_h/G_{vh}. The radial displacements around the tunnel are highly sensitive to the value of E_h/G_{vh}, increasing substantially as E_h/G_{vh} increases.

(d) As the value of K_o increases, the compressive stress concentration at the crown-invert increases and the stress at the springline decreases and changes to tensile.

The dimensionless displacement factor (Ω) at the springline increases (indicating greater inward displacement) as the value of K_o increases. In contrast, the value of Ω at the crown decreases and then changes to outward displacement as K_o increases.

(e) The radial displacement at the springline is insensitive to E_h/E_v for any value of K_o. On the other hand, the magnitude and direction of the radial displacement at the crown-invert is highly sensitive to the value of E_h/E_v, specially for values of ν_{vh} greater than 0.2.

For convenience of application, charts have been prepared for the determination of stresses and displacements for given values of initial stresses and the elastic parameters.

It is believed that the results presented would be useful not only for ready determination of stresses and displacements for design considerations, but also for the interpretation of results of field monitoring in test adits and during construction.

After the stability conditions during construction are satisfied, the long-term deformation and consequent stress built-up in the lining are important design considerations, so as to ensure that the structural integrity of the lining is not affected. In part III, an experimental study is carried out to investigate the characteristic of the time-dependent deformation of Queenston Shale and the mechanism of swelling. From

the present and previous experimental studies, the following conclusions are drawn:

(1) Queenston Shale exhibits important swelling characteristics upon stress relief. Two of the most important characteristics are the long-term time-dependent swelling and the non-linearity with the applied stress. Although the swelling continues to a long period of time (samples under test since 1986 are still swelling till the time of writing of this thesis, 1994), the rate of swelling is decreasing with time.

(2) The long-term time-dependent free swelling is adequately represented by a rheological model consisting of three Kelvin units connected in series.

(3) The model not only represents the swelling strain within the period of time the parameters are calculated (1260 days) but also predicts adequately the strain for much higher values of time (2700 days).

(4) The time-dependent deformation at any given time under an applied stress σ_a decreases with the logarithm of the applied stress.

(5) The stress-dependent swelling can be predicted adequately using the three Kelvin units and the rate parameters calculated from the long-term free swell tests. Only the deformation moduli of the Kelvin units are stress-dependent and their values increase as the applied stress increases. An expression relating the deformation moduli for free swell tests to those under any applied stress is derived.

The follow-up study carried out in 1993 investigation supported the postulation of Lee and Lo (1993) that the following conditions are necessary and sufficient for the swelling of Queenston Shale:

(i)   the relief of initial stresses which serves as an initiating mechanism;

(ii)   the accessibility to water; and

(iii)   an outward salt concentration gradient from the pore fluid of the rock to the ambient fluid.

Using the theory of linear viscoelasticity, closed form solutions for the stresses and displacements in the rock mass and tunnel lining are derived. The long-term time-dependent deformation of the rock is idealized by a model consisting of three Kelvin units connected in series. The time-dependent deformation of the lining is represented by a single Kelvin unit. The anisotropy of the initial stress system and the time elapsed between the excavation and the installation of the lining are accounted for. A semi-analytical solution (nonlinear pressure step-wise approach) is developed to allow for the increase of the values of deformation moduli of the model as the pressure level behind the lining increases. The developed method is then used to predict the stresses in the lining of a tunnel similar to the proposed twin tunnels for the SABNGS No.3 project. The effects of the different parameters on the solution are investigated. From the results of this study, the following conclusion can be drawn:

(1)   The stresses and displacements calculated from the nonlinear approach (suppression of rock deformation as the lining pressure increases is accounted for) are considerably less than those calculated from the linear case (suppression is not accounted for).

(2)   The base-line analysis on the proposed dimensions of the tunnels shows that the stresses in lining do not exceed the tensile or the compressive strengths of the concrete.

(3)   The critical location in the lining for the compressive stress is the inner face at the crown and that for the tensile stress is the inner face at the springline.

(4)   Poisson's ratio of the rock is an important factor in the solution. As Poisson's

ratio decreases, the compressive tangential stresses in the lining at the crown increase and the tensile stresses at the springline increases.

(5)   As the time elapsed between the excavation of the tunnel and the installation of the lining increases, the stresses induced in the lining decrease.

(6)   As the initial stress ratio increases, the tensile stress induced in the lining at the inner face at the springline increases. For the tunnel considered, ratios greater than 5 produces tensile stress which is higher than the tensile strength of the concrete.

(7)   The deformation moduli for the three Kelvin units of the model play an important rule in the final solution. As the values of the deformation moduli increase, the displacements and stresses induced in the lining decrease.

Analysis of Initial Stresses,
Long Term Deformation and
Rock Lining Interaction in Tunnels

VOLUME 2 - APPENDICES

BY

Ashraf Mohamed Hefny

Faculty of Engineering Science

Department of Civil Engineering

Submitted in partial fulfilment
of the requirements for the degree of
Doctor of Philosophy

Faculty of Graduate Studies
The University of Western Ontario
London, Ontario
April 1994

TABLE OF CONTENTS

VOLUME 2

Page

APPENDIX 3A

DETRMINATION OF THE VERTAICAL STRESS AT THE POINT OF MINIMUM TANGENTIAL STRESS IN A VERTICAL BOREHOLE

APPENDIX 3A

DETERMINATION OF THE VERTAICAL STRESS AT THE POINT OF
MINIMUM TANGENTIAL STRESS IN A VERTICAL BOREHOLE

Refering to Figure 3.1, the stress condition before drilling the test hole (point A) is

$$\sigma_\theta = \sigma_h \qquad (3A.1)$$

$$\sigma_r = \sigma_H \qquad (3A.2)$$

$$\sigma_z = \sigma_{zo} \qquad (3A.3)$$

where, σ_h, σ_H are the minimum and maximum in-situ horizontal stresses respectively.

σ_θ is the tangential stress.

σ_r is the radial stress.

σ_z is the vertical stress.

σ_{zo} is the overburden prssure.

The tangential and radial stresses, respectively, at point A after drilling the hole are

$$\sigma_\theta = 3\sigma_h - \sigma_H \qquad (3A.4)$$

$$\sigma_r = 0.0 \qquad (3A.5)$$

The change in the tangential stress ($\Delta\sigma_\theta$) is equal to the difference between the

values of σ_θ after and before drilling the test hole. Therefore,

$$\Delta\sigma_\theta = (3\sigma_h - \sigma_H) - \sigma_h = 2\sigma_h - \sigma_H \qquad (3A.6)$$

Similarily, the change in σ_r is obtained as

$$\Delta\sigma_r = 0.0 - \sigma_H = -\sigma_H \qquad (3A.7)$$

The total change in the stresses in the horizontal direction is equal to sum of $\Delta\sigma_\theta$ and

$\Delta\sigma_r$. Therefore,

$$\Delta\sigma_\theta + \Delta\sigma_r = (2\sigma_h - \sigma_H) - \sigma_H = -2(\sigma_H - \sigma_h) \qquad (3A.8)$$

Adopting plane strain condition, the change in vertical stress $\Delta\sigma_z$ at point A due

to the drilling of the hole is

$$\Delta\sigma_z = v(\Delta\sigma_\theta + \Delta\sigma_r) \qquad (3A.9)$$

Substitution for $(\Delta\sigma_\theta + \Delta\sigma_r)$ from Eq. 3A.8 in Eq. 3A.9 yields

$$\Delta\sigma_z = -2v(\sigma_H - \sigma_h) \qquad (3A.10)$$

The vertical stress at point A after drilling the hole (σ_z) is equal to the sum of the

overburden pressure (σ_{zo}) and the change in the vertical pressure $(\Delta\sigma_z)$ due to

excavation of the hole

$$\sigma_z = \sigma_{zo} - 2v(\sigma_H - \sigma_h) \qquad (3A.11)$$

It should be noted that the vertical stress at point A during the test does not

change and is equal to the value given by Eq. 3A.11. This is because the sum of the

change in tangential and radial stresses due to the increase of internal pressure is always

equal to zero, from elastic solutin of a thick-walled cylinder under an internal pressure.

APPENDIX 3B

CALCULATION OF THE PARAMETER "m" FOR THE DIFFERENT STRESS PATHS

APPENDIX 3B

CALCULATION OF THE PARAMETER "m" FOR THE DIFFERENT

STRESS PATHS

Hoek and Brown's (1980) failure criterion states that

$$\sigma_1 = \sigma_3 + \sqrt{(m\sigma_c\sigma_3 + s\sigma_c^2)} \qquad (3.B\text{-}1)$$

where: σ_1 is the major principal stress

              σ_3 is the minor principal stress

              σ_c is the uniaxial compressive strength of the intact rock material

m and s are constants depend upon the properties of the rock and upon the extent to

which it has been broken before being subjected to the stresses σ_1 and σ_3. For intact

rock, $s=1$. For previously broken rock, $s<1$. Because of selecting the hydro-fracturing

test locations at the depths where the rock is intact, the value of s is taken as unity.

Therefore, the equation becomes

$$\sigma_1 = \sigma_3 + \sqrt{(m\sigma_c\sigma_3 + \sigma_c^2)} \qquad (3.B\text{-}2)$$

In terms of the anisotropic strength parameters, the suitable criteria for stress paths I, II

and III, respectively, are

$$\sigma_1 = \sigma_3 + \sqrt{(m_I \sigma_{cv} \sigma_3 + \sigma_{cv}^2)} \qquad\qquad (3.B-3)$$

$$\sigma_1 = \sigma_3 + \sqrt{(m_{II} \sigma_{ch} \sigma_3 + \sigma_{ch}^2)} \qquad\qquad (3.B-4)$$

$$\sigma_1 = \sigma_3 + \sqrt{(m_{III} \sigma_{ch} \sigma_3 + \sigma_{ch}^2)} \qquad\qquad (3.B-5)$$

Where m_I, m_{II}, and m_{III} are the values of the parameter m for the envelopes required

to represent stress paths I, II, and III, respectively. σ_{cv} and σ_{ch} are the uniaxial

compressive strength in the vertical and horizontal directions, respectively. The value

of m_I can be obtained by substituting $\sigma_1 = 0.0$ and $\sigma_3 = -T_h$ in Eq. (3.B-3), where T_h is

the tensile strength of the rock in the horizontal direction. Similarly, by substituting

$\sigma_1 = 0.0$ and $\sigma_3 = -T_h$ in Eq. (3.B-4) and by substituting $\sigma_1 = 0.0$ and $\sigma_3 = -T_v$ in Eq. (3.B-

5), the values of m_{II} and m_{III} can be obtained. The quantity T_v is the tensile strength

of the rock in the vertical direction. Therefore, the values of m for the three stress paths

are

$$m_I = \frac{\sigma_{cv}}{T_h} - \frac{T_h}{\sigma_{cv}} \qquad\qquad (3.B-6)$$

$$m_{II} = \frac{\sigma_{ch}}{T_h} - \frac{T_h}{\sigma_{ch}} \qquad\qquad (3.B-7)$$

$$m_{III} = \frac{\sigma_{ch}}{T_v} - \frac{T_v}{\sigma_{ch}} \qquad\qquad (3.B-8)$$

APPENDIX 3C

ANALYSIS OF SUBVERTICAL FRACTURES

APPENDIX 3C

ANALYSIS OF SUBVERTICAL FRACTURES

Figure 3.1(a) shows the stress condition at the test location after drilling the hole and before performing the test. The elastic solution for stresses at the location of potential hydraulic fracturing, where the minimum tangential stress occurs (Point A), is given in the figure. The stress condition during the test is shown in Figure 3.1(b). At the breakdown stage (Figure 3.1(c)), the value of P_i (the internal pressure) is equal to the value of P_{cl} (the breakdown pressure). Therefore, the elastic solution at this stage (at Point A) is

$$\sigma_r = P_{cl} \tag{3C.1}$$

$$\sigma_\theta = 3\sigma_h - \sigma_H - P_{cl} \tag{3C.2}$$

$$\sigma_z = \sigma_{zo} - 2\nu(\sigma_H - \sigma_h) \tag{3C.3}$$

where: σ_r = radial stress

         P_{cl} = breakdown pressure

         σ_θ = tangential stress at point A

         σ_h = minimum in-situ horizontal stress

         σ_H = maximum in-situ horizontal stress

         σ_z = vertical stress (plane strain condition)

σ_{zo} = overburden pressure

v = Poisson's ratio

Consider the hydrofracture formed at point A lies in a plane inclined with an angle β to the vertical plane whose strike is parallel to the direction of initial maximum horizontal stress. The component of stress perpendicular to the fracture plane (σ_{N}) is

$$\sigma_{N} = \sigma_{\theta}M^2 + \sigma_{z}N^2 \qquad (3C.4)$$

where: $\qquad M = \cos\beta$, and $N = \sin\beta$

The inclined fracture is assumed to be formed when the normal stress to the plane of fracture is equal to the tensile strength T_{n} of the rock in the normal direction. Therefore,

$$-T_{n} = \sigma_{\theta}M^2 + \sigma_{z}N^2 \qquad (3C.5)$$

$$-T_{n} = (3\sigma_{h} - \sigma_{H} - P_{cl})M^2 + (\sigma_{zo} - 2v(\sigma_{H} - \sigma_{h}))N^2 \qquad (3C.6)$$

The shut-in pressure is equal to the component of stress normal to the fracture plane at this stage. Therefore,

$$P_{s} = \sigma_{h}M^2 + \sigma_{zo}N^2 \qquad (3C.7)$$

After arrangement, the minimum *in situ* horizontal stress is obtained as

$$\sigma_{h} = \frac{P_{s} - \sigma_{zo}N^2}{M^2} \qquad (3C.8)$$

Substituting for the value of σ_h into Eq. (3C.6), the following equation is obtained:

$$-T_n = 3M^2(\frac{P_s - \sigma_{zo}N^2}{M^2}) - M^2\sigma_H - M^2P_{cl} + \sigma_{zo}N^2 - 2\nu N^2\sigma_H + 2\nu N^2(\frac{P_s - \sigma_{zo}N^2}{M^2})$$

After arrangement, the maximum *in situ* horizontal stress is obtained as

$$\sigma_H = \frac{-M^4P_{cl} + (3M^2 + 2\nu N^2)P_s + (-2M^2N^2 - 2\nu N^4)\sigma_{zo} + T_nM^2}{M^4 + 2\nu N^2M^2} \qquad (3C.9)$$

The maximum and minimum *in situ* horizontal stresses (Eqs. 3C.9 and 3C.8, respectively) can be written as

$$\sigma_H = A_1 \; P_{cl} + B_1 \; P_s + C_1 \; \sigma_{zo} + D_1 \; T_n \qquad (3C.10)$$

$$\sigma_h = B_2 \; P_s + C_2 \; \sigma_{zo} \qquad (3C.11)$$

where:

$$A_1 = -\frac{M^4}{F}, \qquad B_1 = \frac{3M^2 + 2\nu N^2}{F}, \qquad C_1 = \frac{-2N^2(M^2 + \nu N^2)}{F},$$

$$D_1 = \frac{M^2}{F}, \qquad F = M^4 + 2\nu N^2M^2,$$

$$B_2 = \frac{1}{M^2}, \qquad C_2 = -\frac{N^2}{M^2}$$

EXAMPLE OF CALCULATIONS - (Case Of Vertical Fractures)

For vertical fractures $\beta = 0.0$, therefore,

$M = 1$, $N = 0$, $F = 1$, $A_1 = -1$, $B_1 = 3$, $C_1 = 0$, $D_1 = 1$, $B_2 = 1$, and $C_2 = 0$.

This leads to

$$\sigma_h = P_s$$

and

$$\sigma_H = 3P_s - P_{c1} + T_n$$

which are the same traditional equations for vertical fractures.

APPENDIX 4A

CALCULATIONS OF INITIAL HORIZONTAL STRESSES
FROM TEST UN1-3
(DARLINGTON GENERATING STATION)

APPENDIX 4A

CALCULATIONS OF INITIAL HORIZONTAL STRESSES

FROM TEST UN1-3

(DARLINGTON GENERATING STATION)

Data:

Data for the test are as follows:

Depth = 101.5 m

Unit weight = 0.026 MN/m^3

Tensile strength (T) = 6.03 MPa

Uniaxial compressive strength (σ_c) = 59 MPa

Poisson's ratio (ν) = 0.32

First Breakdown Pressure (P_{c1}) = 13.10 MPa (measured at ground surface)

Shut-in pressure (P_s) = 5.52 MPa (measured at ground surface)

Head pressure (P_H) = 1.0 MPa

Calculate The Emperical Constant (m)

$$m = \frac{\sigma}{T} - \frac{T}{\sigma} = 9.68$$

Check Stress Path *I*

At breakdown stage, the radial stress at the test location is

$$\sigma_r = P_{cl} + P_H = 13.10 + 1.0 = 14.1 \text{ MPa}$$

And the vertical stress is

$$\sigma_z = \sigma_{zo} - 2\nu(\sigma_H - \sigma_h)$$

$$\sigma_{zo} = 0.026 \times 101.5 = 2.639 \text{ MPa}$$

Therfore, $\sigma_z < 2.639 < \sigma_r = 14.1$

One condition for stress path *I* is that σ_z is the major principal stress. Therefore stress

path *I* is not satisfied.

Check Stress Paths *II* and *III*

The value of the empirical constant "*m*" for Hoek and Brown's failure criterion is

$$m = \frac{\sigma_c}{T} - \frac{T}{\sigma_c}$$

Therefore, *m* = 9.68

The minimum horizontal stress (σ_h) is

$$\sigma_h = P_s + P_H = 5.52 + 1.0 = 6.52 \text{ MPa}$$

The failure criterion for stress path *II* is

$$\sigma_r = 3\sigma_h - \sigma_H - \sigma_r + \sqrt{m\sigma_c(3\sigma_h - \sigma_H - \sigma_r) + \sigma_c^2}$$

Substitution for the values of σ_c, m, σ_r, and σ_h in the above failure criterion leads to the following quadratic equation:

$$\sigma_H^2 + 588.4\ \sigma_H - 6524.66 = 0.0$$

Solution of this equation results in the following value of the maximum horizontal stress:

$$\sigma_H = 10.89\ \text{MPa}$$

Therfore, the value of the vertical stress at test location is

$$\sigma_z = \sigma_{zo} - 2\nu(\sigma_H - \sigma_h) = -0.16\ \text{MPa}$$

And the value of the tangential stress is

$$\sigma_\theta = 3\sigma_h - \sigma_H - \sigma_r = -5.43\ \text{MPa}$$

Therfere, we have the following stress relation at failure:

$$\sigma_r > \sigma_z > \sigma_\theta$$

This means that stess path II is satisfied for Test UN1-3.

APPENDIX 5A

EXAMPLE OF CALCULATING THE INITIAL HORIZONTAL STRESSES
FROM MIXED-MODE FRACTURES

APPENDIX 5A

EXAMPLE OF CALCULATING THE INITIAL HORIZONTAL STRESSES

FROM MIXED-MODE FRACTURES

Test NF4-6 performed for the SABNGS No. 3 project is used for illustration of calculating the initial horizontal stresses from mixed-mode fracturs in anisotropic rocks.

Data: Formation = Queenston Shale

Depth = 106.1 m

Unit weight = 0.026 MN/m^3

Tensile strength (T_v) = 4.6 MPa

Tensile strength (T_h) = 3.4 MPa

Uniaxial compression strength ($\sigma_{cv} = \sigma_{ch} = \sigma_c$) = 25 MPa

Poisson's ratio (v_{hv}) = 0.40

First breakdown pressure (P'_{c1}) = 12.30 MPa   (measured at ground surface)

Shut-in pressure (P_s) = 3.5 MPa   (measured at ground surface)

Head pressure (P_H) = 1.0 MPa

1- Calculate The Emperical Constant (m)

For Stress Path I and II the values of m_I and m_{II} are

$$m_I = m_{II} = \frac{\sigma_c}{T_h} + \frac{T_h}{\sigma_c} = 5.25 \qquad \text{(5A.1)}$$

For Stress Path III the value m_{III} is

$$m_{III} = \frac{\sigma_c}{T_v} + \frac{T_v}{\sigma_c} = 7.22 \qquad \text{(5A.2)}$$

In the following computations, the conditions and expressions used are summarized in Table 3.2.

2- Check Stress Path *I*

At breakdown stage, the radial stress at the test location is

$$P_{cl} = \sigma_r = P'_{cl} + P_H = 12.3 + 1 = 13.3 \; MPa \qquad \text{(5A.3)}$$

And the vertical stress is

$$\sigma_z = \sigma_{zo} - 2\nu_{hv}(\sigma_H - \sigma_h) \qquad \text{(5A.4)}$$

And the value of the overburden pressure is

$$\sigma_{zo} = 0.026 \times 106.1 = 2.756 \; MPa$$

Therefore, $\sigma_z < 2.756 < \sigma_r = 13.3$

One condition for Stress Path I is that σ_z is the major principal stress. Therefore Stress Path I is not satisfied.

3- Check Stress Path *II*

The minimum horizontal stress (σ_h) is

$$\sigma_h = P_s + P_H = 3.5 + 1 = 4.5 \ MPa \qquad (5A.5)$$

The failure criterion for stress path II is

$$P_{cl} = \sigma_r = 3\sigma_h - \sigma_H - P_{cl} + \sqrt{m_{II}\sigma_{ch}(3\sigma_h - \sigma_H - P_{cl}) + \sigma_{ch}^2} \qquad (5A.6)$$

Substitution for the values of σ_c, m_{II}, σ_r, and σ_h in the above failure criterion leads to

the following quadratic equation:

$$\sigma_H^2 + 157.45 \ \sigma_H - 479.64 = 0.0$$

Solution of this equation results in the following value of the maximum horizontal stress

$$\sigma_H = 3.0 \ MPa < \sigma_h = 4.5 \ MPa$$

This means that to satisfy Stress Path II the maximum horizontal stress should be less

than the minimum horizontal stress. Therefore, Stress Path II is not satisfied.

4- Check Stress Path *III*

The only remaining Stress Path is Stress Path III. The condition at failure is

$$\sigma_r > \sigma_\theta > \sigma_z \qquad (5A.7)$$

The modified Hoek and Brown's failure criterion is

$$\sigma_r = \sigma_z + \sqrt{m_{III}\sigma_{ch}\sigma_z + \sigma_{ch}^2} \qquad (5A.8)$$

The vertical stress is

$$\sigma_z = \sigma_{zo} - 2v_{vh}(\sigma_H - \sigma_h) \qquad (5A.9)$$

Therefore,

$$\sigma_z = 2.756 - 0.8 \, (\sigma_H - \sigma_h)$$

Substituting the values of σ_r, σ_z, m_{III}, and σ_c in the failure criterion, letting

$(\sigma_D = \sigma_H - \sigma_h)$ and after arrangement, the following quadratic equation is obtained:

$$0.64 \, \sigma_D^2 + 161.27 \, \sigma_D - 1011.282 = 0.0$$

Solving this equation, the following value for σ_D is obtained:

$$\sigma_D = 6.12 \text{ MPa}$$

Now apply the following condition to obtain the upper limit of both σ_h and σ_H, the first

condition is

$$\sigma_r > \sigma_\theta$$

From notes 4 and 6 in Table 3.2

$$P_{cl} > 3\sigma_h - \sigma_H - P_{cl}$$

After substituting for the value of σ_h in terms of σ_H and σ_D, the following inequality

is obtained:

$$\sigma_H < \frac{2P_{cl} + 3\sigma_D}{2} \quad , \text{ similarly, } \quad \sigma_h < \frac{2P_{cl} + \sigma_D}{2} \qquad (5A.10)$$

Therefore, $\quad \sigma_H < 22.48$ MPa , and $\quad \sigma_h < 16.36$ MPa

To obtain the lower limit of the stress values, the second condition is used

$$\sigma_\theta > \sigma_z \qquad \text{(see notes in Table 3.2)}$$

from which the following inequality is obtained:

$$\sigma_H < \frac{\sigma_{zo} + \sigma_D(3-2v_{hv}) + P_{cl}}{2} \qquad (5A.11)$$

Similarly,

$$\sigma_h > \frac{\sigma_{zo} + \sigma_D(1-2v_{hv}) + P_{cl}}{2} \qquad (5A.11)$$

Therefore, $\sigma_H > 14.76$ MPa, and $\sigma_h > 8.64$ MPa

Now the ranges of the calculated horizontal stress values are

$$14.76 \text{ MPa} < \sigma_H < 22.48 \text{ MPa}$$

and $\qquad\qquad$ $8.64 \text{ MPa} < \sigma_h < 16.38 \text{ MPa}$

5- Elimination of The Inadmissible Range of Stress That Causes Premature Failure

In the stress range computed above, not all values are admissible. Those values of σ_H and σ_h which would cause failure at any point along the cylindrical surface of the test section before the hydraulic fracturing test was conducted are clearly inadmissible. These values of σ_H and σ_h should be excluded from the range. The procedure is to compute the stresses around the circumference and ensure that the state of stress is below the failure envelope. After the test hole is drilled, the vertical (σ_z) and tangential (σ_θ) stresses at the most critical location (Hefny and Lo 1992a) are

$$\sigma_z = \sigma_{zo} - 2\nu_{hv}(\sigma_H - \sigma_h) \tag{5A.13}$$

$$\sigma_\theta = 3\sigma_h - \sigma_H \tag{5A.14}$$

Using the value of $(\sigma_H - \sigma_h) = 6.12$ computed, and the following equation, which gives the stress state at the failure envelope

$$\sigma_\theta = \sigma_{zo} - 2\nu_{hv}(\sigma_H - \sigma_h) + \sqrt{m_{III}\sigma_{ch}(\sigma_{zo} - 2\nu_{hv}(\sigma_H - \sigma_h)) + \sigma_{ch}^2} \tag{5A.15}$$

the maximum permissible value of σ_θ is 13.3 MPa.

Therefore, $\quad \sigma_\theta = 3 \sigma_h - \sigma_H < 13.3$

From this inequality, knowing the value of σ_D (6.12 MPa) obtained before, the upper limits for σ_H and σ_h, respectively, are found to be

$$\sigma_H < 15.83 \text{ MPa}$$

and $\quad \sigma_h < 9.71 \text{ MPa}$

The permissible ranges of the maximum and minimum horizontal stresses are

$$14.76 \text{ MPa} < \sigma_H < 15.83 \text{ MPa}$$

and $\quad 8.64 \text{ MPa} < \sigma_h < 9.71 \text{ MPa}$

The stress paths investigated are graphically illustrated in Figure 5.4 and it is clear that only stress path III satisfies the failure criteria.

APPENDIX 6A

CLOSED FORM SOLUTIONS OF THE STRESSES
AND DISPLACEMENTS AROUND A CIRCULAR TUNNEL DRIVEN IN
CROSS-ANISOTROPIC ROCKS

6A.1 GENERAL

6A.2 CASE OF RELEASING THE HYDROSTATIC INITIAL STRESS COMPONENT (P_o)

6A.3 CASE OF RELEASING THE HYDROSTATIC INITIAL STRESS COMPONENT (Q_o)

6A.4 FINAL STRESSES AND DISPLACEMENTS

APPENDIX 6A

CLOSED FORM SOLUTIONS OF THE STRESSES

AND DISPLACEMENTS AROUND A CIRCULAR TUNNEL DRIVEN IN

CROSS-ANISOTROPIC ROCKS

6A.1   INTRODUCTION

In this Appendix, the solutions of the stresses and displacements around a circular

tunnel driven in a cross-anisotropic medium, Eqs. 6.22 to 6.24, are derived.   As

mentioned in Chapter 6, the tangential stresses are obtained by the superposition of two

cases (Fig. 6.1): case (a) where the infinite medium is loaded by the initial state of stress

(before excavating the tunnel), and case (b) of releasing the initial stresses at the

boundary of the excavated tunnel.   The displacements in the medium due to the

excavation of the tunnel result directly from case (b).   The case of releasing the initial

state of stress is the summation of the case of releasing the hydrostatic initial stress

component (P_o) and the case of releasing the deviatoric initial stress component (Q_o).

Fig. 6A.1 shows the normal stress and the shear stress released at the boundary of the

excavated tunnel for both the hydrostatic and deviatoric initial stress components.

6A.2   CASE OF RELEASING THE HYDROSTATIC INITIAL STRESS COMPONENT (P_o)

Referring to Fig. 6A.1-a and Eq. 6.9-a, the stress boundary conditions at the

tunnel surface are

$$P(ae^{i\theta}) = -P_o \qquad \text{(6A.1)}$$

$$q(ae^{i\theta}) = 0 \qquad \text{(6A.2)}$$

Using Eqs. 6.9-b and 6.9-c, the boundary conditions are represented as

$$-P_o = R_o + \sum_{n=1}^{\infty} R_n \cos n\theta + S_n \sin n\theta \qquad \text{(6A.3)}$$

$$0 = T_o + \sum_{n=1}^{\infty} (T_n \cos n\theta + U_n \sin n\theta) \qquad \text{(6A.4)}$$

Therefore, $R_o = U_o = -P_o$ and all other coefficients being zero.

Substituting the values of the coefficients (R_n, S_n, U_n, and T_n) obtained into Eq. 6.7, the values of the two potential functions $V(z)$ and $W(z)$ are determined as

$$V(z) = -P_o \qquad\qquad W(z) = P_o \qquad \text{(6A.5)}$$

and their complex conjugates are

$$\bar{V}(\bar{z}) = -P_o, \qquad\qquad \bar{W}(\bar{z}) = P_o \qquad \text{(6A.6)}$$

In the following sections, these values of potential functions obtained are used to determine the change in tangential stresses and radial and tangential displacements at the boundary of the excavated tunnel due to the relief of the hydrostatic initial stress component.

(I)   Change in Tangential Stresses

The change in tangential stresses at the boundary of the excavated tunnel, as a

function of the two potential functions, is given by Eq. 6.10 as

$$\Delta\sigma_\theta = \frac{(1+\gamma_1 e^{-2i\theta})(1+\gamma_2 e^{-2i\theta})V(z) + 2(1-\gamma_1\gamma_2 e^{-4i\theta})W(z)}{2(1-\gamma_1 e^{-2i\theta})(1-\gamma_2 e^{-2i\theta})}$$
$$+ \frac{(1+\bar\gamma_1 e^{2i\theta})(1+\bar\gamma_2 e^{2i\theta})\bar V(\bar z)+2(1-\bar\gamma_1\bar\gamma_2 e^{4i\theta})\bar W(\bar z)}{2(1-\bar\gamma_1 e^{2i\theta})(1-\bar\gamma_2 e^{2i\theta})}$$

(6A.7)

As mentioned in Chapter 6 Sec. 6.3, two cases arise:

(a) $\bar\gamma_1=\gamma_1$, $\bar\gamma_2=\gamma_2$

so that γ_1 and γ_2 are real. In this case, $\bar\rho_1=\rho_1$ and $\bar\rho_2=\rho_2$ (i.e. ρ_1 and ρ_2 are real)

(b) $\bar\gamma_2=\gamma_1$, $\bar\gamma_1=\gamma_2$

so that γ_1 and γ_2 are complex conjugates. In this case, $\rho_2=\bar\rho_1$ and $\rho_1=\bar\rho_2$ (i.e. ρ_1 and ρ_2 are complex conjugates).

Case (a) γ_1 and γ_2 are real

Substituting $\bar\gamma_1=\gamma_1$ and $\bar\gamma_2=\gamma_2$ into Eq. 6A.7, the change in radial stress can be written as

$$\Delta\sigma_\theta = \frac{(1+\gamma_1 e^{-2i\theta})(1+\gamma_2 e^{-2i\theta})V(z) + 2(1-\gamma_1\gamma_2 e^{-4i\theta})W(z)}{2(1-\gamma_1 e^{-2i\theta})(1-\gamma_2 e^{-2i\theta})}$$
$$+ \frac{(1+\gamma_1 e^{2i\theta})(1+\gamma_2 e^{2i\theta})\bar V(\bar z)+2(1-\gamma_1\gamma_2 e^{4i\theta})\bar W(\bar z)}{2(1-\gamma_1 e^{2i\theta})(1-\gamma_2 e^{2i\theta})}$$

(6A.8)

Case (b) γ_1 and γ_2 are complex conjugates

Substituting $\bar{\gamma}_1 = \gamma_2$ and $\bar{\gamma}_2 = \gamma_1$ into Eq. 6A.7, the same equation (Eq. 6A.8), derived for the case when both γ_1 and γ_2 are real (case a), is obtained. This means that Eq. 6A.8 can be considered as the general expression for the change in tangential stress in terms of the two potential functions regardless the case of γ_1 and γ_2 (case (a) or case (b)).

Substituting the values of $V(z), W(z), \bar{V}(\bar{z})$, and $\bar{W}(\bar{z})$ into Eq. 6A.8, the change in tangential stress is represented as

$$\frac{\Delta \sigma_{\theta(P_o)}}{P_o} = \frac{-(1+\gamma_1 e^{-2i\theta})(1+\gamma_2 e^{-2i\theta}) + 2(1-\gamma_1\gamma_2 e^{-4i\theta})}{2(1-\gamma_1 e^{-2i\theta})(1-\gamma_2 e^{-2i\theta})}$$
$$+ \frac{-(1+\gamma_1 e^{2i\theta})(1+\gamma_2 e^{2i\theta}) + 2(1-\gamma_1\gamma_2 e^{4i\theta})}{2(1-\gamma_1 e^{2i\theta})(1-\gamma_2 e^{2i\theta})} \qquad (6A.9)$$

After some arrangements Eq. 6A.9 is reduced to

$$\Delta \sigma_{\theta(P_o)} = \frac{A_1}{B_1} P_o \qquad (6A.10)$$

where

$$A_1 = 2 + 2(\gamma_1+\gamma_2)^2 - 6\gamma_1^2\gamma_2^2 - 2(\gamma_1+\gamma_2-\gamma_1\gamma_2^2-\gamma_1^2\gamma_2)(e^{2i\theta}+e^{-2i\theta})$$
$$- 2\gamma_1\gamma_2(e^{4i\theta}-e^{-4i\theta}) \qquad (6A.11)$$

$$B_1 = 2[1 + (\gamma_1+\gamma_2)^2 + \gamma_1^2\gamma_2^2 - (\gamma_1+\gamma_2)(1+\gamma_1\gamma_2)$$
$$(e^{2i\theta}+e^{-2i\theta}+\gamma_1\gamma_2(e^{4i\theta}+e^{-4i\theta})] \qquad (6A.12)$$

Eq. 6A.10 can be expressed in terms of the trigonometric functions ($\cos\theta$ and $\sin\theta$), where $e^{i\theta} = \cos\theta + i\sin\theta$, as

$$\Delta\sigma_{\theta(P_o)} = \frac{A_2}{B_2} P_o \tag{6A.13}$$

where:

$$A_2 = 1 + (\gamma_1 + \gamma_2)^2 - 3\gamma_1^2\gamma_2^2 - 2(\gamma_1 + \gamma_2)(1 - \gamma_1\gamma_2)\cos2\theta \tag{6A.14}$$
$$-2\gamma_1\gamma_2\cos4\theta$$

$$B_2 = (1 + \gamma_1^2 - 2\gamma_1\cos2\theta)(1 + \gamma_2^2 - 2\gamma_2\cos2\theta) \tag{6A.15}$$

Equation 6A.13 represents the change of tangential stress at the boundary of the tunnel due to the relief of the hydrostatic initial stress component P_o.

(II)   Radial and Tangential Displacements

The displacement at the surface of the excavated tunnel ($D = u_x + iu_y$) is given by Eq. 6.12 as

$$D = \delta_1 f(z) + \bar{\rho}_1\bar{f}(\bar{z}) + \delta_2 g(z) + \bar{\rho}_2\bar{g}(\bar{z}) \tag{6A.16}$$

where:

$$f'(z) = \frac{(1 + \gamma_2 \frac{a^2}{z^2})V(z) + (1 - \gamma_2 \frac{a^2}{z^2})W(z)}{4(\gamma_1 - \gamma_2)} \qquad (6A.17)$$

$$g'(z) = -\frac{(1 + \gamma_1 \frac{a^2}{z^2})V(z) + (1 - \gamma_1 \frac{a^2}{z^2})W(z)}{4(\gamma_1 - \gamma_2)} \qquad (6.18)$$

$$\begin{array}{ll} \delta_1 = (1 + \gamma_1)\beta_2 - (1 - \gamma_1)\beta_1 & \delta_2 = (1 + \gamma_2)\beta_1 - (1 - \gamma_2)\beta_2 \\ \rho_1 = (1 + \gamma_1)\beta_2 + (1 - \gamma_1)\beta_1 & \rho_2 = (1 + \gamma_2)\beta_1 + (1 - \gamma_2)\beta_2 \end{array} \qquad (6A.19)$$

$$\beta_1 = S_{12} - \alpha_1^2 S_{22} \qquad \beta_2 = S_{12} - \alpha_2^2 S_{22} \qquad (6A.20)$$

Case (a) γ_1 and γ_2 are real

Substituting the values of $V(z)$ and $W(z)$ into Eq. 6A.17 leads to

$$f'(z) = \frac{-(1 + \gamma_2 \frac{a^2}{z^2})P_o + (1 - \gamma_2 \frac{a^2}{z^2})P_o}{4(\gamma_1 - \gamma_2)} \qquad (6A.21)$$

The value of $f(z)$ is obtained by integrating Eq. 6A.21 with respect to z. Therefore,

$$f(z) = \frac{\gamma_2 a^2 P_o}{2z(\gamma_1 - \gamma_2)} + c_1 \qquad (6A.22)$$

where c_1 is an integration constant. Substituting $z = ae^{i\theta}$ into Eq. 6A.22, the value of $f(z)$ can be written as

$$f(z) = \frac{\gamma_2 a P_o}{2(\gamma_1 - \gamma_2)} e^{-i\theta} + c_1 \tag{6A.23}$$

The complex conjugate of $f(z)$ is

$$\bar{f}(\bar{z}) = \frac{\gamma_2 a P_o}{2(\gamma_1 - \gamma_2)} e^{i\theta} + \bar{c}_1 \tag{6A.24}$$

Similarly, the function $g(z)$ and its conjugate $\bar{g}(\bar{z})$ are obtained by substituting the values of $V(z)$ and $W(z)$ into Eq. 6A.18 and integrating with respect to z. The values obtained for $f(z)$ and $g(z)$, respectively, are

$$g(z) = \frac{-\gamma_1 a P_o}{2(\gamma_1 - \gamma_2)} e^{-i\theta} + c_2 \tag{6A.25}$$

$$\bar{g}(\bar{z}) = \frac{-\gamma_1 a P_o}{2(\gamma_1 - \gamma_2)} e^{i\theta} + \bar{c}_2 \tag{6A.26}$$

Substituting the values of $f(z)$, $g(z)$, $\bar{f}(\bar{z})$, and $\bar{g}(\bar{z})$ into Eq. 6A.16 yields

$$D = \frac{\gamma_2 a P_o}{2(\gamma_1 - \gamma_2)} \delta_1 e^{-i\theta} + \frac{\gamma_2 a P_o}{2(\gamma_1 - \gamma_2)} \rho_1 e^{i\theta}$$
$$- \frac{\gamma_1 a P_o}{2(\gamma_1 - \gamma_2)} \delta_2 e^{-i\theta} - \frac{\gamma_1 a P_o}{2(\gamma_1 - \gamma_2)} \rho_2 e^{-i\theta} + c_3 \tag{6A.27}$$

When the value of P_c is zero, the value of the displacement D should be zero, therefore the integration constant c_3 is equal to zero. By substituting $D = u_x + i u_y$ and $e^{i\theta} = \cos\theta + i\sin\theta$ into Eq. 6A.27 and after arrangements, Eq. 6A.26 is reduced to

$$u_x + iu_y = \frac{aP_o}{2(\gamma_1 - \gamma_2)} \{[\gamma_2(\delta_1 + \rho_1) - \gamma_1(\delta_2 + \rho_2)]\cos\theta$$
$$+ [\gamma_2(\rho_1 - \delta_1) - \gamma_1(\rho_2 - \delta_2)] i \sin\theta\} \qquad (6A.28)$$

Comparing the left hand side of Eq. 6A.28 with the right hand side, the displacements in x-direction (u_x) and y-direction (u_y) respectively are obtained as

$$u_x = \frac{aP_o}{2(\gamma_1 - \gamma_2)}[\gamma_2(\delta_1 + \rho_1) - \gamma_1(\delta_2 + \rho_2)]\cos\theta \qquad (6A.29)$$

$$u_y = \frac{aP_o}{2(\gamma_1 - \gamma_2)}[\gamma_2(\rho_1 - \delta_1) - \gamma_1(\rho_2 - \delta_2)]\sin\theta \qquad (6A.30)$$

Referring to Fig. 6A.2, the radial displacement, $u_{r(P_o)}$, and tangential displacement, $u_{\theta(P_o)}$, in terms of the displacements u_x and u_y , respectively, are

$$u_r = u_x\cos\theta + u_y\sin\theta \qquad (6A.31\text{-}a)$$

$$u_\theta = -u_x\sin\theta + u_y\cos\theta \qquad (6A.31\text{-}b)$$

Substituting for the values of u_x and u_y (Eqs. 6A.24 and 6A.25) into Eq. 6A.30-a, the radial displacement is obtained as

$$u_{r(P_o)} = \frac{aP_o}{2(\gamma_1 - \gamma_2)} \{[\gamma_2(\delta_1 + \rho_1) - \gamma_1(\delta_2 + \rho_2)]\cos^2\theta$$
$$+ [\gamma_2(\rho_1 - \delta_1) - \gamma_1(\rho_2 - \delta_2)]\sin^2\theta\} \qquad (6A.32)$$

After arrangements and making use of the following trigonometric relationships,

$$\cos^2\theta + \sin^2\theta = 1 \qquad \cos^2\theta - \sin^2\theta = \cos 2\theta \qquad \text{(6A.33)}$$

the radial displacement at the tunnel surface due to the relief of the hydrostatic initial stress component is derived as

$$u_{a(P_o)} = \frac{aP_o}{2(\gamma_1 - \gamma_2)}\left[(\gamma_2\rho_1 - \gamma_1\rho_2) + (\gamma_2\delta_1 - \gamma_1\delta_2)\cos 2\theta\right] \qquad \text{(6A.34)}$$

Similarly, by making use of Eqs. 6A.29, 6A.30, and 6A.31-b, the tangential displacement at the tunnel surface is obtained as

$$u_{\theta(P_o)} = \frac{aP_o}{2(\gamma_1 - \gamma_2)}(\gamma_1\delta_2 - \gamma_2\delta_1)\sin 2\theta \qquad \text{(6A.35)}$$

Case (b) γ_1 and γ_2 are complex conjugates

As in case (a), the function $f(z)$ is given by Eq. 6A.23 as

$$f(z) = \frac{\gamma_2 aP_o}{2(\gamma_1 - \gamma_2)}e^{-i\theta} + c_1 \qquad \text{(6A.36)}$$

The complex conjugate of $f(z)$ is

$$\bar{f}(\bar{z}) = \frac{\bar{\gamma}_2 aP_o}{2(\bar{\gamma}_1 - \bar{\gamma}_2)}e^{i\theta} + \bar{c}_1 \qquad \text{(6A.37)}$$

Substitut: g $\bar{\gamma}_1 = \gamma_2$ and $\bar{\gamma}_2 = \gamma_1$ into Eq. 6A.37 leads to

$$\bar{f}(\bar{z}) = \frac{-\gamma_1 aP_o}{2(\gamma_1 - \gamma_2)}e^{i\theta} + \bar{c}_1 \qquad \text{(6A.38)}$$

Similarly, the function $g(z)$ and its conjugate $\bar{g}(\bar{z})$ are obtained as

$$g(z) = \frac{-\gamma_1 aP_o}{2(\gamma_1 - \gamma_2)} e^{-i\theta} + c_2 \qquad (6A.39)$$

$$\bar{g}(\bar{z}) = \frac{\gamma_2 aP_o}{2(\gamma_1 - \gamma_2)} e^{i\theta} + \bar{c}_2 \qquad (6A.40)$$

Substituting the values of $f(z)$, $g(z)$, $\bar{f}(\bar{z})$, and $\bar{g}(\bar{z})$ into Eq. 6A.15 yields

$$D = \frac{\gamma_2 aP_o}{2(\gamma_1 - \gamma_2)} \delta_1 e^{-i\theta} - \frac{\gamma_1 aP_o}{2(\gamma_1 - \gamma_2)} \bar{\rho}_1 e^{i\theta}$$
$$- \frac{\gamma_1 aP_o}{2(\gamma_1 - \gamma_2)} \delta_2 e^{-i\theta} + \frac{\gamma_2 aP_o}{2(\gamma_1 - \gamma_2)} \bar{\rho}_2 e^{i\theta} + c_3 \qquad (6A.41)$$

As mentioned in the previous section, for the case when γ_1 and γ_2 are complex

conjugates, ρ_1 and ρ_2 are also complex conjugates. Therefore, substituting $\bar{\rho}_1 = \rho_2$ and $\bar{\rho}_2 = \rho_1$

into Eq. 6A.41, the displacement D is reduced to

$$D = \frac{\gamma_2 aP_o}{2(\gamma_1 - \gamma_2)} \delta_1 e^{-i\theta} - \frac{\gamma_1 aP_o}{2(\gamma_1 - \gamma_2)} \rho_2 e^{i\theta}$$
$$- \frac{\gamma_1 aP_o}{2(\gamma_1 - \gamma_2)} \delta_2 e^{-i\theta} + \frac{\gamma_2 aP_o}{2(\gamma_1 - \gamma_2)} \rho_1 e^{i\theta} + c_3 \qquad (6A.42)$$

which is the same as Eq. 6A.26. Therefore, the radial and tangential displacements for

this case (where γ_1 and γ_2 are complex conjugates) are given by the same equations

(Eqs. 6A.34 and 6A.35 respectively) derived for the case when γ_1 and γ_2 are real.

6A.3 CASE OF RELEASING THE DEVIATORIC INITIAL STRESS COMPONENT (Q_o)

Referring to Fig. 6A.1-b and Eq. 6.9-a, the stress boundary conditions at the tunnel surface are

$$P(ae^{i\theta}) = -Q_o \cos 2\theta \qquad (6A.43)$$

$$q(ae^{i\theta}) = Q_o \sin 2\theta \qquad (6A.44)$$

Referring to Eqs. 6.9-b and 6.9-c, the boundary conditions are

$$-Q_o \cos 2\theta = R_o + \sum_{n=1}^{\infty} R_n \cos n\theta + S_n \sin n\theta \qquad (6A.45)$$

$$Q_o \sin 2\theta = T_o + \sum_{n=1}^{\infty} (T_n \cos n\theta + U_n \sin n\theta) \qquad (6A.46)$$

Therefore, $R_2 = -Q_o$, $U_2 = Q_o$ and all other coefficients being zero.

Substituting the values of the coefficients (R_n, S_n, U_n, and T_n) into Eq. 6.7, the two potential functions $V(z)$ and $W(z)$ are determined as

$$V(z) = W(z) = -Q_o \frac{a^2}{z^2} \qquad (6A.47)$$

or

$$V(z) = W(z) = -Q_o e^{-2i\theta} \qquad (6A.48)$$

and their complex conjugates are

$$\bar{V}(\bar{z}) = \bar{W}(\bar{z}) = Q_o \frac{a^2}{\bar{z}^2} \qquad (6A.49)$$

or

$$\bar{V}(\bar{z}) = \bar{W}(\bar{z}) = -Q_o e^{2i\theta} \qquad (6A.50)$$

In the following sections, these values of potential functions obtained are used to

determine the change in tangential stresses and radial and tangential displacements at the boundary of the excavated tunnel due to the relief of the deviatoric initial stress component.

(I) Change in Tangential Stresses

The change in tangential stresses at the boundary of the excavated tunnel, in terms of the two potential functions, is given by Eq. 6.10 as

$$\Delta\sigma_\theta = \frac{(1+\gamma_1 e^{-2i\theta})(1+\gamma_2 e^{-2i\theta})V(z) + 2(1-\gamma_1\gamma_2 e^{-4i\theta})W(z)}{2(1-\gamma_1 e^{-2i\theta})(1-\gamma_2 e^{-2i\theta})}$$
$$+ \frac{(1+\gamma_1 e^{2i\theta})(1+\gamma_2 e^{2i\theta})\overline{V}(\overline{z}) + 2(1-\gamma_1\gamma_2 e^{+4i\theta})\overline{W}(\overline{z})}{2(1-\gamma_1 e^{2i\theta})(1-\gamma_2 e^{2i\theta})}$$

(6A.51)

Substituting the values of $V(z), W(z), \overline{V}(\overline{z})$, and $\overline{W}(\overline{z})$ into Eq. 6A.51, the change in tangential stress becomes

$$\frac{\Delta\sigma_{\theta(Q_o)}}{Q_o} = \frac{-(1+\gamma_1 e^{-2i\theta})(1+\gamma_2 e^{-2i\theta}) + 2(1-\gamma_1\gamma_2 e^{-4i\theta})}{2(1-\gamma_1 e^{-2i\theta})(1-\gamma_2 e^{-2i\theta})}$$
$$+ \frac{-(1+\gamma_1 e^{2i\theta})(1+\gamma_2 e^{2i\theta}) + 2(1-\gamma_1\gamma_2 e^{4i\theta})}{2(1-\gamma_1 e^{2i\theta})(1-\gamma_2 e^{2i\theta})}$$

(6A.52)

After arrangements, Eq. 6A.52 is reduced to

$$\sigma_{\theta(P_o)} = \frac{A_3}{B_3} Q_o$$

(6A.53)

where

$$A_3 = 2(3\gamma_1+3\gamma_2-\gamma_1\gamma_2^2-\gamma_1^2\gamma_2)+(-3+\gamma_1^2+\gamma_2^2-\gamma_1\gamma_2+\gamma_1^2\gamma_2^2)(e^{2i\theta}+e^{-2i\theta})$$
$$-(\gamma_1+\gamma_2+\gamma_1\gamma_2^2+\gamma_1^2\gamma_2)(e^{4i\theta}+e^{-4i\theta})+\gamma_1\gamma_2(e^{6i\theta}+e^{-6i\theta})$$

(6A.54)

$$B_3 = 2[1+(\gamma_1+\gamma_2)^2+\gamma_1^2\gamma_2^2-(\gamma_1+\gamma_2)(1+\gamma_1\gamma_2)$$
$$(e^{2i\theta}+e^{-2i\theta}+\gamma_1\gamma_2(e^{4i\theta}+e^{-4i\theta}))]$$

(6A.55)

Equation 6.53 can be expressed in terms of the trigonometric functions ($\cos\theta$ and $\sin\theta$),

where $e^{i\theta} = \cos\theta + i\sin\theta$, as

$$\Delta\sigma_{\theta(Q_o)} = \frac{A_4}{B_4}Q_o \qquad (6A.56)$$

where

$$A_4 = (\gamma_1+\gamma_2)(3-\gamma_1\gamma_2) + (-3+\gamma_1^2+\gamma_2^2-\gamma_1\gamma_2(1-\gamma_1\gamma_2))\cos2\theta \qquad (6A.57)$$
$$-(\gamma_1+\gamma_2)(1+\gamma_1\gamma_2)\cos4\theta + \gamma_1\gamma_2\cos6\theta$$

$$B_4 = (1+\gamma_1^2-2\gamma_1\cos2\theta)(1+\gamma_2^2-2\gamma_2\cos2\theta) \qquad (6A.58)$$

Equation 6A.56 represents the change of tangential stress at the boundary of the tunnel

due to the relief of the deviatoric initial stress component Q_o.

(II) Radial and Tangential Displacements

Case (a) γ_1 **and** γ_2 **are real**

Substituting the values of $V(z)$ and $W(z)$ into Eq. 6A.16 leads to

$$f'(z) = \frac{-(1+\gamma_2\frac{a^2}{z^2})(Q_0\frac{a^2}{z^2}) - (1-\gamma_2\frac{a^2}{z^2})(Q_o\frac{a^2}{z^2})}{4(\gamma_1-\gamma_2)} \qquad (6A.59)$$

After arrangement, Eq. 6A.59 becomes

$$f'(z) = \frac{-2Q_o a^2}{4(\gamma_1-\gamma_2)z^2} \qquad (6A.60)$$

The value of $f(z)$ is obtained by integrating Eq. 6A.60 with respect to z. Therefore,

$$f(z) = \frac{a^2 Q_o}{2z(\gamma_1-\gamma_2)} + c_1 \qquad (6A.61)$$

where c_1 is an integration constant. Substituting $z = ae^{i\theta}$ into Eq. 6A.61, the value of $f(z)$

is obtained as

$$f(z) = \frac{aQ_o}{2(\gamma_1 - \gamma_2)} e^{-i\theta} + c_1 \qquad (6A.62)$$

The complex conjugate of $f(z)$ is

$$\bar{f}(\bar{z}) = \frac{aQ_o}{2(\gamma_1 - \gamma_2)} e^{i\theta} + \bar{c}_1 \qquad (6A.63)$$

Similarly, the function $g(z)$ and its conjugate $\bar{g}(\bar{z})$ are obtained by substituting

the values of $V(z)$ and $W(z)$ into Eq. 6A.17 and integrating with respect to z. The

values obtained for $f(z)$ and $g(z)$, respectively, are

$$g(z) = \frac{-aQ_o}{2(\gamma_1 - \gamma_2)} e^{-i\theta} + c_2 \qquad (6A.64)$$

$$\bar{g}(\bar{z}) = \frac{-aQ_o}{2(\gamma_1 - \gamma_2)} e^{i\theta} + \bar{c}_2 \qquad (6A.65)$$

Substituting the values of $f(z)$, $g(z)$, $\bar{f}(\bar{z})$, and $\bar{g}(\bar{z})$ into Eq. 6A.15 yields

$$D = \frac{aQ_o}{2(\gamma_1 - \gamma_2)} \delta_1 e^{-i\theta} + \frac{aQ_o}{2(\gamma_1 - \gamma_2)} \rho_1 e^{i\theta}$$
$$- \frac{aQ_o}{2(\gamma_1 - \gamma_2)} \delta_2 e^{-i\theta} - \frac{aQ_o}{2(\gamma_1 - \gamma_2)} \rho_2 e^{i\theta} + c_3 \qquad (6A.66)$$

When the value of Q_o is zero, the value of the displacement D should be zero, therefore

the integration constant c_3 is equal to zero. By substituting $D = u_x + iu_y$ and

$e^{i\theta} = \cos\theta + i\sin\theta$ into Eq. 6A.66 and after some arrangements, Eq. 6A.66 is reduced to

$$u_x + iu_y = \frac{aQ_o}{2(\gamma_1 - \gamma_2)} [(\delta_1 + \rho_1 - \delta_2 - \rho_2)\cos\theta \qquad (6A.67)$$
$$+ (-\delta_1 + \rho_1 + \delta_2 - \rho_2)i\sin\theta]$$

Comparing the left hand side of Eq. 6A.67 with the right hand side, the displacements

in x-direction (u_x) and y-direction (u_y), respectively, are obtained as

$$u_x = \frac{aQ_o}{2(\gamma_1 - \gamma_2)} (\delta_1 + \rho_1 - \delta_2 - \rho_2) \cos\theta \qquad \text{(6A.68)}$$

$$u_y = \frac{aQ_o}{2(\gamma_1 - \gamma_2)} (-\delta_1 + \rho_1 + \delta_2 - \rho_2) \sin\theta \qquad \text{(6A.69)}$$

Referring to Fig. 6A.2, the radial displacement (u_r) and tangential displacement u_θ

in terms of the displacements u_x and u_y, respectively, are

$$u_r = u_x \cos\theta + u_y \sin\theta \qquad \text{(6A.70)}$$

$$u_\theta = -u_x \sin\theta + u_y \cos\theta \qquad \text{(6A.71)}$$

Substituting for the values of u_x and u_y (Eqs. 6A.68 and 6A.69) into Eq. 6A.70, the

radial displacement at $r=a$, in terms of Q_o, is obtained as

$$u_{a(Q_o)} = \frac{aQ_o}{2(\gamma_1 - \gamma_2)} [(\delta_1 + \rho_1 - \delta_2 - \rho_2)]\cos^2\theta$$
$$+ (-\delta_1 + \rho_1 + \delta_2 - \rho_2)]\sin^2\theta\} \qquad \text{(6A.72)}$$

After arrangements and making use of the following trigonometric relationships

$$\cos^2\theta + \sin^2\theta = 1 \qquad \cos^2\theta - \sin^2\theta = \cos2\theta \qquad \text{(6A.73)}$$

the radial displacement at the tunnel surface due to the relief of the deviatoric initial

stress component is derived as

$$u_{a(Q_o)} = \frac{aQ_o}{2(\gamma_1 - \gamma_2)} [(\rho_1 - \rho_2) + (\delta_1 - \delta_2)\cos2\theta] \qquad \text{(6A.74)}$$

Similarly, by making use of Eqs. 6A.68, 6A.69, and 6A.71, the tangential

displacement at the tunnel surface is obtained as

$$u_{\theta(Q_o)} = \frac{aQ_o}{2(\gamma_1 - \gamma_2)} (\delta_2 - \delta_1)\sin2\theta \qquad \text{(6A.75)}$$

Case (b) γ_1 and γ_2 are complex conjugates

As in case (a), the function $f(z)$ is given by Eq. 6A.62 as

$$f(z) = \frac{aQ_o}{2(\gamma_1 - \gamma_2)} e^{-i\theta} + c_1 \tag{6A.76}$$

The complex conjugate of $f(z)$ is

$$\bar{f}(\bar{z}) = \frac{aQ_o}{2(\bar{\gamma}_1 - \bar{\gamma}_2)} e^{i\theta} + \bar{c}_1 \tag{6A.77}$$

Substituting $\bar{\gamma}_1 = \gamma_2$ and $\bar{\gamma}_2 = \gamma_1$ into Eq. 6A.77 leads to

$$\bar{f}(\bar{z}) = \frac{-aQ_o}{2(\gamma_1 - \gamma_2)} e^{i\theta} + \bar{c}_1 \tag{6A.78}$$

Similarly, the function $g(z)$ and its conjugate $\bar{g}(\bar{z})$ are obtained as

$$g(z) = \frac{-aQ_o}{2(\gamma_1 - \gamma_2)} e^{-i\theta} + c_2 \tag{6A.79}$$

$$\bar{g}(\bar{z}) = \frac{aQ_o}{2(\gamma_1 - \gamma_2)} e^{i\theta} + \bar{c}_2 \tag{6A.80}$$

Substituting the values of $f(z)$, $g(z)$, $\bar{f}(\bar{z})$, and $\bar{g}(\bar{z})$ into Eq. 6A.15 yields

$$\begin{aligned} D &= \frac{aQ_o}{2(\gamma_1 - \gamma_2)} \delta_1 e^{-i\theta} - \frac{aQ_o}{2(\gamma_1 - \gamma_2)} \bar{\rho}_1 e^{i\theta} \\ &\quad - \frac{aQ_o}{2(\gamma_1 - \gamma_2)} \delta_2 e^{-i\theta} + \frac{aQ_o}{2(\gamma_1 - \gamma_2)} \bar{\rho}_2 e^{i\theta} + c_3 \end{aligned} \tag{6A.81}$$

As mentioned in the previous section, for the case when γ_1 and γ_2 are complex conjugates, ρ_1 and ρ_2 are also complex conjugates. Therefore, substituting $\bar{\rho}_1 = \rho_2$ and $\bar{\rho}_2 = \rho_1$ into Eq. 6A.81, the displacement D is reduced to

$$D = \frac{aQ_o}{2(\gamma_1 - \gamma_2)} \delta_1 e^{-i\theta} - \frac{aQ_o}{2(\gamma_1 - \gamma_2)} \rho_2 e^{i\theta}$$
$$- \frac{aQ_o}{2(\gamma_1 - \gamma_2)} \delta_2 e^{-i\theta} + \frac{aQ_o}{2(\gamma_1 - \gamma_2)} \rho_1 e^{i\theta} + c_3$$

(6A.82)

which is the same as Eq. 6A.66. Therefore, the radial and tangential displacements for this case (where γ_1 and γ_2 are complex conjugates) are given by the same equations (Eq. 6A.74 and 6A.75 respectively) derived for the case when γ_1 and γ_2 are real.

6A.4 FINAL STRESSES AND DISPLACEMENTS

(a) Tangential Stresses

The final tangential stresses at the circumference of the tunnel are obtained by adding the change in tangential stresses from releasing the hydrostatic initial stress component to that from releasing the deviatoric initial stress component. The final tangential stresses are the sum of the initial stresses before excavating the tunnel and the change in stresses induced by the excavation. Therefore, the final tangential stresses are given by the following equation:

$$\sigma_\theta = (P_o - Q_o \cos 2\theta) + \Delta\sigma_{\theta(P_o)} + \Delta\sigma_{\theta(Q_o)}$$

(6A.83)

Substituting for the values of $\Delta\sigma_{\theta(P_o)}$ and $\Delta\sigma_{\theta(Q_o)}$ from Eqs. 6A.12 and 6A.56 ,respectively, into Eq. 6A.83 and after arrangements, the following equation for the tangential stresses at the boundary of the tunnel is obtained:

$$\sigma_\theta = \frac{2 + 2(\gamma_1 + \gamma_2)^2 - 2\gamma_1^2\gamma_2^2 - 4(\gamma_1 + \gamma_2)\cos 2\theta}{(1 + \gamma_1^2 - 2\gamma_1 \cos 2\theta)(1 + \gamma_2^2 - 2\gamma_2 \cos 2\theta)} P_o$$
$$+ \frac{4(\gamma_1 + \gamma_2) - 4(1 + \gamma_1\gamma_2)\cos 2\theta}{(1 + \gamma_1^2 - 2\gamma_1 \cos 2\theta)(1 + \gamma_2^2 - 2\gamma_2 \cos 2\theta)} Q_o$$

(6A.84)

(b)   Radial and Tangential Displacements

The final radial deformation due to the tunnel excavation is obtained by adding the deformations resulting from the release of the hydrostatic and deviatoric initial stresses components, therefore

$$u_a = u_{\alpha(P_o)} + u_{\alpha(Q_o)}$$ (6A.85)

Substituting for the values of $u_{\alpha(P_o)}$ and $u_{\alpha(Q_o)}$, from Eqs. 6A.34 and 6A.74 respectively, into Eq. 6A.85, the following closed form solution for the radial displacement at the circumference of the excavated tunnel is obtained:

$$u_a = \frac{a}{2(\gamma_1 - \gamma_2)} \{P_o(\gamma_2\rho_1 - \gamma_1\rho_2) + Q_o(\rho_1 - \rho_2)$$
$$+ [P_o(\gamma_2\delta_1 - \gamma_1\delta_2) + Q_o(\delta_1 - \delta_2)]\cos 2\theta\}$$ (6A.86)

Similarly, by adding the tangential deformations resulting from the release of the hydrostatic and deviatoric initial stress components, the following expression for the tangential stress at the circumference of the excavated tunnel is obtained:

$$u_\theta = \frac{a}{2(\gamma_1 - \gamma_2)}[P_o(\gamma_1\delta_2 - \gamma_2\delta_1) + Q_o(\delta_2 - \delta_1)]\sin 2\theta$$ (6A.87)
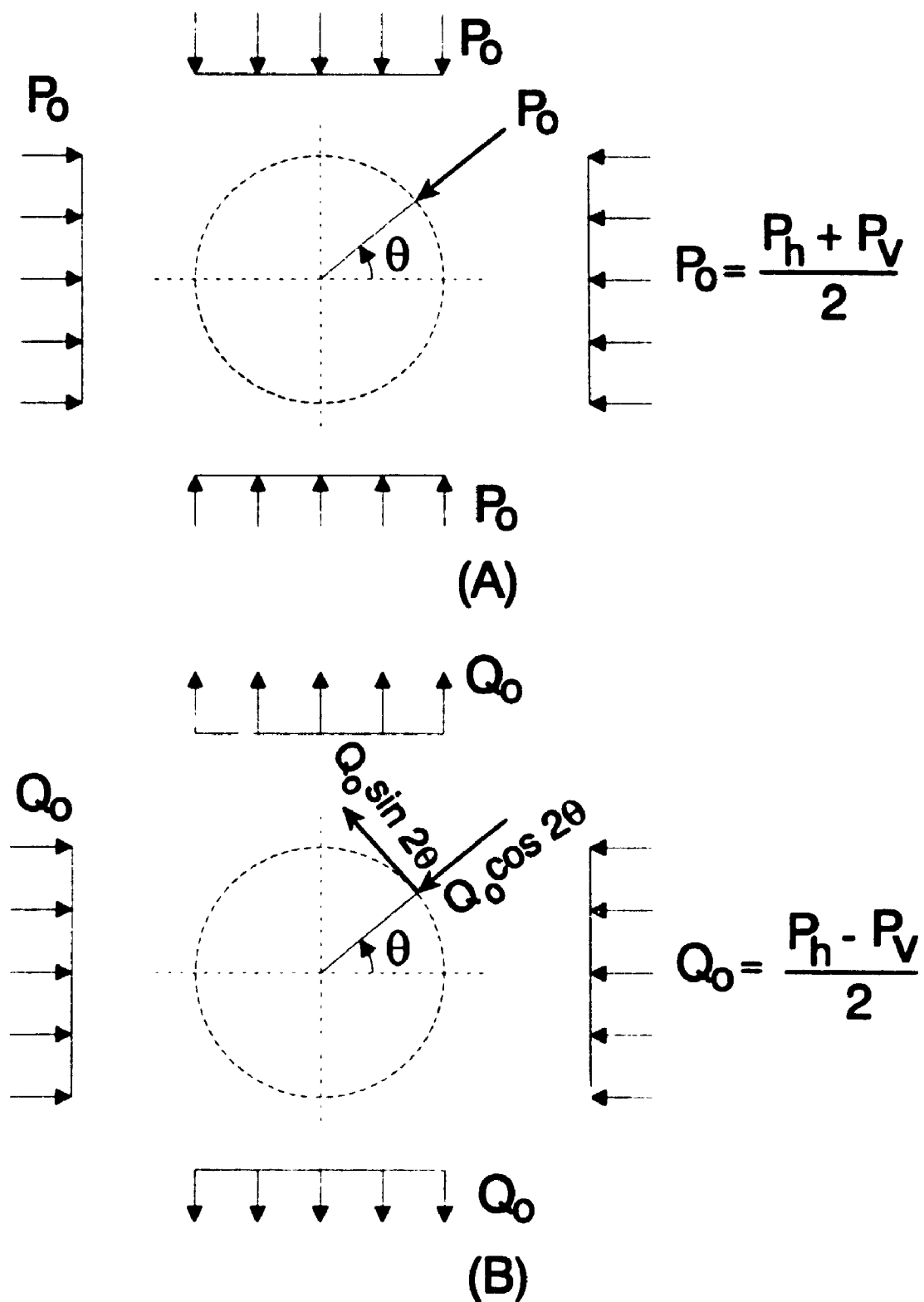
Figure 6A.1 Normal and shear stresses on an imaginary circle in rock
subjected to a biaxial stress system P_h and P_v at infinity.
(A) hydrostatic component P_0, (B) deviatoric component Q_0
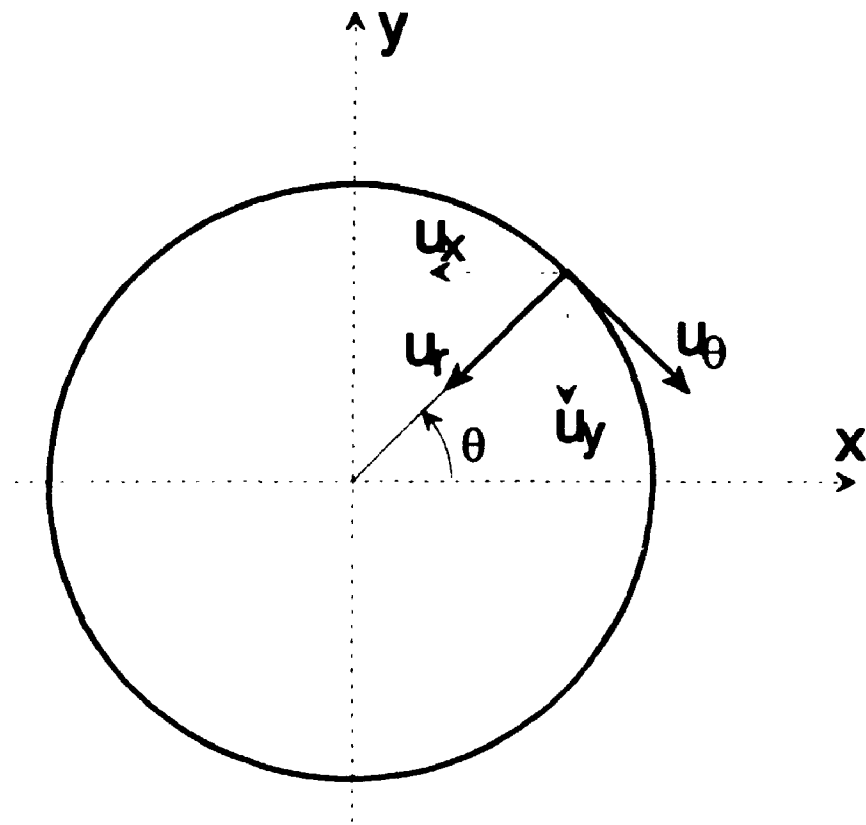
$$U_r = U_x \cos\theta + U_y \sin\theta$$

$$U_\theta = -U_x \sin\theta + U_y \cos\theta$$

Figure 6A.2 Radial and tangential displacements in terms of x and y displacements

APPENDIX 7A

RESULTS OF FREE AND SEMI-CONFINED SWELL TESTS
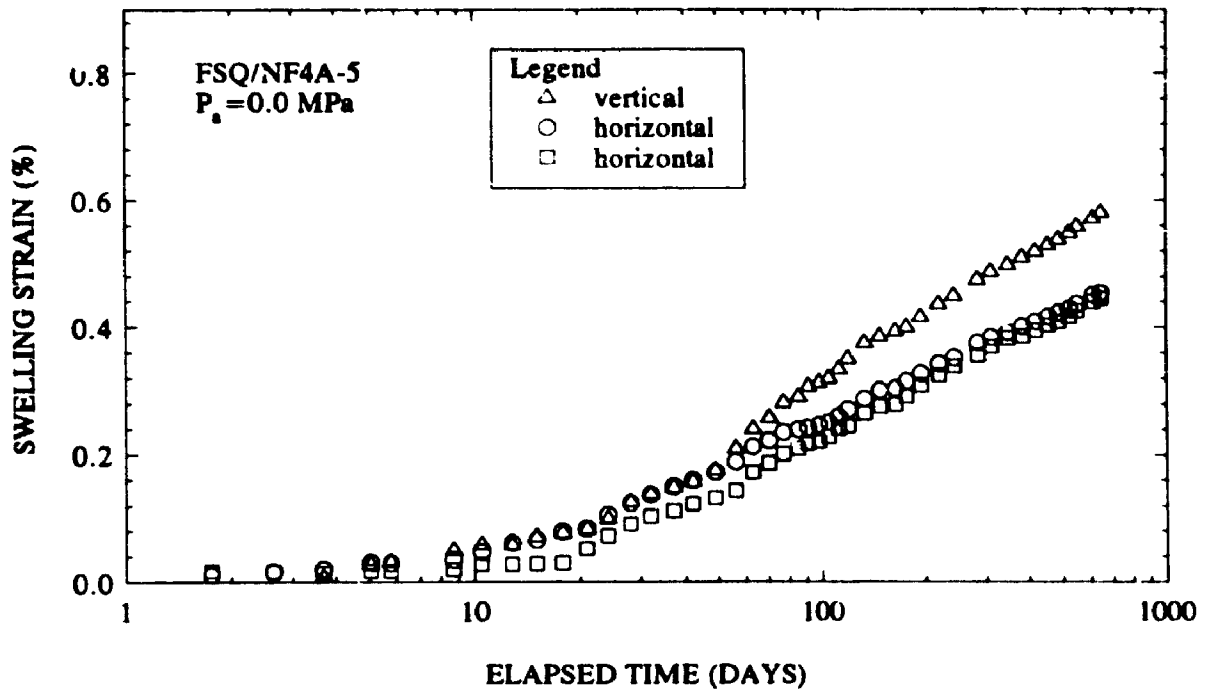ON QUEENSTON SHALE
(SABNGS NO.3 SITE, 1990 INVESTIGATION)
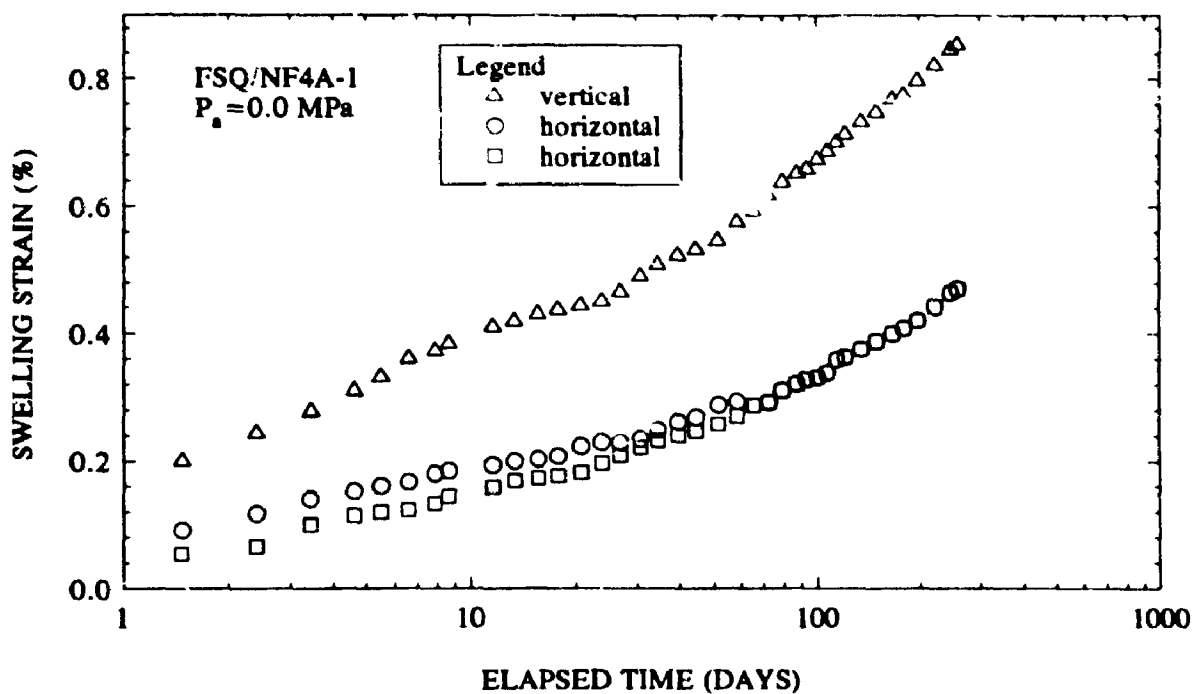
Figure 7A.1 Results of free swell tests on Queenston Shale at SABNGS NO. 3 site
Test No. NF4A-1 (1990 investigation)
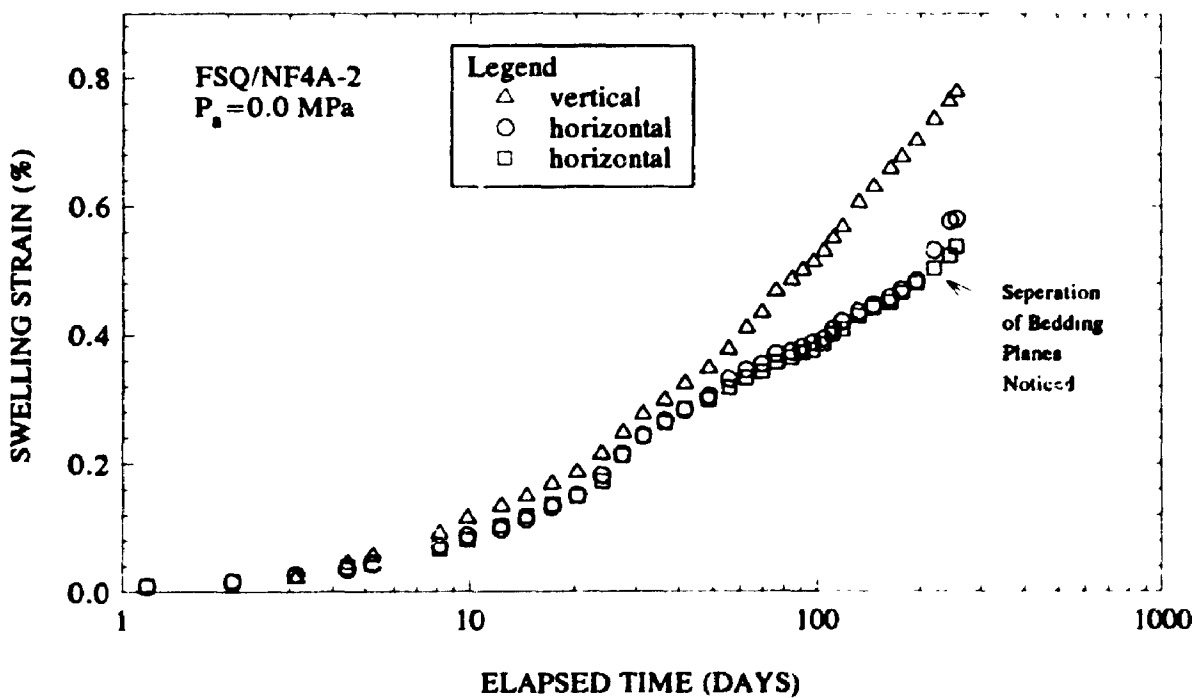
Figure 7A.2 Results of free swell tests on Queenston Shale at SABNGS No. 3 site
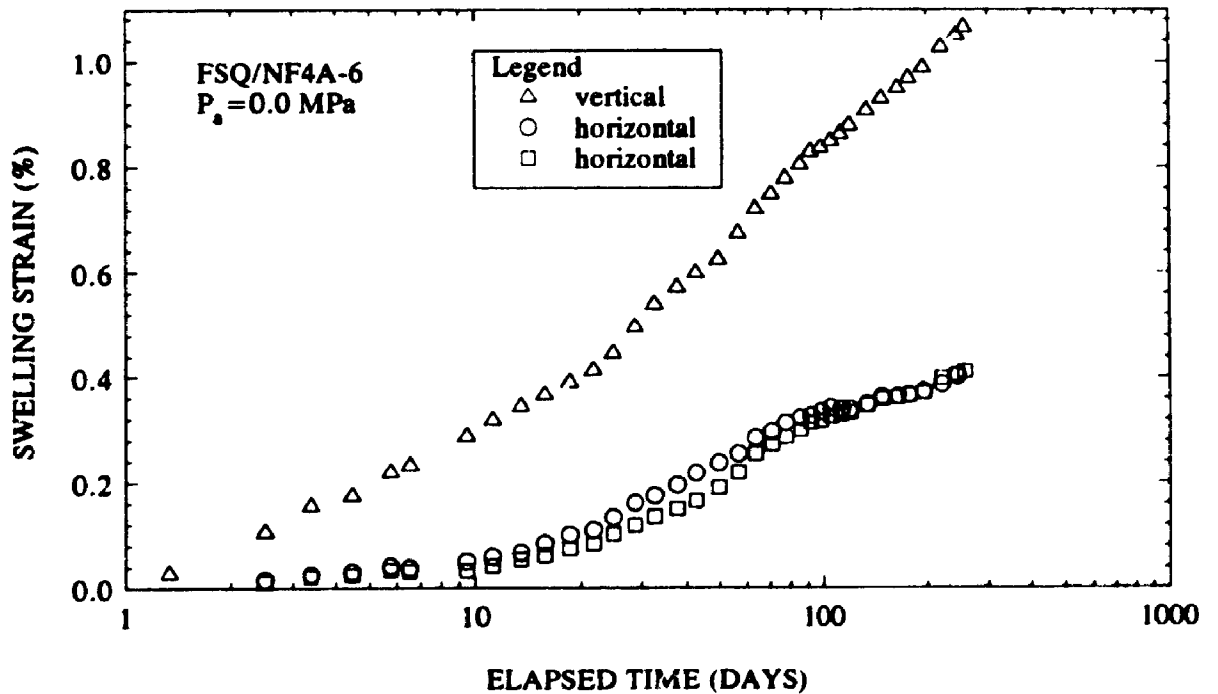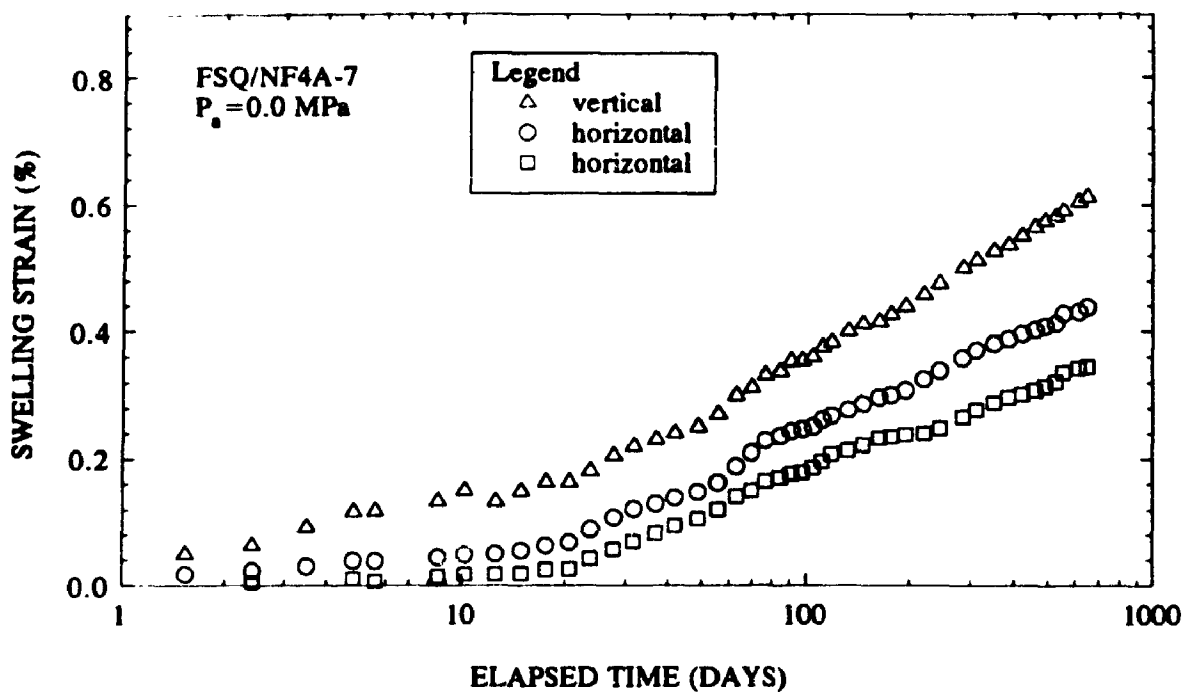Test No. NF4A-2 (1990 investigation)
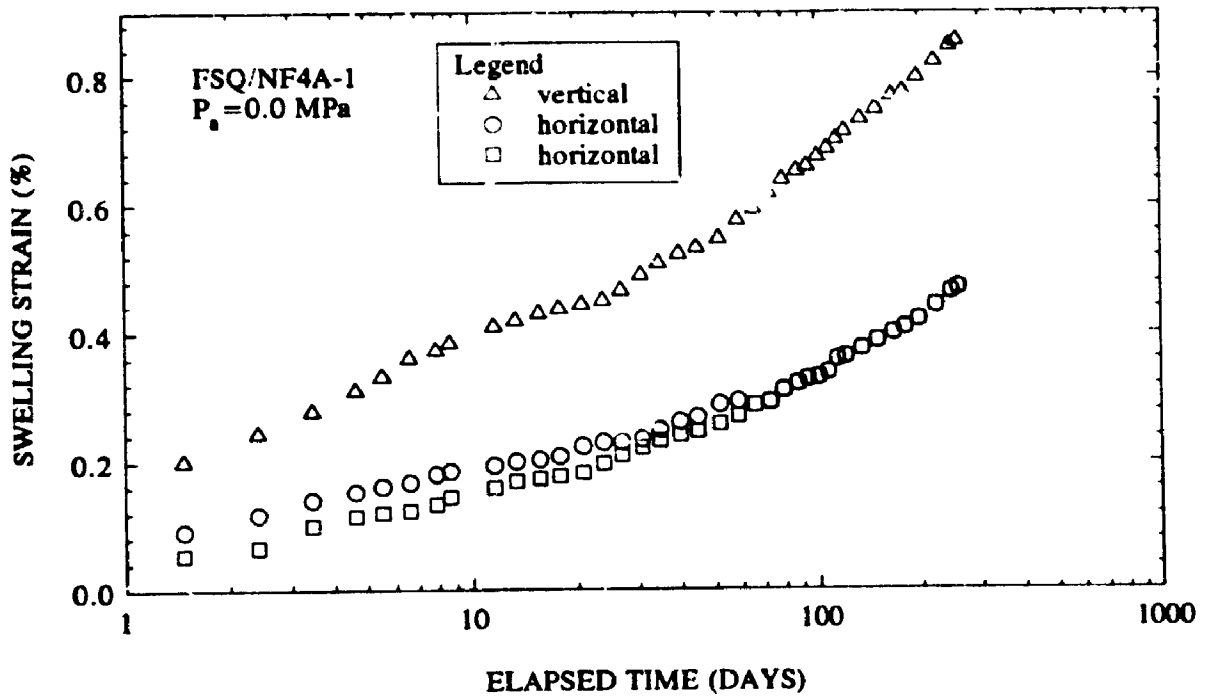
Figure 7A.1 Results of free swell tests on Queenston Shale at SABNGS NO. 3 site
Test No. NF4A-1 (1990 investigation)
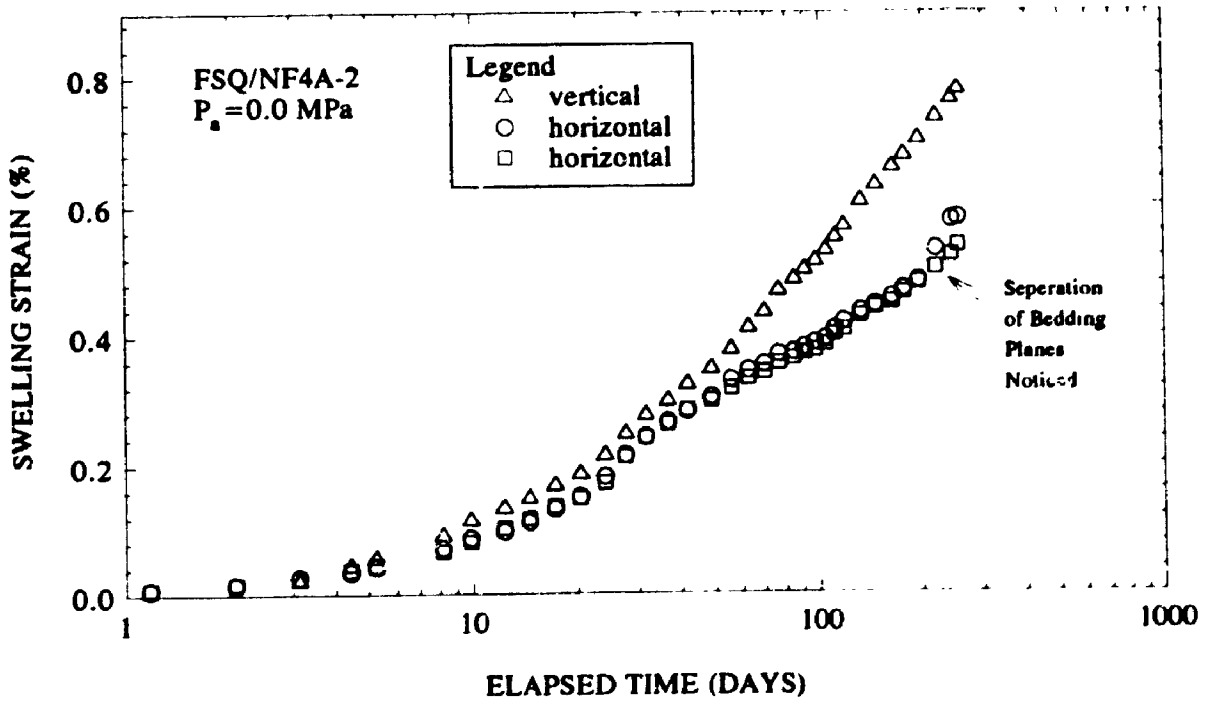
Figure 7A.2 Results of free swell tests on Queenston Shale at SABNGS No. 3 site
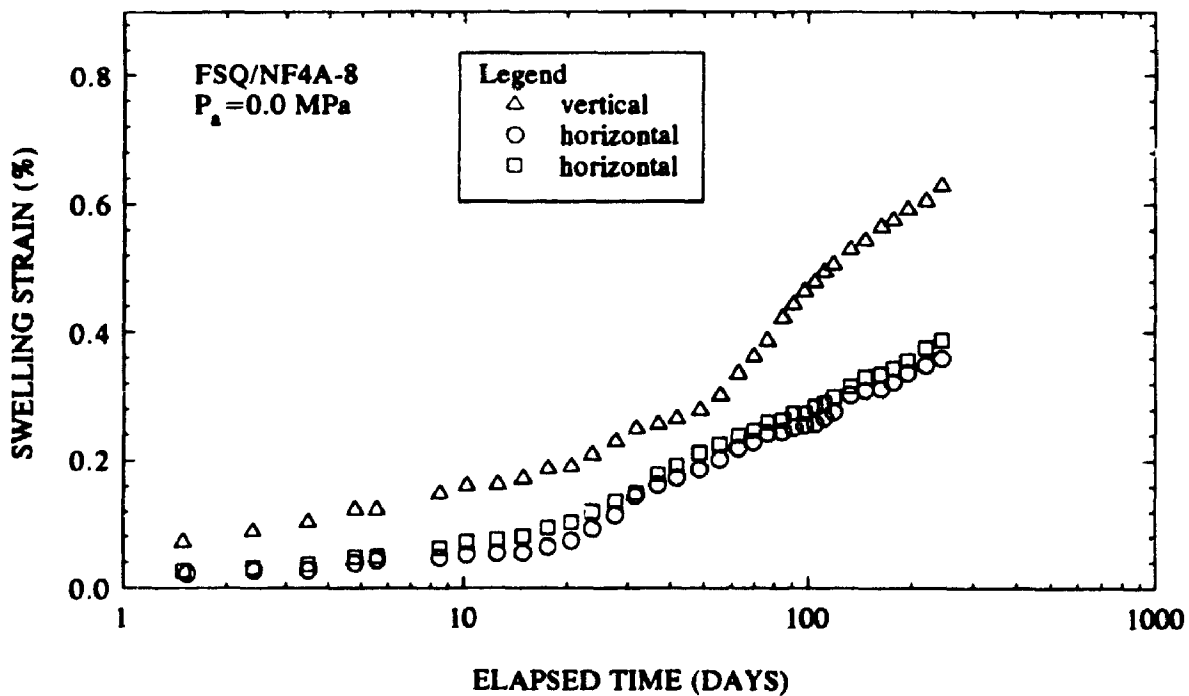Test No. NF4A-2 (1990 investigation)
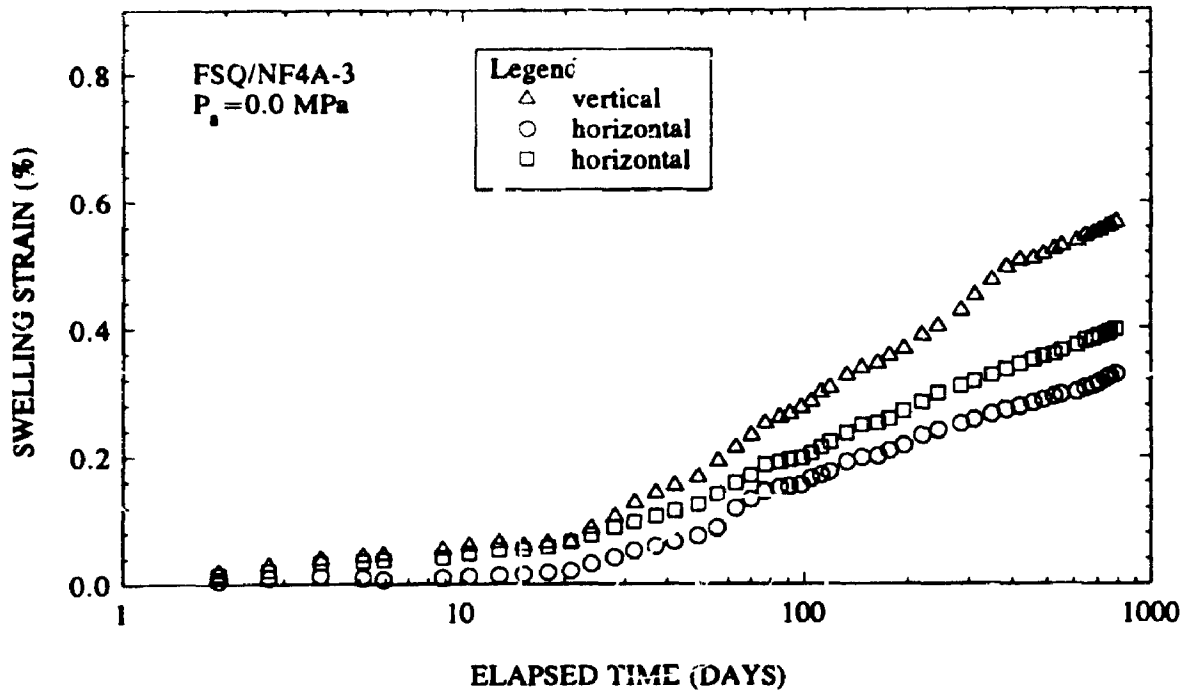
Figure 7A.3 Results of free swell tests on Queenston Shale at SABNGS No. 3 site
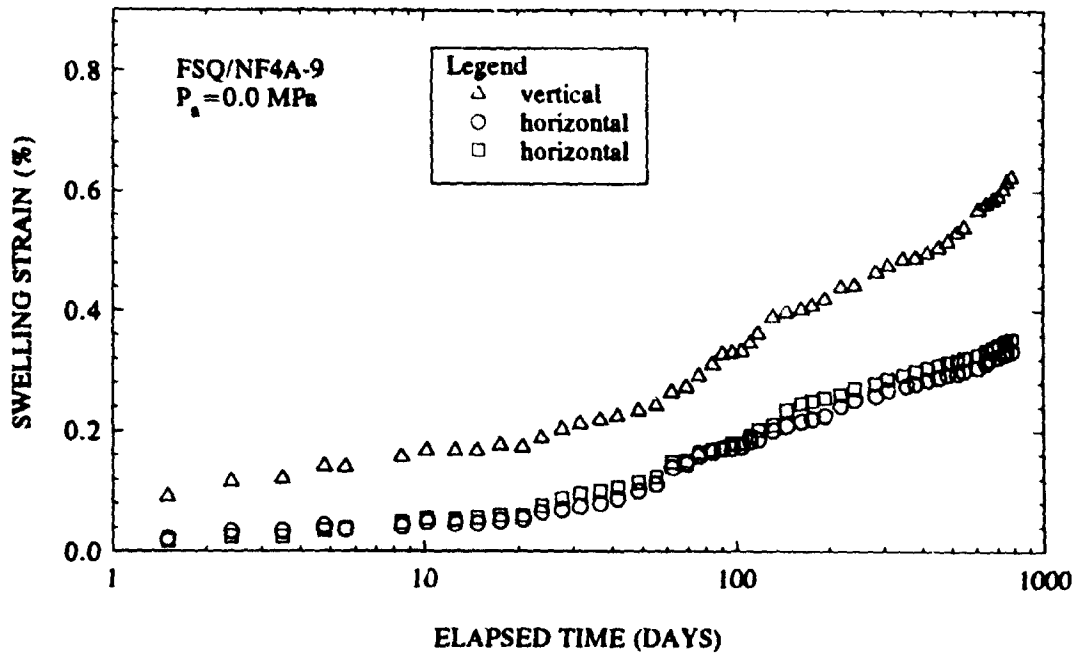Test No. NF4A-3 (1990 investigation)
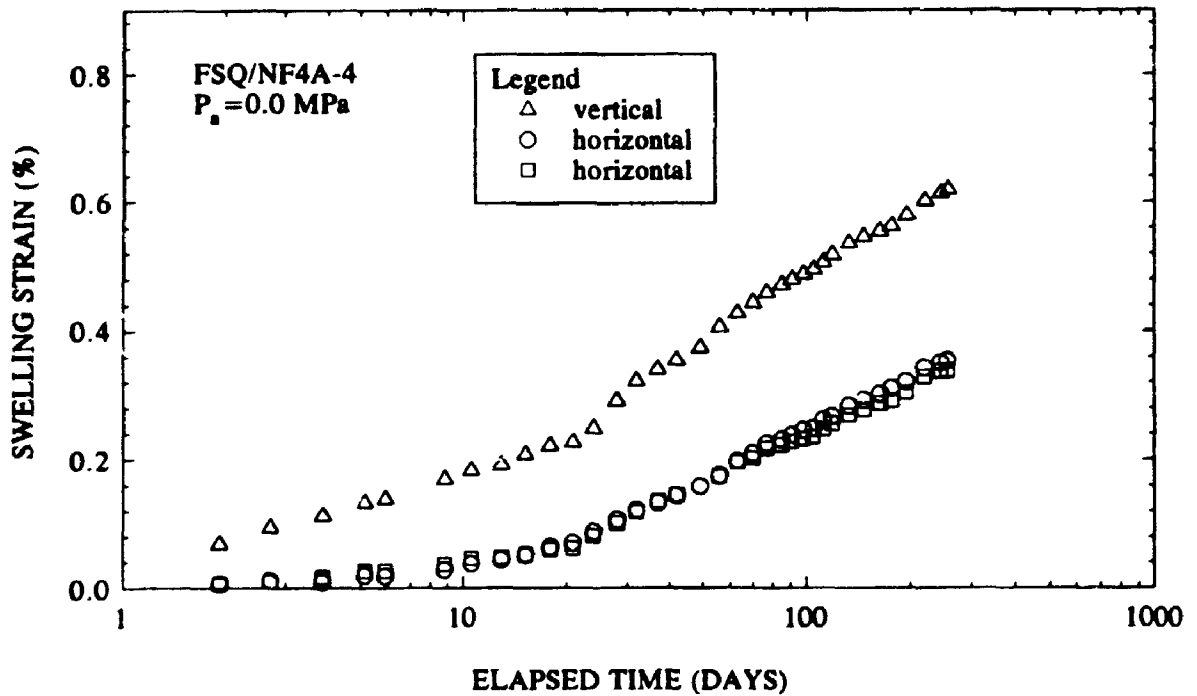
Figure 7A.4 Results of free swell tests on Queenston Shale at SABNGS No. 3 site
Test No. NF4A-4 (1990 investigation)

Figure 7A.5 Results of free swell tests on Queenston Shale at SABNGS No. 3 site
Test No. NF4A.5 (1990 investigation)

Figure 7A.6 Results of free swell tests on Queenston Shale at SABNGS No. 3 site
Test No. 6 (1990 investigation)

Figure 7A.7 Results of free swell tests on Queenston Shale at SABNGS No. 3 site
Test No. NF4A-7 (1990 investigation)

Figure 7A.8 Results of free swell tests on Queenston Shale at SABNGS No. 3 site
Tests No. NF4A-8 (1990 investigation)

Figure 7A.9 Results of free swell tests on Queenston Shale at SABNGS No. 3 site
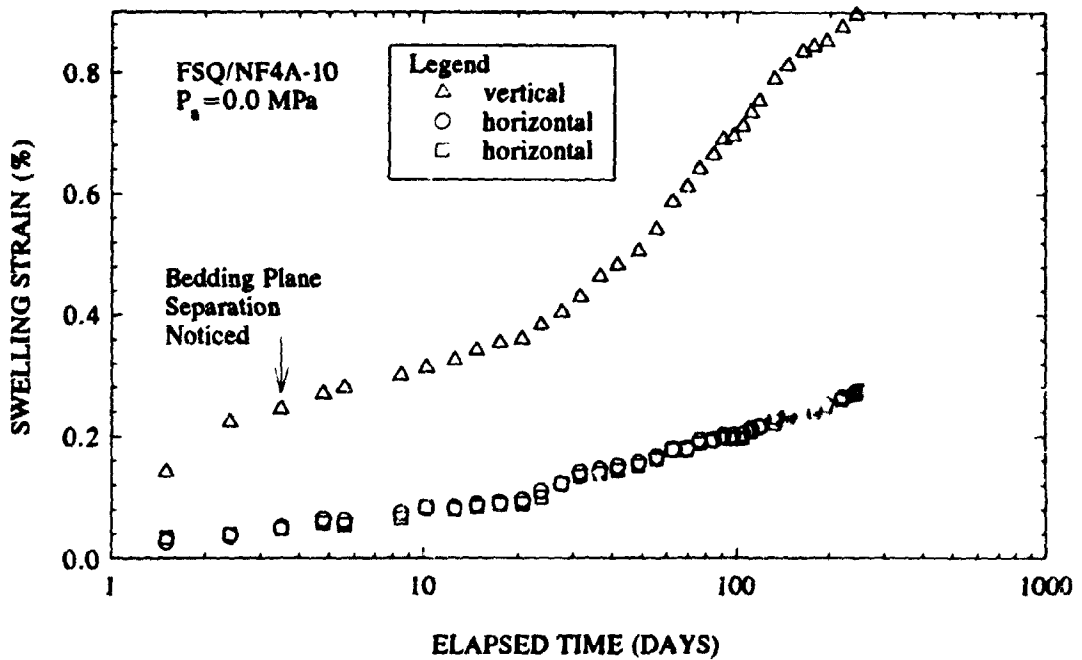Test No. NF4A-9 (1990 investigation)

Figure 7A.10 Results of free swell tests on Queenston Shale at SABNGS No. 3 site
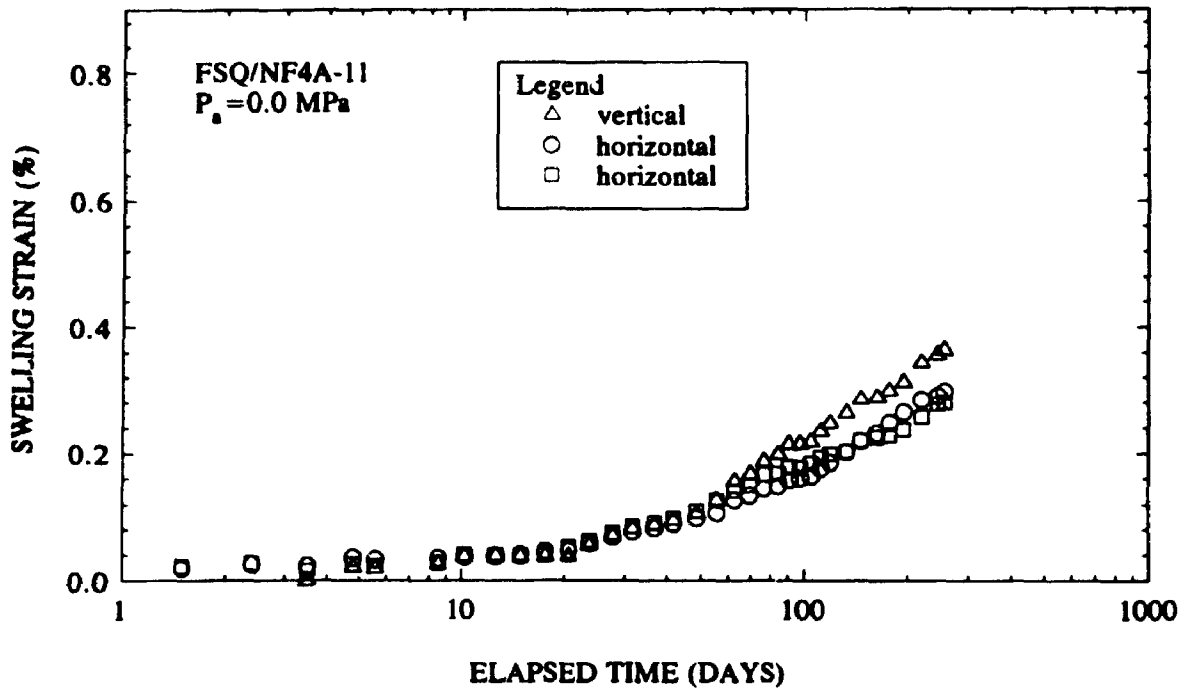Test No. NF4A-10 (1990 investigation)

Figure 7A.11 Results of free swell tests on Queenston Shale at SABNGS No. 3 site
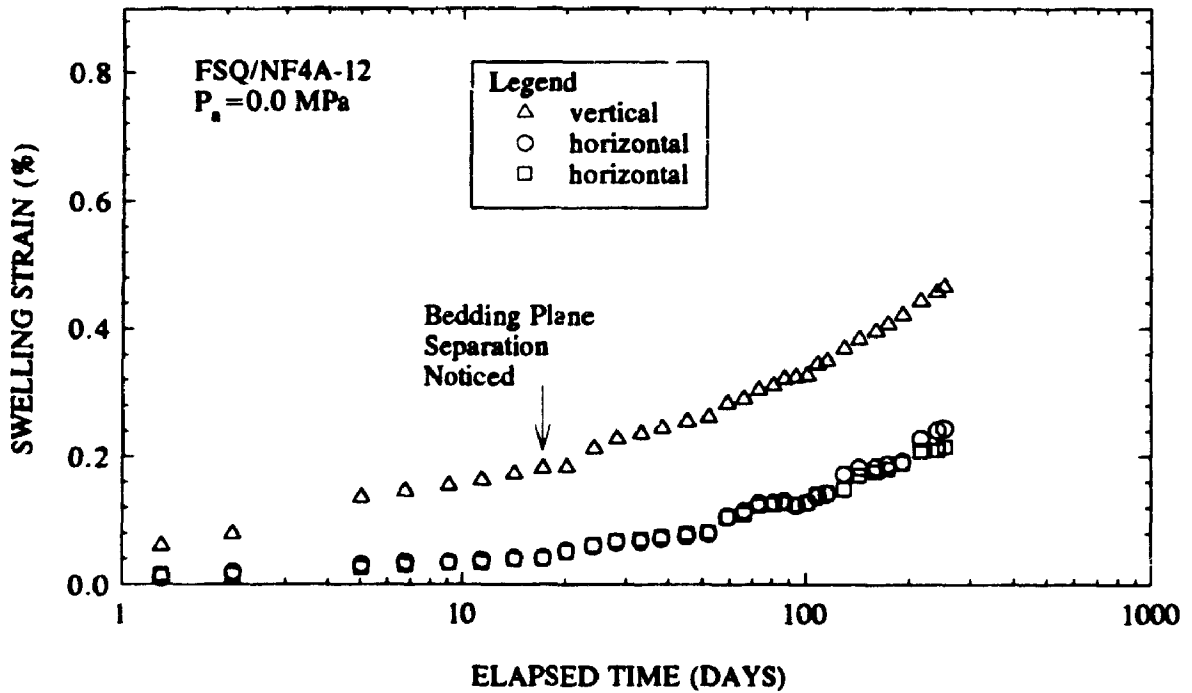Tests NF4A-11 (1990 investigation)

Figure 7A.12 Results of free swell tests on Queenston Shale at SABNGS No. 3 site
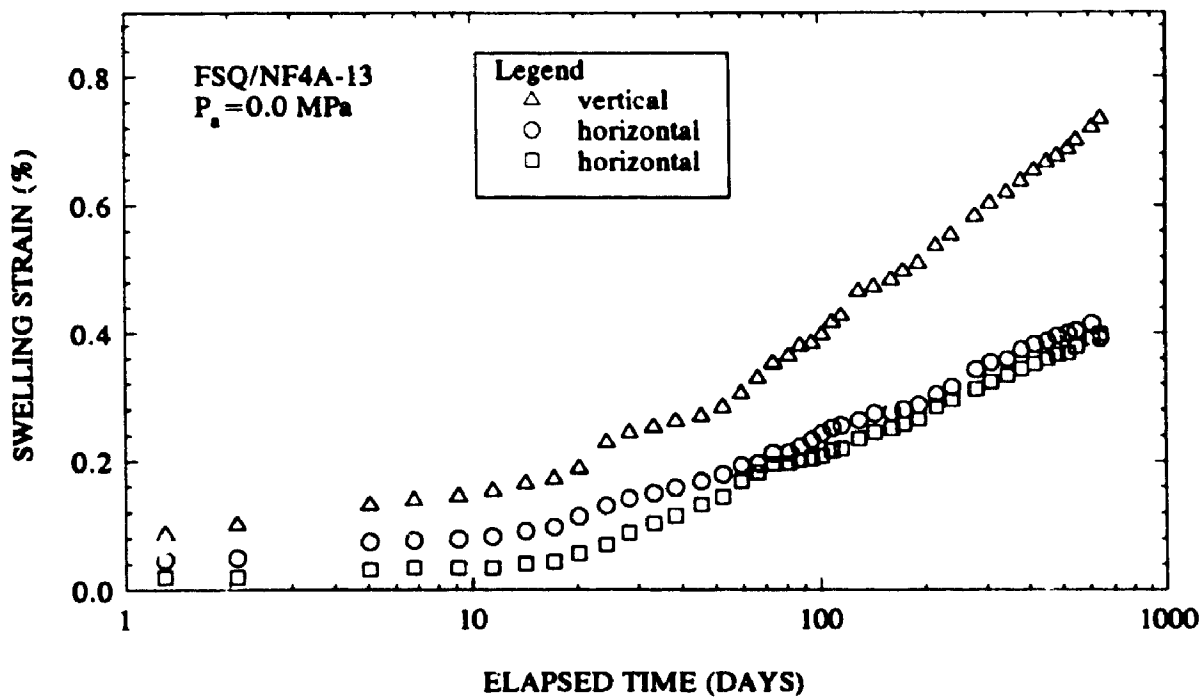Test No. NF4A-12 (1990 investigation)

Figure 7A.13 Results of free swell tests on Queenston Shale at SABNGS No. 3 site
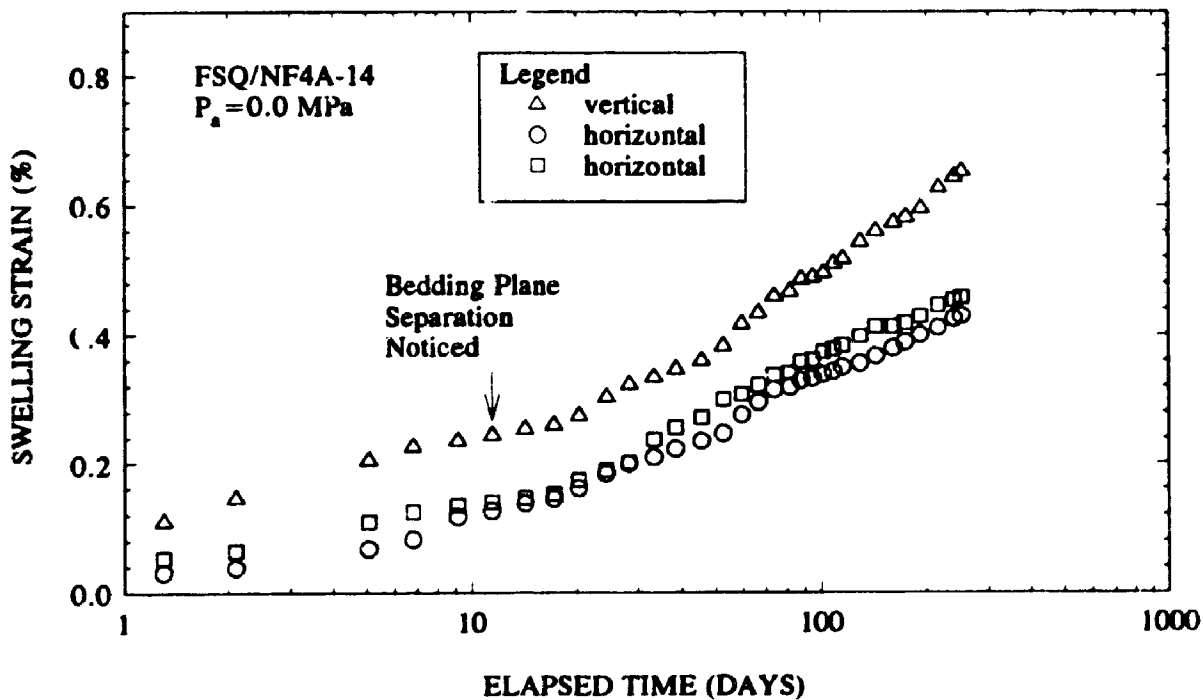Test No. NF4A-13 (1990 investigation)

Figure 7A.14 Results of free swell tests on Queenston Shale at SABNGS No. 3 site
Test No. NF4A-14 (1990 investigation)
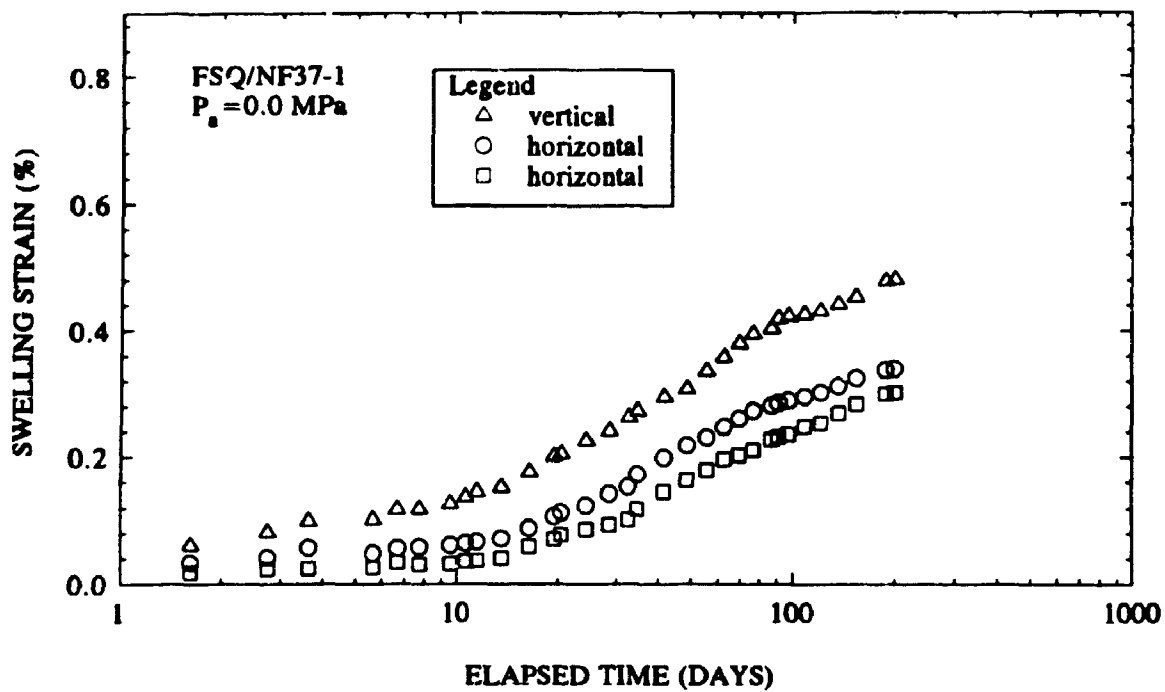
Figure 7A.15 Results of free swell tests on Queenston Shale at SABNGS No. 3 site Test NF37-1 (1990 investigation)
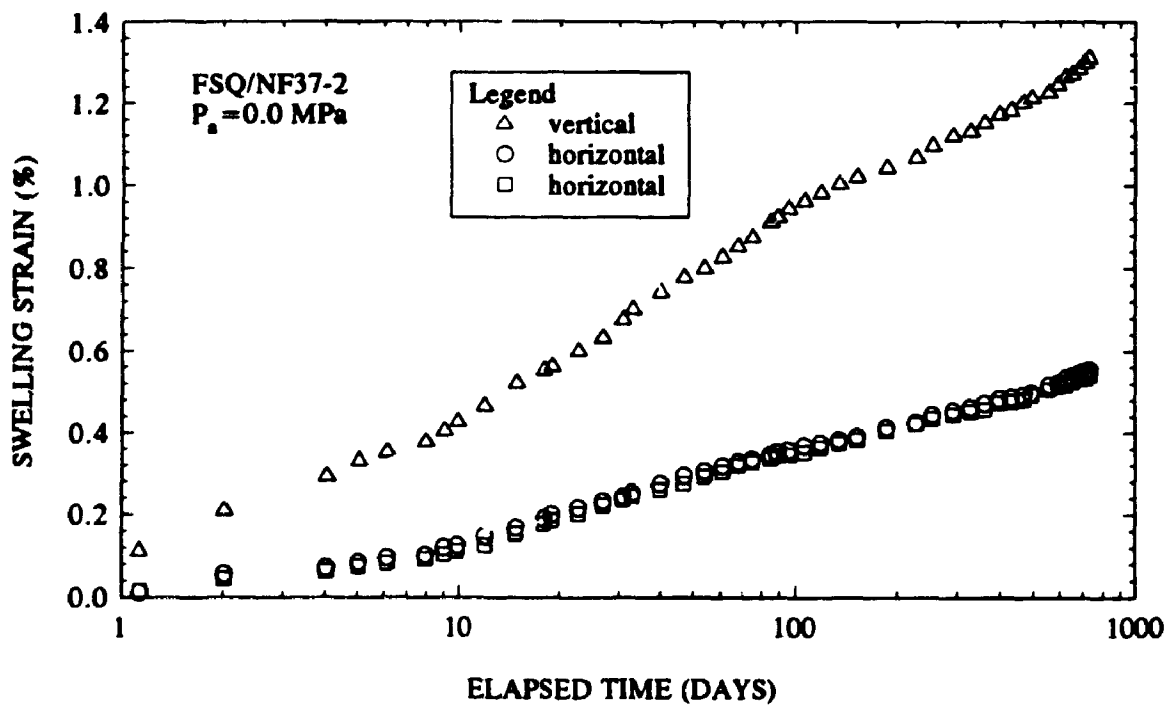

Figure 7A.16 Results of free swell tests on Queenston Shale at SABNGS No. 3 site Test NF37-2 (1990 investigation)

Figure 7A.17 Results of free swell tests on Queenston Shale at SABNGS No. 3 site
Test NF37-3 (1990 investigation)

Figure 7A.18 Results of free swell tests on Queenston Shale at SABNGS No. 3 site
Test No. NF37-4 (1990 investigation)

Figure 7A.19 Results of free swell tests on Queenston Shale at SABNGS No. 3 site
Test No. NF37-5 (1990 investigation)

Figure 7A.20 Results of free swell tests on Queenston Shale at SABNGS No. 3 site
Test No. NF 37-6 (1990 investigation)

Figure 7A.21 Results of free swell tests on Queenston Shale at SABNGS No. 3 site
Test No. NF37-7 (1990 investigation)

Figure 7A.22 Results of Free swell tests on Queenston Shale at SABNGS No. 3 site
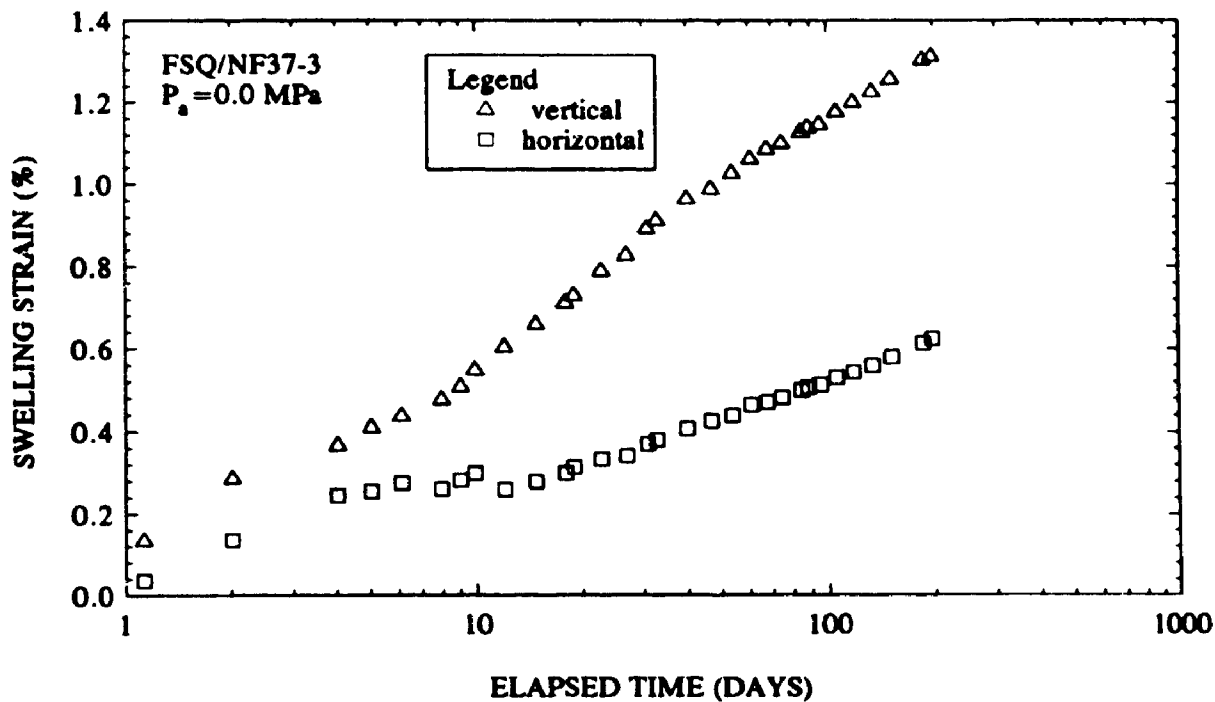Test No. NF37-8 (1990 investigation)

Figure 7A.23 Results of free swell fests on Queenston Shale at SABNGS No. 3 site
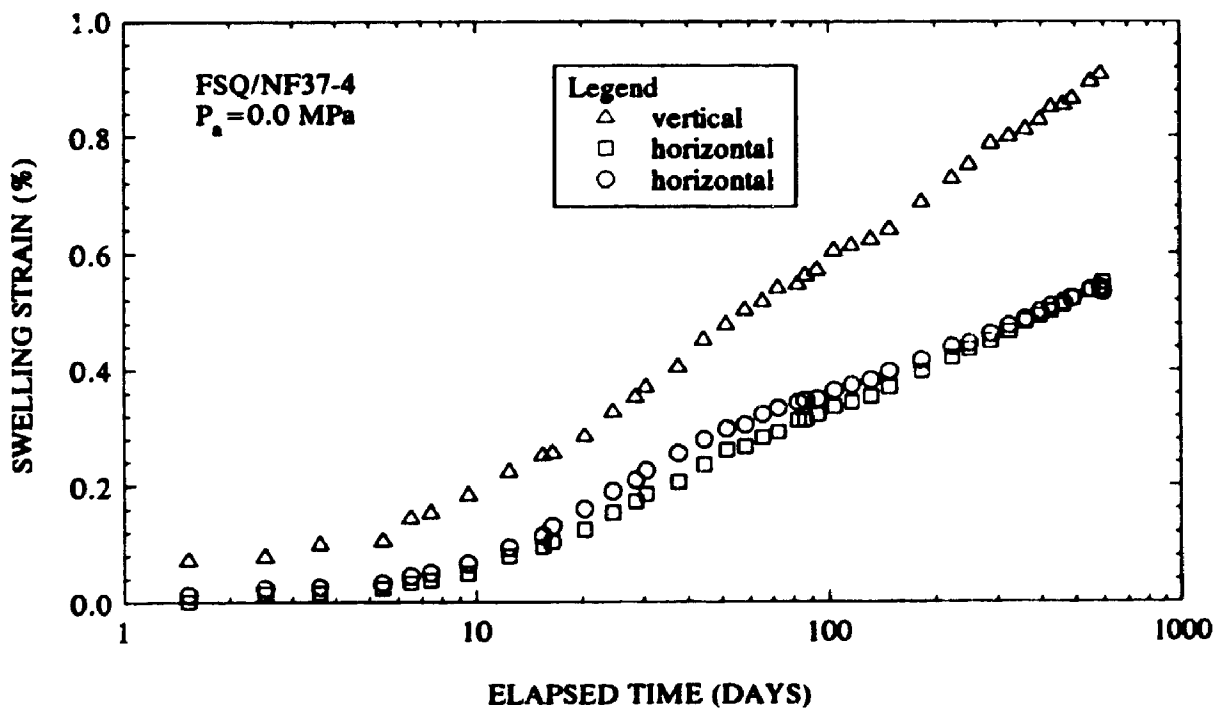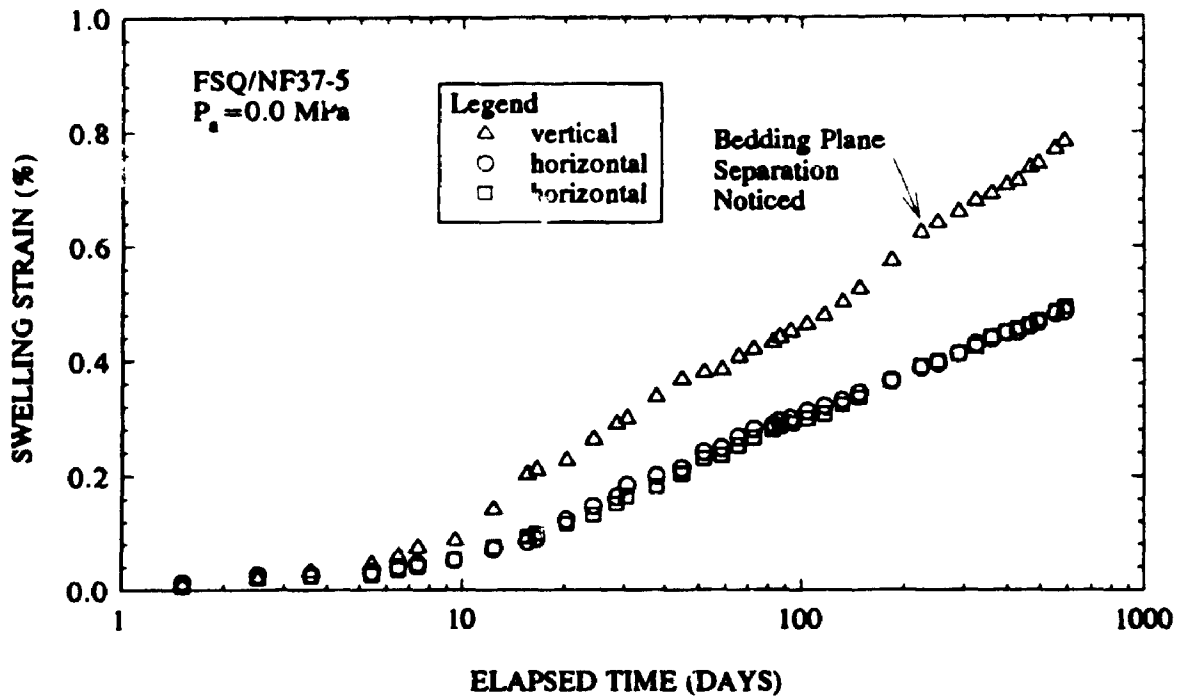Tests NF37-9 (1990 investigation)

Fgure 7A.24 Results of free swell tests on Queenston Shale at SABNGS No. 3 site
Test No. NF37-10 (1990 investigation)
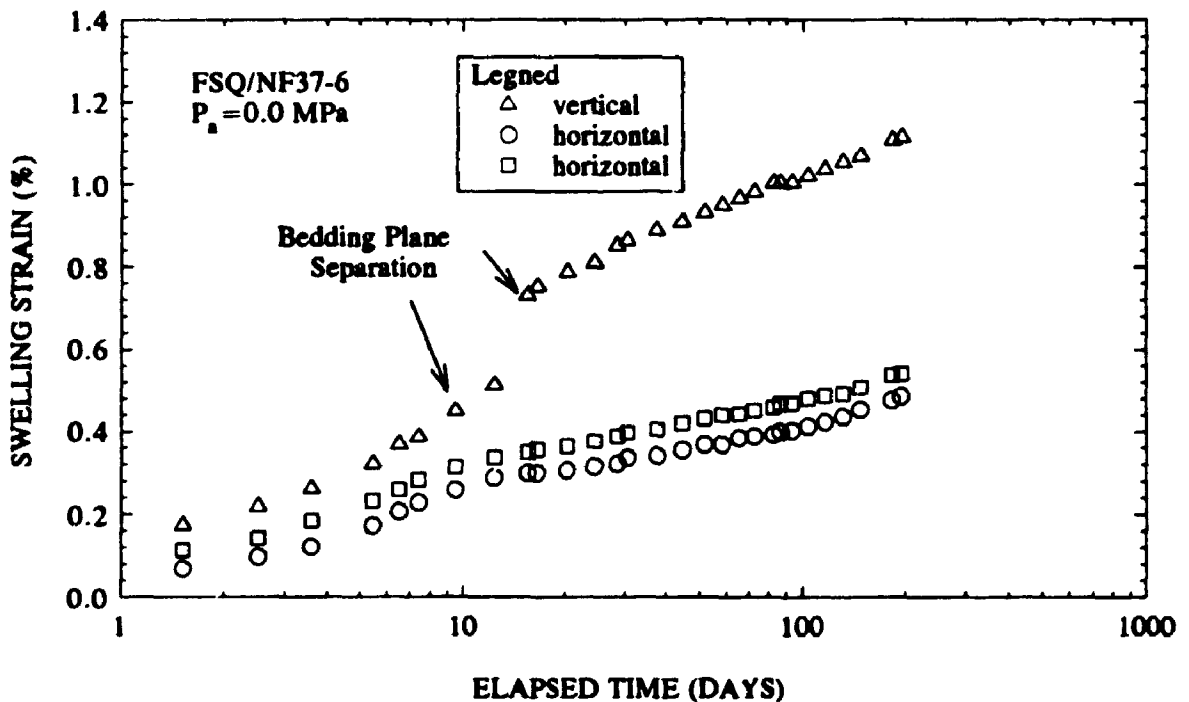
Figure 7A.25 Results of free swell tests on Queenston Shale at SABNGS No. 3 site
Test No. NF37-11 (1990 investigation)

Figure 7A.26 Results of semi-confined swell tests on Queenston Shale at SABNGS
No. 3 site. Test No. NF4A-H1 (1990 investigation)

Figure 7A.27 Results of semi-confined swell tests on Queenston Shale at SABNGS
No. 3 site. Test No. NF4A-H2 (1990 investigation)

Figure 7A.28 Results of semic-confined swell tests on Queenston Shale at SABNGS
No. 3 site. Test No. NF4A-H3 (1990 investigation)
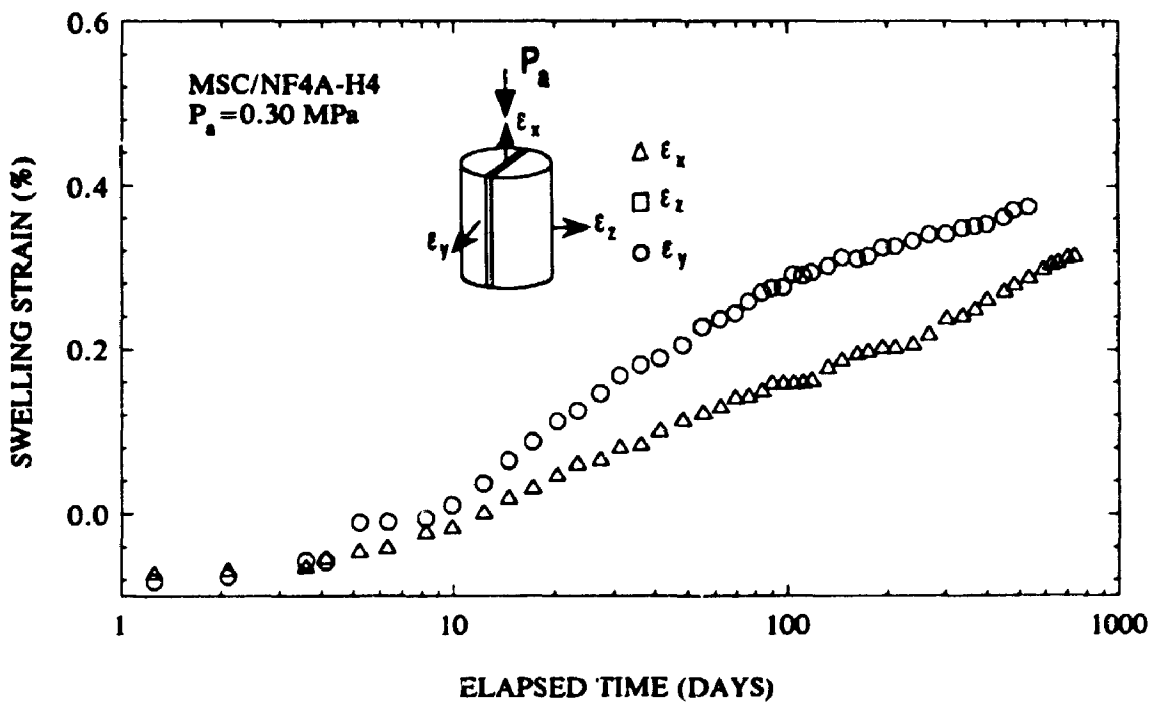
Figure 7A.29 Results of semi-confined swell tests on Queenston Shale at SABNGS
No. 3 site. Test No. NF4A-H4 (1990 investigation)
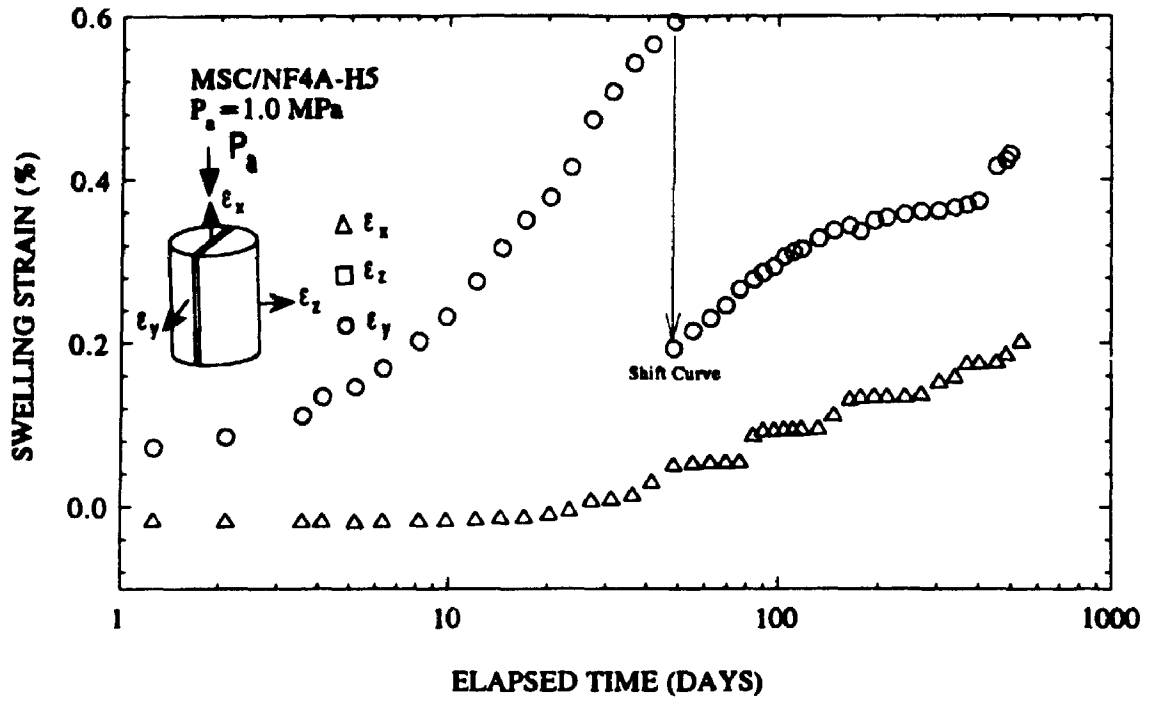
Figure 7A.30 Results of semi-confined swell tests on Queenston Shale at SABNGS
No. 3 site. Test No. NF4A-H5 (1990 investigation)
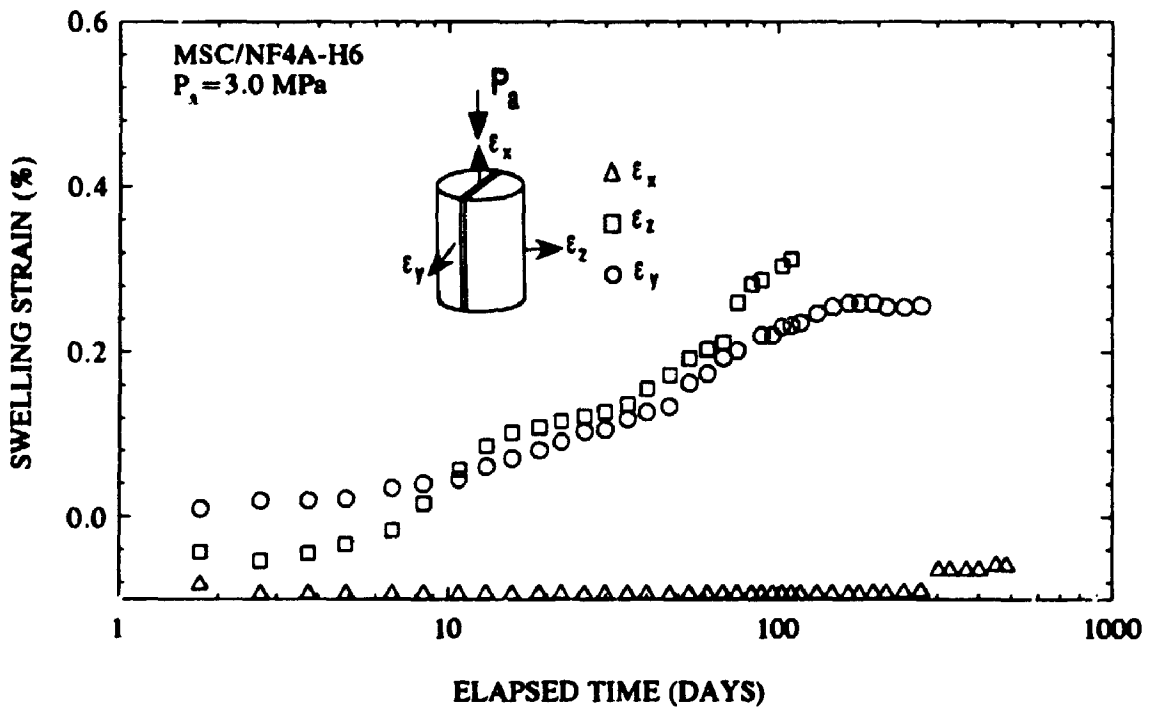
Figure 7A.31 Results of semic-confined swell tests on Queenston Shale at SABNGS
No. 3 site. Test No. NF4A-H6 (1990 investigation)
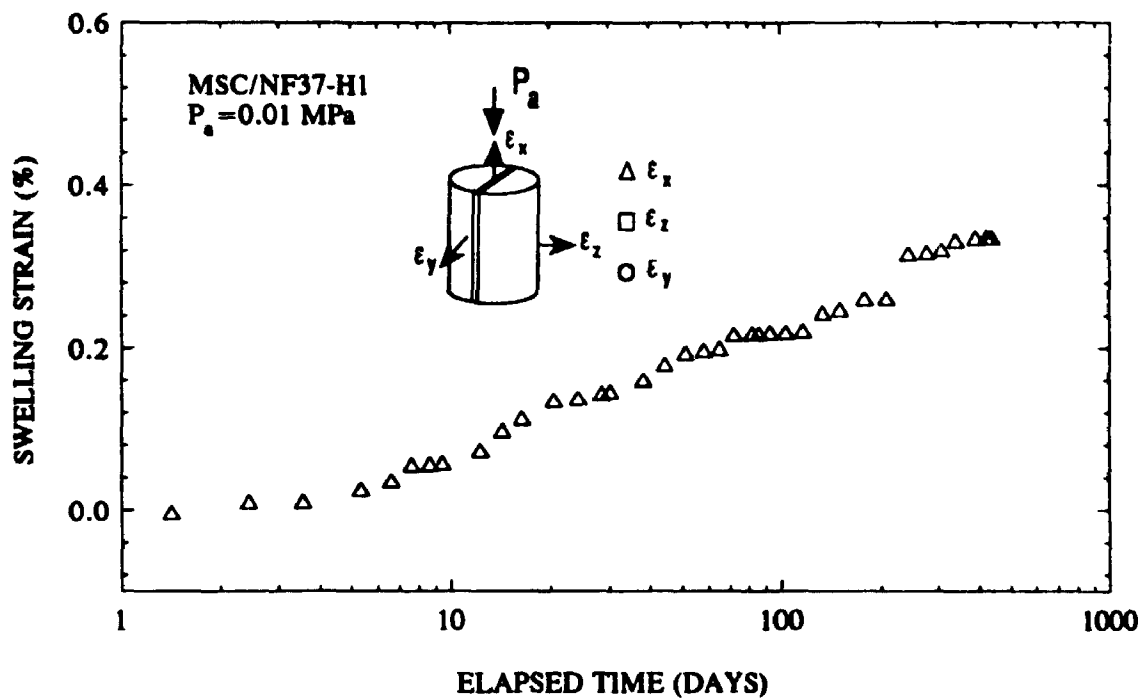
Figure 7A.32 Results of semi-confined swell tests on Queenston Shale at SABNGS
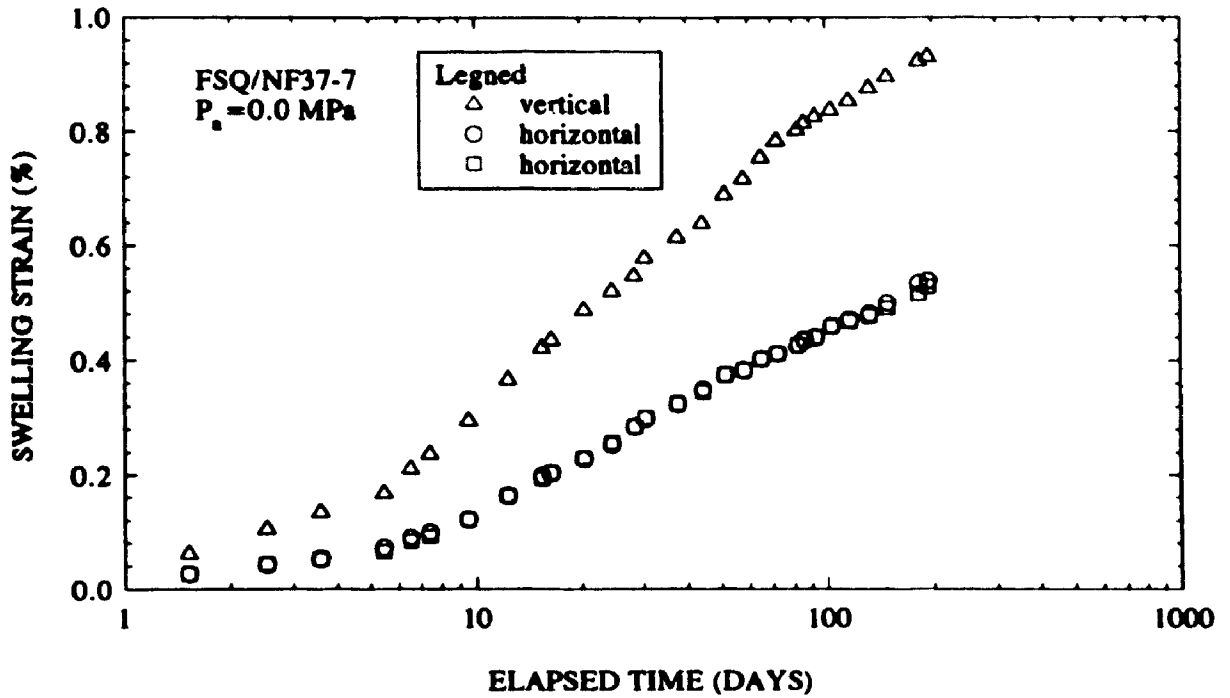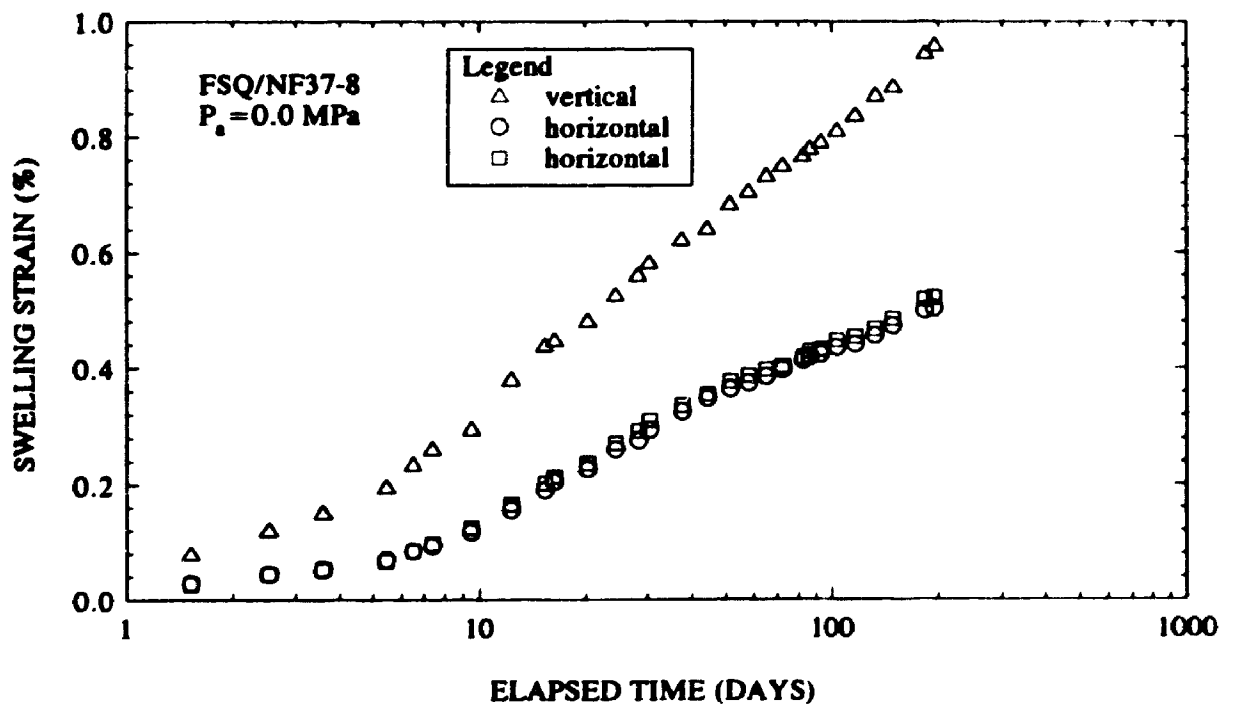No. 3 site. Test No. NF37-H1 (1990 investigation)
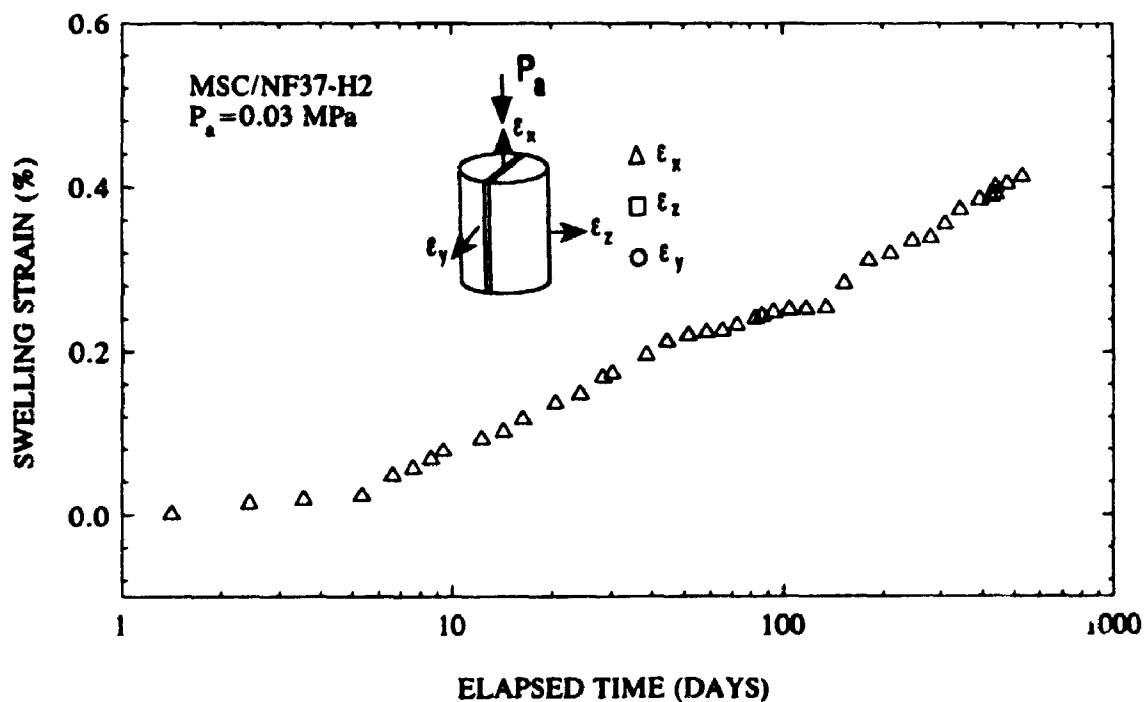
Figure 7A.33 Results of semi-confined swell tests on Queenston Shale at SABNGS
No. 3 site. Test No. NF37-H2 (1990 investigation)
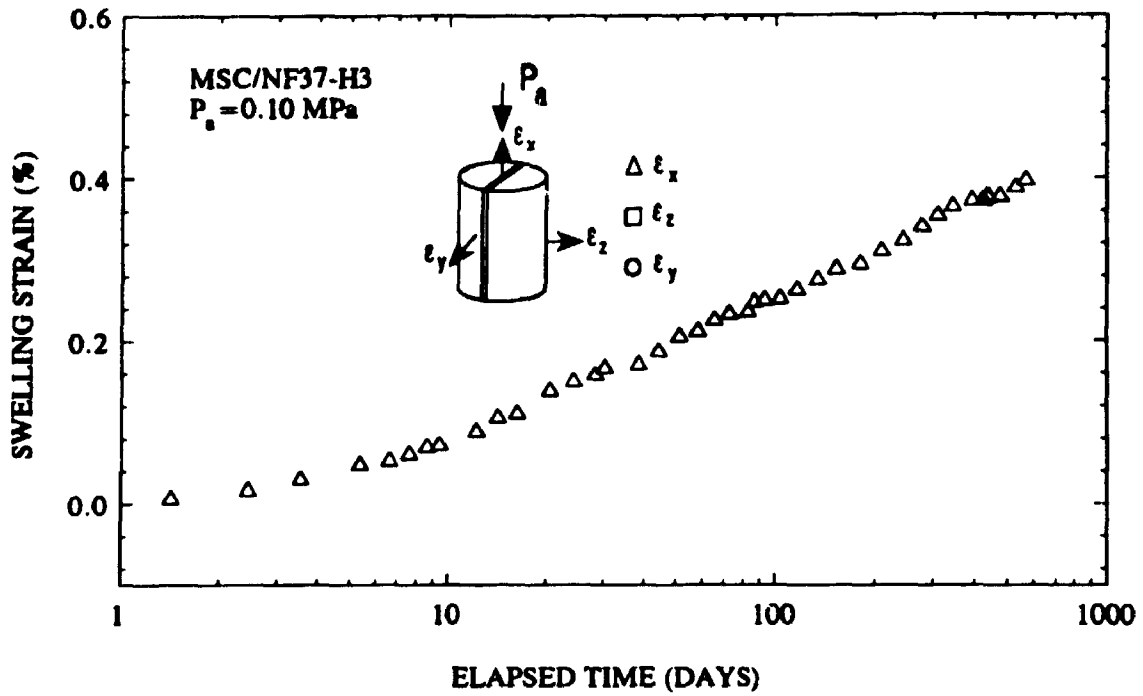
Figure 7A.34 Results of semi-confined swell tests on Queenston Shale at SABNGS
No. 3 site. Test No. NF37-H3 (1990 investigation)
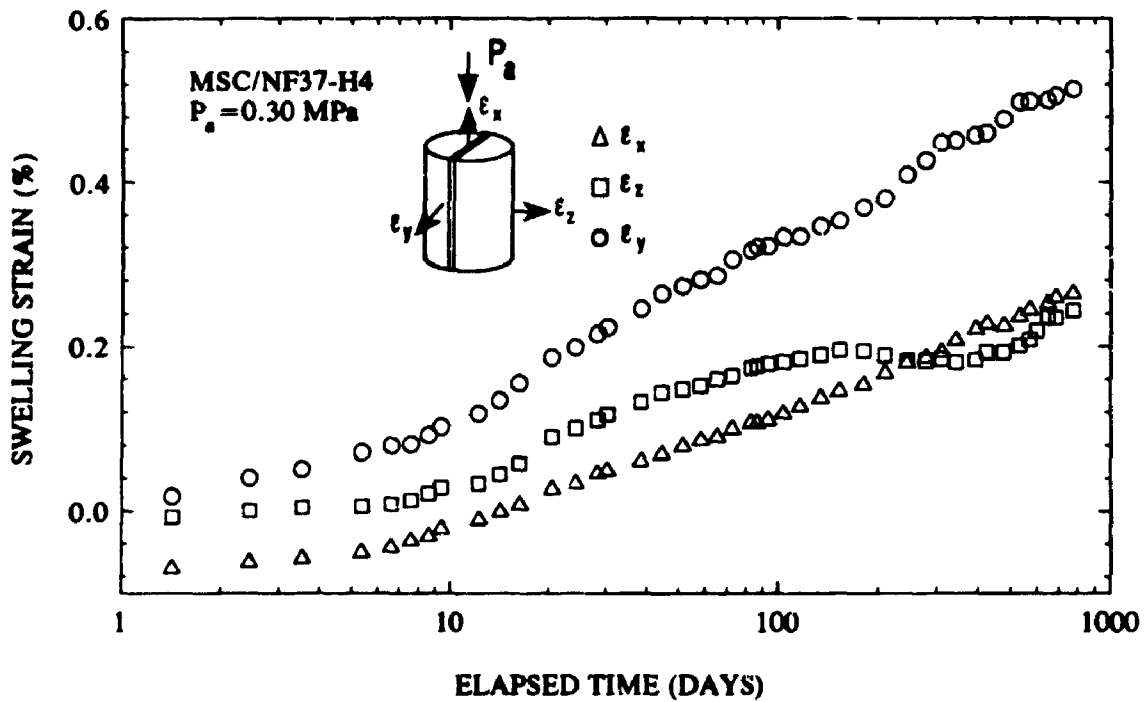
Figure 7A.35 Results of semi-confined swell tests on Queenston Shale at SABNGS
No. 3 site. Test No. NF37-H4 (1990 investigation)
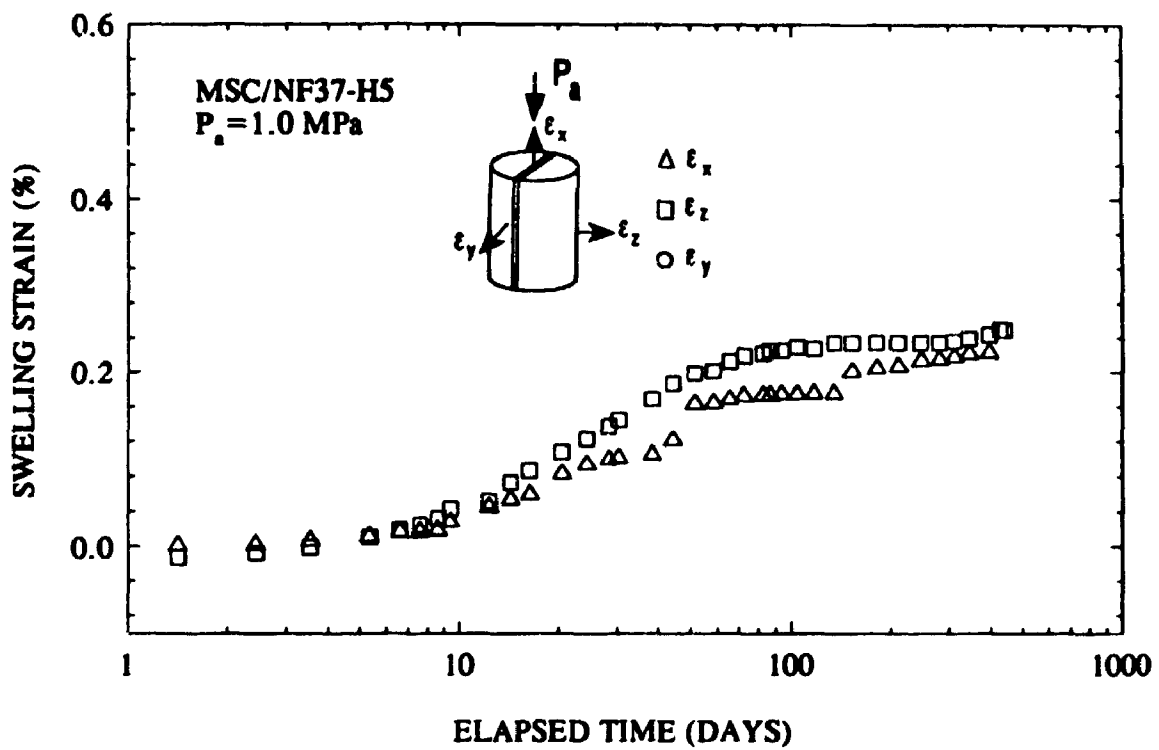
Figure 7A.36 Results of semi-confined swell tests on Queenston Shale at SABNGS
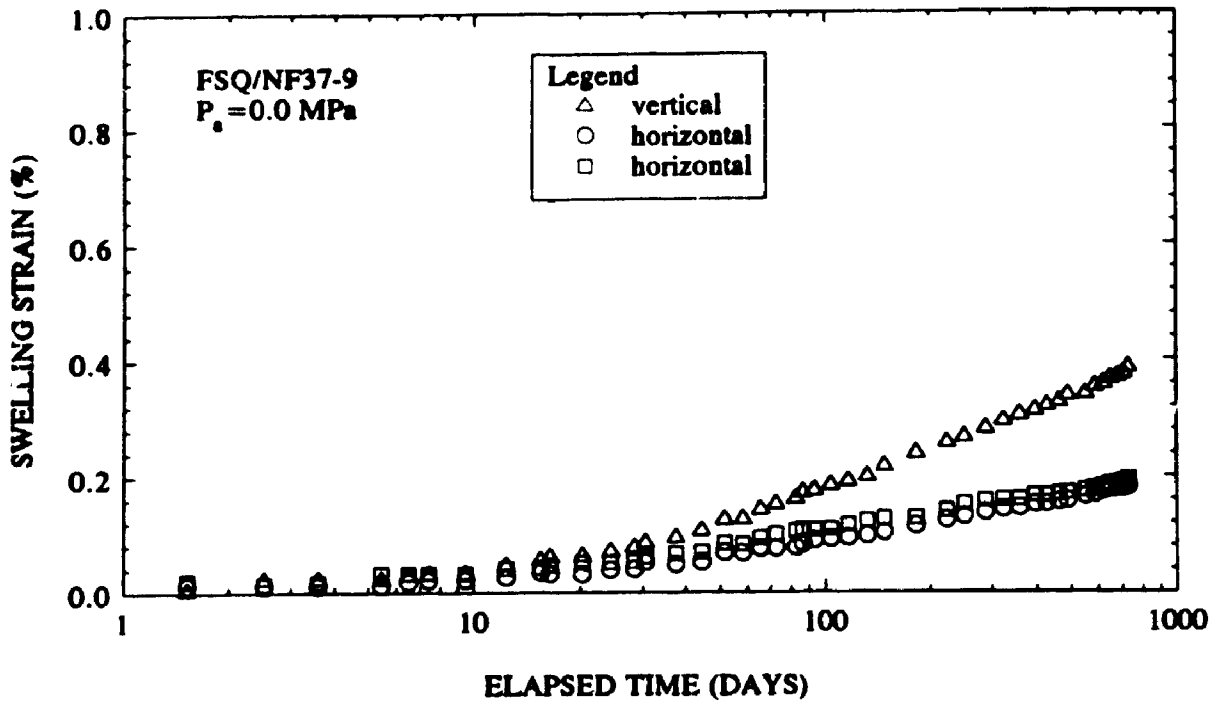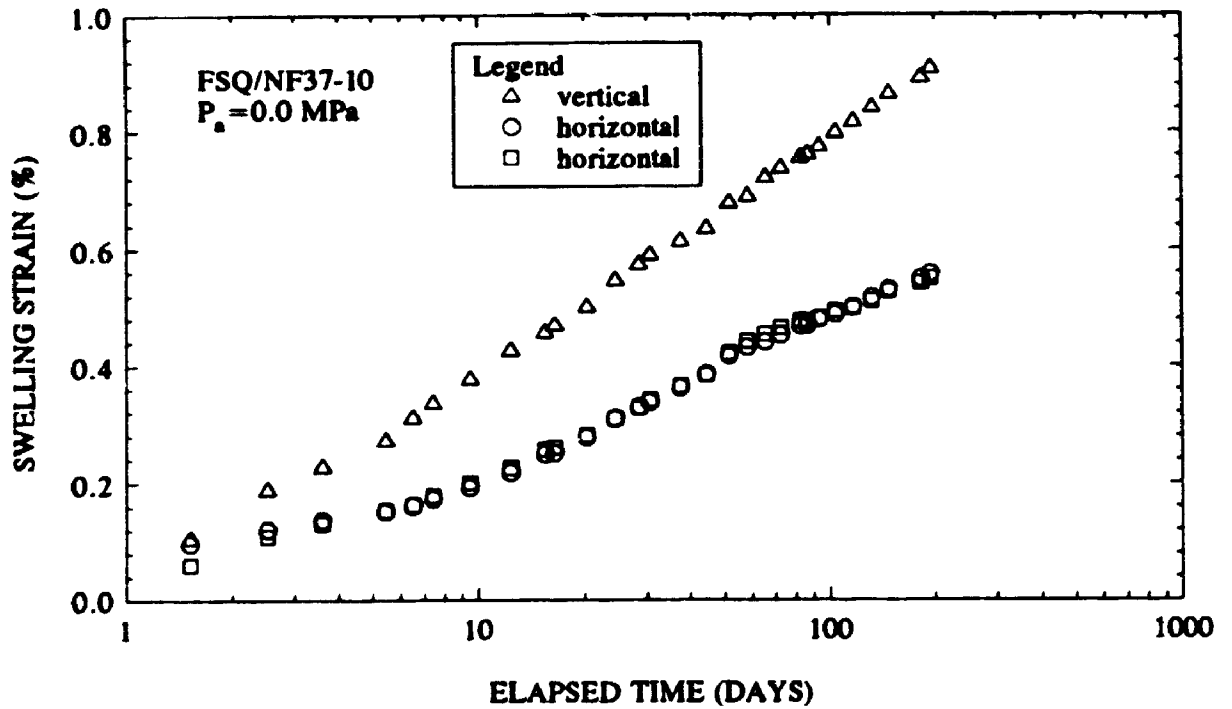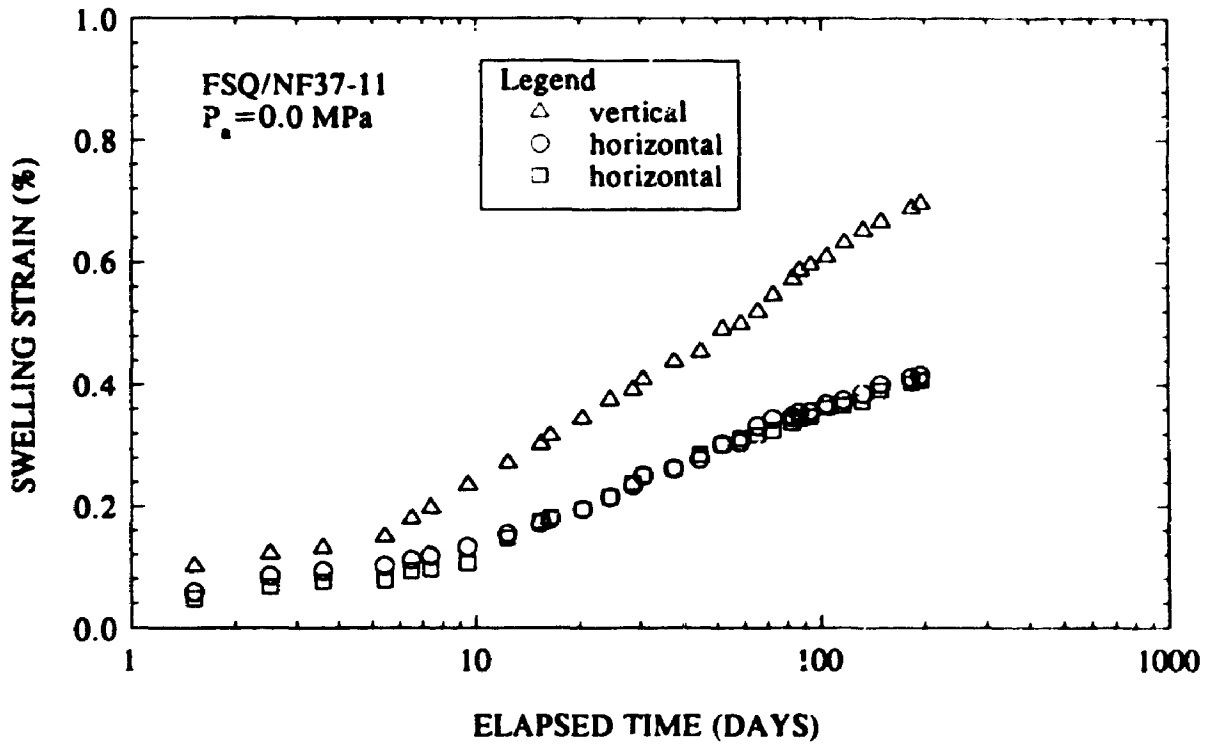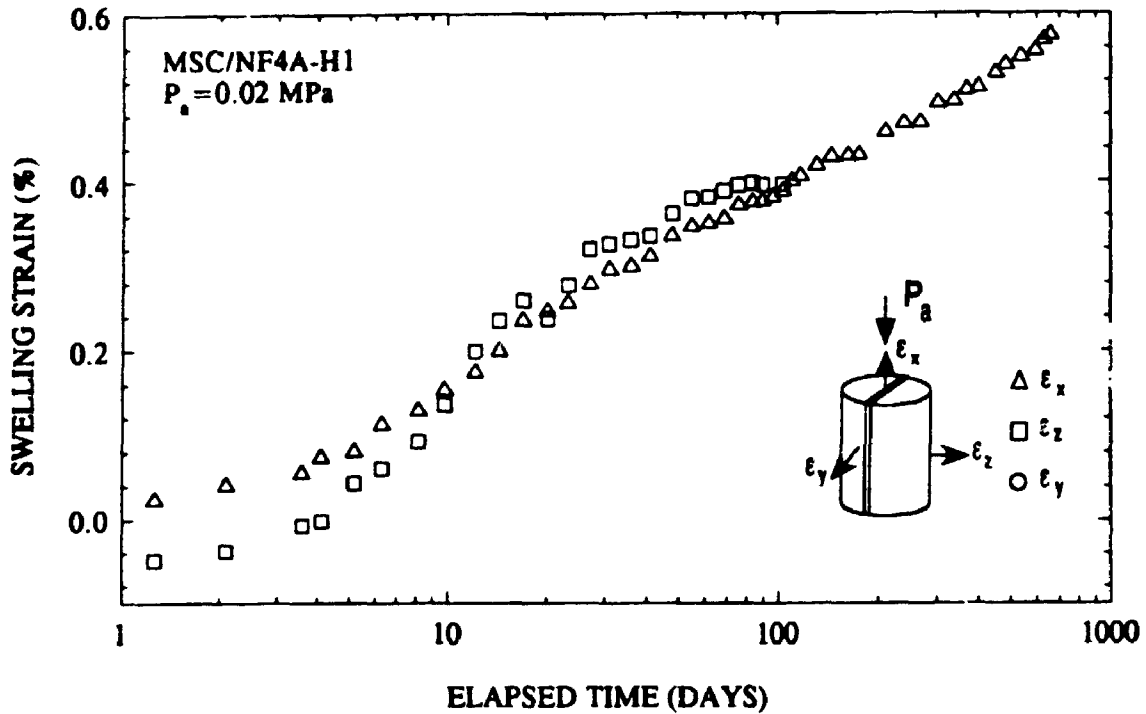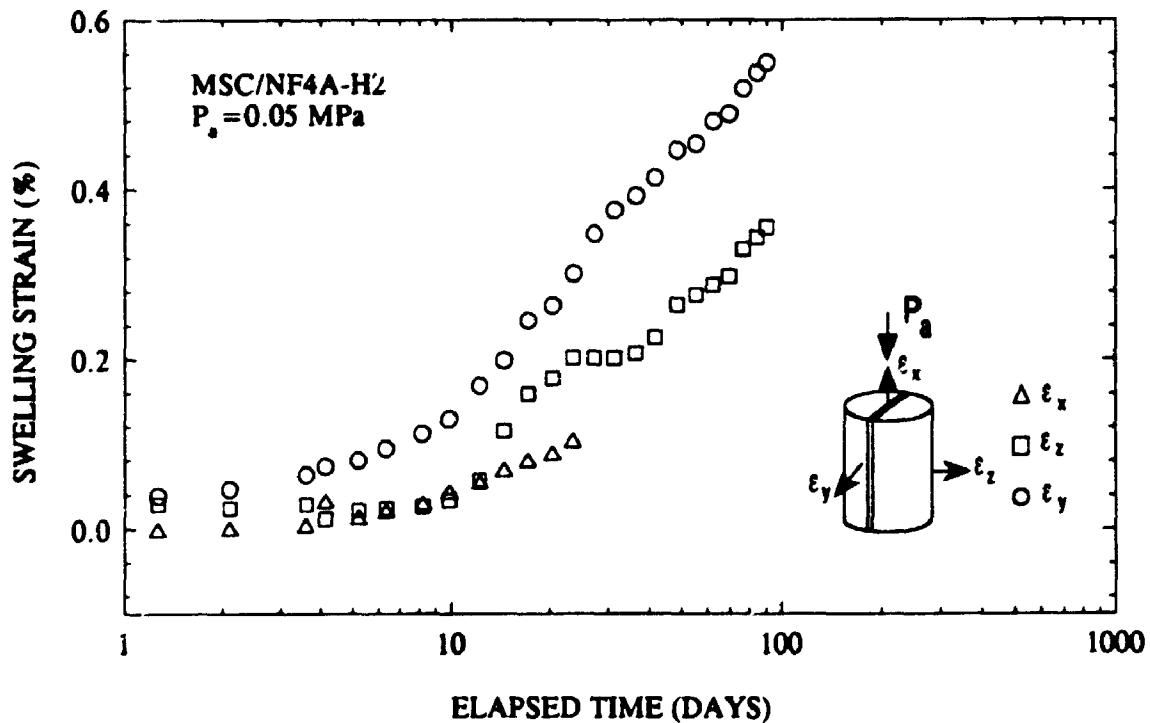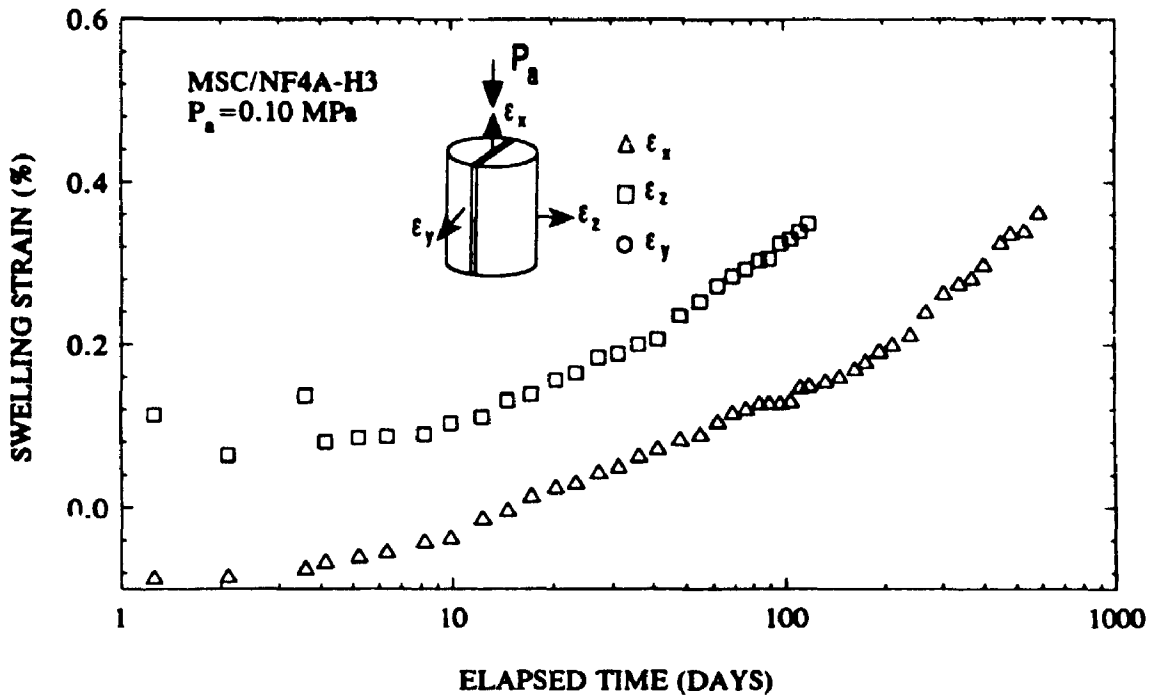No. 3 site. Test No. NF37-H5 (1990 investigation)

APPENDIX 9A

DIFFERENTIAL FORM OF CONSTITUTIVE EQUATIONS
OF VISCOELASTIC MATERIAL
AND THE CORRESPONDENCE PRINCIPLE

APPENDIX 9A

DIFFERENTIAL FORM OF CONSTITUTIVE EQUATIONS

OF VISCOELASTIC MATERIAL

AND THE CORRESPONDENCE PRINCIPLE

9A.1 UNIAXIAL STRESS

(i) Case of a 3-Element Kelvin Model

Consider the simple system shown in Fig. 9A.1 for a spring and a Kelvin unit in series under the action of a uniaxial stress σ. The spring represents the instantaneous elastic strain component (ϵ_e) of the system under σ, and the Kelvin unit represents the time dependent component of strain (ϵ_t). At any time, the total strain of the system is

$$\epsilon = \epsilon_e + \epsilon_t \tag{9A.1}$$

The stress-strain relationship for the elastic component is

$$\sigma = E\epsilon_e \tag{9A.2}$$

and for the time-dependent component is

$$\sigma = E_t\epsilon_t + \eta\dot{\epsilon}_t \tag{9A.3}$$

where E is the elastic modulus

E_t is the modulus of the spring in the Kelvin unit

η is the viscosity of the dashpot in the Kelvin unit

The dot represents derivative with respect to time.

The Laplace transform of any function of time, $f(t)$, is defined as

$$\mathcal{L}\{(f(t)\} = \bar{f}(s) = \int_0^\infty f(t)e^{-st}dt$$

where the bar is an indication that the function has been transformed and it is a function

of the variable s instead of time t.

The application of Laplace transform on both sides of Eqs. 9A.2 and 9A.3

respectively yields

$$\bar{\sigma} = E\bar{\epsilon}_e \tag{9A.4}$$

and

$$\bar{\sigma} = (E_t + \eta s)\bar{\epsilon}_t \tag{9A.5}$$

Multiplying Eq. 9A.4 by $(E_t + \eta s)$ and Eq. 9A.5 by E and adding, the following

equation which relates the transformed applied stress $\bar{\sigma}$ to the transformed total strain $\bar{\epsilon}$

is obtained:

$$(E + E_t + \eta s)\bar{\sigma} = E(E_t + \eta s)\bar{\epsilon} \tag{9A.6}$$

where $\bar{\epsilon} = \bar{\epsilon}_e + \bar{\epsilon}_t$

Transforming back Eq. 9A.6 to the time space yields the following equation:

$$(E + E_t)\sigma + \eta\dot{\sigma} = EE_t\epsilon + E\eta\dot{\epsilon} \tag{9A.7}$$

which can be written in the following form:

$$p_o \sigma + p_1 \dot{\sigma} = q_o \epsilon + q_1 \dot{\epsilon} \qquad (9A.8)$$

where

$$p_o = 1 \qquad p_1 = \frac{\eta}{E + E_t} \qquad (9A.9)$$

$$q_o = \frac{E E_t}{E + E_t} \qquad q_1 = \frac{E \eta}{E + E_t} \qquad (9A.10)$$

Equation 9A.8 is the differential form of the constitutive relationship of the 3-element Kelvin model shown in Fig. 9A.1. This model is used to idealize the time-dependent deformation of the concrete lining of the circular tunnel analyzed in Chapter 10.

(ii) Case of a 7-Element Kelvin Model

Consider the system shown in Fig. 9A.2 for a spring and three Kelvin units (7-element Kelvin model) connected in series under the action of a uniaxial stress σ. The stress-strain relationship for the spring (elastic component) is

$$\sigma = E \epsilon_e \qquad (9A.11)$$

and the stress-strain relationships for the three Kelvin units respectively are

$$\sigma = E_{t1} \epsilon_{t1} + \eta_1 \dot{\epsilon}_{t1} \qquad (9A.12)$$

$$\sigma = E_{t2} \epsilon_{t2} + \eta_2 \dot{\epsilon}_{t2} \qquad (9A.13)$$

$$\sigma = E_{t3} \epsilon_{t3} + \eta_3 \dot{\epsilon}_{t3} \qquad (9A.14)$$

where E_{tk} = modulus of the spring in the kth Kelvin unit

ϵ_{tk} = component of strain of the time-dependent phase resulting from the

kth Kelvin unit

η_k = viscosity of the dashpot in the kth Kelvin unit

The application of Laplace transform on both sides of Eqs. 9A.11 to 9A.14 respectively yields

$$\bar{\sigma} = E\bar{\epsilon}_e \qquad (9A.15)$$

$$\bar{\sigma} = E_{t1}\bar{\epsilon}_{t1} + \eta_1\bar{\epsilon}_{t1}s = (E_{t1} + \eta_1 s)\bar{\epsilon}_{t1} \qquad (9A.16)$$

$$\bar{\sigma} = E_{t2}\bar{\epsilon}_{t2} + \eta_2\bar{\epsilon}_{t2}s = (E_{t2} + \eta_2 s)\bar{\epsilon}_{t2} \qquad (9A.17)$$

$$\bar{\sigma} = E_{t3}\bar{\epsilon}_{t3} + \eta_3\bar{\epsilon}_{t3}s = (E_{t3} + \eta_3 s)\bar{\epsilon}_{t3} \qquad (9A.18)$$

Multiplying Eq. 9A.15 by $(E_{t1}+\eta_1 s)(E_{t2}+\eta_2 s)(E_{t3}+\eta_3 s)$, Eq. 9A.16 by $E(E_{t2}+\eta_2 s)(E_{t3}+\eta_3 s)$, Eq. 9A.17 by $E(E_{t1}+\eta_1 s)(E_{t3}+\eta_3 s)$, and Eq. 9A.8 by $E(E_{t1}+\eta_1 s)(E_{t2}+\eta_2 s)$ and after adding and arrangement, the following equation which relates the transformed applied stress $\bar{\sigma}$ to the transformed total strain $\bar{\epsilon}$ is obtained:

$$L = R \qquad (9A.19)$$

where

$$L = (E_{t1}E_{t2}E_{t3} + EE_{t2}E_{t3} + EE_{t1}E_{t2})\bar{\sigma} + (E_{t1}E_{t2}\eta_3 + E_{t1}E_{t2}\eta_2$$
$$+ E_{t2}E_{t3}\eta_1 + EE_{t2}\eta_3 + EE_{t3}\eta_2 + EE_{t1}\eta_3 + EE_{t3}\eta_1 + EE_{t1}\eta_2$$
$$+ EE_{t2}\eta_1)s\bar{\sigma} + (E_{t1}\eta_2\eta_3 + E_{t2}\eta_1\eta_3 + E_{t3}\eta_1\eta_2 + E\eta_2\eta_3$$
$$+ E\eta_1\eta_3 + E\eta_1\eta_2)s^2\bar{\sigma} + (\eta_1\eta_2\eta_3)s^3\bar{\sigma} \tag{9A.20}$$

and

$$R = EE_{t1}E_{t2}E_{t3}\bar{\epsilon} + (EE_{t1}E_{t2}\eta_3 + EE_{t1}E_{t3}\eta_2 + EE_{t2}E_{t3}\eta_1)s\bar{\epsilon}$$
$$+ (EE_{t1}\eta_2\eta_3 + EE_{t2}\eta_1\eta_3 + EE_{t3}\eta_1\eta_2)s^2\bar{\epsilon} + (E\eta_1\eta_2\eta_3)s^3\bar{\epsilon} \tag{9A.21}$$

$$\bar{\epsilon} = \bar{\epsilon}_e + \bar{\epsilon}_{t1} + \bar{\epsilon}_{t2} + \bar{\epsilon}_{t3}$$

Transforming back Eq. 9A.19 to the time space yields the following differential form of the constitutive relationship of the 7-element Kelvin model (a spring and three Kelvin units connected in series) shown in Fig. 9A.2:

$$p_o\sigma + p_1\dot{\sigma} + p_2\ddot{\sigma} + p_3\dddot{\sigma} = q_o\epsilon + q_1\dot{\epsilon} + q_2\ddot{\epsilon} + q_3\dddot{\epsilon} \tag{9A.22}$$

where

$$p_o = 1 \tag{9A.23}$$

$$p_1 = (E_{t1}E_{t2}\eta_3 + E_{t1}E_{t3}\eta_2 + E_{t2}E_{t3}\eta_1 + EE_{t2}\eta_3 + EE_{t3}\eta_2$$
$$+ EE_{t1}\eta_3 + EE_{t3}\eta_1 + EE_{t1}\eta_2 + EE_{t2}\eta_1)$$
$$/ (E_{t1}E_{t2}E_{t3} + EE_{t2}E_{t3} + EE_{t1}E_{t3} + EE_{t1}E_{t2}) \tag{9A.24}$$

$$p_2 = \frac{E_{t1}\eta_2\eta_3 + E_{t2}\eta_1\eta_3 + E_{t3}\eta_1\eta_2 + E\eta_2\eta_3 + E\eta_1\eta_3 + E\eta_1\eta_2}{E_{t1}E_{t2}E_{t3} + EE_{t2}E_{t3} + EE_{t1}E_{t3} + EE_{t1}E_{t2}} \tag{9A.25}$$

$$p_3 = \frac{\eta_1\eta_2\eta_3}{E_{t1}E_{t2}E_{t3} + EE_{t2}E_{t3} + EE_{t1}E_{t3} + EE_{t1}E_{t2}} \tag{9A.26}$$

$$q_o = \frac{E E_{t1} E_{t2} E_{t3}}{E_{t1} E_{t2} E_{t3} + E E_{t2} E_{t3} + E E_{t1} E_{t3} + E E_{t1} E_{t2}} \tag{9A.27}$$

$$q_1 = \frac{E E_{t1} E_{t2} \eta_3 + E E_{t1} E_{t3} \eta_2 + E E_{t2} E_{t3} \eta_1}{E_{t1} E_{t2} E_{t3} + E E_{t2} E_{t3} + E E_{t1} E_{t3} + E E_{t1} E_{t2}} \tag{9A.28}$$

$$q_2 = \frac{E E_{t1} \eta_2 \eta_3 + E E_{t2} \eta_1 \eta_3 + E E_{t3} \eta_1 \eta_2}{E_{t1} E_{t2} E_{t3} + E E_{t2} E_{t3} + E E_{t1} E_{t3} + E E_{t1} E_{t2}} \tag{9A.29}$$

$$q_3 = \frac{E \eta_1 \eta_2 \eta_3}{E_{t1} E_{t2} E_{t3} + E \bar{E}_{t2} E_{t3} + E E_{t1} E_{t3} + E E_{t1} E_{t2}} \tag{9A.30}$$

This model is used to idealize the time-dependent deformation of the rock material in the design of the circular tunnels analyzed in Chapters 9 and 10.

(iii)   Case of a General Multi-Element Kelvin Model

In general, the differential form of the constitutive relationships for a multi-element Kelvin model can be written as

$$\sigma + p_1 \dot{\sigma} + p_2 \ddot{\sigma} + \dots = q_o \epsilon + q_1 \dot{\epsilon} + q_2 \ddot{\epsilon} + \dots \tag{9A.31}$$

Eq. 9A.31 is commonly written in the following more compact form:

$$P \sigma = Q \epsilon \tag{9A.32}$$

where P and Q are linear differential operators with respect to time:

$$P = p_o + p_1\frac{\partial}{\partial t} + p_2\frac{\partial^2}{\partial t^2} + p_3\frac{\partial^3}{\partial t^3} + \ldots\ldots + p_m\frac{\partial^m}{\partial t^m} \qquad (9A.33)$$

$$P = \sum_{k=0}^{m} p_k \frac{\partial^k}{\partial t^k} \qquad (9A.34)$$

$$Q = q_o + q_1\frac{\partial}{\partial t} + q_2\frac{\partial^2}{\partial t^2} + q_3\frac{\partial^3}{\partial t^3} + \ldots\ldots + q_n\frac{\partial^n}{\partial t^n} \qquad (9A.35)$$

$$Q = \sum_{k=0}^{n} p_k \frac{\partial^k}{\partial t^k} \qquad (9A.36)$$

For a model of a spring and r Kelvin units, $m = n = r$. For example, the model in Fig. 9A.1 consists of a spring and one Kelvin unit, therefore, $m - n = 1$, and only p_o, p_1, q_o, and q_1 appear (refer to Eqs. 9A.8 and 9A.32 to 9A.36).

As another example, the model in Fig. 9A.2 consists of a spring and three Kelvin units, therefore, $m = n = 3$ and only p_o, p_1, p_2, p_3, q_o, q_1, q_2, and q_3 appear (refer to Eqs. 9A.22 and 9A.32 to 9A.36).

Taking Laplace transform for Eq. 9A.32 for zero initial conditions, the following algebraic relationship between the Laplace transforms $\bar{\sigma}(s)$ and $\bar{\epsilon}(s)$ of stress and strain is obtained:

$$\bar{P}(s)\bar{\sigma}(s) = \bar{Q}(s)\bar{\epsilon}(s) \qquad (9A.37)$$

where

$$\bar{P}(s) = p_o + p_1 s + p_2 s^2 + \ldots = \sum_{k=0}^{n} p_k s^k \tag{9A.38}$$

$$\bar{Q}(s) = q_o + q_1 s + q_2 s^2 + \ldots = \sum_{k=0}^{n} q_k s^k \tag{9A.39}$$

s is the transform variable.

Equation 9A.37 represents the constitutive relationship for multi-element Kelvin model in the Laplace space.

9A.2 MULTIAXIAL STRESS STATE

The differential form of the constitutive equation for linear viscoelastic material under uniaxial stress (Eq. 9A.32) can be generalized to the case of linear viscoelastic material under multiaxial stress-multiaxial strain states. Consider the stress tensor σ_{ij} which can be written in the following matrix form:

$$\sigma_{ij} = \begin{vmatrix} \sigma_{11} & \sigma_{12} & \sigma_{13} \\ \sigma_{21} & \sigma_{22} & \sigma_{23} \\ \sigma_{31} & \sigma_{32} & \sigma_{33} \end{vmatrix} = \begin{vmatrix} \sigma_x & \sigma_{xy} & \sigma_{xz} \\ \sigma_{yx} & \sigma_y & \sigma_{yz} \\ \sigma_{zx} & \sigma_{zy} & \sigma_z \end{vmatrix} \tag{9A.40}$$

with shear stresses $\sigma_{xy} = \sigma_{yx}$, $\sigma_{xz} = \sigma_{zx}$, and $\sigma_{yz} = \sigma_{zy}$; or simply $\sigma_{ij} = \sigma_{ji}$. It is convenient in multiaxial stress states to separate the stress tensor σ_{ij} into two components: the hydrostatic (dilatational), $\sigma_v \delta_{ij}$, and the deviatoric (distortional), S_{ij}, components:

$$\sigma_{ij} = \sigma_v \delta_{ij} + S_{ij} \qquad \text{(9A.41)}$$

$$\begin{vmatrix} \sigma_x & \sigma_{xy} & \sigma_{xz} \\ \sigma_{xy} & \sigma_y & \sigma_{yz} \\ \sigma_{xz} & \sigma_{yz} & \sigma_z \end{vmatrix} = \begin{vmatrix} \sigma_v & 0 & 0 \\ 0 & \sigma_v & 0 \\ 0 & 0 & \sigma_v \end{vmatrix} + \begin{vmatrix} S_x & S_{xy} & S_{xz} \\ S_{xy} & S_y & S_{yz} \\ S_{xz} & S_{yz} & S_z \end{vmatrix} \qquad \text{(9A.42)}$$

where σ_v = the average normal stress

$$= \frac{\sigma_x + \sigma_y + \sigma_z}{3}$$

δ_{ij} = Kronecker delta

= 1 when $\quad i = j$

= 0 when $\quad i \neq j$

$\sigma_x \quad = \sigma_v + S_x$

$\sigma_y \quad = \sigma_v + S_y$

$\sigma_z \quad = \sigma_v + S_z$

$S_x + S_y + S_z = 0$

Similarly, the strain tensor ϵ_{ij} can be separated into hydrostatic, $\epsilon_v \delta_{ij}$, and deviatoric, e_{ij}, components:

$$\epsilon_{ij} = \epsilon_v \delta_{ij} + e_{ij} \qquad \text{(9A.43)}$$

$$\begin{vmatrix} \epsilon_x & \epsilon_{xy} & \epsilon_{xz} \\ \epsilon_{xy} & \epsilon_y & \epsilon_{yz} \\ \epsilon_{xy} & \epsilon_{yz} & \epsilon_z \end{vmatrix} = \begin{vmatrix} \epsilon_v & 0 & 0 \\ 0 & \epsilon_v & 0 \\ 0 & 0 & \epsilon_v \end{vmatrix} + \begin{vmatrix} e_x & e_{xy} & e_{xz} \\ e_{xy} & e_y & e_{yz} \\ e_{xz} & e_{yz} & e_z \end{vmatrix}$$

(9A.44)

where ϵ_v = the average normal strain

$$= \frac{\epsilon_x + \epsilon_y + \epsilon_z}{3}$$

$$\epsilon_x = \epsilon_v + e_x$$

$$\epsilon_y = \epsilon_v + e_y$$

$$\epsilon_z = \epsilon_v + e_z$$

$$e_x + e_y + e_z = 0$$

Analogous to Eq. 9A.32, the constitutive equations for isotropic linear viscoelastic materials under multiaxial stress states can take the following forms:

for deviatoric component

$$P' S_{ij} = Q' e_{ij}$$

(9A.45)

and for hydrostatic component

$$P'' \sigma_v = Q'' \epsilon_v$$

(9A.46)

where P', Q', P'', and Q'' are differential operators in time and defined as

$$P' = p_o' + p_1' \frac{\partial}{\partial t} + p_2' \frac{\partial^2}{\partial t^2} + \ldots$$

(9A.47)

$$Q' = q_o' + q_1' \frac{\partial}{\partial t} + q_2' \frac{\partial^2}{\partial t^2} + \dots \qquad \text{(9A.48)}$$

$$P'' = p_o'' + p_1'' \frac{\partial}{\partial t} + p_2'' \frac{\partial^2}{\partial t^2} + \dots \qquad \text{(9A.49)}$$

$$Q'' = q_o'' + q_1'' \frac{\partial}{\partial t} + q_2'' \frac{\partial^2}{\partial t^2} + \dots \qquad \text{(9A.50)}$$

9A.3 CORRESPONDENCE PRINCIPLE

For elastic bodies under constant load, nothing depends on time and the constitutive relationships take the following form:

$$\sigma_v = 3K\epsilon_v \qquad \text{(9A.51)}$$

$$S_{ij} = 2Ge_{ij} \qquad \text{(9A.52)}$$

For viscoelastic bodies, all the stresses, strains and displacements are time dependent and the constitutive relationships are given by Eqs. 9A.45 and 9A.46

$$P' S_{ij} = Q' e_{ij} \qquad \text{(9A.53)}$$

$$P'' \sigma_v = Q'' \epsilon_v \qquad \text{(9A.54)}$$

where P', Q', P'', and Q'' are time differential operators.

The Laplace transforms of Eqs. 9A.53 and 9A.54 respectively yield

$$\bar{P}'(s)\,\bar{S}_{ij}(s) = \bar{Q}'(s)\,\bar{e}_{ij}(s) \tag{9A.55}$$

$$\bar{P}''(s)\,\bar{\sigma}_v(s) = \bar{Q}''(s)\,\bar{\epsilon}_v(s) \tag{9A.56}$$

where $\bar{P}'(s)$, $\bar{Q}'(s)$, $\bar{P}''(s)$, and $\bar{Q}''(s)$ are now polynomials in (s) and $\bar{\sigma}_v$, $\bar{\epsilon}_v$, $\bar{S}_{ij}$, and $\bar{e}_{ij}$

are transforms of σ_v, ϵ_v, S_{ij}, and e_{ij} respectively. Comparison of Eqs. 9A.55 and

9A.56 to Eqs. 9A.51 and 9A.52 shows that Eqs. 9A.55 and 9A.56 describe constitutive

relationships for fictitious elastic body in which the elastic parameters ($\dfrac{\bar{Q}(s)}{\bar{P}(s)}$ and

$\dfrac{\bar{Q}''(s)}{\bar{P}''(s)}$), the stresses ($\bar{\sigma}_v$ and $\bar{S}_{ij}$) and the strains ($\bar{\epsilon}_v$ and $\bar{e}_{ij}$) are functions of the

transform parameter s. For this fictitious elastic body, the correspondence relationships

are

$$2G \rightarrow \frac{\bar{Q}}{\bar{P}} \qquad 3K \rightarrow \frac{\bar{Q}'}{\bar{P}'} \tag{9A.57}$$

Since, $E = \dfrac{9KG}{3K+G}$ and $v = \dfrac{3K-2G}{2(3K+G)}$, the correspondence relationships for E and v

respectively are

$$E \rightarrow \frac{3\bar{Q}'\,\bar{Q}}{2\bar{P}'\,\bar{Q}' + \bar{P}''\,\bar{Q}} \tag{9A.58}$$

and

$$v \rightarrow \frac{\bar{P}\,\bar{Q}' - \bar{P}'\,\bar{Q}}{2\,\bar{P}\,\bar{Q} + \bar{P}'\,\bar{Q}} \tag{9A.59}$$

Therefore, if an elastic solution exists for a particular problem, the associated problem in linear viscoelasticity may be solved by using the principle of correspondence derived above. The procedure is as follows:

(a) replace the displacements and stresses by their Laplace transforms.

(b) replace the actual loads by their Laplace transforms.

(c) replace K, G, E and v in the elastic solution by the transformed operators given in Eqs. 9A.57 through 9A.59.

(d) inversion of the Laplace transforms will give the final viscoelastic solution.
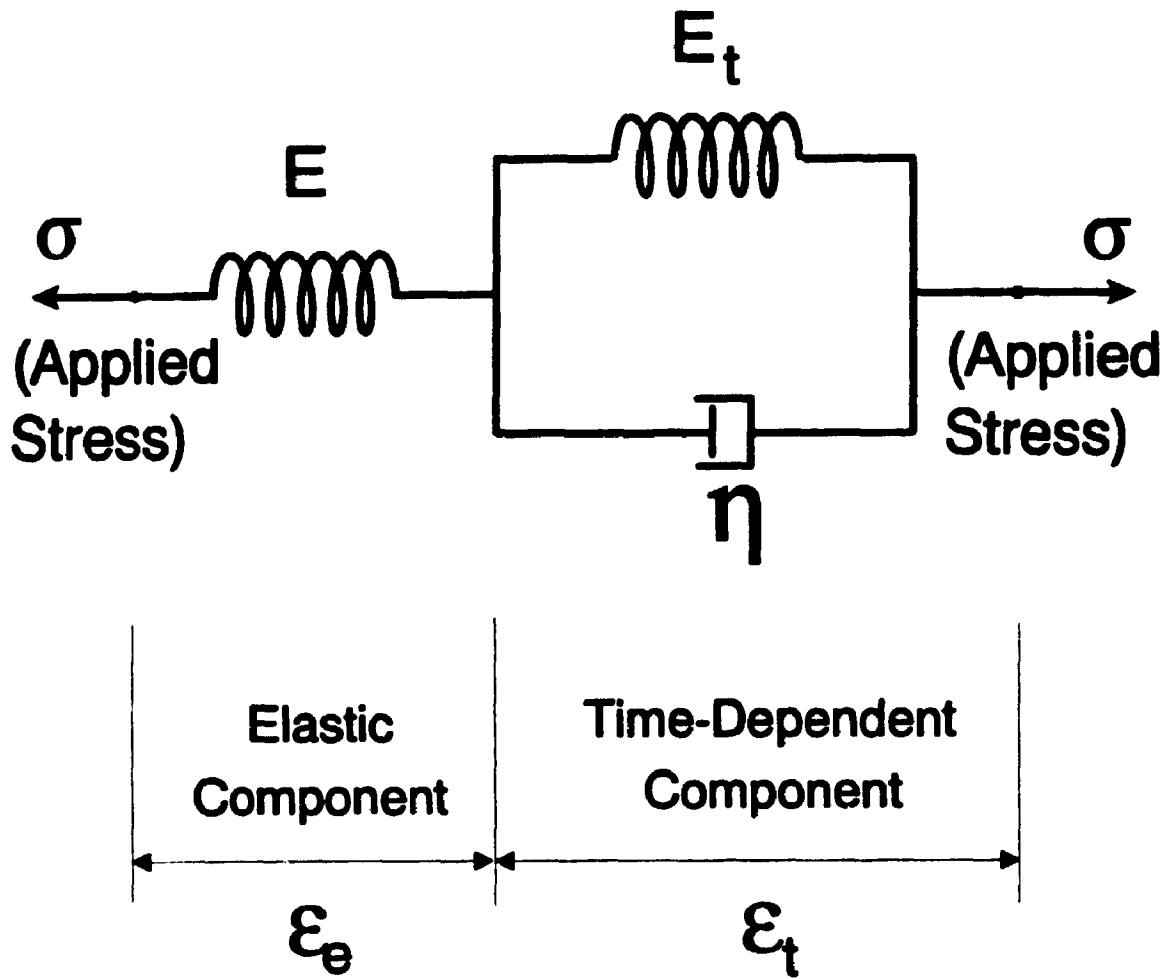
Figure 9A.1 3-Element Kelvin model (a spring and a Kelvin unit connected in series)
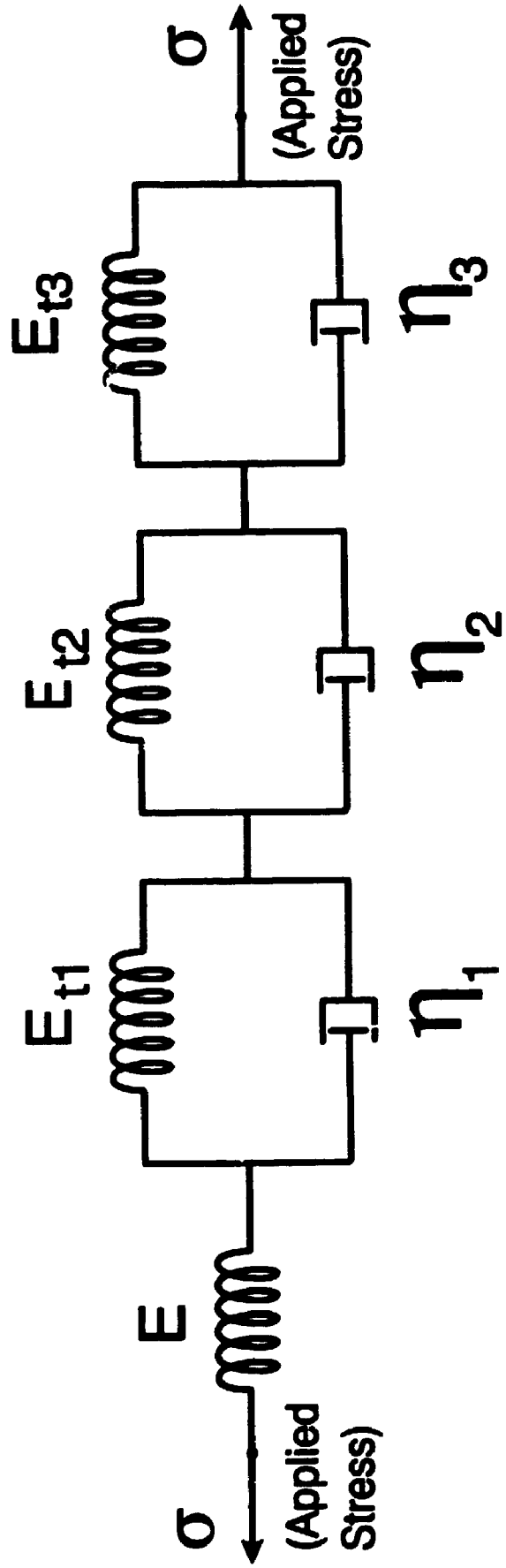
Figure 9A.2   7-Element Kelvin model (a spring and three Kelvin units connected in series)

APPENDIX 10A

EVALUATION OF THE RADIAL DEFORMATION
OF ROCK AND LINING DUE TO REACTIVE LINING PRESSURE
USING THE HEREDITARY INTEGRAL

APPENDIX 10A

EVALUATION OF THE RADIAL DEFORMATION

OF ROCK AND LINING DUE TO REACTIVE LINING PRESSURE

USING THE HEREDITARY INTEGRAL

The time function $J(t)$ derived in Chapter 9 and which relates the viscoelastic

displacement to the elastic displacement is suitable for use when the applied pressure is

maintained unchanged. If at time $t = 0$, the material is subjected to a sudden pressure

and at time $t = t_1$ an increment of pressure is added, the displacement at time $t > t_1$ can

be obtained by the law of linear superposition:

$$u(t) = u_{elastic} J(t) + \Delta u_{elastic} J(t - t_1) \qquad for \ t > t_1 \qquad (10A.1)$$

If the applied pressure is a continuous function of time, the hereditary integral, which

takes into account the history of the applied pressure up to the time of interest, should

be adopted (Flügge 1975).

The expression derived for the time-dependent lining pressure $P_i(t)$ under the

release of the initial hydrostatic stress component (Chapter 10) is

$$P_i(t') = P_{om} (1 - e^{-\alpha t'}) \qquad (10A.2)$$

The lining pressure $p_i(t')$ as expressed in Eq. 10A.2 is a monotonically increasing

function of time. Therefore, the radial displacement in the rock mass and the lining can

be obtained using the hereditary integral as follows.

Referring to Fig. 10A.1, the lining pressure diagram is broken into a sequence

of infinitesimal step functions. In the time step between t_1 to t, the pressure increment is (written in t domain)

$$dP_f(t_1) \cdot \Delta(t-t_1) \tag{10A.3}$$

where

$\Delta(t-t_1)$ = the unit step function

= 1 for $t \geq t_1$

= 0 for $t < t_1$

The pressure increment can also be written in t' domain instead of t domain:

$$dP_f(t'_1) \cdot \Delta(t'-t'_1) \tag{10A.4}$$

where $t' = t-t_o$ and t_o is the time of installation of the lining. Any infinitesimal step function of lining pressure (Eq. 10A.4) can be expressed by the following form:

$$\frac{dp_f(t'_1)}{dt'_1} dt'_1 \cdot \Delta(t'-t'_1) \tag{10A.5}$$

In the following sections, the radial displacement of the rock due to the time-dependent lining pressure is derived, followed by the derivation for the radial displacement for the liner.

(a) **Radial Displacement of the Rock**

According to Eq. 10.6, the radial deformation of the rock at the interface due to

$$\frac{dP_L(t'_1)}{dt'_1} dt'_1 \cdot \Delta(t'-t'_1) \text{ increment of lining pressure is}$$

$$\Delta u_{RlA}(R_2, t) = \left[\frac{dP_L(t'_1)}{dt'_1} dt'_1 \cdot \Delta(t'-t'_1)\right] \frac{(1+v_R)R_2}{E_R} J_R(t-t_1) \tag{10A.6}$$

or

$$\Delta u_{RlA}(R_2, t') = \left[\frac{dP_L(t'_1)}{dt'_1} dt'_1 \cdot \Delta(t'-t'_1)\right] \frac{(1+v_R)R_2}{E_R} J_R(t'-t'_1) \tag{10A.7}$$

The total deformation of the rock from time of installation of lining (t_o) to the arbitrary time (t) or (t') may be obtained by integrating Eq. 10A.7 from t_o to t or form 0 to t'. Therefore,

$$u_{RlA}(R_2, t') = \frac{(1+v_R)R_2}{E_R} \int_0^{t'} \frac{dP_L(t'_1)}{dt'_1} dt'_1 J_R(t'-t'_1) \tag{10A.8}$$

After arrangement,

$$u_{RlA}(R_2, t') = \frac{(1+v_R)R_2}{E_R} \int_0^{t'} \frac{dP_L(t'_1)}{dt'_1} J_R(t'-t'_1) dt'_1 \tag{10A.9}$$

The integral in Eq. 10A.9 is called a hereditary integral (Flügge 1975) and it may be evaluated through integration by parts as follows. First let

$$I = \int_0^{t'} \frac{dP_L(t'_1)}{dt'_1} J_R(t'-t'_1) dt'_1 \tag{10A.10}$$

Through integration by parts, I can be expressed as

$$I = \left| J_R(t'-t'_1) P_f(t'_1) \right|_o^{t'} - \int_0^{t'} P_f(t'_1) \frac{dJ_R(t'-t'_1)}{dt'_1} dt'_1 \tag{10A.11}$$

Knowing that $d(t'-t'_1) = -dt'_1$, Eq. 10A.11 can take the following form:

$$I = \left| J_R(t'-t'_1) P_f(t'_1) \right|_o^{t'} + \int_0^{t'} P_f(t'_1) \frac{dJ_R(t'-t'_1)}{d(t'-t'_1)} dt'_1 \tag{10A.12}$$

Since

$$J_R(t'-t'_1) = 1 + \phi_{R1}\left(1-e^{-\lambda_{R1}(t'-t'_1)}\right) + \phi_{R2}\left(1-e^{-\lambda_{R2}(t'-t'_1)}\right) + \phi_{R3}\left(1-e^{-\lambda_{R3}(t'-t'_1)}\right) \tag{10A.13}$$

the differentiation of $J_R(t'-t'_1)$ with respect to $(t'-t'_1)$ is

$$\frac{dJ_R(t'-t'_1)}{d(t'-t'_1)} = \phi_{R1}\lambda_{R1}e^{-\lambda_{R1}(t'-t'_1)} + \phi_{R2}\lambda_{R2}e^{-\lambda_{R2}(t'-t'_1)} + \phi_{R3}\lambda_{R3}e^{-\lambda_{R3}(t'-t'_1)} \tag{10A.14}$$

Substituting for $P_f(t'_1)$ (Eq. 10A.2) and $\dfrac{dJ_R(t'-t'_1)}{d(t'-t'_1)}$ (Eq. 10A.14) into Eq. 10A.12, the

integral I can be expressed as

$$I = I_1 + I_2 \tag{10A.15}$$

where

$$I_1 = \left| J_R(t'-t'_1) P_f(t'_1) \right|_0^{t'} \tag{10A.16a}$$

$$= \left| \left[1 + \phi_{R1}\left(1-e^{-\lambda_{R1}(t'-t'_1)}\right) + \phi_{R2}\left(1-e^{-\lambda_{R2}(t'-t'_1)}\right) + \phi_{R3}\left(1-e^{-\lambda_{R3}(t'-t'_1)}\right) \right] \cdot P_{om}\left(1-e^{-\alpha t'_1}\right) \right|_0^{t'} \tag{10A.16b}$$

$$= P_{om}\left(1 - e^{-\alpha t'}\right) \tag{10A.16c}$$

and

$$I_2 = \int_0^{t'} P_f(t'_1) \frac{dJ_R(t'-t'_1)}{d(t'-t'_1)} dt'_1 \tag{10A.17}$$

$$= P_{om}\int_0^{t'} \left(1 - e^{-\alpha t'_1}\right)\left[\phi_{R1}\lambda_{R1}e^{-\lambda_{R1}(t'-t'_1)} + \phi_{R2}\lambda_{R2}e^{-\lambda_{R2}(t'-t'_1)} + \phi_{R3}\lambda_{R3}e^{-\lambda_{R3}(t'-t'_1)}\right] dt'_1$$

$$= \sum_{i=3}^{6} I_i$$

$$I_3 = P_{om}\int_0^{t'}\left[\phi_{R1}\lambda_{R1}e^{-\lambda_{R1}(t'-t'_1)} + \phi_{R2}\lambda_{R2}e^{-\lambda_{R2}(t'-t'_1)} + \phi_{R3}\lambda_{R3}e^{-\lambda_{R3}(t'-t'_1)}\right] dt'_1 \tag{10A.18a}$$

$$= P_{om}\left[\phi_{R1}\left(1 - e^{-\lambda_{R1}t'}\right) + \phi_{R2}\left(1 - e^{-\lambda_{R2}t'}\right) + \phi_{R3}\left(1 - e^{-\lambda_{R3}t'}\right)\right] \tag{10.18b}$$

$$I_4 = -P_{om}\int_0^{t'}\phi_{R1}\lambda_{R1}e^{-\lambda_{R1}t'} e^{-(\alpha-\lambda_{R1})t'_1} dt'_1 \tag{10A.19a}$$

$$= \frac{-P_{om}\phi_{R1}\lambda_{R1}e^{-\lambda_{R1}t'}}{\alpha - \lambda_{R1}}\left(1 - e^{-(\alpha-\lambda_{R1})t'}\right) \tag{10A.19b}$$

$$I_5 = -P_{om}\int_0^{t'}\phi_{R2}\lambda_{R2}e^{-\lambda_{R2}t'} e^{-(\alpha-\lambda_{R2})t'_1} dt'_1 \tag{10A.20a}$$

$$= \frac{-P_{om}\phi_{R2}\lambda_{R2}e^{-\lambda_{R2}t'}}{\alpha - \lambda_{R2}}\left(1 - e^{-(\alpha - \lambda_{R2})t'}\right)$$

(10A.20b)

$$I_6 = -P_{om}\int_0^t \phi_{R3}\lambda_{R3}e^{-\lambda_{R3}t'}e^{-(\alpha - \lambda_{R3})t_1}\,dt_1$$

(10A.21a)

$$= \frac{-P_{om}\phi_{R3}\lambda_{R3}e^{-\lambda_{R3}t'}}{\alpha - \lambda_{R3}}\left(1 - e^{-(\alpha - \lambda_{R3})t'}\right)$$

(10A.21b)

Substituting the values of the integrals (Eqs. 10A.16 through 10A.21) into Eq. 10A.15, the radial displacement of the rock at the interface due to the reactive lining pressure in the time interval of t_o to t' is

$$u_{Rlh}(R_2, t') = \frac{(1 + v_R)R_2}{E_R}P_{om}R_h(t')$$

(10A.22)

where

$$R_h(t') = \left(1 - e^{-\alpha t'}\right) - \frac{\phi_{R1}\lambda_{R1}e^{-\lambda_{R1}t'}}{\alpha - \lambda_{R1}}\left(1 - e^{-(\alpha - \lambda_{R1})t'}\right) - \frac{\phi_{R2}\lambda_{R2}e^{-\lambda_{R2}t'}}{\alpha - \lambda_{R2}}\left(1 - e^{-(\alpha - \lambda_{R2})t'}\right)$$

$$- \frac{\phi_{R3}\lambda_{R3}e^{-\lambda_{R3}t'}}{\alpha - \lambda_{R3}}\left(1 - e^{-(\alpha - \lambda_{R3})t'}\right) + \phi_{R1}\left(1 - e^{-\lambda_{R1}t'}\right) + \phi_{R2}\left(1 - e^{-\lambda_{R2}t'}\right) + \phi_{R3}\left(1 - e^{-\lambda_{R3}t'}\right)$$

(10A.23)

At infinity, $R_h(\infty) = 1 + \phi_{R1} + \phi_{R2} + \phi_{R3}$

(b) Radial Displacement of the Lining

Since the reactive lining pressure at the interface is a monotonically increasing function of time (Eq. 10A.2, and Figure 10A.1), the radial displacement of the liner will

be obtained using the hereditary integral as used for the determination of rock displacement in (a) above. The radial deformation of the lining at the interface due to

$\frac{dP_l(t'_1)}{dt'_1} dt'_1 \cdot \Delta(t'-t'_1)$ increment of lining pressure is

$$\Delta u_{lh}(R_2, t) = \left[\frac{dP_l(t'_1)}{dt'_1} dt'_1 \cdot \Delta(t'-t'_1)\right] \frac{C_2(1+v_l)R_2}{E_l} J_l(t-t_1) \qquad (10A.24)$$

or

$$\Delta u_{lh}(R_2, t') = \left[\frac{dP_l(t'_1)}{dt'_1} dt'_1 \cdot \Delta(t'-t'_1)\right] \frac{C_2(1+v_l)R_2}{E_l} J_l(t'-t'_1) \qquad (10A.25)$$

The total deformation of the lining from time of installation of lining (t_o) to the arbitrary time (t) or (t') may be obtained by integrating Eq. 10A.25 from t_o to t or form 0 to t'. Therefore,

$$u_{lh}(R_2, t') = \frac{C_2(1+v_l)R_2}{E_l} \int_0^{t'} \frac{dP_l(t'_1)}{dt'_1} dt'_1 J_l(t'-t'_1) \qquad (10A.26)$$

After arrangement,

$$u_{lh}(R_2, t') = \frac{C_2(1+v_l)R_2}{E_l} \int_0^{t'} \frac{dP_l(t'_1)}{dt'_1} J_l(t'-t'_1) dt'_1 \qquad (10A.27)$$

Now let

$$II = \int_0^{t'} \frac{dP_f(t'_1)}{dt'_1} J_f(t'-t'_1) \, dt'_1 \qquad (10A.28)$$

Through integration by parts, II can be expressed as

$$II = \left| J_f(t'-t'_1) P_f(t'_1) \right|_o^{t'} - \int_0^{t'} P_f(t'_1) \frac{dJ_f(t'-t'_1)}{dt'_1} \, dt'_1 \qquad (10A.29)$$

Knowing that $d(t'-t'_1) = -dt'_1$, Eq. 10A.29 can take the following form:

$$II = \left| J_f(t'-t'_1) P_f(t'_1) \right|_o^{t'} + \int_0^{t'} P_f(t'_1) \frac{dJ_f(t'-t'_1)}{d(t'-t'_1)} \, dt'_1 \qquad (10A.30)$$

Since

$$J_f(t'-t'_1) = 1 + \phi_l\left(1 - e^{-\lambda_l(t'-t'_1)}\right) \qquad (10A.31)$$

the differentiation of $J_f(t'-t'_1)$ with respect to $(t'-t'_1)$ is

$$\frac{dJ_f(t'-t'_1)}{d(t'-t'_1)} = \phi_l \lambda_l e^{-\lambda_l(t'-t'_1)} \qquad (10A.32)$$

Substituting for $P_f(t'_1)$ (Eq. 10A.2) and $\dfrac{dJ_f(t'-t'_1)}{d(t'-t'_1)}$ (Eq. 10A.31) into Eq. 10A.30, the integral II can be expressed as

$$II = II_1 + II_2 \qquad (10A.33)$$

where

$$II_1 = \left| J_l(t' - t'_1) P_l(t'_1) \right|_0^{t'}$$

$$= \left| \left[1 + \phi_l(1 - e^{-\lambda_l(t' - t'_1)}) \right] \cdot P_{om}(1 - e^{-\alpha t'_1}) \right|_0^{t'}$$

$$= P_{om}(1 - e^{-\alpha t'}) \tag{10A.34}$$

and

$$II_2 = \int_0^{t'} P_l(t'_1) \frac{dJ_l(t' - t'_1)}{d(t' - t'_1)} dt'_1 \tag{10A.35}$$

$$= P_{om} \int_0^{t'} (1 - e^{-\alpha t'_1}) \phi_l \lambda_l e^{-\lambda_l(t' - t'_1)} dt'_1$$

$$= II_3 + II_4$$

$$II_3 = P_{om} \int_0^{t'} \phi_l \lambda_l e^{-\lambda_l(t' - t'_1)} dt'_1$$

$$= P_{om} \phi_l (1 - e^{-\lambda_l t'}) \tag{10A.36}$$

$$II_4 = -P_{om} \int_0^{t'} \phi_l \lambda_l e^{-\lambda_l t'} e^{-(\alpha - \lambda_l)t'_1} dt'_1$$

$$= \frac{-P_{om} \phi_l \lambda_l e^{-\lambda_l t'}}{\alpha - \lambda_l} (1 - e^{-(\alpha - \lambda_l)t'}) \tag{10A.37}$$

Substituting the values of the integrals (Eqs. 10A.34 through 10A.37) into Eq. 10A.27, the radial displacement of the lining at the interface due to the reactive lining pressure

in the time interval of t_o to t' is

$$u_{th}(R_2, t') = \frac{C_2(1+v_l)R_2}{E_l} P_{om} L_h(t') \qquad (10A.38)$$

where

$$L_h(t') = (1-e^{-\alpha t'}) - \frac{\phi_l e^{-\lambda_l t'}}{\alpha - \lambda_l}(1-e^{-(\alpha-\lambda_l)t'}) + \phi_l(1-e^{-\lambda_l t'}) \qquad (10A.39)$$

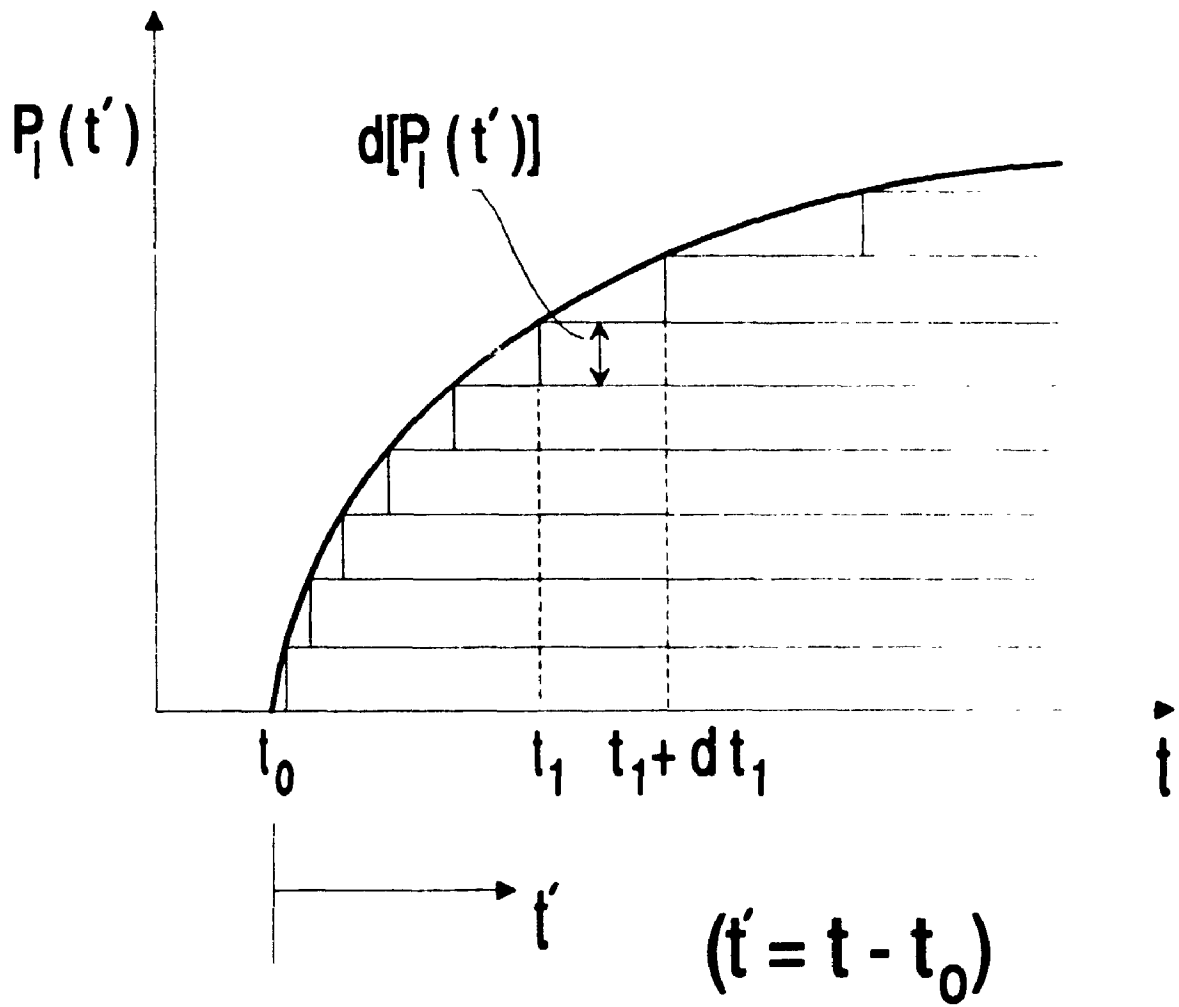At infinity, $L_h(\infty) = 1 + \phi_l$

Figure 10A.1 Time-dependent lining pressure and the derivation of the hereditary integral

REFERENCES

Balasubramonian, B.I. 1972. Swelling of compaction shale. Ph.D. Thesis, University of Alberta, Edmonton.

Beer, F.P., and Johnston, E.R. 1987. Mechanics of materials. McGraw-Hill, NY.

Berk, A., and Grob, H. 1972. Swelling pressure illustrated with the example of the Belchen Tunnel. International Symposium of Underground Openings, Lucernc, pp. 99-119.

Bjarnason, B., Ljunggren, C., and Stephansson, O. 1989. New developments In hydrofracturing stress measurements at Lulea University of Technology. Int. J. Rock Mech. Min. Sci & Gsomech. Abstr. Vol. 26, No. 6, pp. 579-586.

Bredehoeft, J.D., Wolff, R.G., Keys, W.S., and Shuter, E. 1976. Hydraulic fracturing to determine the regional *in situ* stress field, Piceance Basin, Colorado. Gcol. Soc. Am. Bull. 87, pp. 250-258.

Cornet, F.H., and Valette, B. 1984. *In situ* stress determination from hydraulic injection test data. Journal of Geophysical Research, Vol. 89, No. B13, pp. 11527-11537.

Curtis, D.J. 1974 Viscoelastic tunnel analysis. Tunnels and Tunnelling, Nov., pp. 38-39.

Curtis, D.J. 1976. Discussions on circular tunnels in elastic ground. Geotechnique, 26(1), pp. 231-237.

Einstein, H.H., and Bischoff, N. 1975. Design of tunnels in swelling rocks. 16th Symposium on Rock Mechanics, University of Minnesota, Minneapolis, MN, pp. 185-195.

Flügge, W. 1975. Viscoelasticity. Springer-Velag, NY.

Gill, D.E., and Dube, B.P. 1974. Influence des conditions d'Adherence a l'Interface sur les Poussees des Revetements de Souterrains. Proceedings of the 3rd International Congress on Rock Mechanics, Denver, Vol. II-B, pp. 1136-1140.

Gill, D.E., Coates, D.F., and Geldart, L.P. 1970. A mathematical model of a lined circular tunnel driven in a linear viscoelastic medium. Proceedings, 2nd Congress on Rock Mechanics, Belgrade, pp. 625-632.

Goodman, R.E. 1980. Introduction for rock mechanics. John Wiley, NY.

Green, A.E., and Taylor, G.I. 1939. Stress systems in aelotropic plates I, Proc. Roy. Soc., 173, pp. 162-172.

Green, A.E., and Taylor, G.I. 1945. Stress systems in aelotropic plates III, Proc. Roy. Soc., 184, pp. 181-195.

Green, A.E., and Zerna, W. 1968. Theoretical elasticity. Oxford University Press.

Hearmon, R.F.S. 1961. An introduction to applied elasticity. Oxford University Press.

Haimson, B.C. 1978a. The hydrofracturing stress measuring method and recent field results. Int. J. Rock Mech. Min Sci. & Geomech. Abstr. Vol. 15, pp 167-178.

Haimson, B.C. 1978b. Underground nuclear power station study. Hydrofracturing stress measurements. Hole UN-1 Darlington G.S. Report No. 78250. Prepared for geotechnical Engineering Department, Ontario Hydro.

Haimson, B.C. 1985. SAB-NIAGARA GS NO. 3. Hydrofracturing stress measurements and permeability tests in Holes NF-3 and NF4. Report No. 85357. Geotechnical and Hydraulic Engineering Dept.

Haimson, B.C. 1992. Hydraulic fracturing measurements in New York city reaffirm the uniformity of the stress regime in Northeastern United States. Rock Mechanics, Proceedings of the 33rd symposium. Edited by J.R. Tillerson and W.R. Wawersik. Balkema, Rotterdam.

Haimson, B.C and Fairhurst, C. 1969. In-situ stress determination at great depth by means of hydraulic fracturing. In Proc. 11th U.S. Symposium on Rock Mechanics, pp. 559-584.

Haimson, B.C. and Lee, C.F. 1980. Hydrofracturing stress determinations at Darlington, Ontario. 13th Canadian Rock Mechanics Symposium (The H.R. Rice Memorial Symposium), pp.42-50.

Haimson, B.C., Tunbridge, L.W., Lee, M.Y. and Cooling, C.M. 1989. Measuremert of rock stress using the hydraulic fracturing method in Cornwall, U.K. - Part II. Data reduction and stress calculation. Int. J. Rock Mech. Min. Sci. & Geomech. Abstr. Vol. 26, No. 5, pp. 361-372.

Hefny, A.M., and Lo, K.Y. 1992a. The interpretation of horizontal and mixed-mode fractures in hydraulic fracturing tests in rocks. Canadian Geotechnical Journal, Vol. 29, pp. 902-917.

Hefny, A.M., and Lo, K.Y. 1992b. Stresses and Displacements around an unlined tunnel driven in cross-anisotropic rocks. Proceedings of 10th Canadian tunnelling Conference, Banf, Alberta, pp. 115-133.

Hoek, E., and Brown, E.T. 1980. Empirical strength criterion for rock stress determination. ASCE Journal of the Geotechnical Engineering Division, vol. 106(GT9), pp. 1013-1035

Huang, J. 1992. Long-term deformation behaviour of Queenston Shale. M.E.Sc. Thesis, University of Western Ontario, London, Ontario.

Huang, S.L., Anghenbaugh, N.B. and Rockawass, J.D. 1986. Swelling pressure studies of shales. Int. J. Rock Mech. Min. Sci., 23, No. 5, pp. 371-377.

Hubbert, M.K., and Willis, D.G. 1957. Mechanics of hydraulic fracturing. Trans. AIME 210, pp. 153-168

Jaeger, J.C., and Cook, N.G.W. 1976. Fundamentals of rock mechanics. John Wiley, NY.

Kim, K., and Franklin, J.A. 1987. International Society for Rock Mechanics. Commission on testing Methods. Suggested methods for rock stress determination. Int. J. Rock Mech. Min. Sci. & Geomech. Abstr. Vol. 24, No. 1, pp. 53-73.

Kirsch, G 1898. Die theorie der elastizität und die bedurfnisse der festigkeitslehre. Veit. Ver. Deut. Ing. 42, 797-807.

Lee, Y.N. 1988. Stress-strain-time relationship of Queenston Shale. Ph.D. Thesis, The University of Western Ontario, London, Ontario.

Lee, Y.N. and Lo, K.Y. 1993. The swelling mechanism of Queenston Shale. Canadian Tunnelling Journal, pp. 75-97.

Leeman, E.R. and Hayes, D.J. 1966. A technique for determining The Complete state of stress in rock using a single borehole. Proceedings of the first congress (ISRM), Lisbon, Vol. 2, pp 17-24.

Lindner, E. 1976. Swelling rock: a review. Proc. ASCE Specialty Conference on Rock Engineering for Foundations and Slopes, Colorado, U.S.A., vol. 1, pp. 141-181.

Ljunggren, C. and Amadei, B. 1989. Estimation of virgin rock stress from horizontal hydrofractures. Int. J. Rock Mech. Min. Sci. & Geomech. Abstr. Vol. 26, pp. 69-78.

Ljunggren, C., Amadei, B., and Stephansson, O. 1988. Use of the Hoek and Brown failure criterion to determine *in situ* stresses from hydraulic fracturing measurements. Proc. Conf. on Applied Rock Engineering (CARE'88), Newcastle-Upon-Tyne, PP. 133-142.

Lo, K.Y. 1978. Uniaxial compression, thermal expansion and free-swell tests on rock specimens, Darlington Generating Station, Phase I, GEOT-5-78, Report to Ontario Hydro.

Lo, K.Y. 1981. Ontario Hydro. Darlington Generating Station 'A' rock stress measurements and evaluations. Evaluation of rock squeeze problem. Ontario Hydro Report 81192.

Lo, K.Y. 1986. Recent advances in design and evaluation of performance of underground structures in rocks. Keynote address, the 6th Canadian Tunnelling Conference, Niagara Falls, Ont., pp. 5-46. (Reprinted with permission, Tunnelling and Underground Space Technology, Vol. 4, No. 2, pp. 171-183.)

Lo, K.Y. 1989. Results of laboratory tests on rockcores from Boreholes SD2 and SD3, SABNGS No. 3. Report to Ontario Hydro.

Lo, K.Y., and Hefny, A. 1993. The evaluation of in situ stresses by hydraulic fracturing tests in Anisotropic rocks with mixed-mode fractures. Canadian Tunnelling Journal, pp. 59-73.

Lo, K.Y., and Hori, M. 1979. Deformation and strength properties of some rocks in Southern Ontario. Canadian Geotechnical Journal, Vol. 16, pp. 108-120.

Lo, K.Y., and Lee, Y.N. 1990. Time-dependent deformation behaviour of Queenston Shale. Canadian Geotechnical Journal, Vol. 27, pp. 461-471.

Lo, K.Y. and Lukajic, B. 1984. Predicted and measured stresses and displacements around the Darlington Intake Tunnel. Canadian Geotechnical Journal, Vol.21, No. 1, pp. 147-165.

Lo, K.Y., and Morton, J.D. 1976. Tunnels in bedded rock with high horizontal stresses. Canadian geotechnical Journal, Vol. 13, pp. 216-230.

Lo, K.Y., and Yuen, M.K. 1981. Design of tunnel lining in rock for long term time effects. Canadian Geotechnical Journal, Vol. 18, No. 1, pp. 24-39.

Lo, K.Y., Wai, R.S.C., Palmer, J.H.L., and Quigley, R.M. 1978. Time-dependent deformation of shaly rock in southern ontario. Canadian Geotechnical Journal, Vol. 15, No. 4, pp. 537-547.

Lo, K.Y., Lukajic, B., Yuen, C.M.K., and Hori, M. 1979. In situ stress measurement in rock overhang at the Ontario Power Generating Station, Niagara Falls. Proceedings, 4th International Congress on Rock Mechanics, Montreux, Switzerland.

Martin, C.D. 1990. Characterizing *in situ* stress domains at the AECL underground research laboratory. Canadian Geotechnical Journal, Vol. 27, pp. 631-646.

Mindlin, R.D. 1939. Stress distribution around a tunnel. Proceedings of the American society of Civil Engineers, April, pp. 619-642.

Mindlin, R.D. 1948. Stress distribution around a hole near the edge of a plate under tension. Proceedings of Society of Experimental Stress Analysis, pp. 56-68.

Mitchell, J.K. 1973. Influence of mineralogy and pore solution chemistry on the swelling and stability of clays. Proceedings of 3rd International Conference on Expansive Soils, vol. II, Haifa, Israel, pp.11-25.

Mitchell, J.K. 1976. Fundamentals of soil behaviour. John Wiley, NY.

Obert, L., and Duvall, W.I. 1967. Rock mechanics and the design of structures in rock. John Wiley, NY.

Poulos, H.G., and Davis, E.H. 1974. Elastic solutions for soils and rock mechanics. John Wiley, NY.

Rigbey, S.J., Powell, D.B., and Solymar, Z.V. 1992. Design of Underground Powerhouse Complex Niagara River Hydroelectric Development. Proceedings of the 45th Canadian Geotechnical Conference, Toronto, Ontario, pp.102A-1-102A-10.

Sakurai, S. 1974. Determination of initial stresses and mechanical properties of viscoelastic underground medium. Proceedings of the 3rd International Congress on Rock Mechanics, Denver. Vol. II-B, pp. 1169-1174.

Semec, B.P., Huang, J.H.S., and Lee, C.F. 1986. Some geotechnical considerations in the design of twin tunnels for SABNG No. 3, Niagara Falls, Ontario. Proceedings of 6th Canadian Tunnelling Conference, Niagara Falls, Ontario, pp. 93-133.

Schmitt, D.R. and Zoback, M.D. 1989. Pore elastic effects in the determination of the maximum horizontal principal stress in hydraulic fracturing tests-A proposed breakdown equation employing a modified effective stress relation for tensile failure. Int. J. Rock Mech. Min. Sci. & Geomech. Abstr. Vol. 26, No.6, pp. 499-506.

Timoshenko, S.P., and Goodier, J.N. 1970. Theory of elasticity, 3rd ed., McGraw-Hill, NY.

Trow, W.A., and Lo, K.Y. 1989. Horizontal displacements induced by rock excavation: Scotia Plaza, Toronto. Canadian Geotechnical Journal, Vol. 26, pp. 114-121.

Wai, R.S.C. 1977. Time-dependent deformation of some shaly rocks. M.E.Sc. Thesis, University of Western Ontario, London, Canada.

Wittke, W., and Pierau, B. 1979. fundamentals for the design and construction of tunnels in swelling rock. Proceedings of the 4th International Congress on Rock Mechanics, Montreux, Bol. 2, pp. 719-729.

Yong, R.N., and Warkentin, B.P. 1975. Soil properties and behaviour. Elsevier, Amsterdam.

Yuen, C.M.K. (1979): Rock-structure-time interaction in lined circular tunnels in high horizontal stress field. Ph.D. thesis, Faculty of Engineering Science, University of Western Ontario. London, Ontario, 720 p.